Development of a Complete Optical Microsystem for Particle Flow Detection

Ivan Bernat Ubiaga

ADVERTIMENT. La consulta d'aquesta tesi queda condicionada a l'acceptació de les següents condicions d'ús: La difusió d'aquesta tesi per mitjà del servei TDX (**www.tdx.cat**) i a través del Dipòsit Digital de la UB (**diposit.ub.edu**) ha estat autoritzada pels titulars dels drets de propietat intel·lectual únicament per a usos privats emmarcats en activitats d'investigació i docència. No s'autoritza la seva reproducció amb finalitats de lucre ni la seva difusió i posada a disposició des d'un lloc aliè al servei TDX ni al Dipòsit Digital de la UB. No s'autoritza la presentació del seu contingut en una finestra o marc aliè a TDX o al Dipòsit Digital de la UB (framing). Aquesta reserva de drets afecta tant al resum de presentació de la tesi com als seus continguts. En la utilització o cita de parts de la tesi és obligat indicar el nom de la persona autora.

ADVERTENCIA. La consulta de esta tesis queda condicionada a la aceptación de las siguientes condiciones de uso: La difusión de esta tesis por medio del servicio TDR (**www.tdx.cat**) y a través del Repositorio Digital de la UB (**diposit.ub.edu**) ha sido autorizada por los titulares de los derechos de propiedad intelectual únicamente para usos privados enmarcados en actividades de investigación y docencia. No se autoriza su reproducción con finalidades de lucro ni su difusión y puesta a disposición desde un sitio ajeno al servicio TDR o al Repositorio Digital de la UB. No se autoriza la presentación de su contenido en una ventana o marco ajeno a TDR o al Repositorio Digital de la UB (framing). Esta reserva de derechos afecta tanto al resumen de presentación de la tesis como a sus contenidos. En la utilización o cita de partes de la tesis es obligado indicar el nombre de la persona autora.

WARNING. On having consulted this thesis you're accepting the following use conditions: Spreading this thesis by the TDX (**www.tdx.cat**) service and by the UB Digital Repository (**diposit.ub.edu**) has been authorized by the titular of the intellectual property rights only for private uses placed in investigation and teaching activities. Reproduction with lucrative aims is not authorized nor its spreading and availability from a site foreign to the TDX service or to the UB Digital Repository. Introducing its content in a window or frame foreign to the TDX service or to the UB Digital Repository is not authorized (framing). Those rights affect to the presentation summary of the thesis as well as to its contents. In the using or citation of parts of the thesis it's obliged to indicate the name of the author.

Universitat de Barcelona

Tesi doctoral

Development of a Complete Optical Microsystem for Particle Flow Detection

Memòria presentada per

Ivan Bernat Ubiaga

per optar al grau de **doctor en Enginyeria i Tecnologia Avançades**

Departament d'Electrònica

Universitat de Barcelona

Programa de doctorat d'Enginyeria i Tecnologia Avançades

Tesi doctoral dirigida i tutelada per: **Dr. Mauricio Moreno Sereno**

Barcelona, 2013

Departament d' Electrònica

Universitat de Barcelona

Dedicada a mi pequeño rayo de luz.

Gracias por estar ahí,

iluminando mi camino en

los momentos más oscuros.

ACKNOWLEDGMENTS

As a child, I was always attracted to science. I remember myself trying to understand and experiment the most diverse gadgets you can imagine. Every time something new arrived home, I was there, expectant, waiting for it to work. And when it reached the end of its useful life, I was there again, ready to open it, to examine every little circuit, every little mechanical resort with the aim of discovering every little secret.

Now I can compare this thesis with that childish behaviour. I felt attracted not only to the idea of becoming a PhD (Philosophiae Doctor...it sounds great), but also to the chance of doing some research in the electronics field with the spot on point of care testing applications.

During these years of work in the Electronics Department of the Faculty of Physics, at the University of Barcelona, I have had not only the opportunity of developing my technical knowledge in the fields of microelectronic design and optoelectronics for biosensing applications, but also, I have met a lot people who have helped me through this experience. I want to give a thousand thanks to these people, who have become my closest colleagues, especially my partners at the lab 224; and of course I declare my gratitude to the director of my thesis, Dr. Mauricio Moreno, and to the codirector (at least at the beginning), Angel Dieguez.

Thanks to the important persons in my life: my parents and my brother. Mum, I love you so much; you are such an inspiring person and good guide…
Mama (o como te llamamos en casa…Puri), Alex, gracias por estar ahí. Finalmente ya está hecho.
Thanks to my best friend Marc. Marc….te lo puedes creer?

Thanks to all the people of the Electronics Department.
Mauricio, sin ti no lo habría conseguido. Muchas gracias de todo corazón.
Thanks to the staff of the IBM-CNM-CSIC, and in particular to Luis Fonseca for his inestimable assistance.

If I just forget to mention somebody, please accept my most sincere apologies. I have not done it on purpose, and I can assure you that I am really grateful too.

I must admit that these years have been truly the best of my career at the university. I have made good friends, I have known a lot of interesting people, I have worked with incredible scientists...what else could I say?

Thank you!

List of Contents

1 Introduction

2 Conception of the system

3 Optical design

4 Hybrid integration

5 Microfluidics

6 CMOS photodetector array

LIST OF CONTRIBUTIONS

Proceedings:

Towards miniaturization of an optical microbead Flow counter
I. Bernat, K. Loreto, J. Jaramillo, P. Rodriguez-Franco, L. Fonseca, M. Moreno
Poster, EUROPTRODE XII
Barcelona, Spain, April 2012

Particle Detection Microoptical System Based on Hybrid Integration and Silicon Micromachining
I. Bernat, M. Moreno, L. Fonseca
Paper, Congreso: SMART SYSTEMS INTEGRATION 2012
Zürich, Switzerland, March 2012

Design and test of a digital system based on a CMOS 0.350m logarithmic pixel for pulsed laser optical detection
Bernat, I.; Padilla, M.; Moreno, M.; Dieguez, A.; Samitier, J.
Paper, ICECS 2007
Marrakech, December 2007

Design and Test of a Digital System Based on a CMOS 0.35µm Logarithmic Pixel for Time of Flight Measurement Applications
Bernat, I.; Padilla, M.; Moreno, M.; Dieguez, A.; Samitier, J.
Poster, ASICON 2007
Guilin, China, October 2007

Design and test of a CMOS 0.352m pixel with binary output for optical pulsed laser detection
Bernat, I.; Padilla, M.; Moreno, M.; Dieguez, A.; Herms, A.; Samitier, J.
Paper, DCIS 2007
Sevilla, Spain, November 2007

Double Array of 256 photodetectors in 0.35µ CMOS technology with AD Conversion and Derivative output
Bernat, I.; Arbat, A.; Darwish, N.; Moreno, M.; Dieguez, A.; Herms, A.
Paper, DCIS 2006
Barcelona, Spain, November 2006

Binary Pixel for Time Flight Measurement Applications
Bernat, I.; Padilla, M.; Moreno, M.; Dieguez, A.; Samitier, J.
Paper, ODIMAP V
Madrid,Spain, October 2006

Double Array of 256 Photodetectors in 0.35um CMOS technology with AD conversion for laser spot Detection
Bernat, I.; Arbat, A.; Moreno, M.; Dieguez, A.; Samitier, J.
Paper, ODIMAP V
Madrid, Spain, October 2006

A 256-pixels Photosensor CMOS Array for Biosensing Applications
I.Bernat, A.Arbat, N.Darwish, M.Moreno, A.Dieguez
Paper, DCIS 2005
Lisboa, Portugal, October 2005

Numerical study of grating-waveguides for biosensing Applications
N.Darwish, I. Bernat, M. Moreno, J. Samitier.
Paper, IEE Spanish Conference on Electron Devices
Tarragona, Spain, October 2005

CHAPTER I: INTRODUCTION

1.1 Preface

This thesis focuses on the design and fabrication of an Optical Microsystem for Particle Detection based on Hybrid Integration and Silicon Micromachining. Through the following chapters the detailed description of the design and fabrication processes for a functional device, as well as the achieved experimental results with the testing of particles in the range of 10 to 90µm diameter, will be discussed.

However, a previous task of documentation and research is necessary to settle down some useful and basic concepts related to the field we are about to venture in. Therefore, it is recommended to introduce and delimit the concept of particle in the scope of this work, as well as to present a description of the different particle characterization and detection techniques with the purpose of understanding the evolution of the instruments available at this moment.

1.2 Brief introduction to particle characterization and detection

During the last decades, there has been an increasing interest in particle characterization and detection, not only in the scientific and academic fields with the research and development of new methods and techniques, but also in industrial manufacture circles where quality control of materials and products has become fundamental. There are multiple examples of applications in which characterization and detection of particles plays an important role, some of them with direct impact in our everyday lives. Particle size, shape or surface characteristics can influence, for example, the efficacy of a pain-reliever, the efficiency of a catalytic converter, or the resolution of a printer.

In the process of conception of instruments with the ability of performing this kind of operations, several conventional particle characterization methods, such as sieve and sedimentation analysis, have gradually been replaced by non-invasive methods based on light-matter interaction [1], more according with the new standard design criterions: integration, miniaturization, portability, low-cost, facility of use, user-friendly management, low consumption, good performance and multifuncionality are only a few of them.

1.3 Definition of particle and characterization measurement

One possible definition of what is commonly understood by the term “particle” could be “a minute quantity or fragment”[1]. This general conception must be delimited in order to define the type of particles which we are interested in. From all the broadened spectrum of particle sizes, only those in the micrometric range are under our scope (e.g. some bacillus bacteria and paint pigments in the order of a few tens of microns).

Though many theoretical models tend to equal the shape of particles to perfect spheres, we must be aware of the existence of the great diversity of forms which particles can present: linear forms or

[1] Definition from Merriam-Webster's Collegiate Dictionary (10th Edition).

networks such as proteins or gels, ensembles of organic and inorganic molecules such as liposomes, simple spaces such as air bubbles, or just minute pieces of some materials such as metal, sugars or powders.

Again, industry influence is noticeable as the investment in instruments for characterization and detection of particulate systems increases, reaching sectors such as hybrid microelectronics, cleaning and cosmetics drugs or food and beverages, and covering a broad range of particle sizes, even in the submicron region (figure 1.1).

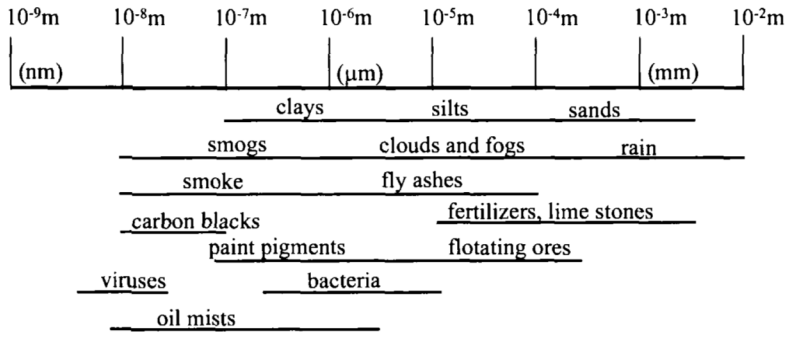

***Figure 1.1**: Range of dimensions for industrial particles, with some particular examples [1].*

Particles usually present themselves in the form of particulate systems, i.e. systems containing a large number of particles in a volume. Each one of these particles may have similar or different physical properties, contributing to the ensemble behavior macroscopically observed. Attending to their properties, particulate systems can be classified in monodisperse or polydisperse, whether the studied property is the same for all particles in the system or it presents different values for all or some particles in the system. Particulate systems also have large specific surface areas (surface area per unit mass) which means they are prone to interfacial phenomena interacting with the surrounding medium and neighboring particles.

The aim in a particle characterization measurement is to obtain information about the geometrical and physical properties of the individual particles present in a sample, such as size, shape, and surface structure. These properties are closely related to the fact that the material is in a particulate form. For other properties such as elemental composition, molecular structure or crystal structure of the particles in the sample, one should refer to particle analysis techniques. In this case, there is no difference whether the material is in a particulate or in bulk form.

During the last two decades, thanks to the development of commercial lasers and microelectronics, the science and technology of particle characterization has experienced important advances. From the initial methods which were constrained to the physical separation of a sample (e.g. sieve analysis) or the analysis of a limited number of particles (e.g. microscopic method), new particle characterization methods take advantage of modern technologies such as light-based systems.

The analytical methods used in particle characterization can be classified into ensemble and non-ensemble methods. Ensemble methods gather information from particles having different properties, in fast and non-intrusive measurements. After a modeling process of the measured signals, information can be retrieved. Laser diffraction and photon correlation spectroscopy are two examples of ensemble methods used in particle size determination.

On the other hand, non-ensemble methods collect information of particles with the same property. This kind of methods often involve time consuming and sample destruction, because of the need of a previous phase to separate or fraction the material (by size exclusion chromatography, for example); but they offer high resolution measurements, detecting or sensing only one particle at a time (with a one-to-one correspondence between the signal and the property of the particle) or a group of particles with the same property. Examples of methods to sense individual particles are optical particle counting and the Coulter Principle (electrical sensing zone method).

The topics described below, gather the basic principles and ideas about particle counting, sizing and characterization techniques. We report not only the most up-to-date methods, but also the traditional ones. Most of them (especially the ones related to light and optics) are non-intrusive methods, i.e. the measurement process does not alter the nature of the analyzed particle, which is especially interesting for the industry, where the material costs are always evaluated and tend to be reduced to minimum. Our classification departures from the distinction between “optical” and “non-optical” techniques for characterization and detection of particles.

1.4 Non-optical techniques for characterization and detection of particles

1.4.1 Classical techniques

1.4.1.1 Sieve analysis – Fractionation and sizing (Application range from 5µm to 10cm)

Basically, sieve analysis requires a test sieve with a screen containing many uniform openings to classify materials into different fractions: the fraction of material larger than the opening of the screen will be retained on the screen, and the fraction smaller will pass through. The openings are either gaps between the woven wires (wire-cloth sieve), perforated holes in a metal plate (punched-plate sieve), or photo-etched holes in a metal sheet (electroformed sieve). Several shapes are possible for these openings (figure 1.2, left).It is interesting to remark that a microfluidic sensor for $CD4^+$ lymphocyte counting [2] has been developed with an approach similar to sieving techniques, though at a different scale (figure 1.2, right).

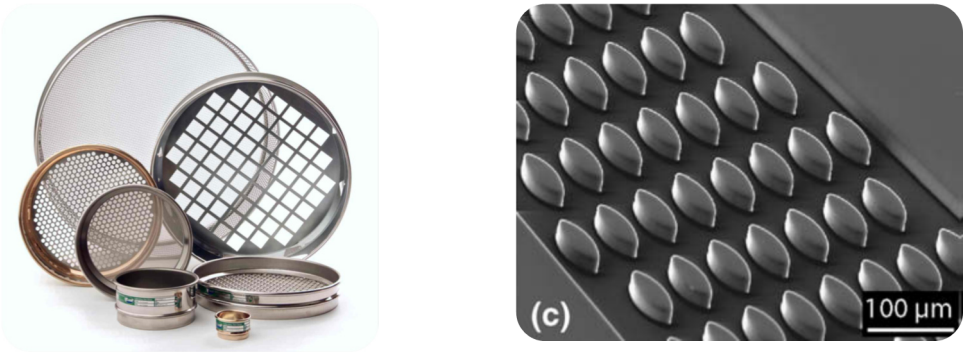

***Figure 1.2**. Left: Sieves of different sizes, shapes and materials. Printed with permission of “Labsupply” webpage. (http://www.labsupply.co.za/shakers%20and%20stirrers/TEST%20SIEVES.pdf). Right: PDMS sensor channel with elliptic-shaped micropillar structures* [2].

Despite its wide usage, sieve analysis presents several inherent drawbacks. Because of the different dimensional grade between the openings on the sieve (three-dimensional considering the round woven wires) and the fractionation process (a function of two dimensions only), two rods of the same

diameter but different lengths may succeed passing through the sieve, and yielding the same result. Besides, this technique presents a strong dependence on particle orientation, on the physical properties of particles, on the mechanics of shaking the sieve and on the time on the process.

1.4.1.2 Sedimentation methods – Sizing (Application range from 0.05µm to 100µm)

Sedimentation methods are based on the rate of settling of particles in a liquid. The settling process can be "natural" (liquid at rest under a gravitational field) or "forced" (under a centrifugal field). The Stokes equation relates the settling velocity and the particle size (d_{st} = Stokes diameter), at low Reynolds numbers. The Stokes diameter (d_{st}) is equal to the equivalent diameter of a spherical particle that has the same density and free-falling velocity as the real particle in the same liquid under laminar flow conditions. There is a distinction between homogenous and line-start sedimentation methods, depending on the position of the particles at the beginning of the measurement. For the first ones, particles are uniformly distributed, while for the second ones, particles are concentrated in a thin layer on top of the solid-free medium.

This technique presents some limitations. At low Reynolds numbers, non-spherical particles are randomly orientation, and consequently there is a wide range of settling velocities. For higher Reynolds numbers, particles orient themselves and settle at the slowest velocity. Samples must have a uniform and known density to avoid the same settling velocity for particles of different size. Additional measurements are necessary to determine the physical properties of particles.

1.4.2 The electrical sensing zone method (ESZ, the Coulter principle) – Particle counting and sizing (Application range from 0.4µm to 1400µm)

Instrumental methods for particle counting are dominated by counters based on electrical sensing zones (e.g. Coulter counter) or by counters based on optical particle detection (through light blockage or light scattering) due in part, to their good integration capacity and the easiness in operation. Both cover a similar range of sizes (≈ order of submicrons). The study of optical particles counters will be exposed in section 1.5.

Electrical sensing method is based on the Coulter principle and has been widely extended since the early 1950's, when it was first used for blood cells counting. Nowadays, a large number of automated counters incorporate this principle, for it can be applied to count and size any particle (of any material) that can be suspended in an electrolyte solution. *Coulter* and *Elzone* are the principal manufacturers. These devices are based on the effect induced in the electrical field applied to an electrolyte when a particle passes through this field. The change produced in the voltage is related to a change in the resistivity of the particle compared to the resistivity of the electrolyte.

The mechanics and instrumentation for a classical experiment is as follows. Particles to analyze must be prepared in an electrolyte solution, at low concentration, to reduce the probability of two particles being sensed at the same time (when passing through the electrodes at the same instant). A tube with an orifice or aperture is placed in that solution. With the help of two electrodes (placed as in figure 1.3), the aperture becomes a "*sensing zone*". These electrodes could also be located along the path of a fluidic channel, where the particles would be flowing. Electrical field is achieved by means of a constant current applied between electrodes. Particles flowing through the "*sensing zone*" produce short-term changes in the resistance across the aperture, because of the displacement of a volume of

the electrolyte solution equivalent to the volume of the particle. The resistance change is measured as a current pulse or voltage pulse. The amplitude of each pulse is proportionally related to the size of particles, and the number of pulses equals the number of particles measured (equation 1.1):

$$U = \frac{V\rho_0 if}{\pi^2 R^4} \tag{1.1}$$

Where U is the amplitude of the voltage pulse, V the particle volume, ρ_0 the electrolyte resistivity, i the aperture current, f the particle "*shape factor*", and R the aperture radius.

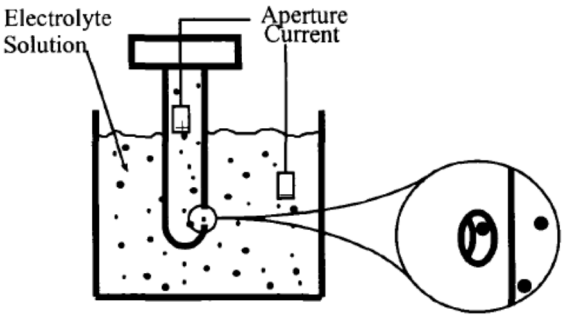

Figure 1.4. Schematic of the electrical sensing zone analyzer.

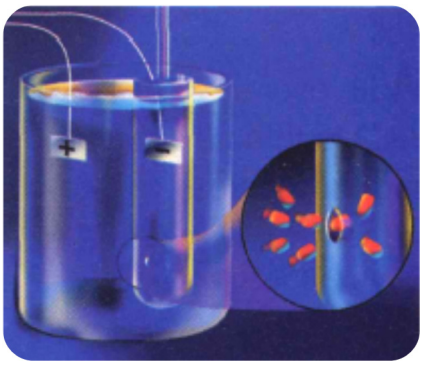

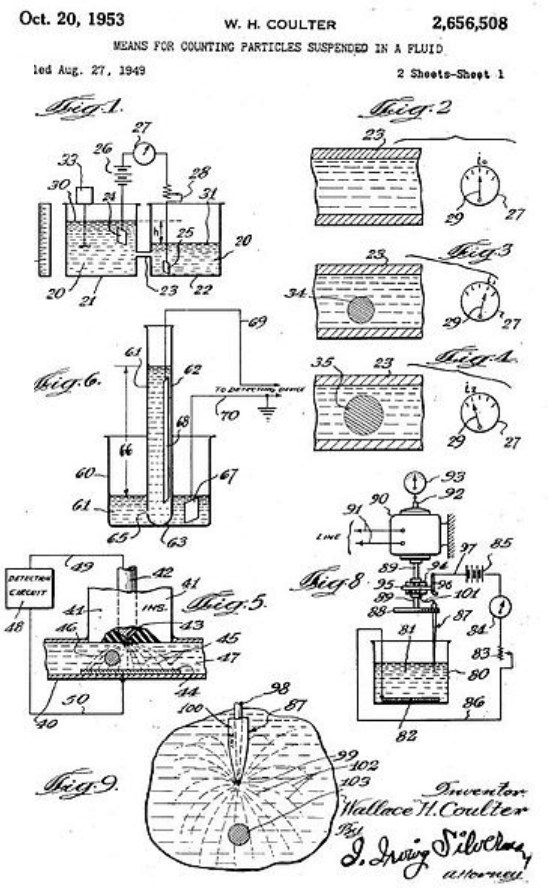

Figure 1.3. *Left: Schematic of the electrical sensing zone analyzer* [1]*. Right: Original Coulter Counter design. Image from US Patent #2,656,508, year 1953.*

Normally, these devices present one of these two typical implementations: the aperture format (already explained, previous figure 1.3) or the flow cell format, where particles flow through a channel with electrodes placed in a particular position.

In both implementations, the Coulter/Elzone counter presents the limitation of fixed aperture or fixed position of the electrodes in relation to the microfluidics channel width. This design restriction implies that only particles whose diameter is within a certain range can be sized; e.g., for the aperture format implementation, the range of sizes is 2%-60% of the nominal aperture diameter, which means apertures of 20µm for 0.4-12µm particles, 200µm for 4-120µm, and 2,000µm for 40-1200µm. Below 2%, particles tend to be confused with electronic noise, and particles much above 60%, tend to block the aperture. Discrimination of noise from the signal of interest, measured with Signal to Noise ratio (SNR) parameter, is quite important to define the lower size limit in Coulter counters. Different noise

sources must be considered (e.g. electronic noise generated by the aperture itself, environmental noise, etc…). Electronics post-processing helps to discriminate noise coupled into the signal, improving the SNR. In practice, apertures smaller than 15µm are not commonly used.

Among the main benefits of Coulter counters we find that their response is independent of shape for particles with the same volume and that fast measurements with high counting and sizing rates (up to 10.000 particles per second) can be performed with good accuracy (within 1-2%).

Commercial manufacturers have designed and fabricated devices based on Coulter principle (e.g. Scepter by Millipore figure 1.4), which demonstrates the high grade of establishment of these counters in the market and the level of miniaturization achieved. In the academic field, especial effort is being made in the development of micro-Coulter counters. In the example of figure 1.4, a hydrodynamic focusing mechanism was integrated in the microfluidic chip, to reduce the probability of wrong measurements, forcing the particles to flow singly aligned.

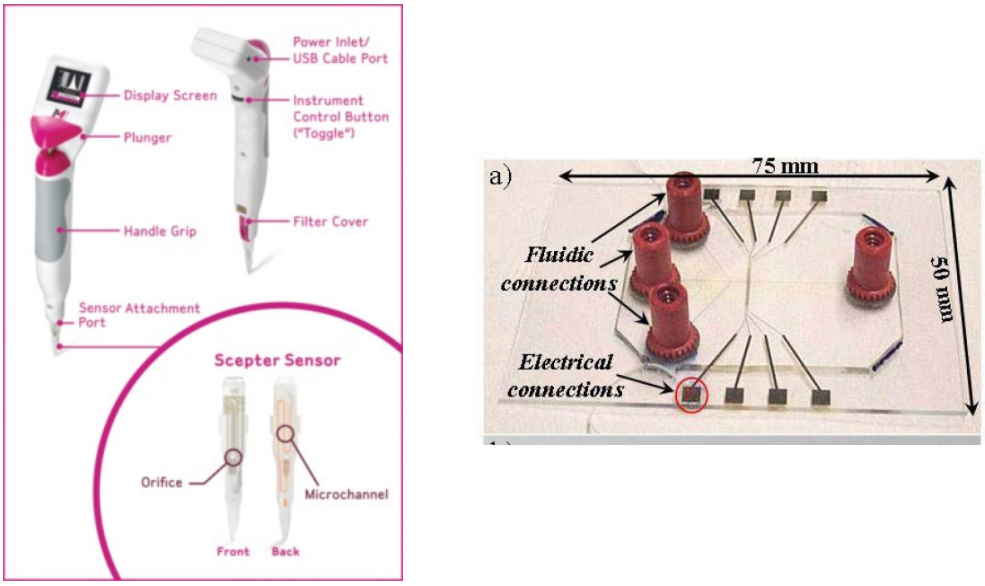

Figure 1.4. *Left: "Scepter" from "Millipore" company. Example of a handheld Coulter counter. Printed with permission of the company. Right: Flow cell format Coulter counter from the PhD thesis of R.Trujillo,"High speed microfluidic devices for particle counting on a chip", U.B. 2008.*

1.4.3 Other techniques

1.4.3.1 Chromatographic methods (Application range from 1nm to 500µm)

In all the techniques for particle characterization based in chromatographic methods, samples injected or placed at one location are moved by a carrier (typically a liquid) following a chromatographic path. Along the way, particles in the sample interact with the chromatographic barriers in different ways, according to certain properties (e.g. the size of the particle). In the process, particles are fractionated, and then detected. All chromatographic analyzers need calibrations for both retention time and concentration determination. The detectors used in particle characterization are usually based on light scattering or UV-vis sensors.

Different techniques are included on the generic subject "Chromatographic methods": Size Exclusion

Chromatography (ESC) or gel permeation chromatography (GPC) with a working range of particles from 0.001 to 0.5µm; Hydrodynamic Chromatography (HDC), either with non-porous bead-packed columns (0.03 to 2µm) or long capillary columns (0.02 to 50µm); Field Flow Fractionation: with a separation range from 0.001 to 500µm.

1.4.3.2 Acoustic analysis (Application range from 0.01µm to 1000µm)

Acoustic analysis is especially interesting to characterize particles present not in diluted suspensions, but in concentrated phase, thanks to the ability of sound waves to travel through concentrated suspensions. With ultrasonic analysis is possible to deal with concentrations up to 60% by volume [3], [4]. Two different methods are considered: Acoustic Spectroscopy (range from 0.01 to 1000µm), in which attenuation of sound waves is measured, since it is specific for a certain particle suspension; and Electroacoustic Spectral Analysis (range of 0.1 and 100µm diameter), which measures the magnitude and phase angle of the sound waves at multiple frequencies to obtain the particle dynamic mobility, and thus the zeta potential and size distribution of particles.

1.4.3.3 Less common techniques

Other techniques are less common or popular than the previous ones, for they are restricted to particular applications. We find for example, Mercury Porosimetry and Capillary Flow Porometry for Pore Size Determination, Streaming Potential Measurement for Zeta Potential Determination, Pulsed Field Gradient Nuclear Magnetic Resonance (PFG-NMR) for Diffusion Coefficient Determination or Dielectric Spectroscopy for Surface Characterization of Liquid-borne Colloids.

1.5 Optical techniques for characterization and detection of particles

1.5.1 Light scattering based techniques

The use of light as a probe permits nondestructive characterization of particles. The light intensity (photon flux) and wavelength (photon energy) are usually too low to damage particles, even delicate biological cells. Light scattering allows to perform in situ measurements; thus particles do not need to be isolated from their natural environment. When scattered light is continuously measured, temporal changes in particle characteristics can also be determined.

When a light beam of a certain wavelength illuminates an object (understood as matter having a dielectric constant different from unity), light is absorbed or scattered, or both. Thus, absorption and scattering contribute to the extinction of the incident light. Light scattering can be defined as the deflection of a ray of light from its theoretical straight path, caused by the irregularities or non-uniformities (known as scattering centers) found in the propagation medium, i.e. particles, bubbles, dust, surface roughness, etc. Scattering will only take place in heterogeneous materials, i.e. the radiation scattered by molecules in a perfectly homogeneous and isotropic material interfere destructively.

Figure 1.5 presents a conceptual illustration for this phenomena: a particle of dust, subdivided into small regions, scattering incident light. When the light wave comes in contact with these small regions, a dipole moment of a certain amplitude and phase, is induced in each one of them. These dipoles oscillate at the same frequency than the incident light, and scatter radiation in all directions, in the

form of wavelets with different phase relations. Size, shape, chemical composition of the dust and the direction at which light is scattered are the parameters that define the scattering of light by dust in this example.

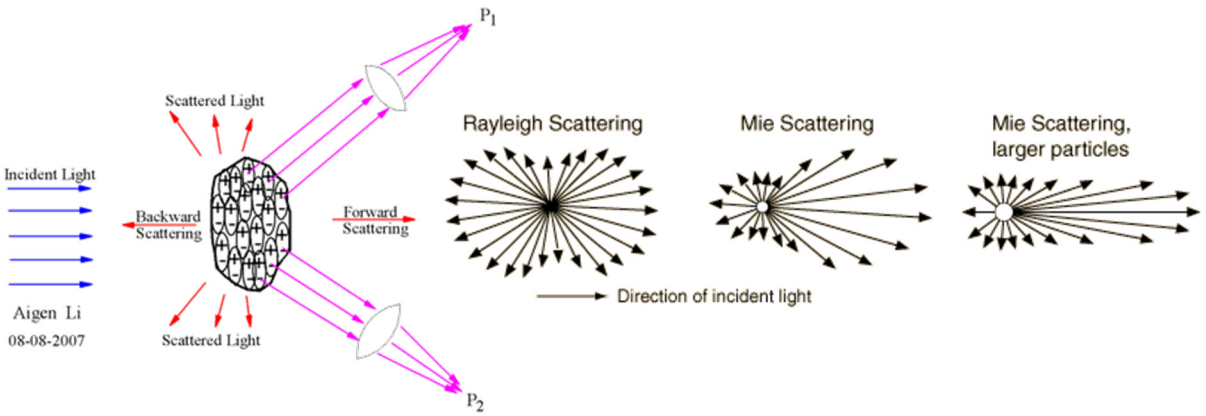

***Figure 1.5**. Left: Graphical representation of the light scattering effect in a particle of dust (Reference: http://ned.ipac.caltech.edu /level5/ Sept07/ Li1/ Li2.html). Right: Light scattering pattern for Rayleigh and Mie theories. (Reference: http://hyperphysics.phy-astr.gsu.edu/hbase/atmos/blusky.html)*

Several theories have been developed to adjust the empirical results of light scattering to the most appropriated model, according to the particle properties (size, shape, relative refractive index) (figure 1.6). Mie theory is a rigorous solution for the scattering from a spherical, homogeneous, isotropic and non-magnetic particle of any diameter in a non-absorbing medium. The scattering of a spherical particle produces a pattern like an antenna lobe. The larger the particles, the sharper and more intense forward lobe (figure 1.5, right). Rayleigh Scattering ($Zero_{th}$-order approximation) is applied when particles are much smaller than the wavelength of light (λ). Light scattered from the particle will be the same as if it was scattered from an oscillating dipole that radiates in all directions (figure 1.5, right). The scattering intensity is dependent on the size of the particles. Rayleigh-Debye-Gans Scattering (First-order Approximation) is useful when the dimensions of the particle do not allow to consider it as a single dipole. The approach is to treat the particle as the sum of many tiny and structureless scattering elements. Rayleigh scattering will be applied independently to each one of these elements. Finally, when the particle dimension is much larger than the wavelength of light (i.e. at values of the ratio D/λ more than 10) or the material is highly absorptive we find Fraunhofer Diffraction. In this case, where the edge effect of particles (i.e. diffraction produced by the bending of light at the particle boundary) contributes much more to the total scattered intensity, diffraction equations can be used to describe the scattering patterns.

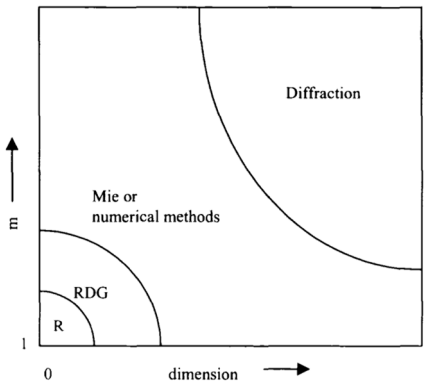

***Figure 1.6**: Light scattering theories and their application ranges (R: Rayleigh, RDG: Rayleigh-Debye-Gans) [1]*

Light scattering also presents some drawbacks. Retrieving the information carried by the scattered light about the particle characteristics is a complex process. Besides, due to the weakness of scattered light, sophisticated detection systems are required. The best results in characterizing particles with this technique are obtained for spherical particles, because of the precision of the Mie model of light scattering by spheres. Measurements for non-spherical and non-homogeneous particles are not so accurate and require numerical computation approaches.

Table 1.1 includes a list of different technologies based on the light scattering phenomena in the field of particle characterization as well as their main applications [1]. From this table, the most commonly used techniques are laser diffraction, single optical particle counting, flow cytometry, photon correlation spectroscopy, and electrophoretic light scattering.

Scattering Frequency Change	Name	Signal	Main Applications	External Field
Elastic	Static LS (including diffraction) [8,9,10,11,12, 13]	Angular scattering intensity pattern	Sizing, particle and macromolecule study	No or Flow
	Optical counting [14]	Single particle scattering	Sizing, counting	Flow
	Focused Beam Reflectance [15,16]	Back scattering using a rotating beam	Sizing	Flow
	Time-of-Transition [17]	Transmission using a rotating beam	Sizing	Flow
	Time-of-Flight [18]	Scattering of accelerating aerosols	Sizing	Flow
	Optical Space-Frequency Analysis [19]	Scattering from masked incoherent light	Sizing	Flow
	Turbidimetry [20]	Transmission	Sizing, composition study	No
	Transient LS [21,22]	Scattering intensity variation in an applied field	Shape study	Electric field
	Forced Rayleigh LS [23,24]	Fringe pattern change due to diffusion	Diffusion study	Intense pulses of light
	Resonance LS [25]	Enhanced scattering due to absorption change	Aggregation study	No
	Flow Cytometry [26,27,28]	Single particle fluorescence and scattering	Cell analysis	Flow
	Pulse Displacement [29]	Refraction and reflection pulses	Sizing and flow velocity study	Flow
Quasi-elastic	PCS (including DWS) [30, 31,32,33,34,35,36,37,38,39, 40]	Scattering intensity fluctuations	Diffusion study, sizing	No
	Electrophoretic LS [41] (including spectrum analysis [42])	Scattering intensity fluctuations	Mobility and diffusion study, sizing	Electric field
	Phase Doppler [43,44,45,46, 47,48]	Scattering frequency shift and phase delay	Sizing, counting, flow velocity study	Flow
	Phase Analysis [49,50]	Scattering phase change	Mobility study	Electric field
	Photon Migration [51]	Optical diffusion of intensity modulated light	Sizing	No
	QELS-SEF [52]	Scattering intensity fluctuations in a sinusoidal field	Dynamic property study	Electric field
	Modulated Dynamic LS [53,54]	Scattering intensity fluctuations of a single particle	Particle mass, diffusion, velocity and shape study	Flow
Inelastic	RCS [55]	Raman scattering intensity fluctuations	Dynamics and composition study	No

***Table 1.1**: Light scattering technologies and applications from the book "Particle Characterization: Light Scattering Methods" by Xu Renliang* [1].

1.5.1.1 Static light scattering or Time-averaged scattering intensity of particles (Application range from 0.01µm to 500µm)

The measurement of time-averaged scattering of particles is based on the assumptions that the scatteters (elements with the ability of scattering the light, i.e. anything that has a different refractive index than that of the medium and is stable throughout the duration of the measurement) are not moving and that the incident light intensity remains constant. Everything is in a static condition, even the components of the experimental setup. That is why the techniques that accomplish the exposed requirements are described as "static light scattering". These techniques deliver the best results when the number of particles in the sample volume is small and the distance between them is large, for under these conditions multiple scattering effects can be neglected and total scattering intensity can be considered as the addition of the scattering from all particles.

1.5.1.2 Dynamic light scattering. Photon correlation spectroscopy (Application range from 0.2nm to 10µm)

Unlike the previous one, Dynamic Light Scattering (DLS) deals with the movement of the particles in the sample. So the first of the assumptions for static light scattering is not considered, as in reality, particles are in constant motion (e.g. random thermal Brownian motion, motion forced by a flow or an electric field, motion from bioactivity…). This motion causes variations in the scattering intensity at a given scattering angle, depending on the nature of the motion and the properties of particles, which are continuously rearranging their configuration. The word "dynamic" refers to the changes of the scattering over time. DLS is the most common technique for sub-micron sizing, delivering information about the diffusion coefficient (D_t), which is related to the hydrodynamic diameter of particles (D_h) through the Stokes-Einstein equation. Hydrodynamic diameter is larger than the diameter measured with a TEM microscope, due to the electric dipole layer formed at the surface of the particle in motion.

To measure the dynamic light scattering of small scatterers in a liquid suspension or solution, Photon correlation spectroscopy (PCS) technology was developed [5], [6]. With PCS, these fluctuations are analyzed in correlation delay time domain to determine the diffusion coefficient. Then, information such as the size of particles or the kinetics of the scatterers can be obtained [7].

Current commercial PCS instruments employ miniature setups utilizing fiber optics and chip correlators with digital signal processing. Manufacturers of commercial instruments such as *Brookhaven, Coulter, and Malvern*, employ 90° scattering and give a mean and standard deviation for the size distribution.

PCS offers some advantages in comparison with other technologies: it is a noninvasive absolute technique; only small amounts of sample are necessary; and it does not require extensive sample preparation. The lower size limit of PCS is determined by the Signal to Noise Ratio parameter: the relation between detectable scattering fluctuations of particles and the experimental noise (i.e. noise created by various sources such as environment disturbances, temperature fluctuations, and the inherent electronic noise). Practically, the lower size limit is below nanometers depending on the refractive index difference between the particles and the medium. The upper size limit is related to the sedimentation limit, as particles that are being analyzed must be stably suspended. In practice, this limit is about a few microns depending on material density and medium viscosity. It is not an appropriated method for larger particles, because of data overlapping.

1.5.1.3 Laser diffraction (Application range from 0.01µm to 1000µm)

In laser diffraction, the information about particle size distribution is obtained by means of scattering intensity measurements of particle suspensions as a function of the scattering angle and the wavelength of light, based on applicable scattering models. This effect was studied in the late 1970s (Cornillault, 1972; Weiss & Frock, 1976; Swithenbank et al., 1977), and through the years, many manufacturers (*Fritsch, Coulter and Horiba*) have joined the original ones (*Cilas Granulometer, Malvern Particle Sizer, and Leeds & Northrup*) in the instrumental implementation of these methods (figure 1.7).

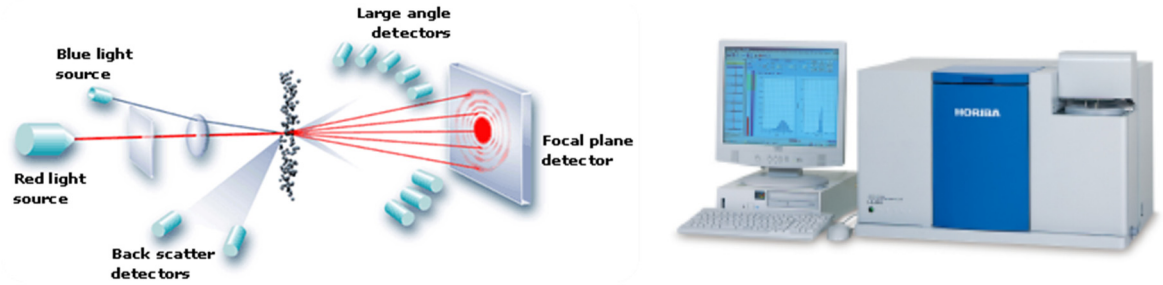

Figure 1.7. *Left: Scheme of laser diffraction technique (printed with permission of Malvern Company). Right: LA300 from Horiba.*

In laser diffraction a light source monochromatic beam is collimated and conditioned to create a Gaussian radial intensity distribution, through optical components. The illuminated sample scatters light, creating unique angular scattering patterns. The pattern is detected by a multi-element photodectector array. The undiffracted light is focused to a point in the centre of the detector, through a lens placed at the focal length from the detector. The photocurrent obtained from photodetectors is converted into a flux pattern. Computers calculate the final conversion according to the appropriate scattering theory, and particle size distribution is presented as the result of the measurement. Problems arise when particles are irregularly shaped, since there are no easy interpretations of the scattering patterns for them. However, modern devices are not restricted to analyze only spherical particles. The results, as in most particle sizing technologies, are apparent values that may differ from real dimension values.

Due to the wide size range of particles that can be analyzed with laser diffraction (high dynamic size range that includes the submicron region), it has become popular in the industry replacing the conventional methods as well as the optical and electron microscopy (used for particles larger than some tens of nanometers). Besides, it offers other advantages such as easiness of use, rapidness, precision and high reproducibility. The evolution of these instruments also includes improvements in the laser light source components, which are often complemented with a light source of continuous wavelength (white light) in order to collect additional information about submicron-size particles based on wavelength and polarization dependencies of scattering intensity.

The lower size limit for laser diffraction technology is defined by the ratio of particle dimension to light wavelength. As particle size becomes smaller, the scattering pattern becomes smoother and less angularly dependent.

1.5.1.4 Electrophoretic light scattering (Application range from 0.3nm to 100µm)

The main use for the electrophoretic light scattering (ELS) technology is the characterization of the surface charges of colloidal particles in liquid media, by measuring the electrophoretic mobility and then calculating the zeta potential. The term "colloidal particles" refers to small particles, from nanometer to micrometer-sized particles, with an extremely large specific surface area (surface area per unit weight). This special characteristic makes colloidal particles very sensitive when in liquid media (liquid-particle interface), affecting the physical properties of colloidal dispersions (e.g. dispersibility and stability). The zeta potential parameter, defined as the value of the electrical potential at the shear plane, is often used in the industrial and academic sectors to characterize the surface of a particle. The most common way to determine zeta potential is to apply an electric field to a colloidal suspension: neutral particles will remain unaffected, while particles carrying surface charges will move oriented according to the direction of the electric field.

1.5.1.5 Flow cytometry (Application range from 0.02µm to 150µm)

Flow cytometry is a scattering/fluorescence measurement technique widely used in cell analysis for the detection of single particles suspended in a liquid solution. It combines a microfluidics block, responsible for the singly alignment of particles when entering into the sensing zone, with laser induced fluorescence measurement and scattering detection performed into the sensing chamber (figure 1.8, left). In a flow cytometer, the stream of fluid is analyzed by a laser beam that interrogates the cell. The cell responses absorbing light and emitting light as forward scatter at small angles, side scatter at large angles and fluorescence. Each one of these signals delivers interesting information about the characteristics of the cell (figure 1.8, right).

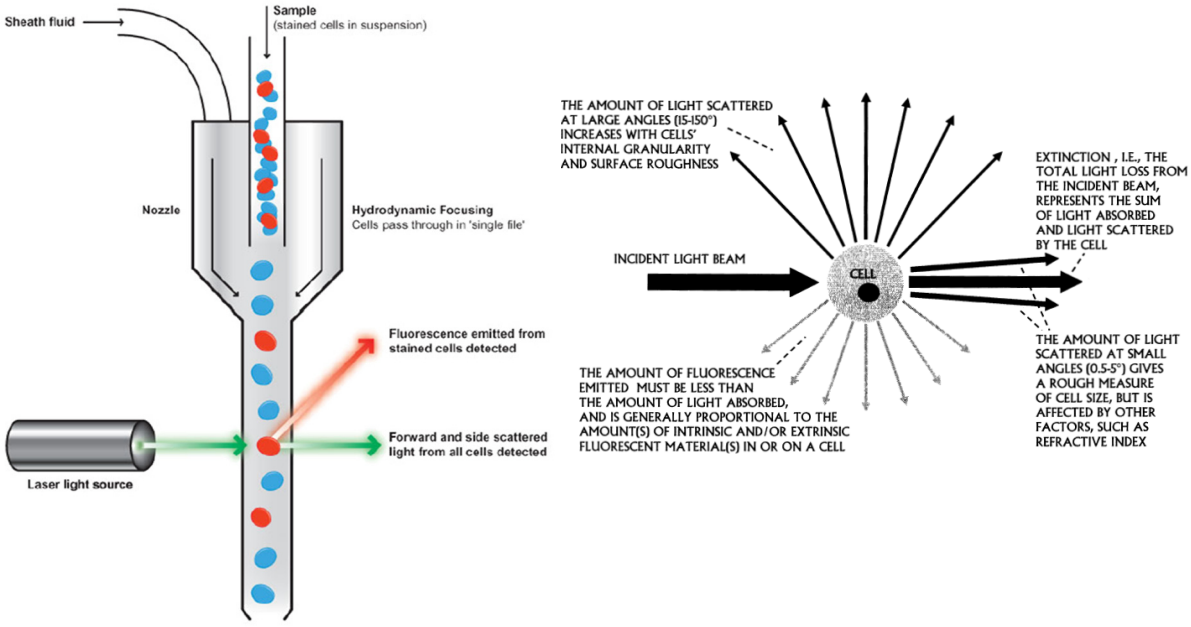

Figure 1.8. *Left: Basic scheme of a flow cytometer. Printed with permission from ABCAM. Right: Information about the particle or cell related to the different signals, generated in response to light excitement.*

Although some molecules are naturally fluorescent (e.g riboflavin, vitamin B2), usually for fluorescence measurements particles and cells must be previously prepared, stained with the appropriate

fluorochrome (the fluorescent label) sensitive to the wavelength of the excitation light, in order to obtain the best response in the intensity of the returning light, at the emitted wavelength.

About the photodetectors in flow cytometers, the commonly used are Photomultiplier tubes (PMT) and Avalanche photodiodes (APD). PMTs offer high gain values (of the order of 10^6) while APDs combine high quantum efficiency with relatively high gains (of the order of 10^3), but they do not match the sensitivity of PMTs. That is the reason why it is a common practice to use photodiodes as detectors for absorption, extinction and forward scatter signals, and PMTs as detectors for orthogonal scatter and fluorescence signals. Additional filters are necessary to avoid damaging the sensors.

The highlights of flow cytometry are selectivity and high sensitivity, but on the other hand it requires expensive equipment and trained technicians. Therefore, there is a current tendency, connected with the development of integration and miniaturization technologies, which tries export the benefits of LoC devices to flow cytometry to offer simplicity of use and low cost fabrication.

1.5.2 Light extinction/obscuration

1.5.2.1 Optical particle counting and sizing (0.5µm to 5000µm)

In contrast to Coulter Counters (based on electrical sensing), optical particle counting is also possible by means of techniques based on the measurement of the signals resulting from the interaction of particles with light. Optical Particle Counters (OPC) can deal with a wider range of sizes in comparison with Coulter counters, as the upper size limit is increased up to 5000µm.

Since more than seventy years ago, when the development of optical particle counting began for the detection of air-borne chemical warfare agents [8], the method has been in constant development to enhance features such as simultaneous counting, sizing, as well as in-situ identification of individual particles in a sample [9]. Initially based on the detection of light scattering[2] from particles, during 1960's Optical particle counters based on light extinction were developed.

Nowadays, optical particle counting technology combines the two different detection methods: light scattering for small particles (as small as 50nm), and light extinction for large particles (as large as 1mm). OPCs are able to detect particles in the form of aerosols, dry powders, or liquid suspensions. The only requirement is that particles must enter individually into the sensing zone by means of pressure, vacuum or a directed flow. Unlike laser diffraction methods, OPCs do not resolve the particle size distribution from an ensemble measurement of the angular scattering intensity pattern, but they count and size particles using the signals generated by individual particles.

The mechanism is as follows: a liquid or gas suspension of particles is prepared, adjusting the concentration to allow particles flow one at a time and singly aligned when entering into the sensing zone (or detection chamber). This sensing zone is uniformly illuminated by a laser or another kind of light source. When a particle passes through the sensing zone, the detectable physical effect is produced: light extinction or light scattering.

[2] Optical particle counting can be achieved by both light scattering and light extinction measurements. The particle detection system presented in this thesis is based on light extinction rather than light scattering, which is presented as a possible detection mechanism in Chapter VIII.

- Light Scattering: As the particles pass through the detection chamber, light energy is either absorbed by them or reflected. Several off-axis photodetectors measure how much light is scattered in order to calculate how many particles have passed through the chamber. This method is typically used for counting small particles in either air or liquid.

- Light Extinction/Obscuration: As larger particles pass through the detection chamber they directly obscure the laser light. The photodetector measures the variation in order to count the particles (figure 1.9). Typically best for counting large particles in liquids.

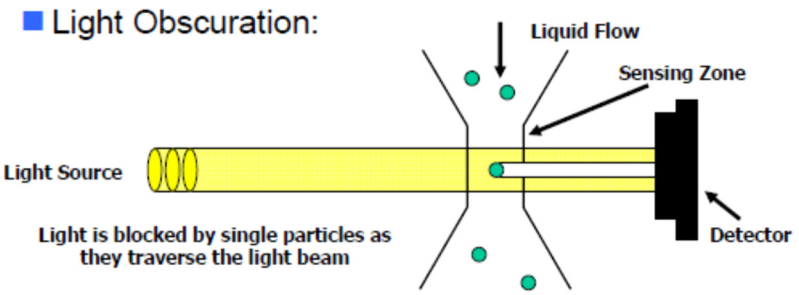

Figure 1.9. *Conceptual scheme for an optical particle counter based on light obscuration/extinction.*

The variations in light signal are detected by photodetectors and converted into electric pulses. The magnitude of the effect depends on the dimensions and optical properties of each particle. The stored data can be analyzed to determine particle count and size according to a calibration curve previously obtained from experiments with control particles of known size. Our attention will focus on the detailed discussion of the light extinction optical particle counting subject, which is related with the aim of this thesis.

OPC is a high resolution technology but with a relatively narrow dynamic range and low statistical accuracy when compared for example to ensemble measurement techniques (i.e. laser diffraction methods). Single optical particle counters are useful devices in the industry for applications such as environmental monitoring or verification and control of product quality. They are widely used, for example, to perform in-situ measurements in contamination analysis (water, clean rooms, hydraulic fluids…), where normally particles are considered undesired substances (figure 1.10, left).

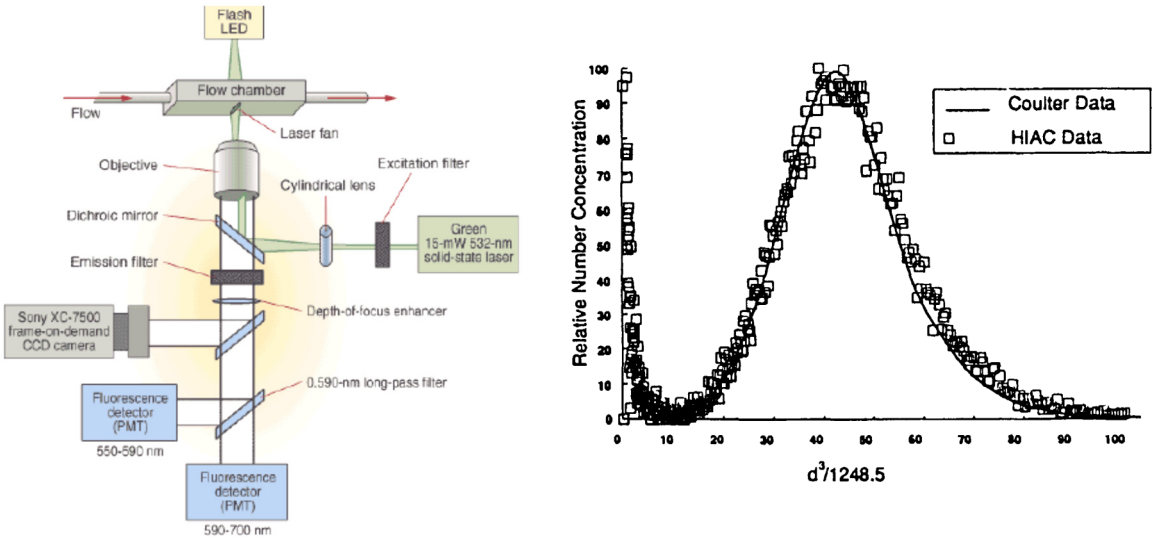

Figure 1.10. *Left: Industrial in-situ optical particle counter in oil samples (from Horiba).Right: Comparison of latex size distributions using a HIAC optical particle counter and a Coulter Counter. Reproduced with permission of The Royal Society of Chemistry.*

The lower sizing limit for detection in air medium is around 30nm using a 1W laser for aerosol particles. In the case of liquid measurements, the detection of small particles is more difficult and requires a higher power laser and a smaller sensing zone. Anyway, thanks to developments in high power laser diodes and the advances in optical designs, detection of particles as small as 50nm in liquid is possible.

In a light extinction measurement of non-spherical particles, the shape of the particle influences the size determination, because the instrument is measuring the projected area according to the orientation of the particle as it passes through the sensing zone. Thus, broadened particle size distributions will be obtained. Comparing the accuracy of OPCs with other particle counting instruments, such as a Coulter Counter, the results are quite similar (figure 1.10, right).

Several factors can affect the counting efficiency and accuracy of OPCs:

1) The zero count. The zero count rate is the background count obtained when measuring using particle-free fluid during a specified time. This background count is generated by the inherent elements of the device (optics and electronics) and affects the measurements of the smallest particles. Thus, the zero count should not exceed 5% of the anticipated count for the smallest particles in the sample.
2) Misalignment of the optical system, producing a distorted calibration.
3) Partial loss of the sample stream in the inlet, so that many particles are not counted. To reduce this undesired effect, the inlet tube should be short and without bends.
4) Recirculation of the sample because of flow eddies, yielding in a higher count.
5) Presence of air bubbles in the sample during liquid measurements, which increases the count as they are considered particles. Sonication or vacuum help to remove air bubbles.
6) Incorrect metering of fluid flowing through the sensing zone produces an erroneous concentration measurement. Correct calibration and a constant flow rate are necessary.
7) Too low particle concentration, since it will reduce the statistical validity of the reported counting and sizing results.
8) Too high particle concentration, which can lead to particle coincidence or electronics saturation. The effect of particle physical coincidence is under-counting of particle number and incorrect particle size determination. The coincident particles are reported as a single one. A double test, consisting of performing a second measurement with a sample of a more dilute concentration, can help to determine the influence of particle coincidence. Electronics saturation refers to the inability of the electronics to detect and sort individual pulses for being too closely spaced in time. This saturation inhibits the electronics to reset and detect separate pulses (one for each particle).
9) High concentration of small particles (outside the specified sizing range). Individually, their effects would be neglected because of the background noise. But if some of them group and enter the sensing zone, they will be detected as an acceptable particle.
10) Flow velocity. Counting efficiency increases with reduced flow velocity.

Nowadays, the best way to value the counting efficiency of an optical particle counter is to carry out a comparative analysis of a monodisperse sample with a “standard” instrument that has been verified to have near 100% counting efficiency.

1.5.2.2 Submicron aerosol sizing and counting (Application range from 1nm to 1µm)

The atmosphere contains plenty of submicron aerosol particles, which require a specific methodology to be characterized because of their size and concentration. First, aerosol particles are classified according to their size. Then, particles pass through a container of evaporated liquid, and when the vapor condenses onto the aerosols, larger particles are obtained. Optical counters can detect and count these particles.

To fraction or classify the aerosol particles, two different schemes can be followed: diffusion battery method (for aerosol particles between 5nm and 200nm) or differential mobility analysis (for particles between 1-1000nm) [10], [11], [12].

1.5.3 Image analysis (Application range from 1nm to 200µm for classical methods, from 0.3µm to 1000µm for holographic methods)

Besides counting the number of particles per sample, image analyzers provide information such as shape and size and even surface texture. As a drawback, the instruments are bulky and the analysis operation requires more time than other techniques. Image analyzers base their counting principle in defining the edges of individual particles captured in images. Nowadays, several companies have developed automated systems to perform the task (e.g. *Cambridge (Quantimet), Leitz, AMS, Kontron).*

Classical image analyzers do not deal with particles in flow, but rather with captured images of samples. Image analysis is based on Microscopic Methods requiring a procedure for image capturing (preliminary task before beginning with image processing and analysis procedure). Several instruments are suitable to capture images. In Optical Microscopy (OM) we find Transmission Microscopy (lower size limit around 3µm), Confocal Laser Scanning Microscopy (offering high image resolution) [13] and Near-field Scanning Optical Microscopy (NSOM) (lower size limit to the submicron range) [14]. With Electron Microscopy (EM), basically we have Transmission Electron Microscopy (TEM) (size range about 0.001-5µm), and Scanning Electron Microscopy (SEM) (0.02-200µm).

When capturing images, sample preparation must accomplish some requirements: minimum number of particles in contact to avoid the effect of pseudoboundaries and special care about staining, shadowing or coating of particles. Once images are captured and digitized (typically in 256 gray levels), with computer image processing valuable information about particles can be extracted (figure 1.11).

An advantage of microscopic analysis over other methods is that it allows to work with particles of a broad size range, offering good levels of resolution and detail [15]. On the other hand, it also presents some weak points. As the information is obtained from 2-D projected particles, particle orientation is a significant factor to consider. In the particular case of electron microscopy, only dried particles can be analyzed, not particles in suspensions, so properties may differ from one state to another. A limited number of particles can be inspected in a field of view. In polydisperse samples, the number of samples to analyze must be increased to obtain the right statistical representation.

The “new image analysis” introduces the Holographic method. This method has been used in the study of airborne and liquid-borne particulate systems in their real environments [16], which represents an improvement compared to the classic image analysis. The 3-D images are constructed by illuminating the samples with coherent light (pulsed laser of a very short duration) to obtain the diffraction patterns

of all the particles and, in a second step, to create a stationary image of the particles at their locations. Regarding to the information provided by this method, besides particle size and shape, also particle orientation and even velocity of particles [17] can be measured.

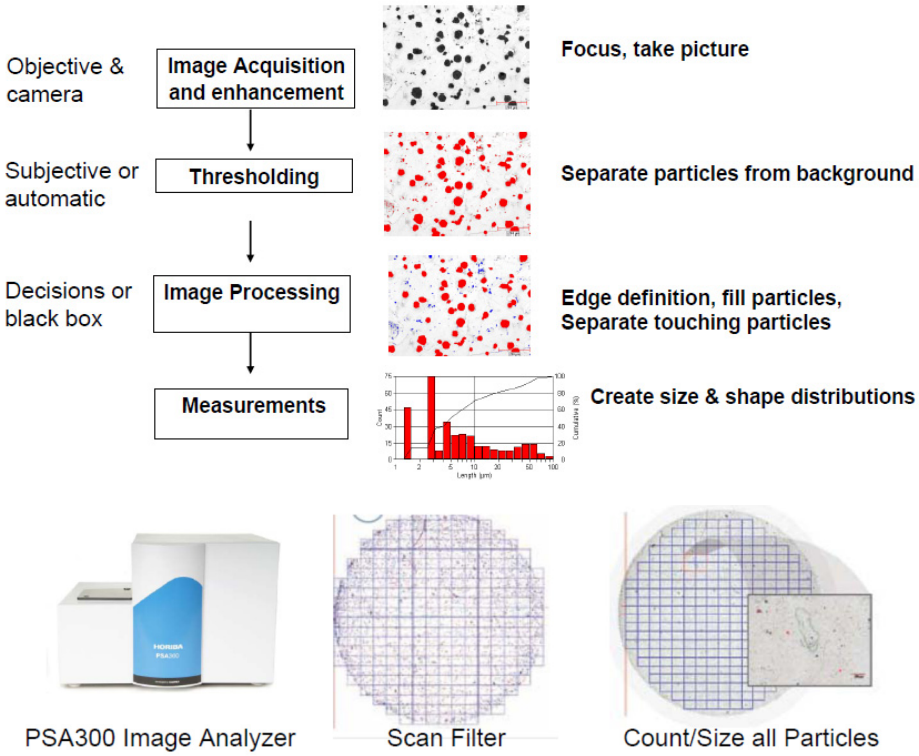

Figure 1.11. *Top: Steps followed in image analysis procedure. Bottom: Horiba PSA300 Image Analyzer. Printed with permission of Horiba company.*

1.6 Particle sizing methods comparison

Figure 1.12 presents a summarized table of the different techniques previously commented and their range of application. This thesis is focused on optical detection of particles, because of the advantages that light and optics based techniques offer over the rest of available technologies, in the fields of biology and life sciences.

It is evident that light scattering techniques cover the best range in sizes, with dynamic light scattering offering the lowest size limit (even below the nanometer scale in some cases). In case of needing a wider range of detection, laser diffraction offers excellent performance. On the other hand, the complexity of this sort of systems (for example, the large number of sources and detectors necessary to perform the measurements in laser diffraction) represents a drawback in terms of integration.

Optical particle counters, and in particular, the ones based on light obscuration technique, are more limited in the range of particle sizes they can deal with, though it can be considered reasonable and acceptable for some biosensing applications. On the on the other hand, the simplicity in their design in comparison with laser diffraction and other light based techniques, makes them the perfect candidate to be miniaturized, exploring the benefits of integration at every level (light sources detectors and fluidics), with the aim of approaching them to the new trend established by the Point of care testing concept.

Comparing light obscuration with electrical sensing methods, both cover approximately the same range of particle sizes, though light obscuration offers a larger upper size limit. However, optical article counters offer other interesting benefits in front of Coulter counters, for example the fact that they are not restricted to measure particles suspended in an electrolyte solution, or that they can provide information not only about the number of particles and their dimensions, but also about their shape, for light is projected over particles creating a shadow that is captured by photodetectors.

Since our actual scope is the detection and counting of particles in the range of 10 to 100µm diameter, light obscuration technique accomplishes our requirements. After the study of the results achieved with the optical detection system introduced in this thesis, the next step will be to reduce the lower limit of detection to 1µm.

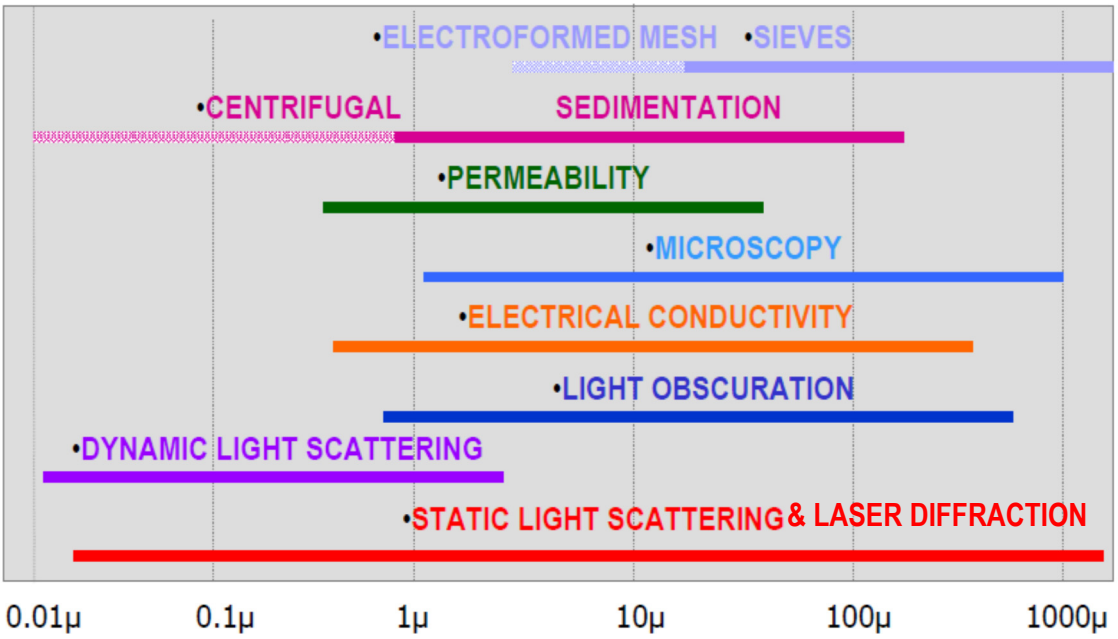

***Figure 1.12**. Size range by technique. Printed with permission from Horiba Company.*

1.7 Industrial and commercial instrumentation for optical particle detection

Apart from the detrimental effects in human health of particles originated by manufacturing processes and by the own use of some commercial products[3], characterization and detection of particles are also considered interesting subjects for the industry. The effects produced by existing contaminants and foreign particles in industrial production processes (for example, in pharmaceutical and automotive industries) are quite negative, even dangerous, and thus, their detection is essential. The paradigmatic example can be found in the "powder technology" branch of chemical industry (e.g. ceramic and paint industries), where the properties and the quality of manmade powders are studied and under control during the manufacturing processes.

Thanks to the interest of industry, fast and precise automated methods of particle size analysis and

[3] Legislation in Europe and North America regulates the mass concentration of particles present in ambient air (from emissions of vehicles, for example), with the aim of reducing damages in the respiratory tract and the cardiovascular system.

particle counting have been developed in the recent years (e.g. Laser particle sizer for fuel spray droplet size) [18]. At present, several companies (e.g. *Malvern, Horiba or HIAC*) offer commercial systems devoted to perform particle characterization. When used in industrial environments, these systems are able to count the number of particles in a sample, to determine their size and shape and even to isolate particles with specific characteristics: "*Malvern Insitec*" systems deliver online continuous particle size analyses for industrial processes, measuring particles in a range of 0.1µm to 2.5mm, by laser diffraction technology (figure 1.13, left); "*Horiba MEXA-2000 SPCS*" series is a laser scattering based particle counter for automotive industry with a lower particle size limit of 40nm (figure 1.13, right). Though these systems offer good accuracy and robustness, usually they are expensive and bulky, which makes them not suitable for measurements in the outside, without the established standard conditions of a testing procedure.

***Figure 1.13**. Left: Malvern Insitec Wet particle size analyzer. Printed with permission of Malvern Company. Right: Horiba MEXA-2000 SPCS particle counter for automotive industry. Printed with permission of Horiba Company.*

In the field of optical particle counting, two types of particle counters are available: air particle counters or liquid particle counters. The difference between them lies in the medium where the particles flow (air or liquid). Both of them include a system (e.g. a small pump) to draw the air or the liquid to be tested into a detection chamber. The first ones are typically used to classify and monitor Cleanrooms. The second ones are commonly used in pharmaceutical (for instance, to control the quantity of particles in liquids for injections) or industrial applications (for example, to monitor the quality of hydraulic oil). Anyway, optical particle counters are present in a large number of industrial areas, such as Life Science, Electronics or Aerospace and Defense. These devices are able to perform full tests with very small sample volumes (≈1ml), yielding in a reduction of the cost and waste to the minimum.

HIAC is one of the main manufacturers for liquid optical particle counters. The *HIAC Particle Counter* was originally developed for aerospace hydraulics applications where a laser particle counter was used to monitor the size and quantity of particles present in the hydraulic liquid. At that time, some experiments were performed to compare *HIAC counters* with well-established *Coulter counters*. The results concluded that the *HIAC counter* undercounted for sizes ≤ 7 µm or ten times the wavelength of light, probably due to the fact that below this limit, particles did not block perfectly the light, and thus diffracted light reached the photodetector sensor.

These values were later confirmed through an *ASTM* comparison (American Society for Testing and Materials international standards organization, 1983). Several analysis technologies were tested

(image analyzer – d_1, Coulter Counter - d_v ,HIAC counter - d_0) to compare the mean sizes of the detected particles, and the following ratios were obtained: $d_0 = 0.77d_1$, $d_v = 0.584d_1$. The study proved that *Coulter Counter* presented the best detection sensitivity, but it was 1983, and since then recent advances in the development of laser light sources and micro-optics have allowed to surpass these limits. Current optical liquid particle counters are able to perform analysis for particles of 0.5µm diameter and even below.

Nowadays, "*HIAC Company*" fabricates a wide range of liquid particle counter systems adapted to the needs of each situation: laboratory or industry measurements (figure 1.14). Especially interesting are the portable systems like the *HIAC PODS* (figure 1.15, left), which is able to perform measurements in 8 channels of dimensions 4, 4.6, 6, 9.8, 14, 21.2, 38, 68µm according to the *ISO-MTD* standard[4] or ~1, 2, 5, 10, 15, 25, 50, 100µm according to the *ACFTD* standard[5], at a flow rate of 15-50 ml/min, with a laser diode as the light source. The concentration limit of the samples is 20.000 particles/ml at 5% coincidence loss (per *ISO 11171*), and the *HIAC PODS* can manage sample volumes of 5, 10 or 20ml. For a portable system, dimensions and autonomy are important parameters. The *PODS* system dimensions are 17.8 D x 33.0 W x 35.6 H cm (7 x 12.5 x 14 inches) and 9.5kg weight (21lbs). About the power supply, the system works with DC Input +24 VDC, 2A, in rechargeable battery Nickel-Metal Hydride, which provides an operating time of 100 samples or 4 hours continuous. The recharge time is about 2.5 hours.

***Figure 1.14**. HIAC Laboratory particle counters for liquid. Left: HIAC 8012 model ideal for testing dark viscous fluid without dilution (viscosities to 1800 cP) with sample volumes as low as 3 ml. The system includes the 8000A Counter and the Syringe Driven Sampler. Middle: HIAC 9703+ specially designed for pharmaceutical USP <788> quality control and research applications. Device presents dimensions of 343 W, 337 D, 482 H mm and 10.7kg weight. Right: HIAC ROC online liquid particle counters are constructed for industrial harsh environments (high pressure and high temperature applications) offering carefree maintenance.*

As an evolution in portability, the same company introduces handheld air particle counters; i.e. lightweight instruments that use the same detection principle and technology (laser based optical systems) in a miniaturized way. Miniaturization has also led to a reduction in the power consumption of the devices, and thus, an improvement in terms of power autonomy. Of course, miniaturization presents other implications: a limitation in the number of channels of the device, and consequently, in the particle size range able to be detected by the instrument. In its catalogue, *HIAC Company* offers for example the *MET ONE HHPC* handheld particle counter (figure 1.15, right). This counter, designed to develop tasks in high technology cleanroom manufacturing environments, presents six channels

[4] Based on the valid filter-test dust standard.
[5] Air-Cleaner-Fine-Test-Dust, the old calibration standard introduced by General Motors.

covering a particle size range of 0.3µm to 10µm (according to *ISO 14644-1* (FS *209E)* industry standard). Its dimensions 27.1 x 9.9 x 5.33 cm are very convenient for single handed operation, and the battery offers over 10 hours of typical us or 5.5 hours of continuous sampling.

Figure 1.15. *Left: HIAC PODS portable liquid particle counter. Right: HIAC MET ONE HHPC 6+ handheld airborne particle counter.*

Anyway, *HIAC* is not the only manufacturer for liquid particle counters based on optical detection. *"Lighthouse*" is another well-established company offering a wide range of choices for these products. Its new "*NanoCount 25+"* based on Solid State Laser particle counting technology, with a detection limit of 25nm, is a good example which proves that industry is continuously evolving to overcome the existent limitations (figure 1.16, left). With dimensions 31.1 W x 30.48 H x 66.80 D cm and 37kg weight, *NanoCount 25+* includes four channels (25nm, 35nm, 50nm, 100nm) of simultaneous count data and can stand a flow rate of 30ml per minute. *Lighthouse Company* also offers handheld airborne particle counters (figure 1.16, right). The *Handheld 2016, 3016 and 5016* particle counters feature 0.2, 0.3 and 0.5µm sensitivities respectively. For the *Handheld 2016* model, 6 channels cover the particle size range from 0.2 to 2µm. An extreme life laser diode is employed as light source in this device with dimensions 22.23 x 12.7 x 6.35 cm.

Figure 1.16. *Left: Lighthouse NanoCount 25+ portable liquid particle counter. Right: Lighthouse Handheld 2016 airborne particle counter.*

Other companies also provide products with similar features and specifications, oriented to detect suspended particles in liquids or in air. Just to name a few examples: *Met One, Climet, IQAir, Kanomax, Fluke, Particle Measuring Systems, Innovatech Labs or Spectrex corporation*.

1.8 Optical particle counting: State of the art

Discussion about the state of the art of optical particle counting is divided in two parts. The first one, focused on advances published in scientific and academic literature from the point of view of biosensing applications. The second one analyzes the reported devices from the point of view of fabrication techniques and integration methods. The optical particle detection system introduced in this thesis has been developed as an early prototype, which intends to become a feasible and operational alternative to current commercial devices.

1.8.1 Point of view: Biosensing applications

During the last years, principally in the research field of biosensing applications, there has been an increasing interest in developing small and portable systems able to perform fast measurements consuming low sample volumes. These devices should also accomplish some other requirements such as **low power consumption**, **integration** and, of course, **cost-effective price**. Lab on a Chip devices and Micro Total Analysis Systems are the perfect examples for this kind of complete systems, and follow the present tendency focused on the concept of **point of care testing** applications, which tries to bring the testing systems closer to the patient, and not in the opposite way. This would result in an improvement in many senses, delivering results to patients in a short period of time near their site, as happens for example with blood glucose testing, pregnancy testing and cholesterol screening. The rapid decision form the expertise would establish the most appropriated treatment for the studied diagnostic.

These minilab testing devices usually include a microfluidic block, where the sample volume is prepared before entering into the sensing stage: the analyte present in the sample (in a variety of forms such as chemical molecules or microparticles) can be directed, focused, aligned, chemically processed, trapped and even sorted. In the optical particle counting field, flow cytometry is one of the most commons and widely used techniques to perform particle counting and characterization in liquid volumes, combining light scattering and fluorescence detection, and scientific research for this subject contains a large number of examples where the same or similar sensing concepts can be found applied to microdevices. The research carried out in the flow cytometry subject, can undoubtedly be applied to optical particle counters.

T. Dong Chung and H. Chan Kim [19] explored the possibilities and benefits of microfluidic flow cytometers as clinical tools in the biomedical research. The great potential of flow cytometry to quantify different characteristics of viruses, bacteria mammalian cells and microparticles at high throughputs make this technique a vital tool for the diagnosis of diseases such as acute leukemia. In front of typical flow cytometers with bulky operating units and peripherals operated by specialists, microfluidic systems offer more volume efficient analysis, more cost-effective units, more sophisticated cellular analysis, better fluid/particle sorting and other interesting features that facilitate on-site measurements. The diagnoses of fetal genetic disorders and infant blood screening test benefit from the fact that microfluidic flow cytometers require reduced cell volumes. Screening and monitoring for human immunodeficiency virus (HIV), complete blood count measurements, and cell screening assays are possible with commercial portable flow cytometers. However, one of the key targets, still in development, for microflow cytometers involves the integration of comprehensive processes (including the pretreatment stage) leading to totally miniaturized systems. Some of the

examples included in their review are discussed below to demonstrate the importance of what could seem a simple application: counting cells and particles.

A commercialized lab-on-a-chip performs detection of rare cell targets such as chronic myeloid leukemia by labeling of CD4 white blood cells (figure 1.17) [20]. A microfluidic channel network system with automated sample staining units has been used for flow cytometric assays of protein expressions and apoptosis in human primary cells [21]. Enumerating leukocytes by flow cytometry is performed routinely for diagnostic purposes, e.g. CD4 + T-lymphocyte counts are essential for detection of HIV [22] and malaria [23]. A single-layer planar on-chip flow cytometer with 3D hydrodynamic focusing integrated with a laser induced fluorescence detection system performs detection of particles equivalent in size to human CD4+ T lymphocytes at high-throughput (>1700 cells s-1) (figure 1.17) [24].

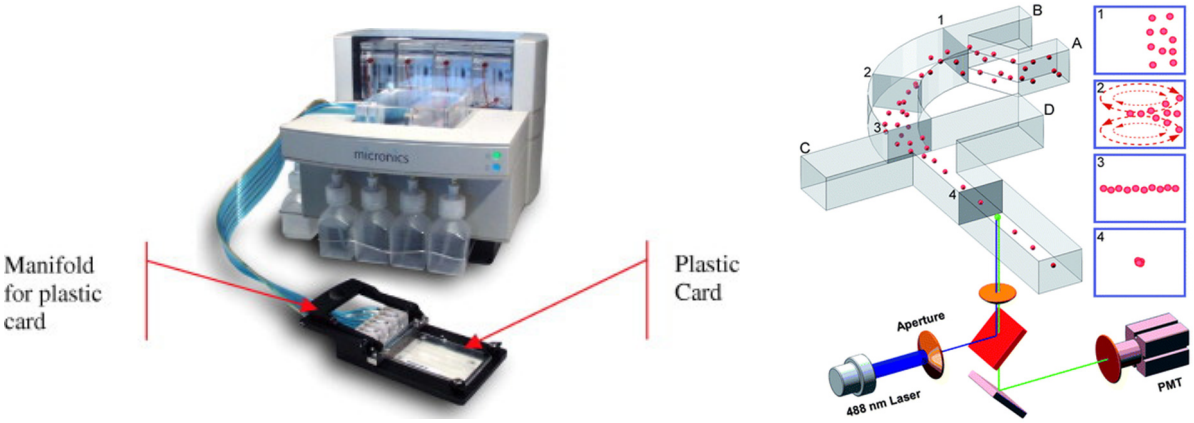

Figure 1.17. *Left: Micronics' microFlow commercial system* [20]*. Right: Schematic of the laser induced fluorescence device setup and 3D hydrodynamic focusing microfluidic drifting mechanism for detection of CD4+* [24] .

Blood analyses requirements are fulfilled by an integrated device constructed from multiple layers of plastic laminates [25]. A whole blood sample is injected and separated into different flow chambers to pretreat different subpopulations of blood, first extracting hemoglobin from lysed red blood cells, to later perform optical counting of red blood cells (6-8µm diameter). There are also studies of enumeration of blood cells using a sheath-free transport system [26]. Viruses can also be rapidly enumerated (approximately in 1 hour) [27].

In his review of the state-of-the-art of Biological Micro-Electro-Mechanical Systems (BioMEMS), Rashid Bashir [28], comments the existing synergy between BioMEMS and optical detection, stating that this one is the most common used detection technique in biology and life sciences. One of the challenges for optical detection biochips is the integration of miniaturized detectors, requiring the fabrication of photo-diodes in silicon substrates or the heterogeneous integration of compound semiconductor LEDs and photodetectors within plastic or polymer platforms. As an example, DNA detection in nano-liter size samples was achieved using a device with integrated fluidic channels, heaters, temperature sensors and on-chip fluorescence detectors (figure 1.18) [29].

G.Minas, J.S. Martins, J.C Ribeiro and others, presented a bio-system for measuring uric acid concentration in serum, plasma or urine, based on the detection of the optical absorption of the uric acid at different concentrations. The optical detector was fabricated through a CMOS standard process and consisted of a set of photodiodes and the readout electronics. A self-designed polystyrene die to

contain the sample was assembled to the CMOS detectors die (figure 1.19) [30]. No optics was used to improve the sensitivity of the system.

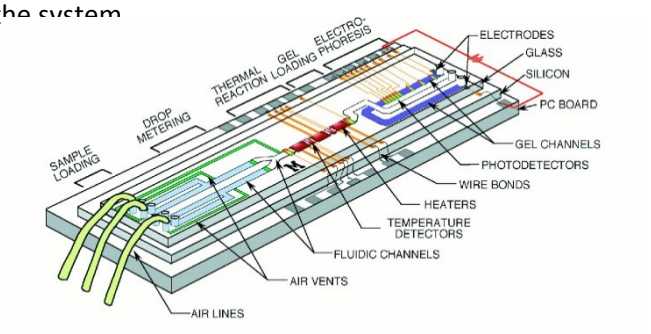

Figure 1.18. *Scheme for a DNA detection integrated device with two liquid samples and electrophoresis gel present. Excitation light source and processing electronics are not fabricated on the silicon substrate* [29].

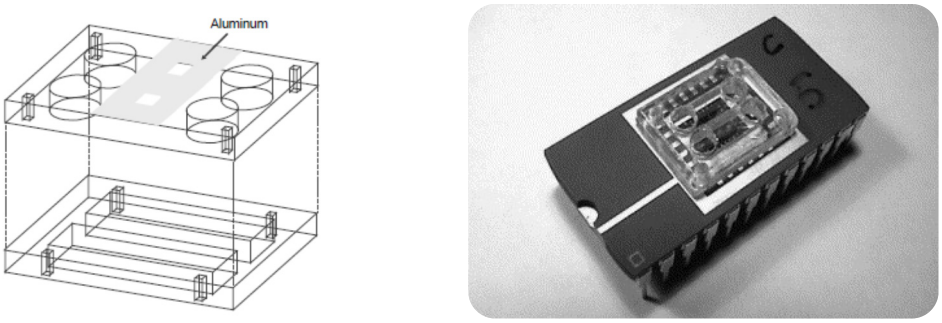

Figure 1.19. *Packaged bio-system composed of two dies: one contains the microchannels to carry chemical reagents and samples (schematic of the polystyrene die on the left side), and the other contains the uric acid concentration detection system based on CMOS detectors* [30].

Sang Uk Son, Yo Han Choi and Seung S. Lee [31] fabricated a micro-cell counter using a boron diffused resistor (BDR) with a photoconductive property at near infrared wavelength, which changed its resistance every time a particle flew through the detection window of a microfluidic channel, shading the illumination it received from an infrared emitting diode (figure 1.20). Authors remark that with this optical detection method, cells remain intact because they are not exposed to an electric field as occurs usually in the impedance spectroscopy method, or attached to fluorescent markers as in the fluorescent detection methods. Experiments with beads from 30 to 100 µm in diameter showed peaks of 8 mV. Reported counting capability is about 7×10^4 events per second.

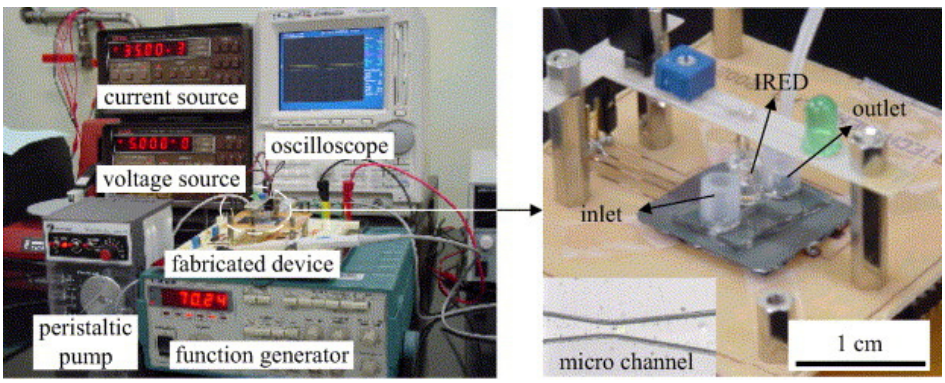

Figure 1.20. *Experimental setup with peripheral equipment and detail of micro-cell counter based on a boron diffused resistor (BDR)* [31].

An optical fiber-based micro-sensor able to detect and count particle food substances by means of light obscuration was fabricated by A.J. Dixon, A.Z. Kouzani and A. Kaynak [32]. They present a compact device with a red laser emitter (655nm), a laser receiver, fiber optic cables, a PDMS microfluidic chip, a microcontroller and the associated electronics and circuitry (figure 1.21). Experiments were conducted on several food substance samples including talcum powder, ground ginger, and soy sauce, most of them with dimensions in the range of 10 to 100µm, and above. It represents an attempt to a total integrated detection device, though robustness is not at its best (fiber optics fragility).

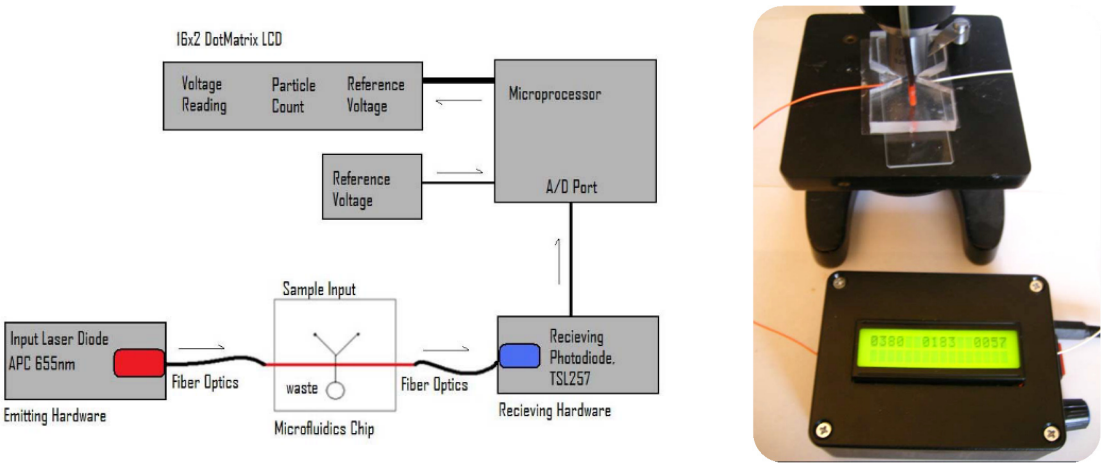

Figure 1.21. *Left: block diagram of the proposed system. Right: complete system including electronics and the PDMS microfludic chip with the optical fibers.*

Another optical detection system using fiber optics but based on fluorescence detection has been developed by n. Hashemi, J.S. Erickson and others, for the characterization of marine algae (dimensions from 1 micron up to hundreds of microns) (figure 1.22) [33]. The authors introduce a new 3D hydrodynamic focusing mechanism consisting of chevron-shaped grooves on the top and bottom of a microchannel. The same hydrodynamic focusing concept was used by the authors in a PDMS microflow cytometer for optical analysis of phytoplankton based on light scatter and fluorescence detection [34].

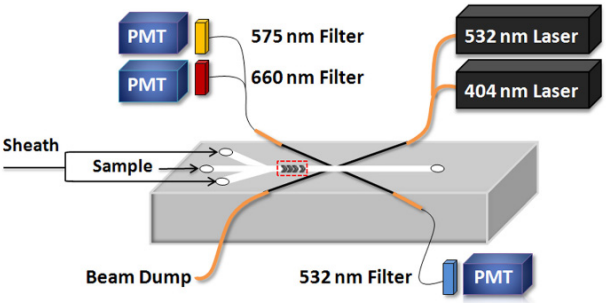

Figure 1.22. *A schematic of the microflow cytometer and the optical and microfluidics setup with lasers, fibers and PMTs* [33].

All the previous references prove that optical detection of particles in microfluidic devices for biosensing applications continues to be a trending topic in research and scientific literature, independently of the method, technique or means employed to achieve results (e.g. optical fibers or optics in combination with light sources and detectors).

1.8.2 Point of view: Fabrication techniques

The “fabrication techniques” approach to optical particle counters and micro flow cytometers also offers quite interesting issues in the scientific and academic literature.

D. Erickson and D. Li [35] discussed about the tendency of integrating microfluidics with electronics and mechanical components onto a single chip substrate. Integration would result in better portability and a decreased reliance on external infrastructure. Scaling down Lab-on-a-Chip devices (LoC) improves the minimization of reagents as well as the reduction in manufacturing costs. Authors review devices for cell handling, sorting and general analysis, such as the micro Coulter particle counter from Gawad et al. for impedance spectroscopy (figure 1.23) [36]. This glass-polymer chip integrates channels and electrodes, and the sample to analyze is introduced into the measurement area via pressure driven flow. Screening rates of 100 samples/s are reported for experiments with latex beads of 5 and 8µm diameter and human erythrocytes (≈6µm).The integrated cell sorter from Fu et al. [37] is also commented. Fabricated through soft-lithography techniques with PDMS, the device incorporates a three valve peristaltic pump. Escherichia coli bacteria was measured in the experimental phase.

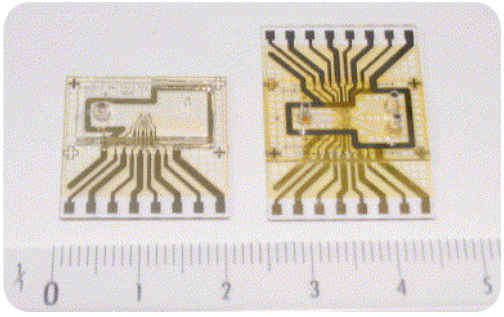

Figure 1.23. *Microfluidic cytological tool, for cell counting and separation, consisting of an integrated microfabricated chip with a PDMS cover and molded fluidic connections* [36].

Erickson and Li also reviewed the integration of optical elements (mainly lenses, waveguides and photodetectors) into microfluidic devices as a requirement to construct a truly portable lab-on-a-chip. They comment for example, the work of Adams et al. [38], who developed a technique for integrating replica molded microchannels with a complementary metal oxide semiconductor (CMOS) imaging chip to create an on-chip adsorption or fluorescence microspectometer in the visible and near-UV wavelength range (figure 1.24). The PDMS device with embedded input and output optical fibers and integrated 2D lenses from Camou et al. [39] increased the sensitivity over a lensless device. Ruano et al. [40] integrated in a sensor device optics and fluidics, describing the necessary microfabrication processes.

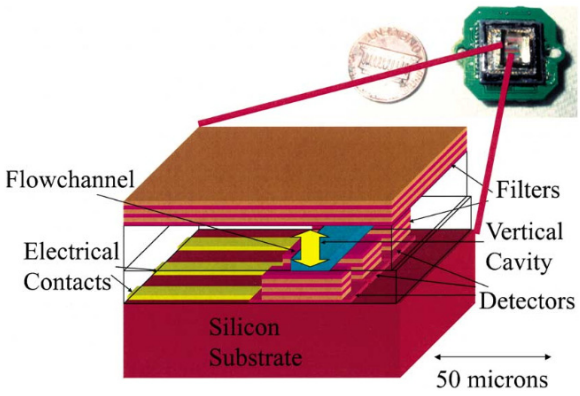

Figure 1.24. *Miniaturization of a spectroscopic measurement system by use of a commercial CMOS imager* [38].

Z. Wang et al. [41] presented a microchip flow cytometer with integrated polymer based optical elements such as waveguides, lenses and fiber-to-waveguide couplers (figure 1.25), fabricated with standard photolithography on SU-8 photoresist. With this design, light from an optical fibre is driven along a waveguide, which ends in an elliptical lens placed in one of the walls of the microfluidic channel. Light is focused on the center of the channel where particles are flowing through, and light is collected by two more waveguides. Three simultaneous signals were measured in the testing with polystyrene beads (from 2.8 to 9.1µm): forward scattering, large angle scattering and extinction. According to the authors, it was the first time that forward scattering and light extinction were measured in a microsystem using integrated optics. However integration was only partially achieved in the microfluidic block, since the light emitting source (HeNe laser - 632.8 nm) and the optical detection block continued to be off-chip. In the same line, we find the recent contribution from the National Oceanography Centre research group at the University of Southampton. Their device is able to analyze the scattered light (collected at two different angles using the optical fibers: 7° for Forward scattering – FSC and 22° for Side scattering -SSC) and fluorescence from tested particles [42].

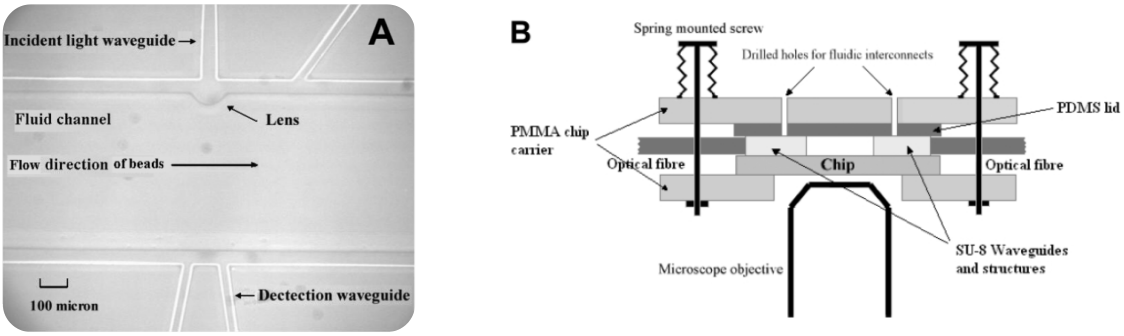

***Figure 1.25**. Left: Microscope images of the polymer optical system at the center of the microchip. Right: Schematic of the chip's packaging* [41].

V. Lien, K. Zhao and Y. Lo depict how a fluidic photonic integrated circuit (FPIC) can enhance the detection sensitivity of fluorescent signals for flow cytometry applications [43]. The device, fabricated in PDMS, includes an array waveguide architecture that provides multiple detection zones for objects flowing through the fluidic channel. Two waveguides near the ends of the channel deliver the optical power for fluorescent excitation while the array of eight waveguide, perpendicular to the fluidic channel, perform the optical interrogation of microbeads with 10µm diameter (figure 1.26).

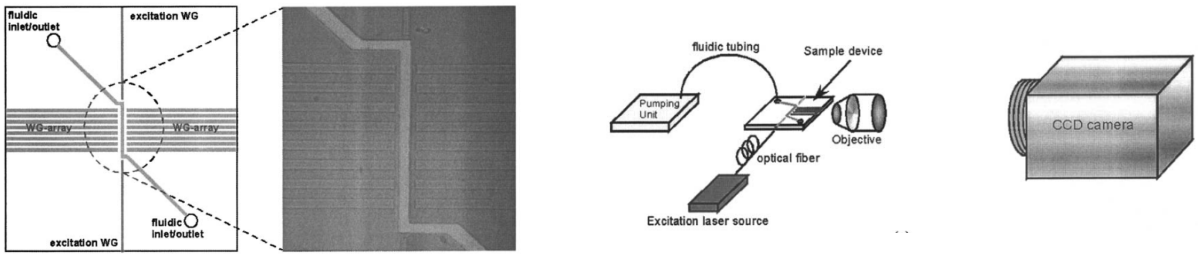

***Figure 1.26.** Illustration and photograph of FPIC. The central fluidic channel and the waveguides are 50µm wide. Experimental setup with off-chip components (laser source and CCD camera)* [43].

A system devoted to optically measure the microfluid velocity by means of integrated waveguides and etched microchannels in glass, was developed by J. McMullin, H. Qiao, S. Goel et al. [44]. With the waveguides, light was carried to certain points in the channel for the detection of fluorescent

microparticles (15µm). Knowing the distance between the detected peaks, which corresponds to the distance between the points of measure, and the time between peaks, determined after processing a recorded video sequence, the velocity of the particles can be easily calculated.

Following with the integration of optical elements with microfluidics, we find the microflow cytometer chip for narrow angle light scattering detection developed by R. Zmijan, D. Spencer, M. Morlew et al. [45] in 2011. The optical detection system consisted of a low Numerical Aperture multimode fibre, a micromachined cylindrical lens and multimode collection fibres. Some grooves were fabricated on the chip to allocate the fibres. The integrated air filled cylindrical micro lens of 150µm radius (figure 1.27), collimates the light from the incident fibre, producing a beam of approximately 34µm FWHM across the channel. External instrumentation was required to drive the microfluidics (peristaltic pumps), to excite the volume sample (laser of 532nm) and to perform detection of the signals (*Hamamatsu PTM*). Polystyrene beads of sizes 10, 15 and 20µm were used for analysis.

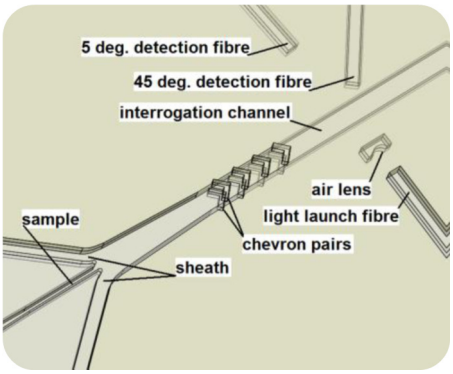

***Figure 1.27**: Schematic view of microflow cytometer chip. The grooves for the optical fibres and the air lens are fabricated on the same substrate than the fluidics* [45].

Optofluidics has also been considered as an alternative to classical optics, for these lenses can modify their optical properties according to the fluid that fills them, adding some versatility to the optical structure. In 2008, S. Hwan, J. Godin, Y. Lo et al. [46] introduced a lab-on-a-chip flow cytometer system integrating microfluidics and photonics (figure 1.28). The system, fabricated by soft lithography techniques, relied on their previous work [47] with fluid-filled two-dimensional on-chip photonic components such as lenses, apertures and slab waveguides for illumination laser beam shaping and optical detection. Again the use of optical fibres was necessary to deliver light into the waveguides of the chip, and the microlenses were planar structures added to the microfluidic chip. There was no integration of a light source. E.Coli and 5µm polystyrene beads were tested.

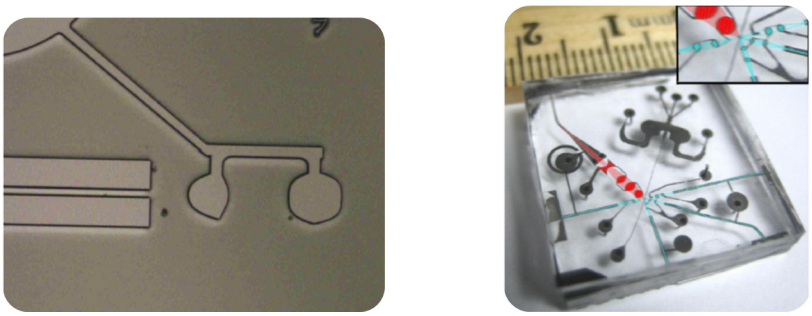

***Figure 1.28.** Left: Images of two-dimensional in-plane optics: custom parabolic optofluidic lenses. Right: Prototype of microfluidic flow cytometer, showing several light lines for incoming and scattered light (in blue) as well as the fluorescence collection line (in red). Each line has two integrated fluidic lenses that are, by fabrication, perfectly aligned to their respective waveguides and to the fluidic channel* [46].

Another attempt to explore the benefits of optofluidics was carried out by M. Rosenauer and Vellekoop [48]. The device included an integrated three-dimensional adjustable optofluidic lens system for forward-scattering/extinction-based measurements (figure 1.29). With optical elements such as polymer (resist/air lens) and fluidic lenses, light was collimated or focused into the microfluidic channel. The single layer microfluidic platform used 3D hydrodynamic sample focusing and incorporated integrated fiber grooves for the insertion of the fibers that connected with the laser light source and the photodiode detectors. These photodetectors were operated by a lock-in-amplifier to improve the sensitivity of the measurements.

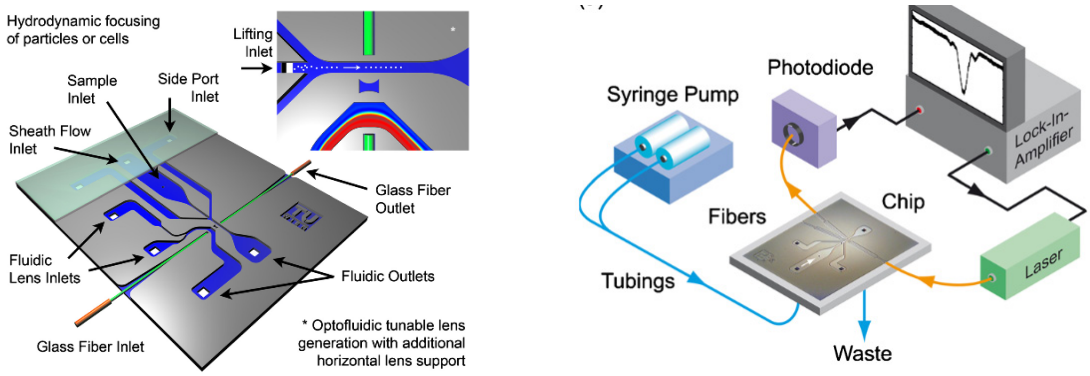

Figure 1.29. *Left: Schematic of the flow cytometric device with an integrated optofluidic lens system to focus the incident light three-dimensionally on cells or particles. Right: Optofluidic measurement setup with standard silicon laser/photodiode and lock-in-amplification. The fluid supply is obtained with infuse/withdraw syringe pumps* [48].

Development in the field of microfluidics has also contributed to deliver more integrated detection systems. In the PDMS microfluidic device from V.Studer, R. Jameson, E. Pellerau et al. [49], the authors introduce active units (mixer, pumps) pneumatically actuated by monolithic soft microvalves (first reported by Unger et al. [50]). Multilayer soft lithography is the technique used for the fabrication. They demonstrate the functionality of their device by sorting 10µm diameter fluorescently tagged objects, such as mammalian cells or beads, randomly distributed in a concentration solution of non-tagged objects. A commercial CCD camera is responsible of the fluorescence optical detection. Six years later, C. Simonnet and A. Groisman [51] introduced their high-throughput and high-resolution flow cytometers based on microfluidic devices made of a single cast of PDMS. Lateral and transverse hydrodynamic focusing allowed to work with a large variety of particles of different shapes and diameters. Throughput rates of 17000 particles/s were obtained with fluorescence detection. For the fabrication of the 3D focusing device they employed a 3 step lithography procedure using two different formulations of SU-8 photoresist (SU-8 2015 and SU-8 2100). In each step, a different level relief was obtained, and consequently the necessary different channel heights for the 3D focalization effect (figure 1.30). Again only the miniaturization of microfluidics was considered, for the excitation light source (488nm argon ion laser) and the detection system (Hamamatsu photomultiplier) were externally connected.

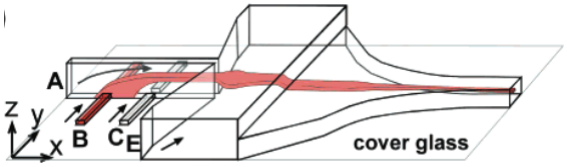

Figure 1.30. *High-throughput device with 3D focusing, fabricated with a 3 step lithography procedure* [52].

L. Cui, T. Zhang and H. Morgan [53] introduced an optical particle detector integrated in a dielectrophoretic lab-on-a-chip for bioparticle counting (figure 1.31). The device included a microfluidic chip to deliver the samples and embedded optical fibers, placed perpendicular to the microfluidic channel at concrete positions thanks to specially etched grooves of 130-150µm wide, to count the particles and measuring their velocities. To insert the optical fibres into the grooves and to align them, a microscope was used. Two optical detection methods were possible: light scattering and fluorescence emission. Laser diodes emitting at 635nm were the excitation light sources. Though measurements of 10um and 45um diameter beads were performed, the use of optical fibers was a limitation in terms of portability.

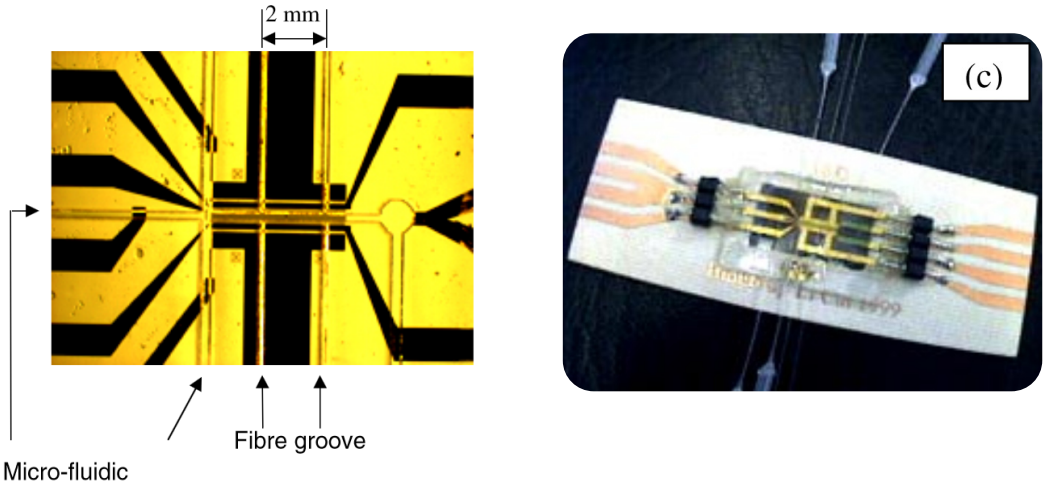

Figure 1.31. *Left: Completed device, comprising the electrode structure, cross-shaped microfluidic channel and parallel grooves for embedding optical fibres. Right: Photographs showing the integrated device with the capillaries for fluid inlets and outlets and two pairs of fibres for particle interrogation* [53].

Fiber optics were also integrated into the micro flow cytometer developed by L. Fu, R. Yang, C. Lin et al. [54] for cell/particle detection (figure 1.32). Instead of the typical hydrodynamic focusing, they employed electrokinetic forces for flow focusing. Fibers were treated with a buffered oxide etchant (BOE) solution to reduce their diameter, and once they were inserted into the etched guides of the fluidic microchip, they were fixed with UV-sensitive glues. Experiments with red blood for cell counting and sorting were satisfactory.

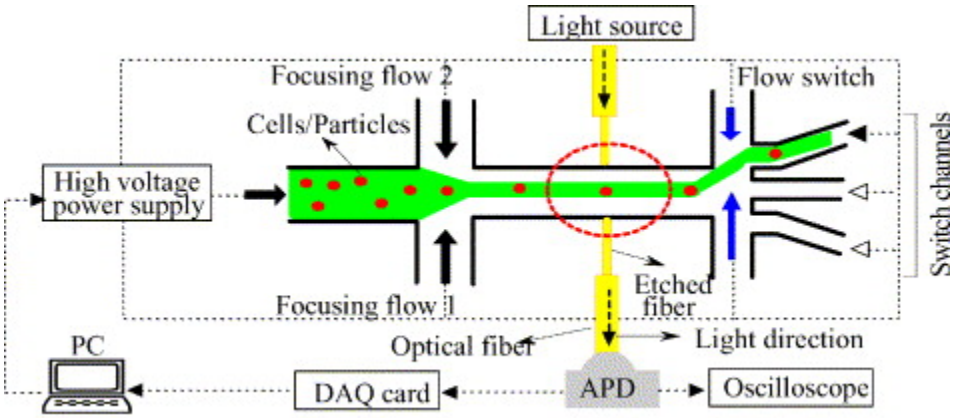

Figure 1.32. *Schematic representation of experimental setup for the micro flow cytometer. Etched optical fibers are used to bring excitation and detected light to the points of interest* [54].

The use of fiber optics is exploited once more in the miniaturized fluorescence excitation platform developed by H. Yang, C.Lee and F. Chang, but this time, besides the etching of V-grooves in the silicon wafer to align the fiber, the lattice plane (111) becomes a reflective micro-mirror added at the end of the fiber to transmit the light to a microchannel placed on the top (figure 1.33) [55].

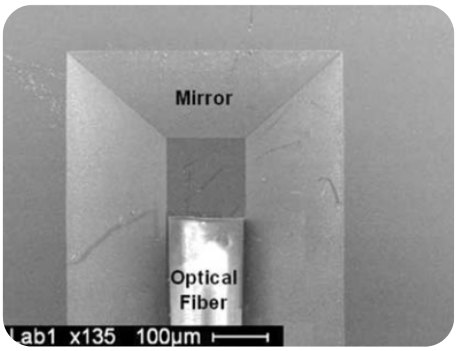

Figure 1.33. *Optical fiber inserted in silicon V-groove. Mirror at the end of the fiber transmits light to the microchannel* [55].

As a summarize of the different technologies reviewed up to now, B. Kuswandi, Nuriman, J. Huskens et al. [56] propose a classification for the two existing approaches in optical sensing systems for microfluidic devices: the off-chip and the on-chip. Authors also describe their progress and applications.

The off-chip approach deals with the coupling of macro-scale detection elements into micron-sized detection areas, for several applications (e.g. absorbance, fluorescence and chemiluminiscence). Highlights of off-chip systems are the low levels of background signal and the high photon sensitive detection offered by devices such as PhotoMultipliers Tubes (PMTs), suitable for single-point detection, and Charged-Coupled Devices (CCD), resulting in very low detection limits.

As for off-chip light sources, several can be used according to the sensing application. For example, in fluorescence detection, lasers offer coherence and low divergence in their light beams, which makes them very convenient to focus on small detection volumes and to obtain high irradiation. Multiple simultaneous laser fluorescence detection can be achieved by using a cylindrical lens to form a laser line suitable to excite a set of the parallel channels [57] (figure 1.34, left). Lamp-based excitation systems surpass the limitation of lasers in terms of available wavelengths. LEDs are effective light sources with compact dimensions requiring low-power driving currents. Therefore, LED-induced fluorescence detection has been reported [58], combining a LED with an optical fiber, without focusing optics (figure 1.34, right). However, due to the broad emission spectra of LEDs, filters are necessary.

In the off-chip approach, the use of optical fibers in optical detection systems, to transport and collect light, is very common. Incorporating optical fibers into the microchip simplifies the detection system, minimizing the number of optical components since focusing becomes unnecessary [59]. On the other hand, optical fibers present some disadvantages when the aim is to achieve miniaturized, portable and robust systems, for the fragility of optical fibers is indeed a critical point.

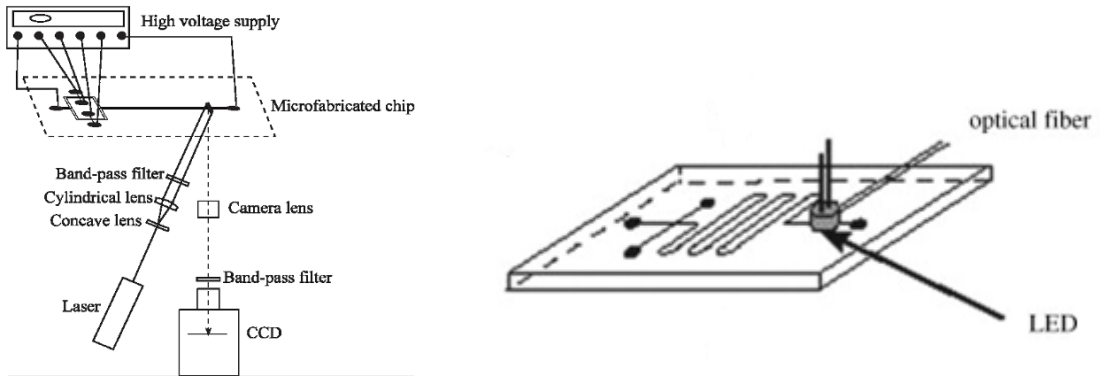

Figure 1.34. *Left: Schematic drawing of the instrumentation setup for the LIF system. With a cylindrical lens, laser beam is focused into a line across the array of microfluidic channels. Excited fluorescence is collected by a CCD camera* [57]*. Right: PDMS microchannel chip incorporating the LED and optical fiber* [58]*.*

In relation with the off-chip approach, even hybrid integration technologies have also been under discussion as opposite to monolithic integration, for they offer interesting advantages [60]. The counting and sorting flow cytometry system presented by S.Yang, S.Hsiung, Y. Hung et al. [61] includes a micromachined flow cytometer device, an optical detection system based on commercial components (solid-state laser diode, collimation lenses, filters and an Avalanche PhotoDiode APD) and a data analysis and control system (figure 1.35). The flow cytometer device, fabricated by means of MEMS technology, integrates serpentine-shaped micro pneumatic pumps (for the hydrodynamic focusing) and valves forming a micro switch block (for cell collection). To hold the micromachined flow cytometer and to align the laser beam with the centre of the sample flow channel a chip holder was used. Optical detection and collection of human lung cells labeled with fluorescent dyes is demonstrated. This portable system of reasonable dimensions and weight, offers also a real-time image of the measurement process thanks to a commercial CCD camera and a LCD panel. Though it can be considered a successful attempt to develop a portable system based on hybrid integration techniques, still the level of integration and miniaturization could be improved for the optical detection block.

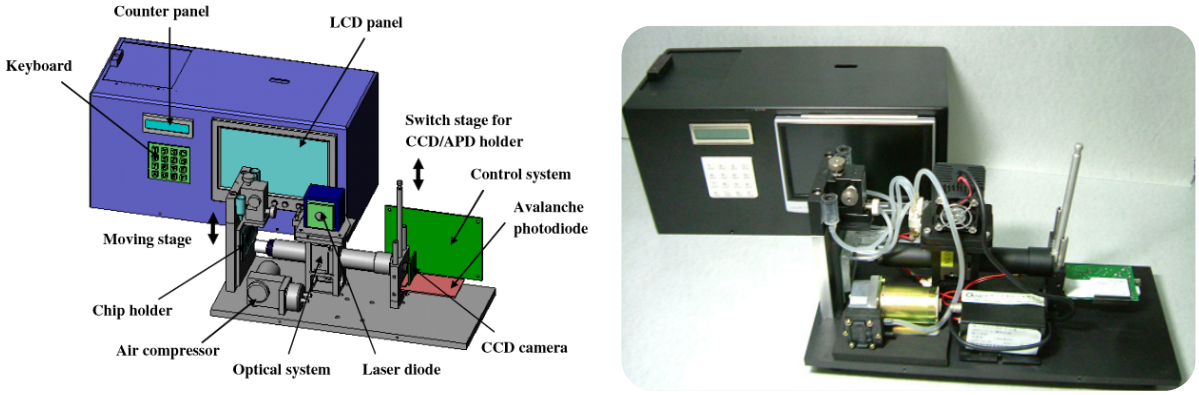

Figure 1.35. *Schematic illustration of the components used to construct the integrated flow cytometer system and photograph of the implemented device* [61].

As for the on-chip approach, the goal is not only the integration of optical components in a microfluidic platform, but also electrical, mechanical and other types of elements. MicroElectroMechanical systems (MEMS) are the demonstration of the integration of mechanical and electrical functionalities into small structures, and is especially interesting the branch directed to the development of Micro-Optical

technologies (MOEMS) with the purpose of replacing macroscopic optical systems.

Combination of complementary metal oxide semiconductor (CMOS) photodetector imaging devices, some of them including Analog to Digital Converters (ADC) to provide a bitstream output proportional to the detected light intensity, with microfluidic chips has been already reported [38]. Integrated optical waveguide technology has been used for the fabrication of miniaturized optical detection systems for sensing in microchannels, along with other assembled components to create higher integrated devices (figure 1.36, left) [62]. Microlenses and planar waveguides have also been integrated in microfluidic devices to improve the detection in fluorescence measurements, for example, focusing the light into channels to increase the excitation power. An array of planar microlenses has been used to focus the light from a LED into a microfludic channel (figure 1.36, right) [63]. Diffraction gratings have been fabricated in waveguides to facilitate the couple-in and couple-out of the light signals [64].

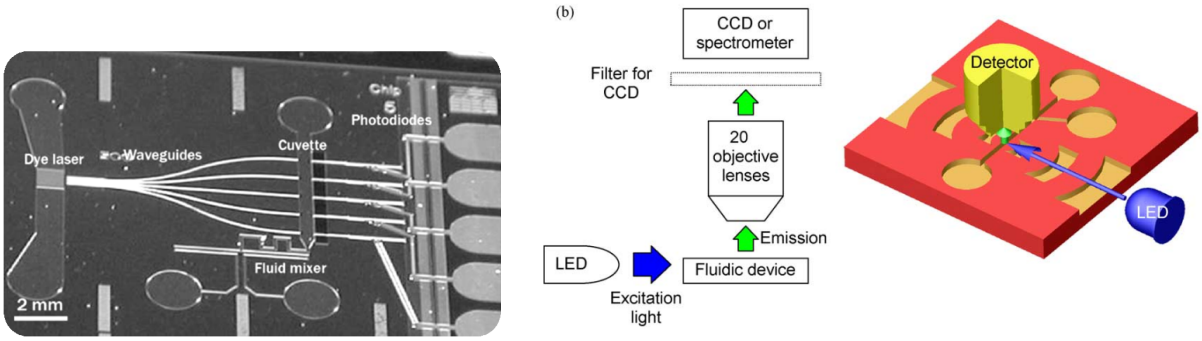

Figure 1.36. *Left: Photograph of the lab-on-chip device with integrated micro-fluidic dye laser, optical waveguides, microfluidic network and photodiodes* [62]. *Right: Disposable integrated microfluidic devices with self-aligned planar microlenses. LED is used as a light source* [63] .

Organic LEDs (OLEDs) have been under study to replace LEDs because of their flat film-like shape which makes them easy to incorporate into microfluidic devices and in close proximity of the channels. Vertical Cavity surface Emitting Lasers (VCSELs) have been monolithically integrated for near-infrared fluorescence measurements. In fact, the semiconductor fluorescence sensor for microfluidic applications developed by E. Trush, O. Levi, L.J. Cook and others (figure 1.37) [65] integrates on a GaAs substrate, a vertical-cavity-surface-emitting laser (VCSEL), PIN photodetectors and optical emission filters. Fluorescence detection of IRDye 800 Phosphoramidite were limited at 250nM due to the laser background levels affecting the sensor sensitivity.

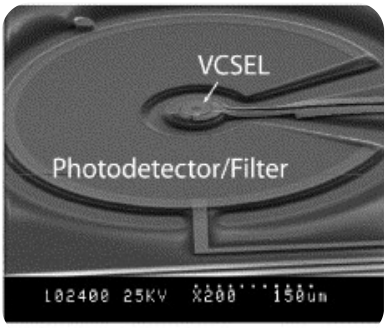

Figure 1.37.*SEM image of the sensor's optoelectronic components(VCSEL, photodetector and emission filter)* [65].

Half way through the off-chip and the on-chip approach, J. Krüger, K. Singh, Al O'Neil and others described the development towards a miniaturized analytical system with functionalities similar to the ones of a flow cytometer [66]. Their low-cost portable instrument was keen to point-of-care diagnosis. Two different blocks were designed, a disposable microfluidic block and an on-chip optical detector block, though finally only the first one was fabricated with rapid prototyping technologies, and tested (figure 1.38). During the experimental setup for fluorescent measurements, the integrated light source (die of LEDs or 635nm laser diodes) of the optical detector block was replaced with an off-chip commercial laser diode. Avalanche Photodiodes (APD) were the optical detectors and flip-chip technique was used to bond them directly over the sorting microchannel. In the microfluidic chip, a leaky waveguide was included, and a micro-prism was used to couple in the light of the laser diode. Testing were performed with 6µm diameter fluorescent beads, and throughput rates of 200 beads/min were achieved. This work represents an example of the feasibility of hybrid integrating optical and solid-state components as part of an on-chip detection system.

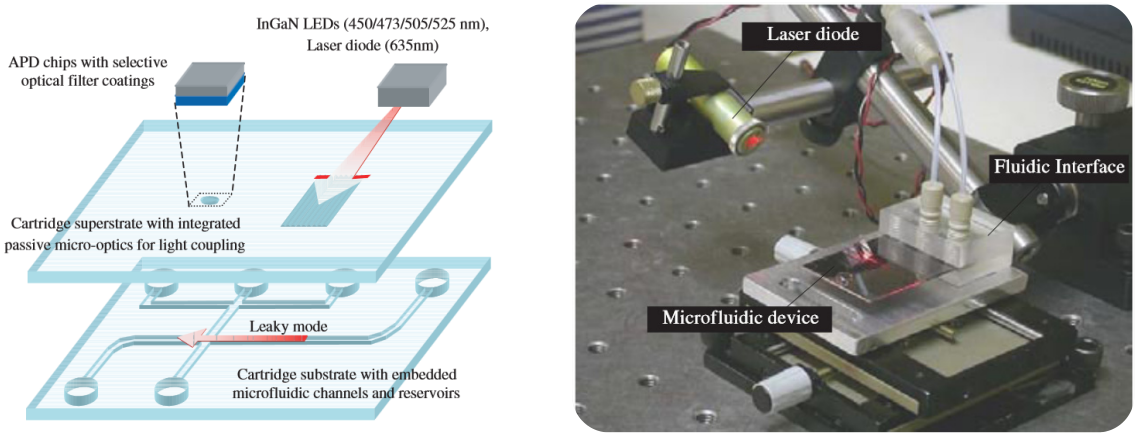

Figure 1.38. *Left: Schematic diagram of microfluidic cartridge and micro-optical fluorescence detection system. Right: The cell sorter chip sits in a plug-in mount, which interfaces microfluidic disposables with external samples. A semiconductor laser excites a high intensity leaky waveguide mode directly in the fluidic channel using prism coupling. Optical detector block, not included* [66].

To conclude, after reviewing the previous references, we can assert that, from the point of view of fabrication, integration of components in all levels (optics, microfluidics, electronics and mechanics) and miniaturization of devices are considered trending topics. With the aim of delivering systems with small dimensions, the field of optical particle counting and characterization applications is in continuous evolution.

The work presented in this thesis is more oriented towards the off-chip approach, though in some aspects, in particular the ones related to Micro-Optical technologies (MOEMS), takes advantage of the benefits offered by the on-chip approach in the field of integration and miniaturization of robust and portable systems.

Anyway, in spite of our proposal for the implementation of a ***"miniaturized, with on chip lenses and integrated light sources, portable, robust, low cost, with acceptable perfomance paramters (i.e. sensitivity and throughput), suitable for point of care testing"*** optical detection system, which discards the use of optical fibers, we can not underestimate the importance of this sort of setups for optical particle counting, detection and fluorescence measurements. Previous references confirm that

a large number of research groups still continue to develop systems based on that methodology, and in fact, we have also explored that possibility in some other works [67], fabricating PDMS devices and testing them with fluorescein dissolutions at different concentrations and particles in the range of 10 to 30µm diameter (figure 1.39).

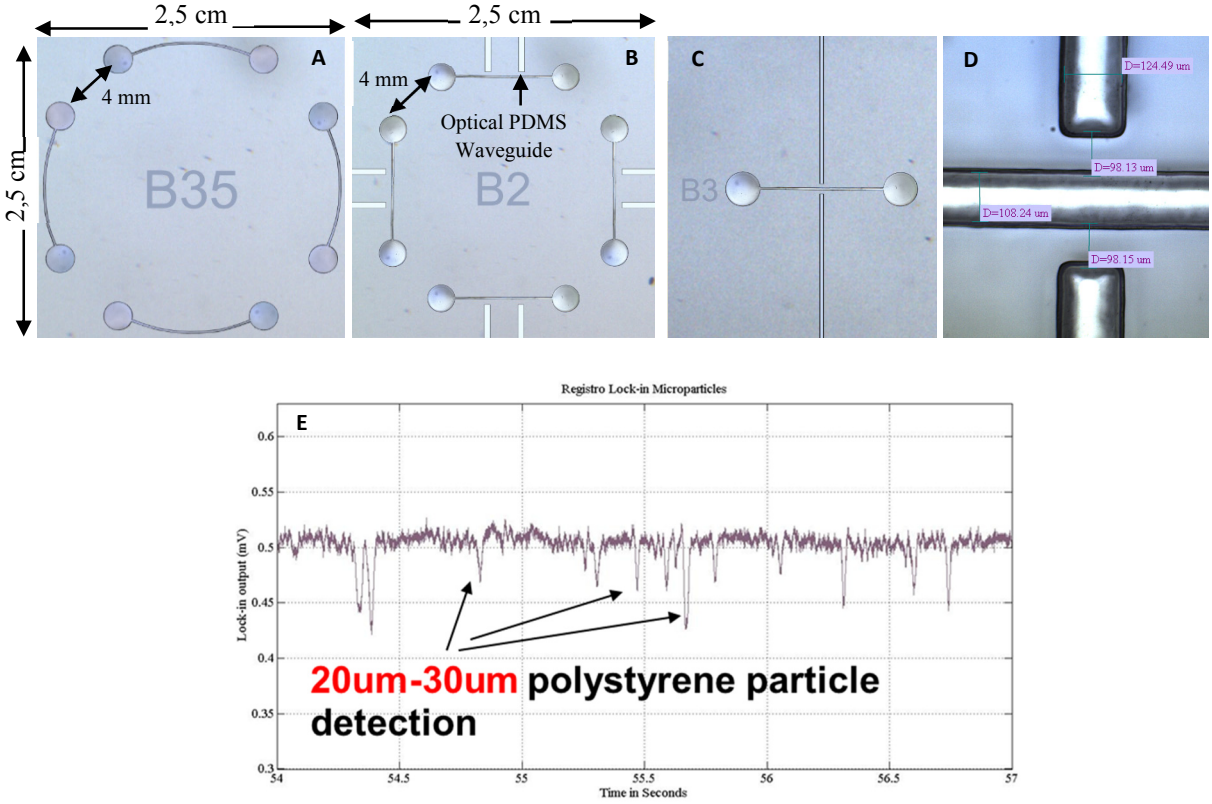

Figure 1.39. *Systems based on optical fibers for excitement and detection. (A and b) Microfluidic chips for detection of fluorescein solutions. (C and d) Microfluidic chips for particle detection. (E) Detection of microparticles achieved with the optical fiber based microfluidic chips* [67].

References

[1] R. XU, Particle Characterization:Light Scattering Methods, Miami, U.S.A: Kluwer Academic Publishers, 2002.

[2] S. Thorslund, R. Larsson, J. Bergquist, F. Nikolajeff and J. Sanchez, "A PDMS-based disposable microfluidic sensor for CD4+ lymphocyte counting," *Biomed Microdevices ,* Issue 10, p. 851–857, 2008.

[3] E. Hackley and T. J. V. A., Handbook on Ultrasonic and Dielectric Characterization Techniques for Suspended Particulates, Westerville: The American Ceramic Society, 1998.

[4] A. S. Dukhin and P. J. Goetz, Acoustic and Electroacoustic Spectroscopy, Langmuir, 1996.

[5] R. Pecora, "Doppler Shifts in Light Scattering from Pure Liquid and Polymer Solutions," *J. Chem. Phys.,* Issue 40, 1964.

[6] "Particle Size Analysis-Photon Correlation Spectroscopy," *International Organization for Standardization (ISO),* p. Geneve, 1996.

[7] R. Finsy, "Particle Sizing by Quasi-elastic Light Scattering," *Adv. Coll. Inter. Sci,* Issue 52, 1994.

[8] Whytlaw-Gray and P. H. S. R., "The Scattering of Light by Individual Particles in Smoke," *Proc. Roy. Soc. London Ser. A.,* Issue 113, 1926.

[9] P. Artaxo, "The Microanalysis of Individual Atmospheric Aerosol Particles by Electron, Proton and Laser Microprobe," *Proc. 2nd World Congress Part. Technol., Kyoto,* 1990.

[10] F. Raes and A. Plomp, "Comparison of Two Condensation Nucleus Counters," *J. Aerosol Sci.,,* 1983.

[11] W. Winkelmayr, G. P. Reischl, A. O. Linder and A. Berner, "A New Electromobility Spectrometer for the Measurement of Aerosol Size Distribution in the Size Range from 1 to 1000 nm," *J. Aerosol Sci.,* 1991.

[12] J. De La Mora, L. De Juan, T. Eichler and Rosell, "Differential Mobility Analysis of Molecular Ions and Nanometer Particles," *Trends Anal. Chem,* 1998.

[13] T. Möller, "Confocal Laser Scanning Microscopy and its Application in Liposomal Research," *Particle and Surface Characterization Methods,* 1997.

[14] H. Shik and R. C. Dunn, "Near-field Scanning Optical Microscopy," *Anal. Chem.,* Issue 71, 1999.

[15] W. C. McCrone and J. G. Delly, "The Particle Atlas Electronic Edition," 1992.

[16] C. S. Vokram, "Particle Field Holography," 1992.

[17] R. Menzel and F. M. Shofner, "An Investigation of Fraunhofer Holography for Velocity Applications," *Appl. Opt,* Issue 9, 1970.

[18] J. P. M. Syvitski, Principles, Methods and Application of Particle Size Analysis, Cambridge University Press, 2007.

[19] K. T. D. Chung and H. Chan, “Recent advances in miniaturized microfluidic flow cytometry for clinical use,” *Electrophoresis-journal,* pp. 4511-4520, 2007.

[20] C. Lancaster, M. Kokoris, M. Nabavi and a. others, “Rare cancer cell analyzer for whole blood applications: Microcytometer cell counting and sorting subcircuits,” vol. 37, pp. 120-127, 2005.

[21] S. Chan, G. Luedke, M. Valer and a. others, *Cytometry A,* vol. 55A, pp. 119-125, 2003.

[22] B. Brando, D. Barnett, G. Janossy and a. others, “Cytometry B Clin. Cytom.,” vol. 42, pp. 327-346, 2000.

[23] T. Hanscheid, “Clin. Lab. Haematol,” vol. 21, pp. 235-245, 1999.

[24] X. Mao, S.-C. S. Lin, C. Dong and T. J. Huang, “Single-layer planar on-chip flow cytometer using microfluidic drifting based three-dimensional (3D) hydrodynamic focusing.,” *Lab on a Chip,* vol. 9, pp. 1583-1589, 2009.

[25] B. Weigl, R. Bardell, T. Schulte and a. o. , “Biomed. Microdevices,” vol. 3, pp. 267-274, 2001.

[26] E. Altendorf, D. Zebert, M. Holl and a. others, “Transducers 97,” 1997.

[27] M. Ferris, M. McCabe, L. Doan and a. others, “Anal. Chem.,” vol. 74, pp. 1849-1856, 2002.

[28] R. Bashir, “BioMEMS: state-of-the-art in detection, opportunities and prospects,” *Advanced DRUG DELIVERY Reviews,* pp. 1565-1586, 2004.

[29] M. Burns, B. Johnson, S. Brahmasandra, K. Handique and a. others, “Integrated manoliter DNA analysis device.,” *Science,* vol. 282, pp. 484-487, 1998.

[30] G. Minas, J. Martins, J. Ribeiro, R. Wolffenbuttel and J. Correia, “Biological microsystem for measuring uric acid in biological fluids,” *Sensors and Actuators A: Physical,* vol. 110, Issue 1-3, 2004.

[31] S. U. Son, Y. H. Choi and S. S. Lee, “Micro-cell counter using photoconductance of boron diffused resistor (BDR),” *Sensors and Actuators A: Physical,* vol. 111, Issue 1, pp. 100-106, 2004.

[32] A. J. Dixon, A. Z. Kouzani, A. Kaynak and B. A. Sexton, “Optical microsensor for counting food substance particles in lab-on-a-chips,” in *in Proceedings of the IEEE International Conference on Systems, Man and Cybernetics, IEEE*, New York, N. Y., 2009.

[33] N. Hashemi, J. S. Erickson, J. P. Golden and F. S. Ligler, “Optofluidic characterization of marine algae using a microflow cytometer,” *Biomicrofluidics,* Issue 5, 2011.

[34] N. Hashemi, J. S. Erickson, J. P. Golden, K. M. Jackson and F. S. Ligler, “Microflow Cytometer for optical analysis of phytoplankton,” *Biosensors and Bioelectronics,* vol. 26, Issue 11, pp. 4263-4269, 2011.

[35] D. Erickson and D. Li, “Integrated microfluidic devices,” *Analytica Chimica Acta,* vol. 507, Issue 1, pp. 11-26, 2004.

[36] S. Gawad, L. Schildb and P. Renauda, “Micromachined impedance spectroscopy flow cytometer for cell analysis and particle sizing,” *Lab Chip,* Issue 1, pp. 76-82, 2001.

[37] A. Y. Fu, H.-P. Chou, C. Spence, F. H. Arnold and S. R. Quake, “An Integrated Microfabricated Cell Sorter,” *Anal. Chem.,* vol. 11, Issue 74, p. 2451–2457, 2002.

[38] M. L. Adams, M. Enzelberger, S. Quake and A. Scherer, "Microfluidic integration on detector arrays for absorption and fluorescence micro-spectrometers.," *Sensors and Actuators, A: Physical,* vol. 104, Issue 1, pp. 25-31, 2003.

[39] S. Camou, H. Fujita and T. Fujiia, "PDMS 2D optical lens integrated with microfluidic channels: principle and characterization," *Lab Chip, 2003,* vol. 3, pp. 40-45, 2003.

[40] J. Ruano, A. Glidle, A. Cleary, A. Walmsley, J. Aitchison and J. Cooper, "Design and fabrication of a silica on silicon integrated optical biochip as a fluorescence microarray platform," *Biosensors and Bioelectronics,* vol. 18, Issue 2, pp. 175-184, 2003.

[41] Z. Wang, J. El-Ali, M. Engelund, T. Gotsæd, I. R. Perch-Nielsen, K. B. Mogensen, D. Snakenborg, J. P. Kutter and A. Wolff, "Measurements of scattered light on a microchip flow cytometer with integrated polymer based optical elements," *Lab Chip,,* vol. 4, pp. 372-377, 2004.

[42] D. Barat, G. Benazzi, M. C. Mowlem, J. M. Ruano and H. Morgan, "Design, simulation and characterisation of integrated optics for a microfabricated flow cytometer," *Optics Communications,* vol. 283, Issue 9, 2010.

[43] V. Lien, K. Zhao and Y.-H. Lo, "Fluidic photonic integrated circuit for in-line detection," *Appl. Phys. Lett.,* Issue 87, 2005.

[44] J. N. McMullin, H. Qiao, S. Goel, C. L. Ren and D. Li, "Integrated optical measurement of microfluid velocity," *J. Micromech. Microeng. ,* Issue 15, 2005.

[45] R. Zmijan, D. C. Spencer, M. C. Mowlem and H. Morgan, "DIFFERENTIATION OF MICRO SPHERES BY NARROW ANGLE SCATTERED LIGHT DETECTION ON LOW COST PMMA MICRO FLOW CYTOMETER CHIP," in *15th International Conference on Miniaturized Systems for Chemistry and Life Sciences* , Seattle, Washington, USA, 2011.

[46] S. H. Choa, J. Godin, C. H. Chen, F. S. Tsai and Y.-H. Lo, "Microfluidic Photonic Integrated Circuits," *Optoelectron Mater Devices. ,* 2008.

[47] J. Godin, V. Lien and Y.-H. Lo, "Demonstration of two-dimensional fluidic lens for integration into microfluidic flow cytometers," *Applied physics letters,* Issue 86, 2006.

[48] M. Rosenauer and M. J. Vellekoop, "Characterization of a microflow cytometer with an integrated three-dimensional optofluidic lens system," *Biomicrofluidics,* Issue 4, 2010.

[49] V. Studer, R. Jameson, E. Pellereau, A. Pépin and Y. Chen, "A microfluidic mammalian cell sorter based on fluorescence detection," *Microelectronic Engineering,* vol. 73–74, pp. 852-857, 2004.

[50] M. A. Unger, H. Chou, T. T. A. Scherer and S. R. Quake, "Monolithic microfabricated valves and pumps by multilayer soft lithography," *Science,* Issue 288, pp. 113-116, 2000.

[51] C. Simonnet and A. Groisman, "High-Throughput and High-Resolution Flow Cytometry in Molded Microfluidic Devices," *Anal. Chem., 2006,* vol. 78, Issue 16, p. 5653–5663, 2006.

[52] C. S. Groisman, "High-Throughput and High-Resolution Flow Cytometry in Molded Microfluidic Devices," *Analytical Chemistry,* vol. 78, Issue 16, pp. 5653-5663, 2006.

[53] L. Cui, T. Zhang and H. Morgan, “Optical particle detection integrated in a dielectrophoretic lab-on-a-chip,” *Journal of Micromechanics and Microengineering,* vol. 12 (2002), pp. 7-12, 2001.

[54] L.-M. Fu, R.-J. Yang, C.-H. Lin, Y.-J. Pan and G.-B. Lee, “Electrokinetically driven micro flow cytometers with integrated fiber optics for on-line cell/particle detection,” *Analytica Chimica Acta,* vol. 507, Issue 1, 2004.

[55] H. Yang, C.-T. Lee and F.-Y. Chang, “Miniaturized fluorescence excitation platform with optical fiber for bio-detection chips,” *Microsystem Technologies,* vol. 13, Issue 11-12, pp. 1623-1628 , 2007.

[56] B. Kuswandi, Nuriman, J. Huskens and W. Verboom, “Optical sensing systems for microfluidic devices: A review,” *Analytica Chimica Acta,* vol. 601, Issue 2, 2007.

[57] Z. Shen, X. Liu, Z. Long and D. Liu, “Parallel analysis of biomolecules on a microfabricated capillary array chip,” 2006.

[58] K. Miyaki, Y. Guo, T. Shimosaka and T. Nakagama, “Fabrication of an integrated PDMS microchip incorporating an LED-induced fluorescence device,” *Analytical and Bioanalytical Chemistry ,* vol. 382, Issue 3, 2005.

[59] H.-F. Li, J.-M. Lin, R.-G. Su, K. Uchiyama and T. Hobo, “A compactly integrated laser-induced fluorescence detector for microchip electrophoresis,” 2004.

[60] I. R. Dr., S. Cova, A. Restelli, M. Ghioni and M. Chiari, “Microchips and single-photon avalanche diodes for DNA separation with high sensitivity,” *ELECTROPHORESIS. Special Issue: DNA SEQUENCING AND GENOTYPING,* vol. 27, Issue 19, 2006.

[61] S.-Y. Yang, S.-K. Hsiung, Y.-C. Hung, C.-M. Chang, T.-L. Liao and G.-B. Lee, “A cell counting/sorting system incorporated with a microfabricated flow cytometer chip,” *Meas. Sci. Technol. ,* Issue 17, 2006.

[62] S. Balslev, A. M. Jorgensen, B. Bilenberg, K. B. Mogensen and e. others, “Lab-on-a-chip with integrated optical transducers,” *Lab Chip, 2006,* Issue 6, pp. 213-217, 2006.

[63] J. Seo and L. P. Lee, “Disposable integrated microfluidics with self-aligned planar microlenses,” *Sensors and Actuators B ,* vol. 99, 2004.

[64] O. Hofmann, G. Voirin, P. Niedermann and A. Manz, “Three-Dimensional Microfluidic Confinement for Efficient Sample Delivery to Biosensor Surfaces. Application to Immunoassays on Planar Optical Waveguides,” *Anal. Chem., 2002,* vol. 74, Issue 20, 2002.

[65] E. Thrush, O. Levi, L. J. Cook, J. Deich, A. Kurtz, S. J. Smith, W. Moerner and J. S. H. Jr., “Monolithically integrated semiconductor fluorescence sensor for microfluidic applications,” *Sensors and Actuators B: Chemical,* vol. 105, Issue 2, 2005.

[66] J. Krüger, K. Singh, A. O'Neill, C. J. A. Morrison and P. O'Brien, “Development of a microfluidic device for fluorescence activated cell sorting,” *Journal of Micromechanics and Microengineering ,* vol. 12, Issue 4, 2002.

[67] K. L. González, “Polymer Technologies for Microoptical Devices and OptoFluidic Applications,” *Master Thesis; University of Barcelona,* vol. Supervised by Mauricio Moreno and Ivan Bernat, 2010.

CHAPTER II: CONCEPTION OF THE SYSTEM

2.1 Summary

After reviewing the contributions commented on previous chapter “Introduction”, it is clear that, nowadays, there is an actual need for particle counting methods, technologies and instrumentation, which spans a wide range of fields.

Controlling and monitoring the concentration of particles is a fundamental task in many situations, for example, to avoid the harmful effects to human health of high concentration of particles in ambient air, or to provide supplies of unpolluted water for agriculture and human consumption. Even in industry, particle detection plays an important role, for example, ensuring the quality of the production environment in manufacturing processes. In medicine and life sciences, point-of-care testing (POCT) has become essential for fast diagnosis and detection of diseases (e.g. diabetes). Many of the tests require counting the number of cells or molecules found in a sample. Several authors and well-known manufacturers have developed instruments able to perform this cell counting (e.g. Millipore Scepter™), but the measurements are often limited to count, normally based on the Coulter principle, and do not consider the benefits that other alternative technologies, such as optical and fluorescence detection methods, can offer. Optical particle counters (OPC) are devoted to perform counting and also characterization of particles.

In an approach closer to the point-of-care testing conception, the present tendency is to develop portable multifunction systems of reduced dimensions, i.e. systems that are able to perform all the necessary steps involved in an analysis process, integrating the different stages in a single and complete device. The word multifunction here, refers to the ability of a single device to perform several tasks (e.g. detection and sorting), avoiding the need of using single specific devices for each one of those tasks.

Lab on a Chip devices (LoC) and Micro Total Analysis Systems (μTAs) are the perfect example of the present trend. Since 1990 the interest in these kinds of biosensors has increased considerably. These devices perform fast measurements using small sample volumes (μl), providing results with good accuracy. All packaged into single and portable devices with low power consumption and low cost fabrication. The same conceptual methodology can be applied in the design and fabrication of devices for a large number of applications eager to explore the benefits offered by miniaturization and integration.

2.2 Miniaturized devices for optical particle characterization

In the field of optical particle characterization, the widely used flow cytometry technique for analyzing and counting of particles suspended in fluid, is a paradigmatic example. In these systems, a sheath flow encloses the particle sample stream to ensure that only singly aligned particles flowing at high speed enter within a detection window, where optical properties of the particles are analyzed by illuminating the zone with collimated laser beams and measuring the intensity of the scattered light and the fluorescence. In elastic light scattering, the intensity of the scattered light is related with the optical properties of particles and medium, but also depends on the dimension and mass of the particles, the sample concentration, and the observation angle and distance.

Though conventional flow cytometry systems provide rapid and reliable analytical cell sampling capabilities, the systems are bulky and expensive. Their operation usually relies on the need for specialized personnel, complicated pretreatment procedures and a relatively high volume requirement of the cell samples to be analysed [1], [2].

Miniaturized devices able to perform precise analysis are necessary. Micromachined-based flow cytometers combining MEMS and microfluidic techniques are a promising alternative to achieve smaller, simpler, more volume-efficient[1] and less expensive instrumentation. Several types of substrates such as glass, silicon and polymer could be used during fabrication, resulting in lower cost disposable chips. However, complete miniaturization should also comprise other elements of the system, often forgotten, such as micropumps and microvalves for the microfluidic chips and light sources and optical detectors for the excitation/detection stages.

Microfluidic flow cytometers work successfully when integrated with optical detection systems, but these systems also present some weak points that still need to be solved. Commonly, pretreatment steps, such as cell modification using markers, are required. Integration of optical elements should equal the level achieved by microfluidics in order to obtain practical systems for POCT. Optical detection systems are expensive and require precise alignment. In terms of costs, optical equipment is more expensive than electronic equipment.

On the other hand, though electrical detection is attractive in terms of miniaturization, simplicity and cost, it also presents some challenges. The fabrication of electrodes facing each other is a complex process that does not ensure reproducibility in the geometry and the electrode characteristics. The existing electric double layer in electrical measurements, reduces the effect of impedance changes caused by cells when using low frequency or DC input bias. Not to forget that electric microfluidic flow cytometers only provide information about cell size and mobility.

Therefore, in the field of optical flow cytometry, different research lines dedicated to fabricate complete miniaturized systems, with performance values similar to the ones offered by benchtop instruments, are being developed by some groups [2]. In this sense, we find several patents that demonstrate the feasibility of new systems able to perform optical particle detection.

In 2004, Philippe J. Goix and Guava technologies registered an American patent [3] for a method and apparatus devoted to detect microparticles in fluid samples. They presented a device which comprised a capillary flow carrier system to transport the particles to the detection zone, and several possible setups for a laser fluorescence detection system to detect the fluorescence substance tagged to a microparticle. In the graphic designs included in the patent, some interesting conceptual ideas can be found.

In 2007, two more American patents from Honeywell International Inc. introduced innovations in flow cytometry. The first one [4] presented an optical alignment system for aligning a light beam with a core flow in a flow stream. The designed optical element could direct the light beam from a light source to the exact position of the core flow. Even an actuator was designed to move the elements of the system (light source, optical element, flow stream) with the purpose of achieving the alignment between the light beam and the core flow. The patent also included the design of a portable flow

[1] Lower sample volumes requiring less high-cost reagents for analysis.

cytometer which used removable bio-analysis cartridges (figure 2.1). This design is indeed inspiring, for it represents the model of what should become the detection system introduced in this thesis.

In the second patent [5], the author Bernard S. Fritz, described an optical detection system which surpass the limitations of conventional flow cytometers using single light sources to interrogate particles. In these instruments, the light beam is normally focused to an elongated shape, ensuring that variations in particle position due to misalignment and changes in the core stream width, will have the minimum effect in the measurement process. However, single laser configuration does not provide a constant illumination across the flow channel and in consequence, sensitivity and accuracy may vary depending on the lateral position of the particle in the beam. Another limitation refers to the impossibility of directly measuring the velocity of each particle, which is important to estimate the particle size from light scattering signals. The presented system overcomes these disadvantages by means of an optical detection system that uses two or more light sources positioned laterally at different distances from the central axis of a flow stream (figure 2.2). With the appropriate optics, light beams are focused onto a common focal point where detectors are placed.

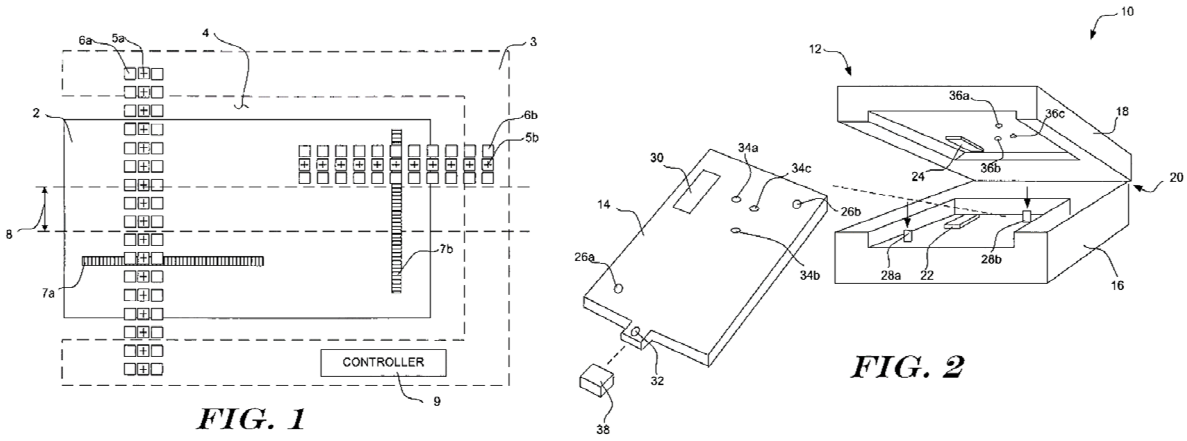

Figure 2.1. *Left: Schematic diagram showing an illustrative embodiment of the invention, including a linear array of sources (5a) and a linear array of detectors (6a). Right: Perspective view of a portable cytometer in accordance with the invention with a removable bio-analysis cartridge* [4].

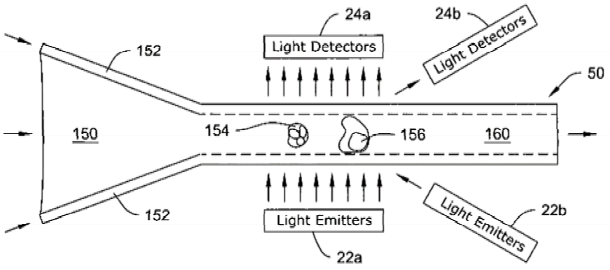

Figure 2.2: *Schematic showing the formation of a flow stream and the position of emitters and detectors* [5].

2.3 Aim of this thesis

After analyzing the academic and scientific literature, some conclusions can be drawn. A reduced number of contributions present a fully integrated detection system, since the use of light sources

continues to be based, in most cases, on off-chip commercial LEDs, diode lasers or laser equipment commonly requiring the use of optical fibers to bring light into the sensing zone. Most of the commented systems are only partially integrated and miniaturized: optical elements are fabricated in the same microfluidic chip, but still light sources are off-chip and the use of optical fibers becomes necessary to bring light into the channel, increasing the fragility of the whole set-up. Besides, in some proposals, the bulkiness of the final system also increases due to the optical detectors and the external instrumentation required to acquire the signals of interest, impacting in the portability of the systems.

With the aim of optimizing factors such as miniaturization, portability and robustness, this thesis explores some of the work developed in the field of optical systems integration, describing the design and fabrication of a microoptical system of reduced dimensions for detection, counting and even characterization of particles flowing through a microfluidic chip, by means of sensing light extinction, and possibly light scattering and fluorescence[2] (for this particular case, being necessary to select a light source with the appropriated wavelength). Basically, system is composed of three blocks: i) an optoelectronic package, ii) a microfluidic chip, and iii) an optical detector. The rendered models are introduced in figure 2.3.

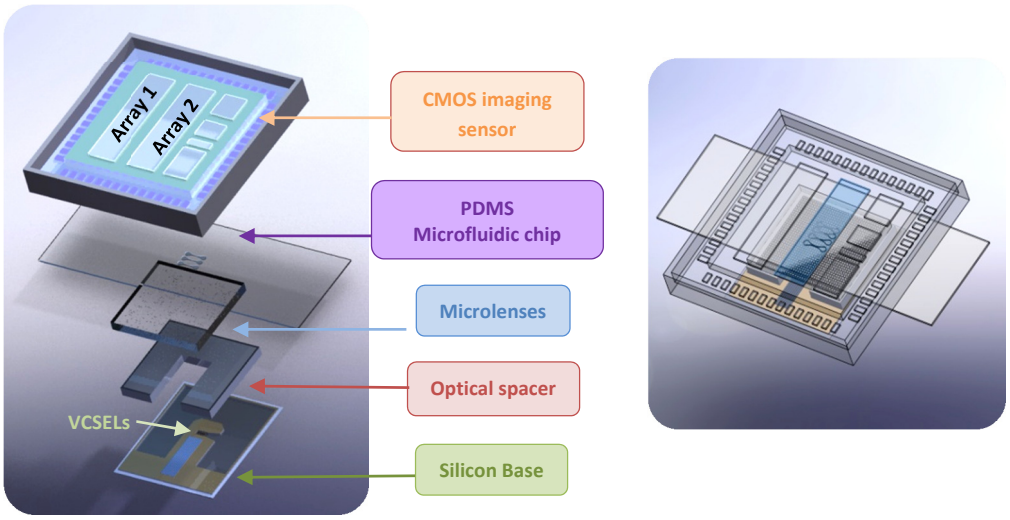

Figure 2.3: *Conceptual images for the components of the optical particle detection system. Silicon base, optical spacer, VCSELs and mcirolenses array compose the optoelectronic package. The microfluidic chip, fabricated in PDMS and glass, contains four microchannels. The chip is placed between the optoelecotronic package and the CMOS image sensor.*

The optoelectronic package includes a solid silicon structure of two pieces (base and optical spacer) for the micro optical commercial components (a die with 4 VCSEL light sources and an array of microlenses). Through optical simulations particular positions for both components are determined with the purpose of defining the shape of the light beams. Silicon micromachining techniques will be employed for the fabrication of the structural pieces of the device, while hybrid integration methodology will be followed for the assembly of the different elements, with special care in the optical alignment, in order to achieve optimal results exploiting the benefits of commercial optical and

[2] Scattering and fluorescence measurements are only presented as possible functionalities of the system. Though in theory the developed device would allow to perform these sort of analysis, no experimental measurements have been yet realized in order to demonstrate the capability of the system. Therefore, both possibilities are discussed in the chapter VIII.

lighting components. A more detailed conceptual design for the optoelectronic package is presented in figure 2.4.

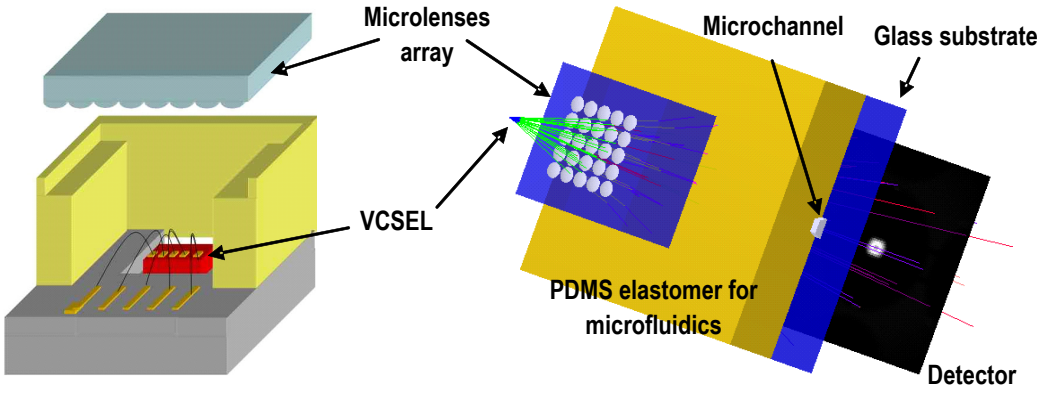

Figure 2.4. *Left: Scheme of the optoelectronic package including a silicon base substrate with VCSELs (red) and electrodes, an array of microlenses and a silicon "U" shaped spacer (yellow) to control the distance between microlenses and VCSELs. Right: Conceptual design for the complete optical particle detection system, including the previous optoelectronic package, the microfluidic chip and the optical detector.*

The Polydimethylsiloxane-glass (PDMS-glass) microfluidic chip contains 4 pressure-driven channels where the liquid suspension with particles will flow. This PDMS chip is disposable and can be easily replaced.

Finally, a full custom designed CMOS double array of photodetectors is responsible of the detection of particles. This "double array" architecture presents some advantages over a single array design, reducing the number of false detections of particles, yielding in a better Signal to Noise Ratio (SNR), and even leaves an open door to the possibility of measuring the velocity of flowing particles (refer Chapter VIII for more details). Pixels of the camera are fabricated in CMOS 0.35µm technology. Other functionalities such as control of the CMOS imaging sensor or RF/USB data transmission are implemented in a PCB with a microcontroller, not shown in the figure.

As can be appreciated in previous figures, the optoelectronic package includes commercial and silicon custom-fabricated components to provide a set of collimated or focused laser beams, offering spots with small dimensions and with high power at the image plane, i.e. the microfluidic channels. With every laser light beam directed to an independent microfluidic channel, the system is suitable to perform measurements such as particle detection/counting.

The VCSEL light beams, together with the custom designed camera based on two linear arrays of 256 pixels, allow the detection by light extinction, of microbeads flowing through microfluidic channels (figure 2.5). As a result, the fabricated system is able to perform 4 parallel measurements, but even more could be fulfilled depending on the selected commercial components. Since optical sensing is the working principle, the device can be considered a special approach to flow cytometers and handheld optical particle counters, with the added benefits of LoCs (e.g. miniaturization and low cost).

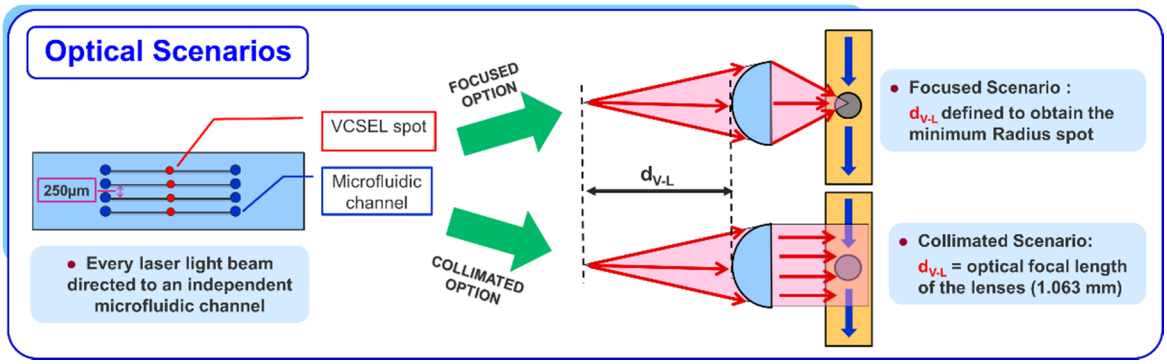

Figure 2.5: *Scheme for the two different optical scenarios considered: collimated or focused light beams. On the left side, a model for the microfluidic chip with 4 channels separated 250µm. Focused or collimated light spots, coming from VCSELs, illuminate each one of the channels. The optical effect (collimation or focusing) can be controlled with variable d_{V-L}, i.e. the optical distance between light sources and microlenses.*

The expected multifunctionality of the presented device and its architecture/design refers not only to the previously commented ability of being suitable for performing different optical measurements, but also to the wide range of counting/detection applications in which the system can be useful due to its particular design: the easiness in replacing the microfluidic chip allows to select the appropriate channels for each scenario according to the sizes of particles or the alignment method of particles into the sensing zone (hydrodynamic focusing or geometrical confinement); the simplicity in the operation (user-friendly device), for example in the alignment between the optoelectronic package, the microfluidic chip and the sensor, but also the possibility of fine adjustment for a particular setup; and the facility of performing multiple measurements simultaneously because of the integration of several independent light sources, even combining sources of different wavelengths to fulfill for example light blockage and fluorescent measurements in two different microfluidic channels. These are the main features of the system.

2.4 Outline of this thesis

In this thesis, I present the work developed in the Optoelectronics laboratory of the Department of Electronics at the University of Barcelona, which also includes the results of the collaboration with the Spanish National Center of Microelectronics - Barcelona Microlectronics Institute (IMB-CNM-CSIC).

This thesis details all the steps involved in the design and fabrication processes of a low cost and robust miniaturized Optical Microsystem for Particle Flow Detection based on silicon micromachining techniques and hybrid integration methodology, suitable for point of care testing applications.

This intended to be low cost optical particle counter, whose detection principle is primarily based on light extinction, is able to detect and count particles in liquid suspensions with diameters ranging from tens to a hundred of microns flowing in microfluidic channels, providing satisfactory results. This system was tested using polystyrene and polybead ® beads that were representative of biological cells.

This work is perfectly aligned with the current tendencies in fabrication procedures, and introduces a new way of fabrication for optical particle counters, based on hybrid integration and silicon micromachining. The presented concept is suitable not only to perform optical particle detection, but

also fluorescence measurements at least in theory, resulting in a miniaturized, compact and versatile system with a sensitivity according to the standard present values.

The following chapters explore not only the previously mentioned fabrication, assembly and packaging techniques, but also present the tasks developed in other complementary fields, with the aim to obtain a complete device: microelectronics design for the CMOS camera array, microfluidics analysis and fabrication techniques for the microfluidics channels and optical design for the microoptics included on the device.

In previous chapter 1, the concept of particle and the different particle characterization techniques, as well as a description of the state of the art for optical particle counting have been reported.

Present chapter 2 has been devoted to the conception of the system, offering a general idea about the aim of this thesis and the implemented device. The different elements that integrate the final device have also been introduced.

Chapter 3 will continue with the detailed explanation of the optical design and simulations, based on a commercial fused silica array of microlenses and a linear array of infrared VCSELs light sources. Hybrid integration of commercial components and silicon micromachined pieces is discussed in chapter 4. This chapter also deals with the fabrication procedures followed in the Clean Room of the IMB-CNM-CSIC to process the silicon wafers.

The design and fabrication of the microfluidics channels in biocompatible materials (PDMS and glass) with a low-cost fabrication procedure based on soft lithography techniques is the focus of chapter 5.

Chapter 6 refers to the ASIC microelectronic design and fabrication of the CMOS double array camera, responsible for the optical detection of the particles by means of measuring the changes in light intensity.

The experimental setup for the final device and the testing carried out are the purpose of chapter 7. The development of the first prototype of a low-cost optical particle counter based on hybrid integration and silicon micromachining proves to be successful. A set of measurements corresponding to the counting and sizing of particles in the range of 10 to 93µm diameter is presented. Double array configuration for the CMOS sensor is also tested.

To conclude, chapter 8 summarizes the conclusions of this thesis and leaves an open door for possible future work, especially in the field of fluorescence detection methods.

References

[1] S.-Y. Yang, S.-K. Hsiung, Y.-C. Hung, C.-M. Chang, T.-L. Liao y G.-B. Lee, «A cell counting/sorting system incorporated with a microfabricated flow cytometer chip» *Meas. Sci. Technol. ,* 2006.

[2] T. D. Chung and H. C. Kim, «Recent advances in miniaturized microfluidic flow cytometry for clinical use» *ELECTROPHORESIS,* vol. 28, Issue 24, 2007.

[3] P. J. Goix, «Method and apparatus for detecting microparticles in fluid samples». US Patent US 6710871 B1, 23 Mar 2004.

[4] T. Rezachek, A. Padmanabhan and B. Fritz, «Optical alignment for flow cytometry». US Patent US 7215425 B2, 8 May 2007.

[5] B. S. Fritz, «Optical detection system for flow cytometry». US Patent US 7262838 B2, 28 Ago 2007.

CHAPTER III: OPTICAL DESIGN

3.1 Introduction

In flow cytometers, optics plays a prime role ensuring that the light spot illuminating the detection zone accomplishes some requirements, such as a particular shape and size. The focused or collimated light beam (usually coming from a laser source) used to interrogate the particles is often shaped into an ellipse that covers the entire detection window area, thus uncertainty in particle position due to misalignment and variations in the width of the core stream does not affect the measurements. However, a single laser source does not provide constant illumination intensity across the width of the stream. Particles passing more towards the edge of the core stream may not be as illuminated as particles that pass near the center. As a result, sensitivity and accuracy of the system may vary depending on the lateral position of the particle through the focused elongated shape beam [1].

Optics integration leads to the use of on-chip lenses. This kind of lenses allows to obtain collimated or focused light beams, with reproducible results and reduced cross-talk effect. Levels of background light collection can also be minimized. In flow cytometry, lenses can be used to improve not only interrogation, but also the sensitivity[1] in the detection process, allowing to collect light signals of lower intensities by means of lenses with high numerical apertures. Most systems employing on-chip lenses for light collection also involve a form of slab-waveguiding [2].

Considering flow cytometers as the model to follow in the field of optical particle detection, some conclusions can be deduced from the fabrication alternatives of miniaturized flow cytometers already discussed in previous chapters.

Though most authors take advantage of commercial or self-fabricated microlenses with the purpose of reducing divergence of light and improving interrogation and detection processes, usually other external optical elements, such as optic fibres, are necessary to accomplish the objective, resulting in bulky or fragile systems. Other authors explore the possibility of substituting those external elements by others integrated into the fluidic chips (e.g. waveguides), but again the use of external light sources represents a drawback in terms of miniaturization. Finally, we find a reduced number of authors who truly works in the line of integrating microlenses and light sources with the aim of obtaining more robust and portable devices. The work presented in this thesis moves toward this direction, emphasizing fully miniaturization and integration of optical systems as essential tasks.

In this chapter devoted to optics, we present and discuss the results of the optical simulations performed to define the best optical conditions of the system in each one of the analysed scenarios, under the premises of obtaining a minimum or acceptable size for the light spot in the plane of the microfluidic chip, but with the necessary power to carry out optical detection of microparticles flowing through the defined detection area.

[1] If light collection process improves, low intensity light signals corresponding to smaller size particles might also be detected.

One of the important constraints in the optical design process, was that the fabrication of the detection system should integrate commercial components in an optoelectronic package (i.e. a die of VCSELs and an array of microlenses). In an early stage of system conception, some custom optical designs based on the fabrication of structures with self-designed microlenses, were also considered as a possible alternative to the present hybrid system, though finally discarded due to the complexity of the fabrication process [3], [4]. When dealing with self-designed microlenses arrays, there are two important questions to consider: the ability in the fabrication process to precisely pattern and model the lenses for creating optical elements with good performance parameters, and the ability to position each one of these individual lenses following a particular two dimensions pattern [5]. Being able to combine these two abilities requires experience, know-how and investment. Unfortunately, nowadays, our self-fabricated lenses could not equal the quality of the ones offered by the market. For this reason, though the "custom designed lens" subject is introduced at the end of this chapter, where some suggestions to improve optical integration are discussed, the election of a commercial array of microlenses was clear. Therefore, as one of the preliminary tasks, it was necessary to search in the market the best-suited components that would accomplish with the criterions of design.

As a result of the simulation processes, the positional parameters of the optoelectronic packaging elements will be obtained.

3.2 Micro-optics: integration of VCSELs and microlenses

3.2.1 Defining the optoelectronic package

The aim of the optical system is to provide a set of four controlled light beams to illuminate the sensing zone of four microfluidic channels. To avoid light interferences with neighbouring channels, low divergence light beams and light spots with minimum or suited size (diameter) illuminating each one of the detection windows, are necessary. Whether the light beams should be collimated or focused will depend on the results obtained from simulations, but also on the expected performance for the planned measurement; e.g. in theory, focusing light beams into the detection region would be an excellent option for fluorescence detection methods.

The source optoelectronic package gathers 4 elements (figure 3.1). Two of them are commercial components (a die of VCSELs and an array of microlenses) and the other two are specifically designed pieces, fabricated with Silicon micromachining procedures. These two silicon pieces, joined together, build a solid optical structure where commercial elements can be accurately placed. By means of this silicon structure, the system accomplishes the requirements of the optical design, and also provides the necessary electrical connections to power the system. Hybrid integration methodology offers high quality results, allowing the use of commercial components, but as a counterpart, the criterions of design are restricted to the selected commercial components.

Optics was simulated using ray tracing simulator *ZEMAX Radiance* software working in sequential and non-sequential modes. The former, to obtain the preliminary geometry of the system, as well as the shape of the light spots, and the latter to simulate a more complex and realistic scenario, modelling the VCSEL sources and including special detectors to visualize the estimated light intensity profile at certain interesting planes and locations.

With simulations, the optimum positions and dimensions of the elements are determined, analysing two possible scenarios: pure collimated light beams system or focused light beams system. In the first case, the goal is to control the spread and divergence of the beam, trying to keep ray lights in parallel paths. To achieve it, light source must be placed at the focal length of the lens. In the second case, the aim is to optimize a figure of merit defined by the minimum size (radius) of the laser beam spot. This figure of merit is calculated for a beam focused in the fluidic channel where microparticles are flowing.

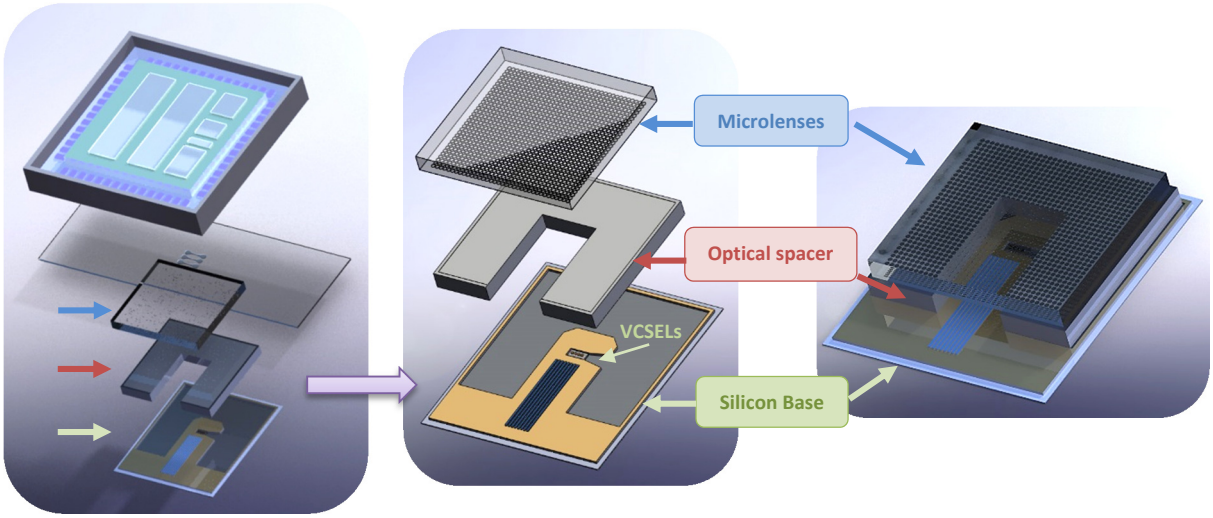

Figure 3.1. *Left: 3D-rendered image of the components of the Micro-Optical Particle Detection System. Middle: Scheme of components of the optoelectronic package: Silicon substrate with VCSELs and electrodes (bottom), "U" shaped optical spacer (middle) and the array of microlenses (top). Right: 3D-rendered image of the optoelectronic package. Silicon pieces joined and commercial components positioned (hybrid integration).*

3.2.2 Vertical-cavity surface-emitting laser (VCSEL)

The selected commercial light sources are VCSELs from "*ULM Photonics*", in particular the model *ULM850-05-TT*. Though commonly used in the field of optical communications, these devices are becoming popular in other researching fields that require integrated light sources with good performance (figure 3.2). Manufacturer offers a catalogue of micro lasers emitting at several different wavelengths (from 760nm to 948nm), but for this work, chosen VCSELs emit at Near Infra-Red (NIR) 850 nm wavelength, which is the most common in the market, and are commercialized in dies forming linear arrays of 4 or 12 lasers, with an emission area of 25µm, a pitch[2] of 250µm and both contacts, anode and cathode, on the top side (figure 3.3). For the 4 VCSEL array, total dimensions are 350 x 1000 x 150µm (w-l-h). Typical values for threshold current and voltage are 1.5mA and 1.7V, while optical output power is about 1.5mW at $I_{forward}$ 5mA. Their divergence angle presents a maximum value of 25° (full width 1/e^2) at $I_{forward}$ 5mA. Optics is necessary to correct this undesired effect and avoid interferences between two near light beams, as well as for allowing the focusing or collimating of the light beams.

[2] Due to their main use in the field of optical communications, the commercially available VCSEL arrays typically have a pitch of 250µm that matches with the standard pitch used in fibre-ribbon cables and connectors. However, it has been demonstrated that they can be fabricated with smaller pitches [14].

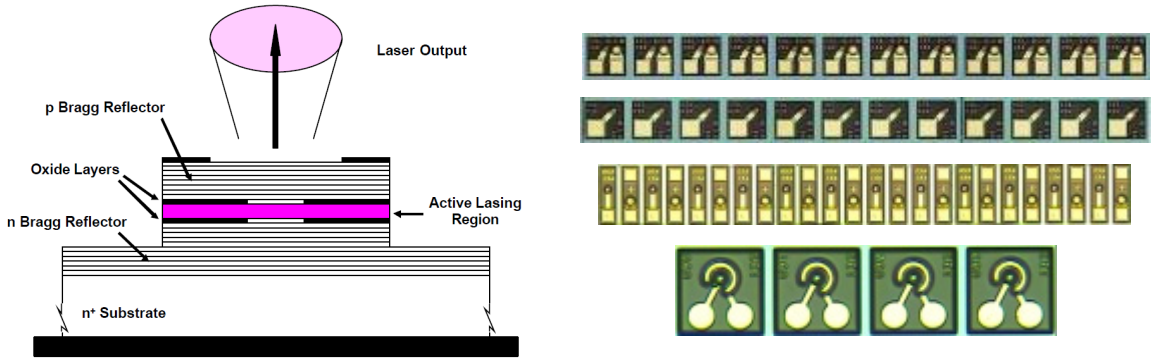

Figure 3.2. *Left: Diagram for simple VCSELs (from NEPP NASA webpage). The different layers compounding the laser can be appreciated. Vertical resonant cavity is confined by the two Bragg reflectors. The lasing current is laterally confined by the oxide layers. Metal contact is usually placed on the top side. Right: Pictures of commercialized arrays of VCSELs 1x12 and 1x4 (from ULM photonics).*

Though Light-Emitting Diodes (LEDs) were also considered as possible light sources for our system [6], VCSELs offer more advantages [7], [8]. The divergence of VCSEL light beams is smaller by a factor of 2 or more, and rotationally symmetric (compare the typical angle divergence value of 20° for VCSELs with typical values of 60° or even 80° for LEDs), which means better optical coupling efficiency into miniature applications. About driving currents, VCSELs require typically 1mA for reaching their threshold level, while for example, Low current LEDs from *VISHAY semiconductors* require 2-5mA DC forward current, being the typical value for standard LEDs 20mA. VCSELs also offer higher optical power once they reach the threshold current: from 1 to 10mW, which is almost up to 60 times more than a LED. Besides, VCSELs produce a narrow beam of coherent light in front of scattered incoherent light emitted by LEDs, and narrow spectral width emissions (VCSELs $\Delta\lambda$ = 0.01nm versus LEDs $\Delta\lambda$ = 50nm) with low spectral tuning because of temperature or current, which is useful for example in fluorescence detection methods (figure 3.4).

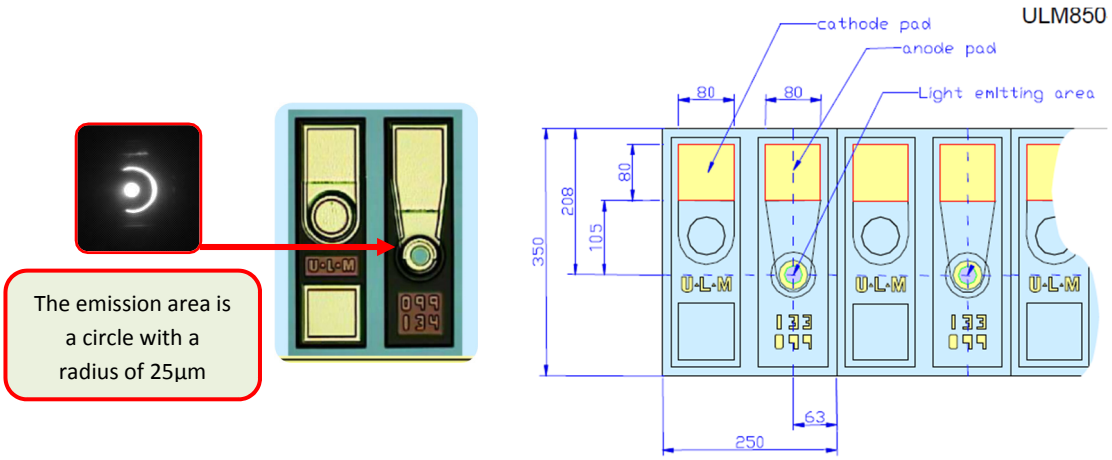

Figure 3.3: *Single VCSEL "ULM Photonics". Image of the light emitted from the VCSEL captured with a commercial camera (UI-1545LE-M uEye from IDS) and focused with an aspheric lens of 4mm diameter. The "arc" surrounding the central spot is due to spontaneous light emission. This effect is neglected. On the right side, dimensions for the die of VCSELs. Pitch distance is 250µm.*

The optical efficiency parameter impacts directly into cost and size. When a light source presents high divergence, optics is necessary to reduce the emission angle producing a narrower beam, for only the light that strikes the detector provides useful signal. Dimensions of the employed optics will depend

on the divergence of the source. The larger the divergence value, the larger diameter of the lens necessary to collect the emitted light (of course, other optical parameters influence in the decision and should be also considered, for example, the numerical aperture of the lens or the distance between the lens and the light source). Figure 3.4b shows the illumination beam patterns for a VCSEL and a LED at a constant distance. It is clear that the VCSEL will require the smallest lens.

Thinking about integration, miniaturization and handheld systems, it is mandatory to study the electrical efficiency parameter. Electrical power for VCSELs, with common values of 5mW, is lower compared to LEDs (according to *VISHAY semiconductors*, LED values are in the range from 40mW for low current models to 75mW for highbright devices), which is translated in an increased battery lifetime for a particular application. The difference in lifetime can be more than two orders of magnitude. The extremely low power required by VCSELs is an advantage for applications where electrical power is at a premium.

In spite of the benefits of solid-state sources over LEDs previously exposed, the main drawback for VCSELs is the limited range of available wavelengths. Nowadays, research and development is being carried out by manufacturers to deliver VCSELs emitting in the visible range (e.g. *Laser components UK*, 650-670nm red colour VCSELs), but there is still work to be done if the aim is to expand the list of wavelengths.

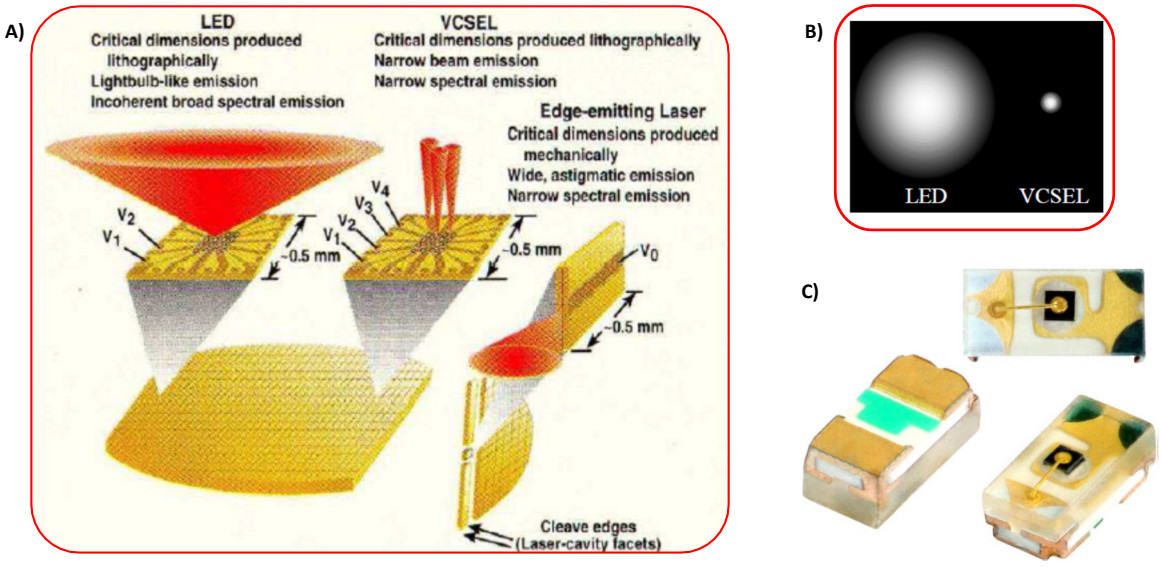

***Figure 3.4**: (a) Comparison of the optical characteristics of three optoelectronic light sources: LEDs, VCSELs and Edge-emitting Lasers. Printed with permission of Fiber Vision Technolgies Limited. (b) Beam patterns without optics for a LED and a VCSEL, at a constant distance. Printed with permission of Honeywell VCSEL Products* [8]. *(c) Ultrabright SMD 0402 ChipLED from VISHAY semiconductors, with dimensions 1.0 mm x 0.5 mm x 0.35 mm (L x W x H).*

A special remark should be made with respect to a novel technology that, though being currently still under development in some aspects, could be the perfect alternative to VCSELs when it becomes more mature. We are referring to the microLEDs (µLEDs) delivered by *InfiniLED company* in collaboration with *Tyndall National Institute* (figure 3.5). According to manufacturer, these devices will enable a new generation of low cost and miniature diagnostic equipment with minimal energy consumption (optimal battery life). They are presented as the key piece for a new generation of fluorescence measurements due to the broad range of available wavelengths (at present, from UV 360nm to green 525nm and IR

950nm up) and their good performance qualities, combining the benefits of lasers and LEDs to offer "*enhanced optical performance of fluorescence-based systems by simplifying the optical path, controlling the excitation spectrum and minimizing the wasted light (scattered light), and enhancing system performance through reduced power consumption and system size*" [9]. Instead of the Gaussian profile emission from standard light sources (both LEDs and lasers), microLED emission profile delivers a top-hat profile, allowing the uniform coverage of the target area with light, which indeed is an important issue for fluorescence detection applications.

A standard single 20µm diameter microLED pixel, fabricated using LED-type material, can produce a quasi-collimated emission beam (Angle (Θ½) < 25°) directly from a single surface of the chip, similar to a semiconductor laser, delivering light intensities larger than 300 W/cm^2. In addition, these devices do not require threshold currents or complex heat sinking to ensure stable performance. Minimum drive current (in the order of nanoAmpers) is required to generate light, though for emitting with an optical output power of 1mW, for example at 410nm, typical $I_{forward}$ values are higher than 2mA and threshold voltages around 5V are necessary. MicroLEDs, designed to be attached with flip chip technique, also have been fabricated as addressable arrays of emitters or lines.

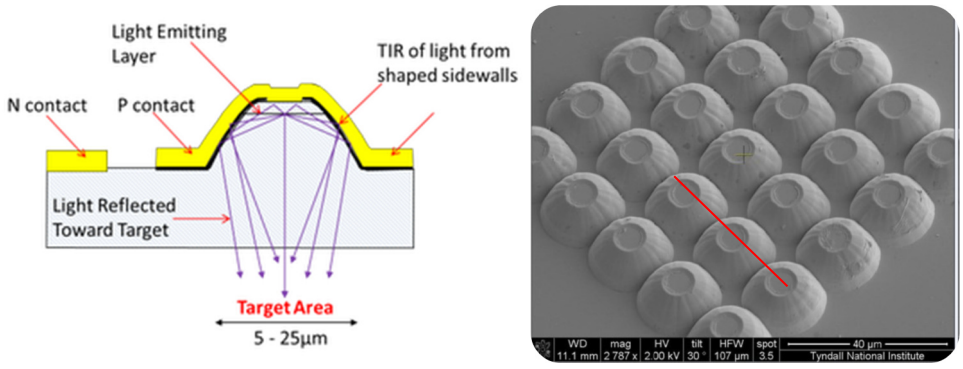

Figure 3.5. *Right: MicroLED device structure: integration of light control optics directly at the site of light generation. Left: Array of MicroLEDs. Red line equals 40µm length. Both images printed with permission of INFILED Company.*

3.2.3 Microlenses

The designed system also includes a microlenses array from "*SUSS MicroOptics*" (figure 3.6, left), fabricated in fused silica material, with dimensions 10x10x1.2mm^3 (w-l-h). *SUSS MicroOptics* uses high-quality Fused Silica Wafers made of SCHOTT Lithosil Q1, Hereaus Infrasil or equivalent, with a transmission above 90% in the range of 850nm, the wavelength emitted by the VCSELs (figure 3.6, right). Lenses can also be fabricated in silicon material, though they are best suited for other optical applications in the NIR regime, working with wavelengths above 1200nm (silicon is absorbent in the visible and NIR, with a transmission less than 10% for wavelengths below 1200nm).

The shape of the lenses define the applications in which they best fit. Cylindrical and square microlenses are commonly used for beam homogenizing and shaping, while circular microlenses are suitable for fiber coupling, imaging and collimation, as in our case of study (figure 3.7). Different configurations and arrangements for microlenses are available in the market. *SUSS MicroOptics* offers circular lenses arranged in linear arrays and quadratic and hexagonal grids.

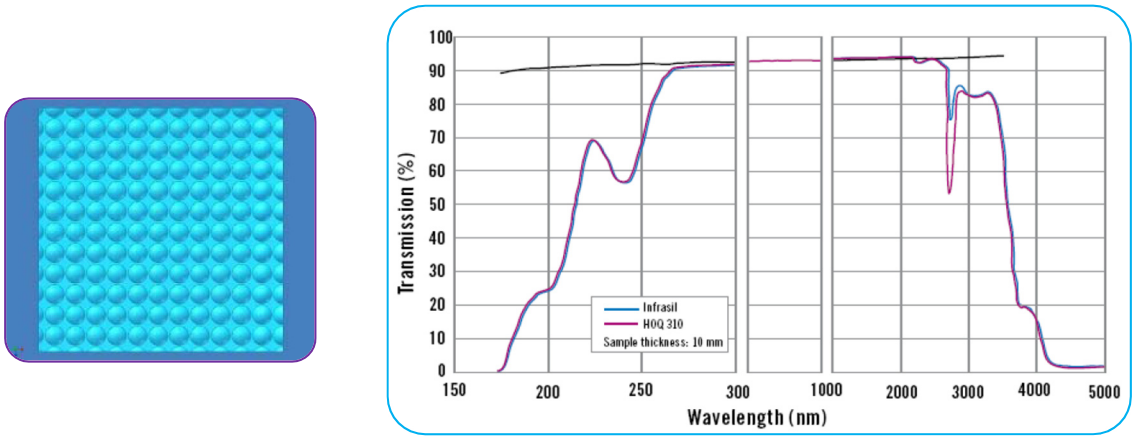

***Figure 3.6**. Left: Picture of the quadratic grid of circular fused silica microlenses from "SUSS MicroOptics", with dimensions 10x10x1.2mm. Right: Typical Transmission of Infrasil including Fresnel reflection losses (10 mm path length) (Specifications from Hereaus Quarzglas).*

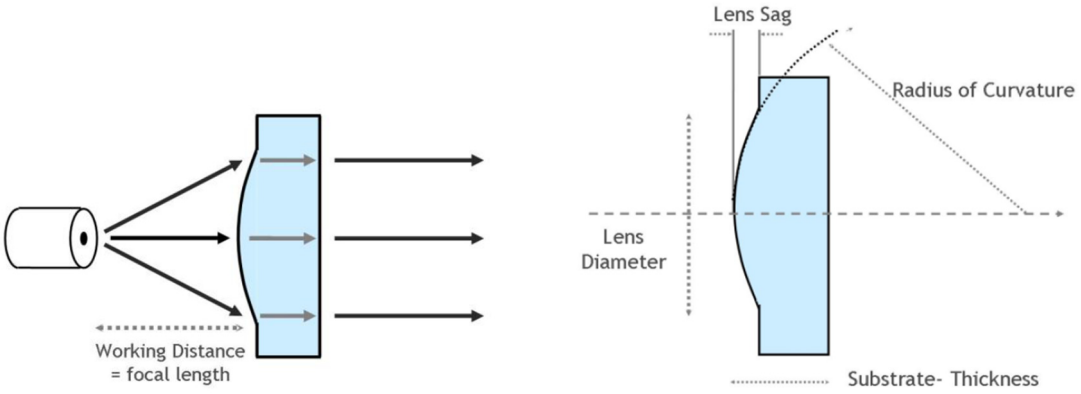

***Figure 3.7.** Left: Circular lenses are suitable for collimation applications, when the working distance of the system equals the focal length parameter of the lens. Right: Typical parameters of a lens. Images printed with permission of "SUSS MicroOptics".*

The selected circular microlenses present an effective focal length of 1.063mm, a radius of curvature (ROC) of 0.487mm, a sagittal depth (or lens sag, h) of 14µm and a pitch of 250µm. Comprehensive diagrams are included in figure 3.8. One of the constraints for selecting the array of microlenses was undoubtedly the pitch parameter. The fact that the pitch of the VCSELs is also 250µm allows a perfect alignment between the center of a lens and the center of the VCSEL emission area. Table 3.1 contains a comparison of different microlenses commercialized by the same company in terms of optical lens parameters.

***Table 3.1:** Comparative table for different microlenses offered by SUSS MicroOptics. Several parameter are observed: distance between centres (pitch), radius of curvature of the lenses (ROC), the effective focal length (fe), the numerical aperture (NA) and the radius (a) and diameter of the lens. Below this table, some boxes with helpful information: other characteristics of the selected microlenses and some optics equations.*

Circular Lenses, quadratic grid					
Pitch (mm)	**ROC (mm)**	**fe (mm)**	**NA**	**a (mm)**	**Lens diameter (mm)**
0.25	0.535	1.1681	0.11	0.1284	0.2569
0.25	0.487	1.0633	0.11	0.1169	0.2339
0.25	0.47	1.0262	0.12	0.1231	0.2462
0.25	0.297	0.6484	0.18	0.1167	0.2334

Microlenses	
Fused Silica	Visible and infrared spectrum
Typology of Lens	Plane-convex, convergent
Refractive index	1,458

Equations
fe= *ROC/(n-1)*
NA = *a/fe*
Sagittal depth = *ROC* - $\sqrt[2]{ROC^2 - a^2}$

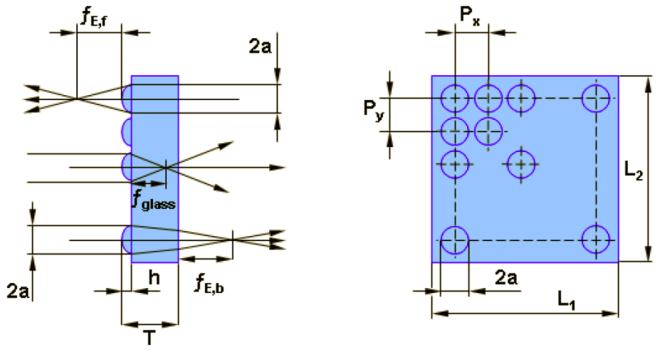

Definitions	
Lens width	$2a_1$, $2a_2$
Lens pitch	P_x, P_y
Lens sag	h
Radius of curvature	R_C
Effective front focal length	$f_{E,f}$
Effective back focal length	$f_{E,b}$
Focal length in glass	f_{glass}
Refractive index glass	n
Wavelength	λ

Figure 3.8. *Useful information about physical and optical parameters for circular microlenses arranged in a quadratic grid. With permission of "SUSS MicroOptics".*

3.2.4 Preliminary simulation results

With *ZEMAX Radiance* software we simulated the optical system. Angular intensity distribution of VCSELs was defined according to the real emission profile provided by the manufacturer ULM photonics (figure 3.9), and the rays were traced following a Sobol distribution algorithm, which generates a uniform distribution in probability space, rather than generating random numbers.

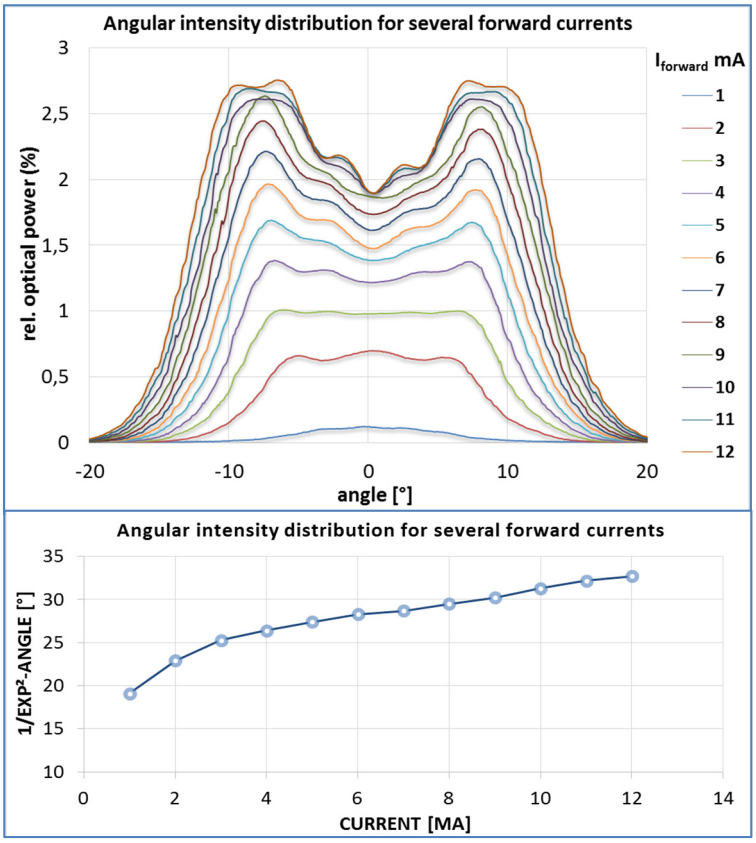

Figure 3.9: *(a) Angular intensity distribution for several forward currents, with the doughnut-like pattern typical for VCSELs. (b) Angular distribution measured as 1/e² full width for different currents. Images printed with permission of ULM Photonics.*

When measuring the simulated radiance[3] in a detector plane placed at 100µm from the VCSEL light sources, for $I_{forward}$ 8mA, we obtained the same angular intensity profile (figure 3.10). From images in both figures, a deviation can be appreciated in the values of the beam divergence parameter with respect to the information published in the datasheet of the commercial component. In concrete, with $I_{forward}$ 5mA beam divergence should be in the range of 20-25°, but a value of 27° is found (figure 3.9b).

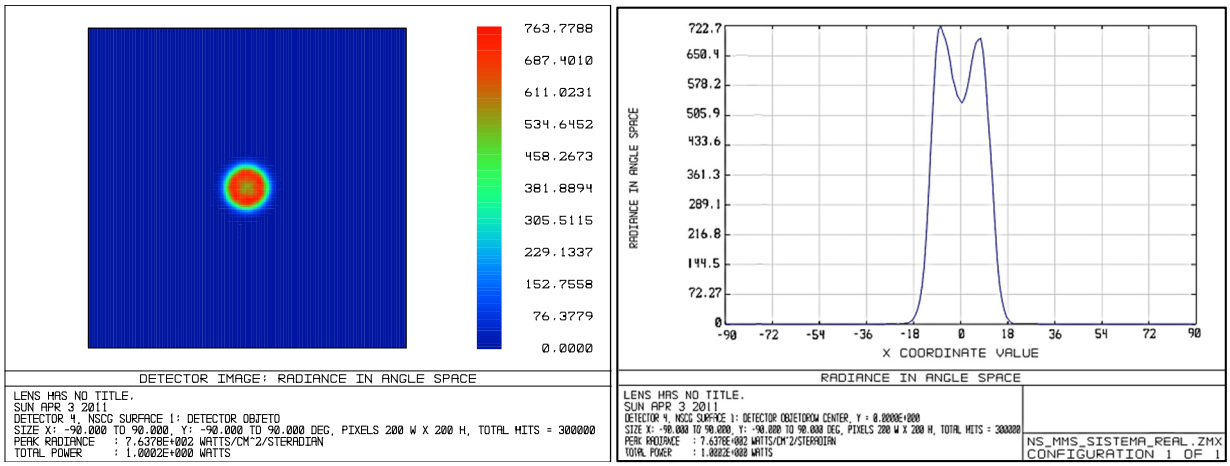

Figure 3.10. *Left: Radiance measured in angle space for a detector plane placed at 100µm from the VCSELs, and $I_{forward}$ 8mA. Right: Cross-section of the radiance angular distribution. Same doughnut-like pattern as in the curves provided by manufacturer, in concrete for the curve of $I_{forward}$ 8mA. At $1/e^2$ a total value of 29° is obtained.*

An explanation should be made before continuing with the exposition of simulation results. Although in the conceptual design of the optical detection system 4 VCSELs are included, and so is the number of VCSELs on the commercial die, for simulations only 3 active light sources are defined in order to simplify the simulation scenarios and to reduce the processing time. Anyway, results offer the same reliability and validity.

Results of first simulations in sequential mode[4] (figure 3.11) proved the collimation effect achieved when placing the array of microlenses at the focal length (1.063mm), and how variations in this parameter distorted the size and distribution of the spots in the image plane, placed at 1cm from the light sources[5] (black line on the right side of the layout figures). This image plane, with dimensions 3mm height, represents the linear sensor array of the detection system. In a collimated system, rays follow parallel paths with no divergence until reaching the image plane (figure 3.11a). Three clear and well-defined spots (one for each VCSEL) can be observed in the image plane (figure 3.11b). However, in a non-ideal scenario (figure 3.11c), variations in the position of the array of microlenses, increasing or reducing the focal length distance, produce non-parallel and divergent light rays and overlapped spots. Note that the replicas that appear in the diagrams of the spots, can be underestimated for being

[3] Radiance is a measure of the quantity of radiation that passes through or is emitted from a surface and falls within a given solid angle in a specified direction.

[4] In sequential ray tracing all of the rays traced must propagate through the same set of surfaces in the same order, i.e. all ray propagation occurs through surfaces which are located using a local coordinate system. Sequential mode is limited to the analysis of imaging systems.

[5] In a micro-optical system, this distance is considered large enough to observe the collimation effect. Increasing this distance has a positive effect, avoiding the apparition of replicas. This separation distance also responds to practical issues, since in the final system a microfluidic chip must be placed in the space between optics and sensor.

out of range in the real system (out of the vision field of the sensor), since the final detector has a delimited area (≈ 3mm height x 0.3mm width).

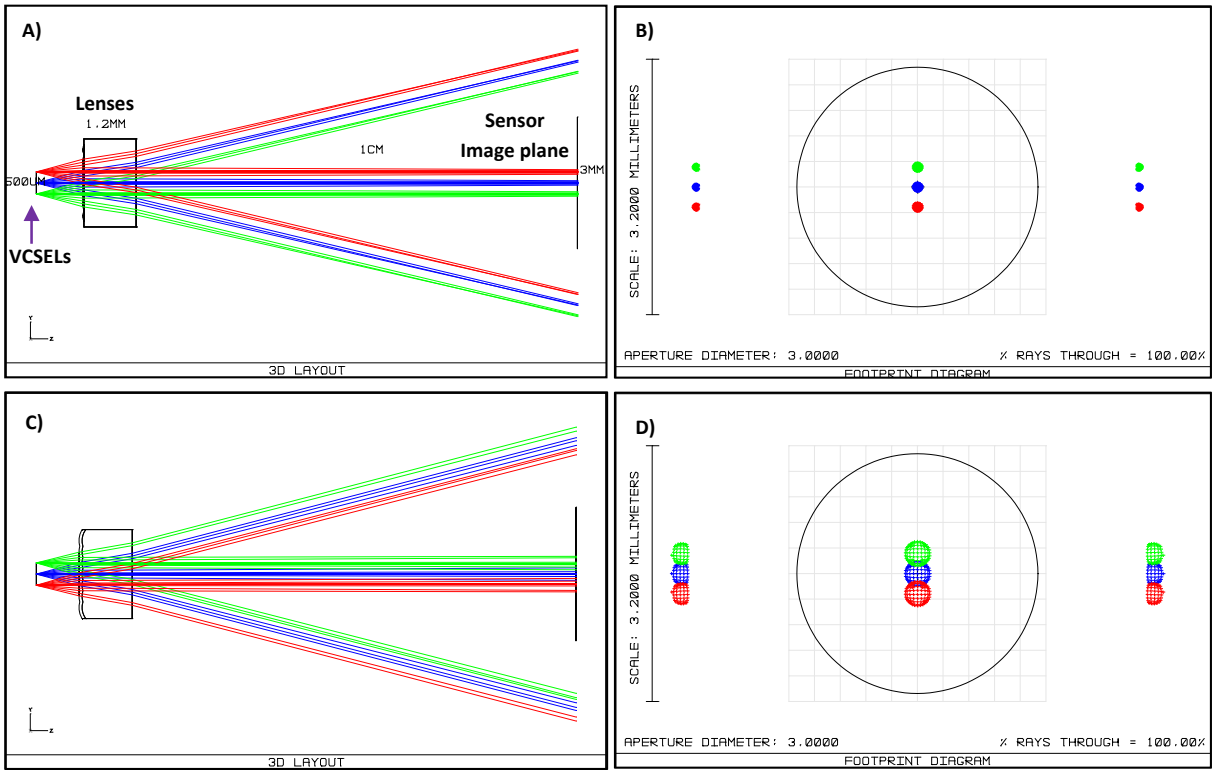

Figure 3.11: *ZEMAX ray tracing simulations in sequential mode for a collimation system with 3 VCSEL light sources separated 250µm (pitch) and an array of microlenses. Image plane at 1cm. (a) Layout of the ideal scenario, with the array of microlenses placed at the focal distance (1.063mm). No divergence observed in rays until reaching the image plane. (b) Shape and size of the spots at the image plane. Some replicas can be observed at both sides. (c) Layout of a non-ideal scenario with lenses placed at a distance of 0,960mm (focal 1,063mm - 100µm). Parallel paths of rays are distorted. (d) Shape and size of the spots also experiment a deviation from ideal scenario.*

A basic study to remark the importance of optical alignment was also performed analysing several cases: decenter of light sources with respect to microlenses in X and Y axes (figure 3.12), tilt factor in Z axis (figure 3.13a) and tilt factor applied to all three axes (figure 3.13b).

After the preliminary study to comprehend the basis of a collimated system, more sophisticated analysis is required. In non-sequential mode[6], size of the spots and light profile in the microfluidic channel were determined by placing detector viewers at fixed positions. For the pure collimated scenario, the detector was placed behind the microlenses, varying its position with respect to the light sources and analysing the variations in the radius of the spot. In this case of study, the microfluidics block was not considered. In the focused light beams scenario, detector viewers were placed just in front of and behind the microfluidic channel, in parallel planes referred to the VCSELs and the microlenses.

[6] Non-sequential ray tracing implies that there is no predefined sequence of surfaces which rays that are being traced must hit. The objects that the rays hit are determined solely by the physical positions and properties of the objects as well as the directions of the rays. Each object is placed globally at an independent x, y, z coordinate with an independently defined orientation. Non-sequential mode can be used to analyze stray light, scattering and illumination in both imaging and non-imaging systems.

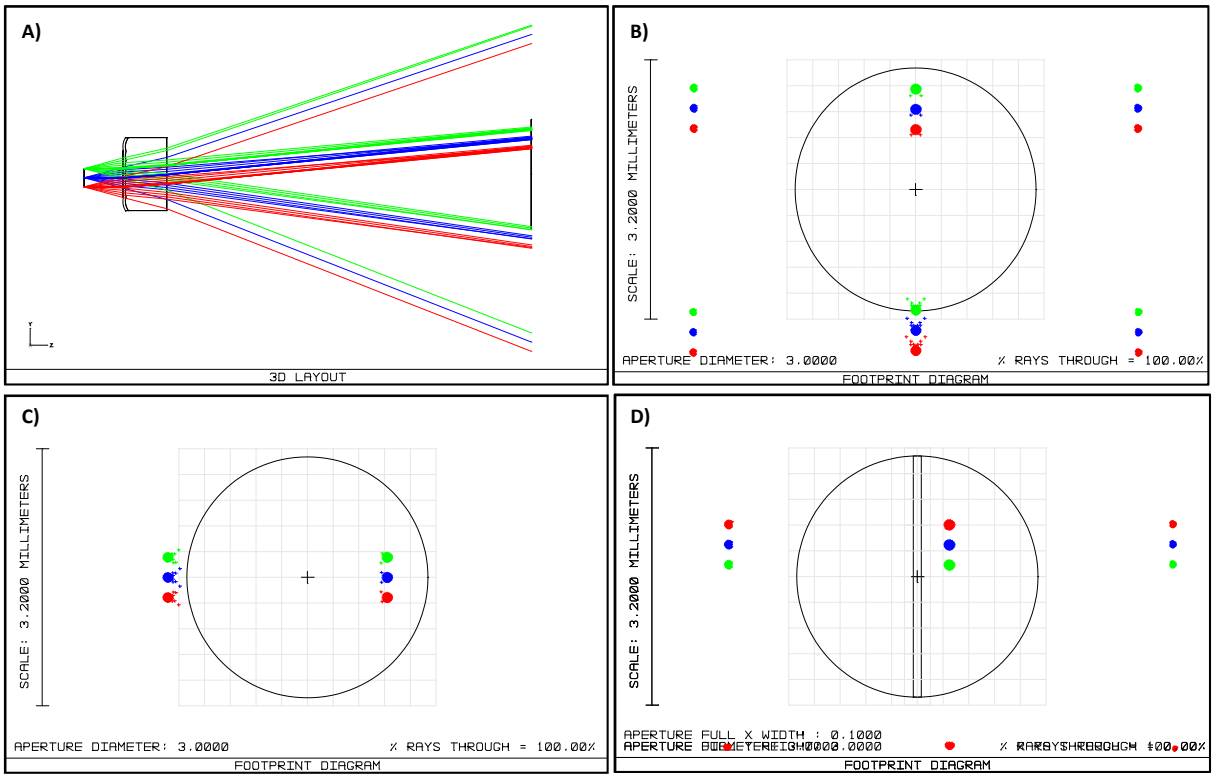

***Figure 3.12**: Simulation results for a collimated system with decentering of the light sources with respect to the microlenses. Layout (a) and spots diagram with a decenter of 100µm in Y (b) and X (c) axis respectively. Decenter of 40µm on both axes XY (d).*

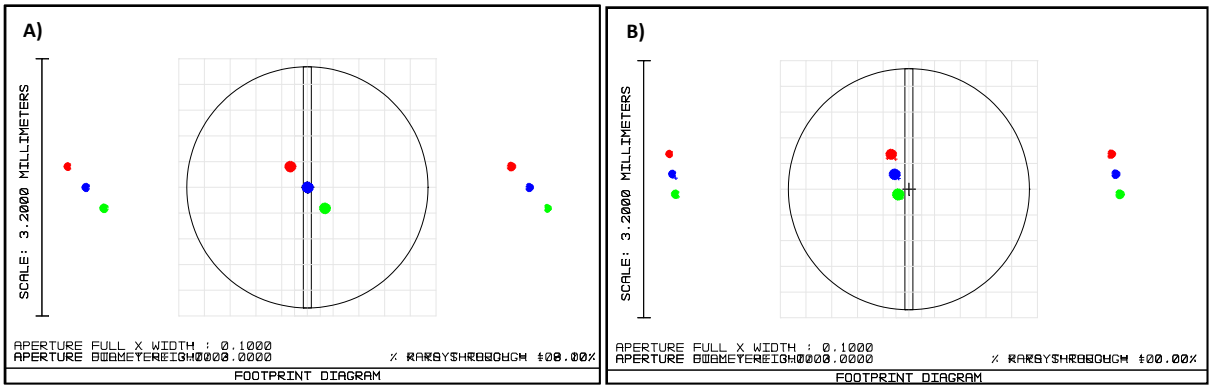

***Figure 3.13:** Simulations results for a collimated system with a tilt factor applied to the light sources. The rectangle in the detector area, represents one of the arrays of photodetectors (0.1x3mm). (a) Tilt factor of 5° in Z axis, which represents approximately a deviation of 100µm in the parallelism between the light sources and the microlenses planes. Two of the spots appear to be out of range and would not be detected (b) Tilt factor of 1° in all axes XYZ.*

3.3 Pure collimated scenario

The following figures show some examples of the results obtained with non-sequential simulations for the pure collimated scenario. Positioning the microlenses at the theoretical effective focal distance (1.063mm) not only corrects the divergence effect of the VCSEL light sources (figure 3.14), but also provides spots of controlled dimensions with small variations in their radius even placing the detector at large distances of 30mm from the source point, which indeed is a great distance in the field of micro-optics [10].

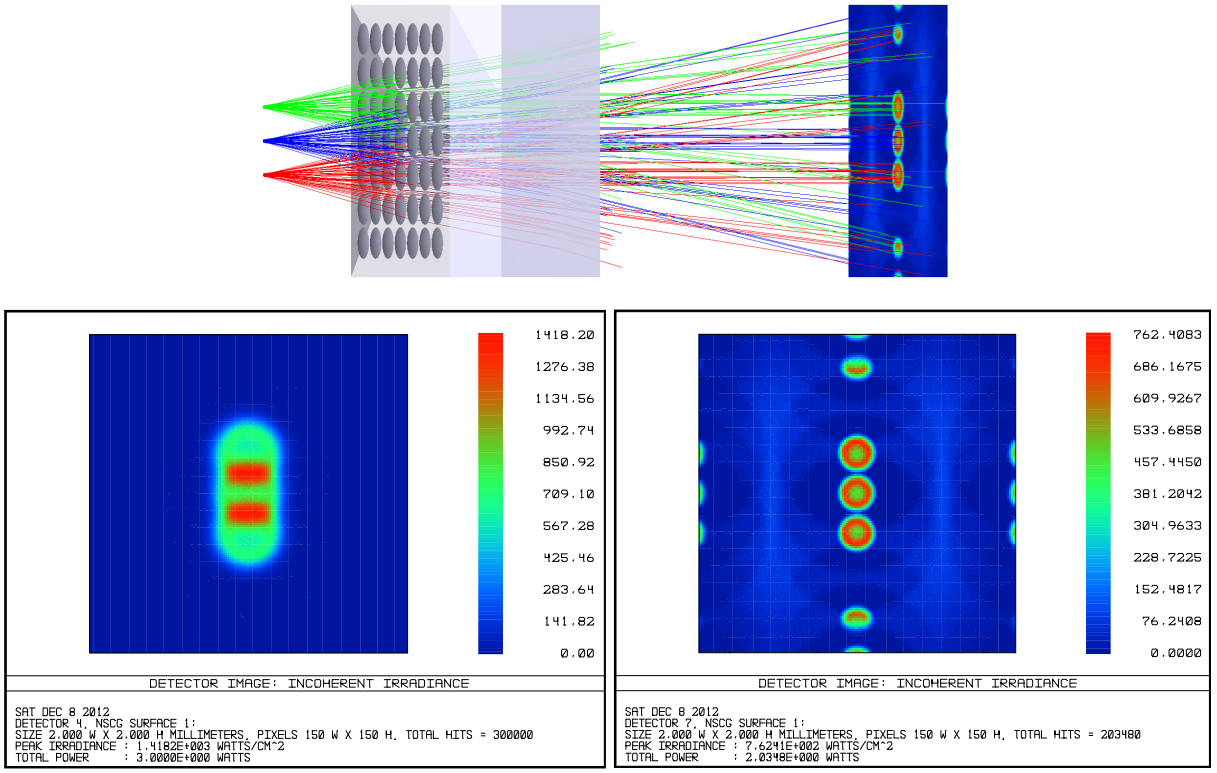

***Figure 3.14**: ZEMAX non-sequential mode ray tracing simulations for a collimated system. Top: 3D model of the system with 3 VCSEL light sources, $I_{forward}$ 8mA, the array of microlenses and a detector plane of dimensions 2x2mm^2 located at a distance of 5mm from the VCSELs. Bottom: On the left side, Irradiance[7] measured at a detector viewer located at a distance of 1mm from the VCSELs, previous to the microlenses. The natural effect of light divergence, when no optics is used, can be observed. On the right side, collimation effect can be observed in the rear detector viewer (5mm). Some replicas also appear.*

Results in previous figure show clearly the collimation effect achieved by optics. Three well-defined independent spots of ≈150µm radius are obtained in the image plane of the detector, placed at 5mm from the VCSELs light sources, with $I_{forward}$ 8mA. Comparing this results with the ones in the same figure but without optics, where there was overlapping between the emissions of the three VCSELs, gives an idea of the benefits of collimation. The typical doughnut-shape of VCSELs emission profile is also observed in the irradiance image. Some replicas also appear, due to the proximity of the image plane to the array of microlenses. In the real scenario, the optical detector would be place at a larger distance, thus replicas would have no effect as they would fall out of the sensitive area of the sensor.

The same simulations were repeated for VCSELs with $I_{forward}$ 1mA and 2mA. In the first case, $I_{forward}$ 1mA, the positions of all the elements were maintained. Results in figure 3.15 show the comparison of the irradiance at the detector plane with and without microoptics. Again the improvement of collimation is evident. In the second case, $I_{forward}$ 2mA, the detector was placed at a distance of 30mm from the VCSEL light sources. This time, results (figure 3.16) are not so satisfactory (overlapping of light spots and increased radius ≈ 250-300µm) due to the large distance that light rays must cross (which could

[7] Irradiance is the power of electromagnetic radiation per unit area (radiative flux) incident on a surface. The SI units are watts per square meter (W/m^2).

be considered equivalent to infinite in the macro-optics world) but still the collimation effect presents positive effects over the case without microoptics.

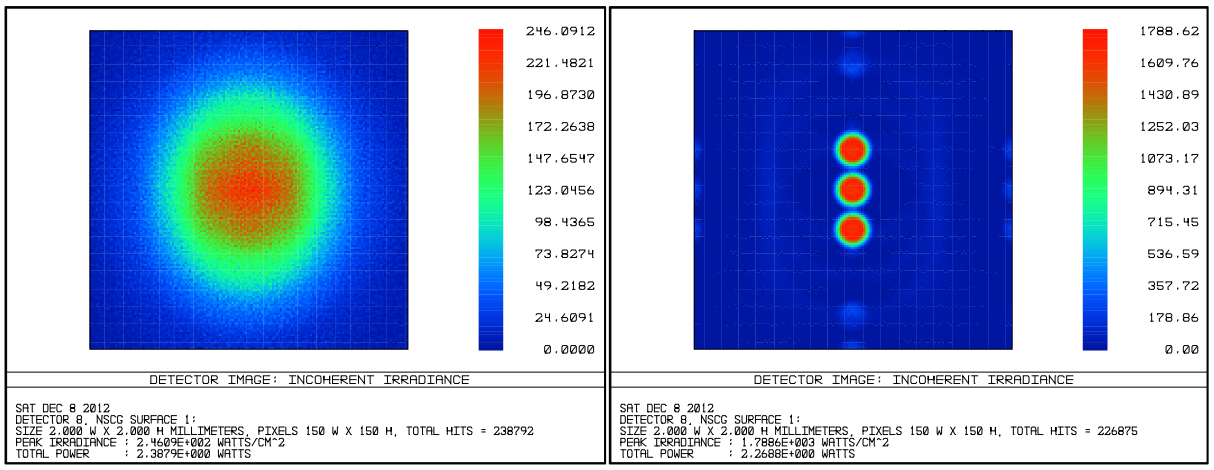

Figure 3.15: *Comparative results for a non- collimated system without optics (left) and a collimated system (right). Detector plane located at 5mm from the 3 VCSEL light sources, with $I_{forward}$ 1mA. In the system without optics (left), the three individual spots overlap into a single one due to the uncorrected divergence of the light sources.*

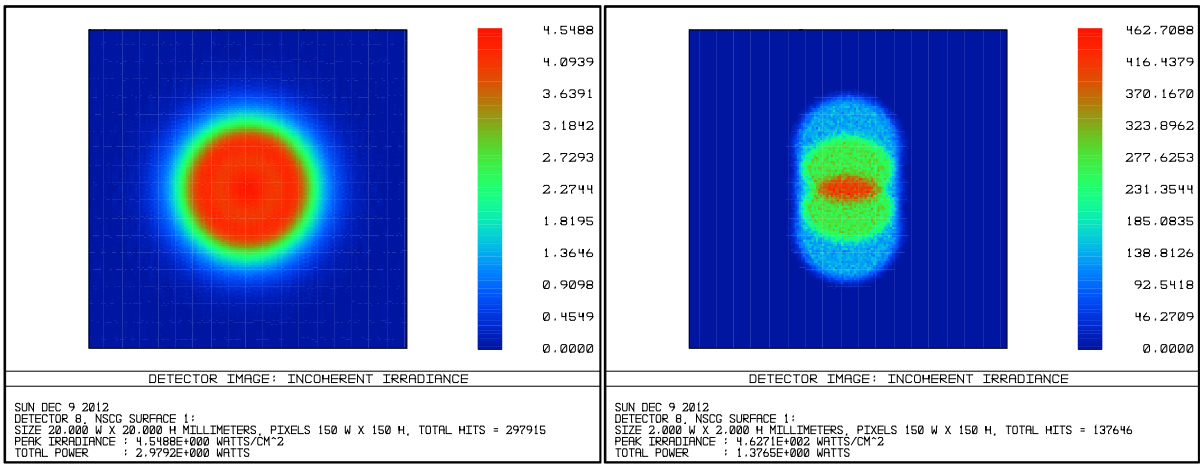

Figure 3.16: *Comparative results for a non-collimated system without optics (left) and a collimated system (right). Detector plane located at 30mm from the 3 VCSEL light sources, with $I_{forward}$ 2mA. Even in this case, the effect of micro-optics appears to be positive as in the image of the right side, it is possible to deduce the existence of 3 light sources, though the large distance (equivalent to the infinite in macro-optics) in the position of the detection plane deteriorates the result.*

The purpose for the set of simulations performed with the collimated system scenario was to determine the goodness of the collimation effect, i.e. the variation in the radius of the spots captured by a detector object (image plane). Several cases were analysed, setting the variable of study as the position of the detector and increasing the distance between that element and the origin point (the position of the light sources). To simplify the system, only one VCSEL was considered, but the effects of the others can be easily extrapolated as they present the same behaviour. Simulations were performed for several VCSEL $I_{forward}$ values (8mA, 2mA and 1mA).

We defined a merit function by means of several *ZEMAX* specific non-sequential (NSC) operands to calculate the centroid (equation 3.1) and the Root Mean Square (RMS) radius[8] of the spot obtained in the detector. The RMS value of the radius considers all the contributions in the detector plane, understood as the distances between the impact points of incident ray lights with respect to the central point (the centroid).

$$c_x = \frac{\int x.I(x,y)dxdy}{\int I(x,y)dxdy} \;\; ; \;\; c_y = \frac{\int y.I(x,y)dxdy}{\int I(x,y)dxdy} \tag{3.1}$$

As an example of the results obtained, figure 3.17 (next page) shows the case of study for the merit function with VCSELs $I_{forward}$ 1mA, along with information from the irradiance captures in the detector for some concrete cases. Separation distance between VCSEL light sources and detector was increased from 0 to 30mm, with the array of microlenses placed at the effective focal length (1.063mm). A minimum RMS radius of ≈75μm is obtained for a distance of 5mm between the VCSELs and the detector.

In the same figure, it can be appreciated that there is a range of position values (from 0 to 5mm approximately) where the tendency is distorted. This is due to the fact that merit function is dependent on the area of the detector used for the simulation. In this case, detector area was defined large enough to cover the whole range of simulations (700x700μm^2) and this caused that in short distances, near the light source, this area captured not only the spot of interest but also some replicas. Merit functions for cases with $I_{forward}$ 2mA and 8mA offer similar results: a minimum RMS radius value of ≈80μm is obtained in a detector placed at a distance of 5mm from the VCSEL light sources.

We can conclude that even in a collimated scenario, where in theory divergence is corrected, simulations demonstrate that there is an increasing tendency in the values of the spot radius from ≈75μm to ≈240μm, though surely lower than the one existing in a system without optics.

After merit function simulations, each one of the images provided by the detector was then processed with *Matlab* software to fit the most suitable Gaussian curve to the cross section of the irradiance profile (power per unit area) as in figure 3.18a. Then, values of the width of the beam (≈ diameter of the spot) were determined according to $1/e^2$ standard. In a Gaussian beam, the $1/e^2$ width is equal to the distance between the two points on the marginal distribution that are $1/e^2$ = 0.135 times the maximum value, i.e. optical intensity drops to 13.5% from the maximum (figure 3.18b). The Full Width at Half Maximum (FWHM) standard (understood as the distance between two diametrically opposite points at which the irradiance is a ½ fraction of the beam's peak irradiance) was not considered, since measuring the width of the beam with that criterion would not provide information about the total dimensions of the spot, i.e. the full width in the worst case.

The summarised data of the simulation results for the pure collimated scenario and the comparative study of a system with and without optics, can be consulted in tables 3.2 and 3.3, and in the enclosed figures.

[8] According to *ZEMAX* user's manual, the RMS spot radius is the root-mean-square radial size. The distance between each ray and the reference point is squared, and averaged over all the rays, and then the square root is taken. The RMS spot radius gives a rough idea of the spread of the rays, since it depends upon every ray.

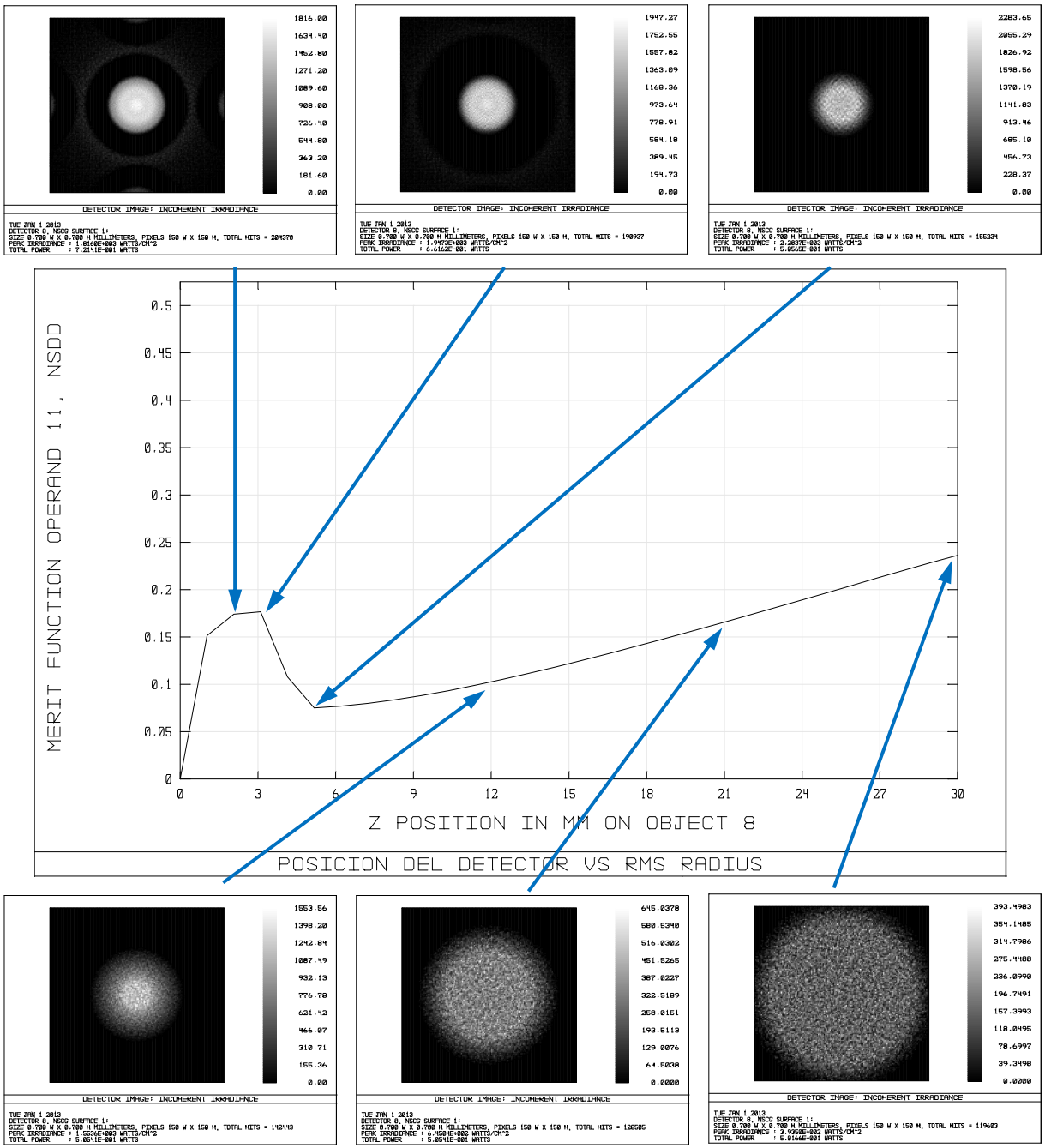

Figure 3.17: *ZEMAX non-sequential mode ray tracing simulations. In the middle, "RMS radius VS position of the detector" merit function for a collimated system: X-axis refers to the location of the detector plane (770x700µm²) in absolute values (the origin is the VCSEL light source), Y-axis presents the RMS radius value (mm) of the captured spot. Position of the detector varies in the range of 0 to 30mm. The intensity emission profile of the light source is defined for a forward current of 1mA. At the top and bottom, detector captures with information about irradiance at concrete positions: 2.3, 3, 5, 12, 21 and 30mm. A minimum RMS radius value of ≈75µm is obtained for a distance of 5mm. For cases in the range from 0 up to 5mm, values of RMS radius in the figure of merit are distorted, due to the effect of undesired replicas captured in the area of the detector (e.g. capture for case 2.3mm). For better quality images, please refer to Appendix.*

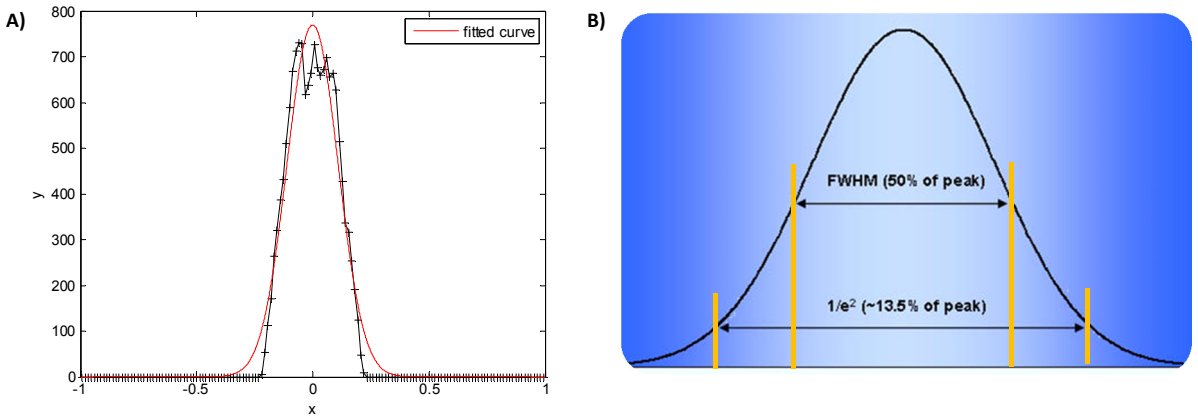

Figure 3.18. *(a) Matlab Gaussian adjustment for the cross section of the irradiance profile for a spot captured in a detector located at a distance of 15mm. (b) Scheme of the $1/e^2$ and FWHM standards defined to statistically measure the width of the beam (diameter of the spot). FWHM is discarded.*

Tables 3.2: *Summary of the merit function simulation results of the spot sizes (radius) measured as ZEMAX RMS radius and $1/e^2$ standard, for a collimated scenario. Image plane was located at different distances from the VCSEL light source to evaluate the collimation effect achieved by the micro-lenses. Results are presented for several VCSEL forward intensities (8mA, 2mA and 1mA), but it can be appreciated that there is no significant difference in the values obtained. The RMS radius is always lower because of the calculation of the parameter as a RMS value.*

Radius of the spots with micro-lenses in µm. Collimation effect: RMS | $1/e^2$	Distance between VCSELs and detector (image plane) in mm. Detector of dimensions 700x700µm²				
Simulation results for several VCSEL forward intensities (mA)	**5**	**10**	**15**	**20**	**30**
8	82/119	96/146	124/188	159/236	236/340
2	80/128	94/145	123/187	159/231	236/338
1	75/115	91/138	121/185	158/230	236/348

Table 3.3: *Summary of the simulation results of the spot sizes (radius) measured as $1/e^2$ for a non-collimated scenario; no micro-lenses were used to correct the divergence of light sources. Image plane was located at different distances from the VCSEL light source. Results are presented for several VCSEL forward intensities (8mA, 2mA and 1mA). For these simulations, ZEMAX detector area was adjusted according to the needs of each particular case. In a non-collimated system, the more far the detector is placed, the more increase in the radius. Detector size must be large enough to capture the whole spot.*

Radius of the spots without micro-lenses in µm: $1/e^2$	Distance between VCSELs and detector (image plane) in mm. Detector with variable dimensions.			
Simulation results for several VCSEL forward intensities (mA)	**5**	**10**	**15**	**20**
8	1313	2626	3939	5252
2	991	1982	2973	3964
1	842	1608	2412	3216

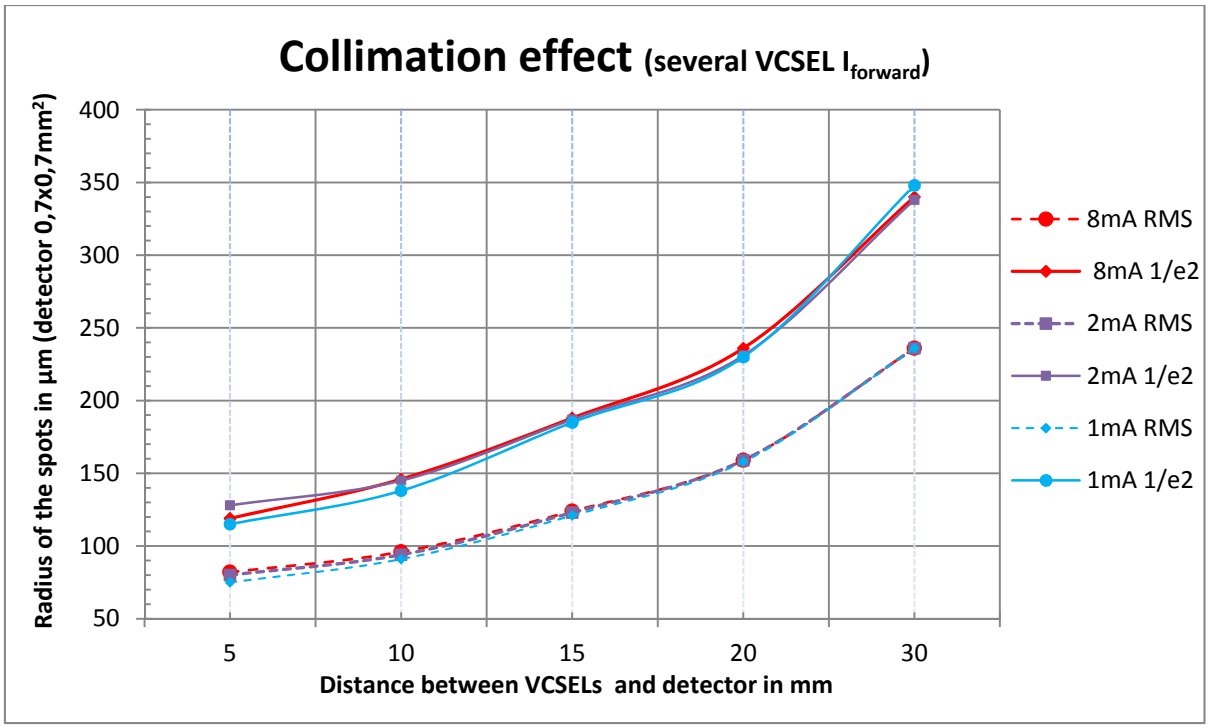

Figure 3.19: *Comparison graph of the spot radius calculated as ZEMAX RMS value and 1/e² standard for several VCSEL forward intensities (8, 2 and 1mA) in the collimated scenario. At the view of the results, different angular intensity distributions of VCSELs exert a minimum effect in the definition of the dimensions of the spot. For the 1/e² standard, a Gaussian adjustment is performed with Matlab software. RMS values are lower, for they are calculated as the quadratic mean value considering all the contributions of rays impacting the detector.*

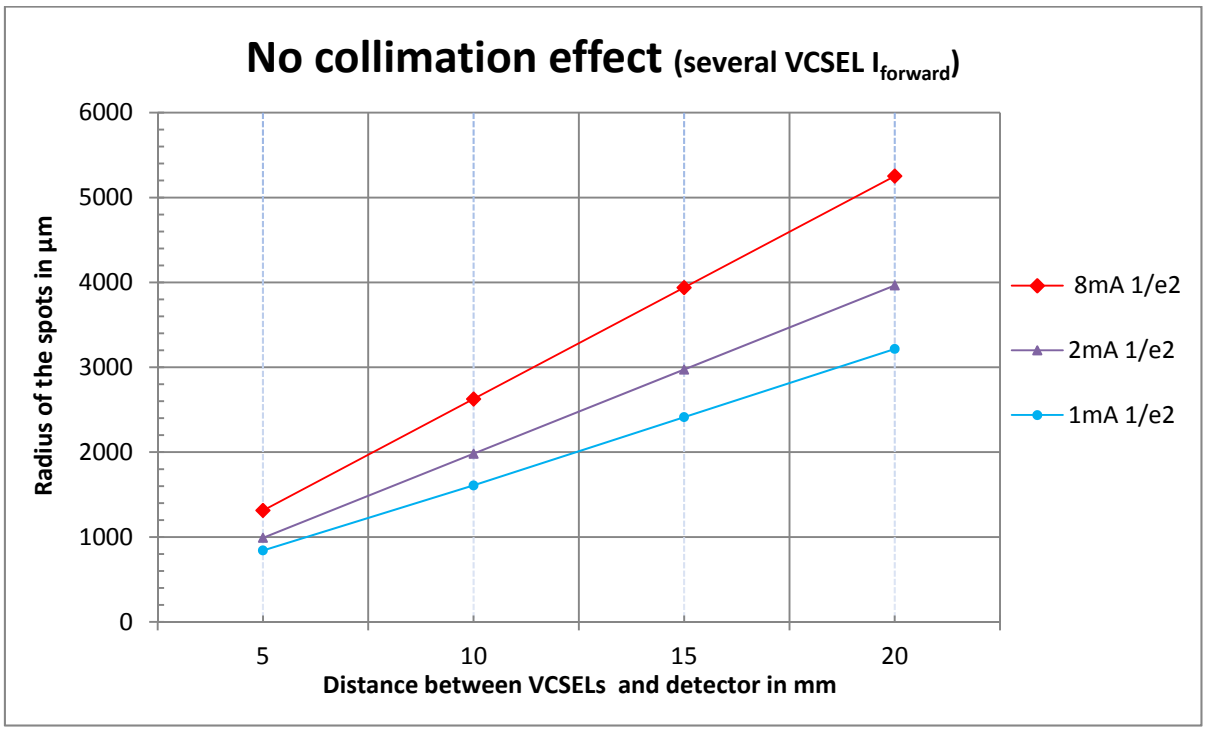

Figure 3.20: *Comparison graph of the radius values for several VCSEL forward intensities (8, 2 and 1mA) measured as 1/e² standard. Gaussian adjustments performed with Matlab software. No microlenses were used for these simulations. Large values of spot sizes are obtained in all cases. An increasing linear tendency is observed.*

As can be appreciated in previous graphs, for a system without micro-optics the radius of the spot in the detector plane increases linearly with distance, due to the fact that there is no optical correction. The correction introduced by the micro-lenses reduces the natural beam divergence of the VCSEL light sources (approximately 25°- 30° measured as full width $1/e^2$ according to manufacturer) to only ≈ 3.5° for a detector placed at a distance of 5mm from the VCSEL light sources (figure 3.21). At the view of the results, the collimated system is suitable to work within the range from 5 to 10mm, delivering acceptable results with an increment of only ≈15µm (≈+18%) in the radius of the spot (refer to figure 3.19 containing RMS radius values). Outside this range, the collimation effect can not be guaranteed: although certainly there is a correction in the divergence angle, radius values suffer an increment larger than expected. For example, the increase in the divergence angle for the range of distances from 10mm to 20mm is ≈ 0.38° (according to RMS radius values), which is translated in an increment in the radius of about 60µm (≈+93%). We suppose that to achieve perfect collimation, a system of multiple lenses should be necessary.

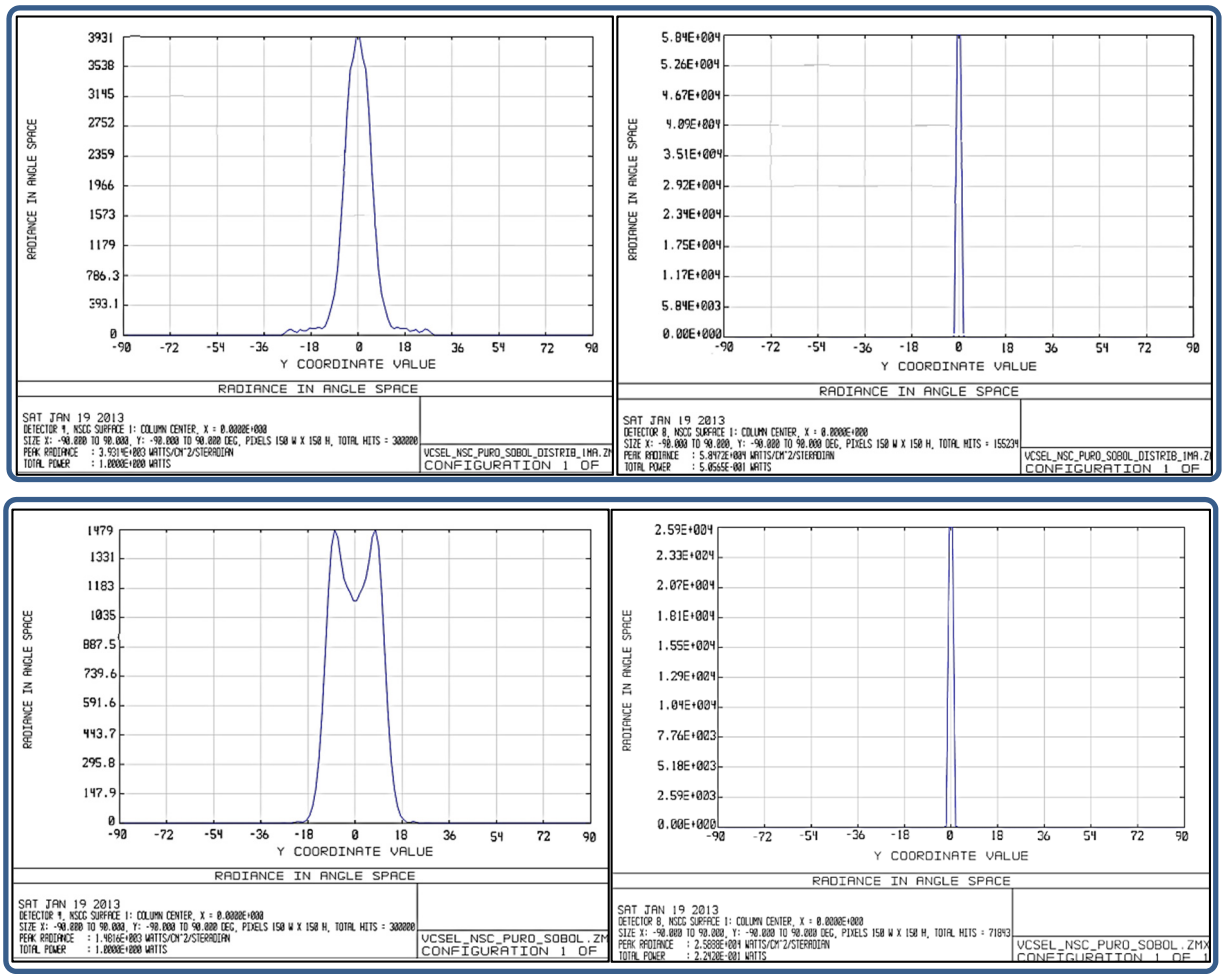

Figure 3.21: *Comparison of the results for the divergence effect in a collimated system, with a detector plane located at 5mm from the VCSEL light sources. Images on the left: natural radiance emission profile in angle space of the light source for $I_{forward}$ 1mA with divergence of 18° (top) and 8mA with divergence of 30° (bottom); divergence of 18°. Images on the right: corrected radiance emission profile after micro-optics; in both cases, $I_{forward}$ 1mA (top) and 8mA (bottom) divergence becomes 3.5°.*

Finally, simulations performed for the collimated scenario prove that a radius as small as 115µm ($1/e^2$) or 75µm (RMS) can be obtained for a VCSEL with $I_{forward}$ of 1mA and a separation distance between the

VCSEL and the detector plane of 5mm. Attending to the real dimensions of the microfluidic block (placed between the optical system and the detector), a more realistic working hypothesis would place the detector (i.e. microfluidic chip) at a distance of 10mm. In this case, the radius value becomes 138µm ($1/e^2$) or 91µm (RMS).

3.4 Focused light beams scenario

In the focused light beams scenario, simulation results for the diagrams of impacts and irradiance in the detector viewers were analysed in order to determine the expected behaviour of the system, with the aim of defining the best conditions to obtain a spot of reduced dimensions and high power efficiency. A focused spot is useful to concentrate the maximum power in a defined area, improving for example the detection of fluorescence particles (refer to Chapter VIII). For these simulations, besides the VCSEL light sources (with 1mW optical power) and the micro-lenses, the system layout was completed with the microfluidic chip (figure 3.22). Several VCSEL forward intensities (8, 2 and 1mA) were considered for analysis.

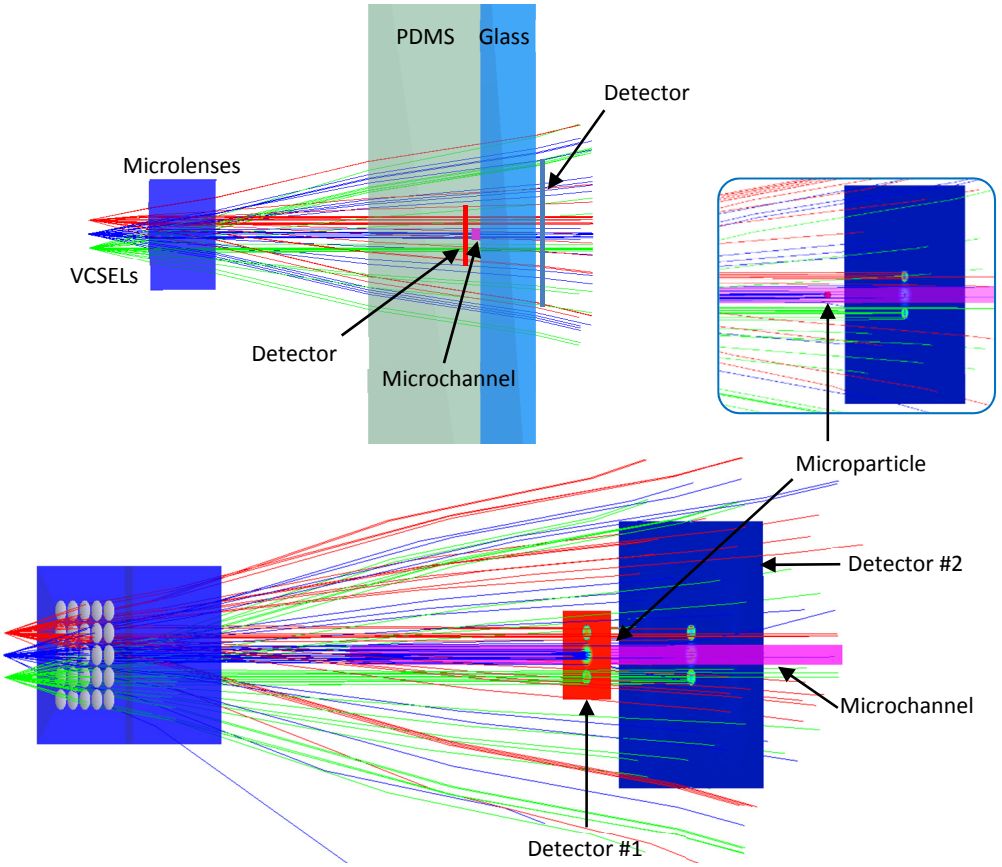

Figure 3.22: *Simulations for the complete system, including the microfluidic stage. Top: 3D model of the system with 3 VCSEL light sources (red, blue and green), the array of microlenses (dark blue) and the microfluidic block (PDMS in soft green and glass in light blue). In the center of the microfluidic block, a microchannel (pink) of dimensions 150x200x225µm³ (height, width top, width bottom) is defined. Some detectors can be appreciated: detector #1, previous to the plane (in the PDMS layer) where the channel lies, and detector #2, behind the microfluidic chip. Bottom: 3D layout with an improved view of the microchannel and the detectors. The effect of a microparticle of 50µm diameter (red colour) located in the channel is captured by the final detector #2, as well as the three well-defined light beams coming from the VCSELs (Zoom).*

Detector elements included in the simulation layout (4 in total) were placed in defined positions of interest. Two of them inside the microfluidic chip, and the other two located behind the microfluidic block, in the position that would correspond to the real CMOS photodetectors array.

To obtain proper results, according to the real dimensions of CMOS imaging sensor, one of these rear detectors was defined to have total dimensions of 0.100x3mm^2 with a number of 256 pixels in a single column, so that each pixel presented dimensions of ≈ 100x11µm^2, equivalent to the real values of the fabricated array (refer to Chapter VI). In simulations, *ZEMAX* will average out the value of the irradiance intensity for these pixels, just as in a real measurement, in which all the light contributions exciting the area of one pixel determine its final intensity value.

The microfluidic stage was defined following these design parameters: a PDMS layer of 2mm thickness (refractive index 1.47), a glass layer of 1mm thickness (refractive index 1.51), and a microfluidic channel of 150µm height, 200µm width for the top side and 225µm for the bottom side. The difference in the width for top and bottom sides creates a more real channel with non-parallel side walls (figure 3.23).

Different channel geometries produce different optical effects: the less parallelism between the channel walls, the more refraction of light. In the image captured by the final detector, this effect will show up as black lines (absence of light) along the length of the channel. Channel is filled with Isopropanol (refractive index 1.37) and a spherical particle of 50µm diameter is placed in the center.

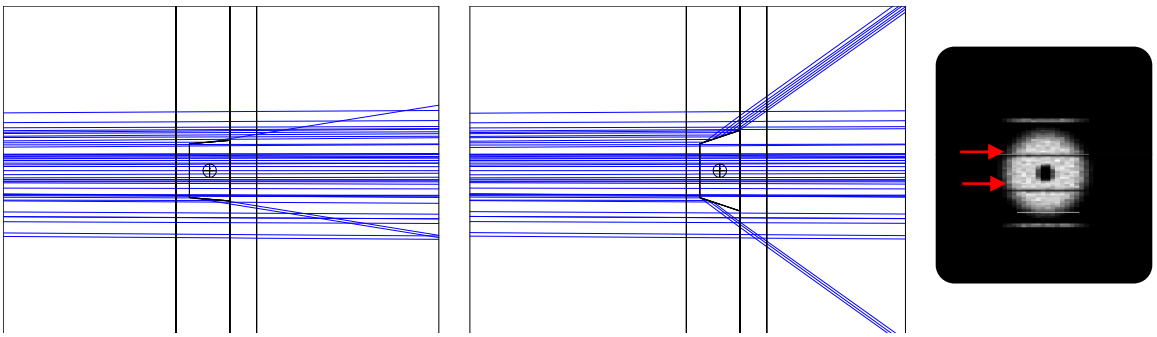

Figure 3.23*: Effects of the geometry of the microfluidic channel in simulations. Channel on the left side with dimensions 200µm for top face and 225µm for bottom face. Channel on the right side with dimensions 200µm for top face and 300µm for bottom face. The black lines (absence of light) in the image captured by the detector, are the result of light refraction produced by the walls of the channel.*

Simulation process was as follows: with the detector located inside the microfluidic chip, right previous to the plane where the microchannel lies, the optimal radius of the spot responsible for lighting the particles (optical detector #1 in figure 3.22) was determined. The “intermediate” detector right behind the microchannel (in the glass substrate) offered an image of the direct effect produced by the microparticle inside the channel. The final detectors, which represented the CMOS photodetectors array, as in the experimental setup (optical detector #2 in figure 3.22), provided an estimation of the variation in the intensity distribution after the microfluidic stage, due to the flowing of particles.

Simulations demonstrate that a relation exists between the radius of the particles and the effect they produce on the final detector, as can be seen in the following figures. Figure 3.24 presents the results of the merit function that defines the power captured in the detector depending on the radius of the particle. As the particle increases its volume, the total amount of power received in the detector

decreases, following the natural tendency in which a large object blocks more light. Increasing the thickness of the PDMS layer from 2mm to 3.5mm almost have no effect on the final values: for a particle of 10microns radius, the power in the detector only decreases 4.46%.

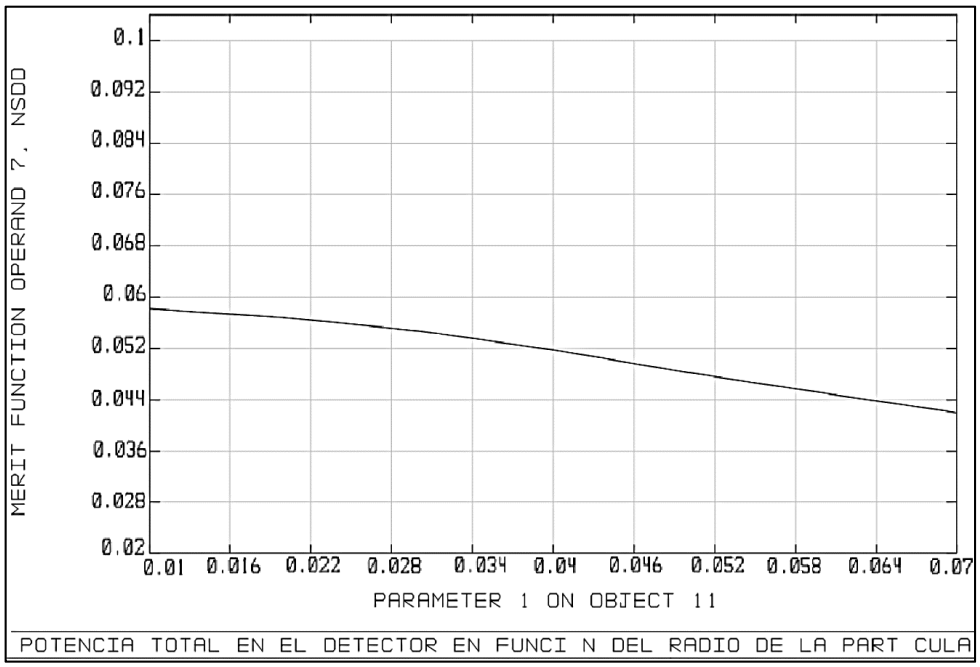

***Figure 3.24**: "Total power in Watts (Y-axis) VS radius of the particle (X-axis)" merit function. Radius of particles from 10 to 70 microns. VCSEL source forward intensity of 8mA and 1mW optical power. Separation distance of 20mm between the VCSEL and the PDMS layer. Detector area in both cases is 0.100x3mm. Results for a PDMS thickness layer of 2mm (left) and 3.5mm (right).*

A detailed study of the effect of particle size in the irradiance captured by the final detector is shown in figure 3.25, with examples for two different particles: 10µm and 50µm diameter. Images captured from the detectors offer visual information of the shadows (light blockage) caused by particles, while in cross-sections views the decrease in the light intensity can be easily observed.

***Figure 3.25 (next page):** Simulations for a VCSEL forward intensity of 8mA and a PDMS thickness layer of 2mm. First set of pictures correspond to simulation results for a particle of 50µm radius (green color). Second set, to a particle of 10µm radius (orange color). On the left, images captured by the final detectors (dimensions 3x3mm, 0.100x3mm) behind the microfluidic block. It is clearly noticeable the effect of the particle of 50µm radius (black circle inside the grey spot) as well as the shadow caused by the walls of the microchannel (two black lines inside the grey spot). On the right side, cross-section of the images. The effect (decrease in light intensity) of the particle of 10µm radius can be appreciated in the cross-sectional figures.*

Particle of 50µm radius

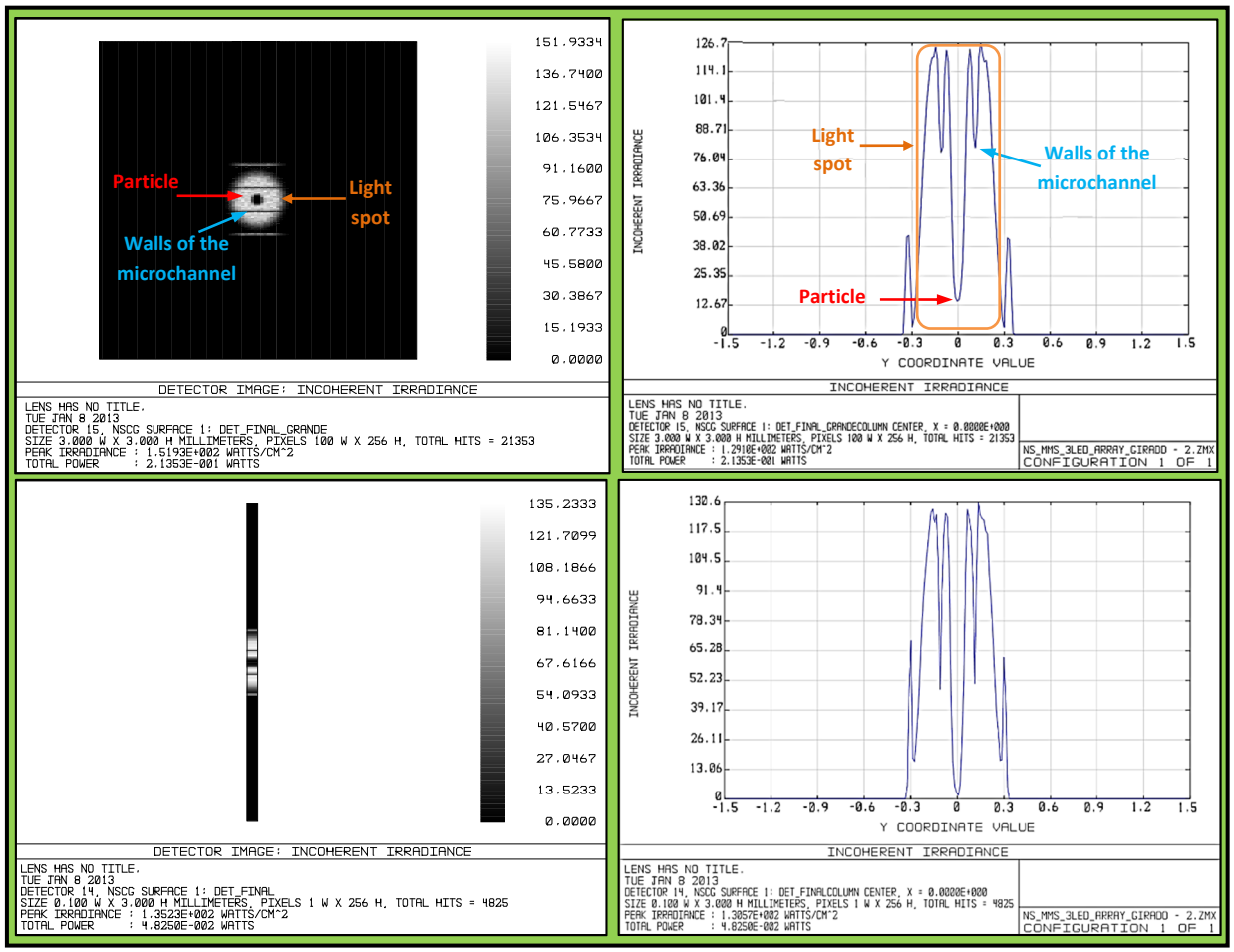

Particle of 10µm radius

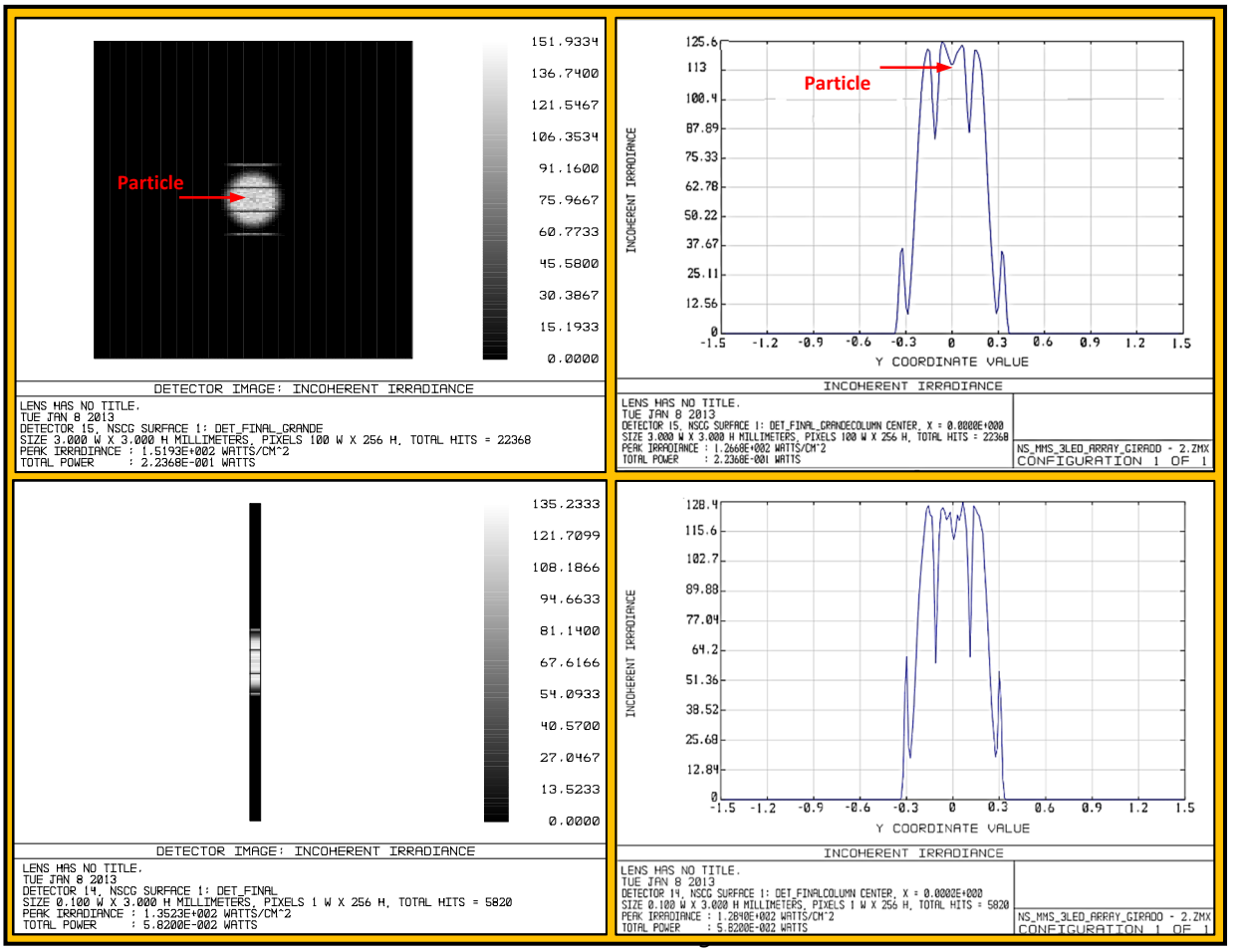

To calculate the minimum radius of the spot focused onto the microchannel (≈position of optical detector #1 in figure 3.26), two variables were defined in our parametric analysis: the separation distance ($d_{V\text{-}D}$) between the VCSEL light sources and the final detector located at the rear of the system (optical detector#2 in figure 3.26) representing the real CMOS photodetectors array; and the distance ($d_{V\text{-}L}$) between the VCSELs and the microlenses array.

Though simulations covered a large range of values (from 9mm to 33mm) for variable $d_{V\text{-}D,}$ in practice, the initial value was limited to 18mm (equal to a distance of 15mm from the VCSELs to the top side of the PDMS). With this lower limit, simulations were more adjusted to the real dimensions of the rest of the components of the system; for example, regarding the physical manipulation of the microfluidic chip for the placement and replacement of the different elements and pieces.

As for variable for variable $d_{V\text{-}L}$, considering the value of the effective focal length for microlenses (1.063mm), we decided that an appropriate range of values would be from 0.5 to 1.5mm.

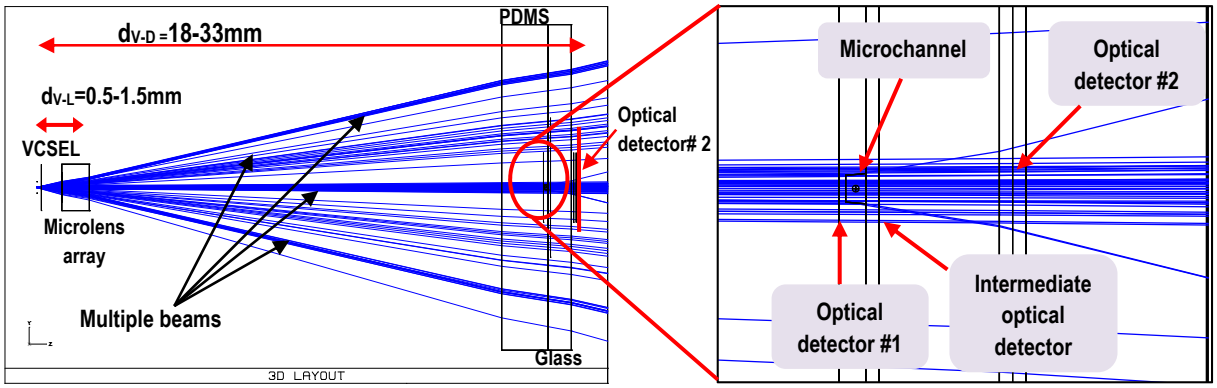

***Figure 3.26**: Simulations with 100.000 analysis rays and a VCSEL emitting at 850nm. Left: Layout of the complete microoptical system. Right: Detail of the microfluidic channel in the simulations. Detector#1 is used to optimize the RMS radius of the spot focused on the microchannel (merit function). Intermediate detector placed right behind the microchannel captures directly the light blockage effect of particles. Detector#2 simulates the CMOS photodetectors array.*

A merit function returning the RMS value for the radius of the spot in the microfluidic channel (detector#1) was obtained for each one the cases of study: setting the value of variable $d_{V\text{-}D}$, a swept for variable $d_{V\text{-}L}$ was performed with the purpose of calculating the optimal position of the micro-lenses array resulting in the smallest light spot. The cycle was repeated for a new $d_{V\text{-}D}$ value.

Figure 3.27 is just an example for one of the simulated cases, where $d_{V\text{-}D}$ = 18mm. The VCSEL source was defined to have $I_{forward}$ 1mA, and dimensions for detector#1 were 1x1mm^2. The effect of a particle of 50µm diameter (shadow = blockage of light) is presented in the captures for detector#2 for different values of variable $d_{V\text{-}L}$.

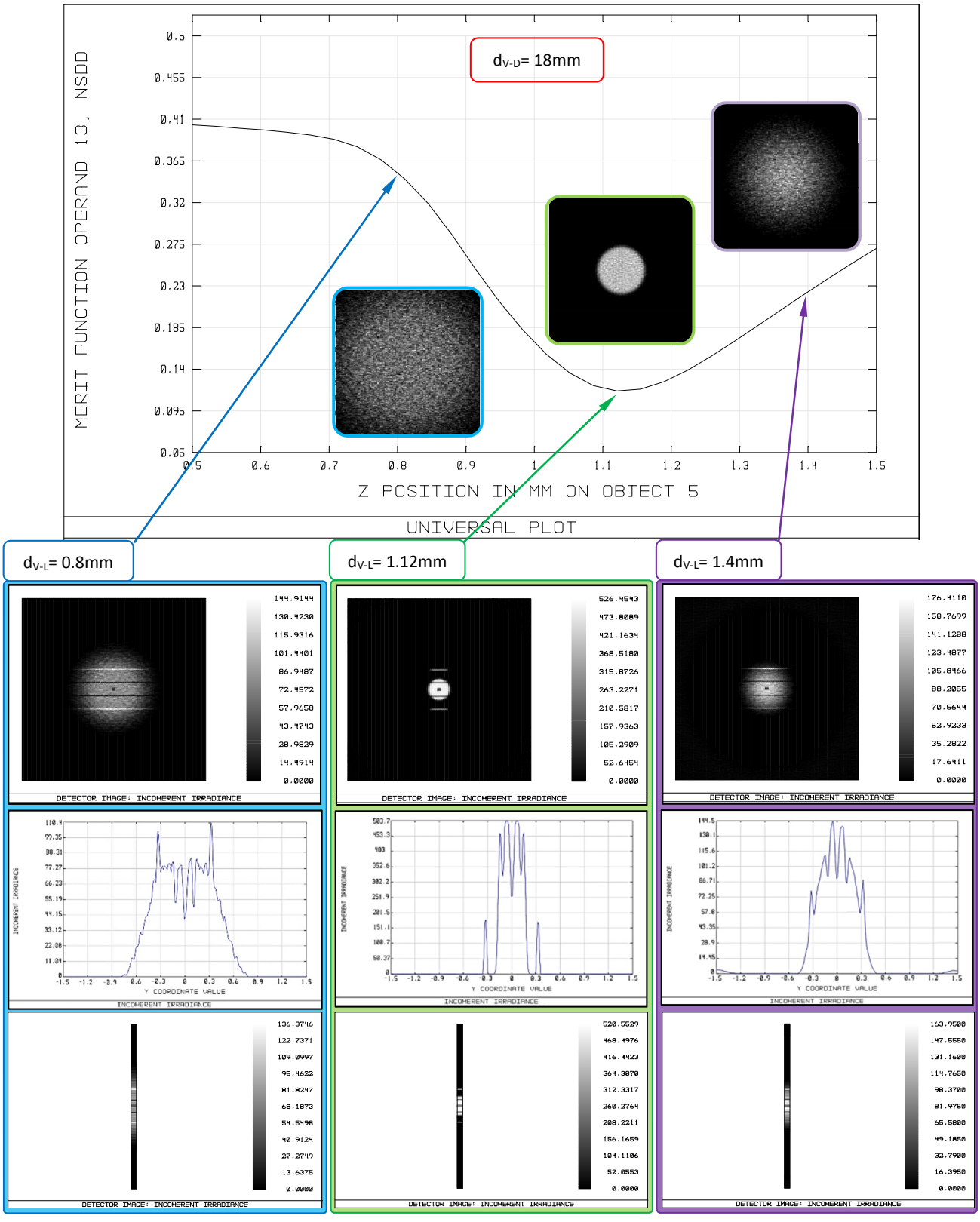

Figure 3.27: *Merit function simulations for the focused system with VCSEL $I_{forward}$ of 1mA and $d_{V\text{-}D}$ 18mm. Variable $d_{V\text{-}L}$ represented in X-axis. RMS radius value of the spot captured in detector#1 (1x1mm²) represented in Y-axis. Inserted images contain the capture of the spot focused onto the channel (at detector#1). Each coloured box corresponds to a particular case: blue box for $d_{V\text{-}L}$ of 0.8mm, green box for $d_{V\text{-}L}$ of 1.12mm (minimum radius spot) and pink box for $d_{V\text{-}L}$ of 1.4mm. First and second rows include images and cross-sections respectively from the irradiance captures at the final detector#2 with dimensions 3x3mm²; third row refers to the same captures for a detector of dimensions 0.100x3mm². For better quality images, please refer to Appendix.*

Through the comparison of the results for the different analysed cases, some conclusions can be drawn for the light beam focused scenario (figure 3.28). There is no significant difference between the results provided by the merit functions for the two VCSEL forward intensities studied (1mA and 8mA) in terms of the minimum RMS radius value focused at the position of the microfluidic channel. In both cases the tendency is the same. Looking at the results, we find that the minimum RMS spot radius in this scenario corresponds to a value of ≈38μm for $d_{V\text{-}L}$≈1.29mm and $d_{V\text{-}D}$≈9mm. Note that this RMS value is very close to the radius of the emission area of the VCSEL (≈25μm).

However, attending not only the purpose of obtaining the minimum spot radius but also considering the physical restrictions of the designed system, some precisions must be pointed. This theoretical RMS radius of ≈38μm could be inefficient in the particle detection process, yielding unsuccessful detections in some conditions. If we observe the image for irradiance in the final detector#2 corresponding to this particular case (figure 3.29), we will not see the black lines which define the limits of the microchannel due to the refraction of light in the walls of the channel. Therefore, it can be assumed that the entire spot falls inside the area of the channel, and even, depending on the dimensions of the particular channel (i.e. the width), the spot could be small in comparison.

According to the optical detection theory widely applied in flow cytometry[9], the optimum size of a light spot should cover and even surpass the whole width of the fluidic channel to avoid that particles not flowing in the central path be undetected (figure 3.30). Besides, it also must be considered that simple spherical lenses do not modify the natural properties of light passing through them, and consequently, provided spots are very intense in the central region but with brightness decreasing out toward the edges, for they follow the typical Gaussian profile of laser sources. Hence, for much reduced spots, the microfluidic system must ensure the confinement of particles in a well-defined path through the beam [11].

All this reflexions lead us to conclude that the size of the spot should be in accordance with the dimensions of the channels in the microfluidic chip. Concerning our design criterions, where the width of the microfluidic channel was set to ≈200μm, it is clear that the desired spot should have at least the same diameter. Adding some other material restrictions, like the ones previously commented (e.g. handle and replacement of the microfluidic channel, or connection of the flextubes to the inlets and outlets), we considered that the minimum separation distance between the optical package and the microfluidic block should be at least 15mm, which means that the distance between the VCSELs and the final detector (CMOS array sensor) is $d_{V\text{-}D}$= 18mm.

With these constraints, a minimum RMS spot radius of ≈116μm is obtained for $d_{V\text{-}L}$≈ 1.118mm. This value accomplishes perfectly with the exposed requirements: the dimensions of the microfluidic channels (200μm width for a channel with hydrodynamic focusing driving particles of 10-100μm diameter) and the separation between two adjacent VCSELs (250μm) (figure 3.27).

[9] In flow cytometry, the optimum spot should present an elliptical shape: it covers the entire width of the channel, and also avoids multiple particles being illuminated at the same time. Unfortunately, in spite of the existence of some references describing their fabrication [15], [16], the catalogue of commercial microlenses from *SUSS Microoptics* do not include this sort of lenses. The alternative to achieve the desired shape in the spot would be the fabrication of self-designed microlenses.

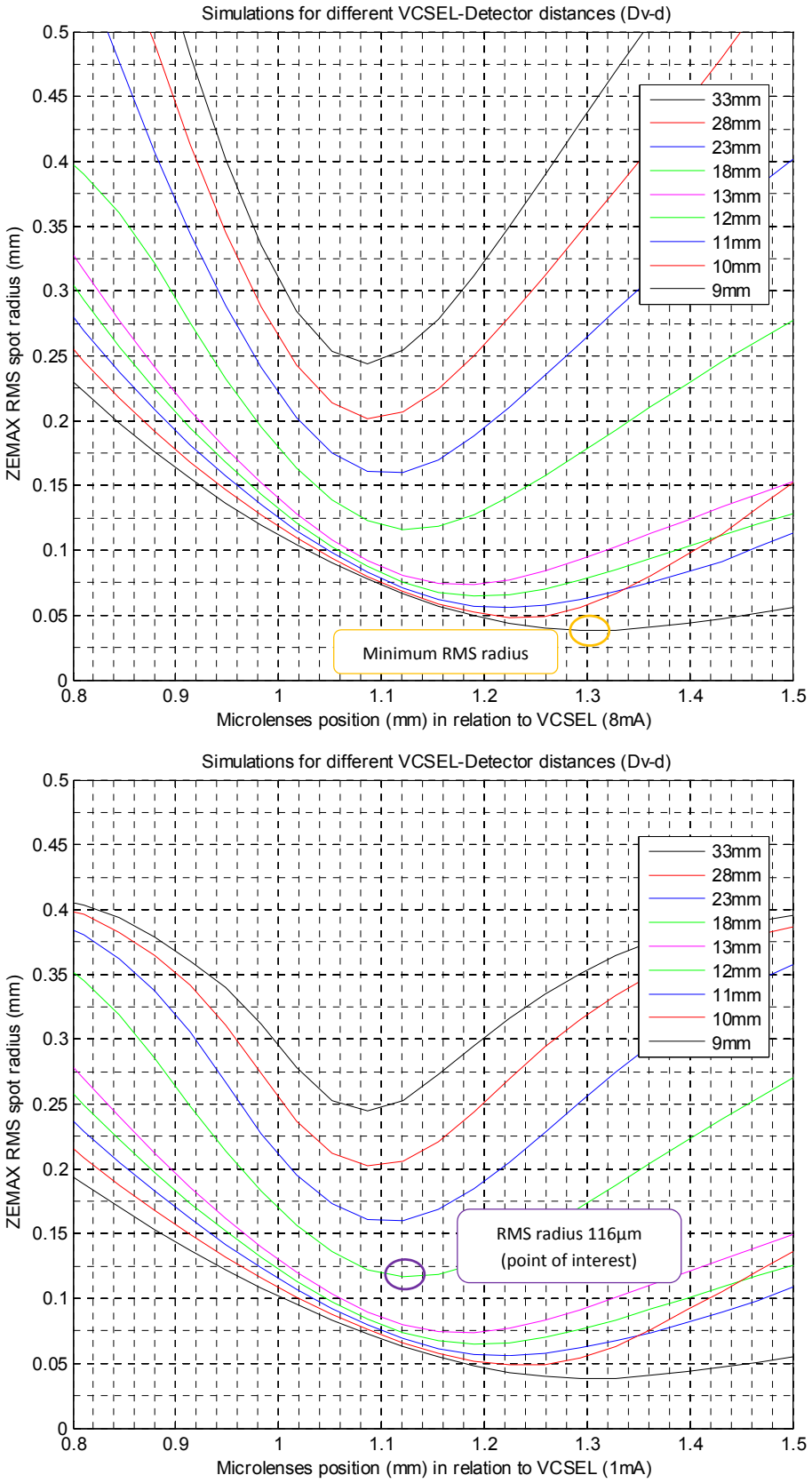

Figure 3.28: *Results of the defined merit function for multiple analysed cases. Two different VCSEL forward intensities studied: 8mA and 1mA. Minimum RMS spot radius (38µm) is obtained for the case where the distance between the VCSELs and the final detector#2 is equal to* $d_{V\text{-}D}$*≈9mm with* $d_{V\text{-}L} \approx$ *1.29mm. Real point of interest according to design criterions, offers a RMS radius of 116µm, for to* $d_{V\text{-}D}$*≈18mm with* $d_{V\text{-}L} \approx$ *1.118mm.*

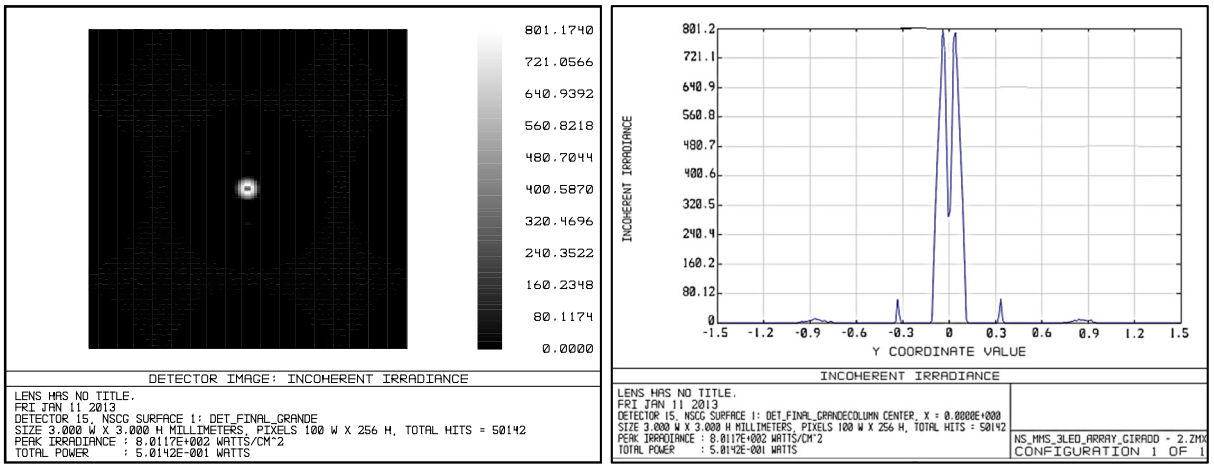

***Figure 3.29**: Simulations for a focused light beam scenario. Conditions for minimum RMS radius (≈38µm in detector#1) with VCSEL $I_{forward}$ 1mA. Images correspond to irradiance capture (left) and cross-section (right) from the detector behind the microfluidic channel (detector #2).*

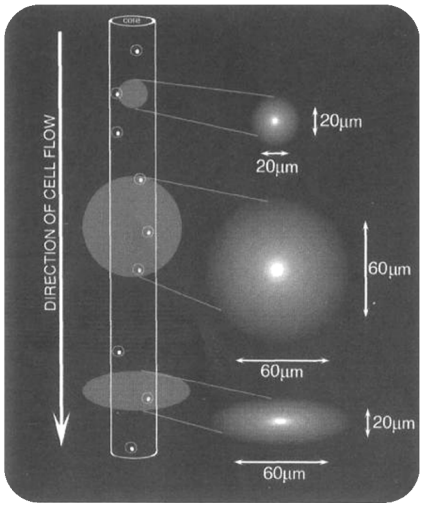

***Figure 3.30:** Flowing cells crossing light beams of different profiles and dimensions. Small circular beam does not illuminate particles equally if they flow at the edge of the stream core. The large circular beam illuminates the cells equally, but multiple cells are included in the spot at the same time if flow rate and concentration of solution are not controlled. Elliptical spots represent the optimum alternative. Printed with permission of Alice Longobardi Givan from "Flow Cytometry: First Principles", John Wiley & Sons Editors, 2004.*

3.5 Discussion on the results for both studied scenarios

From the results obtained after the study of both scenarios (collimated light beams and focused light beams) it can be concluded that, with the defined design restrictions ($d_{V\text{-}D}$ = 18mm), the optimal position of the microlenses array for the focused light beams scenario ($d_{V\text{-}L}$≈ 1.118mm) is very similar to the focal length parameter of the microlenses, fixed in the collimated case ($f_e = d_{V\text{-}L}$ = 1.063mm). Thus, a comparison between simulation results in both scenarios returns that final radius values are quite similar (Table 3.4). In micro-optics, the far field image plane of detector #2 at the fixed distance $d_{V\text{-}D}$ 18mm, can be compared with the infinite image plane where the collimated light beams would converge. At the view of these results, it is deduced then, that there is no considerable difference in any of the two proposed scenarios with the defined working conditions. Both solutions offer

acceptable results (spots with adjusted dimensions) and are suited to be included in the final optical particle detection system. Furthermore, the collimated scenario could be the best option for it presents more technical possibilities, as it delivers RMS radius values of 102µm and 133µm (both spots covering the whole width of the microfluidic channel) for $d_{V\text{-}D}$=13mm and $d_{V\text{-}D}$=18mm respectively (with $I_{forward}$ 8mA). If the mechanics of the final system allowed us to work in the range of $d_{V\text{-}D}$=13mm, the whole system would be more miniaturized.

Table 3.4: *Summary of the simulation results for the source optoelectronic package including the microfluidic block and analyzing two different scenarios: focused and collimated light beams. Values of the spot sizes (RMS radius) are presented for a detector located at the microfluidic channel position (detector#1). From $d_{V\text{-}D}$ 18mm the differences in the values obtained for each scenario are below 15%. Best values for spot dimensions according the requirements of the system are achieved for the focused scenario with $d_{V\text{-}D}$ 18mm, where a RMS radius of 116µm is achieved. Anyway, the collimated scenario can be also considered a good solution for it offers RMS radius values of 102µm and 133µm for $d_{V\text{-}D}$ 13mm and $d_{V\text{-}D}$ 18mm respectively.*

	Focused $I_{forward}$ = 8mA	Collimated $I_{forward}$ = 8mA		Focused $I_{forward}$ = 1mA	Collimated $I_{forward}$ = 1mA	
$d_{V\text{-}D}$ mm	RMS radius µm	RMS radius µm	Difference µm / %	RMS radius µm	RMS radius µm	Difference µm / %
9	38	86	48 / 126	38	80	42 / 111
10	48	89	41 / 85	48	83	35 / 73
11	55	92	37 / 67	55	87	32 / 58
12	64	97	33 / 52	65	92	27 / 42
13	73	102	29 / 40	73	98	25 / 34
18	116	133	17 / 15	116	130	14 / 12
23	165	169	4 / 2	159	167	8 / 5
28	201	207	6 / 3	202	207	5 / 2
33	243	247	4 / 2	243	247	4 / 2

The description of the hybrid assembly process of the commercial components introduced in this chapter, as well as the explanation of the adopted solution to place them in the defined positions according to the simulation results, will be the subject of the next chapter.

3.6 Alternatives of design

Two alternatives are presented in this section. Both are based on the design and fabrication of more complex structures redefining the initial conceptual idea, and even one of the proposals explores the idea of using self-designed microlenses instead of commercial components. None of them has been fabricated, and they are only included here as an introduction of what sort of future work could be developed.

3.6.1 Monoblock design

This alternative represents not only a new departure point in the design process, but also in the fabrication methodology. The detection system is based on a single “one piece block” which includes optics and microfluidics fabricated in PDMS. In the work discussed up to now, the array of microlenses and the microfluidic chip were separated pieces, independently designed and fabricated in different materials, which ended up being joined according to the positional parameters obtained in optical simulations, to create the structure of the final detection system. The monoblock design incorporates

both elements on the same PDMS substrate by means of a two-step fabrication process: a first PDMS slab with microlenses array on the top side would be bonded to a second PDMS slab including a microfluidic channel, delivering a single PDMS block. Thickness of PDMS slabs defines the particular position of interest for the microfluidic channel inside the final PDMS block (figure 3.31). In this proposal, to simplify the process, lenses could be replicated in PDMS from a commercial array, like for example, the "*SUSS microoptics*" array of microlenses presented in this chapter.

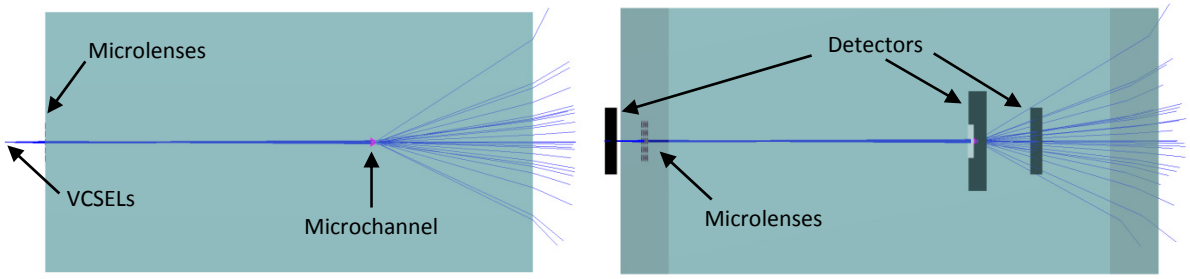

***Figure 3.31**: ZEMAX ray tracing simulations for the PDMS monoblock system integrating the array of microlenses and the microfluidic channel. (a) 3D model of the system with 1 VCSEL light source emitting rays (blue lines). In this example, the channel (pink color) is positioned at a distance of 11mm from the VCSELs, and the microlenses on the top face of the monoblock at 1.22mm from the light sources. (b) View of the detectors used for simulations.*

The results of the merit function that define the optimal position of the microlenses with respect to the VCSELs to obtain the minimum RMS radius spot in the plane of the microfluidic channel, are presented for different positions of the microfluidic channel inside the PDMS block (figure 3.32).

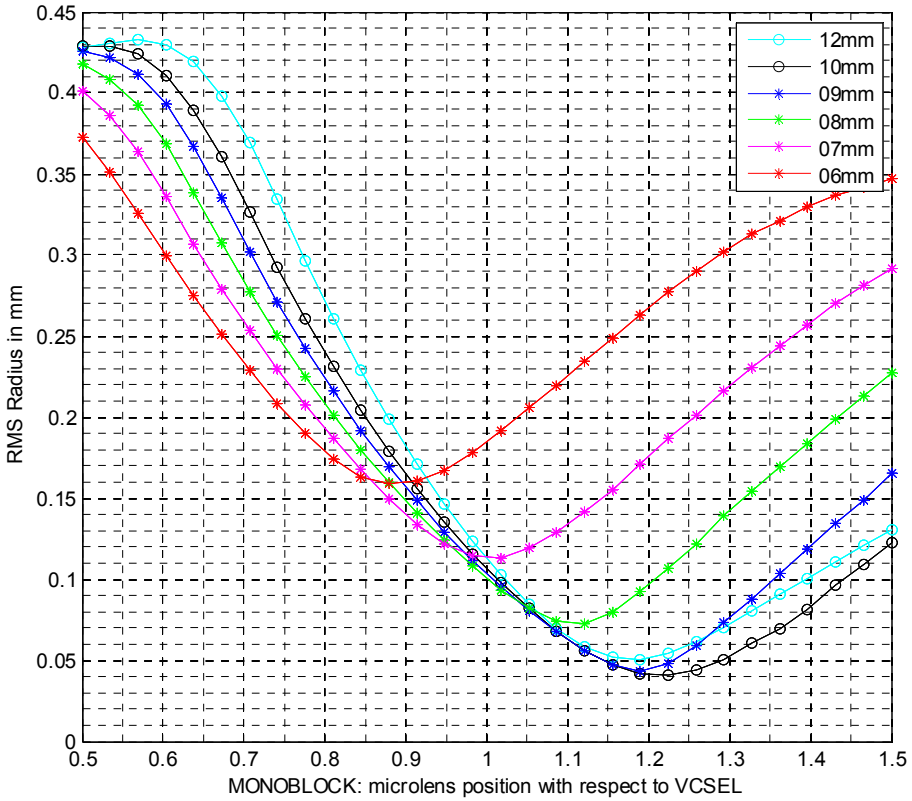

***Figure 3.32**: Merit function simulation results for the monoblock system with RMS radius versus microlenses position with respect to VCSELs. Each curve corresponds to a position of the microfluidic channel inside the PDMS block with the reference of the top side of the microlenses.*

The tendency in these results tells us that as the separation distance between the VCSEL light sources and the microfluidic channel decreases, the RMS radius value of the spot increases: lower RMS radius values are obtained for distances in the range of 8 to 12mm.

Positioning the microlenses at 1.22mm from the VCSELs and the microchannel at a distance of 11.22mm from the light sources (= 10mm from the top face of the microlenses; black curve from previous figure), a minimum RMS radius of 41µm is obtained for the spot in the detector of the microfluidic channel (figure 3.33). This value is in accordance with the minimum value obtained in the previous studies discussed in this chapter, i.e. RMS value of ≈38µm for $d_{V\text{-}D}$ ≈ 9mm, but with the benefit that the monoblock does not present physical restrictions in terms of the minimum space necessary to place and manage the microfluidic chip. Otherwise, with the system based on independent blocks and a distance $d_{V\text{-}D}$ fixed at 9mm, it would be a quite difficult task to operate the fluidics.

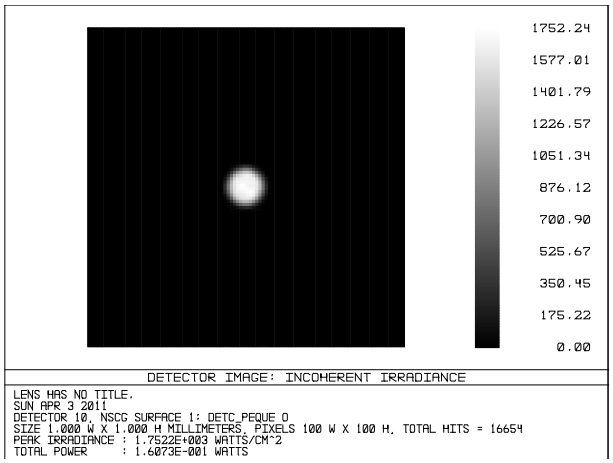

Figure 3.33*: Irradiance image of the spot obtained (RMS radius 41µm) in the detector placed previous to the microfluidic channel. Microlenses are positioned at 1.22mm from the VCSEL light sources, and the channel at 11.22mm from the same source.*

With the same variables, a study of the power collected by the detector placed previous to the microfluidic channel was also performed (figure 3.34). In all cases, power captured by the detector diminishes with distance as expected. Anyway, it may be quite interesting to sacrifice the target of obtaining the minimum RMS radius of the spot in benefit of an increase of the power impacting the microfluidic channel. As can be appreciated in figure 3.34, the power collected presents some maximums for certain VCSEL-microlenses positions, and these positions correspond to RMS radius values other than the minimum. Increasing the power would be especially useful for sensing applications requiring a powerful light source to excite the samples, e.g. fluorescence measurements. A compromise between these two parameters (dimensions of the spot and power) should be settled.

Centred in a particular case, the analysis of the power captured by the final detector (i.e. CMOS sensor array) placed behind the monoblock, in relation to the dimensions of the particles flowing through the channel, proves the functionality of the system to detect particles. In the example of figure 3.35, the case analysed corresponds to the minimum RMS radius value previously determined; i.e. microlenses positioned at 1.22mm from the VCSELs and the microchannel at a distance of 11.22mm from the same light sources (= 10mm from the top face of the microlenses; black curve from previous figure). Blockage

effect of light increases with larger particles, and consequently less power is collected by the final detector.

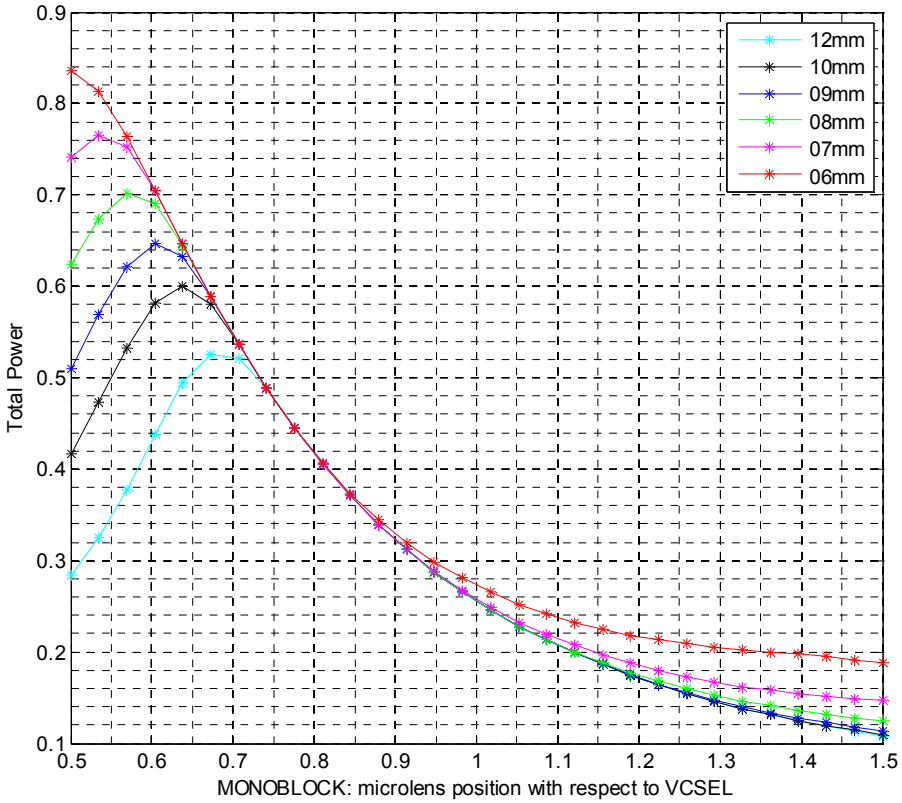

Figure 3.34: *Merit function simulation results for the monoblock system with total power collected by the detector positioned previous to the microfluidic channel versus separation distance between microlenses and VCSELs. Each curve corresponds to a position of the microfluidic channel inside the PDMS block with the reference of the top side of the microlenses. Distance units in mm, and power in Watts.*

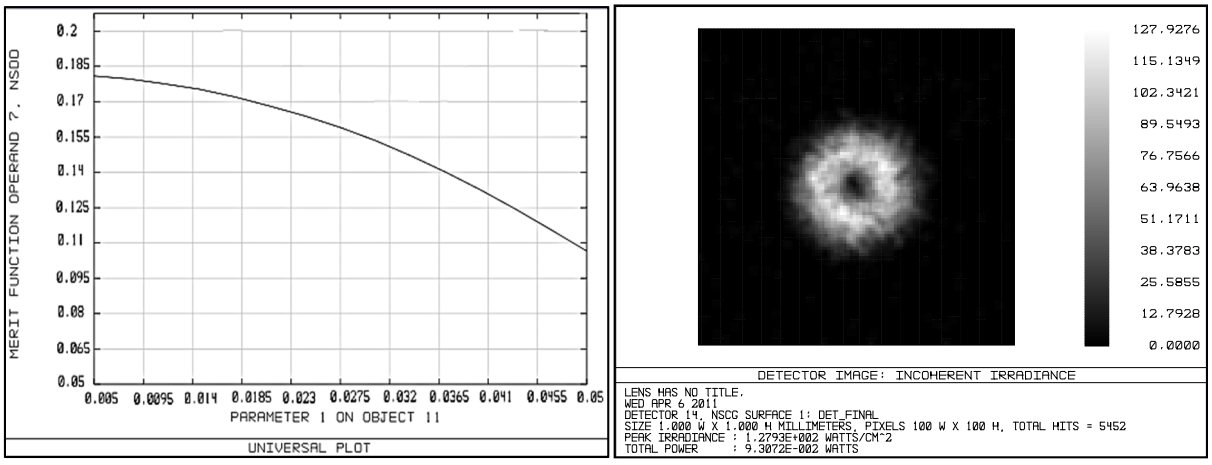

Figure 3.35: *"Total power in Watts (Y-axis) VS radius of the particle in millimetres (X-axis)" merit function for the monoblock. Range of particles from 5 to 50 microns radius. (a) Simulation results for a particular case: microlenses positioned at 1.22mm from the VCSEL light sources, and channel at 11.22mm from the same source VCSEL. (b) Irradiance image captured at final detector for a particle of radius 50µm, with a clear light blockage effect.*

The monoblock would be a great advance in terms of integration. However, as the microfluidic channel is embedded in the fabricated PDMS block, no replacement or substitution of this single part would be

possible without wasting also the microoptics, for example, in case of clogging of the channel or when performing measurements with particles of different dimensions requiring another paticular microfluidic chip. On the other hand, due to the low cost materials used for the fabrication (PDMS), we could reconsider the functionality of the monoblock from another point of view, presenting it as a low cost disposable device. Certainly, in this case each disposable chip should be designed and optimized to work within settled conditions.

A point of study has been omitted in the presentation of this alternative, and it has to do with the alignment between VCSEL light sources and the monoblock. Anyway, and with the certainty that this question would be solved, monoblock alternative is an ambitious approach to a completely miniaturized and integrated optical particle detection system.

3.6.2 Advanced monoblock: self-designed microlenses + PDMS microfluidics

This second alternative sets out from the previous one, but in this case, the optical block includes self-designed microlenses fabricated over a selected substrate, fused silica in the example of figure 3.36, though the block could be completely fabricated in PDMS.

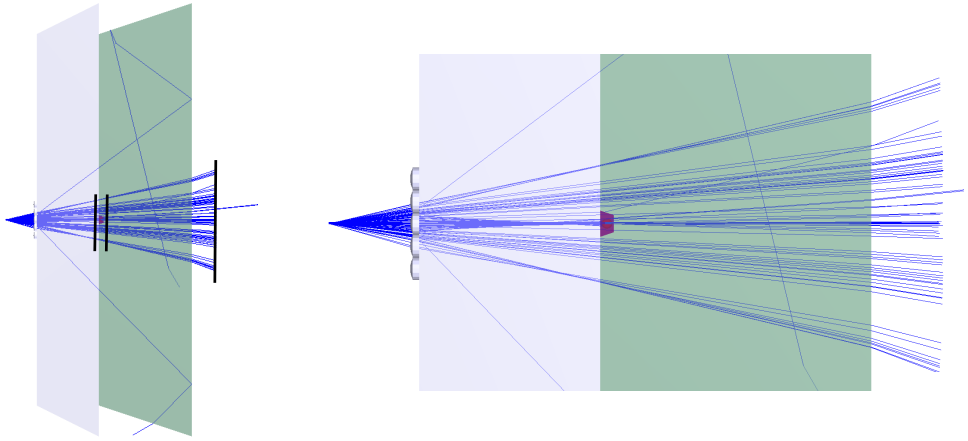

Figure 3.36: *ZEMAX ray tracing simulations for the "two blocks" system. (a) 3D model of the system with 1 VCSEL light source emitting rays. Fused silica self-designed microlenses on the top face of the optical block. A microfluidic channel (pink color) in the PDMS block. Detectors located at different positions (black lines). (b) 3D model with zoom effect. A red coloured particle can be appreciated inside the fluidic channel.*

Optical parameters for the lenses such as diameter, ROC or the sagittal distance could be tailored according to the particular needs of each case. The microfluidic block would be fabricated in PDMS material. In this case, for the definition of the closed geometry of the channel, the substrate of the optical block would be used instead of the typical glass layer, creating a more compact and integrated system, though on the other hand, there would be no possibility of replacing the microfluidic chip, as in the previously studied case.

With this system, with the position of the microfluidic channel determined according to a criterion of design (i.e. the thickness of the fused silica substrate or the PDMS slab), we studied the relation of the separation distance between the VCSELs and the microlenses with the radius of curvature (ROC) of the microlenses for defining the minimum light spot on the microfluidic channel. Example results are shown in figure 3.37 for a case in which the microfluidic channel was positioned at 3mm from the

VCSELs. With this design constraint, a minimum RMS radius spot equal to 30µm was achieved for a separation distance between the VCSELs and the microlenses of 0.90mm (black curve), and microlenses with a ROC of 0.28mm. *SUSS Microoptics* offers arrays of microlenses with similar ROC values (0.297mm), so we assume that the fabrication of our self-designed microlenses is feasible.

Note also that the range of possible values defined for the separation distance between the VCSELs and the microlenses (from 0.8 to 1.1mm) would allow the fabrication of a silicon piece to be used as an optical spacer, from a standard thickness silicon wafer in a similar way as in the other studies presented in this chapter. Details on the subject will be discussed on Chapter IV.

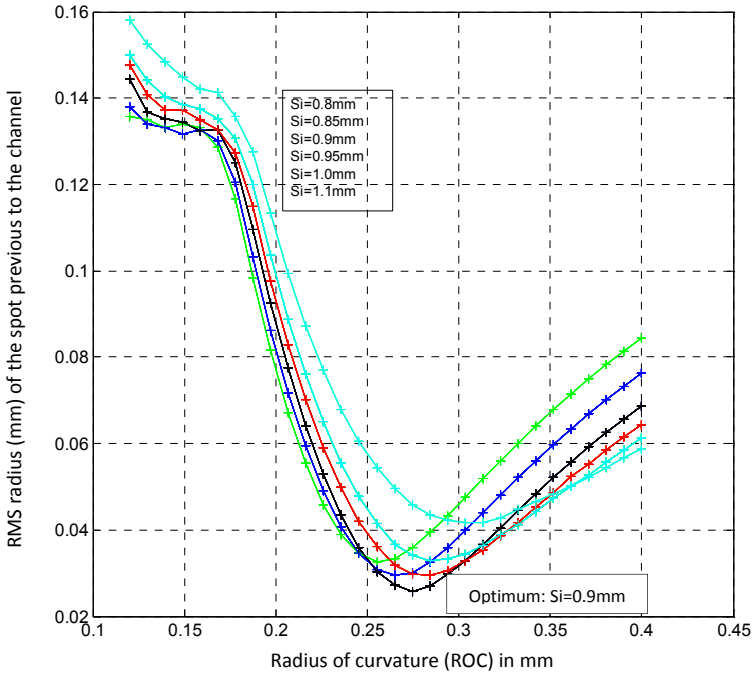

Figure 3.37: *Merit function simulation results for the "advance monoblock" system with radius of curvature (ROC) of the microlenses versus RMS radius of the spot located in the detector previous to the microfluidic channel. Each curve corresponds to a particular distance between the VCSELs and the microlenses, with the microfluidic channel positioned at 3mm from the VCSELs.*

With the same working conditions, the effect of a 50µm diameter particle on each one of the detectors was studied. Following pictures (figure 3.38) demonstrate that particle detection would be also possible with this alternative design: in the two detectors placed behind the microfluidic channel, the black circles in the center of the spot are the result of light blockage caused by the particle.

Finally, an analysis of the power captured by the final detector in relation to the dimensions of the particles flowing through the channel was performed. Parameters for the simulation were settled for the optimal case (minimum RMS radius spot 30µm). Figure 3.39 confirms the existing relation between the two variables. Increasing the dimensions of particles yields a much more notorious reduction of the power captured at the final detector than in the monoblock system: for a particle of radius 50µm, the total power captured by the detector (≈0.01W) is about 100 times less than the power emitted by the source (1W).

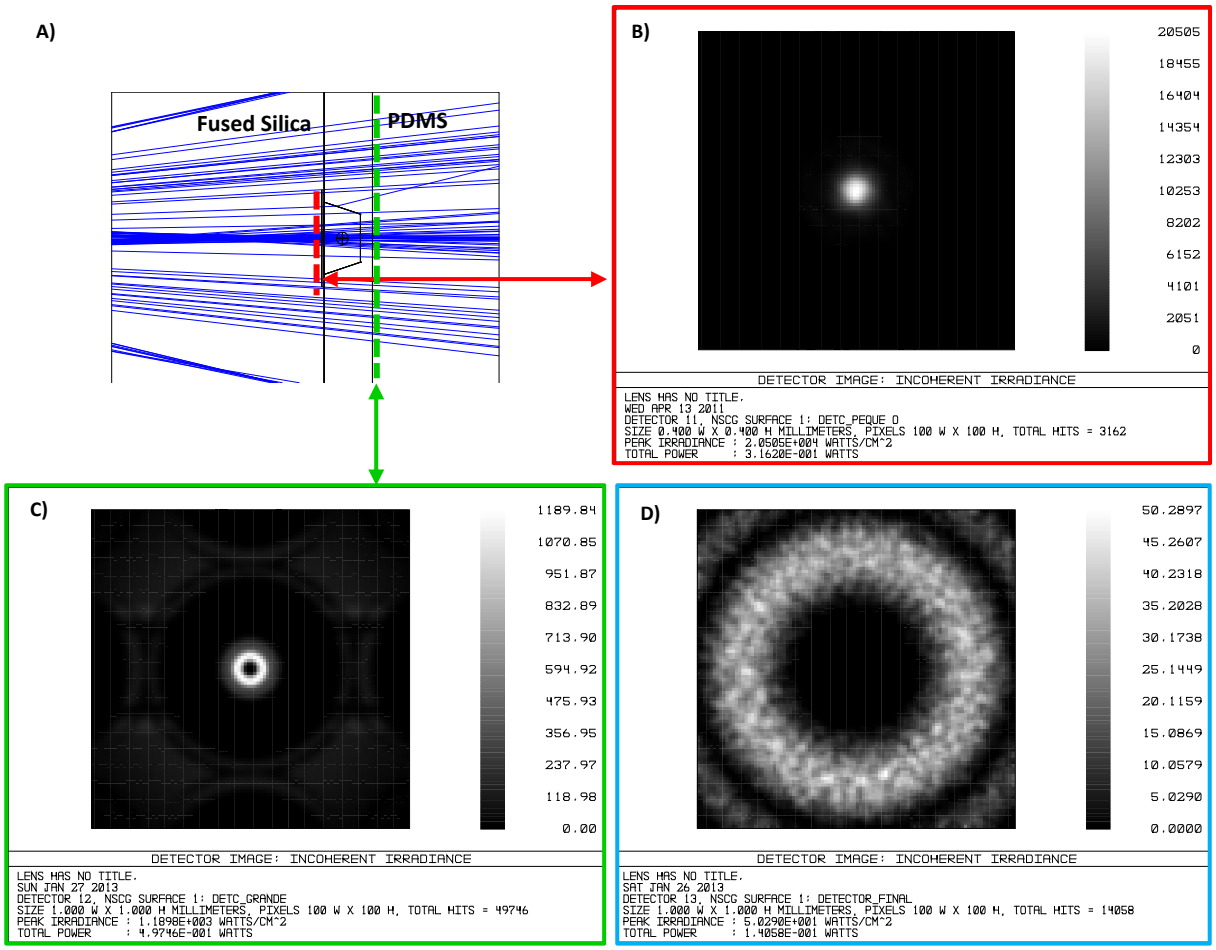

***Figure 3.38**: Effect of a 50µm diameter particle on the detectors of the "two blocks" system, for the working conditions that define a spot with RMS radius of 30µm. (a) Layout zoom in the microchannel containing the particle. (b) Image of the spot obtained (RMS radius 30µm) in the detector (0.4x0.4mm) placed previous to the microfluidic channel. (c) Image captured at the detector right behind the microfluidic channel. (d) Image captured at the final detector. In both cases (c and d) detectors present dimensions 1x1mm.*

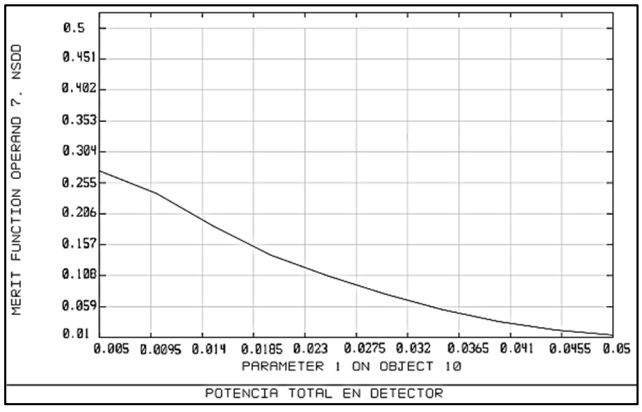

***Figure 3.39:** "Total power in Watts (Y-axis) VS radius of the particle in millimetres (X-axis)" merit function for the "advanced monoblock". Range of particles from 5 to 50 microns radius. Study of a particular case: microlenses with a ROC of 0.28mm are positioned at 0.90mm from the VCSEL light sources, and the channel at 3mm from the same source. Resulting spot size of 30µm radius located in the microfluidic channel.*

A brief discussion about the benefits and drawbacks of this alternative design is presented below. Simulations have demonstrated that with self-designed microlenses the light blockage effect produced by particles can be improved, which yields in a better detection. On the other hand, the fabrication process for the microlenses becomes more complex than simply replicating, requiring a well-defined procedure suitable to deliver microlenses fulfilling the established criterions of design with an acceptable quality degree [12], [13]. Besides, as in the monoblock case, no replacement of the microfluidic channel would be possible. A more detailed study relating the costs of the fabrication with the performance and usability of the system should be carried out.

APPENDIX: Detailed images from ZEMAX simulations

- Figure 3.17

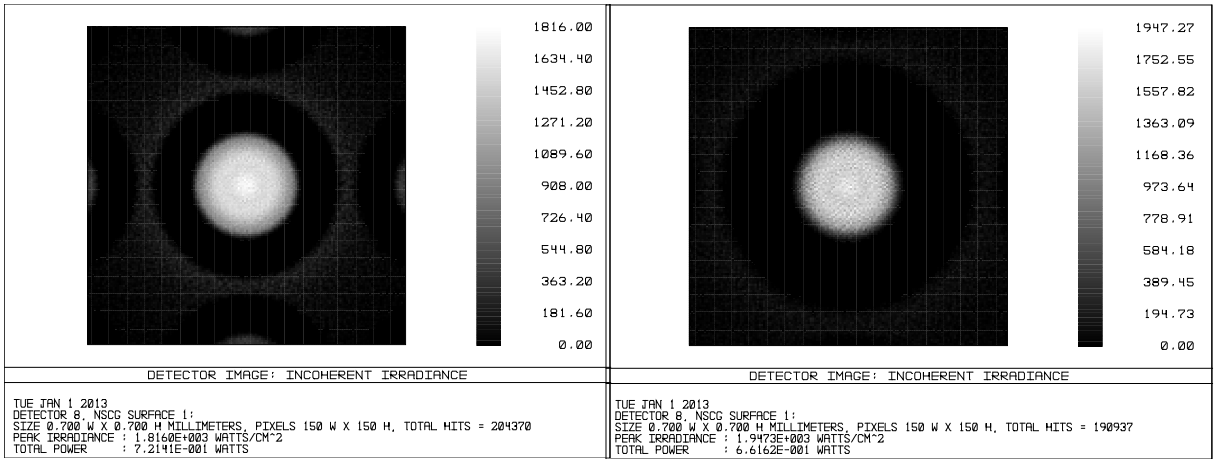

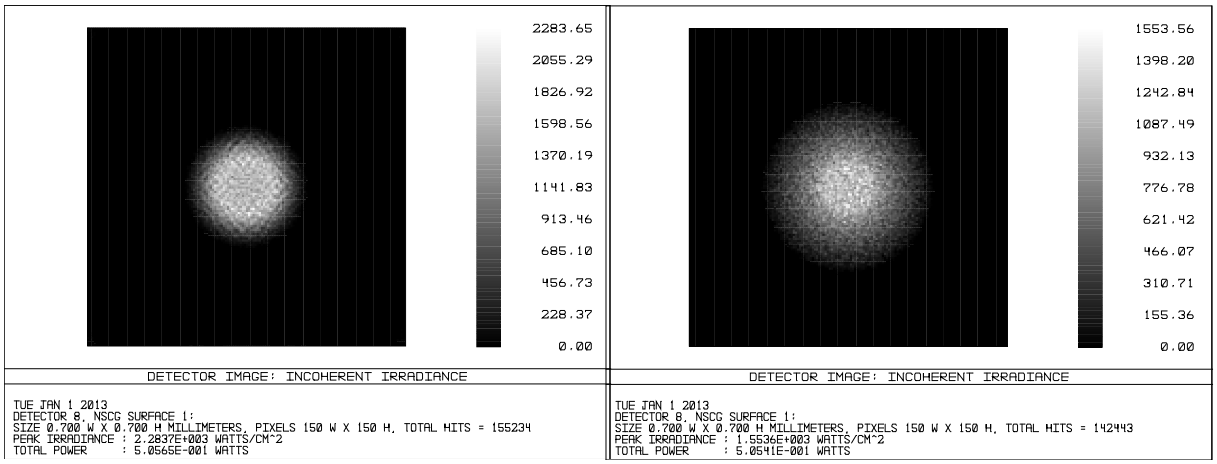

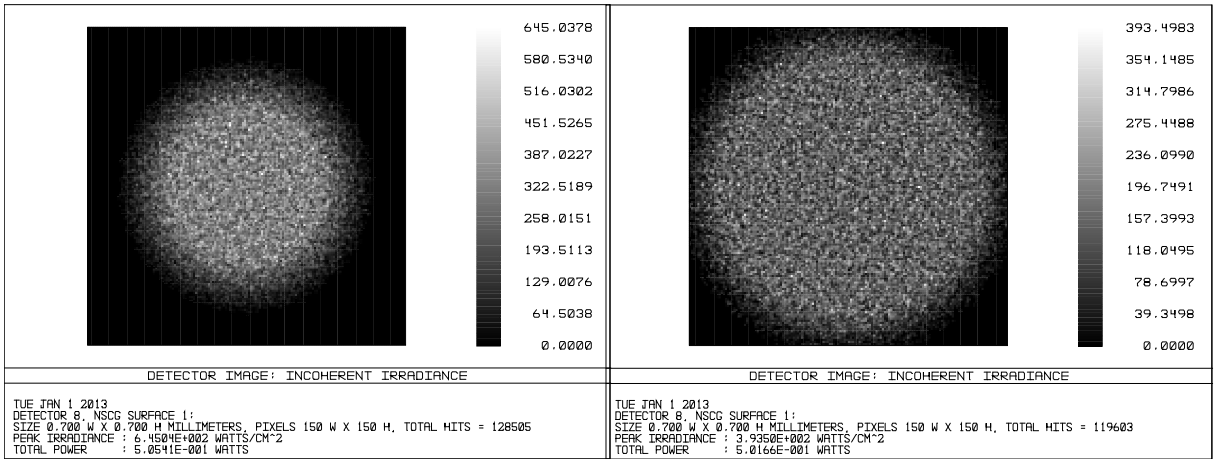

- Figure 3.27 (next page)

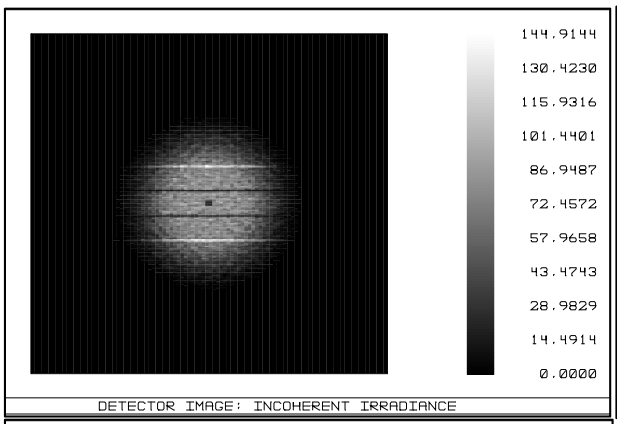
144.9144
130.4230
115.9316
101.4401
86.9487
72.4572
57.9658
43.4743
28.9829
14.4914
0.0000
DETECTOR IMAGE: INCOHERENT IRRADIANCE

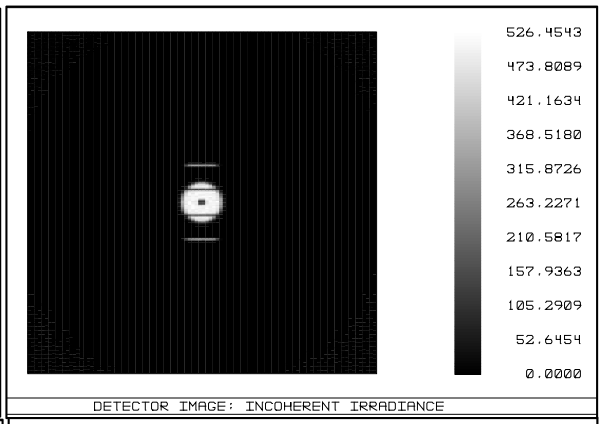
526.4543
473.8089
421.1634
368.5180
315.8726
263.2271
210.5817
157.9363
105.2909
52.6454
0.0000
DETECTOR IMAGE: INCOHERENT IRRADIANCE

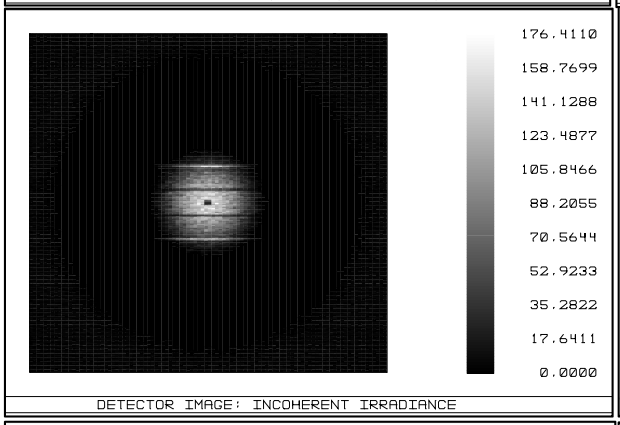
176.4110
158.7699
141.1288
123.4877
105.8466
88.2055
70.5644
52.9233
35.2822
17.6411
0.0000
DETECTOR IMAGE: INCOHERENT IRRADIANCE

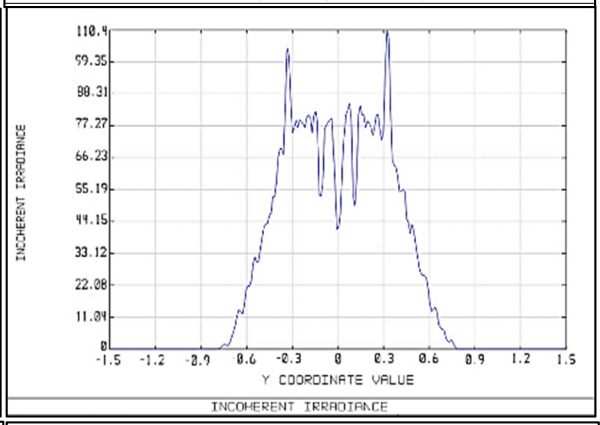
INCOHERENT IRRADIANCE
Y COORDINATE VALUE
INCOHERENT IRRADIANCE

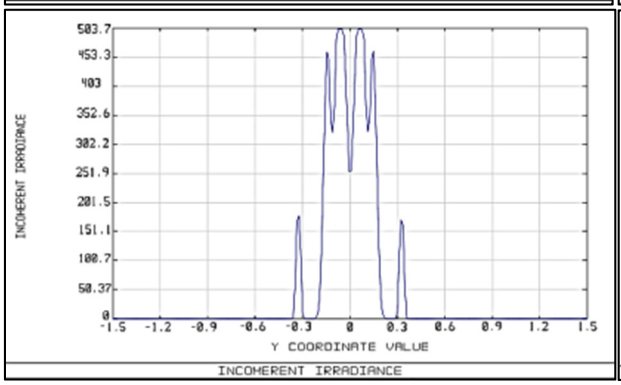
INCOHERENT IRRADIANCE
Y COORDINATE VALUE
INCOHERENT IRRADIANCE

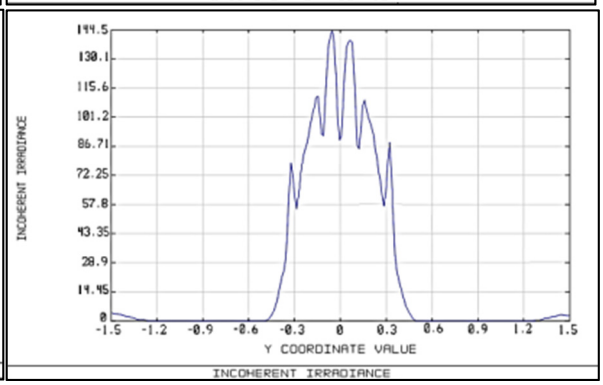
INCOHERENT IRRADIANCE
Y COORDINATE VALUE
INCOHERENT IRRADIANCE

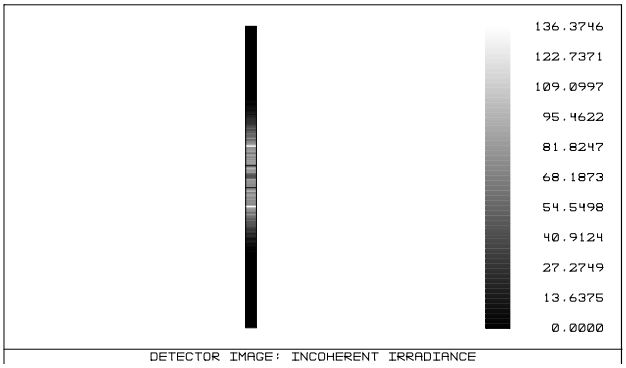
136.3746
122.7371
109.0997
95.4622
81.8247
68.1873
54.5498
40.9124
27.2749
13.6375
0.0000
DETECTOR IMAGE: INCOHERENT IRRADIANCE

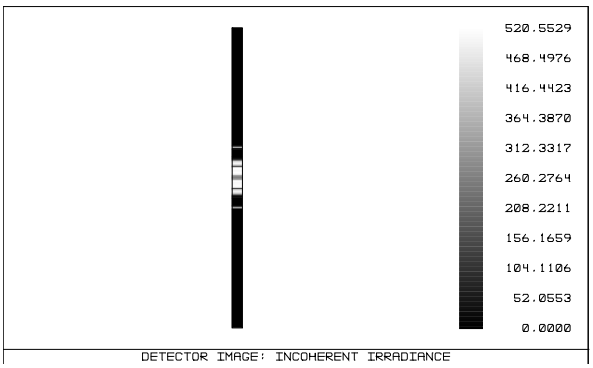
520.5529
468.4976
416.4423
364.3870
312.3317
260.2764
208.2211
156.1659
104.1106
52.0553
0.0000
DETECTOR IMAGE: INCOHERENT IRRADIANCE

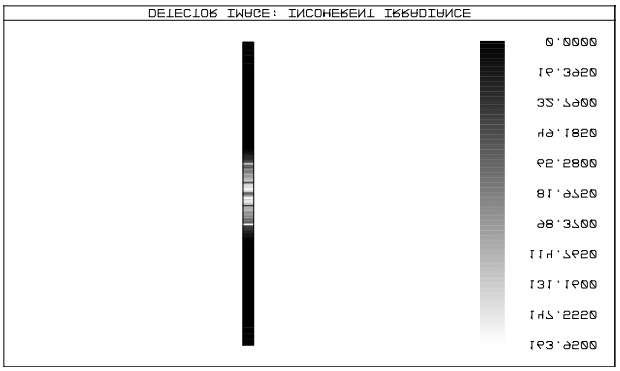
DETECTOR IMAGE: INCOHERENT IRRADIANCE

References

[1] B. S. Fritz, «OPTICAL DETECTION SYSTEM FOR FLOW CYTOMETRY». United States Patente US 7,262,838 B2, 28 August 2007.

[2] J. Godin, C.-H. Chen, S. H. Cho, W. Qiao, F. Tsai and Y.-H. Lo, «Microfluidics and photonics for Bio-System-on-a-Chip: A review of advancements in technology towards a microfluidic flow cytometry chip», *J Biophotonics,* vol. 1, Issue 5, p. 355–376, 2008.

[3] J.-N. Kuo, C.-C. Hsieh, S.-Y. Yang and G.-B. Lee, «An SU-8 microlens array fabricated by soft replica molding for cell counting applications», *J. Micromech. Microeng.,* vol. 17, Issue 4, 2007.

[4] M.-K. Wei, J.-H. Lee, H.-Y. Lin, Y.-H. Ho, K.-Y. Chen, C. Ci, Lin, C.F. Wu, H.-Y. Lin, J.-H Tsai and T.-C. Wu, «Efficiency improvement and spectral shift of an organic light-emitting device by attaching a hexagon-based microlens array», *Journal of Optics A,* vol. 10, Issue 5, 2008.

[5] N. F. Borrelli, «Microoptics Technology: Fabrication and Applications of Lens Arrays and Devices», Marcel Dekker, 2005.

[6] B. Kuswandi, Nuriman, J. Huskens and W. Verboom, «Optical sensing systems for microfluidic devices: a review», *Analytica Chimica Acta,* Issue 601 (2), pp. 141-155, 2007.

[7] C.Griffin, «Beam divergence measurements of InGaN/GaN micro-array lightemitting diodes using confocal microscopy», *Appl. Phys. Lett.,* Issue 86, 2005.

[8] J. G. Tatum, «Sensors, VCSEL Based Optical» *Honeywell VCSEL Products,* 2002.

[9] William Henry (Infiniled), «MicroLEDs Enabling New Generation of Fluorescence Instruments» *Biophotonics,* 2013.

[10] P. Savander and H. -J. Haumann, «Microlens array used for collimation of linear laser-diode array», *Meas. Sci. Technol,* vol. 4, Issue 4, 1993.

[11] A. L. Givan, «Flow Cytometry: First Principles», John Wiley & Sons Editors, 2004.

[12] K. L. González, «Polymer Technologies for Microoptical Devices and OptoFluidic Applications», *Master's Thesis supervised by Dr. Mauricio Moreno and Ivan Bernat,* 2011.

[13] F. Badar, «Fabrication of Microlens in Polymers with Thermal Reflow», *Master's Thesis supervised by Dr. Mauricio Moreno and Ivan Bernat,* 2012.

[14] F. Koyama, «Recent Advances of VCSEL Photonics», *Journal of Lightwave Technology,* vol. 24, Issue 12, pp. 4502-4513, 2006.

[15] P. Nussbaum, R. Völkel, H. P. Herzig, M. Eisnert and S. Haselbeck, «Design, fabrication and testing of microlens arrays for sensors and microsystems», *Pure Appl. Opt.,* vol. 6, pp. 617-636, 1997.

[16] K. Mersereau, R. Nijander, P. Townsend, J. Crisci, Y. Feldblum and D. Daly, «Design, fabrication and testing of refractive microlens arrays», *IOP Short Meeting Series,* vol. 30, 1991.

CHAPTER IV: HYBRID INTEGRATION

4.1 Introduction

4.1.1 Preface

When the selection of the commercial components or the design and fabrication of new ones, according to the established parameters, has been accomplished, the different pieces of the system must be connected and assembled to form a unique and complete device. The present chapter deals with concepts such as integration, assembly and packaging. Maybe because these steps are performed in the final stages of the global development process, they may seem unimportant or simple. On the contrary, they are fundamental for the successful implementation of conceptual systems, in order to prove their feasibility in view of the real market.

Therefore, these subjects become necessary and critical. Necessary to manipulate and protect the final device and to interconnect the different components; critical because sometimes the package itself plays an important role in the conceptual definition of the system: placement of the components at concrete positions becomes so vital that without a way to assure it, the device becomes useless.

This chapter will focus on the assembly and packaging of the optoelectronic elements for the designed system. Through the next sections, the process followed to develop a solid optical structure will be described, and the reader will be able to comprehend its complexity.

4.1.2 State of the art

Different proposals and techniques to integrate and assemble micro-optical components (basically micro-lenses, but also optical fibers and waveguides) in structures for optical communications or in optical detection systems have been reported by many research groups, with the aim of improving the optical coupling efficiency in optical fibers or the sensitivity of the optical detection. Our attention will be focused on the work developed for the miniaturization of optical systems and in particular, for the integration and assembly of light sources and microlenses.

In 2000, S. Eitel, S.J Fancey et al. [1] described the fabrication of an 8x8 array of VCSELs and its alignment and integration with an array of microlenses to shape the beams according the needs of each application. They created a vertical spacing between the microlens array and the VCSELs by placing a machined ring around the chip itself (figure 4.1). This ring helped them to achieve the necessary distance to produce a beam with the desired focal units. Lateral alignment of the microlens array was the critical point. The authors used reflective Fresnel zone plates positioned at the top-level in the corners of the VCSEL array as a mechanism to create alignment lighting spots on the top surface of the microlenses, which should be coincident with the markers on that surface. An estimated lateral alignment precision of ≈ 2µm was obtained.

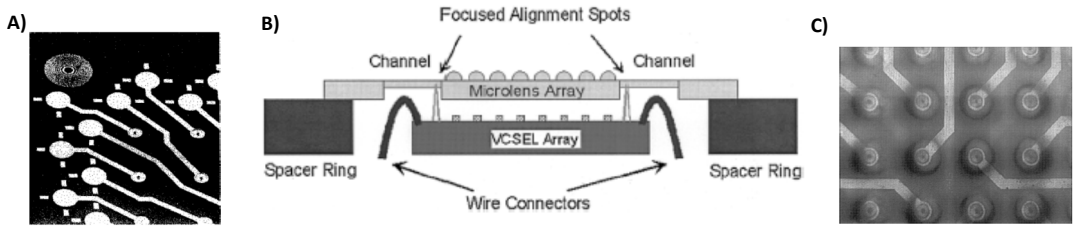

Figure 4.1: *(a) Image showing one of the three Fresnel zone plates deposited on the VCSEL array with the top-layer metal. (b) Integration scheme showing the supporting ring and the Fresnel lenses for lateral alignment. (c) VCSEL array viewed through the microlens array after attachment* [1].

E. Trush, O. Levi, L. J. Cook et al. [2] monolithically integrated a semiconductor fluorescence sensor for microfluidic applications (figure 4.2). The sensor was based on a VCSEL, a PIN photodetector and an emission filter; all they integrated in a GaAs substrate. The system was completed with an external aspheric lens and a microfluidic chip placed at the focal plane of the lens, separated by a distance of ≈20µm. The excitation spot provided by the laser presented a diameter of about 90µm. To position and align the different components, an aluminum chuck was used. The lens was mounted in an aluminum housing and then screwed into the chuck. The microfluidic chip was placed on top of the chuck. With the help of micrometers on top of the chuck, the microfluidic channel and the lens were aligned.

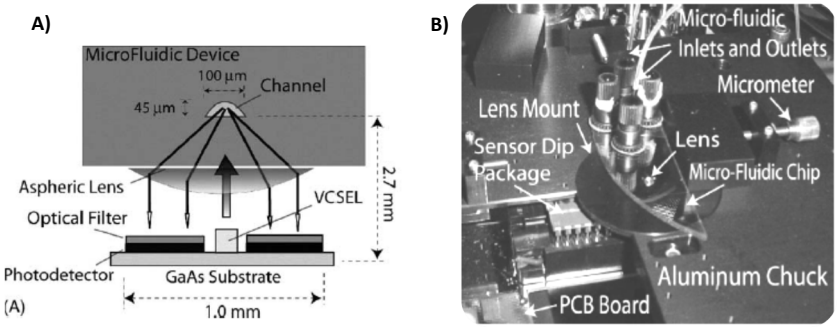

Figure 4.2: *(a) Sensor design: schematic of sensor architecture (b) Photograph of the experimental setup used to align the components* [2]

Two American patents from 2007 [3] and 2008 [4] presented several alternatives for achieving optical alignment in integrated systems. The first patent, devoted to flow cytometry applications, exposed the need of using optical elements to define the shape and size of the beam, and proposed a dynamic alignment of the optics with the microfluidics controlled with some actuators, with the aim of delivering the best fine adjustment for each case of study. The second patent proposed interesting solutions for the hybrid integration of a microlens array structure with a photonic device containing VCSELs. The alignment of the optics during the assembly process was achieved by means of "special legs" fabricated in the lower surface of the microlens substrate (figure 4.3). These legs also defined the optimal distance between the VCSELs and the lenses. In one of these solutions, complementary patterns fabricated on the top surface of the VCSELs substrate improved the alignment procedure.

The previous references represent a brief overview of the state of the art in the field of integration of optical components for different applications. This integration is carried out at high levels, i.e. in the assembly and packaging stages, when the components of the system have been separately designed

and fabricated for optimized performance in a cost effective manner, improving the economical production.

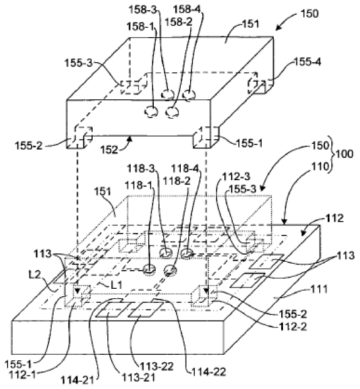

Figure 4.3: *Hybrid integration: Image of the alignment proposal to assemble a substrate of VCSELs with an array of microlenses. Special "legs" fabricated on the lower surface of the substrate of the lenses help in the process* [4].

Lenses are usually integrated with light sources, avoiding the use of optical fibers and waveguides and simplifying the design of the chips where the sensing is carried out (e.g. microfluidic chips), for it is not necessary to include embedded lenses in them, and therefore, the optical performance of the system can be adjusted and even modified according to the needs of each particular case of study. In this context, optical alignment gains special relevance, being considered as one of the critical subjects. This approach is named hybrid integration, and it is an alternative to the limitations imposed by the integration of optical elements at low levels.

4.2 Assembly and optical alignment: overview of techniques

4.2.1 Monolithic integration and Hybrid assembly

The different components of the optical particle detection system need to be assembled in order to create a functional system. In this process, optical alignment is a critical issue due to the micrometer positioning accuracies required. Two conceptual approaches for integration of components in optical systems have evolved: monolithic integration and hybrid assembly [5].

Monolithic integration combines all the necessary components on a substrate, usually a semiconductor, and by means of a unique technology, these elements are fabricated simultaneously. Active, passive and electronic components can be fabricated on a single chip. This kind of integrated systems has been mainly developed in the field of optical communications applications where we find, for example, waveguide-based optical circuits fabricated on InP. Similar results have been achieved using silicon photonics technologies with planar lightwave circuits, integrating all the components on a silicon chip but the light-emitting sources. With monolithic integration, the final systems are compact, without the need for any post-processing alignment or assembly, but on the other hand, the technological processes are complex and expensive, and thus, have a limited industrial relevance.

On the other hand, hybrid assembly is more versatile and economically feasible than monolithic integration. In hybrid systems, components fabricated with different technologies are aligned and assembled (e.g. systems can combine silicon semiconductors with polymers, glass, metals and other

materials). The previously commented US patent of 2008 [4] is a perfect example of hybrid integration, where separately fabricated components (the VCSEL device and the microlens structure) are precisely aligned and assembled, creating an opto-photonic system. The same approach is used by "*EMCORE*" company for example in the optochip presented in figure 4.4, proving that circuits developed for optical communications applications are not restricted to monolithic integration.

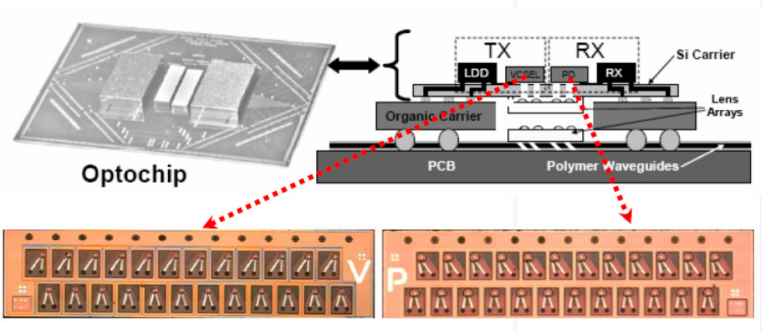

Figure 4.4: *Optochip from EMCORE with 2x12 VCSELs and PhotoDtectors Arrays. The chip presents hybrid integration of microlenses arrays with VCSELs and PDs by using the flip-chip alignment technique. Printed with permission of EMCORE Corporation.*

For the optical detection system presented in this thesis, hybrid integration approach is chosen in front of monolithic integration, since it offers the benefits of working with high quality and reasonable priced commercial components fabricated with optimum materials, in combination with custom designed elements to create complete devices tailored to the requirements of the application. Compared to monolithic integration, which is almost restricted to planar structures, hybrid assembly is able to deal with three-dimensional configurations, as commonly used in micro-optics as the waveguide-based integrated optics. However, this conceptual approach requires special attention in the alignment and assembly of the optical components.

4.2.2 Active and passive alignment

Aligning micro-optical components is the most critical step in the hybrid assembly process due to the fact that tolerances in micro-optics world are in the order of micrometers and even submicrometers. Two principles are commonly followed to perform alignment of components achieving these accuracies: active and passive alignment.

In active alignment, the optimal position of the elements is determined by the measurement of the optical system properties (e.g. output field, beam profile, intensity) when light is coupled into the system. This information is used as a feedback for closed loop control [6]. During this process, the position of the components can be manipulated, normally using a sis-axis manipulator, and when the read values are the expected, optics is fixed in the best position. This process leads to high coupling efficiencies, but it requires a considerable effort and long assembly times, without considering that once the component is positioned in the correct place, this position must be maintained until it can be fixed by applying, for example, glue, UV-curable epoxy, or laser welding.

Some examples for this approach can be found in the work of M. Gale, J. Pedersen and H. Schütz [7], where the active alignment of replicated microlens arrays on a charge-coupled device imager was performed through the mechanical jig presented in figure 4.5, or in the research about hybrid

integration from C. Ke, X. Yi et al. [8], where the authors used a commercial aligner (*MJB3 IR/Visible* aligner) with a precision of 0.3µm.

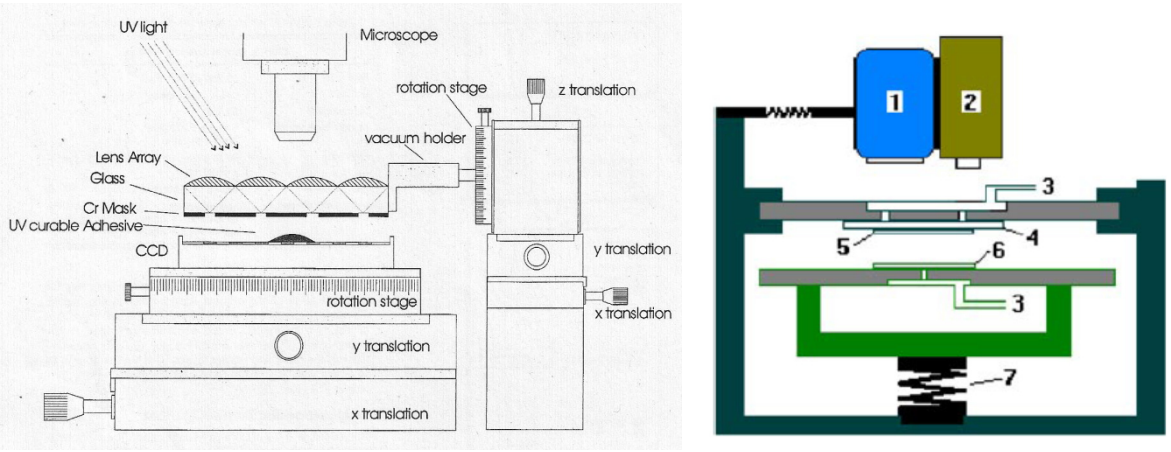

Figure 4.5. *Left: Set-up for active alignment of replicated microlens array based on a microscope, 3-axis positioners and rotation control. Right: Block diagram of the experimental set-up with the MJB3 IR/Visible aligner: (1) UV source, (2) microscope, (3) pipe for suction, (4) glass sheet, (5) microlens array, (6) charge-coupled device (CCD) chip and (7) displacement control* [8].

On the other hand we find passive alignment, which is based on the geometrical properties of the components and structures employed. Through physical alignment features and self-alignment processes, components are oriented and positioned with respect to each other. Typical physical alignment features include slots, bars, edges, binary circular pins and grooves etched on semiconductors, metals, glass or ceramic substrates, acting as mechanical "stops" for the optical components [9]. Especially interesting are the V-grooves useful for the alignment of optical fibers. But there are other techniques that can also facilitate passive alignment, such as the flip-chip bonding (figure 4.6).

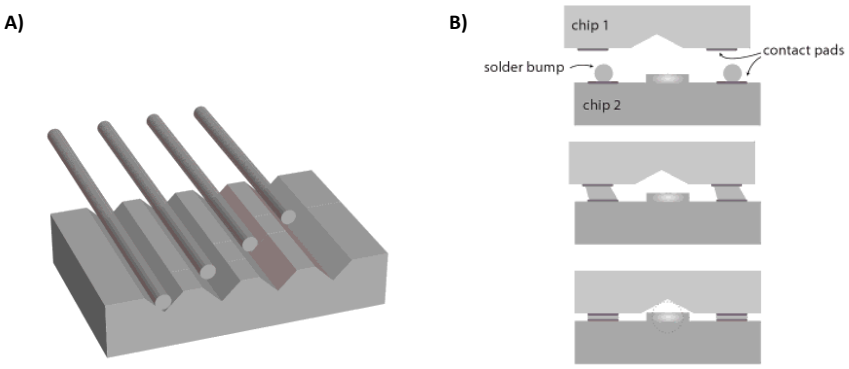

Figure 4.6*: (a) V-grooves fabricated in silicon using an anisotropic wet etch. The width is designed to position optical fibers at bottom. (b) Flip-chip process uses surface tension of molten solder (solder bumps) to align chips face-to-face* [5].

With the flip-chip technique, originally developed for electronics packaging, two chips mounted face to face are aligned using the surface tension of molten solder and, at the same time, electrical connections between them are created. For this process, contact pads are defined photolithographically on the top surfaces of both chips. Then, solder balls are deposited over the contacts of one of the chips. The other chip is flipped and roughly aligned, so contact pads coincide.

Rising the temperature of the substrate above the melting point of the solder, the balls melt, pulling the two chips into alignment due to the surface tension created. What defines the accuracy of this alignment process (which can be better than 1µm) is the precision in the definition of the contact pads on both chips (dimensions and positions).

Passive alignment can also be performed by means of visual methods, as in the work of S. Hwan, J.Woon and B. Sup [10]. With the help of the 2-sight camera of a pick-and-place machine from "*SUSS MicroTec*" (*TRIAD 05* flip-chip bonder) the authors assembled a VCSELs die and a microlens array for optical communications. Besides those two components, the system also included an upper spacer, a lower spacer and a silicon optical bench (SiOB) (figure 4.7). With the 2-sight camera placed between the SiOB and the microlens array, both the upper and lower views were available, so the centers of the VCSELs and the center of the lenses were aligned.

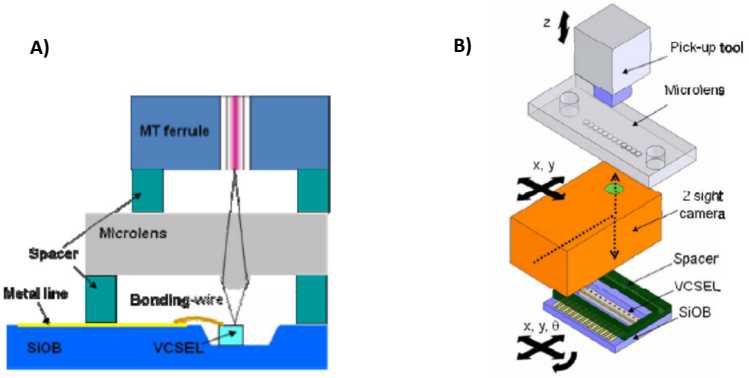

Figure 4.7: *(a) Schematics of the VCSEL OSA in cross-sectional view. (b) Passive alignment technique for the OSA packaging with the 2-sight camera* [10].

Though passive alignment offers lower accuracies than active alignment, the cost is much lower in economical and timing terms.

4.3 Optoelectronic package: assembly and packaging of components for a collimated light beams system

For the real implementation of our optical detection device, we have opted for a system based on hybrid integration of commercial components and silicon micromachined pieces, and passive alignment for the micro-optical elements. In this section, different alternatives for the optical support structure will be discussed, in terms of fabrication techniques, possible materials and their processing technologies. Issues such as packaging methodologies will also be introduced.

Regarding the simulation results presented in previous chapter, two different scenarios are possible for the optical detection system: collimated or focused light beams. Since it has been demonstrated, the collimation configuration does not differ considerably, in terms of optical design, from the theoretical system for focused beams, and even present one extra advantage: the optoelectronic package, considered as an independent block, offers more versatility as it could be integrated in other applications not so restricted to the geometry and physical dimensions of our conceived detection system. In our technological supposition with a collimated system, the separation distance between VCSELs and the microfluidic block could be reduced to 10mm ($d_{V\text{-}D}$ = 13mm) yielding a global system of small dimensions, and still the optoelectronic source package would provide spots with RMS radius

of 98µm, fulfilling the requirements to perform optical detection. Concluding, the following discussion deals with the implementation of an optoelectronic package providing collimated light beams.

To obtain a solid and robust structure for placing the selected commercial elements (VCSELs and microlenses array), respectful with the defined optical parameters (effective focal length, f_e), three different fabrication technologies were analyzed: micromachining of silicon structures to create a micro-opto-electromechanical system (MOEMS), low temperature co-fired ceramic (LTCC) technology and stereolithography (SLA). In an early stage also machining in aluminum was estimated, but soon was discarded for several reasons: the lack of accuracy and the risk of material fracture (mechanical stress of the structures) due to the tools and the mechanical procedures used (drilling, cutting, polishing…). Some of these problems could have been solved working with ultra-high precision machining using single-crystal diamond cutting tools and high resolution position control systems (≈ 0.01 µm). Grooves of 85µm wide and 70µm deep in aluminum foils of 100 µm thick have been reported [11]. Unfortunately this technology was not available for us.

4.3.1 Micromachining of silicon structures: Microsystems technology (MST)

Microsystems are systems with an overall size in the order of millimeters, with features in the micrometer range. MicroSystems Technology (MST) emerged from a combination of IC-processing and conventional miniaturized fabrication technologies based on Silicon. Through microsystems technology is possible to integrate electronic, mechanical and optical elements delivering Micro-Electro-Mechanical (MEMS) and Micro-Opto-Electro-Mechanical Systems (MOEMS) (figure 4.8).

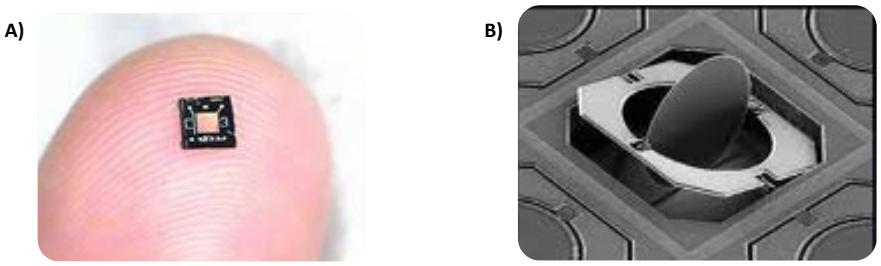

Figure 4.8: *(a) Photograph of a silicon micromechanical microphone for a mobile telephone or a hearing aid. (b) An example of MOEMS: Scanning mirrors. Printed with permission of "Intellisense" company.*

Silicon is the reference material for its good mechanical properties (high strength and elasticity, good hardness and relatively low density) and its well-established processing techniques. The basic processing technologies are the same used in the fabrication of integrated circuits, but with some differences: aspect ratios (height-to-width ratio of the features) and device sizes in microfabrication are generally much greater than in IC fabrication, and structures often include cantilevers, bridges and other shapes requiring gaps between layers. This three-dimensional features and geometric structures are built in single-crystal silicon wafers by means of Bulk (e.g. anisotropic chemical wet etching or Deep Reactive Ion Etching – DRIE with plasma) or Surface micromachining procedures.

In Bulk Micromachining, mechanical elements are fabricated etching away unwanted parts from a single-crystal silicon wafer. The parts left are useful mechanical devices. This is a relatively simple and inexpensive fabrication technology, and is well suited for applications which do not require much complexity, and which are price sensitive.

On the contrary, Surface Micromachining refers to planar structuring of the substrate surface, using much more shallow etching. Surface Micromachining builds devices up from the wafer layer-by-layer, in a repetitive sequence of depositing thin films on a wafer, photopatterning the films, and then etching the patterns into the films. Surface Micromachining is more expensive than Bulk Micromachining for it requires more fabrication steps, but it is able to create much more complicated devices suitable for applications requiring more sophisticated mechanical elements.

To summarize, silicon micromachining is a well-established technology which offers good accuracy at a reasonable price, when standard techniques are used and the number of steps developed in a Clean Room is reduced.

4.3.2 Low temperature co-fired ceramics (LTCC)

Basically, LTCC can be defined as a multi-layer glass composite technique that offers the possibility of fabricating 3D structures, such as cavities and wells. LTCC allows the integration of photonic devices and electrical circuits into a ceramic substrate, making possible to implement precision structures for optical alignment [12]. It is one of the most interesting options since it also allows the possibility of integrating passive components and creating electrical connections in the same process that develops the physical structure. Due to this multilayer structure, high packaging density is achieved. Mechanical tolerances in the order of 10-20 micrometers are obtained in the alignment of the components and different layers. The material commonly used as LTCC substrate to implement structures for micro-optical alignment is Dupont 951 (figure 4.9).

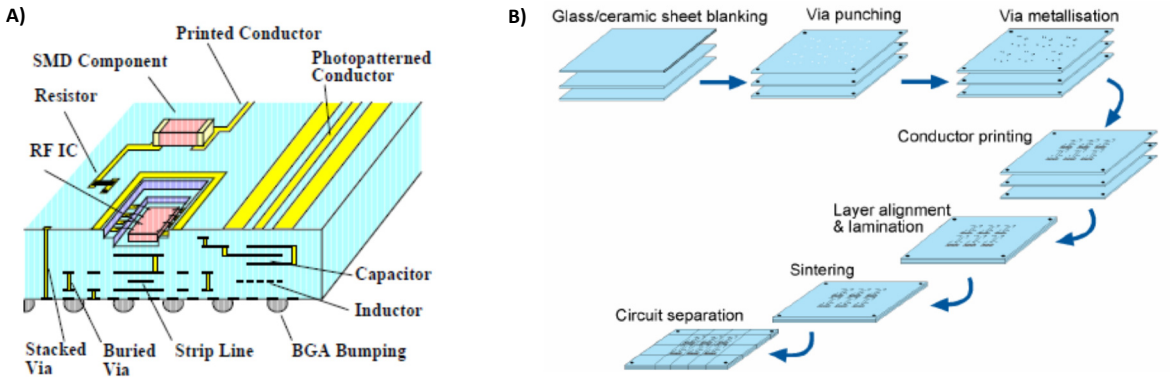

Figure 4.9: *(a) Schematics (cross-sectional view) of an LTCC multi-chip module illustrating the possibilities offered by the technology. (b) Manufacturing process of LTCC wiring boards. Both images printed with permission of VTT* [12].

In 2005 [13] and 2006 [14], J. Melin, K. Hedsten, A. Magnusson et al. presented two contributions regarding microreplication techniques of micro-optical elements for silicon integration. The interesting point in these works is the integration of the fabricated lenses into Micro-Opto-Electro-Mechanical Systems (MOEMS). For the assembly and packaging of their optical system, consisting of the fabricated lens and a VCSEL (figure 4.10), the authors used Low-Temperature Co-fired Ceramics (LTCC) substrates (tape material was DuPont 951) developed by VTT (Finland). Four layers were necessary for the carrier, placing the VCSEL in a 250µm depth cavity (matching the height of the VCSEL), half way through the substrate. Electrical connectors were placed in the inner layers. The lens (resting over a silicon layer) was assembled on top of the LTCC carrier and centered above the VCSEL with the help of mechanical

translators to adjust the lateral position while measuring the intensity distribution of the laser beam in an active alignment procedure.

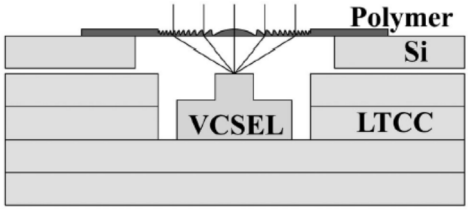

***Figure 4.10**: A transmissive diffractive optical element on a silicon substrate positioned above a VCSEL mounted on a LTCC (low-temperature cofired ceramic) carrier* [13].

We considered LTCC as a serious alternative to silicon micromachining for fabricating the optical structure required in our hybrid integration process. Two proposals, elaborated with the technical support of *VTT Technical Research Centre of Finland - Business from technology*, were discussed.

In the first, a cavity for the VCSELs would be created in the LTC substrate. Then, the substrate would be ground precisely to the desired thickness, in accordance with the optical parameters of the microlens array mounted on the top surface of the LTCC structure (figure 4.11). Active alignment of the micro-lens array would correct errors with the dimensions of the cavity and with the placement and orientation of the VCSELs (they could be slightly tilted during the process). This proposal would be the best for a low cost proof-of-principle demo device with active alignment of the optical components.

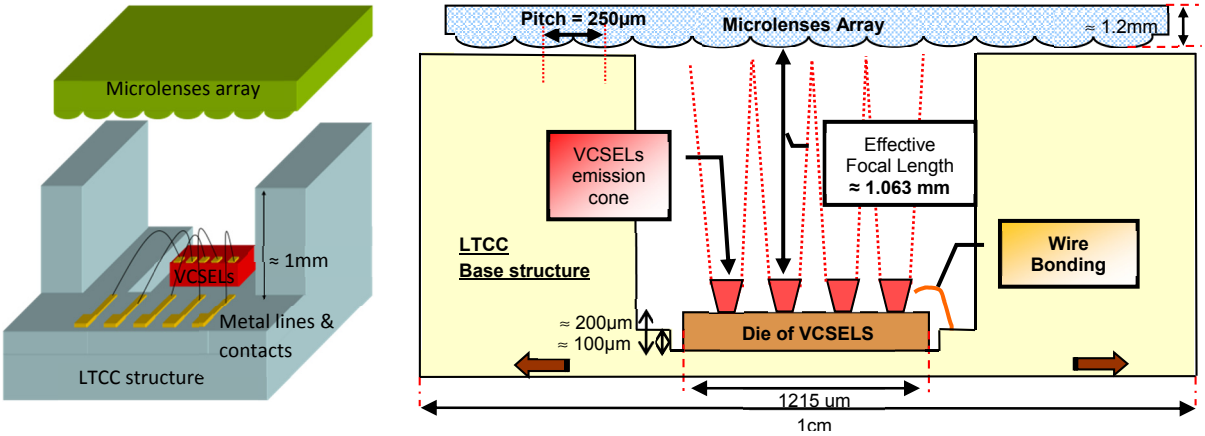

***Figure 4.11**: Schemes for a LTCC support structure. It is almost equivalent to the final proposal for the structure based on silicon micromachining technology, but with some differences: it is a single piece block, the microlens array is mounted on a plane surface and active alignment is required.*

The second proposal consisted on a different approach. The VCSEL would be flip-chipped on the bottom side of the LTCC structure. The LTCC bottom layer would be 90µm thickness with 80µm diameter apertures for the VCSELs. VCSELs bonding could be carried out with an accuracy of 5µm or even better using stud bumps and thermocompression bonding. On the top layer, the microlenses array could be actively aligned using a "*Newport*" system, or passively using a flip-chip bonder along with accurate alignment marks on LTCC package. Finally, the package with flip-chipped VCSELs on the bottom side would be surface mounted on a J-type lead frame (figure 4.12). This proposal would be the appropriate for a low cost large production of devices, since the flip-chip version offers cost benefit, especially if passive alignment methods are used instead of active alignment.

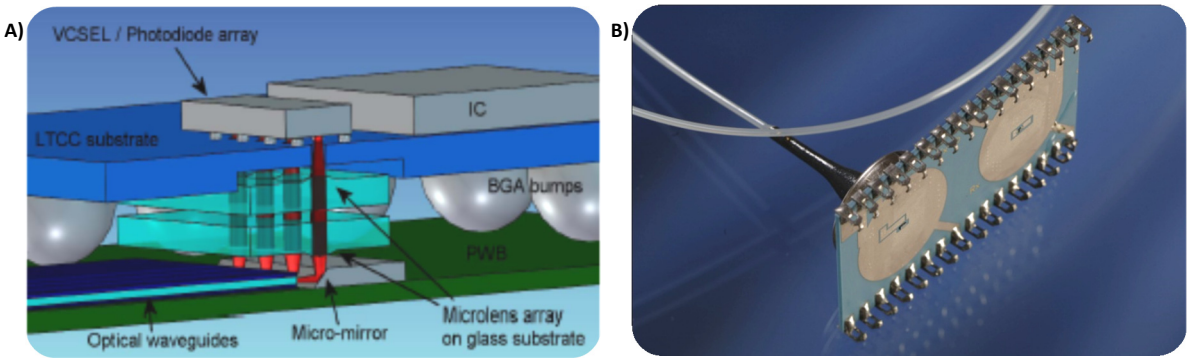

Figure 4.12: *(a) Scheme for a LTCC support structure based on flip-chip technique for the VCSELs. Circular apertures allow the emitted light beams from VCSELs pass through. Microlenses could be active or passive aligned. (b) LTCC package with flip-chipped VCSELs on the bottom side surface mounted on a J-type lead frame.*

In both proposals UV-curable epoxy would be used to fix the mounted microlens array once aligned. Very accurate alignment requirements would, of course, increase the cost. At the same time, if the thickness of the optical support structure, where the microlenses would be placed, must be controlled very precisely, it could be possible to grind the top surface of the LTCC structure. It should be noted that dielectric material layers used in the process present specific thicknesses (90, 130, 200µm), with a typical tolerance about 2%. For that reason, achieving a particular thickness respectful with the defined optical parameters could be difficult without additional machining processes, which would end up raising the cost.

Estimated costs for each one of the proposals were calculated. The first option, with a price of 10k€, would include only the substrate for the proof-of-principle demo. Bonding the VCSELs would increase the price. The second option, i.e. the demonstration of a solution suitable for volume manufacturing (using "passive alignment"), would cost a minimum of 30k€.

Though LTCC technology has proven to be a good alternative to well-established technologies, offering new ways and possibilities of integrating electrical components such as electrical connections, metal paths, resistors and capacitors in the same process by using layers of different materials, the fact that these layers can shrink in a factor of about 15% in Z-axis (though at present there are several research projects focused on zero-shrinkage materials), represents a drawback since the optical parameters of the system would not be reliable. In addition, the estimated high costs of the production relieve this technology at a second place. Again, the benefits of standard microelectronic processes and the good compatibility of silicon in terms of electronic integration come out into the open.

4.3.3 Stereolithography

Stereolithography is included in the group of rapid prototyping technologies, along with 3D-Printing and the micro and nanostereolithographies. Rapid prototyping allows the fabrication of conceptual designs into functional and technical prototypes at low cost and reduced time, delivering reduced time-to-market product development.

Stereolithography (SLA) is based on the use of especial curable resins that modify their physical characteristics when excited with laser light. Through a complex system of optical mirrors, the modulated laser light comes in contact with the resin at concrete points, curing these sections and shaping and forming the final structure according to a 3D-data model design previously introduced on

a computer and analyzed with specific software. This software creates a slice model from the initial one, so that it can be divided into multiple layers that are sequentially treated. Pieces of great complexity can be obtained. The same conceptual idea of sliced model is used in 3D printing, but this time, a print head deposits the material (polymers, metal o ceramic powder) at certain positions of interest (figure 4.13a).

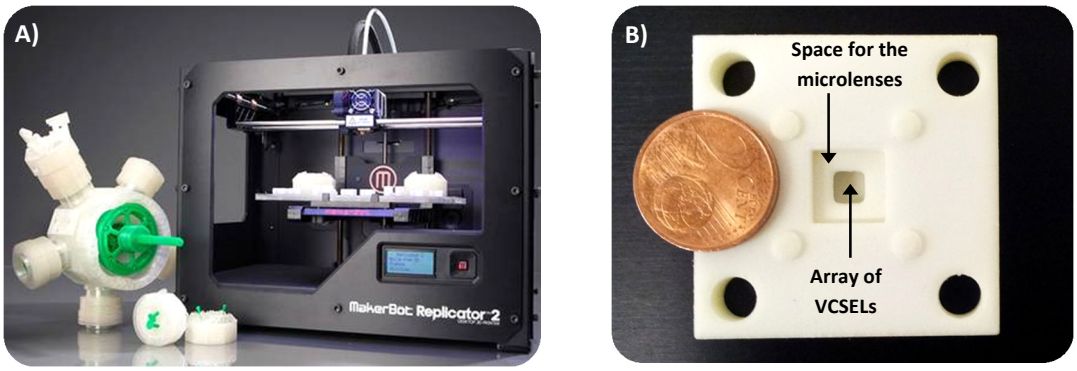

Figure 4.13: *(a) Photograph of a commercial 3D printer (Makerbot's new Replicator 2). (b) 3D printed piece: a structure for placing an array of VCSELs and microlenses. Printed with permission of SIC group.*

When working with stereolithography technology, there are several factors that need to be considered such as the volume of the final piece, the number of pixels per plane, pixel dimensions and layer thickness in Z-axis. The values of these parameters limit the level of resolution and detail of the final piece; for example, in standard stereolithography layer thickness in Z is about 50 to 100µm, while in ministereolithography the values vary from 25 to 50µm, thus detail level is increased in a 100%. In microstereolithography (MSTL), layer thickness is about 5µm and the smallest structural detail (accuracy) is 1µm, which is better than the 10µm precision of stereolithography. Microstereolithography achieves an average production rate of 1.5mm per hour. Even more interesting results are obtained with nanostereolithography. This technology works with acrylic and epoxy materials, and designs present details in the submicron level (nm). Of course, the fabrication cost increases[1].

Regarding to a feasible, price-reasonable and complete structural packaging solution for our optical detection system, both standard and ministereolithography would be suitable options. However these technologies present some drawbacks: first, the accuracy and resolution levels are not as good as with Microsystems technologies, so the final device probably could not satisfy the optical requirements because of the error introduced in the effective focal length; and second, the materials used and the technology itself do not allow creating electrical connections or other electronic compatible elements embedded into the final structure as with silicon material. Anyway, stereolithography (and its variations) and 3D printing are useful techniques for rapid prototyping and conception models, such as the example shown in previous figure, developed by the SIC research group (Electronics Department of the University of Barcelona): a structure for the placement of an array of VCSELs along with microlenses.

[1] Micro and nanostereolithography with transparent materials were also studied as an alternative to soft lithography for the fabrication of the microfluidic chip. Advantages of these methods are accuracy, precision and production time; being the main drawback the high fabrication cost. This fact led to choose the well-known soft lithography technique which allows low cost production of a large number of microfluidic chips from a single master.

4.3.4 Conclusions

After analyzing and discussing about the different alternatives, micromachining of silicon wafers is selected as the most convenient fabrication technology for it offers great accuracy, good quality, reasonable price and the entire process could be developed at the clean room of the Barcelona Microelectronics Institute of the National Microelectronics Centre-CSIC (IMB-CNM-CSIC) in Barcelona with the support of its staff, thanks to a research fellowship (GICSERV Program 6th call NGG-190). Thus, the optics supporting structure necessary for the hybrid integration of the commercial components will be fabricated on silicon material through microsystems technology. The know-how of our group to carry out the technological procedures and the future possibility of fabricating and integrating electronic circuits (e.g. VCSELs) on the same support structure, thanks to the compatibility offered by Silicon, have also been pondered in order to take the decision.

4.4 Concept for the Optoelectronic package

The hybrid assembly of the VCSELs and the microlenses must accomplish the requirements of *ZEMAX* simulations, discussed on previous chapter. To achieve that goal and integrate those elements in a solid structure, two silicon pieces (named “base” and “optical spacer”) are designed and fabricated with microsystems machining procedures, according to the geometrical and physical constraints imposed by the commercial components. The die of VCSELs will be placed in a particular position of the base, facing upward[2], while the array of microlenses will be aligned and mounted on the top surface of the optical spacer. The decision of creating two independent pieces instead of a single block structure obeys to some practical reasons: a single block structure would require a non-standard thickness silicon wafer and more complex micromachining processes, which indeed would increase the costs of production. As a result, base and optical spacer pieces will join to create a complete optoelectronic package, like the one presented in the following figures (figure 4.14). Their design and fabrication processes will be detailed in the following sections.

In this design process we also focus on passive alignment of optical components as one of the key points. The thickness of the optical spacer must guarantee that the microlenses are placed at a certain position/distance, according to the results of the simulations and the finality pursued by the optical design. The thickness of this silicon piece is the key to accomplish with the requirement of the optical path. For a collimated light beams scenario, lenses must be positioned at their effective focal length distance, thus the distance between light sources (at the top side of the commercial die) and the microlenses array ($d_{V\text{-}L}$) is equal to the focal length of the lenses f_e=1.063mm.

Two different proposals[3] are presented to achieve this target: single etched base and double etched base. The difference between them yields in the depth of the cavity where the VCSELs are placed (base piece) and, consequently, in the necessary thickness of the optical spacer.

[2] Flip chip for VCSELs was discarded in spite of the benefits offered by this technique in the optical alignment process. In comparison with classical soldering and wire bonding, flip-chip adds an extra difficulty. Flip-chip technique uses solder balls/bumps to create electrical connections and force alignment between components. The dimensions of solder balls after the soldering and reflow should ensure that the final value of the focal length is in accordance with the expected to achieve the desired collimation effect.

[3] The particular design for each silicon piece will be described in the following sections of this chapter. However, to introduce and justify the different proposals, it is necessary to refer to some concrete elements and features defined in those designs, such as the cavity for the VCSELs or the “U” shaped well created in the base piece.

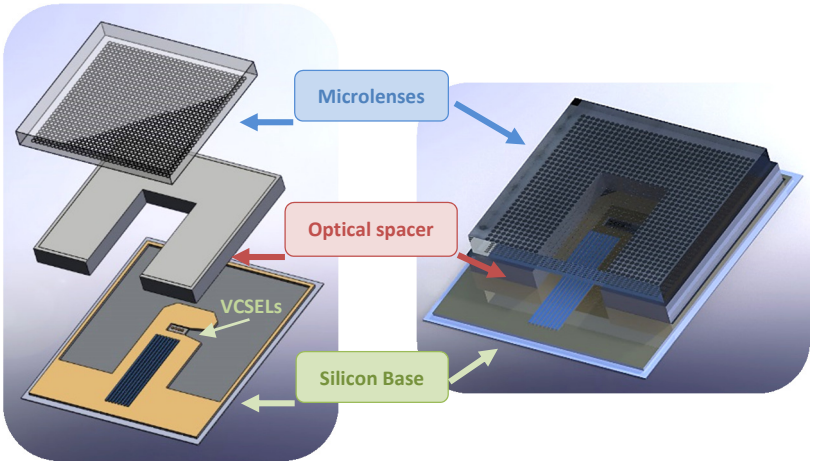

Figure 4.14: *Optoelectronic package. Left: Components fabricated in silicon material (base and optical spacer) and microlenses array. The base hosts a die of VCSELs along with metal paths and electrodes. Microlenses array will be aligned and mounted on the top surface of the "U" shaped optical spacer. Right: 3D-rendered image of the base and optical spacer pieces joined together.*

4.4.1 Single etched base and special optical spacer

The determination of the thickness for the optical spacer piece responds to the following reasoning (figure 4.15). For a single etched base, the depths[4] of the well, used as a guideline for the join with the optical spacer, and the cavity for the placement of VCSELs, are defined as 150µm. The optical spacer is also etched 15µm on the top side to create a pattern of pillars for passive alignment. If the optics must be placed at f_e= 1.063mm, the negative effects of the etchings must be compensated. Thus, the thickness for the optical spacer piece should be:

$$Thickness = 1063\mu m + 150\mu m + 15\mu m = 1228\mu m \approx 1230\mu m \pm 5\mu m \qquad (4.1)$$

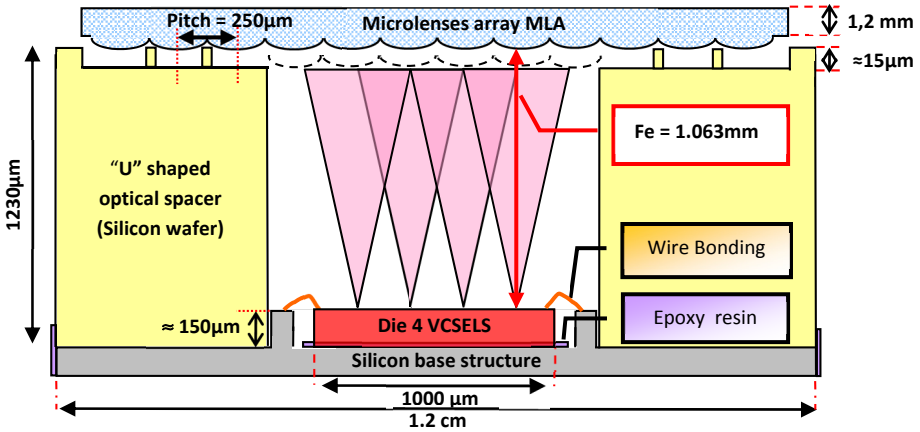

Figure 4.15: *Cross-sectional view of the complete assembly for a single etched base structure. The optical spacer is fabricated in a silicon wafer with thickness 1230µm. A pattern of pillars is etched on the top side to help in the alignment of optics. The depth of the etching for the base piece is 150µm, equal to the height of the die of VCSELs.*

[4] Silicon wafers of 500µm thickness are used for the fabrication of the base pieces. The depth of the defined patterns (150µm) guaranties the robustness of the produced pieces. At the same time, the etching corresponds to the thickness of the die of VCSELs (*ULM Photonics*).

To process these special optical spacer pieces, a silicon wafer with a thickness of 1230µm is necessary. As these wafers required special manufacturing processing, *"Si-Mat Silicon Materials"* company was contacted. They served us a total of 10 wafers with the parameters presented in table 4.1.

Table 4.1: *Summary of the parameters of the silicon wafers provided by "Si-Mat Silicon Materials" company.*

Silicon wafers			
Diameter	100 mm	**TTV**	< 10 µm
Type/Dopant	P/Boron	**Bow/Warp**	< 30 µm
Orientation	<100> +/- 0.5 deg.	**Front Surface**	polished
Growth Method	CZ	**Back Surface**	polished
Resistivity	1-20 ohm.cm	**Flats**	2 SEMI
Thickness	1230 +/- 5 µm		

4.4.2 Double etched base and standard optical spacer

In this case, there is no need of silicon wafers with special thickness requirements (figure 4.16). More common wafers of 1000µm can be used to fabricate the optical spacer pieces with results within the expected values. With a double etched base (350µm in total[5]), the depth of the etching for the well (150µm) has no effect on the calculation of the effective focal distance. From the remaining 200µm depth in the VCSELs cavity, 150µm are consumed by the height of the VCSELs die according to the dimensions of the manufacturer, thus only 50µm are added to the 1000µm thickness of the wafer. The etching of the pattern of pillars on the top side of the wafer, reduces the previous value to 1035µm (equation 4.2).

$$f_e = 1000\mu m \text{ (thickness of the wafer)} + 50\mu m \text{ (extra distance created by the double etching)} - 15\mu m \text{ (etching of the pillars)} = 1035\mu m \quad (4.2)$$

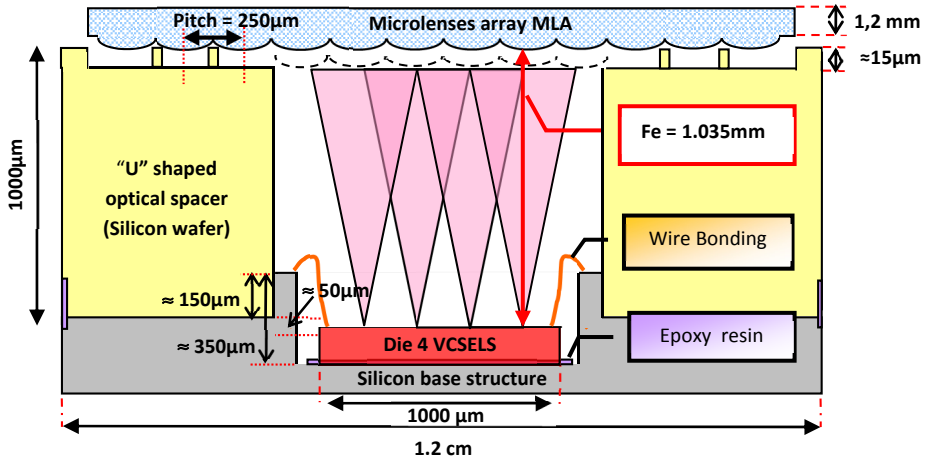

Figure 4.16*: Cross-sectional view of the complete assembly for a double etched base structure. The optical spacer is fabricated in a silicon wafer with 1000µm thickness. The base is double etched: first step creates the cavity for the VCSELs with a depth of 200µm, second step of 150µm increases the depth of the cavity up to 350µm and creates the "U" shaped well.*

[5] Base pieces are processed on a 500µm thickness silicon wafer. To avoid the fabrication of extremely fragile silicon pieces a total etching of 350µm was defined, resulting in pieces with 150µm thickness in some parts of the base structure. This minimum thickness was considered enough to ensure the correct manipulation and handling of these pieces.

The resulting effective focal distance is f_e= 1.035mm, which represents a Δf_e= -28µm with respect to the theoretical desired value of 1.063mm. With a fine adjustment of the fabrication parameters, the final result could be improved, reducing the difference between theoretical and real values. The effect of the reduction in the value of the f_e parameter on the RMS radius for the spot located at the position of the microfluidic channel was simulated. Results are shown in table 4.2. The RMS radius increases in a mean value of 15µm, which still is acceptable according to the functionality of the system.

Table 4.2: *RMS values of the spot radius at the microfluidic channel (detector#1) for ZEMAX simulations, with the array of microlenses placed at a distance f_e=1035µm from the VCSELs light sources. VCSEL $I_{forward}$ = 1mA. Dimensions of the detector were 1x1mm^2. To compare with results obtained in previous simulations (chapter III), variable $d_{V\text{-}D}$ corresponds to the distance between the VCSELs and the CMOS array of photodetectors (detector#2).*

Distance in mm $d_{V\text{-}D}$	RMS radius in µm Fe=1063µm	RMS radius in µm F_e=1035µm	Difference µm / %
13	98	111	13/13
18	130	145	15/12
23	167	182	15/9
28	207	222	15/7
33	247	262	15/6

4.4.3 Base structure

The design for the base structure is shown in figure 4.17. Both images are equal, except for the inclusion of the microlenses array pattern on the left one. This pattern becomes useful for alignment purposes during the design process.

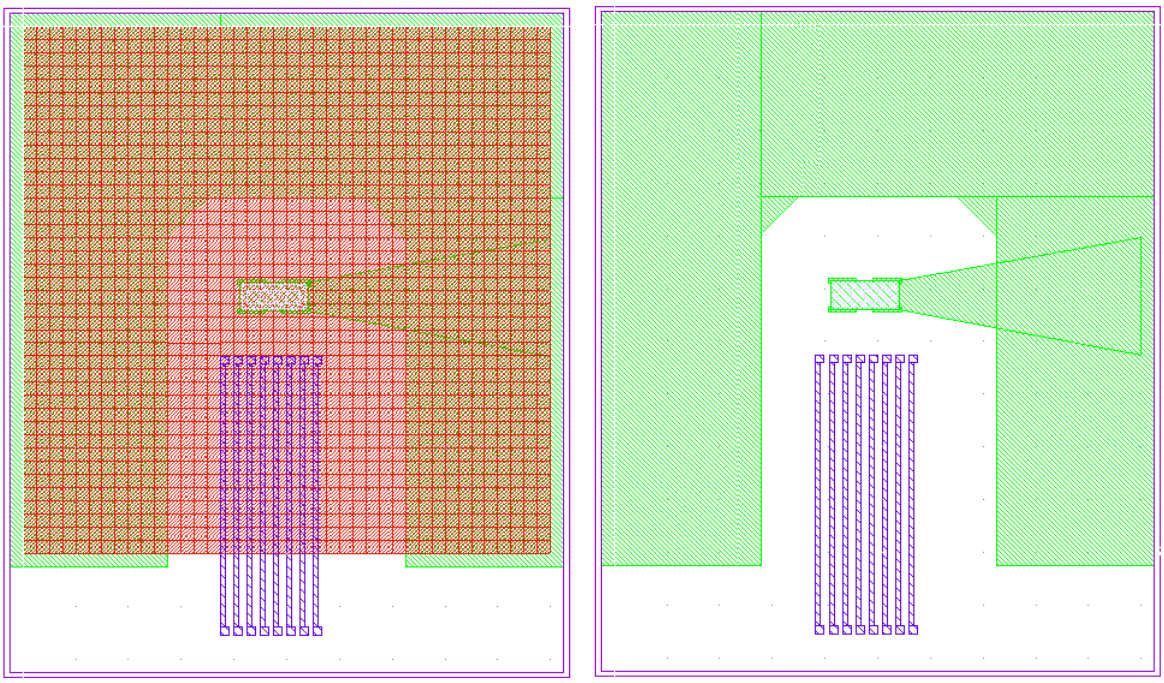

Figure 4.17: *Design schemes for the base structure silicon piece. Left: Scheme including the microlenses array layer (in red color) for alignment purposes. Right: Scheme of the base structure with the central cavity for the VCSELs, a surrounding well (green color) to allow the fitting of the "U" shaped optical spacer and the metal paths (blue color) for the powering electrical connections.*

The outline (violet colour) marks the boundaries of the base structure (12.70mm x 10.70mm). Though these dimensions are determined in part by the commercial microlenses array (red colour), they are still very acceptable for the purpose of our device. These boundaries will also be the guide to follow during the dicing of the chips in the last step of fabrication process.

There is a first etching (green colour) on the silicon base structure whose aim is to create the well (10.50mm x 10.50mm) for the placement of the "U" shaped optical spacer for the microlenses, and for this reason, this well shares the same "U" shape. When joined together, the two pieces will match. The election of the "U" shape for the well of the base and the optical spacer piece, also responds to another reason: to create electrical connections with the die of VCSELs, metal paths must be paced closer to it in order to allow wire bonding machines work properly. The "open way" to the die of VCSELs achieved with the "U" shape, simplifies the creation of these metal paths,

Since the etching of the base will be achieved through a DEEP RIE process and these microelectronic processes are anisotropic, attention must be paid to the corners of the well we expect to obtain, for they will present a curved profile. As a consequence, the "U" shaped spacer may not fit properly into the well. To correct this undesired effect, the inner corners of the well are replaced with triangles (figure 4.18).

The dimensions for this well (with the shape of an inverted "U" vowel) must assure the stability of the optical spacer structure.

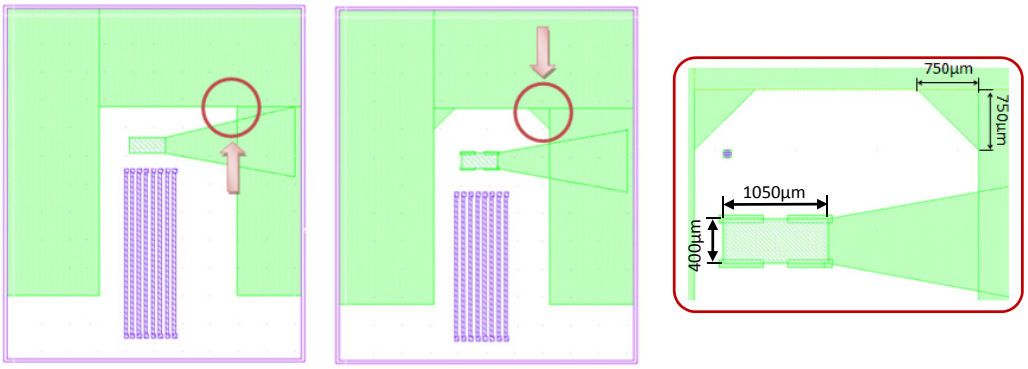

Figure 4.18: *The rectangular inner corners of the base structure (image on the left) must be substituted by triangles (750µm x 750µm) (images in the middle and on the right) in order to avoid mismatch problems in the assembly of base and spacer pieces, caused by the anisotropic etching processes used in the fabrication.*

In the center of the base structure lies a rectangular cavity (green colour) of 400microns x 1050microns to accommodate the array of VCSELs (350microns x 1000microns). The dimensions defined for this cavity consider possible tolerances present in the die of VCSELs. The cavity is located so that a passive alignment of the microlenses array with the VCSELs is possible. A funnel on the right side will also be etched on the silicon wafer to ease the placement of the die of VCSELs inside the cavity. The effective length of this funnel is about 1.5 times the length of the die (figure 4.19a). To accurately align the die inside the cavity, rectangular reference marks are included (figure 4.19b). This central cavity, the funnel and the rectangular alignment marks are also achieved with the first etching process.

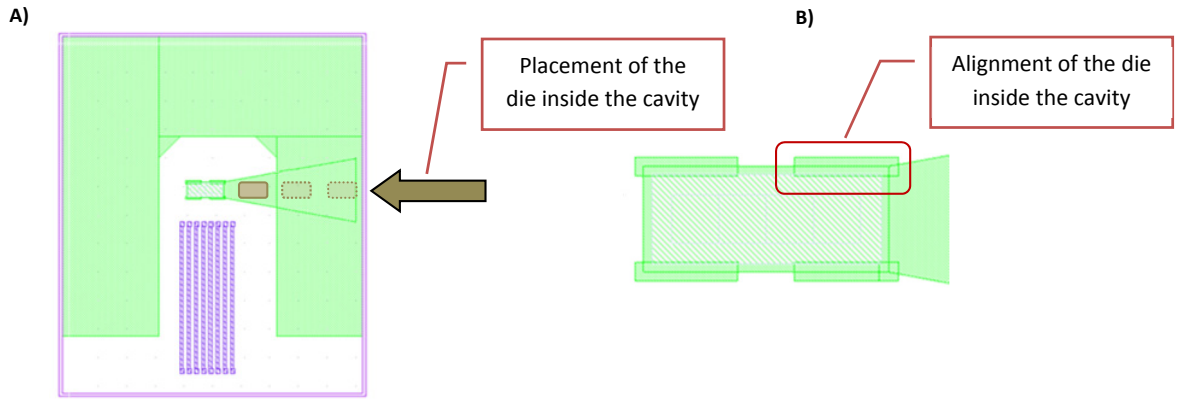

Figure 4.19: *(a) On the right side of the base structure, a special funnel is etched to ease the placement of the VCSEL die inside its own cavity. (b) The VCSEL cavity contains its own alignment marks to help the positioning and orientation of the die of VCSELs. All the features are etched in the same DEEP RIE process.*

The second layer (violet colour) is designed to create the metal paths that will be used for powering the VCSELs. The number of paths is eight: one for each anode and one for each cathode of the VCSEL lasers. The paths are large enough (length 5.750mm) to facilitate the bonding of the inner pads near the boundary of the chip with external pads found, for example, in a printed circuit board. The distance between the cavity for the VCSELs and the metal paths is 850µm and the dimensions of the metallic pads are 150µm x 150 µm (figure 4.20). The width of the metal paths is 100µm, more than enough to endure a maximum intensity of 8mA.

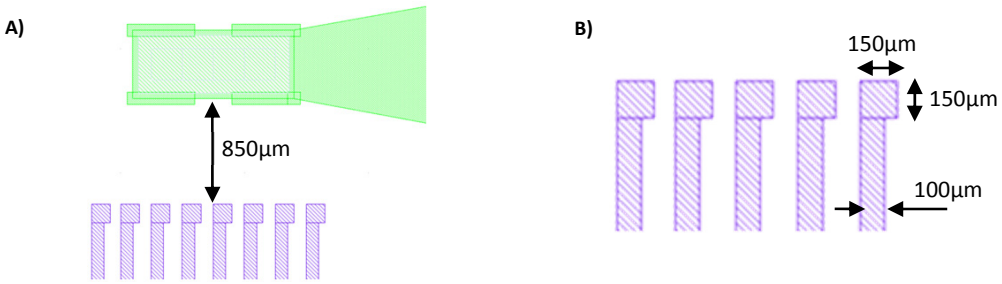

Figure 4.20: *(a) Following photolithographic design rules, metal paths are placed at a separation distance of 850µm from the VCSEL cavity. (b) The metal deposition phase will create metallic paths of 100µm width and bonding contacts of 150x150µm.*

4.4.4 Optical spacer

The optical spacer must guarantee not only the placement of the microlenses array on its top surface at the optical distanced determined by simulations, but also the passive alignment between the optical components of the system (VCSELs and microlenses). The design in “U” shape (green colour) for the piece offers good stability for the microlenses array and creates a window to allow the alignment between VCSELs and microlenses (figure 4.21). Again, the outline (violet colour) marks the boundaries of the piece.

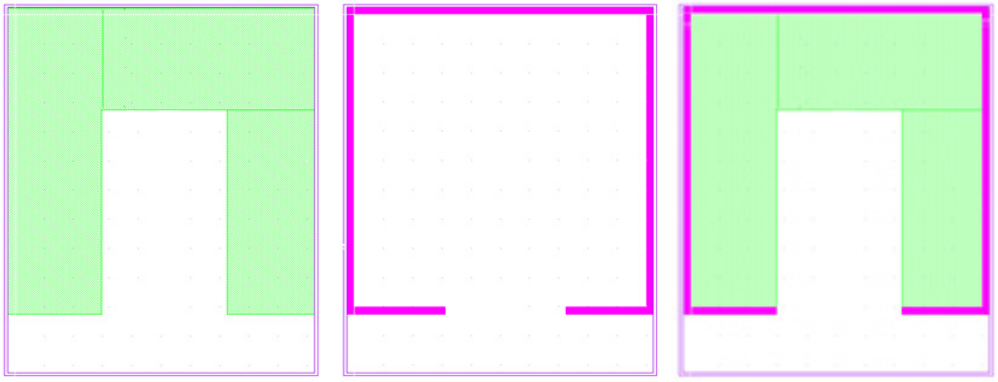

Figure 4.21: *Design scheme for the optical spacer structure. Left: the "U" shaped optical spacer (green colour). Middle: definition of the flange (pink colour) surrounding the top surface of the optical spacer. Right: "U" shape optical spacer with the flange on the top surface.*

To ensure the accurate positioning of the microlenses array and to avoid undesired lateral displacements during the alignment process, the initial idea was to define a flange (pink color) surrounding the top side of the optical spacer (figures 4.21, 4.22), according to the dimensions of the microlenses array, so that the optics would fit perfectly into the created cavity. In this way, we corrected lateral displacements between the emission axis of the light sources and the optical axis of the microlenses that would result in a loss in the efficiency of the system and possible crosstalk effects (light captured by a lens but coming from a neighboring VCSEL).

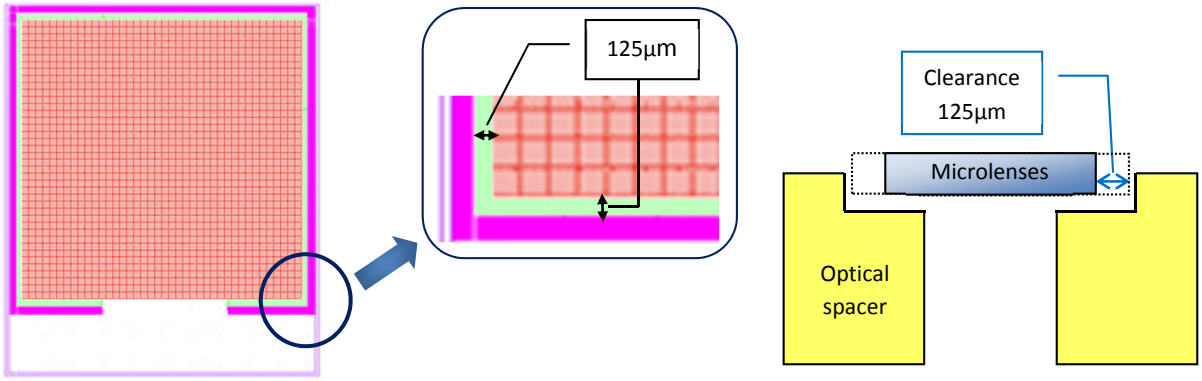

Figure 4.22: *Design scheme for the optical spacer structure. Left: the "U" shaped spacer (green colour) along with the pattern for the microlenses array. Middle: definition of the flange (pink colour) surrounding the top surface of the optical spacer. Right: Cross-sectional view of the "U" shaped optical spacer with the flange on the top surface.*

But the irregularities in the edge profile of the microlenses array (figure 4.23), due to the manufacturing process, brought some extra notes. The two silicon pieces (base and spacer) were designed so that after the assembly process, the microlenses array would be perfectly centred and aligned with the VCSEL light sources. Dimensions and positions of the aligning elements (cavities and wells) in both pieces were designed and adjusted according to the dimensions and the uniform profile of an ideal array of microlenses. To consider the flange design as a valid alignment method would require that either the definition of the flange was adjusted to the real profile of the microlens array or that the dimensions of the flange allowed the fitting of the microlenses array with enough tolerance.

The former would entail a previous study of the profile for each commercial array of microlenses. The latter, that the accuracy of the passive alignment defined strategy would have no sense, because in the case of study, the necessary tolerance was about 125µm (half of a lens) (figure 4.22).

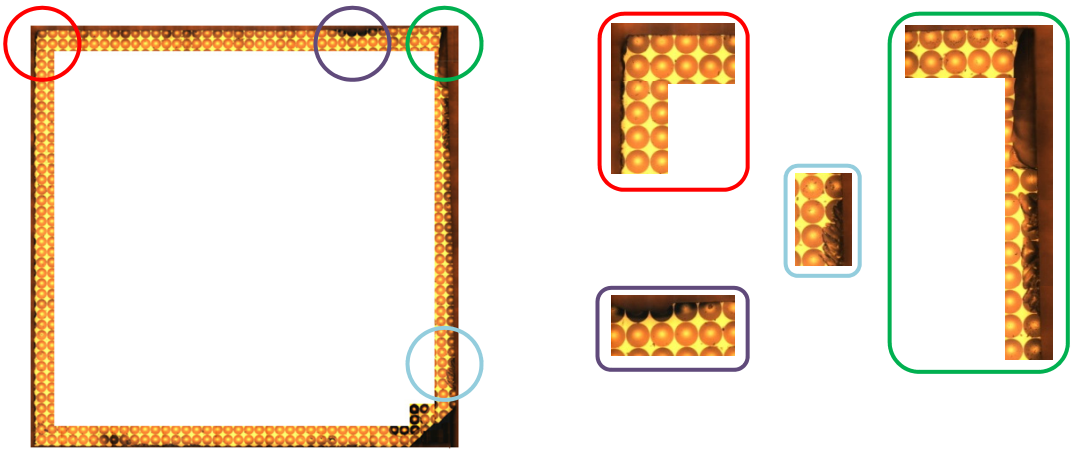

***Figure 4.23**: Microscope photography of the commercial microlenses array, with some zoomed details. The edge profile is plenty of irregularities due to the manufacturing process (dicing). In some zones, incomplete microlenses can be found.*

None of them were acceptable solutions for us, so the hybrid assembly approach demanded an additional passive alignment mechanism. The proposed solution was that the optical spacer also included a pattern of pillars on the top side. These pillars were specifically designed according to the geometry of the microlenses array, with a diameter of about 70-80µm and a height of 14-15µm (almost equal to the sagittal height of the lenses). The pillars helped to self-align the microlenses array with the VCSELs. Each one of the pillars was supposed to be placed in the intersection of 4 individual microlenses (figure 4.24).

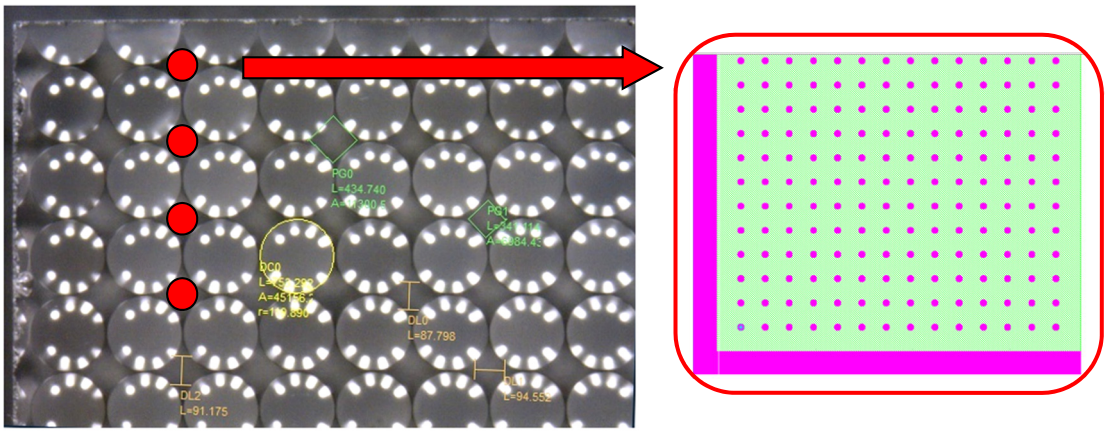

***Figure 4.24:** Microscope photography of the commercial microlenses array with several measurements of the dimensions of the lenses. A pattern of pillars on the top side of the "U" shaped optical spacer improves the passive alignment between the optical components.*

Once the question about the passive alignment was solved, other issues concerning the design of the optical spacer were discussed. As it will be detailed in the following section, the fabrication process for the optical spacer requires an etching on both sides of the silicon wafer. One of these etching processes will completely drill parts of the wafer (etching the total thickness of the wafer) and as a result, a free

piece will be obtained. In order to maintain the pieces subjected to the wafer, connection points are necessary, as the ones shown in figure 4.25. To release the processed pieces, these special "ribs" should be easily broken by applying a little force.

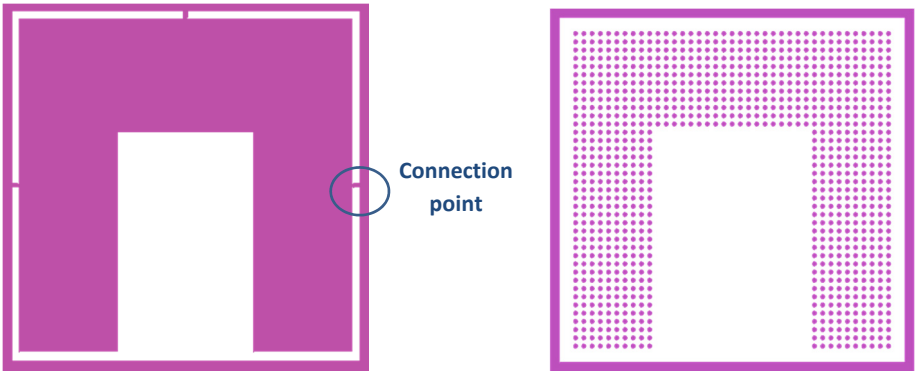

Figure 4.25: *Final design for the optical spacer structure. On the left side, the "U" shaped optical spacer with three connection points ("ribs") to the silicon wafer. On the right side, the pattern of pillars for the top side of the piece.*

Previous experiences (figure 4.26) have proven that after releasing the pieces, it is very likely to find some protuberances in their outlines, in the positions where the "ribs" lied. These non-uniformities depend on the strength exerted and on the crystallographic planes of the wafer.

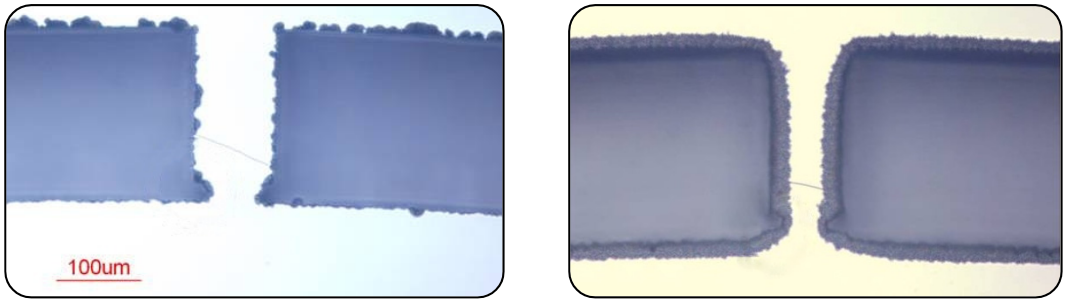

Figure 4.26*: Examples of different "ribs" fabricated on a silicon wafer for previous research projects. Printed with permission of the IMB-CNM-CSIC in Barcelona.*

Three different designs were considered (figure 4.27), following the rule that the "ribs" should be narrower near the optical spacer structure to favor the rupture reducing the creation of protuberances in the final piece.

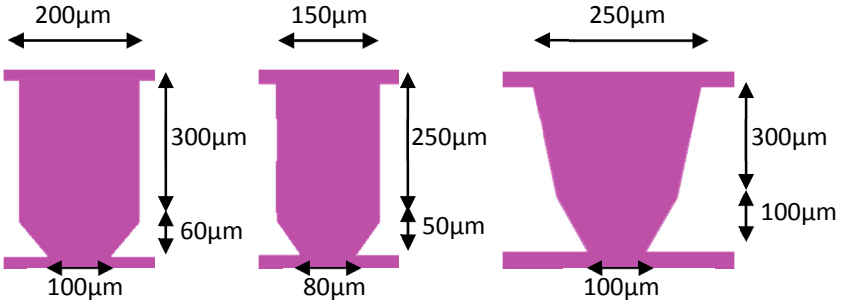

Figure 4.27: *Three designs for the "ribs", each one with different dimensions. The narrower part is near the optical spacer piece.*

Anyway, if these protuberances appeared, it would be difficult to fit the optical spacer chips into the base structure (figure 4.28).

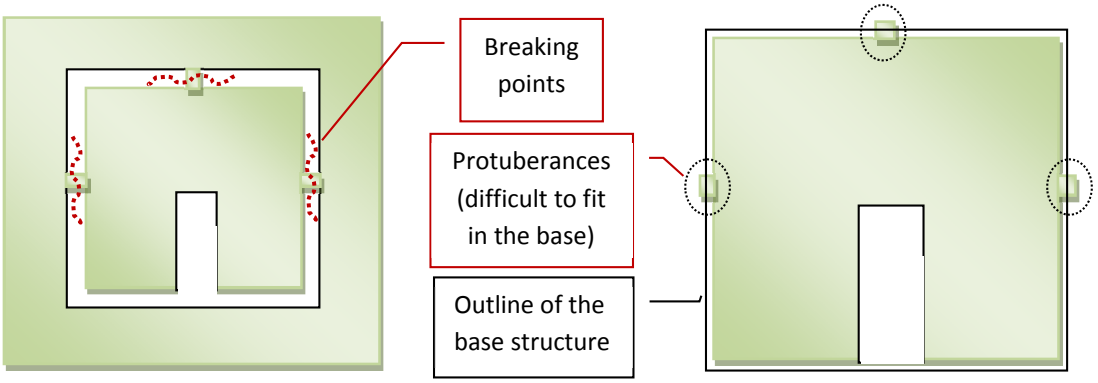

***Figure 4.28**: Schemes showing the difficulty of fitting the optical spacer into the base because of the existence of protuberances. The protuberances are consequence of the release process ("breaking the ribs") of the optical spacer piece from the substrate wafer.*

Since mechanically polishing these protuberances would be a costly task to carry out, the base structure was redesigned increasing the lateral dimensions and redefining the contour of the piece to adapt it to the shape of the "rib" (figure 4.29).

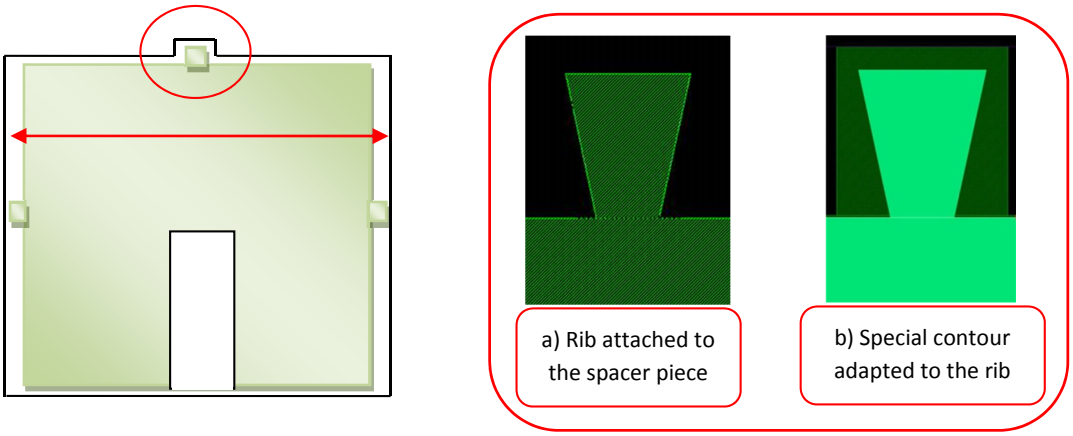

***Figure 4.29.** Left: To ease the fitting process of the optical spacer (green colour) with the base (black line), a redesign of the base is suggested: increasing the lateral width of the base structure and adapting the contour of the upper zone. Right: A special contour (dark green square on image "b") is defined on the base structure to allow the fitting of the remaining "rib".*

4.4.5 Comments on design tolerances

By now, the presented designs are almost ideal designs, regardless of the tolerances of a real fabrication process such as the anisotropic DEEP RIE. To ensure a successful assembly, the base structure was modified, adding tolerances in the dimensions of the "U" shaped well where the optical spacer should be placed (figure 4.30). The considered lateral tolerances were 5, 10 and 20µm. A special case of a base with a loose-fitting design for the "U" shaped well was also included for study, since it offered more freedom in the orientation and positioning of the optical spacer into the base (though this case was not valid for passive alignment of the components).

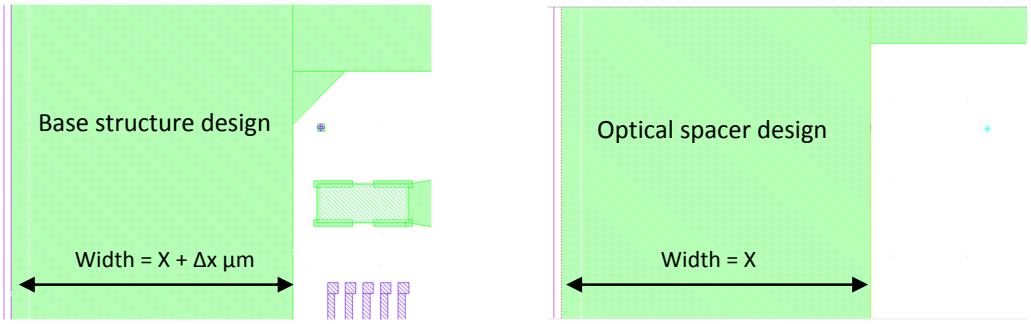

Figure 4.30: *Design of a base structure including lateral tolerances to ensure the matching and fitting with the optical spacer. Several cases for tolerance Δx are considered: 5, 10 and 20µm.*

4.5 Fabrication of the silicon pieces

The silicon pieces (the base structure and the "U" shaped optical spacer) were fabricated at the clean room of the IMB-CNM-CSIC in Barcelona (fellowship GICSERV Program: 6th call (NGG-190)). Silicon microsystems processes such as bulk micromachining or metal layer deposition were developed following standard procedures. Entire silicon wafers (100mm diameter) were processed.

For each one of the pieces a set of chromium masks was designed with *Cadence Software* (orientation chrome down, right reading). The 5 inches masks were fabricated by *Delta Mask Company*, in sodalime material. Each mask corresponds to a specific photolithographic step in the micromachining process of the silicon wafers; thus, alignment marks were included on them. The masks can be divided into two subsets. The first includes the masks elaborated for the silicon base structure. The second subset contains the masks for the "U" shaped optical spacer.

4.5.1 Base structure

For the fabrication of the base structure, two different silicon micromachining processes are described: single etching and double etching. Note that the same processes described in this section could be followed to fabricate a system providing focused light beams, adapting the etching depth parameter to the new configuration.

In both cases, a standard single side polished Silicon wafer of 500µm thickness was used for the process. All the photolithography and etching steps were performed on the polished side of the wafer.

4.5.1.1 Single etching on silicon substrate

For the single etched base, the depth of the VCSELs cavity and the "U" shaped well is the same and equal to the height of the VCSELs die, according to manufacturer dimensions, i.e. 150µm (figure 4.15). Metal paths to power the lasers are created by aluminum layer deposition of 1-2 microns.

Two masks are used for the fabrication of the piece:

- Mask for the deposition of the metal layer (NGG190 MET1, figure 4.31, left). This mask contains the metallic outline that defines the dimensions for each one of the 31 chips, the electric contacts and the

8 paths to power the lasers, a pattern of crosses to define the scribe lines for the dice phase, and necessary alignment marks for the lithography process. The mask is designed in bright field: the black lines and polygons of the picture (the metal depositions) represent chrome on the mask and the white color, transparency. The external circle defines the area of the wafer and it is used only for guidance.

- Mask for the Deep Reactive Ion Etching (DRIE) process to create the cavity for the die of VCSELs, the funnel feature and the "U" shaped well to fit the optical spacer (NGG190 RIE, figure 4.31, right). The chips are distributed as follows: 5 chips with a lateral tolerance of 5µm, 12 chips with a lateral tolerance of 10µm, 12 chips with a lateral tolerance of 20µm and 2 chips (central column, rows 3 and 6) for the special case of the base with the loose-fitting design. Contrary to the previous mask, this one is designed with the dark field criterion: figures in white color (transparent) represent the zones which will be attacked during the process, while black zones (chrome in the mask) will remain protected.

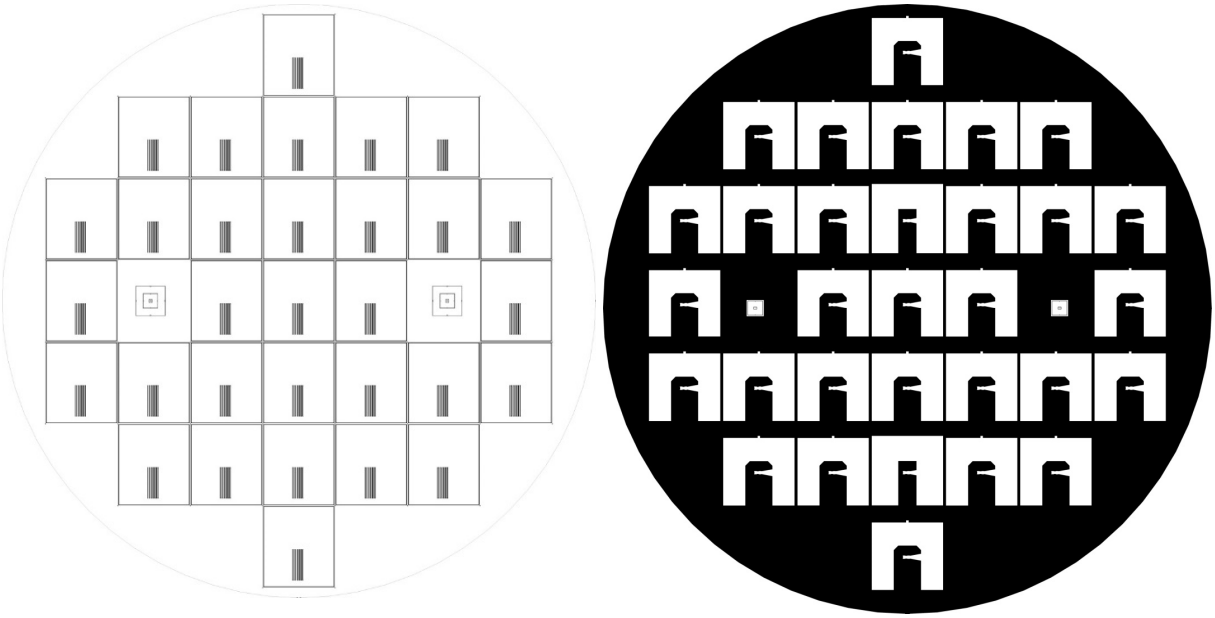

Figure 4.31: *Photolithographic masks for use in the Clean Room. Left: NGG190 MET1, metal layer deposition. Right: NGG190 RIE, DRIE processing of the silicon wafer.*

4.5.1.2 Double etching on silicon substrate

The double etched base follow the same guidelines described for the single etched base, but with a difference in the depth of the cavity for the VCSELs (figure 4.16). With a double step DRIE process, the depth of the cavity for the VCSELs is increased, maintaining the depth of the "U" shaped well at 150µm. As a result, an initial DRIE of 200µm produces the first etching step for the VCSELs and with a second DRIE of 150µm, the "U" shaped well is created and the depth of the VCSELs cavity is increased to a total value of 350µm. This design offers an interesting advantage: the possibility of using standard wafers of 1mm thickness to fabricate the "U" shaped optical spacer (refer to section 4.4.2 Double etched base and standard optical spacer"). For processing this double etching, a new mask is added to the previous ones:

- Mask for the first step of the Deep Reactive Ion Etching (DRIE) process. With this mask, the initial etching of 200µm depth for the cavity of VCSELs and the funnel feature is carried out (NGG190 RIE2, figure 4.32). The mask is designed in the dark field: figures in white color represent the zones that will be attacked during the process.

For the second step of the DRIE process, the previously introduced mask (NGG190 RIE) is used.

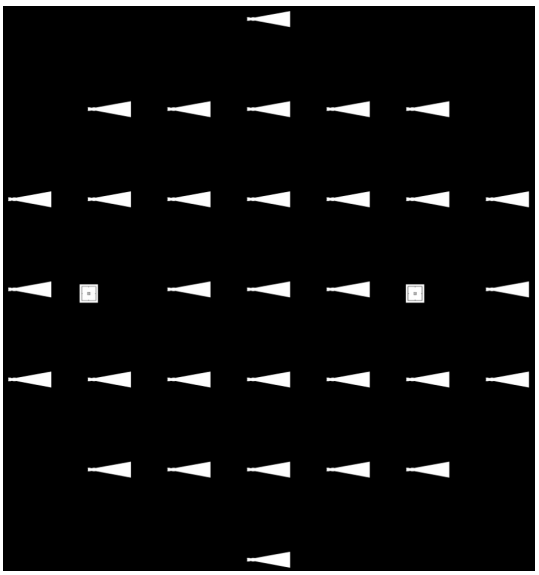

***Figure 4.32**: Photolithographic mask (NGG190 RIE2) for use in the Clean Room during the first step of the two phases double etching DRIE processing.*

4.5.2 Optical spacer

Optical spacer pieces are processed in their own silicon wafer. The thickness of these wafers will be different whether the base structure is single or double etched. For example, a single etched base requires a silicon wafer of a specific thickness of 1230µm. These silicon wafers must be fabricated upon request to manufacturers. However, for a double etched based, a standard wafer of 1mm could be used with acceptable results. Anyway, for both cases double side polished Silicon wafers are necessary, since both sides will be processed.

On the top side of the wafer, the pattern of pillars for optical passive alignment of the microlenses will be etched through a RIE process with a depth of 15µm. The processing of the bottom side will define the "U" shape of the piece, by means of a DRIE with an etching depth equal to the thickness of the wafer. The piece will remain subjected to the wafer thanks to three connection points.

Two masks are required for the fabrication of the optical spacer pieces:

- Mask for the Reactive Ion Etching (RIE) process on the top side of the silicon spacer (NGGC190 LENT, figure 4.33, left). This mask defines the side of the optical spacer in contact with the microlenses. A total of 14 chips are included: 8 with the pattern of pillars and 6 without the pattern. Chips without the pattern of pillars were included to study alternative alignment methods. In these chips, the degrees of freedom in the alignment process are increased, which allows to perform other passive alignment methods, such as visual alignment, and even an active alignment of the array of microlenses. The mask

is designed in bright field, so that the polygons in the design appear in chromium on the mask. The white zones will be attacked during the RIE process. The disposition of the chips on the mask prevents undesired effects during and after the processing of the silicon wafer, such as unexpected breakages related to the silicon crystallographic planes. The reduced number of chips attends the same reasons; the etching of the total thickness of the wafer necessary for the fabrication of the pieces is an aggressive process.

- Mask for the Deep Reactive Ion Etching (DRIE) process on the bottom side of the silicon spacer (NGGC190 LENB, figure 4.33, right). This mask defines the "U" shape geometry of the optical spacer and the connection points. The mask is designed in bright field, with the white zones being attacked through a DRIE process that will drill completely the wafer.

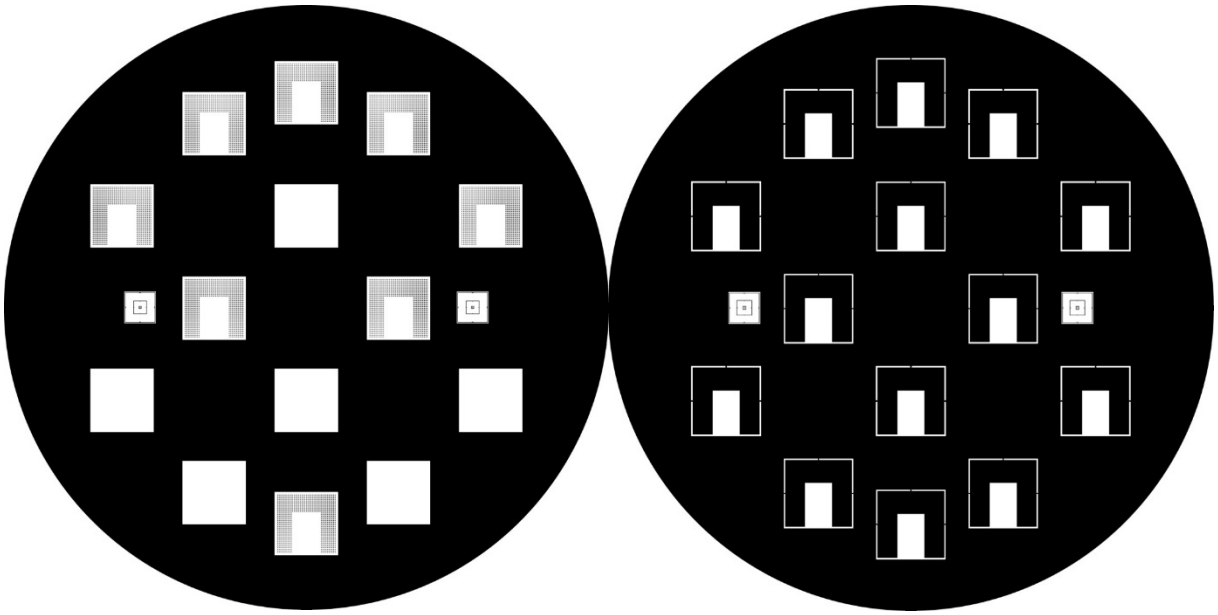

***Figure 4.33**: Photolithographic masks to be used in the Clean Room, Left: NGG190 LENT, RIE processing of the silicon wafer for the top side of the optical spacer pieces. Right: NGG190 LENB, DRIE processing of silicon wafer for the bottom side of the optical spacer pieces.*

4.5.3 Definition of RUNs for the fabrication at the Clean Room

A total of four RUNs were defined for the fabrication of the silicon pieces. The detailed descriptions containing the technical information about the followed processes can be consulted in the appendixes. Schemes in figures 4.34 and 4.36 describe graphically the basic photolithography steps followed during the fabrication of the base and the optical spacer structures.

Several confocal microscopy measurements were also performed with the *LEICA DCM3D* instrument to evaluate the agreement between fabrication parameters and real obtained values (figures 4.35, 4.37 and 4.38).

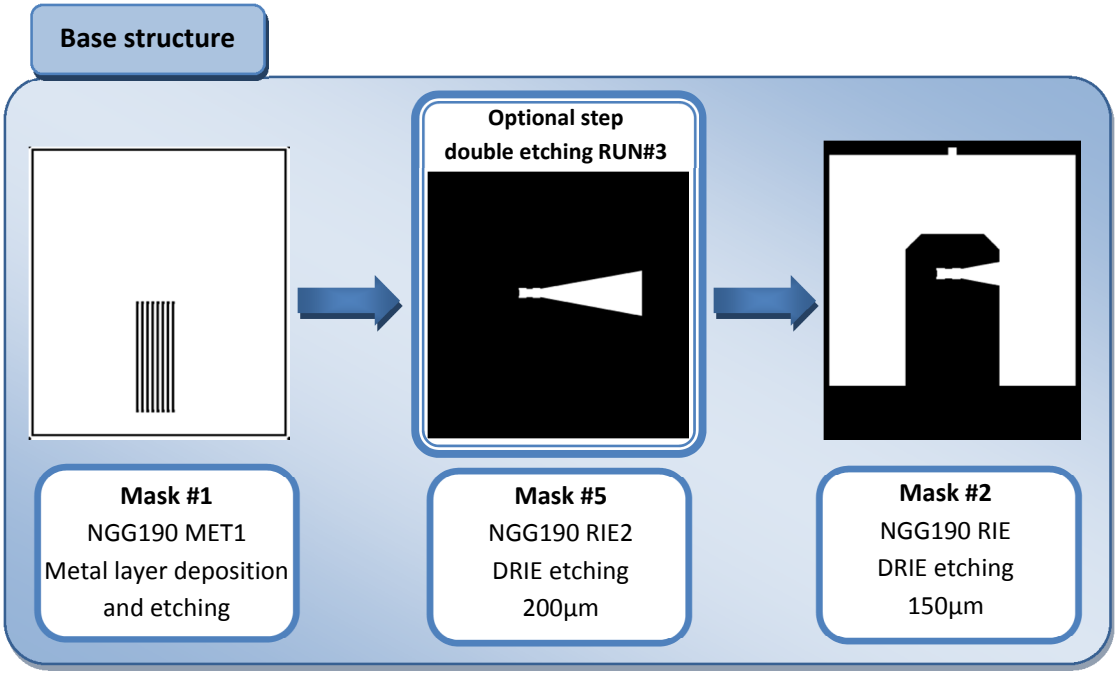

***Figure 4.34**: Scheme of the photolithography steps followed for the fabrication of the base structure. There is an optional step that will be necessary in case of processing a double etched base.*

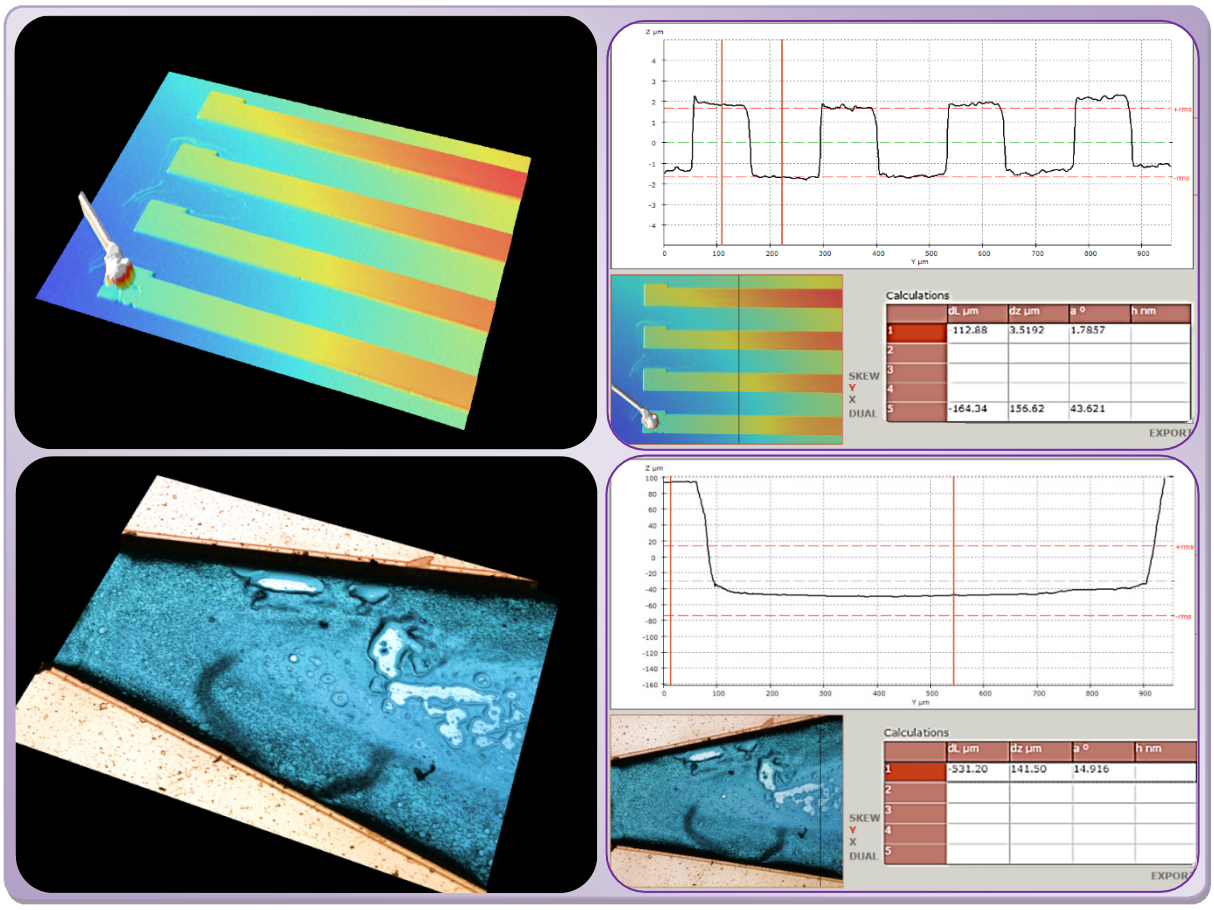

***Figure 4.35:** Confocal microscopy measurements for a single etched base. First: metallic paths of 3.5µm thickness. Second: funnel zone on the "U" shaped well with an etching depth of 141µm. Values agree with the expected.*

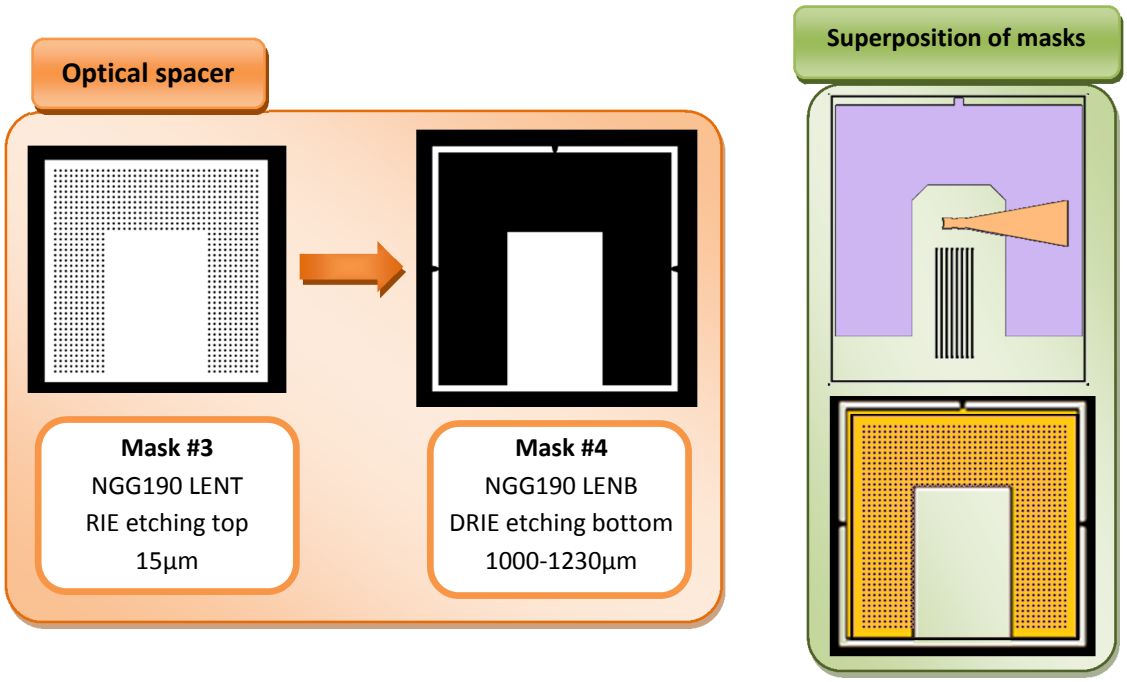

Figure 4.36. *Left: Scheme of the photolithography steps followed for the fabrication of the optical spacer. Right: Coloured superposition of photolithography masks for each one of the fabricated silicon pieces.*

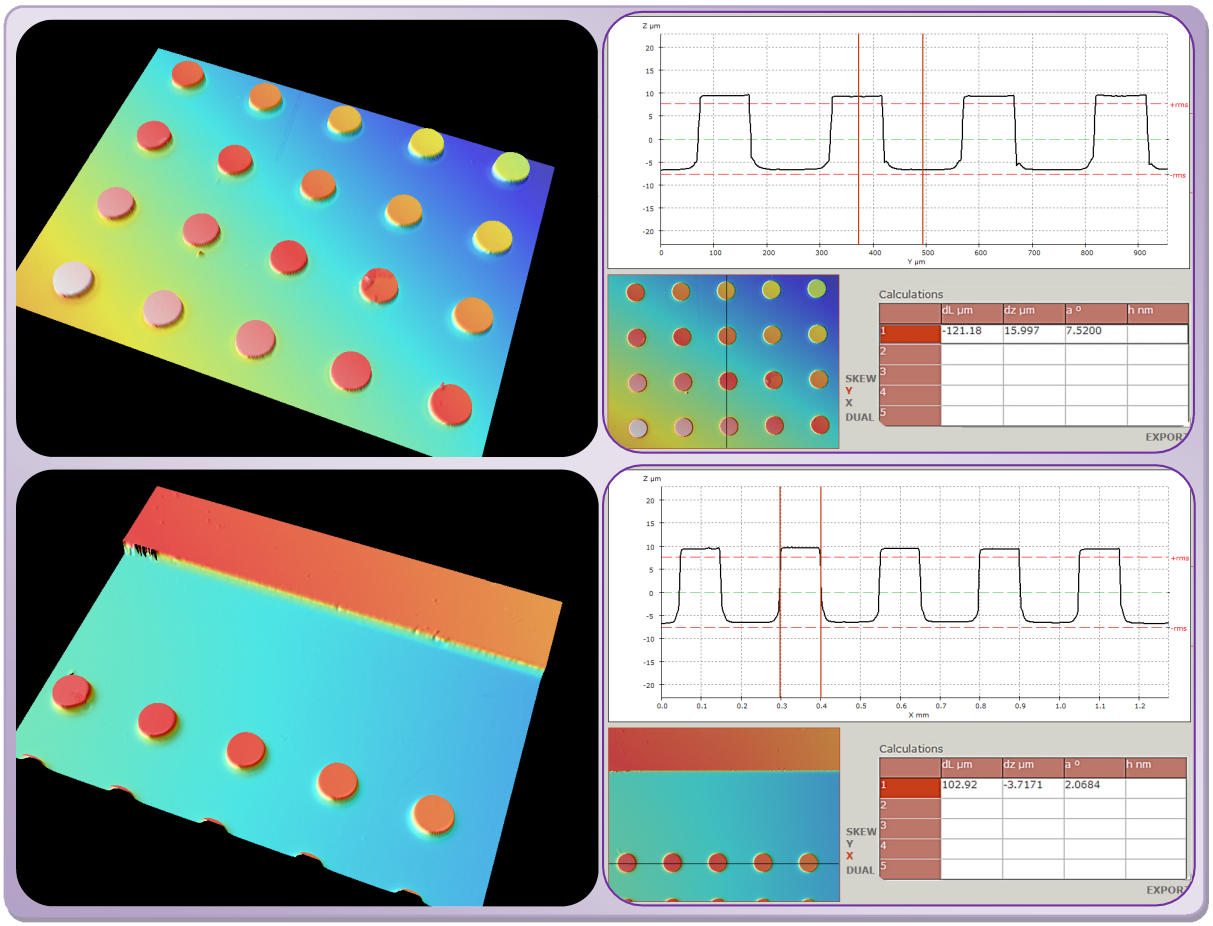

Figure 4.37*. Confocal microscopy measurements for the optical spacer. Dimensions of the fabricated pillars can be appreciated (≈16µm height and ≈100µm diameter).*

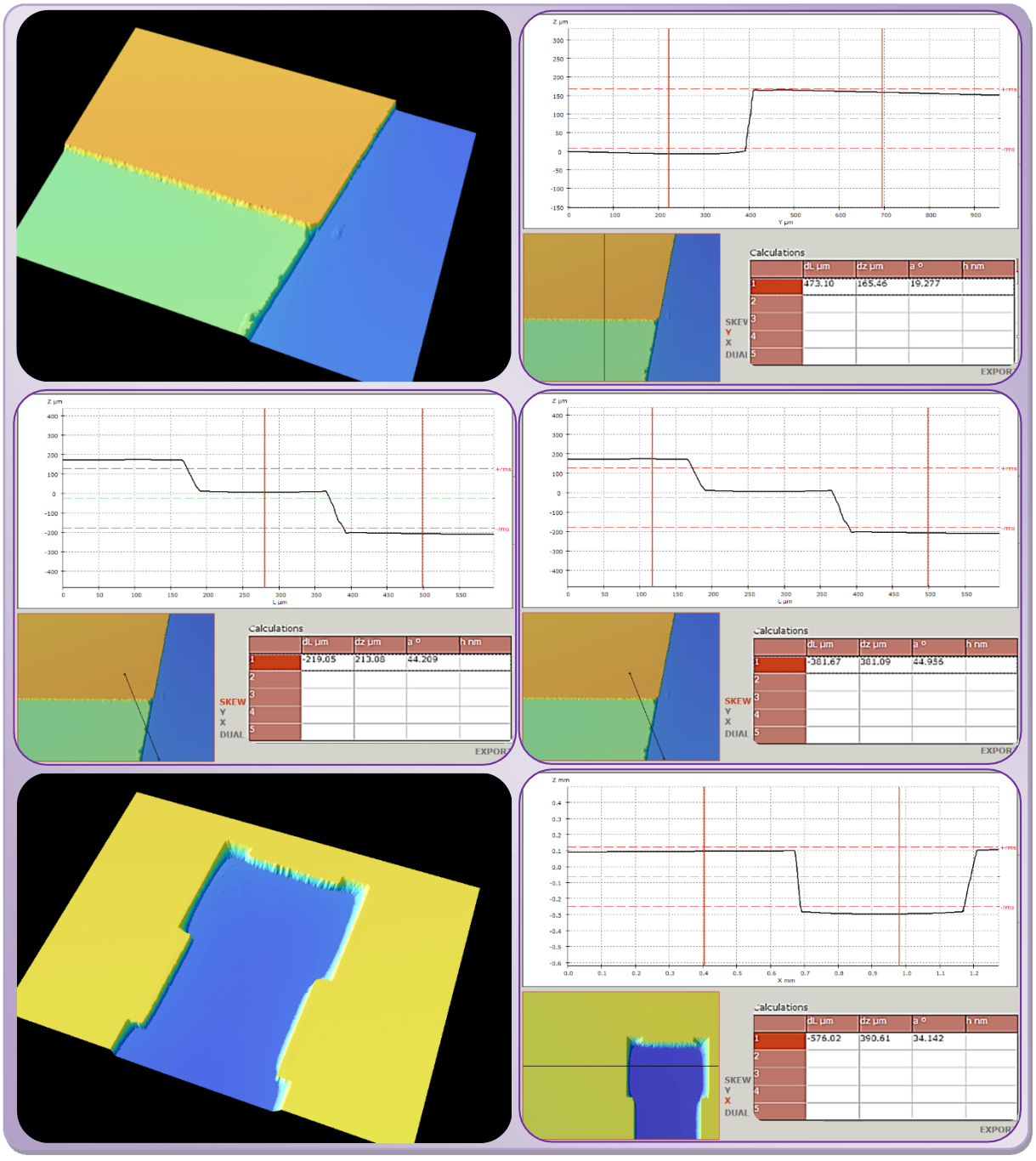

Figure 4.38: *Confocal microscopy measurements for a double etched base. First group of pictures correspond to measurements in a zone with single and double step etchings (part of the base level, part of the "U" shaped well and part of the funnel). An etching depth of ≈165µm is achieved in the "U" shaped well. The funnel presents an etching depth of ≈213 µm with respect to the "U" shaped well. Total etching depth is ≈ 381µm. Second group of images shows part of the cavity for the die of VCSELs, with a double etching process and a real value of 390µm.*

4.5.4 Results: fabricated silicon pieces

This section gathers images from the fabricated base and optical spacer silicon pieces.

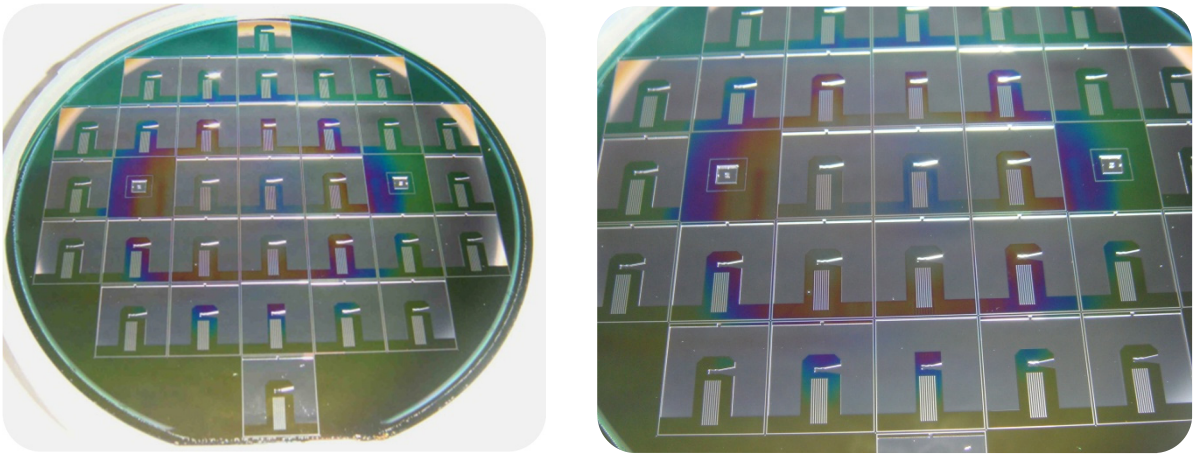

Figure 4.39: *Photography of the processed silicon wafer for the "base" pieces, before dicing the chips.*

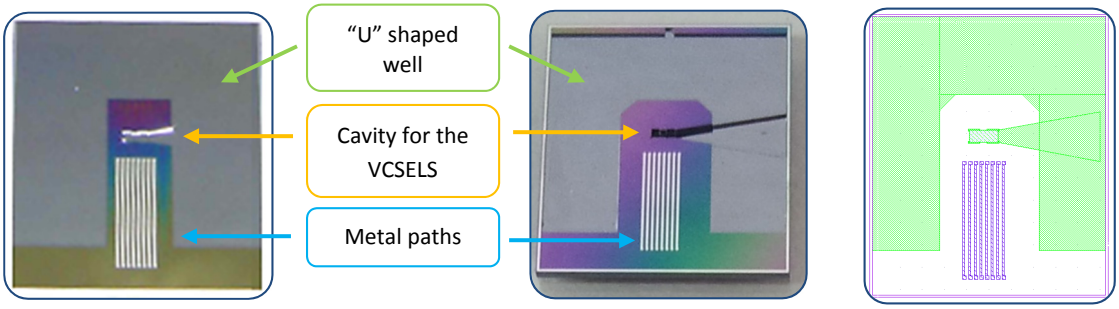

Figure 4.40: *Photographs of silicon "base" chips. Left: single etched base. Right: double etched base. On the right side, schematic design of the expected base piece.*

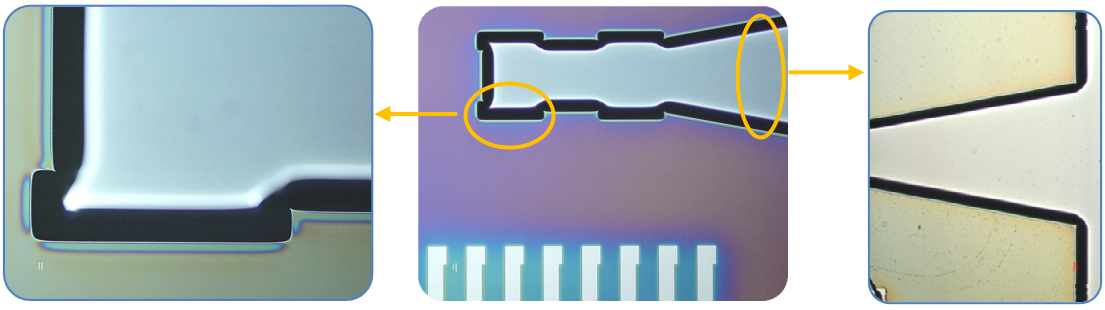

Figure 4.41: *Details for a silicon single etched "base" chip. Left: Zoom of the alignment marks in the cavity for the die of VCSELs. Center: Cavity for the VCSELs. Right: Zoom of the funnel geometry.*

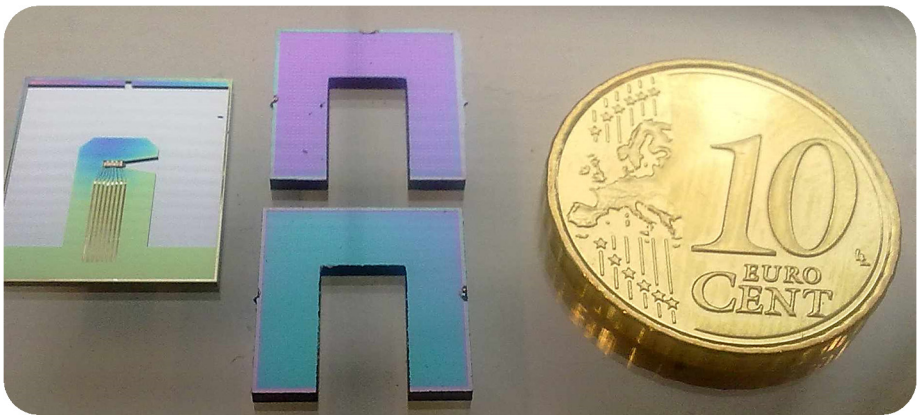

Figure 4.42: *Photographs of the real dimensions and sizes of a silicon base chip and two silicon optical spacers ("U" shape) with and without the pattern of pillars (top and bottom respectively).*

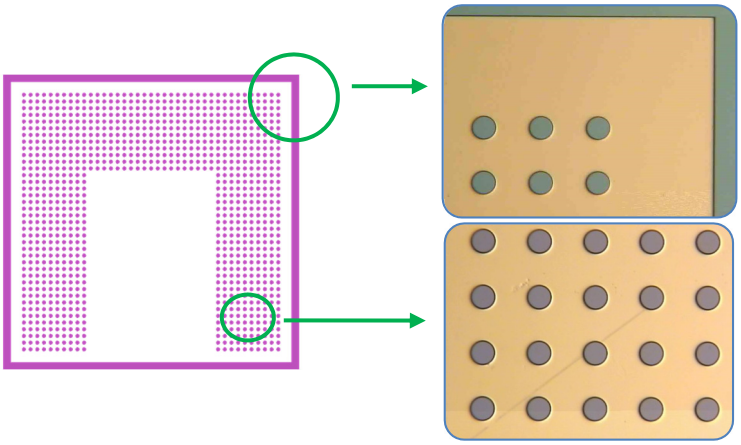

Figure 4.43: *Detail of the mask used to process the top side of the silicon optical spacer. The mask includes a pattern of pillars. On the right side some photographs of the fabricated patterns.*

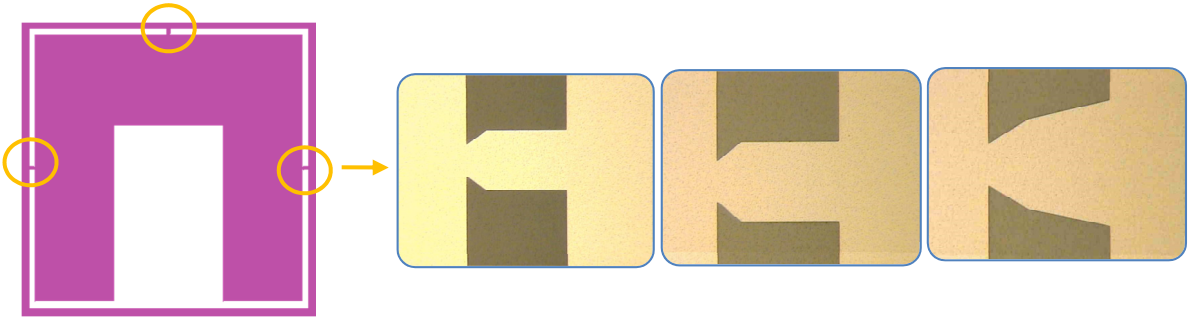

Figure 4.44: *Detail of the mask used to process the bottom side of the silicon optical spacer. The mask includes the "ribs" designed to maintain the piece connected to the wafer during the fabrication phase. On the right side some real photographs of the different designed "ribs".*

4.6 Comments on the fabrication results

Concerning the real etching values obtained during the fabrication of the double etched base (RUN #3 in appendix), a comparative study of the deviation in the RMS radius value of the spot located at the plane of the microfluidic channel (detector #1 in optical simulations of Chapter III) with respect to the expected values, was performed.

Two different thickness values were considered for the optical spacer piece: 1000 and 1100µm, according to the processed wafers in RUN #2 (appendix). These two values in combination with expected and achieved etching depths[6] in the base piece define a range of possible effective focal distances (table 4.3) when applying equation 4.3:

f_e = thickness of the optical spacer wafer
+ depth of the first etching (cavity for VCSELs die)
– depth of the second etching ("U"shaped well of the base for the placement of the spacer)
– depth of the etching on the top side of the optical spacer (pattern of pillars) *(4.3)*

Table 4.3: *Possible effective focal distances (fe) for the real values of silicon pieces obtained after fabrication.*

	Focal length in µm		
	Base expected etching values	Base experimental etching values (fabrication process)	
Optical spacer thickness	First etching 200µm Second etching 150µm Total etching 350µm	First etching 173µm Second etching 166µm Total etching 339µm	First etching 183µm Second etching 166µm Total etching 339µm
1000µm	1035µm	1008µm	1018µm
1100µm	1135µm	1108µm	1118µm

From the results of the study (table 4.4, next page) we can deduce that the minimum deviations in the RMS value of the radius are obtained for f_e = 1018µm (optical spacer fabricated from a wafer of 1000µm thickness) and f_e = 1108µm (optical spacer fabricated form a wafer of 1100µm thickness). In both cases the Δf_e (understood as $f_{e\_theoretical}(1.063) - f_{e\_real}$) in absolute values is 45µm.

For f_e= 1018µm the RMS radius increases in a mean value of $\Delta_{RMS\ radius}$ = +26µm, 11µm more than the expected optimal case for f_e 1035µm. However, for f_e=1108µm the values of the RMS radius are even lower than the expected for f_e 1035µm, becoming closer to the values calculated for the theoretical collimated scenario with f_e 1063µm. The deviation in the radius of the spot is only of $\Delta_{RMS\ radius}$ = -8 µm (mean value) in front of the increment of 15µm mean value for the case f_e=1035µm.

Though these values could be still considered as acceptable, even when they represent a deviation from the perfect collimated light beams scenario, they respond to simulated calculus. For the real deviations in terms of f_e distance, it is necessary to perform the measurements once the hybrid assembly of the system is completed. Several factors can influence the final values, e.g. tilt factor in the die of VCSELs due to manual placement and soldering processes or differences in the etching depth of the cavity for the VCSELs depending on the position of the chip in the silicon wafer (the etching process is not uniform along the wafer; small variations can be found between different zones).

[6] Refer to figures 4.16 and 4.34 for the graphic representation of the double etched base fabrication process.

Table 4.4: *Comparative table of ZEMAX simulations results for the RMS radius of the spot located at the microfluidic channel (detector#1) with the array of microlenses placed at different f_e distances from the VCSELs light sources, according the values obtained after the fabrication of pieces. Ideal values for f_e=1063µm are included for comparison, as well as values for f_e=1035µm and 1135µm (theoretical expected values after fabrication). VCSEL $I_{forward}$ = 1mA. Dimensions of the detector used in simulations were 1x1mm^2. To compare with results obtained in previous simulations (chapter III), variable $d_{V\text{-}D}$ corresponds to the distance between the VCSELs and the CMOS array of photodetectors (detector#2). Results are also presented as values of deviation with respect to ideal case (f_e=1063µm).*

	RMS radius in µm/ Difference in µm/Difference %						
	Desired	Expected		Experimental			
Distance in mm $d_{V\text{-}D}$	Fe 1063µm	Fe 1035µm	Fe 1135µm	Fe 1008µm	Fe 1018µm	Fe 1108µm	Fe 1118µm
13	**98**	111/13/13	145/47/48	125/27/28	**119/21/21**	**82/-16/-16**	80/-18/-18
18	**130**	145/15/12	191/61/47	162/32/25	**155/25/19**	**117/-13/-10**	116/-14/-11
23	**167**	182/15/9	242/75/45	203/36/22	**195/28/17**	**159/-8/-5**	159/-8/-5
28	**207**	222/15/7	289/82/40	245/38/18	**235/28/14**	**202/-5/-2**	205/-2/-1
33	**247**	262/15/6	323/76/31	287/40/16	**277/30/12**	**247/0/0**	251/4/-2
Mean $\Delta_{RMS\ radius}$	**-**	≈15µm	68µm	34µm	**26µm**	**-8µm**	-9µm

4.7 Hybrid Assembly of the pieces

The first step in the assembly process is the placement of the die of VCSELs into the designed cavity (figure 4.46), to follow with the wire bonding of the pads (anodes and cathodes) to the metallic paths of the base chip.

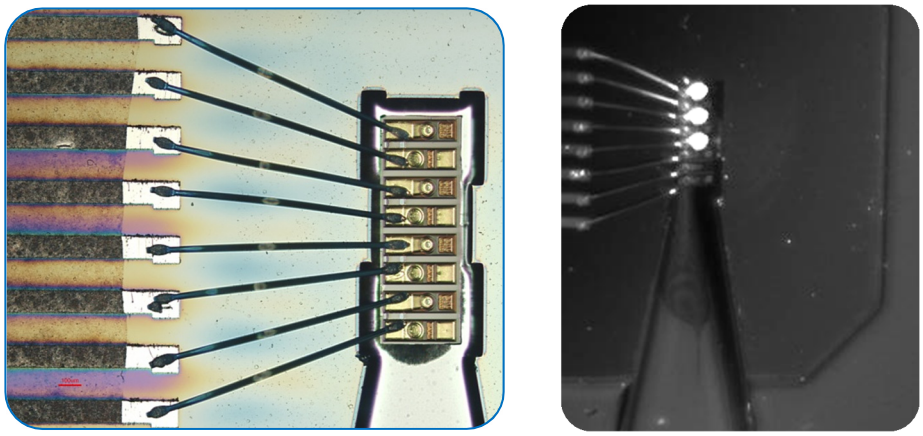

Figure 4.45. *On the right side, microscope photograph for the placement of the die of VCSELs inside the designed cavity and the wire bonding of the electrical connections. On the right side, microscope photograph of the die of VCSELs assembled on the base piece, with three lasers emitting.*

The next step consists in joining the base with the optical spacer (figure 4.47). This operation is manually achieved thanks to the design of both pieces, which facilitates the mechanical join. To permanently fix the pieces, glue or epoxy resin can be used.

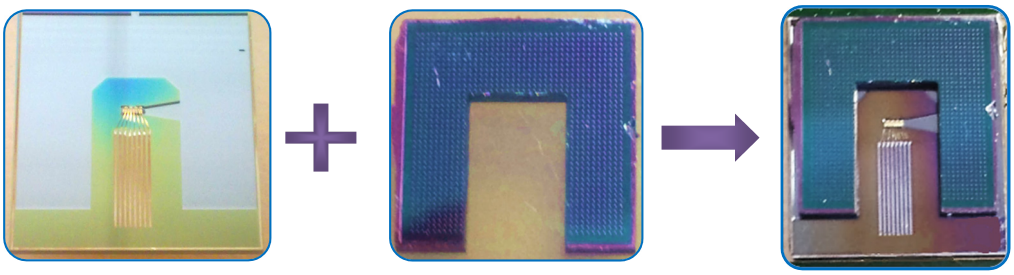

Figure 4.46: *Joining of the silicon base and the silicon optical spacer. The process can be manually done, without any special instrumentation. Left: detail of a silicon base with a single "U" etched zone, the die of VCSELs, the metal paths and the wire bonding. Center: silicon optical spacer with pattern of pillars. Right: result of the joining process. Epoxy resin/special glue is used to fix the pieces.*

We are only one step away to have a complete optoelectronic device: the passive alignment of the array of microlenses with the VCSEL light sources. The hybrid assembly between the silicon optical spacer and the array of microlenses is one of the most critical steps of the process. The accuracy in the assembly process defines the level of optical alignment achieved. The photographs in figure 4.47 show the result of the passive alignment of both elements, in a manual process. For this case, the silicon optical spacer structure presents a pattern of pillars on the top side which helps in the alignment process yielding in an accuracy of ≈5µm.

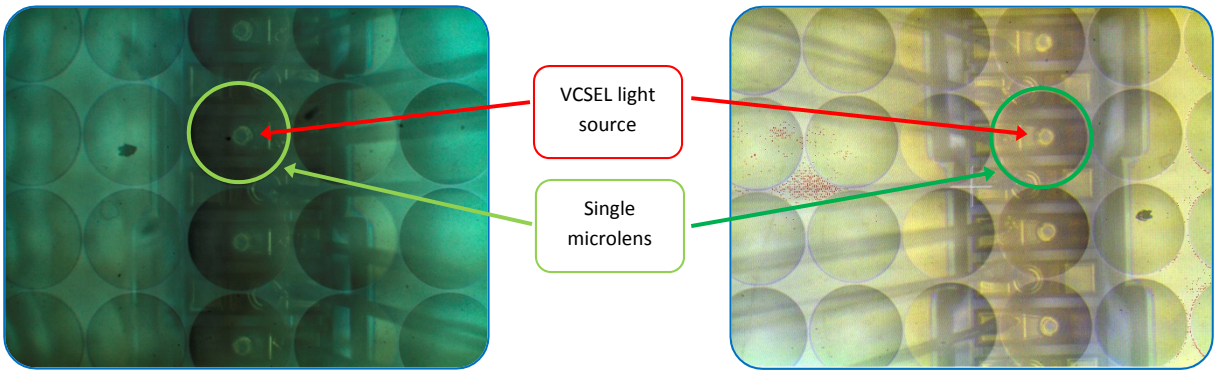

Figure 4.47: *Microscope photograph for the result of the hybrid assembly and passive alignment of the VCSEL light sources and the array of microlenses. Each VCSEL is almost perfectly centred on a microlens. The pattern of pillars on the top side of the optical spacer piece improves the optical alignment process, which is carried out manually.*

4.8 Packaging

To handle the optoelectronic device, it is necessary to package it. Packaging the device will also bring the necessary electrical power supply to the light sources. Two alternatives were considered: the first, based on commercial packages, and the second, on a self-designed printed circuit board (PCB). Due to the difficulties in finding packages with the necessary dimensions to contain the device, the PCB option was implemented.

The optoelectronic device was placed and fixed, by means of epoxy resin, in a custom designed PCB with flash gold electrical contacts and paths (good conductivity and resistance to oxidation), and the integrated electrical components (resistors and switches) necessary to control and power the light

sources (1-2mA at 2.3V_{dd_MAX}) (figure 4.48). Electrical connections from the metal paths on the silicon base piece of the optoelectronic device to the contacts in the PCB were created with wire bonding.

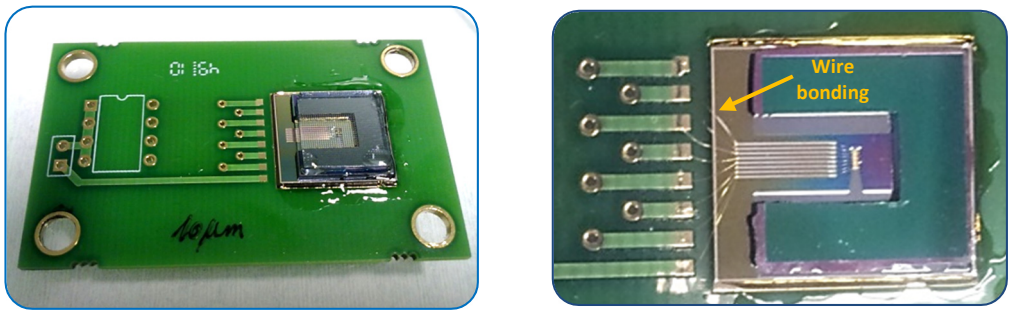

Figure 4.48: *Packaging of the final device. Left: Photograph of the final miniaturized system with the optoelectronic device mounted on the PCB. Right: Detail of the wire bonding connections between the metal paths of the silicon base piece and the electrical flash gold contacts of the PCB. In this picture, the array of microlenses is not present to offer a better view of the zoom.*

Through integration, assembly and packaging processes we have obtained a miniaturized and robust optoelectronic system, which provides four collimated laser light beams, and that can be easily managed, handled and operated to be included on an optical particle detection application.

4.9 Optical testing

A set of optical testing measurements was performed with the fabricated optoelectronic package, in order to determine the goodness of the collimation effect. The set-up for the measurements is presented in figure 4.49.

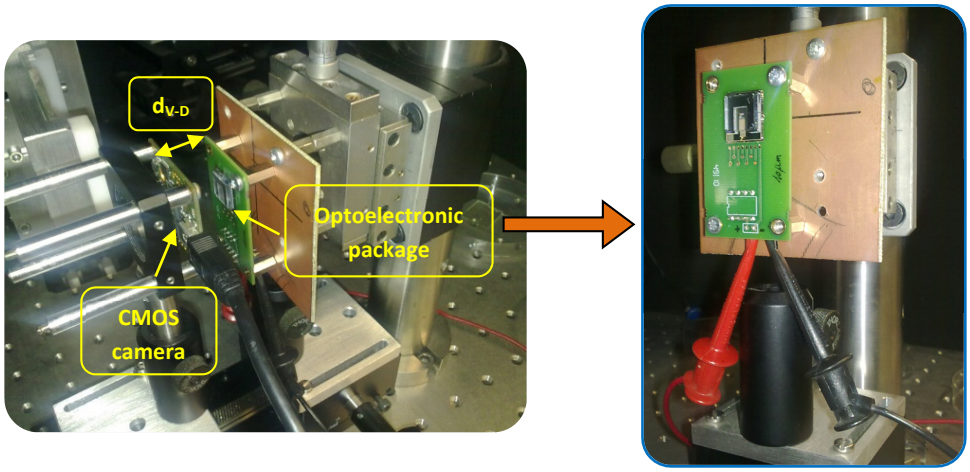

Figure 4.49: *Set-up for the optical testing measurements. Optoelectronic package is mounted on a 2-axis micropositioner. In front, a commercial CMOS camera is placed at a controlled distance* d_{V-D}.

Once the position of the optoelectronic package was fixed, with the help of a commercial 2D CMOS camera (*UI-1545LE-M uEye from IDS*) faced front in a parallel plane, we captured real images of the spots. The plane corresponding to the CMOS camera equals the plane where the microfluidic channels would be placed (according to optical simulations, Chapter III). The measurements were repeated for several distances d_{V-D} (VCSELs – plane of detector) varying the position of the commercial camera. The resulting images showed the variation in the diameter of the spot for a single VCSEL, depending on the

distance to the image plane. Table 4.5 contains de values obtained for these measurements. In the captured images of the spots, the typical spontaneous emission[7] existing in VCSELs can be appreciated.

Table 4.5: *Summary of the collimation effect measurements for the experimental setup. As distance $d_{V\text{-}D}$ increases, radius of the spot follows the same increasing tendency, though more reduced and controlled. Red circles delimit the area of the spot considered in the measurements. Anyway, it can be concluded that experimental results for the collimation effect are satisfactory.*

$d_{V\text{-}D}$ (VCSEL- Detector)	Spot radius	Captured images from CMOS camera
3 to 9mm (Δ=1mm)	124 µm	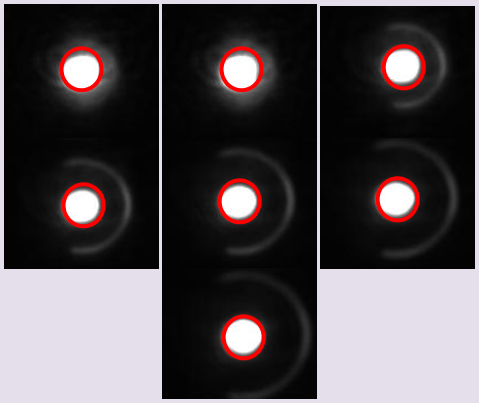
1cm	130 µm	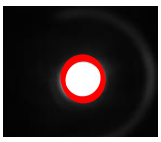
2cm	166 µm	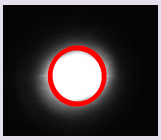
3cm	213 µm	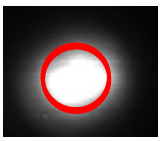

From the analyzed data, it can be concluded that in the range of values for variable $d_{V\text{-}D}$ that goes from 1cm to 3cm, divergence in the light beam increased only in 0.234°, while in the range of distances from 0.3 to 0.9cm there was no significant variation in divergence, i.e. the RMS radius kept almost constant at the minimum value (124µm). Results demonstrate that the system accomplishes the expectations according to optical simulations with good values of collimation. Though during fabrication and assembly processes some deviations have been introduced with respect to theoretical values, the impact of these tolerances proves to be minimum.

The effect of optical replicas can be appreciated in figure 4.50, where a single VCSEL is active, but secondary spots created by the neighboring microlenses appear in the picture. Adjusting the

[7] Before threshold is reached, a laser produces spontaneous emission, for it essentially behaves like a light emitting diode (LED). Once threshold is reached, the additional input power is coupled into the coherent lasing radiation mode and is superimposed on the background LED spontaneous emission [15], [16].

separation distance $d_{V\text{-}D}$ it is possible to eliminate them. In the figure, for $d_{V\text{-}D}$ = 1cm, the effect of replicas can be underestimated, thus a single VCSEL source will result in a single light spot in the plane of the CMOS double array sensor (replicas do not appear in the field of view of the sensor).

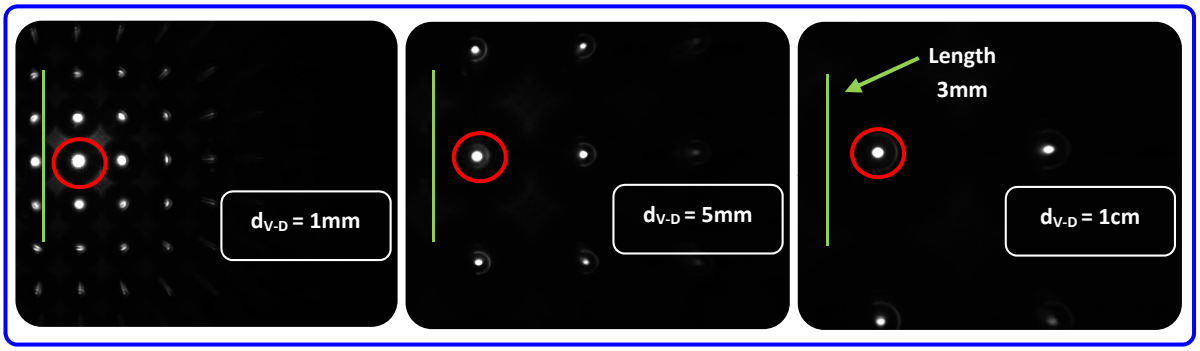

Figure 4.50: *Images captured with the commercial 2D CMOS camera. Only one VCSEL is switched on. As the distance between the VCSEL light source and the camera (image plane) increases, replicas disappear. In this series of pictures, $d_{V\text{-}D}$ corresponds to 0.1, 0.5 and 1cm respectively. Red circle identifies the main spot. Green line of 3mm length represents the length of the CMOS double array sensor.*

Some comparative images that demonstrate the benefits of collimation effect are shown in the following images (figure 4.51) for the case when two VCSELs are active.

Figure 4.51: *Images captured with the commercial 2D CMOS camera to compare the benefits of the integration of micro-optics (collimation effect in the figures on the left side) with the natural response of the light sources (figures on the right side). Two VCSELs are active (the second and the fourth from the four available in the integrated die). In this series of pictures, $d_{V\text{-}D}$ is equal to 1 and 2cm. Red circle identifies the main spots.*

With 2 VCSELs are active, it is interesting to remark that when distance $d_{V\text{-}D}$ increases from 0.1 to 3cm, the distance between the centers of the captured light spots at the image plane keeps constant thanks

to the collimation effect. The second and the fourth VCSELs are switched on with a distance between the centers of the spots ≈520µm, which corresponds to almost two times the pitch of the VCSELs in the die as expected. The study also states that from $d_{V\text{-}D}$ = 1 to 3cm, the divergence between the spots (considering for the measurement the variation of the total distance between the outer points for both spots) increases ≈1° (figure 4.52). A rotational effect in the spots axis can be observed in the presented results when $d_{V\text{-}D}$ increases, due to the tilt introduced in the optical system during the assembly process (i.e. the placement and soldering of the die of VCSELs in the cavity of the base piece).

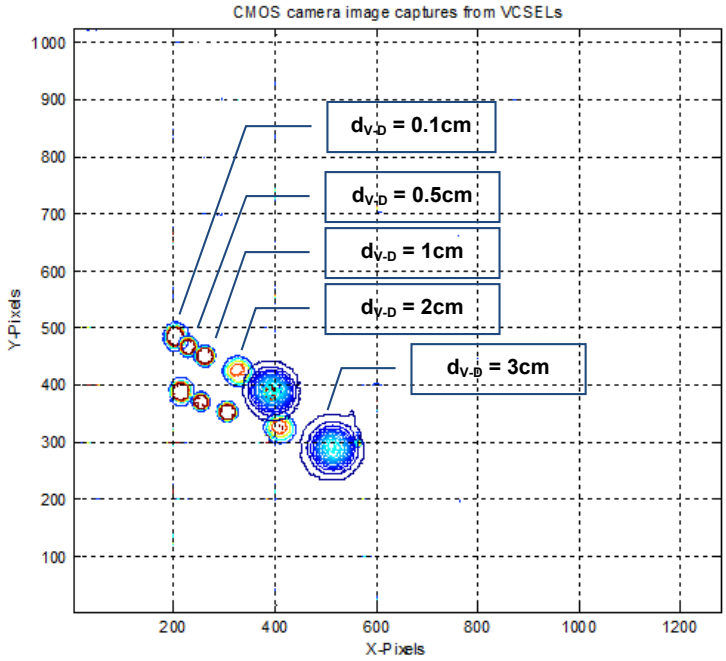

Figure 4.52: *Study of the effect of distance $d_{V\text{-}D}$ in the divergence between two spots. The separation distance between centers keeps constant at a value of 520µm trough the experiment. According to fabricant, pitch between VCSELs is 250µm, which means that the distance between two non-consecutive VCSELs should be 500µm.*

Finally, images in figure 4.53 compare simulations with experimental results for several active VCSELs and a distance $d_{V\text{-}D}$ = 0.5cm.

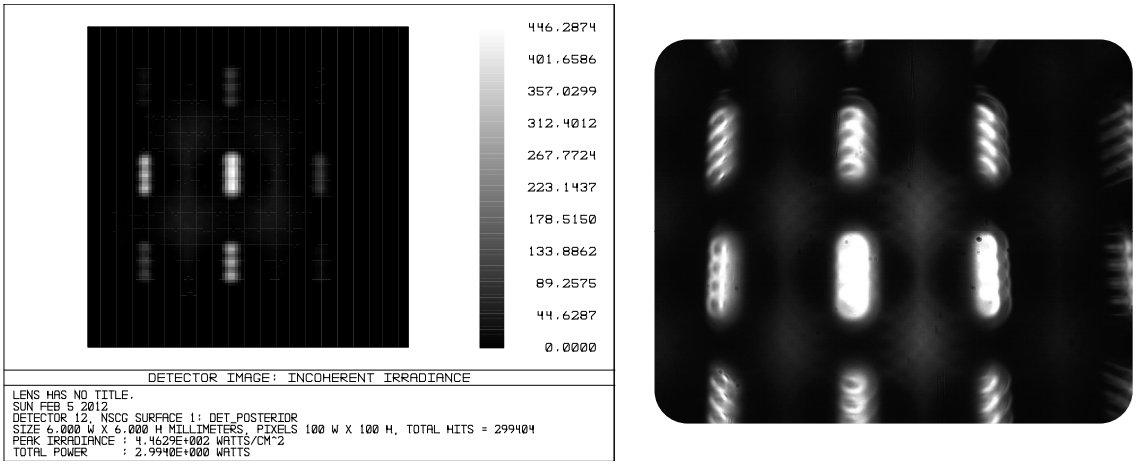

Figure 4.53: *Comparison of simulated and experimental results for several active VCSELs and a distance $d_{V\text{-}D}$ = 0.5cm. Distribution of spots and replicas coincide in both cases.*

The summarized data of the simulation results for the pure collimated scenario compared with experimental results can be consulted in table 4.6 and figure 4.54. Table 4.7 and figure 4.55 present the results of the measurements in the same conditions but without the use of microlenses. From the experimental data, the collimation effect is quite noticeable: at a distance $d_{V\text{-}D}$ = 2cm, the radius of the system with microoptics reduces from ≈2mm to ≈166µm.

From the graphs we can conclude that experimental results are even better than the ones from simulations, which is very noticeable in the case of large distances ($d_{V\text{-}D}$ greater than 10mm). The correction of the divergence of light beams achieved by the optical collimation system implemented in the optoelectronic package is maintained along a wider range of distances. As a result, the radius of the spots in the plane of interest, fits the optical design requirements. And when considering the real distances ($d_{V\text{-}D}$ from 1 to 2 cm) imposed by the physical limitations of the optical detection system, the radius of the obtained spots is perfectly suitable to work with. Integration of optics in an optoelectronic package yields a positive collimation effect. We assume that the deviations in the real values with respect to simulations are due to the tolerances introduced during the fabrication, assembly and packaging processes, which results in a system with a tendency to focus rather than to collimate, with an effective focal length larger than theoretical value 1.063mm.

Table 4.6: *Comparison between simulation results of the spot sizes (radius), calculated as ZEMAX RMS and $1/e^2$ standard, and experimental measured values for a collimated scenario (system with micro-lenses). Image plane was located at different distances from the VCSEL light source. Simulation results are presented for several VCSEL forward intensities (8mA, 2mA and 1mA). ZEMAX detector area was 700x700µm². No microfluidics block considered.*

Radius of the spots with micro-lenses in µm. Collimation effect: RMS | $1/e^2$	Distance between VCSELs and detector (image plane) in mm ($d_{V\text{-}D}$)				
Simulation results for several VCSEL forward intensities (mA)	**5**	**10**	**15**	**20**	**30**
8	82/119	96/146	124/188	159/236	236/340
2	80/128	94/145	123/187	159/231	236/338
1	75/115	91/138	121/185	158/230	236/348
Experimental values ($1/e^2$)	**124**	**130**	**-**	**166**	**213**

Table 4.7: *Comparison between simulation results of the spot sizes (radius), calculated as $1/e^2$, and experimental measured values for a non-collimated scenario; no micro-lenses were used to correct the natural divergence effect of light sources. Image plane was located at different distances from the VCSEL light source. Simulation results are presented for several VCSEL forward intensities (8mA, 2mA and 1mA). ZEMAX detector area was adjusted according to the needs of each particular case. No microfluidics block considered.*

Radius of the spots without micro-lenses in µm: $1/e^2$	Distance between VCSELs and detector (image plane) in mm ($d_{V\text{-}D}$)			
Simulation results for several VCSEL forward intensities (mA)	**5**	**10**	**15**	**20**
8	1313	2626	3939	5252
2	991	1982	2973	3964
1	842	1608	2412	3216
Experimental values	**1150**	**1460**	**1820**	**1958**

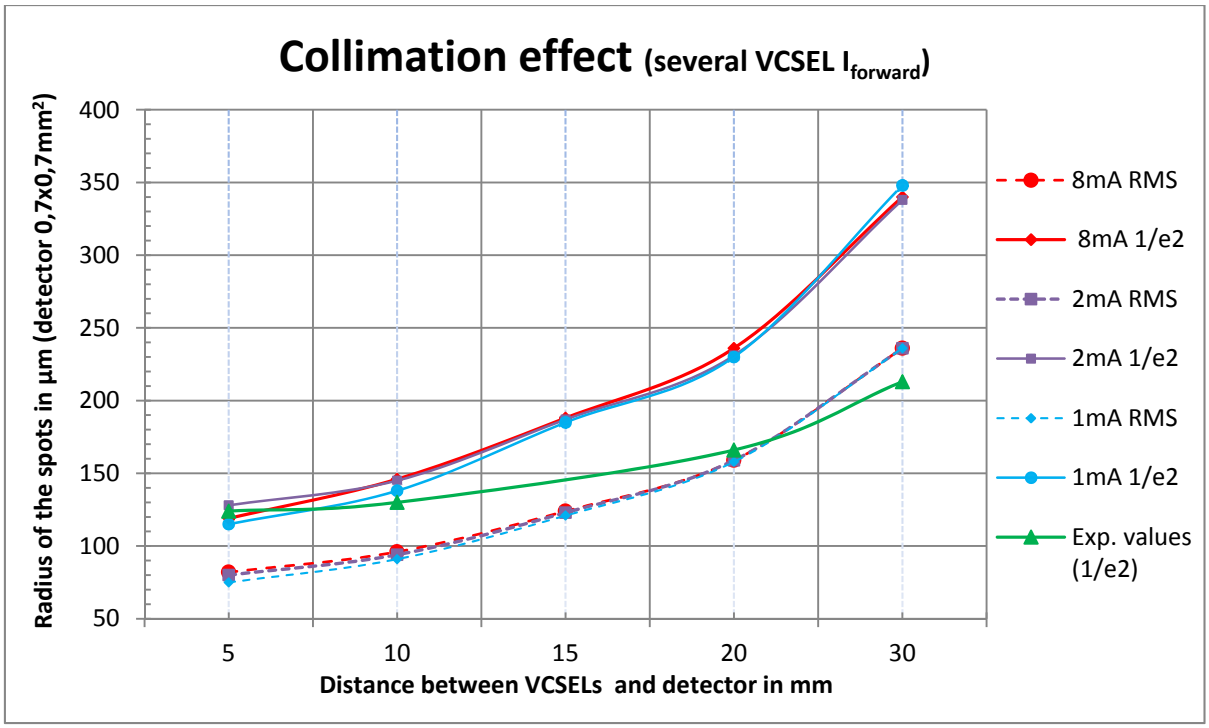

Figure 4.54: *Comparison graph of the radius values, measured as ZEMAX RMS and 1/e², between simulations for several VCSEL forward intensities (8, 2 and 1mA), and experimental results (as 1/e²). A Gaussian adjustment is performed with Matlab software, and then width of the spot (radius) is calculated as 1/e² from the maximum value of the curve. Experimental values are satisfactory.*

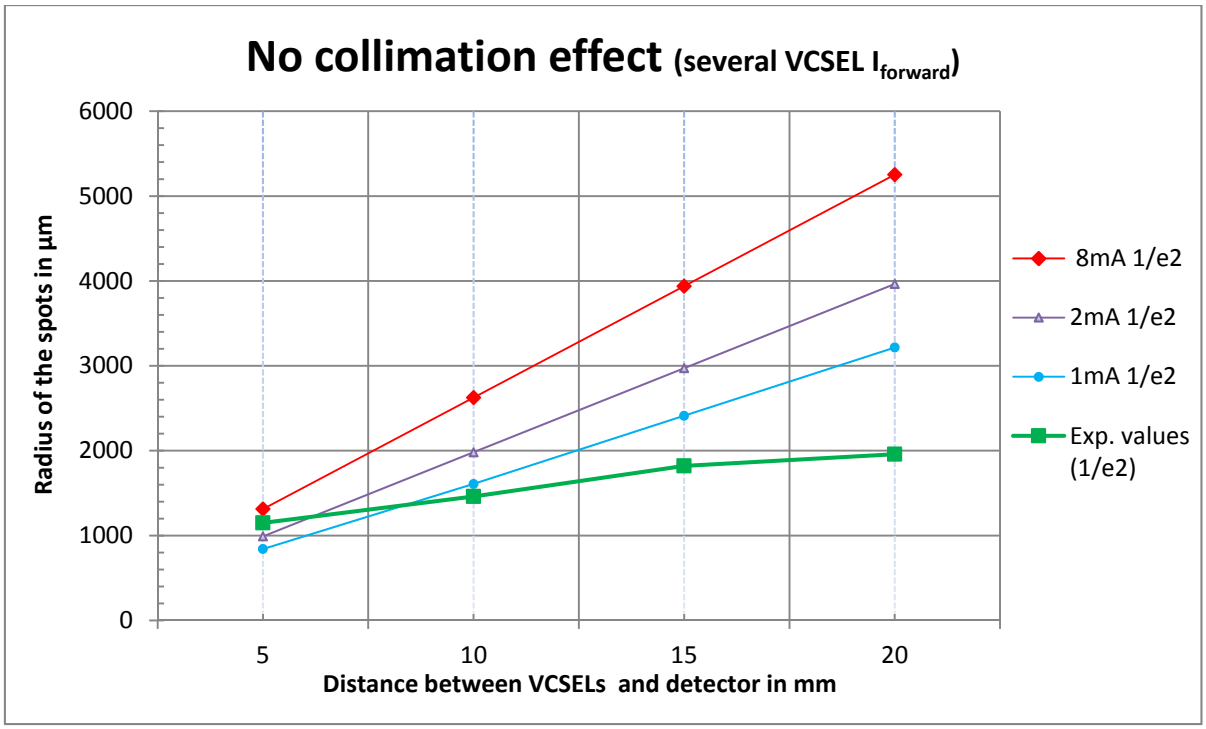

Figure 4.55: *Comparison graph of the radius values measured as 1/e² for several simulated VCSEL forward intensities (8, 2 and 1mA), and for experimental results. No optics used. A Gaussian adjustment is performed with Matlab software. The difference between simulated and experimental values can be owed to the acquisition parameters (e.g. integration time) of the commercial sensor used for the experimental captures.*

APPENDIX: Technical definition of RUNS for the micromachining of silicon pieces

A detailed technical description of the steps followed at the clean Room of the IMB-CNM-CSIC in Barcelona for the fabrication of the base and the optical spacer silicon pieces is presented below. Four RUNS were defined to process the different silicon wafers. The photolithographic masks used in each one, are also indicated.

This appendix also includes a graphical scheme of the process followed to achieve the double etching necessary for the double etched based structure.

RUN #1 (#5469 @ IMB-CNM-CSIC) – Single etched base structure

- **Creation of the outline for the chips, the metallic paths and the electrodes**.
  - Deposition of the layer of aluminum (1 micron) on the wafer.
  - Photolithography step with Mask #1 NGG190 MET1.
  - Etching of the aluminum.

- **Creation of the cavity for the die of VCSELs and the "U" shaped well.**
  - Photolithography step with Mask #2 NGG190 RIE.
  - Etching of the silicon wafer through a DRIE of 150μm.

- Two silicon wafers (500μm thickness) processed with 31 chips/wafer.

- Results of the etching:
  - Wafer 1: 153μm (mean value)
  - Wafer 2: 155μm (mean value)

RUN #2 (#5474 @ IMB-CNM-CSIC) – "U" shaped optical spacer

- **Creation of the patterns (pillars/no pillars) for the top side of the optical spacer.**
  - Photolithography step with Mask #3 NGG190 LENT.
  - Etching of the top side of the silicon wafer through a RIE of 15μm.

- **Definition of the "U" shape for the optical spacer.**
  - Deposition of a protective layer of aluminium (1 micron thickness) on the bottom side of the wafer. This layer substitutes the resin and will persist the deep etching process.
  - Photolithography step with Mask #4 NGG190 LENB.
  - Etching of the total thickness of the wafer from the bottom side through a DRIE of 1mm-1.1mm. This large etching process introduces a non-orthogonality factor in the walls of the optical spacer. However it has no effect in the functionality of the piece.

- Two silicon wafers (1000μm and 1100μm thickness) processed with 14 chips/wafer.

- Results of the etching on the top side:
  - Wafer 1: 15μm (mean value)
  - Wafer 2: 15.5μm (mean value)

RUN #3 (#5605 @ IMB-CNM-CSIC) – Double etched base structure[8]

- **Creation of the outline for the chips, the metallic paths and the electrodes.**
  - Deposition of the layer of aluminium (1 micron) on the wafer.
  - Photolithography step with Mask #1 NGG190 MET1.
  - Etching of the aluminium.

- **Creation of the cavity for the die of VCSELs and the "U" shaped well.**
  - Photolithography step with Mask #5 NGG190 RIE2.
  - First etching of the silicon wafer through a DRIE of 200µm. Only the cavity for the die of VCSELs and the funnel feature are attacked.
  - Photolithography step with Mask #2 NGG190 RIE.
  - Second etching of the silicon wafer through a DRIE of 150µm. The cavity for the die of VCSELs and the "U" shaped well are attacked. The total etching depth for the cavity is 350µm.

- Two silicon wafers (500µm thickness) processed with 31 chips/wafer.

- Results of the first etching:
  - Wafer 1: 173µm (mean value)
  - Wafer 2: 183µm (mean value)

- Results of the second etching (= etching depth for the "U" shaped well)[9]:
  - Wafer 1: 168µm (mean value)
  - Wafer 2: 168µm (mean value)

- Results for the total etching of the central cavity:
  - Wafer 1: 339µm (mean value)
  - Wafer 2: 339µm (mean value)

RUN #4 (#5606 @ IMB-CNM-CSIC) - "U" shaped optical spacer – special wafers

- **Creation of the patterns (pillars/no pillars) for the top side of the optical spacer.**
  - Photolithography step with Mask #3 NGG190 LENT.
  - Etching of the top side of the silicon wafer through a RIE of 15µm.

- **Definition of the "U" shape for the optical spacer.**
  - Deposition of a protective layer of aluminium (1 micron thickness) on the bottom side of the wafer. This layer substitutes the resin and will persist the deep etching process.
  - Photolithography step with Mask #4 NGG190 LENB.
  - Etching of the whole thickness of the wafer from the bottom side through a DRIE of 1.2mm. This large etching process introduces a non-orthogonality factor in the walls of the optical spacer. However it has no effect in the functionality of the piece.

- Two silicon wafers (1230µm thickness) processed with 14 chips/wafer.

- Results of the etching on the top side:
  - Wafer 1: 15µm (mean value)
  - Wafer 2: 15µm (mean value)

[8] Refer to figure 4.56 for a graphical scheme of the double etching process.
[9] The increasing of 18µm in the second etching step with respect to the theoretical etching depth (150µm) tries to compensate the decrease in the expected etching depth of 200µm for the first etching step.

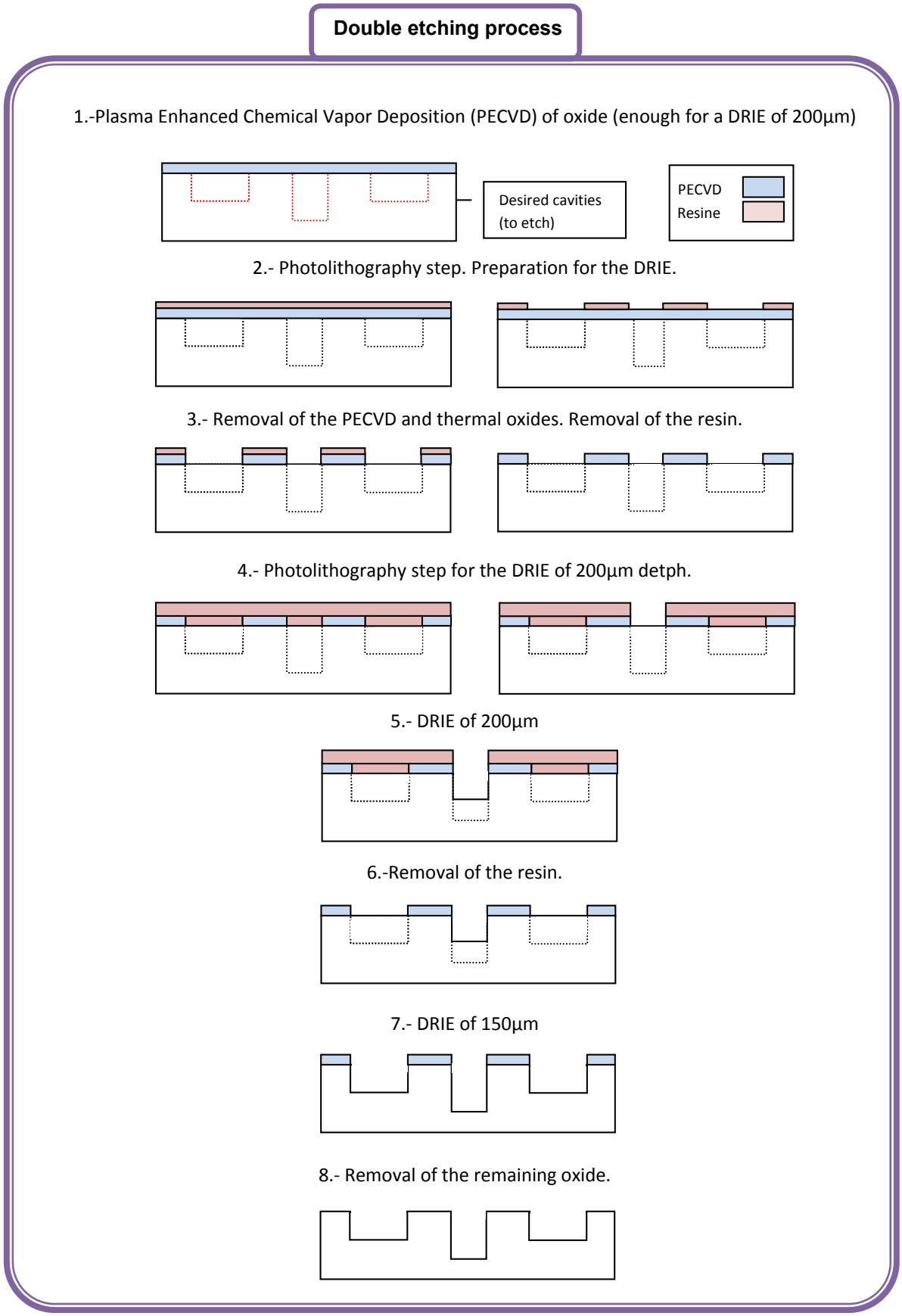

Figure 4.56: *Graphical scheme of the double etching process used for the fabrication of the double etched base structure.*

APPENDIX: Optical effects of the misalignment

Due to manual operations, errors introduced during the critical steps of the integration, assembly and alignment processes yield in misalignment between the VCSEL light sources and the array of microlenses, producing undesired optical effects such as rotation of the spots.

Figure 4.57 shows a microscope image of an undesired case of study: microlenses are not aligned nor centered with the emission area of the VCSELs, and the die of VCSELs presents a tilt factor in the Z-axis resulting in non-parallel planes between the microlenses and the light sources.

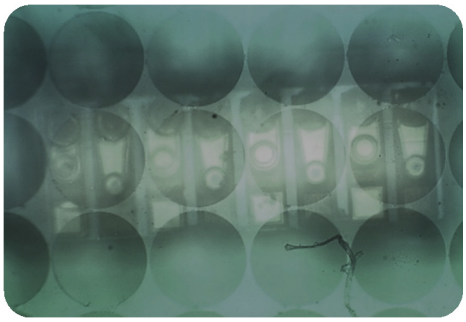

Figure 4.57: *Microscope photograph of a misaligned system with microlenses not centered with VCSELs, and a tilt factor in Z-axis.*

This effect was simulated and experimental measurements confirm the results (figure 4.58). The more distance between the image plane and the light sources, the more rotation of the spots (i.e. deviation of the line of spots from the normal). Though the system is able to collimate light beams, the misalignment in the spots makes it not suitable for measurements in combination with a microfluidic block, since there would be no coincidence between the locations of the detection windows of the channels and the optical spots.

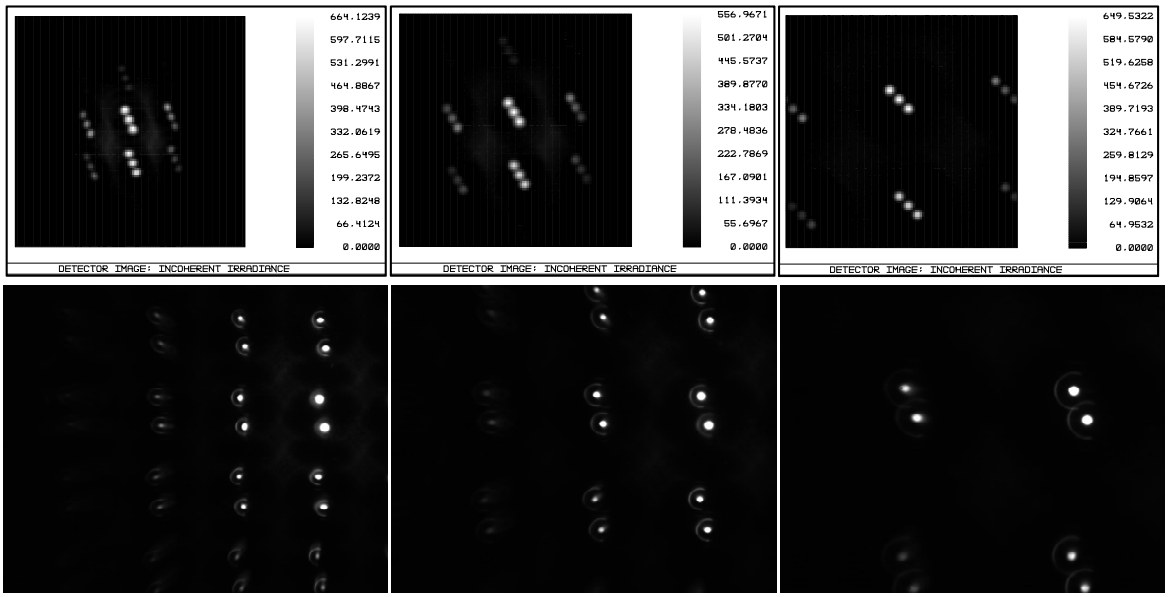

Figure 4.58: *Comparison of simulation (top) and experimental (bottom) results for a misaligned optical system. Distance $d_{V\text{-}D}$ with values 0.3, 0.5 and 10mm respectively. The consequence is a rotational effect in the axial position of the light spots when distance $d_{V\text{-}D}$ increases. Simulations were performed with 3 active VCSELs, while measurements, only with 2 active VCSELs.*

References

[1] S. Eitel, S. J. Fancey, H.-P. Gauggel, K.-H. Gulden, W. Bächtold and M. R. Taghizadeh, «Highly Uniform Vertical-Cavity Surface-Emitting Lasers Integrated with Microlens Arrays», *IEEE PHOTONICS TECHNOLOGY LETTERS,* vol. 12, Issue 5, MAY 2000.

[2] E. Thrusha, O. Levia, L. J. Cooka, J. Deichb, A. Kurtzb, S. J. Smithc, W. Moernerb and J. S. Harris, «Monolithically integrated semiconductor fluorescence sensor for microfluidic applications», *Sensors and Actuators B ,* Issue 105, p. 393–399, 2005.

[3] T. Rezachek, A. Padmanabhan and B. Fritz, «Optical alignment for flow cytometry». Patent 7215425, 8 May 2007.

[4] C. L. Chua, M. A. Rosa, P. Y. Maeda and E. Peeters, «Photonic device with integrated hybrid microlens array». Patent 7324717, 29 Jan. 2008.

[5] H. Zappe, "Fundamentals of micro-optics", Cambridge University Press, 2010.

[6] M. Mohaupt, E. Beckert, R. Eberhardt and A. Tünnermann, «Alignment Procedures for Micro-optics», *Precision Assembly Technologies and Systems; 5th IFIP WG 5.5 International Precision Assembly Seminar Proceedings,* pp. 143-150, 2010.

[7] M. T. Gale, J. Pedersen, H. Schütz, H. Povel, A. Gandorfer, P. Steiner and P. N. Bernasconi, «Active alignment of replicated microlens arrays on a charge-coupled device imager», *Opt. Eng. ,* Issue 36(5), pp. 1510-1517, May 01, 1997.

[8] C. Ke, X. Yi, J. Lai and S. Chen, «Research on hybrid integration technology between charge-coupled devices and diffractive», *J. Micromech. Microeng.,* Issue 14, p. 125–128, 2004.

[9] A. Stockham, J. A. Hammer, J. G. Smith and L. M. Nelson, «Assembly of micro-optical systems with mechanical positioning», *Society of Photo-Optical Instrumentation Engineers,* 2006.

[10] S. H. Hwang, J. W. Lim and B. S. Rho, «120 Gb/s-level VCSEL array optical subassembly using passive alignment technique», *Proceedings - Electronic Components and Technology Conference,* 2008.

[11] M. P. Groover, "Fundamentals of Modern Manufacturing:Materials, Processes, and Systems", John Wiley & Sons, 2010.

[12] M. Karppinen, «High bitrate optical interconnects on printed wiring board», *Thesis VTT PUBLICATIONS 698,* 2008.

[13] J. Melin, K. Hedsten, A. Magnusson, D. Karlén, H. Rödjegård, K. Persson, J. Bengtsson, P. Enoksson and F. Nikolajeff, «Microreplication in a silicon processing compatible polymer material», *J. Micromech. Microeng.,* Issue 15, 2005.

[14] K. Hedsten, A. Magnusson, J. Melin, P. Enoksson, J. Bengtsson, F. Nikolajeff, D. Karlén, H. Rödjegård and G. Andersson, «Replication of continuous-profiled micro-optical elements for silicon integration», *Applied Optics,* vol. 45, Issue 1, pp. 83-89, 2006.

[15] A. Onischenko and J. Sarma, *IEEE Proc. Optoelectron 144,* Issue 39, 1997.

[16] E. Thrush, O. Levi, W. Ha, K. Wang, S. J. Smith and J. S. H. Jr., «Integrated bio-fluorescence sensor», *Journal of Chromatography A,* Issue 1013, p. 103–110, 2003.

CHAPTER V: MICROFLUIDICS

5.1. Brief introduction to microfluidic devices

In the most general way, microfluidics is defined "as the study of transport processes in microchannels" [1]. Though this definition only refers to the term "microchannel", thanks to the evolution achieved in integration and fabrication techniques, valves, filters and pumps are also very common elements in microfluidic devices. Most of the scientific literature and research studies in the field of biological sensing applications consider microfluidics as a fundamental piece in the processes carried out. These complex devices are able to perform laboratory operations such as metering, dilute, pumping and particle separation, with great accuracy and low cost. In terms of design and operation, we must praise the flexibility of microfluidic devices, for multiple designs and combinations of elements in a single chip are possible: from simple linear channels to more advanced structures with nonlinear paths, mixers and switches, leading to parallel analysis performed simultaneously.

Since the first total-chemical-analysis systems (TAS) built in the 80s connecting multiple lengths of Tygon tubing and plastic components [2] until present days, where BioMEMS devices are especially relevant, microfluidics has undergone through some important changes. Nowadays, medicine and life sciences are the main markets for this sort of devices, becoming the most profitable when comparing the sales of other MEMS devices.

As we have already discussed in the Introduction chapter, the increasing use of Lab on a Chip (LoC) devices and Micro Total Analysis Systems (μTAs), where microfluidics is essential, is in partly explained thanks to the biocompatibility of the materials used in their fabrication, yielding high quality microfluidic chips suitable for bioapplications. It is very common the use of microfluidic chips in optical sensing applications, such as Laser Induced Fluorescence (LIF) assays, where the interest lies in measuring the intensity of the light emitted by cells or beads targeted with special fluorochromes and excited with the appropriate light wavelength, when flowing through a detection zone; and it is also quite normal to relate the term microfluidics with flow cytometry techniques. Most of these innovative sensing procedures require not only the presence of microfluidics devices, but also sensors able to detect the changes and variations caused by the flow of particles through the microchannel. The type of sensor used depends on the signal to be measured: while Coulter counters sense resistivity variations, and thus the sensor needed will be sensitive to electrical changes, sensors for optical particle counters must sense light variations (i.e. light extinction, light scattering or light emission).

To fabricate optically and biologically compatible microfluidic channels two basic materials are commonly used: glass and polymers. Some studies also include silicon as a valid material because of its resistance to high temperatures and strong solvents, but due to its opacity it is not suitable for optical detection applications. Glass offers good features as it is transparent to visible light, non-fluorescent and presents Electro Osmotic Flow properties, but the fabrication of microchannels in this material is a complex process involving patterning through photolithographic techniques and etching with hydrofluoric acid, though recently, modern fabrication techniques facilitate the task (e.g. laser micromachining or laser ablation). Polymers offer low cost and ease of fabrication, besides good physical properties. Plenty of fabrication techniques with polymers are possible including the ones

based on lithography and replica molding (such as the commonly used soft lithography, but also LIGA, thick resist lithography and microstereolithography), micromolding (i.e. injection of thermoplastic polymer materials), polymeric surface micromachining and also the previously mentioned laser micromachining (for example, with laser ablation using femtosecond lasers or infrared lasers), as well as laser-induced micro-joining and laser-assisted micro-replication tools [3]. The advantage of non-contact laser machining in polymers over replica molding lies in the fact that the features are not subject to dimensional changes as they can be fabricated directly in pre-cured polymer. On the other hand, we found the economical factor, being the latter more profitable (e.g. soft lithography is excellent in economic terms).

The choice of the fabrication materials depends then, on the final application and the level of accuracy required in the fabrication processes. Consider for example laser ablation techniques for producing accurate glass microfluidic channels in comparison to the lower cost per unit of replicated polymer devices, which are normally disposable.

This thesis focuses on the use of light emitting sources and photo sensors in combination with micro-optics and microfluidics applied to optical particle detection; and this chapter is devoted to microfluidics. For this research work several transparent microfluidic chips were fabricated in biocompatible materials (glass and PDMS), with the aim of performing optical analysis of their circulating flow. Our goal design consists of a chip with 4 parallel channels and passive focusing of particles, though some other alternatives are also considered (e.g. single channel chips with active hydrodynamic focusing). Soft lithography techniques were chosen for the fabrication of the microfluidic chip, for several reasons. The know-how in our department in the fabrication of polymer microfluidic devices, the low cost of the materials employed during the design and fabrication processes or the possibility of obtaining functional and operative chips in a short time, were only a few of the advantages we considered in order to justify our decision. In the testing phase, the injection of the sample volume (a liquid suspension of particles) and the control of the flow rate were achieved by pressure driven flown with the use of an external peristaltic mini pump.

5.2. State of the art

One of the most trending topics in microfluidics is the one related to the hydrodynamic focusing of the flow as an alternative to other passive (e.g. geometrical focusing) and even active focusing methods (such as electrophoresis or dielectrophoresis). The control of the flow (shape and flow rate) is indeed a mandatory condition to achieve a defined stream of particles. Particles in fluid suspensions need to be singly aligned to be accurately detected. Several proposals have been presented towards this purpose.

The improvement of the volume and power efficiency of microfluidic systems was introduced in a study about the use of air-liquid two-phase flow in disposable flow cytometers, developed in 2002 [4]. When using ambient air as sheath fluid, the supply becomes unlimited and the typical procedures used to recycle sheath liquid are no longer necessary. However most of the microfluidic systems discussed in literature continue with the extended methodology of using liquid as sheath fluid for hydrodynamic focusing.

In 2003, S.Chung, S.J. Park et al. [5] designed and fabricated plastic (PDMS) microchips for flow cytometers with 2 and 3 dimensional hydrodynamic focusing. Three dimensional focusing was achieved by lowering the height of the sample inlet through a double level lithography process. In laser-induced fluorescence measurements of microbeads, two-dimensional focusing caused broadening of the signal intensity due to the fact that sample particles were more widely distributed in vertical direction than in the three-dimensional case.

C. Simonnet and A. Groisman described the fabrication and testing of another three-dimensional flow focusing PDMS device to be used in flow cytometry, offering high throughput and high resolution [6]. Lateral ports connected to the central channel create the vertical focusing effect, previous to the lateral focusing. Authors explain the benefits of hydrodynamic focusing in front of the use of chambers and cross sections of small depths: the parabolic velocity profile of flow produces highly non-uniform velocities in particles flowing in channels with streams confined by walls. High throughput in these channels would expose cells to high mechanical stresses.

C. Tsai, H. Hou and L. Fu [7] studied how to optimize three-dimensional focusing for micro-flow cytometers. With a first pair of sheath flows liquid is horizontally compressed, and the focusing in the vertical direction is obtained with a second pair of sheath flows. The flow passes over a micro-weir structure positioned beneath an optical detection system. Anyway, from the point of view of fabrication, the system is complex, and the focusing requires wasting more sheath fluid as the number of inlets increases.

In 2008, P. Howell, J. golden, L.Hilliard et al. [8] offered a new proposal for three dimensional hydrodynamic focusing with two simple designs (stripe design and chevron-based design) that accomplished full sheathing using only one sheath input (figures 5.1a and 5.1b). A different approach to three-dimensional hydrodynamic focusing was presented by X.Mao, S.Steven, C. Dong et al. [9] in 2009. This time, 3D focusing was achieved in a single-layer planar chip thanks to Dean vortex effect induced in a 2D curved channel, thus eliminating the need of a multilayer fluidic structure. Four inlets were required (figure 5.1c).

Passive focusing of particles was considered by H. Chen and Y. Wang [10] for their microflow cytometer. The microfluidic chip consisted of a main channel of 200µm width and 30µm height, and a detection gate with 50µm width and 200µm length. The flow was electroosmotically driven.

The review of X. Xuan, J. Zhu and C. Church [11] summarizes the different techniques used in microfluidic devices for particle focusing. It offers a complete overview of focusing mechanisms, classifying the contributions from researchers in two categories: sheath flow focusing and sheathless focusing systems. Some of the discussed techniques include grooved microchannels, Dean flow effect, vertical confinement, acoustic focusing, AC dielectrophoretic focusing and passive sheathless techniques based in inertial focusing or hydrophoretic focusing.

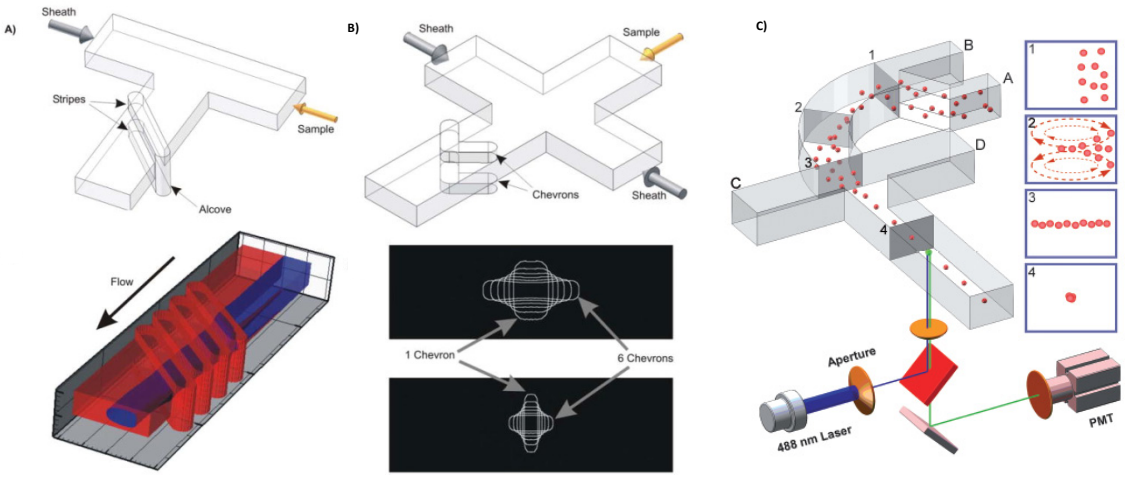

***Figure 5.1**: Different designs to achieve hydrodynamic focusing through the inclusion of simple patterns in the microfluidic channel: stripes (a) and chevrons (b)* [8]*. (c) 3D hydrodynamic focusing achieved in a single-layer planar chip thanks to Dean vortex effect* [9]*.*

In the topical review of microfluidics for flow cytometry from D. huh, W. Gu, Y. Kamotani et al. [12], the focus is set on microfluidic systems which use microfabricated structures. A very recommendable reading to have an overview of the fabrication techniques employed in microfluidics (e.g. micromachining and soft lithography), pumping and switching schemes useful to drive the flow, and commentaries on hydrodynamic focusing (e.g. sheath and no sheath based systems).

Not only microfluidics is present in integrated flow cytometers. Micro-Coulter counters also take advantage of microfluidic chips for particle counting applications. In 2007, R. Trujillo, C.A.Mills, J. Samitier and G.Gomila fabricated a low cost micro-Coulter counter with biocompatible materials such as PDMS, gold and glass [13]. The device included hydrodynamic focusing in the microfluidic block which allowed to probe particles with a wide range of sizes. They successfully tested the system counting latex particles of 20 microns diameter.

A year later, the same group brought in an improvement for their micro-Coulter counter. This time, the microfluidic block achieved two dimensions hydrodynamic focusing by adding an extra inlet to the previous three (figure 5.2). Thus, the authors state increased detection sensitivity by a factor of 1.6 when compared to one dimension focusing conditions, resulting in signals of higher amplitude. Confining particles becomes more accurate and efficient with lateral and vertical focusing [14].

In spite of the vast number of examples related to hydrodynamic focusing and the unquestionable benefits offered by this technique, our main interest was set on obtaining a microfluidic chip with several parallel channels and a reduced number of inlets, relying on a passive focusing design to align particles. In addition, the device should be easily fabricated in short times. Therefore, we prioritized integration and miniaturization in front of high sensitivity, but accomplishing the purpose of the system: optical particle detection. Anyway, previously introduced works have guided us in the design and fabrication processes of our microfluidic chips.

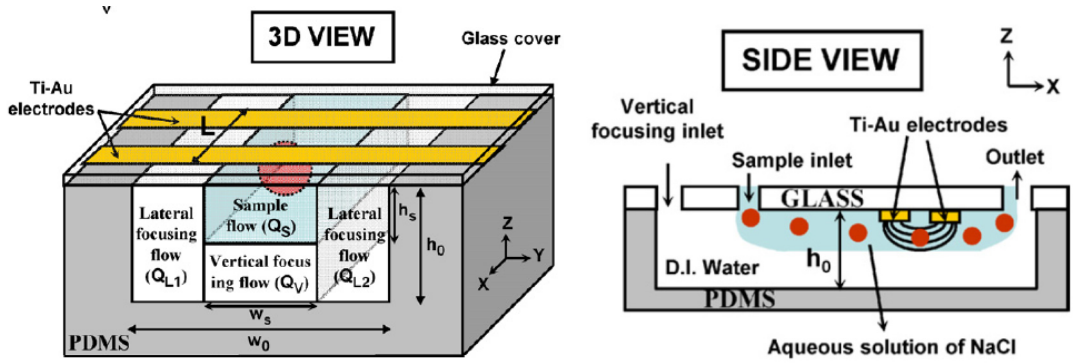

***Figure 5.2**: Improvement of micro-Coulter counter in the microfluidic block, achieving hydrodynamic focusing in three dimensions* [14].

5.3. Concepts related to microfluidics

In order to design a microfluidic chip in accordance with our needs, concepts relative to the physics of fluids at the micro scale must be considered. Some authors define microfluidics as the manipulation of fluids (gases and liquids) constrained in channels whose cross sectional dimension is in the order of ten to a few hundreds of micrometers (µm) and thus, the volume contained in them is about some nanoliters (nl) or even femtoliters (fl) [1] [15]. The reduced dimensions of these devices offer some good advantages such as their low cost of fabrication, the low volumes of reagents and solvents needed for the analysis, or the short-time required to complete the operation.

Understanding how the fluid behaves in such small scale devices is an important issue to discuss. According to the characteristic dimension, *Lc*, of the systems, we can change from the macro to the nanoscale [16]. When Lc > 200µm we refer to macroscale systems, and when Lc moves between 100nm and 200µm, we speak of microscale systems. Nanoscale systems are the ones with Lc < 100nm. At the micro scale, the most important transport properties for fluids are viscosity (i.e. a measure of the fluid resistance to flow when an external force acts), diffusivity (i.e. random walk of small particles in suspension in a fluid) and conductivity (i.e. a measure of the ability of the fluid to conduct electricity). The determination of the Lc value is useful for the study of the fluid-mechanics properties of the system, but the flow in microchannels is also influenced by kinematic, thermodynamic and other parameters (e.g. surface tension and surface accommodation coefficients) [17].

It is not the purpose of this thesis to study in detail the complexity of modeling the flow and the behavior of liquids injected into microchannels, depending on dimensional design parameters (length, width and height of the channels) and physical properties of the fluids (density, viscosity and velocity of the fluids), but some ideas, concepts and basic calculations need to be presented in order to justify the adopted decisions. In the following discussion it is assumed that the fluids are Newtonian, i.e. the shear stress is directly proportional to the rate of strain within the fluid.

5.3.1 Sample size

Small volume means less analyte (the target substance, molecule or particle that will be studied), so the existing relationship between the sample volume (V) and the analyte concentration (A_i) must be considered (equation 5.1):

$$V = \frac{1}{\eta_s N_A A_i} \tag{5.1}$$

Where N_A is the Avogadro's number and η_s the sensor efficiency (a value between 0 and 1).

If sample volume is too small, it may not contain the analyte of interest. The necessary volume of the sample will depend on the analyte concentration (copies/ml): the lower analyte concentration, the more sample volume required. As the purpose of the presented system is the optical detection of microparticles, a commitment must be made between these two parameters such in a way that the concentration of particles in the sample volume do not lead to the clogging of the channel and favor particles to flow singly aligned. In our case, we have opted to work with rather low concentrations, which means according to equation 5.1 a large amount of sample volume.

5.3.2 Laminar flow

In microfluidics the flow is considered laminar if particles in the fluid move through the channel not randomly but in parallel paths to the flow direction. Laminar flow is opposite to turbulent flow, and the dimensionless Reynolds number (equation 5.2) tells us what to expect depending on the channel geometry and the viscosity, density and velocity of the fluid. Simple microfluidic channels with width and height less than 1mm, and velocities less than a centimeter per second, work in the regime of laminar flow [18]:

$$R_e = \frac{\rho V D_h}{\mu} \tag{5.2}$$

Where ρ is the fluid density, V the mean fluid velocity, D_h the diameter of the channel and μ the fluid viscosity.

Previous equation can be transformed considering the typical rectangular geometry of most of the microfluidic channels, where the height and width are comparable. For a rectangular channel of width W and height H:

$$R_e = \frac{\rho V D_h}{\mu} = \frac{\rho V}{\mu}\frac{2HW}{(H+W)} = \frac{\rho Q}{\mu A}\frac{2HW}{(H+W)} \tag{5.3}$$

With Q being the volumetric flow rate. Table 5.1 presents some example calculations of the Reynolds number for channels with similar dimensions to the ones of our interest. Calculations are based on water (viscosity = 10^{-3}kg/(s.m) and density = 10^3 kg/m^3 at 20°C) and isopropanol (viscosity = 2,2*10^{-3} kg/(s.m) and density = 786 kg/m^3 at 20°C) as fluids of interest for this thesis.

***Table 5.1**: Physics of microfluidics. Calculations of Reynolds number and fluidic resistance for several microfuidic channels.*

Flow rate	Height	Width	Fluid	Reynolds number	Length	Fluidic resistance
10µl/min	100µm	60µm	Water	2	5mm	1.10^{12} Pa s/m^3
10µl/min	60µm	60µm	Water	2,67	5mm	$1,25.10^{13}$ Pa s/m^3
20µl/min	100µm	60µm	Water	4,13	30mm	6.10^{12} Pa s/m^3
20µl/min	60µm	60µm	Water	5,50	30mm	$7,51.10^{13}$ Pa s/m^3
10µl/min	100µm	60µm	Isopropanol	0,715	5mm	$2,2.10^{12}$ Pa s/m^3
10µl/min	60µm	60µm	Isopropanol	0,953	5mm	$2,75.10^{13}$ Pa s/m^3
20µl/min	100µm	60µm	Isopropanol	1,47	30mm	$1,32.10^{13}$ Pa s/m^3
20µl/min	60µm	60µm	Isopropanol	1,97	30mm	$1,65.10^{14}$ Pa s/m^3

Results confirm that these microfluidic channels work in the regime of laminar flow. In the microfluidics scale, laminar flow for rectangular channels corresponds to Reynolds numbers below 200, being possible to have values even lower than 1 [19]. With laminar flow, particles and molecules can be transported in a relatively predictable manner through microchannels.

5.3.3 Fluidic resistance

Fluidic resistance refers to the forces which act on a solid object in the direction of the relative fluid flow velocity. These forces oppose the motion of the object. Equation 5.4 confirms the existing relationship between fluidic resistance and the flow rate within a microchannel:

$$Q = \frac{\Delta P}{R} \tag{5.4}$$

Where *Q* is the flow rate, *ΔP* is the pressure drop across the channel, and *R* is the channel resistance. For rectangular channels, the resistance can be calculated by means of equation 5.5:

$$R = \frac{12\mu L}{h^3 w} \tag{5.5}$$

Where μ is the fluid viscosity, *L* is the channel length, *h* is the channel height, and *w* is the channel width. The previous formula is restricted to channels with high aspect ratio (w>>h). For a rectangular microchannel with a low aspect ratio (w≈h), the formula can be approximated to:

$$R \approx \frac{12\mu L}{wh^3(1-0.630\frac{h}{w})} \tag{5.6}$$

From these equations, it can be deduced that long narrow channels present high fluidic resistance, while short wide channels, low fluidic resistance. Some example calculations are shown in previous table 5.1.

5.3.4 Surface Area to Volume ratio (SAV) and surface tension

In the microscale, Surface Area to Volume ratio (SAV) ratio presents large values (e.g. a microchannel of 50µm height, 50µm wide and 30mm long has a SAV ratio of 800cm^{-1}). Surface forces tend to dominate over volume forces; i.e. capillary and interface phenomena become dominant. Large SAV ratios have an effect in transport processes (discussed in next section): though capillary electrophoresis becomes more efficient in microchannels because of rapid removal of excess heat, on the other hand, when transporting fluids by establishing an electrokinetic flow, the efficiency of pumping is reduced due to rapid diffusion and adsorption of macromolecules to channel surfaces [20].

At the microscale, surface tension also has a great effect, for the lengths liquids will travel based on capillary forces are quite significant. This parameter is important in the study of droplet-based microfluidics [21].

5.3.5 Flow transport processes: pressure driven flow vs electrokinetic flow

Transport of fluid and particles trough microchannels can be achieved by several methods, but the two more commonly used are pressure driven flow and electrokinetic flow (based on the electrokinetic phenomena).

Pressure driven flow method needs a pressure drop to initiate the transport action [22], [23]. Generally, this drop is created by applying a positive pressure at the inlet of the channel while the outlet is open to atmospheric pressure. An external pumping source, such as a syringe or a peristaltic pump, is needed to create the pressure. The benefits of using a peristaltic pump over a syringe are evident: mini peristaltic pumps present smaller dimensions compared to setups based on syringes, reservoirs are easy to refill and to replace, and accurate control of the flow is possible.

For a pressure driven laminar flow, the basic laws of fluid mechanics define a parabolic velocity profile within the channel according to Poiseuille flow (figure 5.3). Poiseuille flow is an exact solution of the more general Navier-Stokes equations, the differential equations that govern the motion for Newtonian fluids. The solution provided by Poiseuille flow, establishes the no-slip boundary condition: the fluid velocity at the walls must be zero.

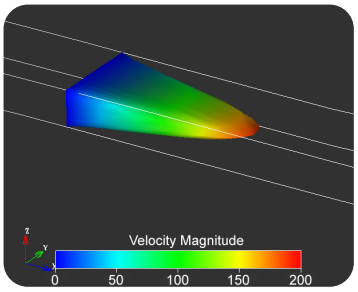

Figure 5.3: *Velocity profile in a rectangular microchannel under conditions of pressure driven flow. Velocity is assumed to be zero at the walls in most treatments of transport of liquids. Printed with permission of Paul Yager, Ph.D. University of Washington, Microfluidic Tutorial.*

On the other hand, we find transport processes based on electrokinetic phenomena, which are also commonly used in µTAS and LOC devices, and comprise several techniques for transport fluids and particles in microchannels [1]. Their common point is the existence of a certain electrical charge and how this charge can be profitable to produce movement in the fluid. Sometimes, an electric field is externally applied (e.g. in electro-osmosis and in electrophoresis) and others the electric field is consequence of the inner nature of the particles suspended in the liquid fluid (such as in dielectrophoresis). Thanks to electrokinetics, cell and particle trajectories can be instantly and finely adjusted [24].

- Electro-osmosis: through the application of an electric field, which induces the formation of an electric double layer (EDL), fluids move relative to a stationary charged or conducting surface.

- Electrophoresis: in the presence of an electric field, an electrostatically charged particle can be induced to move relative to the stationary or moving liquid (bulk liquid phase). It is widely used as a separation technique.

- Streaming potential: By applying hydrostatic pressure, an aqueous ion containing solution is forced to flow through a microchannel, producing a resistance to flow, known as electroviscous effect. This resistance is due to the streaming potential created along the channel walls [25].

- Dielectrophoresis: the movement of dielectric particles in a spatially nonuniform electric field [26].

Both transport processes methods present advantages and disadvantages. Pressure driven flow can be a relative inexpensive approach to pumping fluids through microdevices and a good candidate in terms of miniaturization and integration of compact systems due to the increasing efforts at developing functional mini and micro pumps. The main drawback is that the distribution of particles and molecules is influenced by the parabolic velocity profile.

On the other hand, the velocity profile of electrokinetic flow avoids many of the diffusion non-uniformities that occur with pressure driven flow, though other undesired effects can appear, such as sample dispersion as in the case of electro-osmosis. Electrokinetic flow also produces variability in the surface properties of the microchannel walls (because of the adsorption of proteins and other molecules), yielding unpredictable long-term time dependencies in the fluid flow. Electrokinetic based transport processes often require high voltage electric fields, difficult to obtain without off-chip power supplies, besides the fact that these huge potential gradients in most cases are fatal for cells. As an example, to achieve a flowing velocity of 100µm/s in a microchannel of 4mm length, filled with water, it is necessary to apply a voltage of 23V, corresponding to an electrical field of 5,76KV/m.

From the above exposed reasons and especially the ones referred to integration and miniaturization, in this research work pressure driven flow is the transport method adopted for the developed microfluidic chip.

5.4. Fabrication of microfluidic channels

As one of the necessary blocks in our optical particle counter, this section is devoted to describe the procedure followed to fabricate the channels for the microfluidic chip, using soft lithography techniques. The fabrication procedure was carried out at the 1000 class clean room of the Faculty of Physics at the University of Barcelona.

Soft lithography refers to a family of techniques whose aim is to replicate structures using molds (masters produced in hard material). Soft lithography techniques are an evolution of the standard photolithography ones, offering better feature resolutions and lower production costs. The term “soft” comes from the elastomeric materials used in the replication phase. PolyDiMethylSiloxane (PDMS) is one of the most commons, but others can be also utilized (e.g. PolyMethylMethacrylate - PMMA). Some of these replication methods are widely used, for example contact printing and hot embossing, but others are less known, such as MicroTransfer Molding (µTM) [27], MicroMolding In Capillaries (MIMIC) [28] and Solvent/Assisted MicroMolding (SAMIM) [29]. In our case, Replica Molding Technology (REM) is the soft lithography technique chosen to duplicate the relief structures defined in the surface of a master, due to its simple use, low cost and good resolution (about 30nm) [30].

With REM technology all the three-dimensional master information (shape, morphology and structure) is duplicated in a single step, thanks to the characteristics of the PDMS in its precursor prepolymer form (not cured). PDMS is a homogeneous and optical transparent material down to about 300nm, it

is cheaper than Silicon, durable, more flexible and it bonds easier to other materials, like glass [22], [31]. PDMS also adapts itself to non-planar surfaces, is waterproof and permeable to gases. It is a natural hydrophobic material, though this behavior can be radically changed converting it into hydrophilic by modifying its surface properties through the exposure to oxygen plasma. PDMS is often used in soft lithography because once cured, it is easy to release it from the master due to its elastomeric characteristics.

Unfortunately, the same elastomeric properties present some disadvantages when replicating certain kinds of structures with PDMS. The replicas can collapse because of gravity, adhesion and capillary forces. If aspect ratio of the structures is too large, they fall under their own weight. The adhesion process between the PDMS replica and a supporting substrate can also cause sagging of the structures, when their aspect ratio is too low. Finally, PDMS can also shrink (about 1%) upon curing, modifying the geometrical structure of the replicated pattern (figure 5.4) [30].

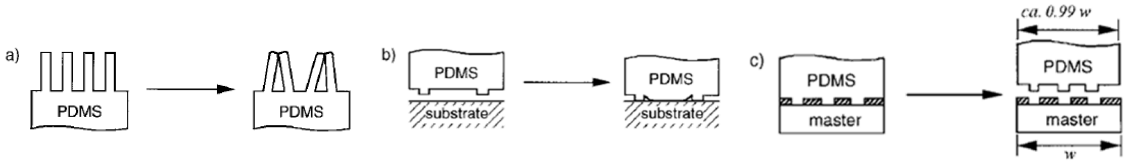

Figure 5.4: *Undesired effects when replicating with PDMS. a) For large aspect ratio, structures collapse and fall under their own weight. b) Sagging of the PDMS structures in the adhesion. c) PDMS shrinks when cured* [30].

In conclusion, soft lithography itself is not diffraction limited like the classic photolithography and offers good results in the fabrication of quality microstructures, usually at low costs. However, results depend on the availability of well-defined and accurate masters, fabricated, for example, using microlithographic or standard photolithography techniques combined with surface micromachining [32], [33], [34], [35], [36].

The fabrication process four our microfluidic chips can be divided in three phases. The first one, devoted to design and fabricate the master with the micrometric patterns that define the geometry of the fluidic channels. A standard photolithography procedure was followed for the fabrication. Materials used were glass and SU-8, a negative photoresist available at different viscosities. In the second phase, master is replicated, and finally, in the third phase, replica is bonded to a glass substrate in order to form the channels. The complete process does not take more than 24 hours.

5.4.1 Master design

For the fabrication of the master, a photolithographic mask is required. This mask, will be used in the photolithography step and contains the planar drawn of the features which are going to be created in the master. This mask must accomplish some design rules: because SU-8 photoresist is a negative resist, transparent zones in the mask will remain on the hardened resist layer of the master at the end of the process, while opaque zones will be removed.

Photolithography has been widely used in microtechnology since its invention in 1959 [37], [38], [39]. To transfer the pattern of the mask onto a thin film of photoresist (SU-8 in our case) spin-coated on a substrate (glass), several methods can be used during the exposure phase. Contact and proximity exposures are the most simple, while for Very Large Scale Integration (VLSI) photolithography projection is used.

In photolithography, the theoretical limit set by optical diffraction is about λ/2, but normally the minimum feature size that can be obtained is approximately the wavelength (λ) of the light source used. That is the reason why illuminating sources used in photolithography tend to shorter wavelengths. For example, with an Ultra Violet i-line Hg lamp, the resolution is about 350nm, and with advanced lithography sources like Extreme UV[1] (EUV, 13nm) the theoretical resolution is lower than 100nm. However, these new sources and their applications are still in early stages, so there are no economic studies in terms of cost of production [40]. While contact lithography offers better resolution than proximity lithography (resolution limited by the square root of the product of the wavelength and the gap distance), it is frequent to damage both the mask and the spin-coated substrate.

By now, some ideas about standard photolithography should be considered: besides being an expensive technique suitable only for using with a limited set of photoresists, it is ineffective in generating three-dimensional structures (patterning non-planar surfaces becomes a difficult process) [41], [42], [43]. The high cost of standard photolithography is partly due to the expensive chromium glass masks utilized in the process. Instead of them, in soft lithography, simple and non-expensive acetate masks are commonly used in what is known as rapid prototyping [44]. Feature resolution achievable by these low cost masks depends on the quality of the commercial printer used to print them. The best resolution, the higher cost. Nowadays, it is possible to find companies offering feature resolutions below 10µm (e.g. CAD/Art Services, Inc.).

We designed a set of acetate masks, drawing the patterns for the channels with *Freehand software* from *Adobe®*. From simple designs with a set of fluidic channels of different shapes and dimensions (figure 5.5a – red color), to advanced schemes more oriented to accomplish the target requirements of our optical detection system including 4 parallel microchannels with passive focusing based on geometry confinement and a separation between centers of 250µm (figure 5.5b&c – blue color). Extra masks were designed to study hydrodynamic focusing (figure 5.5d&e – green color). For more details refer to section 5.6.2.

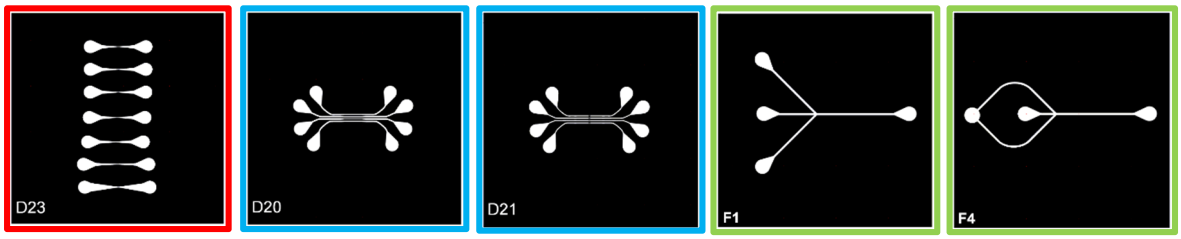

***Figure 5.5**: Rapid prototyping. Examples of acetate masks with several designs of microfluidic channels. (a,red) Several channels with different geometries and dimensions. Useful for first microfluidic experiments (b,blue) Final design in agreement with the requirements of the optical particle detection system. 4 parallel channels with a pitch of 250µm. Passive focusing based on geometry: in the central zone channels width decrease from 150µm to 90µm. (c,blue) Variation of the previous design, with a shorter focusing zone ranging from 100µm to 60µm width. (d,green) Channel design based on 2D hydrodynamic focusing. Central channel width of 200µm. (e,green) Alternative design to classical 2D hydrodynamic focusing, reducing the number of inlets.*

[1] According to ASML (manufacturer of high-tech lithography machines for the semiconductor industry), shipments and installations for the first two NXE:3300B EUV systems will happen in Q2 and Q3 2013. These systems will be used by customers to validate EUV lithography in preparation for its adoption in high-volume manufacturing.

Masks were printed by Spanish company LEICROM, S.L. offering an acceptable resolution of 10µm at a very reasonable price (about 35€). Acetate masks would not be durable or dimensional stable for use in commercial manufacturing processes, but they are perfect for the rapid production of simple prototypes [45], [46], [47], [48], [49], [50].

5.4.2 Master fabrication

Once the acetate photolithography mask has been designed and printed, the procedure to fabricate the SU-8 master can begin. The following steps describe the full process [51], [52], [53]:

1.- **Pretreatment** of the glass substrate (dimensions 25x25x3 mm). This is a cleaning process which includes 2 consecutive immersions (first in acetone, second in isopropanol) of the substrate under an ultrasound bath for 5 minutes to follow with a rinsing in Deionized (DI) water.

2.- **Dehydration** of the glass substrate on a hot plate at 95°C for 15-20 minutes. This step improves adhesion between the substrate and the SU-8 photoresist.

3.- **Spin-Coating** of the SU-8 photoresist (figure 5.6). With this process, a SU-8 resist layer is deposited on the glass substrate, covering the whole surface and defining the thickness of the layer:

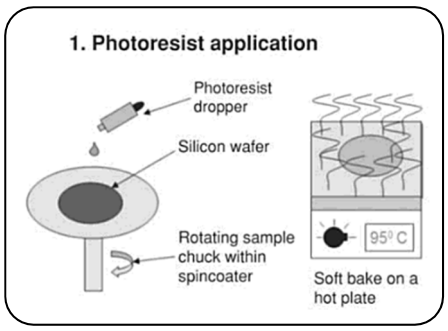

- Pouring 1 ml of selected photoresist per square inch of the substrate. Viscosity of the chosen SU-8 photoresist defines maximum and minimum limits for the thickness of the layer obtained after the spin-coating process. According to *Microchem* manufacturer with SU-8 10, SU-8 50 and SU-8 2150 is possible to obtain layers of thickness from 10µm to 150µm (table 5.2).

***Figure 5.6**: Fabrication process of a microfluidic channel using soft lithography techniques (REM). Spin-coating phase and soft bake* [52].

- Configuration and programming of the parameters of the spinner (*SUSS MicroTec Delta 6RC Spin coater*): acceleration ramp, target velocity in rpm and hold time. Their values define the final thickness of the resin layer, i.e. the height of the microchannels. As reference, *Microchem* manufacturer offers spin curves for each one of its photoresists (figure 5.7).

In the first step of the spin-coating process ("coating"), where the spinning velocity is low (usually 500 rpm), the dispensed resin is spread uniformly all over the substrate. In the second step ("spinning"), an acceleration ramp is applied, increasing spinning velocity until target value is reached. Final velocity is held for a period of time. The combination of these parameters (velocity and time) results in a certain thickness deposition. For a channel of 100µm height and SU-8 50, two steps are programmed. In the first, spinning velocity is set to 500 rpm for 5 seconds. In the second, velocity of 1000 rpm is applied for 27 seconds. Some defects may appear in this phase, like bubbles and edge beads. If that is the case, post-coating relaxation time (from 5 minutes to 24 hours) before next step can be helpful. Relaxation improves uniformity of the layer reducing defects.

Photoresist	Thickness (µm) = Height of the channel
SU-8 10	10 - 30
SU-8 50	40 - 100
SU-8 2150	100 - 150

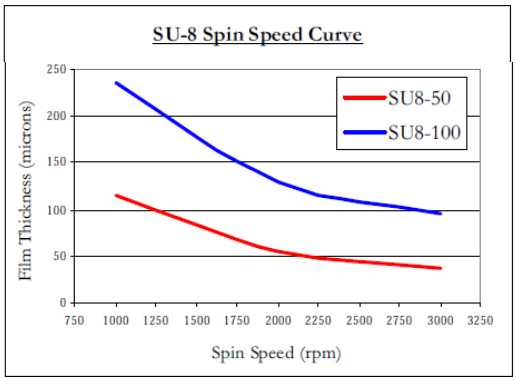

***Table 5.2**: SU-8 photoresist and film layer thicknesses, according to Microchem datasheets.*
***Figure 5.7**: SU-8 50 and SU-8 100 spin speed curves from Microchem. The spin speed parameter (rpm) defines the thickness in microns of the film layer.*

4.- **Soft Bake (prebake)** of the substrate on a hot plate to remove solvents and stress, and to promote adhesion of the resist (figure 5.6). It is recommended to apply an increasing temperature ramp of at least two steps. The temperature values depend on the thickness of the spin-coated resist layer, but for a film layer of 100µm thickness a first 10 minutes step at 65°C temperature and a second 30 minutes step at 95 °C temperature are recommended. Pre-exposure relaxation for 20 minutes is suggested.

5.- **UV Exposure** performed in the mask aligner system (*SET France MG 1410 Mask Aligner*). With exposure, the designed pattern in the mask is transferred to the photoresist. A near ultraviolet lamp (320 to 450nm) is used for exposure because of the absorbance and transmission parameters of the SU-8 photoresist: high absorption for wavelengths less than 365nm (i-line) and high transmission for wavelengths above 405nm (h-line). Exposure dose in time may differ from one resist to another, and thus, manufacturer provides some reference doses depending on the thickness of the photoresist and the power of the lamp source (figure 5.8). For a UV lamp of 25 mWatts/cm^2, exposure doses from 10 to 20 seconds are enough (e.g. 20 seconds for a film layer of 100µm thickness).

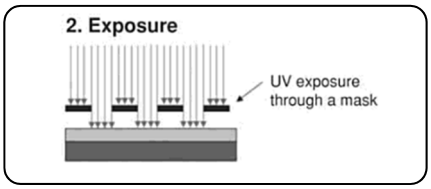

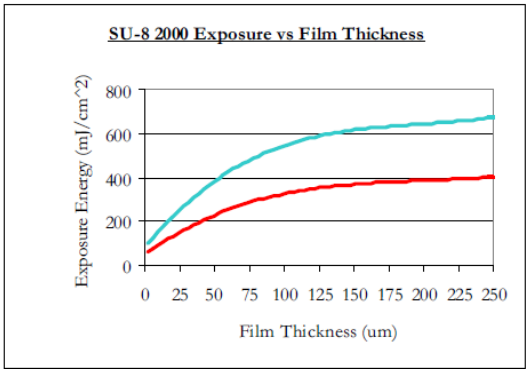

***Figure 5.8.** Left: Fabrication process of a microfluidic channel using soft lithography techniques (REM). Exposure phase* [52]*. Right: Recommended exposure doses for SU-8 resin. Data from Microchem.*

In the exposure phase, T-topping effect (non-parallel walls and formation of a hard skin at the surface of SU-8) may appear in some channels when the top layer is strongly exposed while the bottom part is not (figure 5.9). This effect is related to the duration of the exposure and the absence of a filter in the UV-lamp (to cut wavelengths shorter than 350nm). Dividing the total exposition time in multiple exposures and waiting short times between them can solve the problem [51].

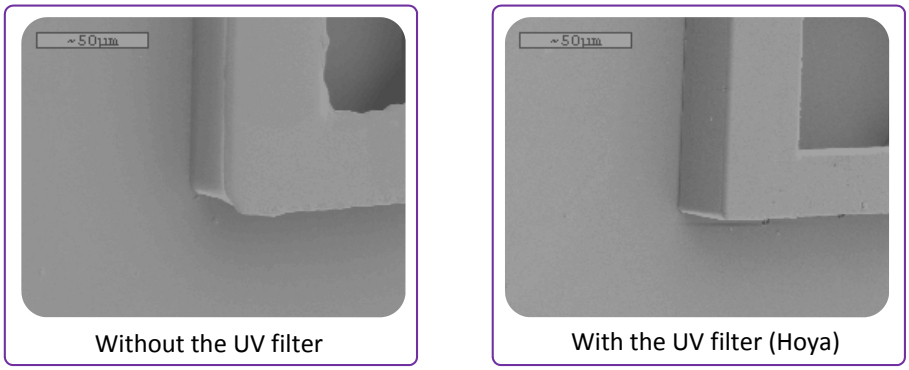

Figure 5.9*: T-topping effect in SU-8 structures. The use of a filter can avoid the geometric defect. From Steven Hobson, Fraunhofer USA.*

6.- **Postexposure Bake** of the substrate to cross-link (cure) the exposed regions of SU-8. With high temperature the polymerization process accelerates. The baking takes place in a hot plate, and two temperature steps are recommended. Again, depending on the thickness of the resist layer, temperatures may vary. For a film layer of 100µm thickness, a first 1 minute step at 65°C temperature and a second 10 minutes step of 95 °C temperature are recommended (figure 5.10).

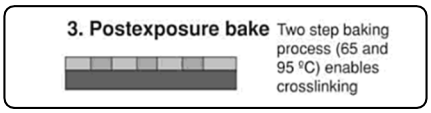

Rapid cooling should be avoided to prevent from residual stresses and cracking.

Figure 5.10: *Fabrication process of a microfluidic channel using soft lithography techniques (REM). Master postexposure phase.*

7.- **Development** of the substrate with SU-8 developer to remove the resist not exposed. Substrate is immersed into the liquid developer (wet development) for a period of time(figure 5.11). Approximately 10 minutes for a film layer of 100µm thickness. Development process can be optimized with agitation.

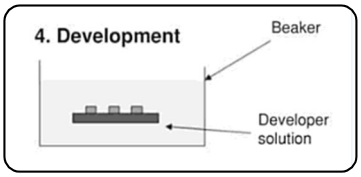

After completion, substrate can be dipped into a fresh SU-8 developer solution to eliminate the final residues (white spots) typical for underdevelopment. Following development, substrate must be rinsed with isopropyl alcohol (IPA).

Figure 5.11: *Fabrication process of a microfluidic channel using soft lithography techniques (REM). Master development phase.*

7b.- **SU-8 double processing**. It is possible to fabricate SU-8 masters containing channels of different heights repeating the process from steps 3 to 7 with the necessary parameters to obtain the desired film thickness of the new photoresist layer. Combining channels of different heights increases the versatility of the microfluidic chip. Refer to appendix "Double processing for SU-8 in a single master" for more information.

8.- **Hard Bake (postbaking)** of the substrate to remove residual solvents and promote adhesion of the resist. Through the development process, resist has been weakened by developer penetration. The hardness of the final master is improved with this final baking (temperature set at 120°C for 20 minutes). Before continuing the process, substrate must be cooled down slowly.

5.4.3 Master replication

1.- **Silanization of the SU-8 master.** This optional step should be performed previously to the replication process with PDMS (figure 5.12). Some authors report that silanization of the master prevents adhesion of PDMS and improves the release from PDMS once it is cured.

2-**Preparation of the PDMS** (*Sylgard 184 kit, Dow Corning, NC, USA*) by manually mixing the necessary amount of base and curing agent in 10:1 weight proportion. To degas the PDMS mixture we used a desiccator for 15 minutes.

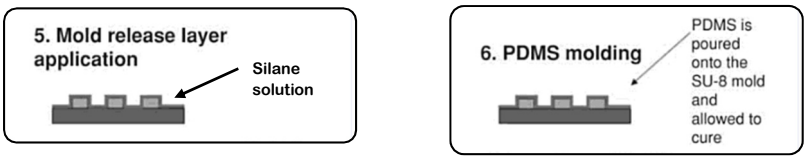

Figure 5.12: *Fabrication process of a microfluidic channel using soft lithography techniques (REM). Master silanization phase. PDMS molding (pouring and curing).*

3.-**PDMS molding**. The master was placed in a petri dish, with the SU-8 relief structures facing up and then PDMS mixture was poured. Curing process can be accelerated at high temperatures (65°C-70°C for 1-1.5 hours), but at ambient temperature the process requires at least 24 hours.

4.-**Peel PDMS**. After cooling, cured PDMS can be carefully peeled off from the master. As a result a transparent PDMS polymer sheet containing the designed channels is obtained. These channels correspond to the positive relief of the SU-8 photoresist. Depending on the PDMS volume poured into the container, the thickness of the PDMS sheets may vary.

5.-**Cut out** the cured PDMS sheet and with a needle 18G (0.8mm diameter) holes were punched into the inlets and outlets. The choice of the needle gauge depends on the external flextubes that will connect to the inlets and outlets.

5.4.4 Bonding of the PDMS

To form the microfluidic channels it is necessary to bond or seal the PDMS sheets to a flat surface of glass. Several types of bonding are possible, being the simplest one to attach the PDMS sheet with the channel side facing down, directly to the glass substrate. Of course, this bonding is the weakest one and liquid samples should be drawn from the channel with negative pressure using a syringe pump. As a benefit, the PDMS sheet can be retrieved from the glass substrate at any time. More complex reversible and irreversible bonding methods are possible using oxygen plasma cleaner. Just by decreasing exposure time of the samples below 1 minute, an irreversible bonding is obtained (reversible bonding requires 3 minutes exposure). After oxygen plasma treatment, the resulting microfluidic chip should be heated in a hotplate at 95°C for 5 minutes. Irreversible bonding yields channels that can withstand high pressures, both positive and negative.

Oxygen plasma treatment transforms PDMS surface into a hydrophilic material, but the effect is not permanent and due to the migration of short uncrosslinked PDMS chains to the surface, hydrophobicity is recovered in a short time [54]. Besides, application of oxygen plasma for extended

periods of time causes cracking of the oxidized surface due to stress. For these reasons, some authors have explored the benefits of exposing the PDMS sheets to UV/ozone cleaner besides Plasma cleaner, which still is necessary for the bonding [55]. This exposure would enhance microfluidic performance (i.e. increasing electroosmotic flow stability), which is rather low when comparing PDMS to other materials such as glass or quartz. High hydrophobicity and poor surface properties of PDMS would also be improved with UV/ozone treatment converting PDMS into a silica-like material, thanks to a deeper oxidation of the material. Tests have been performed with 14µm thickness PDMS sheets and UV/ozone treatment. Oxidation process in these thin membranes is complete, transforming the PDMS into a glass-like hydrophilic material for reported periods of more than 3 months.

In our case, we have simply chosen the irreversible oxygen plasma bonding method exposing the PDMS sheets and glasses to oxygen plasma for 30 seconds at 100W in a *Harrick Plasma Cleaner* (figure 5.13). No need to expose the samples to UV/ozone treatment, because the thickness of our PDMS sheets is undoubtedly greater than 14µm, and the effects of the mentioned special treatment would have no impact.

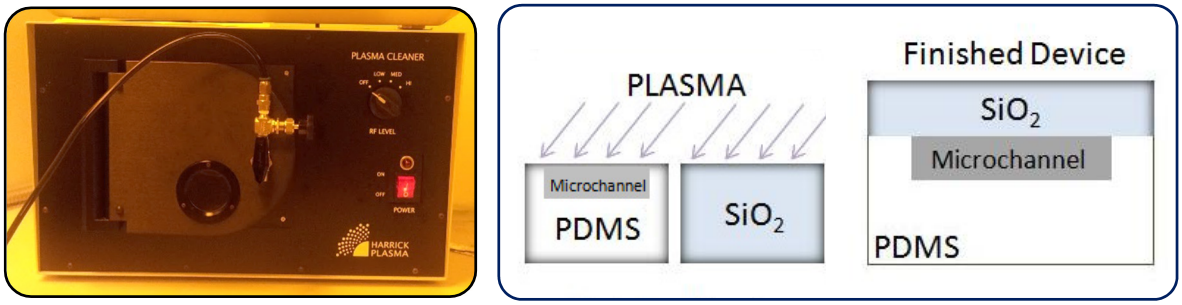

***Figure 5.13**. Left: Harrick Plasma Cleaner in the Clean Room of the Faculty of Physics, University of Barcelona. Right: PDMS to glass bonding process with plasma cleaner to create the microfluidic channels.*

5.5. Comments on Fabrication

Figure 5.14 shows a collection of microscope photographs with several of the fabricated SU-8 masters for the microchannels. In this case, pictures correspond to the design oriented to fulfill the requirements of the optical particle detection system: 4 parallel microfluidic channels with a pitch of 250µm.

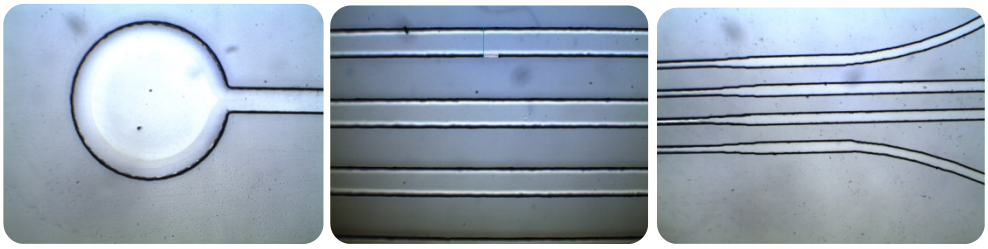

***Figure 5.14:** Microscope pictures from SU-8 fabricated master. Left: 1mm diameter inlet/outlet of one microchannel. Center: zoom for 3 parallel channels of 100µm width, with a pitch of 250µm. Right: 4 parallel channels which gradually reduce their width (passive focusing). Scheme of used mask in figure 5.5b.*

First aspect to comment about the described process concerns the real thickness of the spin-coated layers of SU-8 photoresist during the master fabrication step. With our set of experimental parameters, expected thickness and subsequently, height of the microfluidic channel, is achieved with an accuracy of ±10% (e.g. for a channel of desired thickness 50µm, real obtained values are in the range of 45-55 µm).

The profile of the side walls of the master is also a critical point to be considered in microfluidics. With lithography techniques, it is very common to appreciate defects in the resist wall profiles of the obtained masters which deviate from the expected. Two typical resist wall profiles are the undercut or lift-off profile and overcut profile (figure 5.15) [56].

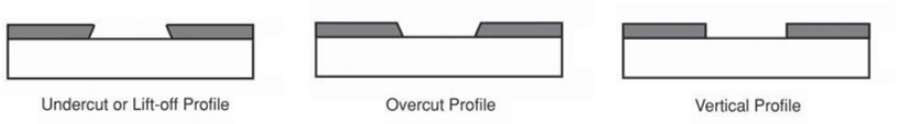

Figure 5.15*: Three different photoresist profiles. (a) The undercut (lift-off) profile is found mostly when patterning of metals in a process called "lift-off". (b) The overcut profile is normally obtained from a positive-tone photoresist. (c) The vertical profile achieves the best pattern fidelity, but is relatively difficult to obtain* [56].

The verticality of the resist wall profile of the master has a direct impact in the way light rays interact with the edges of the microfluidic channel, as has been discussed on Chapter III, where ZEMAX optical simulations for different wall profiles were performed. In particular, results for two selected channel wall profiles, with slopes of 85° and 63° respectively, demonstrated the different behavior of light rays in each case: the less vertical wall profile, the more refraction and loss of collimation effect, yielding deviated light rays which interfere with neighboring sensitive zones in the optical sensor element.

Fortunately, the resist wall profile can be controlled by adjusting mainly parameters such as resist tone, exposure dose time, developer concentration and development time.

To determine the real resist wall profile of the fabricated masters, we measured them with two instruments: a profilometer (*Veeco Dektak 6M Stylus Profilometer*) and a confocal microscope (*Leica TCS-NT*) (figures 5.16 and 5.17). Though both instruments deliver useful information, confocal microscopy presents some extra advantages: in addition to the possibility of exploiting data in 3D models, non-contact measurements are feasible, and consequently masters are not mechanically stressed in the process.

Results conclude that the resist wall profiles of our masters can be considered almost vertical. Thus, the followed fabrication procedure, though based in rapid prototyping techniques, delivers microfluidic chips with an acceptable quality.

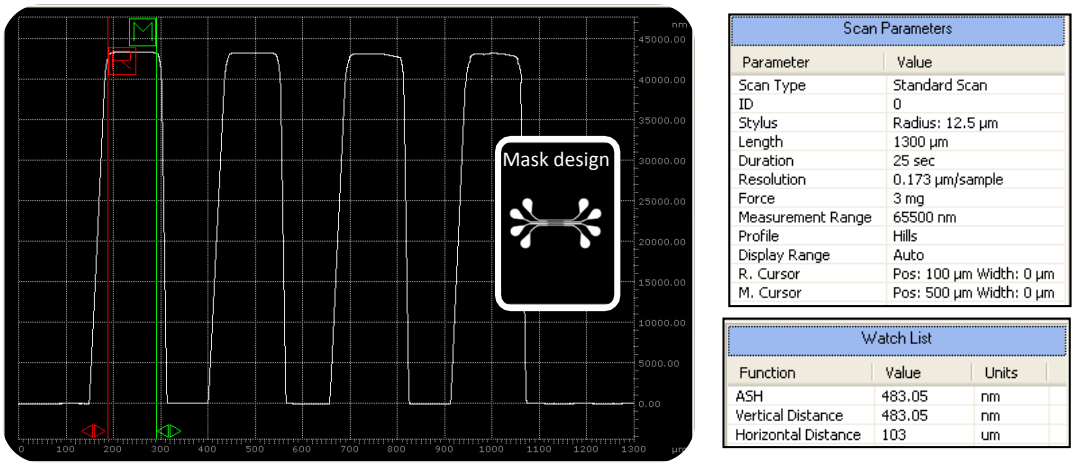

***Figure 5.16**: Profilometer measurement to determine dimensional parameters and resist wall profile of a fabricated SU-8 master. The measured master corresponds to mask design presented in figure 5.5b, with 4 parallel channels and a pitch of 250µm. Height and width of the channels are 45µm and 100µm respectively.*

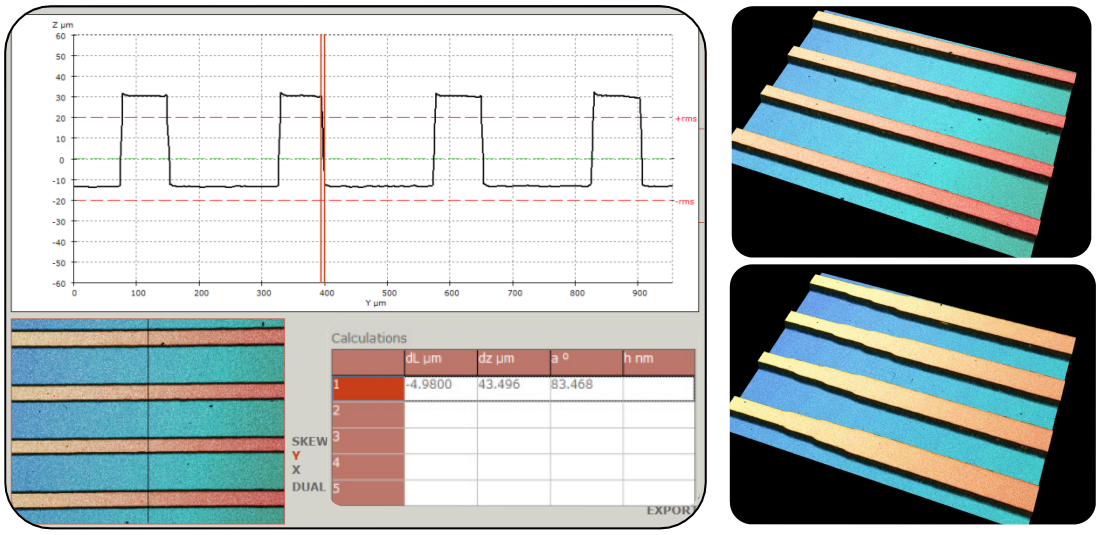

***Figure 5.17**: Confocal measurement to determine the resist wall profile of a fabricated SU-8 master. Same mask design as in previous figure. Only a difference of 4.9µm in the verticality of the wall is obtained, which makes it almost a vertical profile. Funnel design passive focusing) can be observed in the bottom right corner image.*

5.6. Testing of the microfluidic channels and redesign of the channels

5.6.1 Experimental procedures

A set of experiments was performed to test the fabricated microchannels. The setup was based on "pressure driven flow" transport process and a group of suspensions with different concentrations of microbeads and fluids.

In the first trials, liquid suspensions were directly injected into the microchannels with a syringe. This uncontrolled way to create a pressure driven flow, was substituted by the use of a *GILSON* peristaltic pump. This change allowed to obtain a better, more controlled and more constant flow rate through all the experiments (figure 5.18).

Previous to the injection of the solutions into the channels, a cleaning protocol was executed: circulation of deionized *MiliQ* water for 5 minutes, followed by circulation of Isopropanol for 5 minutes, to finish with circulation of deionized *MiliQ* water [57].

Two reservoirs were prepared. One for the inlet, containing the target suspension of particles at a specific concentration, and the other connected at the outlet for collecting the wasted suspension after circulating through the channel (the residual liquid with particles).

In all the experiments a liquid suspension containing microbeads was prepared with the concentration of beads adjusted to favor particles flow singly aligned through the detection sensing window of the microchannel. Translucent *Polybead®* microspheres of 45µm and 75µm diameter, black dyed *Polybead®* polystyrene microspheres of 10µm and 45µm diameter, and black dyed polyethylene *Cospheric®* microspheres of 53-63µm and 75-90µm diameter were used.

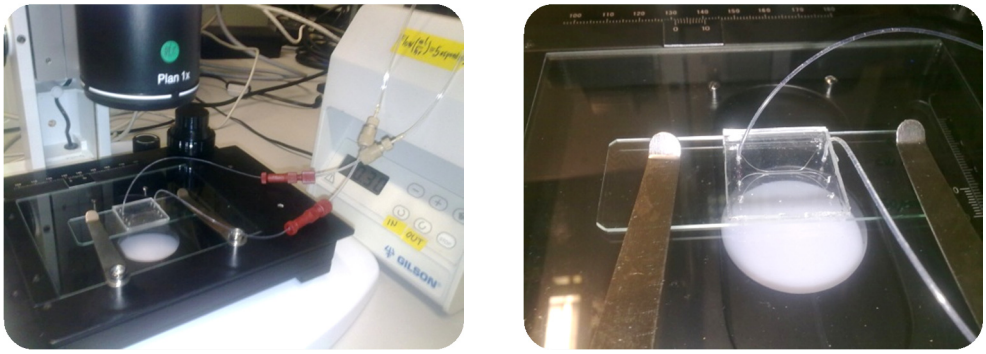

***Figure 5.18**: Experimental setup for testing the PDMS microfluidic channels. A peristaltic pump was used to create a pressure driven flow. Flextubes and fittings from UPCHURCH. Channels were observed under a SZP-8 - Binocular Stereo Zoom Microscope from OPTIKA.*

To improve the flowing of the microbeads and to avoid undesired effects (such as the formation of aggregates or the adhesion of beads to the walls of the channel leading to its clogging), several fluid mediums were considered with the purpose of trying to equal the densities of both, microparticles (≈ 1.2-1.3g/cc) and fluids: *MiliQ* water, isopropanol, ethanol and TRIS buffer. The latter was discarded, since, in these trials it was not necessary to maintain pH within a relatively narrow range, for we were dealing with non-biological synthetic particles. From the other three liquid mediums, best results were observed with water and isopropanol. Note that, when testing polyethylene *Cospheric®* microspheres suspended in water, anionic detergent (Sodium dodecyl sulfate - SDS or *Triton X-100*) was added to the liquid in order to reduce the hydrophobicity of particles.

Clogging effect was studied with the first tested microchannels. They were simple straight linear and elongated PDMS channels (length >4cm) fabricated in rectangular glass substrates (figure 5.19, table 5.3).

Despite acceptable results were obtained with suspensions at low concentrations, these channels presented some fluidic problems due to their length (i.e. larger fluidic resistance): tests demonstrated that after a short time of use microbeads blocked parts of the channel path and even accumulated in the inlets and outlets (figure 5.20), leading in most cases to the irreversible clogging of the channel.

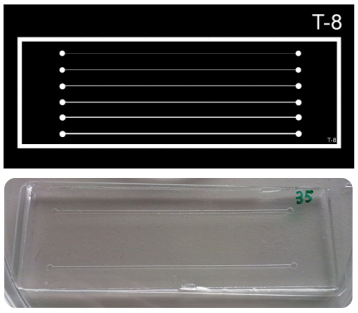

Channel	Length (mm)	Width (µm)
1	54	50
2	54	100
3	54	150
4	54	200
5	54	250
6	54	300

***Figure 5.19**: (a) Acetate mask for a set of long linear microfluidic channels. (b) PDMS microfluidic chip with long microchannels.*
***Table 5.3:** Geometrical parameters for the channels of mask in figure 5.19a.*

The same effect was observed in shorter channels, though after a longer time of use. This fact denotes that fabricated channels have a limited lifetime when using them in experimental measurements. Several reasons could contribute to this effect:

- the weight of the beads,
- the flow rate used in the experiment,
- the larger value of the fluidic resistance parameter, directly proportional to the length of the channel,
- the increased error rate in the fabrication process (the more length of the channel, the more errors may appear in the master fabrication),
- the inherent imperfections of the PDMS replicas (e.g. roughness of the channel walls),
- the lack of a focusing mechanism (active or passive) to correct and avoid the random flowing of particles near the walls,
- the narrowness of the channels in comparison with the diameter of the microbeads,
- the wrong adjustment in the concentration of the sample, and in consequence the high rate of aggregates formation (groups of particles flowing together).

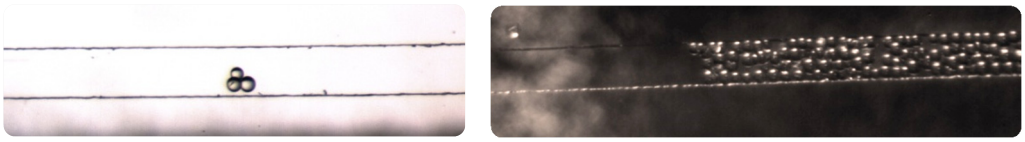

***Figure 5.20:** Undesired effects in microfluidic channels. Pictures for particles of 50µm diameter flowing in long channels. Left: Formation of aggregates. Right: Clogging of the channel.*

An empirical relationship has been established for circular silicon channels and suspensions of polyethylene particles, between particle concentration ϕ, flow rate Q, the mean diameter of particles d, the mean diameter of channels D and the time to channel blockage [58], [59]. The presence of particles flowing through a channel, compromise the reliable operation of microfluidic devices. Particles deposit successively on channel walls producing a blocking effect, and thus, device failure. This effect is observed in channels with Reynolds number below 10, as in our case [58]. Even a model has been developed to prove that particles flowing within a distance of 10nm from the sidewall of the channel will end up depositing on the wall [60].

According to Mustin et al. [61] not only particle size parameter (mean particle diameter) of monodisperse suspensions contributes to channel blockage through successive particle deposition, but also there is a relation between the blockage effect of the channels and particle size distribution of the suspension: relative large particles in a suspension present a major effect on the blockage of a channel, reducing the average time for this effect to appear. It is a quite logical deduction.

Other authors consider that electrostatic repulsion forces, van der Waals forces and hydrodynamic force, pushing the flowing particles towards the deposited ones, are the main causes of multilayer deposition. These causes could be induced by increasing the flow velocity or the ionic strength of the suspension [62].

Stoeber and Liepmann [59] reported that the particle deposition effect could be controlled by reducing the particle concentration. However, this solution is not feasible for all experimental situations, for example a case of drug delivery through human skin, as it would be necessary to deliver a larger amount of suspension to achieve the same drug concentration, and skin has a limited absorption capacity.

To sum up, two are the main reasons that lead to the blockage of a channel: size exclusion of particles that are larger than the flow passage, and reduction of the cross section of the channel due to successive particle deposition. According to previously commented authors, several factors influence the clogging of the channels; some of them previously deduced by our own experiences:

- Suspension type: at same concentrations and pressure conditions, the mean times leading to channel blockage vary according to suspension type (i.e. surface treatment applied to particles).
- Particle size: larger particles contribute to faster channel blockage.
- Particle concentration: higher particle concentration leads to faster channel blockage.
- Driving pressure: higher hydrodynamic forces overcoming electrostatic repulsive forces between particles produce a rise in multilayer particle deposition.

As a conclusion, the following rule can be applied: the time to channel blockage presents a linear dependency with the flow rate, and is inversely proportional to particle concentration [61].

Concerning these statements, to avoid fast clogging in our microfluidic channels some corrections were made. Channels were redesigned reducing their length, increasing their width and adding a focusing mechanism to direct the flow of particles. In the subsequent experiments, flow rate and concentration of particles in the tested suspensions were readjusted.

5.6.2 Redesign of the microfluidic channels

Regarding the focusing mechanism, two solutions were developed. The first one, based on passive geometrical focusing by adding a special geometry feature at the center of the linear path of the channels. As seen in figure 5.21, we introduced a funnel that gradually reduced the width of the channel to direct and singly align the flow of particles in a passive way, without the use active hydrodynamic focalization techniques [63]. A rectangular cavity with certain dimensions defined a detection window where only one single particle could be located at an instant of time. This solution does not require sheath fluid; thus the microfluidic chip consumes small sample volumes at rather

modest flow rates, minimizing fluid mechanical stresses on the cells and producing small amounts of waste liquid. Besides, inlets and outlets defined in the previous designs as simple 1mm diameter circles, adopted a teardrop shape, which helped the transition of particles into the channel.

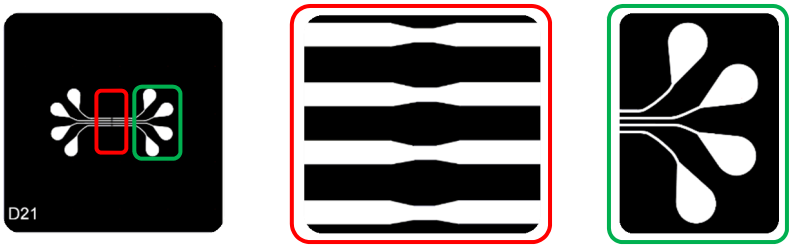

***Figure 5.21**: Passive confinement of particles into the detection window by means of a funnel geometry which defines a focusing zone of 60µm width (detail in the middle). In the right figure, zoom of the inlets/outlets. The teardrop shape improves the flowing of particles towards the channel path.*

The second solution was based on 2D active hydrodynamic focalization. In this technique, a typical Y-mixer design is complemented with a central third input line, where the sample suspension with particles is injected, while the sheath flow injected from the other two input lines from the Y-mixer exert a confining action, delimiting the width of the central path flow (figure 5.22). The relationship between the central and the lateral flow rates define the width of the central path according to equation 5.7 [64].

$$\frac{w_s}{w} = \frac{1}{g(\lambda)} \cdot \frac{Q_s}{Q_s + Q_F} \tag{5.7}$$

$$with\ \lambda = {}^{height}/_{width}\ and$$

$$g(\lambda) = 1\ , when \lim_{\lambda \to 0} (h \ll w)\ or$$

$$g(\lambda) = (1+\lambda)^2(1 - 1.3553\lambda + 1.9467\lambda^2 - 1.7012\lambda^3 + 0.9564\lambda^4 - 0.2537\lambda^5)$$

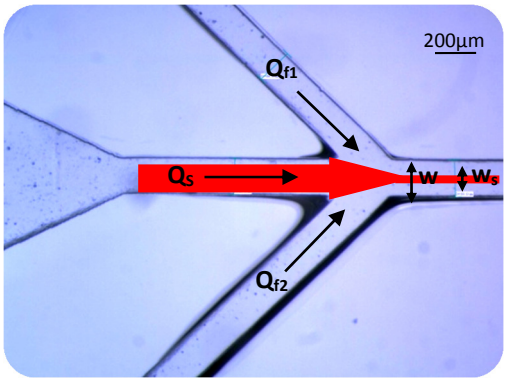

***Figure 5.22:** Fabricated channel based on a design with 2D hydrodynamic focusing. Channel height h=100 µm. Channel width w=200µm. Qs is the sample flow rate. Q_{f1} and Q_{f2} are the flow rates of the lateral sheath fluids, with $Q_F = Q_{f1} + Q_{f2}$. The width of the central path (w_s) is defined by equation 5.7.*

Due to the fact, that normally the same flow rate is applied in both lateral inlets, it is possible to simplify the design, joining both lateral input lines into a single one and minimizing the number of inputs (figure 5.23).

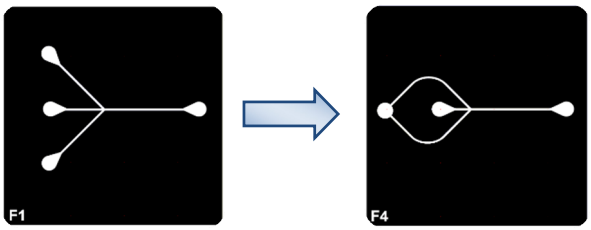

***Figure 5.23**: Alternative design to classical 2D hydrodynamic focusing, reducing the number of inlets. Central channel width of 200µm.*

According to previous equation, for a desired w_s of 50µm in a channel of dimensions h =100µm and w=200µm, the ratio between the flow rates Q_F/Q_s should be 1.7425. The larger the ratio Q_F/Q_s, the narrower central channel. An interesting case occurs when the flow rate is equal for all the inlets. Then the theoretical width of the central channel w_s would be 68.5µm. Graphical results from calculations can be consulted in figure 5.24.

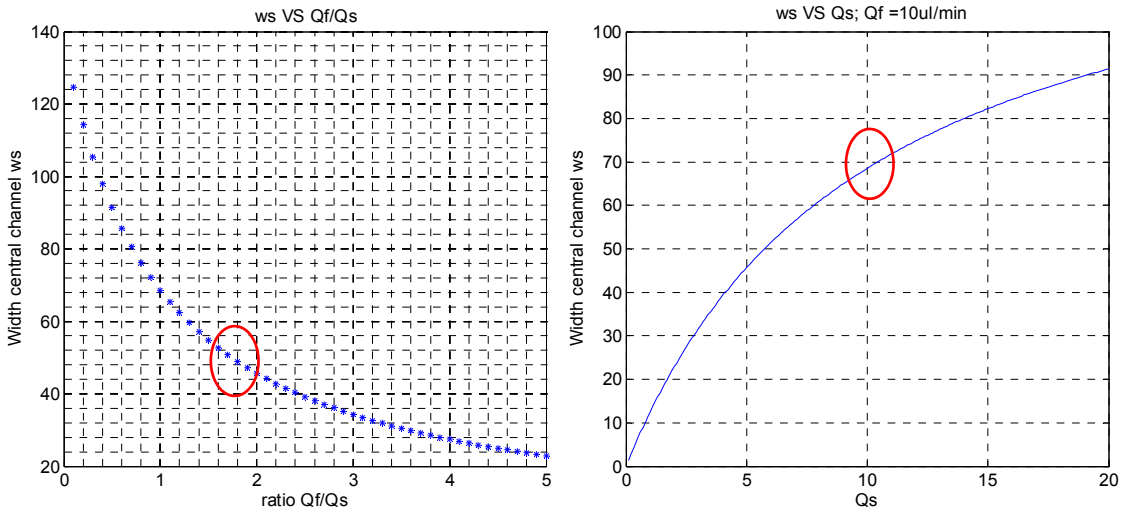

***Figure 5.24**: Calculations for a 2D hydrodynamic focusing scenario with a channel of 200µm width (w) and a height of 100µm (h). Left: according to the geometry of the channel, ratio Q_F/Q_s defines the width of the central channel. For a w_s of 50µm, ratio Q_F/Q_s should be 1.7425 (red circle). Right: particular analysis for a typical value of Q_F 10µl/min. When ratio Q_F/Q_s = 1, w_s is equal to 68.5µm (red circle).*

With *COMSOL* software, we simulated both designs to validate the functionality of these new approaches: funnel geometry and 2D hydrodynamic focalization. *COMSOL* software works with models and studies to solve the Navier Stokes equations for each scenario. In the fluids simulation module, the parameters used for the models defined a laminar flow through the channel, while in the particle tracing module, parameters established the motion of particles from the inlet to the outlet due to drag forces. The first step was to perform stationary studies of the flow to determine the velocity and pressure profiles of the fluid in the geometries of the microchannels. With this information, in a second step, time dependent studies were performed to trace the path followed by particles of 50µm diameter along the channels.

For the simulations, a typical flow rate of 10µl/min at the inlet/outlets was considered. The selected flow rate corresponds to a velocity of 82.83E-10 m/s for a flextube of outer diameter 1/32 inches (=0.793mm) and 0.016 inches (=0.406mm) inner diameter ("*Upchurch Scientific*" manufacturer). These values were later applied in the experimental testing. In the case of hydrodynamic focusing, all the

inlets were defined to have the same flow rate, and suspension with particles was injected into the central path (ws ≈ 70µm width). The fluids in the channels were defined as Newtonian, and water and isopropanol were the liquids for suspensions under study in two different scenarios.

The results confirm that particles flow aligned in both designs (figures 5.25, 5.26 and 5.27). According to velocity profile simulation results, in the funnel geometry case velocity increases when channel becomes narrower near the detection window, as expected. This effect not only favor particles to flow singly aligned when passing through that zone, but also reduces the probability of channel clogging. In both cases of 2D hydrodynamic focusing (with 3 and 2 inputs), a similar effect is observed. The high velocity profile present in the central channel, built by the action of lateral sheath fluids, maintains particles flowing aligned along the path until reaching the outlet.

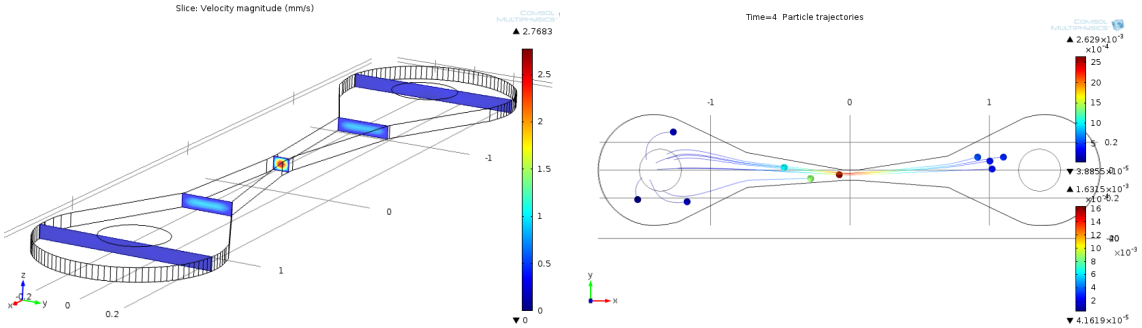

***Figure 5.25**: COMSOL simulations for a microfluidic channel design based on passive geometrical focusing. Inlet on the left side, outlet on the right side. Left: Velocity profile. Right: Particles trajectory.*

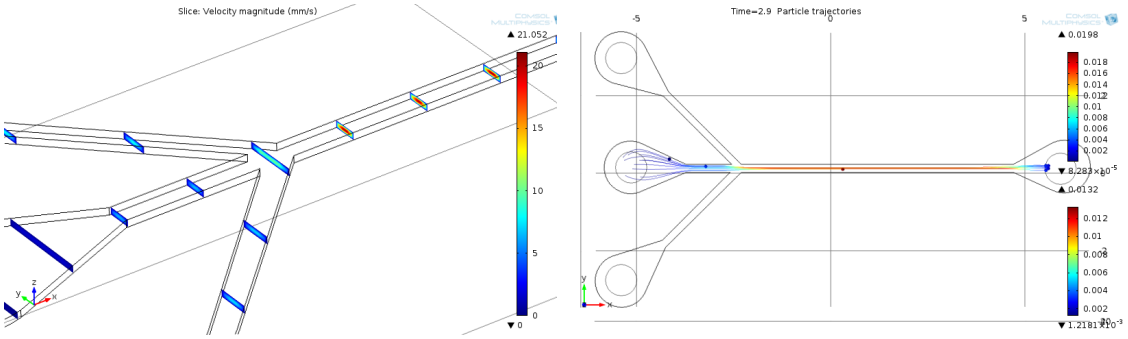

***Figure 5.26:** COMSOL simulations for a microfluidic channel based on classical 2D hydrodynamic focusing design. Inlets on the left side, outlet on the right side. Same flow rate applied to all inlets. Left: Velocity profile. Right: Particles trajectory.*

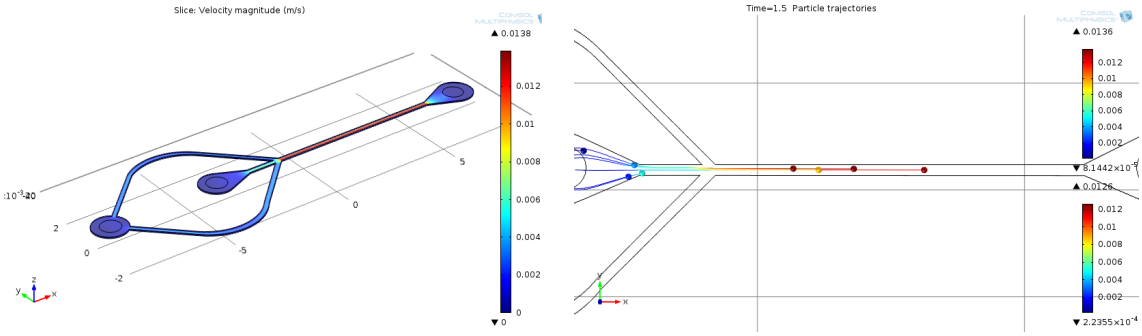

***Figure 5.27**: COMSOL simulations for a microfluidic channel based on an alternative 2D hydrodynamic focusing design. Inlets on the left side, outlet on the right side. Same flow rate applied to all inlets. Left: Velocity profile. Right: Particles trajectory.*

We also performed some experiments to confirm the 2D hydrodynamic focusing effect of the alternative design (figure 5.28). In the top pictures, same flow rate (10µl/min) was applied to all the inlets, defining a ratio Q_F/Q_s =1. The experimental width of the central channel w_s results in ≈65µm, which is quite similar to the theoretical value of 68.5µm (red circle in figure 5.24, right). In bottom pictures, different flow rates were applied to each one of the inlets: for the sheath inlet 10µl/min, while for the sample inlet 20µl/min. These values deliver a ratio Q_F/Q_s =0.5, and according to theoretical calculus, w_s should be 91.4µm (figure 5.24, right). Experimentally, a value of 90µm is obtained. Results prove that with the described design is possible to predict and control the width of the central channel by adjusting the ratio between flow rates.

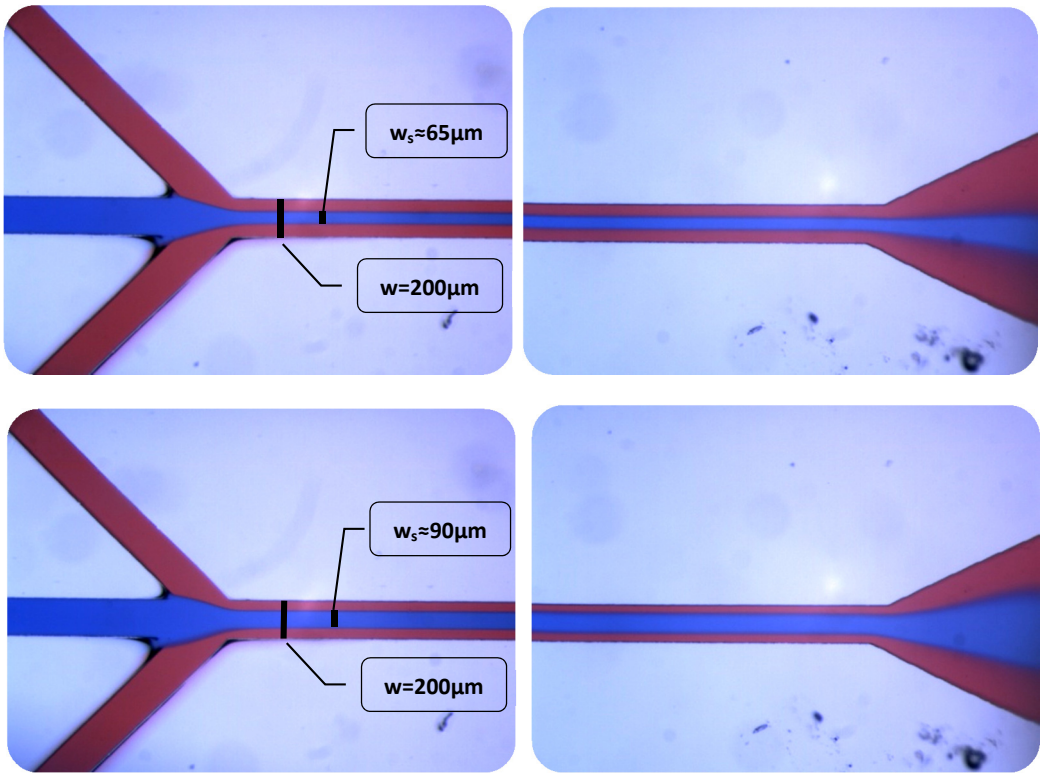

Figure 5.28: *2D hydrodynamic focusing technique implemented in a channel of 200µm width and 100µm height. The ratio between the flow rates of the central inlet (sample liquid – blue color) and the lateral inlets (sheath liquid – red color) defines the width of the central path w_s (narrow in the top images, wide in the bottom images). This path is maintained along the length of the channel.*

Anyway, in order to design the final masks for the system, including four parallel channels, whatever the selected focusing method is, an important design restriction should also be considered. The pitch between two consecutive VCSELs (from *ULM Photonics* manufacturer) follows the optical communications standard of 250µm. According to the optical design, the micro-optical package provides a set of collimated light beams. Therefore, in the microfluidic mask, the sensing zone of the parallel channels should maintain the same separation distance of 250µm between centers (figures 5.29 and 5.30).

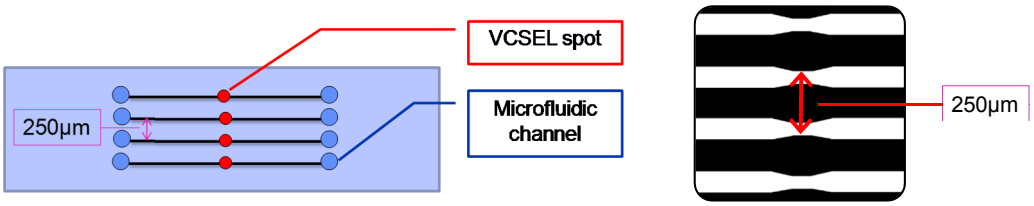

Figure 5.29: *Design restrictions for parallel optical detection in the microfluidic channels. A pitch of 250µm between the centers of the channels is mandatory.*

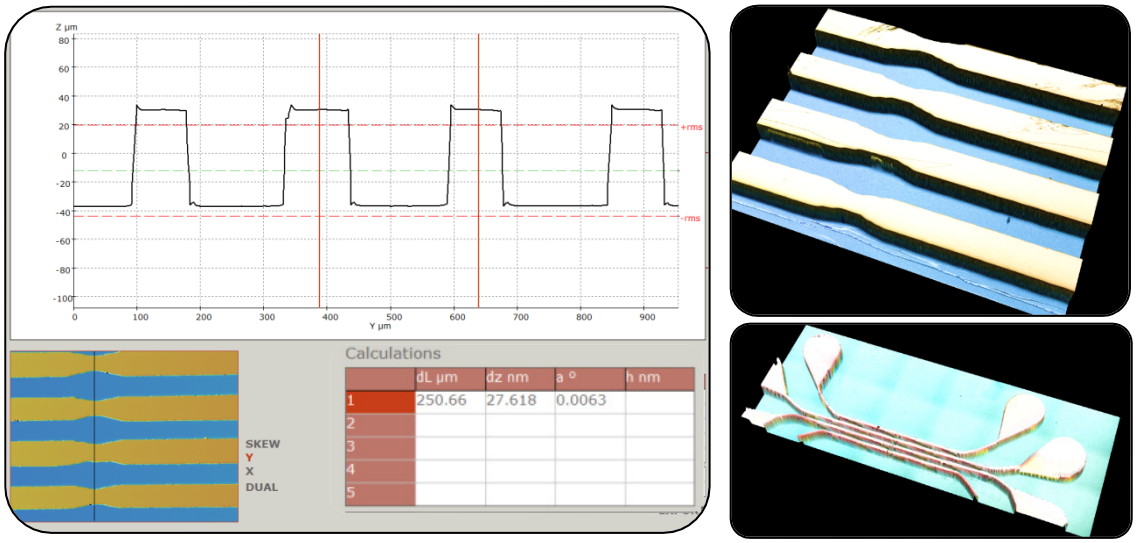

Figure 5.30*: Confocal microscope measurement of the pitch between parallel channels (≈250µm) for a fabricated master. In this case, height of the channels was ≈65µm.*

Finally, both focusing methods were tested connecting inlets and outlets of the fabricated microfluidic chips to the UPCHURCH flextubes (outer diameter of 1/32 inches) of the external injection circuit. Tracing of sample suspensions containing 45µm diameter microbeads was observed under microscope, delivering positive results (figures 5.31 and 5.32).

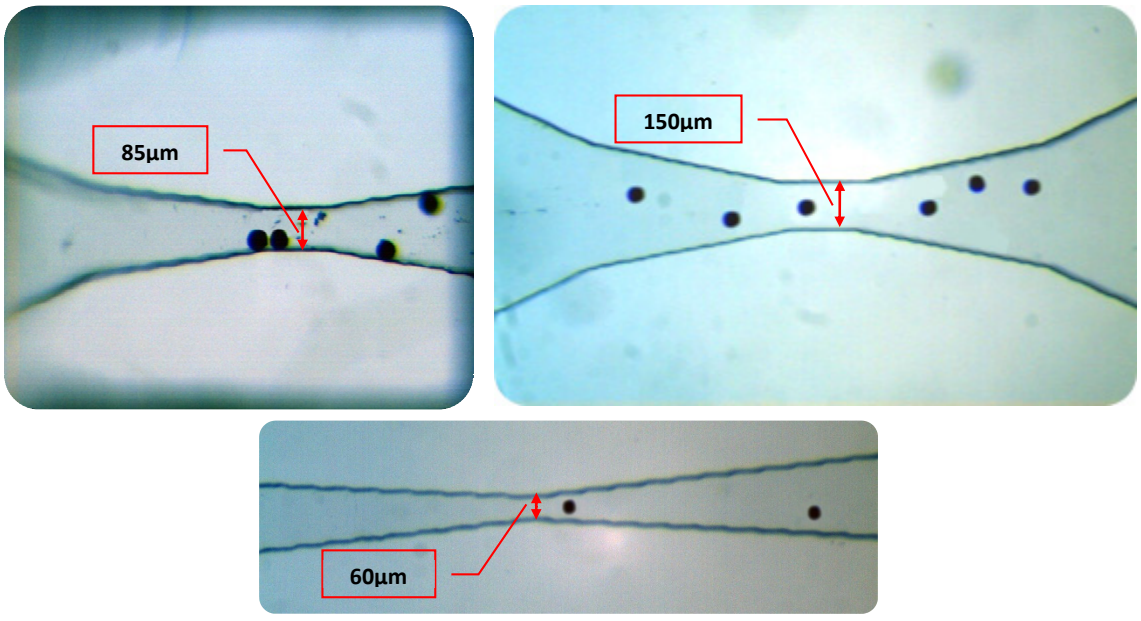

Figure 5.31: *Sheathless passive focusing based on the geometry of the channel. Testing with 45µm diameter black dyed polyethylene beads. Microchannels observed under microscope. Left: detection window of 85µm width. Right: detection window of 150µm width. Bottom: detection window of 60µm width.*

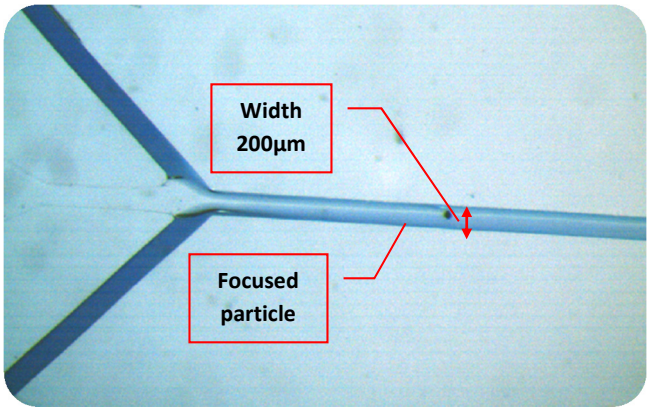

Figure 5.32: *Example of 2D hydrodynamic active focusing of particles. Microchannel observed under microscope. Width of the channel is 200µm. 45µm diameter black dyed polyethylene bead flowing aligned in the central path defined by the lateral sheath liquids.*

5.6.3 Conclusions

Hydrodynamic focusing is a common and widely used technique to serialize and align the flow of particles in many applications such as flow cytometry, and indeed for this thesis some microfluidic channels have been fabricated according to a 2D hydrodynamic focalization simplified design. However, passive focusing achieved by means of a funnel geometry design, combined with pressure driven flow transport process and low concentrated samples, has proven to be good enough to obtain the expected results. This microfluidic chip avoids the need of large amounts of sheath liquid pumped at high flow rates in order to process small volume samples, and also the microfluidic circuitry becomes simpler; a single peristaltic pump is enough to drive the system.

APPENDIX: Double processing for SU-8 in a single master

As previously commented in section "5.6.4 Master fabrication", it is possible to fabricate SU-8 masters for microfluidic channels including on the same chip channels with different heights (figure 5.33). This combination improves the versatility of the microfluidic block allowing to perform simultaneous measurements of microparticles with different size ranges without the need of replacing the fluidic chip. Fabrication process requires a double processing for the SU-8 film layer.

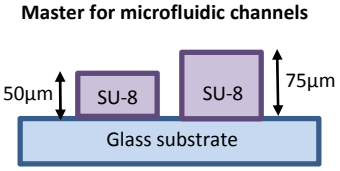

***Figure 5.33**: Scheme of a SU-8 master with channels of different heights. Cross section view.*

Some of these chips were fabricated with satisfactory results (figure 5.34):

- First processing: channel of 50µm height

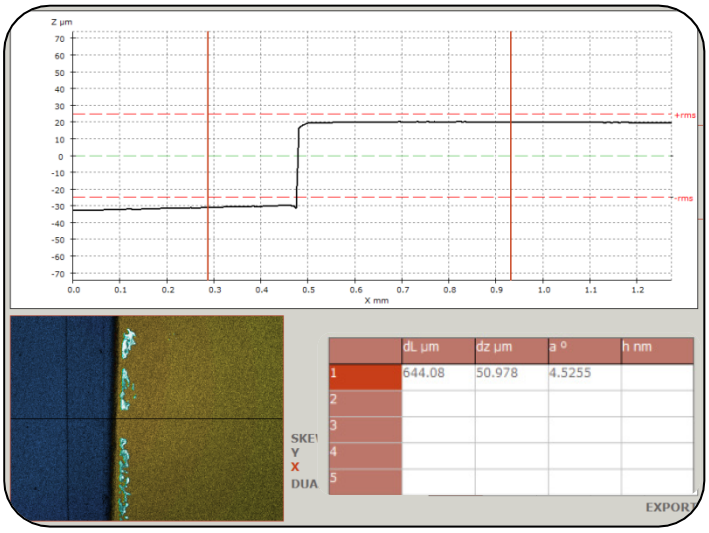

- Second processing: channel of 75µm height

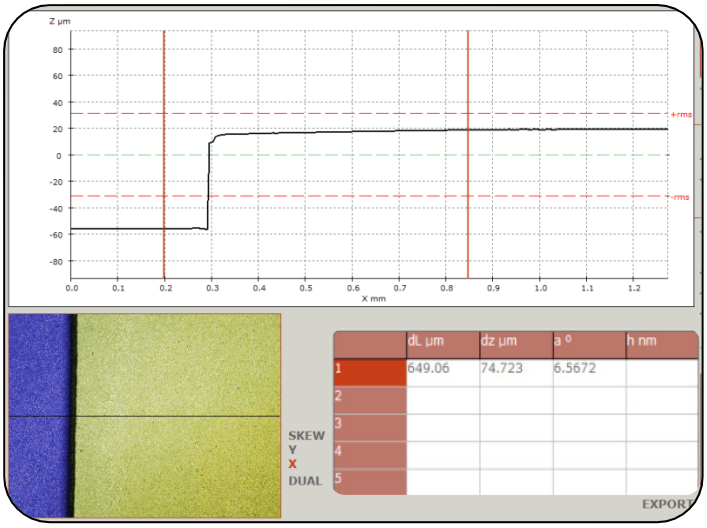

***Figure 5.34**: Confocal microscopy measurements for a SU-8 master with double processing on a single substrate. First image corresponds to a channel of 50µm height, and second to a channel of 75µm height.*

References

[1] S. Saliterman, «Fundamentals of BioMEMS and Medical Microdevices», SPIE Press, 2006.

[2] A. Berg and P. Bergveld, «Micro Total Analysis Systems», de *Proceedings of the [micro]TAS '94 Workshop*, MESA Research Institute, University of Twente, The Netherlands, 1994.

[3] C. G. K. Malek, «Laser processing for bio-microfluidics applications (part II)», *Analytical and Bioanalytical Chemistry,* vol. Volume 385, Issue 8, pp. 1362-1369, August 2006.

[4] D. Huh, Y.-C. Tung and H.-H. Wei, «Use of Air-Liquid Two-Phase Flow in Hydrophobic Microfluidic Channels for Disposable Flow Cytometers», *Biomedical Microdevices 4 (2),* pp. 141-149.

[5] S. Chung, S. J. Park, J. K. Kim, C. Chung, D. C. Han and J. K. Chang, «Plastic microchip flow cytometer based on 2- and 3-dimensional hydrodynamic flow focusing», *Microsystem Technologies,* vol. 9, Issue 8, pp. 525-533, October 2003.

[6] C. Simonnet and A. Groisman, «High-Throughput and High-Resolution Flow Cytometry in Molded Microfluidic Devices», *Anal. Chem,* vol. 78 , Issue 16, p. pp 5653–5663, 2006.

[7] C.-H. Tsai, H.-H. Hou and L.-M. Fu, «An optimal three-dimensional focusing technique for micro-flow cytometers», *Microfluidics and Nanofluidics,* vol. 5, Issue 6, pp. 827-836, December 2008.

[8] P. B. P. Howell, J. P. J. Golden, L. R. L. Hilliard, J. S. J. Erickson, D. R. D. Mott and F. S. F. Ligler, «Two simple and rugged designs for creating microfluidic sheath flow», *Lab Chip,* vol. 8, Issue 7, pp. 1097-103, 2008.

[9] X. Mao, S.-C. S. Lin, C. Dong and T. J. Huang, «Single-layer planar on-chip flow cytometer using microfluidic drifting based three-dimensional (3D) hydrodynamic focusing», *Lab Chip,* vol. 9, pp. 1583-1589, 2009.

[10] H.-T. Chen and Y.-N. Wang, «Optical microflow cytometer for particle counting, sizing and fluorescence detection», *Microfluidics and Nanofluidics,* vol. 6, Issue 4, pp. 529-537, April 2009.

[11] X. Xuan, J. Zhu and C. Church, «Particle focusing in microfluidic devices», *Microfluidics and Nanofluidics,* vol. Volume 9, Issue 1, pp. pp 1-16, July 2010.

[12] T. D. Chung and H. C. Kim, «Recent advances in miniaturized flow cytometry for clinical use», *Electrophoresis,* vol. 28, p. 4511–4520, 2007.

[13] R. Rodriguez-Trujillo, C. A. Mills, J. Samitier and G. Gomila, «Low cost micro-Coulter counter with hydrodynamic focusing», *Microfluid Nanofluid,* 2006.

[14] R. Rodriguez-Trujillo, O. Castillo-Fernandez, M. Garrido, M. Arundell, A. Valencia and G. Gomila, «High-speed particle detection in a micro-Coulter counter with two-dimensional adjustable aperture», *Biosensors and Bioelectronics,* vol. 24, Issue 2, pp. 290–296, October 2008.

[15] J. C. McDonald, D. C. Duffy, J. R. Anderson, D. T. Chiu, H. Wu, O. J. A. Schueller and G. M. Whitesides, «Fabrication of microfluidic systems in poly(dimethylsiloxane)», *ELECTROPHORESIS,* vol. 21, Issue 1, pp. 27–40, January 2000.

[16] D. Li, «Electrokinetics in Microfluidics», Volume 2 (Interface Science and Technology), Esevier, November 8, 2004.

[17] N.-T. Nguyen and S. T. Wereley, «Fundamentals and Applications of Microfluidics», ARTECH H O U S E, 2002.

[18] Bousse, Cohen, Nikiforov, Chow, Kopf-Sill, Dubrow and Parce, «Electrokinetically controlled microfluidic analysis systems,» *Annu Rev Biophys Biomol Struct.,* Issue 29, pp. 155-81, 2009.

[19] S. Saliterman, «Fundamentals of BioMEMS and Medical Microdevices», SPIE Press, 2006.

[20] D. J. Beebe, G. A. Mensing and G. M. Walker, «Physics and applications of microfluidics in biology», *Annu. Rev. Biomed. Eng.,* pp. 261–86, 2002.

[21] D. Mampallil and S. D. George, «Microfluidics – A Lab in Your Palm», *Resonance,* vol. 17, Issue 7, pp. 682-690, 2012.

[22] S. SK and W. GM., «Microfluidic devices fabricated in poly(dimethylsiloxane) for biological studies», *Electrophoresis,* vol. 24, Issue 21, pp. 3563-76, 2003.

[23] B. H. Weigl, R. L. Bardell and C. R. Cabrera, «Lab-on-a-chip for drug development», *Advanced Drug Delivery Reviews,* vol. 55, pp. 349–377, 2003.

[24] T. D. Chung and H. C. Kim, «Recent advances in miniaturized microfluidic flow cytometry for clinical use», *Electrophoresis,* vol. 28, pp. 4511–4520, 2007.

[25] C. Li, L. Ren and Dongqing, «Electroviscous effects on pressure-driven flow of dilute electrolyte solutions in small microchannels», *Journal of Colloid and Interface Science,* vol. 274, pp. 319–330, 2004.

[26] G. Medoro, N. Manaresi, A. Leonardi, L. Altomare, M. Tartagni and R. Guerrieri, «A lab-on-a-chip for cell detection and manipulation», *IEEE Sensors Journal - IEEE SENS J,* vol. 3, Issue 3, pp. 317-325, 2003.

[27] X.-M. Zhao, Y. Xia and G. M. Whitesides, *Adv. Mater,* vol. 8, pp. 837 ± 840, 1996.

[28] E. Kim, Y. Xia and G. M. Whitesides, *Nature,* Issue 376, pp. 581 ± 584, 1995.

[29] E. Kim, Y. Xia, X.-M. Zhao and G. M. Whitesides, *Adv. Mater.,* Issue 9, pp. 651 ± 654, 1997.

[30] Y. Xia and G. M. Whitesides, «Soft Lithography», *Angew. Chem. Int. Ed.,* Issue 37, pp. 550 ± 575, 1998.

[31] S. R. Quake, «From Micro- to Nanofabrication with Soft Materials», *Science,* Issue 290,pp. 1536, 2000.

[32] J. L. Wilbur, A.Kumar, E. Kim and G. M. Whitesides, *Adv. Mater. ,* vol. 6, pp. 600 ± 604, 1994.

[33] A. Kurnar, N. L. Abbott, E. Kim, H. A. Biebuyck and G. M. Whitesides, «Acc. Chem. Res.», vol. 28, pp. 219 ± 226, 1995.

[34] G. M. Whitesides and C. B. Gorman, «Handbook of Surface Imaging and Visualization», pp. 713 ± 733, 1995.

[35] J. L. Wilbur, A. Kumar, H. A. Biebuyck, E. Kim and G. M. Whitesides, *Nanotechnology,* vol. 7, pp. 452 ± 457, 1996.

[36] Y. Xia, X.-M. Zhao and G. M. Whitesides, *Microelectron. Eng. ,* vol. 32, pp. 255 ± 268, 1996.

[37] S. Okazaki and J. Vac., *Sci.Technol. B ,* vol. 9, pp. 2829 ± 2833, 1991.

[38] H. J. Jeong, D. A. Markle, G.Owen, F. Pease, A. Grenville and R. v. Bünau, *Solid State Technol.,* vol. 37, pp. 39 ± 47, 1994.

[39] L. Geppert, *IEEE Spectrum ,* vol. 33, pp. 33 ± 38., 1996.

[40] B. Wu and A. Kumar, Extreme Ultraviolet Lithography, McGraw-Hill Professional; ISBN 0-07-154918-8, May 2009.

[41] W. M. Moreau, Semiconductor Lithography: Principles and Materials, New York: Plenum, 1988.

[42] A. Reiser, H.-Y. Shih, T.-F. Yeh and J.-P. Huang, «General reviews on photoresists», *Angew. Chem.,* Issue 108, pp. 2609 ± 2620, 1996.

[43] Several authors, «General reviews on nanolithography,» *Microelectron. Eng.,* Issue 32, pp. 1 ± 418, 1996.

[44] D. C. Duffy, J. C. McDonald, O. J. A. Schueller and G. M. Whitesides, «Rapid Prototyping of Microfluidic Systems in Poly(dimethylsiloxane)», *Anal. Chem.,* Issue 70, pp. 4974-4984, 1998.

[45] N. C. MacDonald, «General reviews on microelectromechanical systems (MEMS)», *Microelectron. Eng.,* Issue 32, pp. 49 ± 73, 1996.

[46] A. Goffeau, «General reviews and highlights on microanalytical systems», *Nature ,* Issue 385, p. 202 ± 203, 1997.

[47] M. C. Wu, L. Y. Lin, S. S. Lee and C. R. King, «Recent reports on microoptics», *Laser Focus World ,* Issue 32, pp. 64 ± 68, 1996.

[48] J. Bryzek, «General reviews on microsensors», *Sensors,* Issue 7, pp. 4 ± 38, 1996.

[49] «Recent reviews on combinatorial synthesis», *Chem. Rev.,* Issue 97, pp. 347 ± 509, 1997.

[50] D. Qin, Y. Xia and G. M. Whitesides, *Adv. Mater. 1996,* Issue 8, pp. 917 ± 919, 1996.

[51] W. Wang and S. A. Soper, «Bio-MEMS: Technologies and Applications», CRC Press, 2006.

[52] S. D. Minteer, «Microfluidic Techniques: Reviews and Protocols», Springer, 2006.

[53] K. E. Herold and A. Rasooly, «Lab on a Chip Technology, Volume 1: Fabrication and Microfluidics», Horizon Scientific Press, 2009.

[54] H. Hillborg, J. Ankner, U. Gedde, G. Smith, H. Yasuda and K. Wikstrom, «Crosslinked polydimethylsiloxane exposed to oxygen plasma studied by neutron reflectometry and other surface specific techniques», *Polymer ,* Issue 41, pp. 6851–6863, 2000.

[55] Y. Berdichevsky, J. Khandurina, A. Guttman and Y.-H. Lo, «UV/ozone modification of poly(dimethylsiloxane) microfluidic channels», *Sensors and Actuators B ,* vol. B, Issue 97, pp. 402–408, 2004.

[56] R. Zaouk, B. Y. Park and M. J. Madou, «Introduction to Microfabrication Techniques», *Microfluidic Techniques Methods In Molecular Biology,* vol. 321, pp. 5-15, 2006.

[57] J.-C. Roulet, R. Völkel, H. P. Herzig, E. Verpoorte, N. F. d. Rooij and R. Dändliker, «Microlens systems for fluorescence detection in chemical microsystems», *Opt. Eng. ,* vol. 40, Issue 5, pp. 814-821 , 2001.

[58] Stoeber, Español and Liepmann, «Operational limits of suspension flow through sudden contractions», de *Proceedings of the 2001 ASME international mechanical engineering congress and exposition*, New York, U.S.A., 2001.

[59] L. Stoeber B, «MEMS syringe, technical digest of the 2002 solid-state sensor and actuator workshop, Hilton Head Island, South Carolina, U.S.A.», pp. 77-80, 2002.

[60] Wyss, Blair, Morris, Stone and Weitz, «Mechanism for clogging of microchannels», *Phys Rev E,* vol. 74, 2006.

[61] B. Mustin and B. Stoeber, «Deposition of particles from polydisperse suspensions in microfluidic systems», *Microfluidics and Nanofluidics ,* vol. 9, Issue 4-5, pp. 905-913, 2010.

[62] Ramachandran and Fogler, «Multilayer deposition of stable colloidal particles during flow within cylindrical pores», *Langmuir,* Issue 14, pp. 4435–4444, 1998.

[63] S. U. Son, «Micro-cell counter using photoconductance of boron diffused resistor (BDR),» *Sensors and actuators,* 2004.

[64] Stiles, «Hydrodynamic focusing for vacuum-pumped microfluidics,» *Microfluid Nanofluid,* pp. 280–283, 2005.

CHAPTER VI: CMOS PHOTODETECTOR ARRAY

6.1 State of the art of optical detectors

Optical detectors are under constant study, not only in the industry but also in the scientific community. As advances in optical applications have proven to be more evident in recent years, optical detectors have evolved in the same way, yielding a visual interaction with the real world in a more natural way.

Complementary Metal-Oxide-Semiconductor (CMOS) image sensors have been a trending topic in literature, in part due to their good performance as optical detectors and the possibility to integrate on-chip signal processing electronics in the same fabrication process. These optoelectronic devices represent a good alternative to the classical Charge-Coupled Devices (CCD), even more when considering price and cost as parameters to evaluate. CCD has been the common technology used for imaging devices with advantages such as high resolution and high Signal to Noise ratio (SNR). But it also presents some drawbacks: CCD chips must be driven in a very specific way with operating voltages above 10V, which makes it difficult to integrate these devices within a standard digital chip, commonly biased at 3.3V or even lower. On the contrary, CMOS technology is a standard microelectronics technology and allows including on the same chip analog photosensor devices along with digital control and processing circuitry [1]. This combination makes possible to obtain structures like the one presented in this chapter. The every time more reduced dimensions of CMOS transistors by means of using newer foundry technologies, is also a positive quality to consider, as it is related for example, with the working frequency and power consumption of the integrated circuit. Custom design is possible with CMOS technology and here, almost all can be tailored to the application [2], [3], [4].

Low cost of CMOS technology is an extra that also stimulates the research in other fields, such as life sciences. The use of CMOS optoelectronic devices in the everyday life is getting more common (e.g. mobile telephones with integrated cameras), and even some authors have proven that these new devices can be used to perform measurements in biosensing applications, such as fluorescent flow cytometry [5], [6] (figure 6.1, left). CMOS devices combined with grating couplers and waveguides can also act as light spot position detectors in order to measure variations in the refractive index of particular mediums or analytes (figure 6.1, right). It is clear that CMOS technology offers better opportunities to design and develop integrated and compact systems [7] .

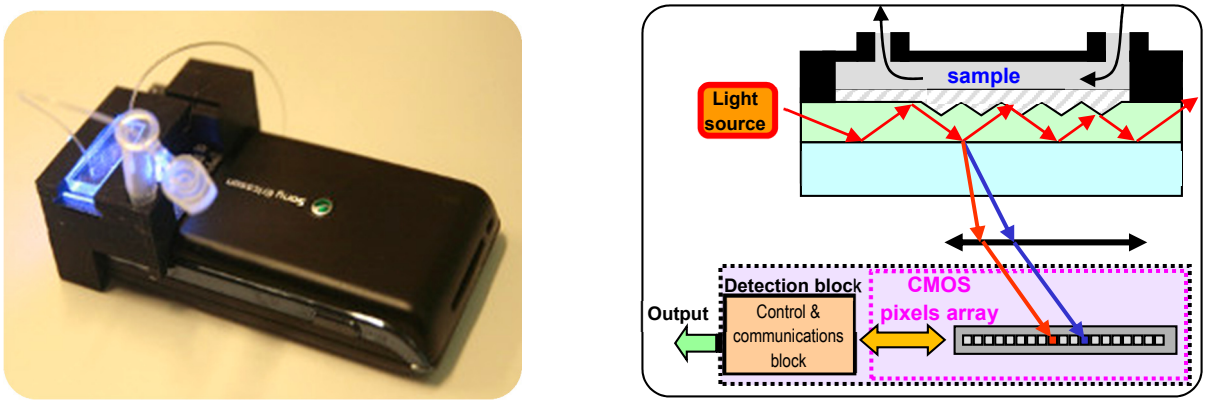

Figure 6.1. *Left: Biosensor for fluorescent flow cytometry measurements based on CMOS phone camera as optical detector* [5]*. Right: Example of application for a CMOS array of pixels combined with a grating coupler* [7].

The following table gathers information about the wide range of applications (industrial, medical and science) in which CMOS image sensors are included as sensing elements. Some detailed examples are discussed below.

***Table 6.1**: Examples of applications for CMOS image sensors. From "CMOS Image Sensors", Albert Theuwissen, 2005.*

Major consume markets	Professional applications
camcorders	machine vision
surveillance	dentistry
digital photography	cardio-vascular
video conferencing	mammography
web-cams	aerospace
PC cameras	target tracking
mobile phones	astronomy
automotive	broadcast
toys	process control
fingerprint identification	motion analysis

In 2000, S. Kavadias et al. developed a logarithmic response CMOS image sensor with on-chip calibration mechanism for correcting the variations in the "sensitivity to pixel" parameter introduced during the fabrication process [8]. Two years later, a high-sensitivity and wide-dynamic range pixels array with logarithmic response was designed by Y. Oike, M.Ikeda et al. for position detection and 3D measurements [9]. Many contributions demonstrate that CMOS image sensors are also present in the field of centroiding techniques for object location, for example, calculating the position of a laser spot in a linear array (figure 6.2) [10-16]. Especially interesting are the publications from the group at the *Center for scientific and technological research* in Trento [10], [11].

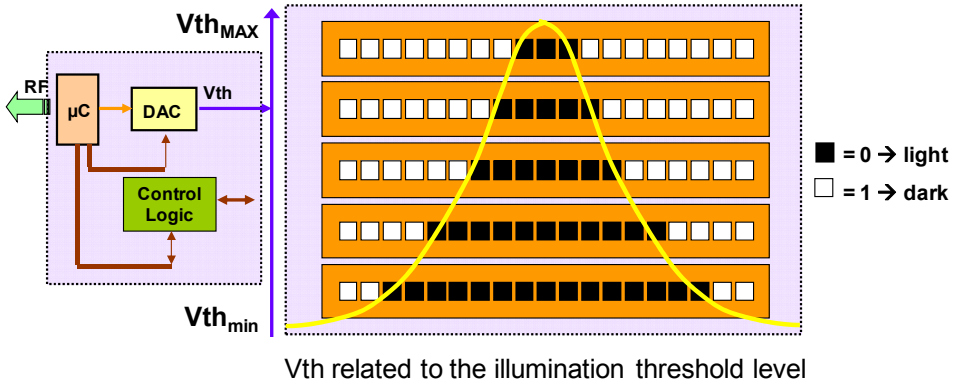

***Figure 6.2:** Simple example application of centroiding technique used to determine the position of the most illuminated pixels in a linear array of pixels. CMOS imaging sensor based on digital pixels whose detection threshold is controlled by the V_{th} signal.*

Some of the main challenges for CMOS imagers in industrial and scientific applications are their blooming immunity at high illumination levels and their relatively large dark current and random noise, especially at low light conditions. To improve their performance in the latter conditions, H. Ji and P. Abshire proposed a new pixel design which increased both signal to noise ratio (SNR) and dynamic range (DR) [12]. D. Stoppa, M. Vatteroni, D. Covi et al. also improved the dynamic range of their CMOS

image sensor and added a programmable power responsivity feature to the device, exploiting the benefits of electronics integration offered by CMOS technology [13].

M. Hadi and K. Karim simulated that it was possible to use 0.18µm CMOS pixels for digital X-ray mammography applications with a high dynamic range and large signal linearity [14]. Arrays of CMOS photodetectors have proven to work successfully for spectrophotometry and fluorescence detection applications [15], [16]. S. Li, S. Kleinfelder, L. Jing and N. Xuong introduced an active pixel sensor array which could be applied to the study of nanostructures and biological samples offering high resolution results [17]. Even some CMOS image sensors have been designed as retinal prosthesis to help in the solution of degenerative diseases such as age-related macular degeneration (AMD) and retinitis pigmentosa (RP) [18].

In case of needing great sensitivity, at levels of photon detection, some CMOS image sensors have been developed based on single photon avalanche diodes operating in Geiger mode (with reverse bias above the breakdown voltage) [4],[19]. However, high voltages are required to bias this kind of photodiodes, and quenching (active or passive) is needed to restore the device after an avalanche event has been triggered, if another event wants to be registered.

Besides the benefits provided by CMOS technology, also the improvement of classical laser systems has played an important role in the development of new applications (e.g. integration of Vertical-cavity surface-emitting lasers - VCSELs).

6.2 CMOS photodetector double linear array for optical particle detection

Optical sensing block is an essential part of the particle detection system we are introducing. From the simple photodiodes based on a PN junction to the high sensitive photon counters Avalanche Photodiodes (APD), including devices such as the Photomultiplier tubes (PMT), there is a wide range of available solid-state optical sensors. To optically detect the variations in light intensity caused by particles flowing through microfluidic channels, we present in this chapter an Application-Specific Integrated Circuit (ASIC) fabricated on 0.35µm *CMOS-OPTO* "*AustriaMicrosystems*" technology. The sensing element of this full-custom integrated circuit is a double linear array of 256 analog pixels, designed to match the requirements of our target application: multiple detection of particles in parallel microfluidic channels. Each one of the pixels contains a photodiode able to transform light into an electrical signal, delivering an electrical charge proportional to light intensity. When the pixel is addressed and selected, the charge is transported directly to the output of the array, thus the pixel returns an analog signal, which afterwards can be digitally processed.

The double array architecture improves detection process by discarding false positives, which also has a favorable effect in the Signal to Noise ratio (SNR). To consider a detection event as a valid one, the event must be detected by both arrays. Otherwise, the event could be originated by another source, not a particle flowing through a defined path. This feature will be especially useful in the detection of small sizes particles, in the order of 10 microns diameter and below, for in these cases, events are not easily distinguished from the noise present in the electrical signal.

The designed ASIC also includes an embedded 10 bits Analog to Digital Converter (ADC), which provides digital output for the analog values of the photodetectors, as well as internal control logic to address the pixels, and a differentiator circuit, whose purpose is to improve the total process time devoted to detect the most illuminated pixel, by reducing in a fast way, the range of pixels to work with. The device is placed on a printed circuit board along with a PIC microcontroller from *Microchip* ® and a RF transmission system.

Working together with the rest of the elements already described and discussed in the previous chapters, it is possible to achieve the desired functionality. The detection operation of the complete system is as follows: when a bead flowing through a microfluidic channel interferes with the collimated light path emitted by one of the VCSELs, the variation of light due to the blockage effect is detected by the optical sensor (i.e. the double linear array of 256 pixels), placed just behind the microfluidic block. The measurement of these variations is useful to detect and count particles and to provide information about other physical parameters, such as the size.

Experimental results obtained during the testing of the image sensor architecture will be presented. Benefits of CMOS technology for this kind of devices will also be discussed. All designs (schematics and layouts) and simulations were performed with *Cadence Design Software*.

6.3 Double linear array: microelectronic design and simulations

Though in this section an architecture for a CMOS image sensor based on active pixels is introduced, a few comments about passive pixels should be made. Due to their simplicity, with passive pixels is possible to achieve high-density imaging arrays with high quantum efficiency, yielding in the highest fill factors for a given pixel pitch [20]. The classical configuration consists of a photodiode/phototransistor and a selection transistor [21],[22]. Compared to the simple configuration of passive pixels, active pixels include in their design a buffer/amplifier that improves the pixel performance lowering the levels of readout noise. Active pixels also offer better signal-to-noise ratio, dynamic range and scalability, in exchange for lower fill factor and loss in optical signal (the latter could be partly solved using microlenses). Active pixels are the perfect solution for large size arrays.

The pixel architecture presented in this section follows a double linear array design with 256 pixels. A schematic overview of the ASIC is shown in figure 6.3, where the rest of the components embedded in the sensor are also included. Differentiator and ADC can be connected to the analog outputs of the array of pixels through a multiplexer controlled by the user. Dimensions of the different blocks can be consulted in table 6.2.

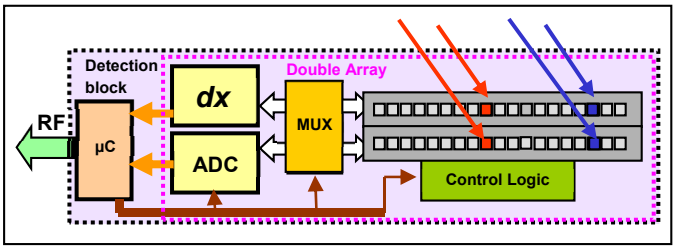

***Figure 6.3**: Diagram of blocks for the 256-pixels double linear array CMOS image sensor (pink dotted line). Sample (red colour) flowing through a microfluidic channel crosses the top array first, and then the bottom one. A different sample could be analyzed with a second channel (blue color). Diagram also contains off-chip electronics not included on the CMOS image sensor: microcontroller and communications ports (RF is available).*

Table 6.2. *Dimensions of the blocks included on the CMOS image sensor.*

Component	Dimensions	Area
Double Array	3710µm X 500µm	1.85mm^2
Control Logic	1000µm X 150µm	0.15mm^2
ADC	323µm X 263µm	0.085mm^2
Differentiator	471µm X 131µm	0.062mm^2
Multiplexer	18µm X 16µm	0.00029mm^2

6.3.1 Pixel design

Each one of the two arrays contains 256 pixels linearly arranged, designed in 0.35µm CMOS *c35b4 "AustriaMicroSystems"* technology. The active pixel structure (10µm pitch x 200µm length) is based on a CMOS photodiode, an analog memory element (capacitor), a buffer, and reset and selection transistors (figure 6.4) [23], [24], [25].

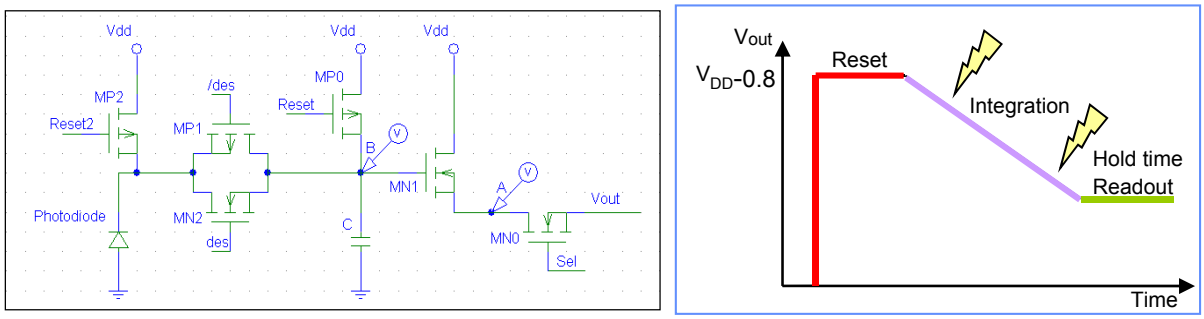

Figure 6.4*. Left: Graphical scheme for the structure of the active pixel. Right: Evolution of the electrical charge at the analog memory component of the pixel (Capacitor "C"). With the Reset, the charge is set up to a high level voltage, which decreases during Integration time due to the generated photocurrent. After that, remaining electrical charge (voltage) is "saved" until the pixel is addressed for the Readout step.*

The expected signal response for one pixel when exposed to light conditions is represented in figure 6.4. According to the applied control signals three different phases can be established: Reset, Integration and Readout. *Photodiode* acts as a light sensor generating photocurrent proportionally to the incident light. In the reset stage, *Reset* transistor (MP0) initializes the pixel state charging the capacitor at a voltage of 3.3V. *Reset2* transistor avoids parasitic currents effects (detailed in the following paragraphs). During the period of time when *transmission gate* (MP1 and MN2) is switched on, *capacitor* (C) discharges linearly due to the generated photocurrent (I_{ph}). The duration of this "*integration time*" plays an important role in the integration phase: the larger this time, the lower noise and the greater sensibility to little light excitement (equation 6.1).

$$V_{out\_capacitor} = V_{DD} - \frac{I_{ph}}{C} t_{integration} \tag{6.1}$$

The *output buffer* (MN1), in the source follower configuration, improves the performance of the pixel and the memory effect of the *capacitor* by avoiding its discharge during the readout process, but introduces a drop at the output voltage of approximately 0.8V (V_{th}, the threshold voltage of the transistor). The W/L ratio for this transistor is especially high compared to the others in order to have

the maximum output voltage swing, and hence the minimum gate-source voltage V_{GS} (MOSFET equations in the saturation region, equation 6.2):

$$V_{GS} = \sqrt{\frac{I_{bias}}{k\left(\frac{W}{L}\right)}} + V_{th} \tag{6.2}$$

Where *W* is the transistor width, *L* the transistor length, I_{bias} the bias current, V_{GS} the gate-source voltage, V_{th} the threshold voltage and $k=\mu_n.C_0/2$, being μ_n the mobility of electrons and C_0 the capacitance per area unit.

Capacitor (C) value must guarantee that voltage will be held enough time in this phase. The whole cycle takes place in all the pixels simultaneously. Switching on *Selection transistor* (MN0) enables pixel reading when it is addressed.

Photodiode is perhaps the most important element in the design. To capture light in the most efficient way, the photodiode area must be large enough. Relying on the results obtained in previous research works the chosen photodiode area was 1000µm^2 [23], [25]. We distributed this area in a long and narrow photodiode, resulting in a width of 10µm and a height of 100µm (good resolution level and large area for light capturing). With the defined pitch between consecutive pixels (≈10µm), the crosstalk effect for neighboring photodiodes is reduced [23].

For schematic simulations, the effect of the photocurrent generated by the photodiode was modelled with a continuous current supply (I_{dc}) in parallel with a diode and a capacity (figure 6.5). According to the process parameters of the technology employed for the fabrication of the CMOS array, the inherent capacity of a 10x100µm photodiode is equal to 0.89pF (equation 6.3); a value very close to the one selected for simulations, 1 pF.

$$For\ a\ N_{DIFF} - P_{WELL}\ diode:$$

$$C_{JN} = \frac{0.84fF}{\mu m^2}\ and\ C_{JSWN} = \frac{0.25fF}{\mu m^2}$$

$$Capacity = 1000\mu m^2 * \frac{0.84fF}{\mu m^2} + 220\mu m * \frac{0.25fF}{\mu m^2} = 0.89pF \tag{6.3}$$

With C_{JN} being the area junction capacitance and C_{JSWN} the sidewall junction capacitance. Similar capacity value is also confirmed in later simulations performed in the AC regime. Although this approximate model does not consider the possible variations of the photo-junction capacity, it serves well to our purposes, since in this design the photodiode does not switch between different states at high frequencies.

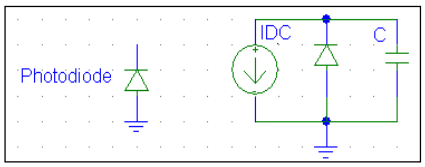

Illumination (Lux)	Iph (nA)
100	0,44
500	2,4
750	12
1000	25,6

Figure 6.5. *Photodiode model: ideal current source in parallel with a diode and a capacitor of 1pF.*
Table 6.3: *Experimental measurements of the photocurrents generated at different illumination levels for a n-difussion photodiode of 1000µm^2.*

For the combination of layers used in the design of the photodiode and the defined area, typical values for the current supply (I_{DC}) are in the range from I_{dc}=1nA to 20nA. These levels are equivalent to an illumination range from 10 to 1000 lux (table 6.3).

Experimental and simulated results on previous pixel designs with 0.35µm CMOS technology returned a short hold time (poor memory effect) for the voltage at the *capacitor (C)*, which rapidly decreased its voltage, due to parasitic currents and charge movements through the *transmission gate* (MP1 and MN2 transistors) [23], [24], [25]. This hold time (i.e. effective time to perform the reading of the analog memory) was dependant on the photocurrent for a constant integration time according to simulations (figure 6.6). The lower generated photocurrent, the larger hold time.

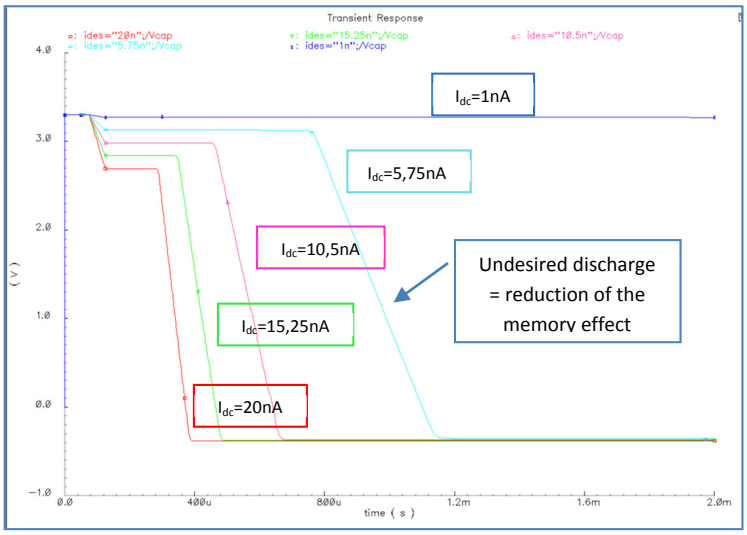

***Figure 6.6**. Parametric simulations showing the fast discharge of the voltage at the capacitor (C) for different photocurrents (I_{dc} from 1nA to 20nA). Thus, the analog memory effect is reduced.*

To avoid this undesired effect and to ensure that the saved voltage after integration phase was present at the output of each pixel, without losses, during the sequentially readout of the whole array, a second *Reset transistor* (MP2) controlled by *Reset2* signal was included in the pixel design. The negative counterpart of this second reset is that the held value at the capacitor increases in ≈3-4mV. It represents the loss of 1 bit resolution in the digital conversion of the output.

As for the *capacitor (C)*, the large the capacity value, the better memory effect is obtained. A large capacitance also minimizes the charge injection effects of the transmission gate into the capacitor. Considering area restrictions, a final value of 562fF was established. As it will be demonstrated in the experimental phase, the addition of *Reset2* transistor in combination with the large area of the capacitor, yields a memory effect lasting enough for a complete reading cycle of the 256 pixels.

As a general rule, dimensions of the transistors were as reduced as possible to ensure good integration and to low power consumption.

Concerning the layout design, each photodiode is defined by an N+ structure over P-type substrate (i.e. n-diffusion photodiode). Guard rings isolate each pixel to avoid parasitic leakage current and coupled noise between neighboring pixels. Two dummy pixels are placed at the beginning and the end of the array as a protection and to ensure the maximum symmetry. Seven Metal-2 paths placed

horizontally connect all the functional transistor gates. Selection signals to activate the different pixels are placed vertically also in Metal-2. Pixels outputs are connected to a unique Metal-2 path placed horizontally. We can appreciate these details in figure 6.7.

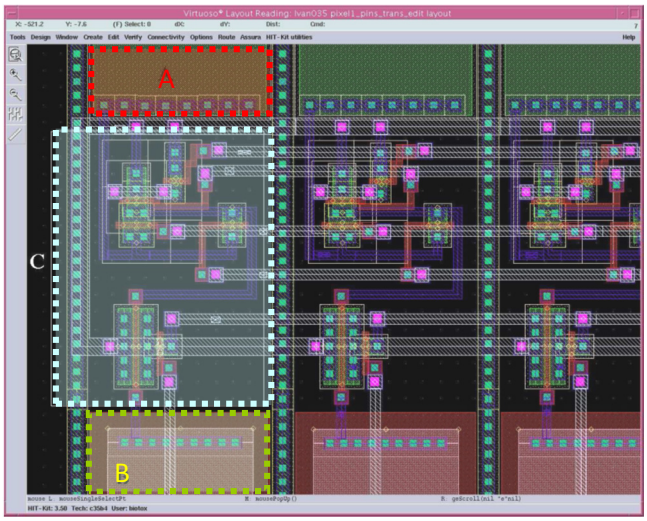

Figure 6.7: *Detail of the 256 pixels linear array layout. Picture contains the partial schematic layout of three pixels: "A" marks the photodiode area, "B" the capacitor and "C" the logical transistors. A guard ring encloses every pixel. Total dimensions for the double array are 3710µm X 500µm.*

Detailed information for every component in a single pixel is included in table 6.4. Fill factor of the pixel is about 60%. The dimensions and the number of pixels determine the total length of the array (≈3.7mm) as well as the resolution achieved in the detection for the selected application. With the defined length multiple parallel measurements will be possible.

Table 6.4: *Dimensions and functionality of the electronic components in the pixel structure.*

Transistor	Function	W	L
MP0	Reset	1.1µm	0.35µm
MP1	Transmission Gate	1.55µm	0.35µm
MP2	Reset2	0.5µm	0.35µm
MN0	Selection	0.9µm	0.35µm
MN1	Buffer	4.4µm	0.35µm
MN2	Transmission Gate	1.1µm	0.35µm
Photodiode	Light sensor	10 µm	100 µm
Capacitor	Analog Memory (562fF)	10.5µm	80µm

6.3.2 Double linear array

Double array architecture represents an improvement in system execution and response times, since it offers the possibility of performing double-check measurements for samples, increasing the SNR and discarding false positive detections. A second array also allows to calculate the average/mean value of two measurements with a single sample without having to reprocess the sample (i.e. recover the sample from the waste reservoir to reintroduce it into the microfluidic chip). The efficiency of the whole detection system is improved.

Each one of the arrays can be internally connected either to a differentiator or to a 10 bits ADC through a multiplexer controlled by the user in order to define the range of pixels excited by a laser source or to convert the pixel signals to digital data. Analog outputs of the arrays can also be directly read thanks to output pads present in the chip.

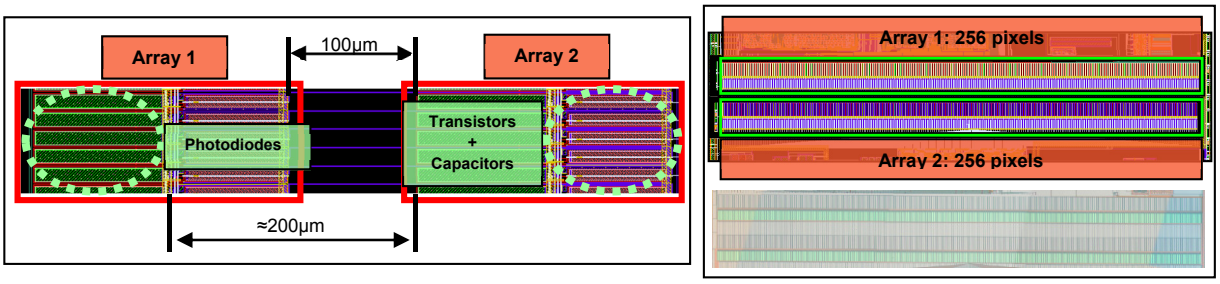

Figure 6.8: *Double linear CMOS array. Left: Detail of layout for the double array. Both arrays are separated a distance of 100µm. Distance between photodetectors is ≈200µm. Pixel pitch 10µm. Right: At the top, complete layout for the double array. Below, microscope photograph.*

The layout does not differ very much from a single array layout (figure 6.8). The single array structure is copied and placed it below at a distance of 100µm. The width of power supply metal paths is resized to avoid that intensity peaks of consumption damage the circuitry. Both arrays share the paths for control signals.

6.3.3 Simulations for the double linear array

Simulation results for the double array, from the extracted layers of the layout design, met our expectations. In the temporal transient response of figure 6.9, the effect of a simulated light spot (width of 2 pixels) can be appreciated for each array. This light spot is intentionally located in a different range of pixels in each case to prove the independent behavior of both array structures. Average intensity consumption is about 1mA (i.e. digital components = 0.35mA; analog components = 0.74mA).

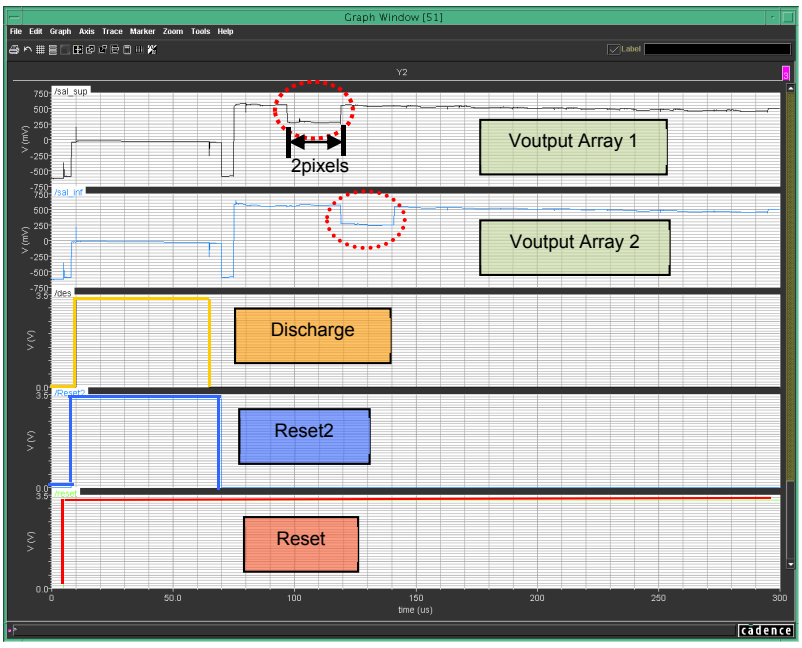

Figure 6.9: *Extracted simulation results from the layout of the CMOS image sensor. Basic control signals are also represented as well as voltages at the output of the array during the readout process. For this case, an integration time of 55µs was established. Red circles mark the position of the simulated light spot excitement in both arrays.*

6.4 Other electronic circuitry included on the CMOS image sensor

6.4.1 Multiplexer

Multiplexer design is based in the combination of two transmission gates (schematic in figure 6.10 left, layout in figure 6.10 right). Applying complementary signals to the gates, the analog outputs of the arrays ($Input_A$ and $Input_B$ in the figure) can be connected to the ADC or to the differentiator structure. Selection signal is controlled externally by the user, while an internal inverter allows generating the complementary signals. Dimensions of transistors are presented in table 6.5.

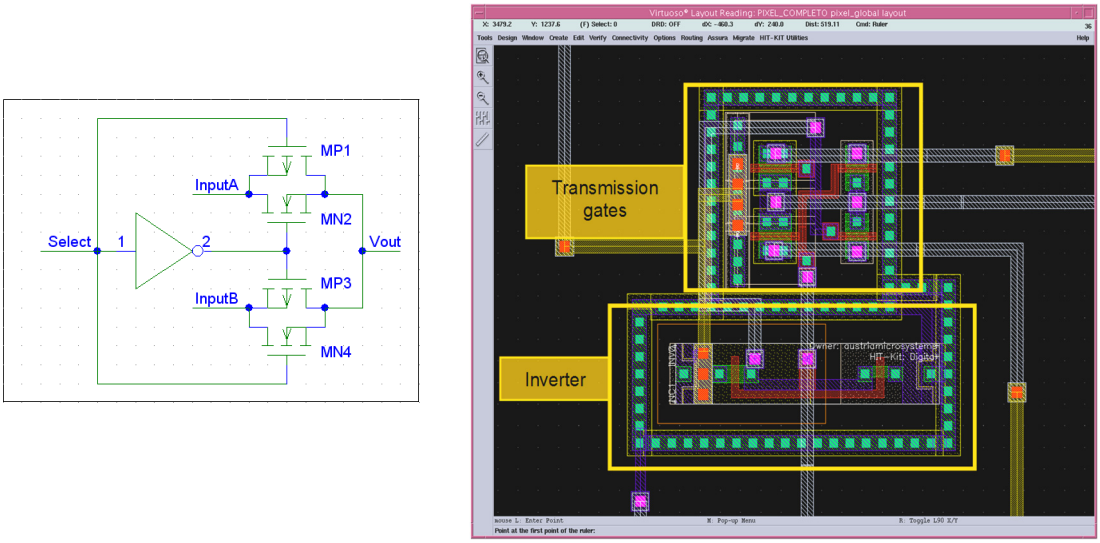

***Figure 6.10**. Left: Scheme for the multiplexer device based on transmission gates and an inverter. Right: Layout wit dimensions 18µm X 16µm.*

Logical behavior for the multiplexer follows the flow chart shown in figure 6.11. User decides which one of the arrays should be connected to the ADC and which one to the differentiator.

Transistor	W	L
MP1, MP3	1.6µm	0.35µm
MN2, MN4	1.1µm	0.35µm

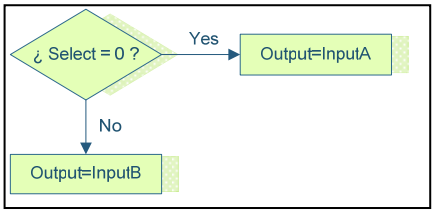

***Table 6.5:** Dimensions of the transistors employed for the multiplexer.*
***Figure 6.11:** Flow chart for the multiplexer device. "Select" signal controls which one of the inputs connects to the output.*

6.4.2 10 bits Analog to Digital Converter

The 10 bits Analog To Digital Converter (ADC) included in the presented ASIC was designed by the *"Microelectronics design group"* of the Electronics Department at the University of Barcelona [26].The converter operates at a maximum frequency of 500 KHz and it takes 11 clock cycles (22µs) to perform a complete conversion of the analog voltage at the output of the array of photodetectors, to digital values. ADC can be connected to one of the arrays via the multiplexer.

Design of ADC is based on the successive approximations method and it is composed by a Digital to Analog Converter (DAC), a comparator and a Successive Approximation Register (SAR) (figure 6.12). SAR generates different digital values that are converted into analog voltages by the DAC. Comparing these values with the analog voltage at the ADC input, the definition of the digital value at the output is obtained bit by bit. If the analog input value is greater than the one produced by the SAR+DAC, then SAR increments its count, generating a new digital value greater than the previous. This digital value is converted again by the DAC and compared with the ADC input. See table 6.6 for ADC technical specifications.

ADC specifications	
Range	0-3.3V
Resolution	10 bits
Power supply	3.3V
Max. frequency	500KHz
LSB	3.22mV

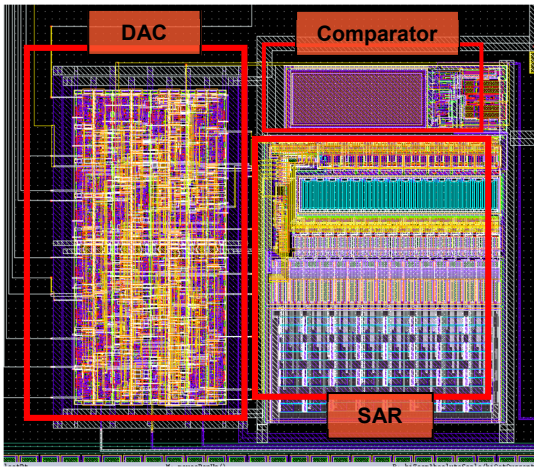

Table 6.6: *Specifications for the 10 bits analog to digital converter (ADC).*
Figure 6.12: *Layout for the 10 bits ADC based on successive approximations method. Dimensions 323µm X 263µm.*

6.4.3 Differentiator structure

For the differentiator design a compensated architecture with an operational amplifier (OPAMP) was implemented (figure 6.13 left, equation 6.4). Simulations proved that this kind of architecture provides better response than the non-compensated one: the signal is centred in the offset voltage applied at the positive terminal of the OPAMP, there are no perturbations, no oscillations at high frequencies and no intensity peaks of consumption. The additional elements added in the compensated differentiator (*Cd* and *Rd* marked with red circles in figure 6.13), determine two points of interest (f_1 and f_2) in the range of working frequencies: *Rd* determines the maximum frequency with gain (f_1), while *Cd*, the frequency (f_2) from which attenuation of signal is produced (low-pass filter). For frequencies lower than f_1, differentiator is very stable. In the standard configuration, f_1 and f_2 present equal values.

$$V_{out} = -RC\frac{dV_{in}}{dt}$$

$$f_1 = \frac{1}{2\pi R_d C} \quad f_2 = \frac{1}{2\pi R C_d} \tag{6.4}$$

The differentiator structure is useful to determine the range of pixels excited by a laser source (figure 6.13, right). Instead of addressing each one of the pixels of the whole array (256 pixels) during the readout phase, the voltage peaks produced by the differentiator point out the initial and the final pixels excited by the light source, which results in a reduction of the processing time, improving efficiency of the device. Each peak corresponds to a change of voltage in the analog array output (V_{in}): the first peak appears when voltage level starts decreasing (beginning of excited pixels) while the second peak appears when voltage level starts rising (end of excited pixels). Sensitivity of the differentiator is

adjusted by design to deliver an output when the variations in input signal present a particular range of estimated slopes.

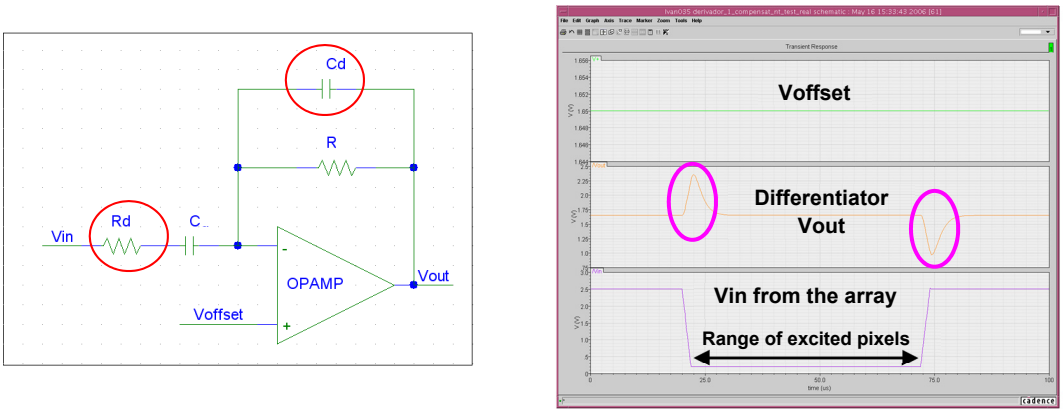

Figure 6.13. *Left: Differentiator structure scheme based on a compensated architecture with and OPAMP. Right: Simulation results for the differentiator structure. The peaks corresponding to the changes in V_{in} voltage are marked with pink circles.*

The chosen operational amplifier (*OPAMP OP05B*) belongs to the group of Standard Cells from "*AustriaMicrosystems*". This internally compensated OPAMP with PMOS input stage is designed for low power switched capacitor applications. With parametric simulations the best capacity and resistor values were determined, constrained by the target of reduced dimensions. The combination of different values for these two components modifies the width of the peaks, which mark the changes in the input voltage (V_{in}) (table 6.7).

Table 6.7*. Detection peak width Δt for different values of R and C in the differentiator structure.*

C_d	R_d	Δt (peak width)
10 pF	100 KOhms	13,9μs
5 pF	50 KOhms	3,13 μs (too narrow)
1 pF	10 KOhms	No valid data

With the values for components *Cd* (10pF) and *Rd* (100kΩ), for the layout design (figure 6.14) "*cpoly*" layer (capacity obtained from polisilicon) was used to build the capacitors while "*rnwell*" layer (resistivity obtained from n-well) for the resistors, since it offers larger electrical resistance and lower area consumption than other alternatives. Final dimensions for components are presented in table 6.8.

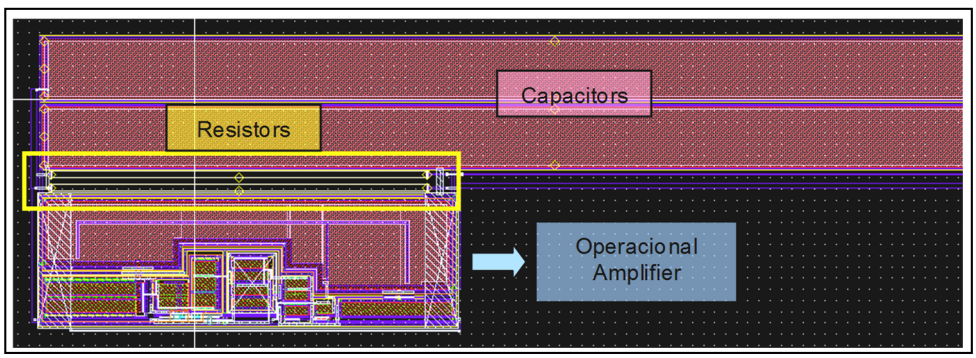

Figure 6.14*. Layout for the compensated differentiator. Dimensions 471μm X 131μm.*

***Table 6.8**. Dimensions of the components for the differentiation structure.*

Component	Dimensions	Value
OP05B	60.35µm X 190µm	-
Resistor (Rd)	3µm X 170µm	100kΩ
Capacitor (Cd)	25µm X 461µm	10pF

6.4.4 Array Control Logic

The control logic integrated on chip generates the necessary signals for sequentially selecting the pixels in the readout phase. These signals are applied at the same time to both arrays. An external clock signal (*selection clock*) fixes the working frequency. The elements for this block are: a digital counter, an enable block and a decoder. The 8 bit counter increases its count from 0 to 255 with every clock. The count number is then decoded by the 8:256 decoder, and a pixel is selected, transferring its saved voltage value to the output line. During the operation, enable block activates the decoder. The control logic was designed using verilog high level language and synthesized in 0.35µm CMOS tech(figure 6.15).

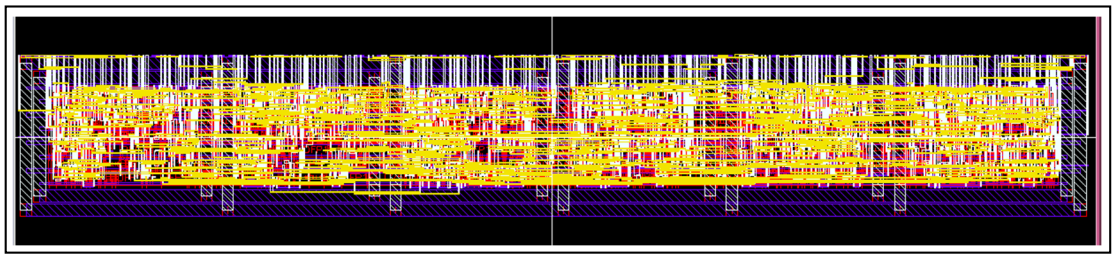

***Figure 6.15.** Layout of the internal logic control containing an 8 bit counter, an 8:256 decoder and an enable block. Dimensions 1000µm X 150µm.*

Flow chart in figure 6.16 explains how the control logic block works with the rest of operating signals of the CMOS image sensor, and which conditions must be accomplished in order to begin with the readout phase. The selection process for the pixels starts when E*nable* signal becomes a logical “1”. To achieve that condition, *Reset, Discharge* and *Selection clock* signals must present particular values.

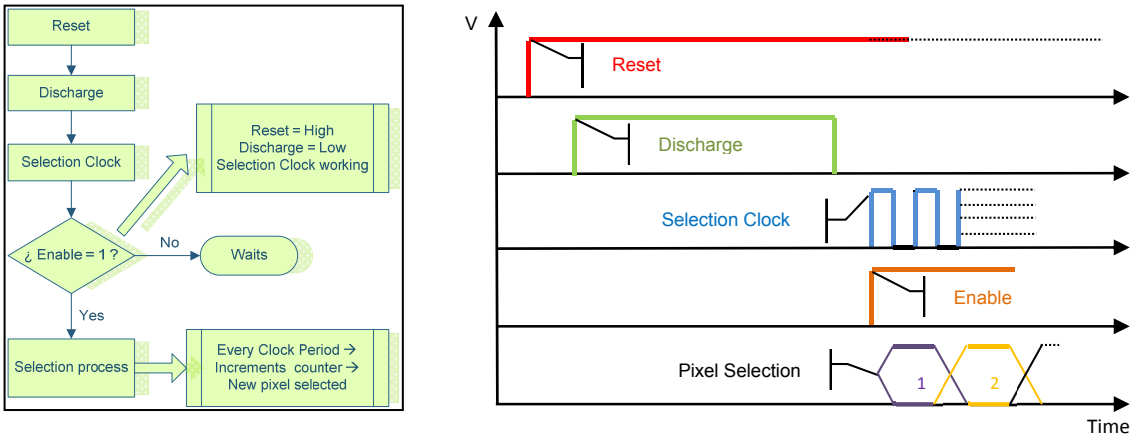

***Figure 6.16.** Left: Flow chart for the control logic block, which manages the readout phase of the CMOS image array. Right: Timing chronogram of the signals involved in the pixel selection process.*

6.5 Fabrication and packaging

CMP Circuits Multi-Projects Company fabricated the CMOS image sensors in 0.35 CMOS-Opto *C35B4O1* "*AMS*" technology. This process offers 4 metal and 2 poly layers and it is suitable for prototyping and low volume production, providing enhanced optical sensitivity for embedded photodiodes and high density CMOS camera products, with supply voltages of 5V or 3.3V. The company delivered us a set of dies and subsequently some of them were wire-bonded and packaged in taped lid ceramic packages, compatible with commercial sockets.

A microscope photograph of one of the dies can be observed in figure 6.17. Surrounding the central part of the chip, a ring of analog and digital pads is found: analog pads for the analog outputs of the arrays and the differentiator structure, and digital pads for the ADC and other control signals.

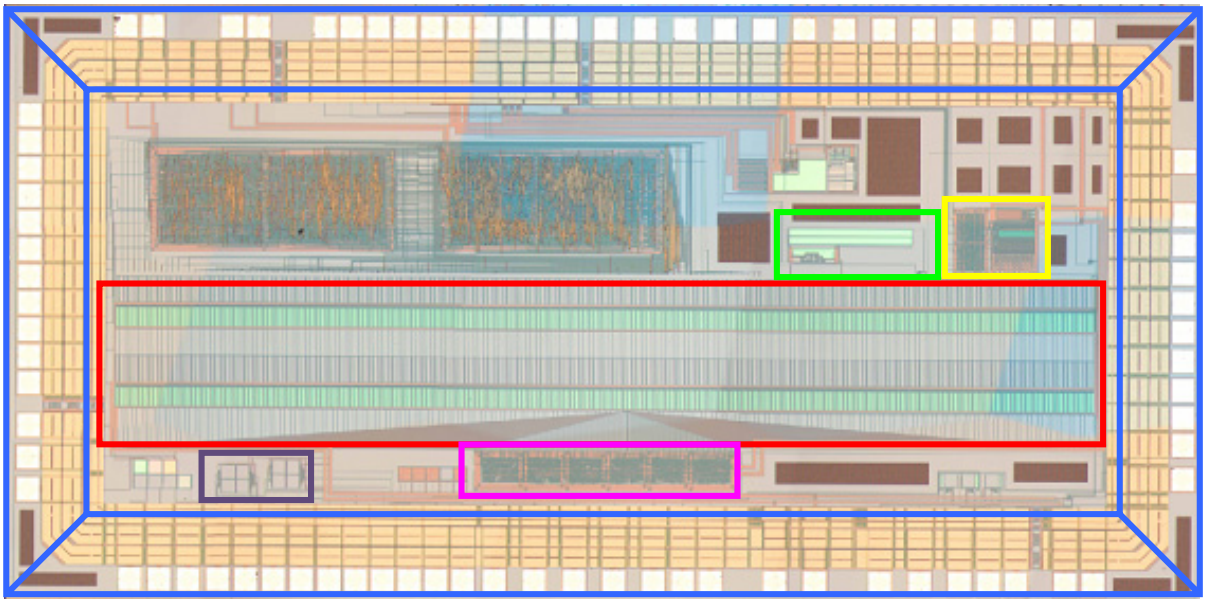

Figure 6.17: *Microscope photograph for a single die. In blue colour: the ring of pads; in green: differentiator structure; in yellow: ADC; in red: 256 pixels double array; and in pink: control logic for the array. Pixels with binary output are marked in lilac colour. The rest of blocks correspond to several testing photodiodes and other electronic circuitry not related to this thesis.*

As for the packaging of the dies, ceramic chip carrier JLCC was selected. This package presents a rectangular shape with contacts on all four edges and J-shaped metal leads for connections by a socket. Two versions were implemented: the JLCC84 and the JLCC44, with 84 and 44 contacts respectively.

For wire-bonding diagrams of both versions and photographs of the packaged devices refer to figures 6.18 and 6.19 respectively.

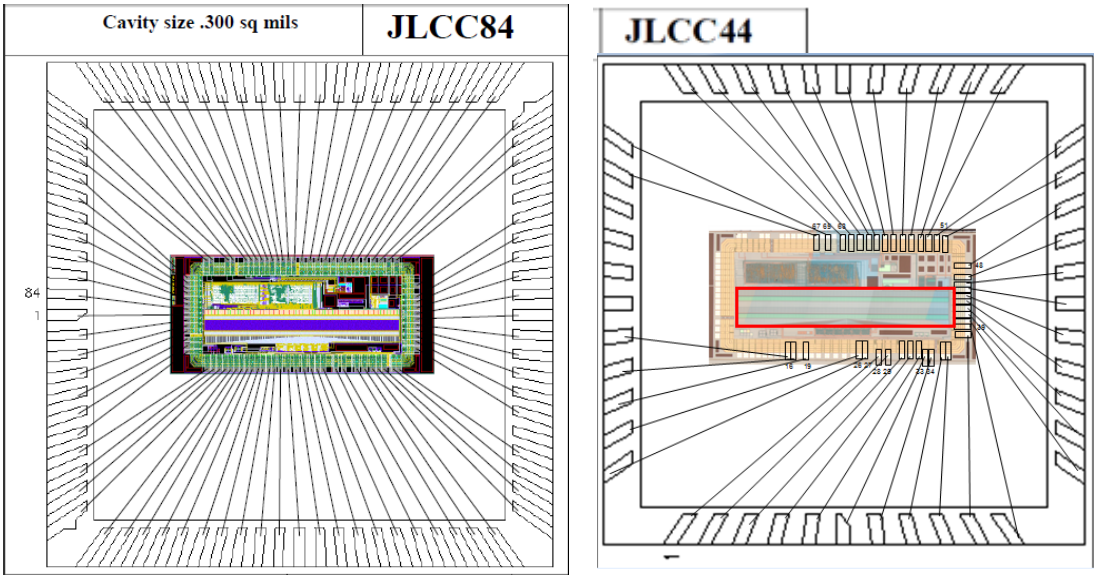

Figure 6.18: *Wire-bonding plans for ceramic chip carrier JLCC84 (left side, layout of the chip in the center) and JLCC44 (right side, photograph of the chip in the center).*

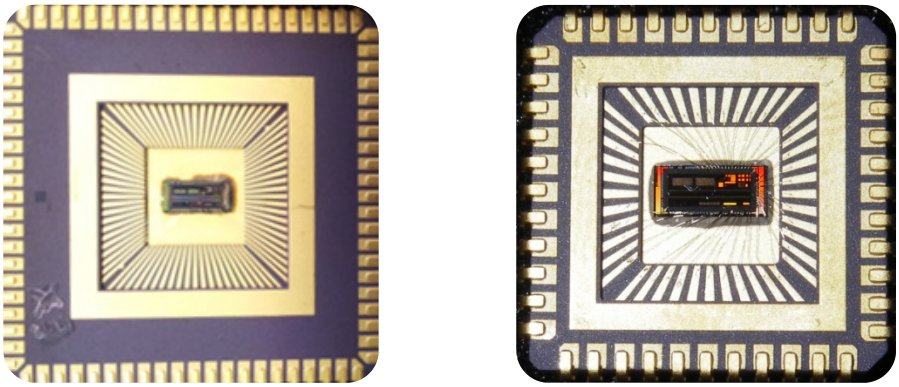

Figure 6.19: *Packaged dies in ceramic chip carriers JLCC84 (left side) and JLCC44 (right side).*

6.6 Microcontroller and electronics for managing the CMOS image sensor

A printed circuit board (PCB) is designed to contain the off-chip electronics necessary for managing and controlling the CMOS image sensor (figure 6.20). The packaged double array of pixels is placed in this board, which also includes an on-board programmable *PIC* microcontroller devoted to generate the external control signals of the system. Besides, the board allows transmission of data via USB or RF communication protocols.

Specific software running in a receptor system has been developed in *Labview* and *Matlab* to manage the acquisition parameters of the CMOS imaging array during the measurement process (e.g. integration time) and to represent graphically, in real time, the information read from the transmission system. Note that two 1MΩ resistors are connected at each one of the analog outputs of the CMOS double array.

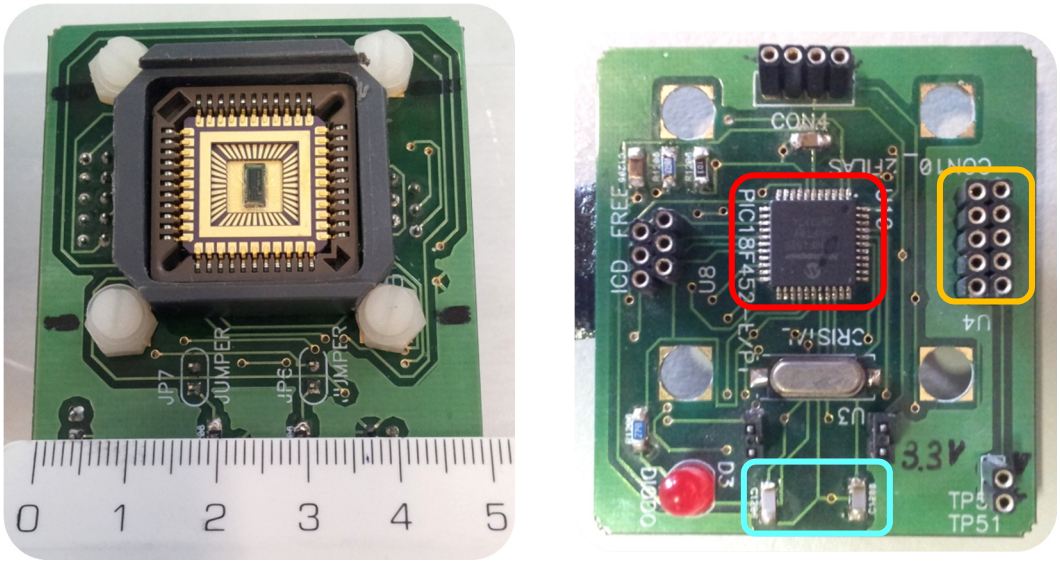

Figure 6.20: *PCB for the JLCC44 packaged CMOS image sensor array. Left side: front face with the socket for the sensor. Right side: rear face with the PIC microcontroller (red), the communications port (orange) and two 1MOhm resistors connecting the analog outputs of the arrays to ground (blue).*

The *18F458 PIC* microcontroller from *Microchip* is an EEPROM device with a large RAM memory bank and enhanced features and peripherals. This intermediate memory is used to save the digital data coming from the ADC of the image sensor and to send it later via RF or USB to the receptor. By means of 7 signals (i.e. *Reset, Reset2, Discharge, Selection Clock signal, ADC Clock, ADC Start* and *ADC Reset*) microcontroller also manages the readout phase of both arrays, the Analog-to-Digital conversion and the data transmission process (figure 6.21).

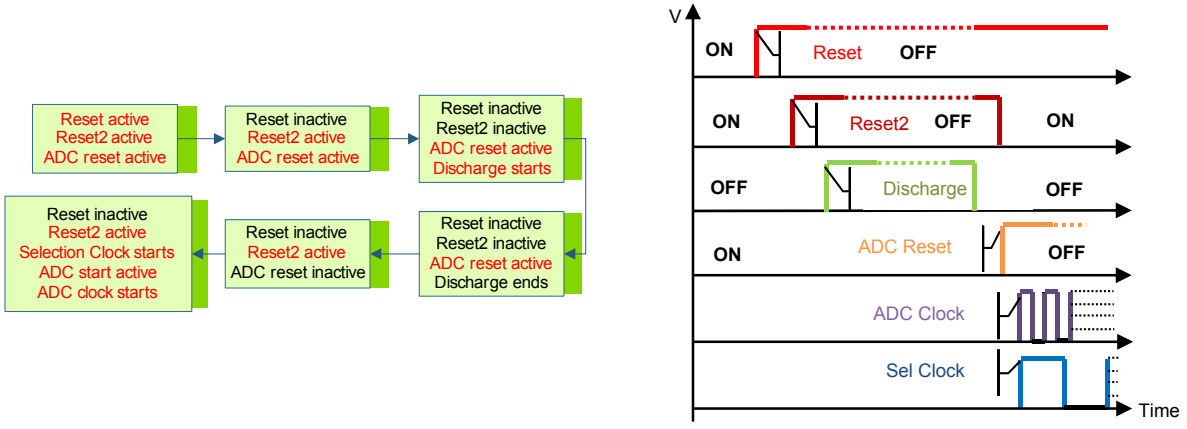

Figure 6.21. *Left: Flow chart for the external control signals produced by the microcontroller. First and second blocks correspond to the Reset phase; third and fourth blocks to the Discharge phase, and fifth and sixth to the Readout and the digital Conversion phases. Right: Timing chronogram of the signals generated by the external control block.*

The operation of the complete CMOS image sensor, including off-chip electronics, and the actions carried out in each one of the phases are presented in the next figure.

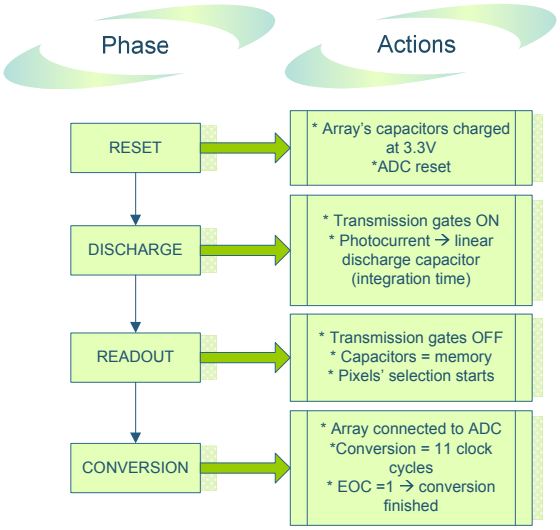

Figure 6.22: *Flow chart for the sequence followed to perform a measurement with the CMOS image sensor. Control signals are generated by the external control block (off-chip electronics and microcontroller).*

6.7 Testing and Characterization of the 256-pixels CMOS double linear array

In this section, results of the experimental measurements for the fabricated CMOS double linear array imaging sensor are presented. First, characterization of the designed pixel is reported, to continue with the study of the performance parameters for the linear array of photodetectors, including the AD conversion, when excited with diode laser and VCSEL emitting sources. Results for the differentiator structure are commented in a separated section.

6.7.1 Characterization of the pixel: Responsivity

Experimental measurements of the linear response of a single pixel are presented in figure 6.23. At fixed illumination levels, different integration times were applied, and the voltage at the output of the pixel was measured. From these values responsivity of the pixel can be calculated (table 6.8). The resulting mean value (6,09V/lux*s) is in accordance with standard values from other developed sensors [23], [27].

Table 6.8*: Responsivity values for different illumination levels. A mean value of 6,09V/lux*s is obtained.*

Illumination (lux)	117	210	300	508	626	825	1030
Slope (V/µs)	0,0005	0,0015	0,0022	0,0034	0,004	0,0051	0,0048
Responsivity (V/lux*s)	4,27	7,14	7,33	6,69	6,38	6,18	4,66

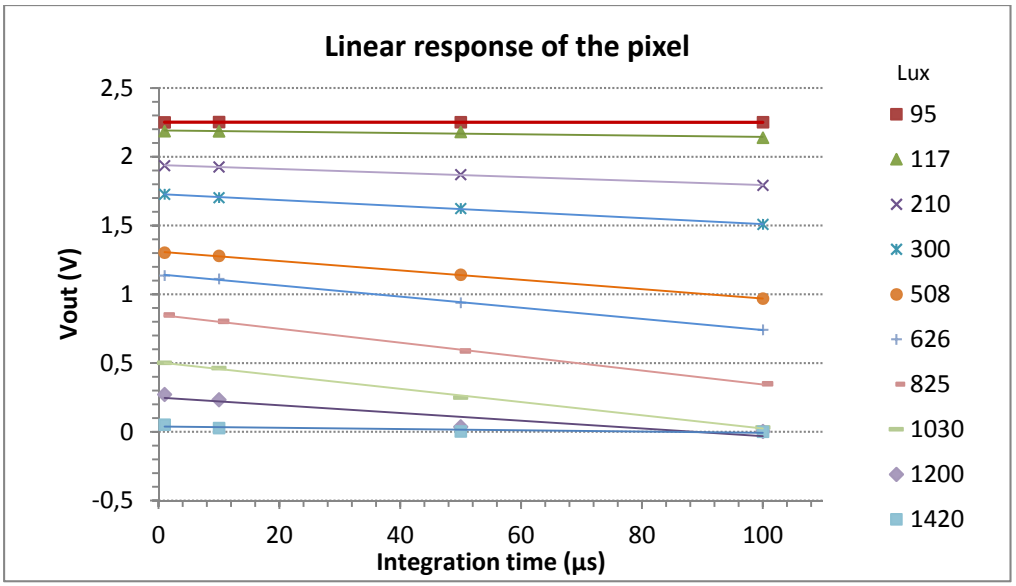

Figure 6.23: *Responsivity of a single pixel. Experimental results of the voltage at the output of the pixel, with different integration times for a set of fixed illumination levels.*

The same linear tendency can be observed in the response of the pixel in relation with the integration time under different illumination conditions (figure 6.24).

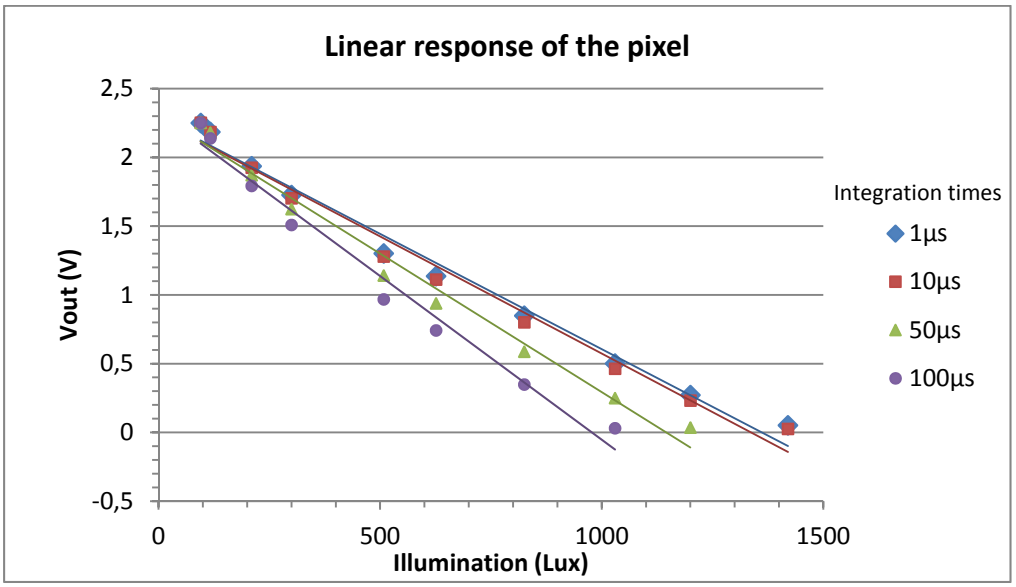

Figure 6.24: *Responsivity of a single pixel. Experimental results of the voltage at the output of the pixel under different illumination levels for fixed integration times.*

6.7.2 Characterization of the pixel: Spectral Response

The setup for the study of the spectral sensitivity of the fabricated photodiode consisted on a white light source, a monochromator to select the concrete wavelength of study (λ) and a chopper working together with a lock-in-amplifier to measure the amplitude value of the signal delivered by the photodiode, reducing the effects of environmental illumination noise. A lens placed behind the

chopper improves the focusing of the light into the sensitive area of the photodiodes. A special software designed in Labview controlled the instruments of the setup and saved the results. These results are presented in the form of normalized spectral responsivity (figure 6.25). The whole visible range is covered presenting a peak around 700 nm. We believe that the observed ripple effect in the figure is due to the oxide layers deposited during the fabrication CMOS process.

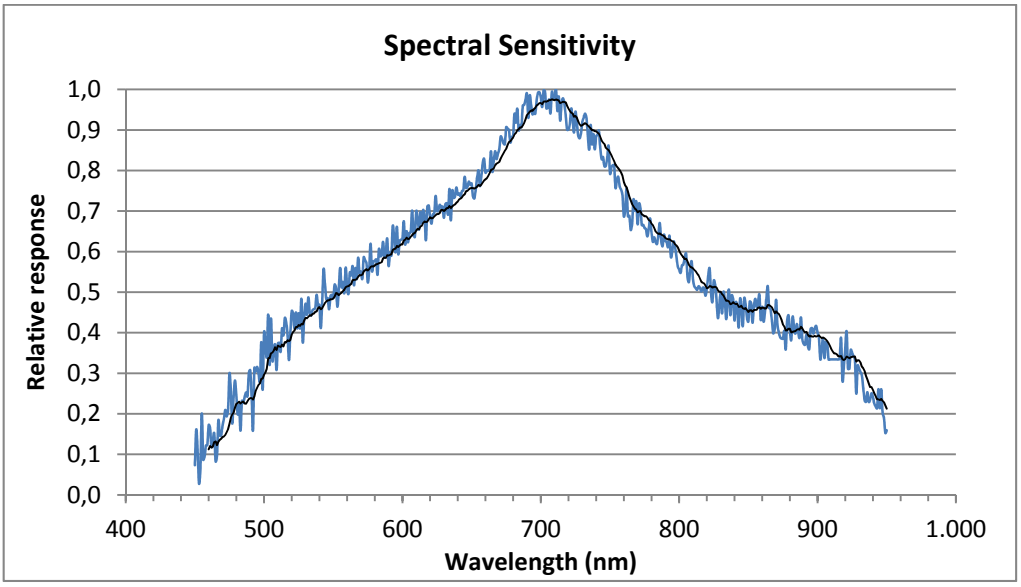

Figure 6.25: *Normalized spectral responsivity for a silicon photodiode (N-plus diffusion over P-substrate). The peak is presented around wavelength 700nm.*

6.7.3 Characterization of the pixel: Dark Current

To determine the value of the Dark Current of the pixel, several measurements were performed in dark conditions (0 Lux) at different integration times (from 1 to 100µs). The mean value of these measurements is presented in figure 6.26.

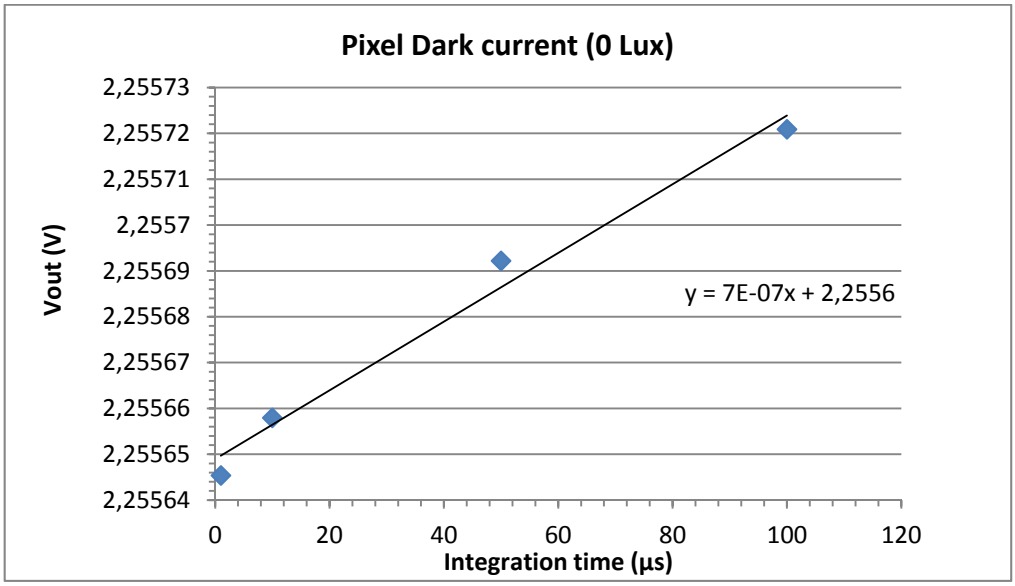

Figure 6.26: *Dark current of a pixel. Experimental results of the voltage at the output of the pixel under dark conditions for fixed integration times.*

From the expression of the linear tendency observed in the previous graph and considering the value of the capacity integrated in the pixel, we can conclude that the mean value of the dark current is 0.393fA/μm² (equation 6.5):

$$i_{dc} = C * \frac{dV}{dt} = 562fF * 0{,}7\frac{V}{s} = 393\frac{fA}{pixel} = 0{,}393\frac{fA}{\mu m^2} \quad (6.5)$$

6.7.4 Characterization of the pixel: Fixed Pattern Noise in Dark

Fixed Pattern Noise (FPN) is defined as the variation in the response of identical pixels under equal illumination conditions, due to reasons such as variations in the doping levels, sizes or threshold voltages. For the study of this parameter, several measurements were performed in dark conditions (0 Lux), reading the output of all the pixels in the array for a fixed integration time. The multiple readings were averaged to remove temporal noise.

In the case presented in the figure 6.27, integration time was set to 10μs. Measurements for different integration times offer the same results, which means that FPN is independent of this parameter. FPN can be expressed in several ways, but in our case we present the peak to peak value. The measured FPN is 74mV (≈3% of the saturation level, V_{sat} = 2.5V).

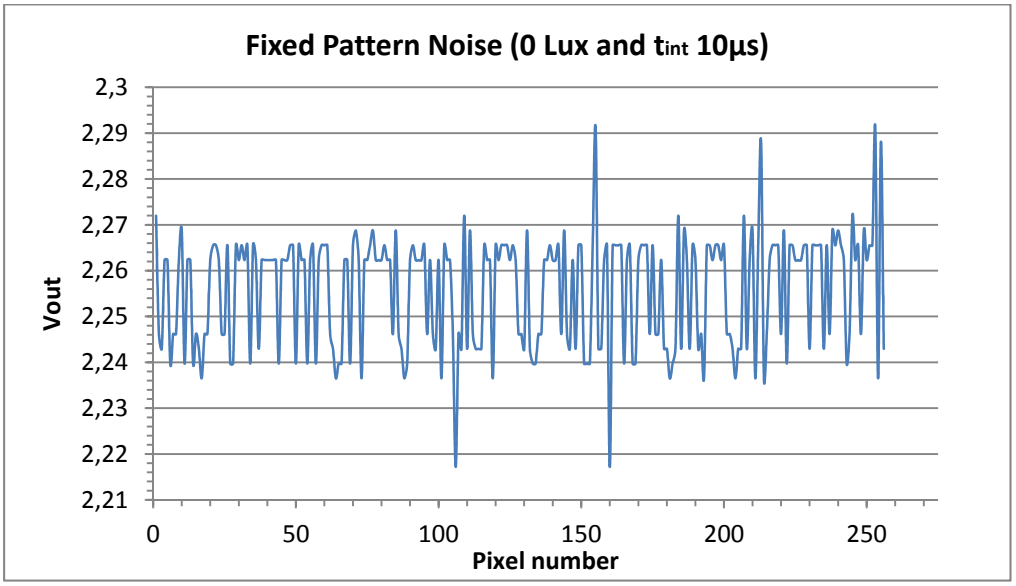

Figure 6.27: *Fixed pattern noise of the CMOS imaging array at 0 Lux and with an integration time of 10μs.*

6.7.5 Characterization of the pixel: Photocurrent

The combination of layers used for the fabrication of the photodiode integrated in the pixel, produces a characteristic response in terms of generated photocurrent. A white light source in addition with a set of attenuation filters (absorptive neutral density filters from *Spectra-Physics*) was used for these measurements. Photocurrents were measured with a pico-amperimeter. As can be appreciated in the qualitative results presented in figure 6.28, higher illumination levels deliver higher photocurrent values. A value of 95,4pA/lux is obtained for a photodiode with a sensitive area of 1000μm².

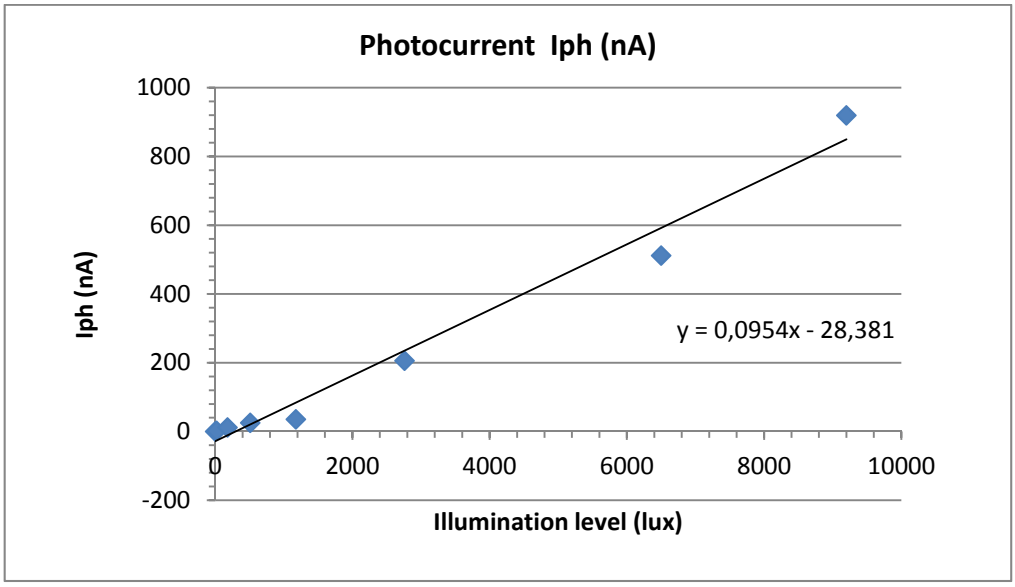

Figure 6.28: *Photocurrent generated by a single photodiode (1000µm²). Experimental results of the current under different illumination levels for the set of layers used in the fabrication of the component (N-plus diffusion over P-substrate).*

6.7.6 Temporal response of a single pixel

These experimental measurements were performed with the aim of analyzing the temporal response of a single pixel. The setup for this testing comprised the PCB with the optical sensor, an oscilloscope, a red visible emitting laser diode from *Monocrom* and a power supply (3.3V). From the CMOS image sensor, analog outputs were the signals of interest, leaving for later the study of the analog to digital converter. Laser diode was used to excite the pixels, generating a photocurrent in the range of 1nA to 20nA (figure 6.29).

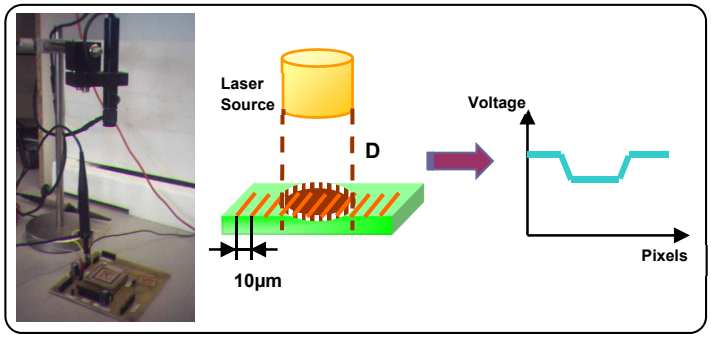

Figure 6.29: *Experimental setup for initial testing. As the diameter of the light spot from the laser diode is > 10 µm, several pixels are excited (low voltage level).*

The signal obtained from the direct reading of the analog output of one of the arrays is in accordance with the simulation results (figure 6.30). In the response of the pixel, the three stages corresponding to the evolution of the electrical charge previously discussed can be observed: reset, integration and hold.

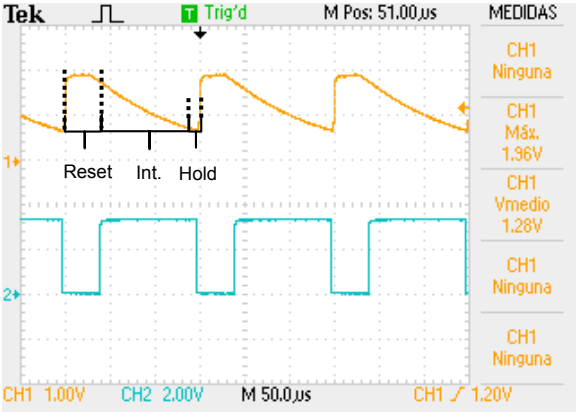

Figure 6.30: *Oscilloscope capture. Response of a single pixel when illuminated (orange colour) and Reset signal (blue colour). The three characteristic states for the evolution of the electrical charge can be observed: reset (high level), integration (lineal decreasing) and hold (voltage is stable).*

6.7.7 Temporal response of the array of pixels and AD conversion

Experimental results for a total reading of the array (256 pixels) are presented in figure 6.31. The same red laser diode from *Monocrom* was used to excite the CMOS image array. As the pixel pitch was fixed in 10µm in the design phase, it is obvious that several pixels will be illuminated depending on the diameter of the laser spot (figure 6.29). Thus, the analog output signal presents several pixels with lower voltage level compared to the others. These lower voltage levels mark the position of the laser spot.

Three complete readings of the array are shown in the oscilloscope captures of figure 6.31. The narrow dips point out the range of pixels corresponding to one reading cycle. With a fixed level of light excitement, increasing integration time (from 10µs to 100µs) is possible to improve the response of the image sensor to low light levels and even to reach saturation of the pixels.

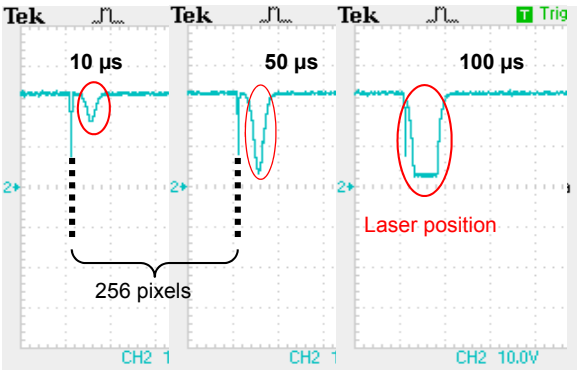

Figure 6.31: *Complete array reading (256 pixels) for different integration times (t_1=10µs<t_2=50µs<t_3=100µs) with the same light excitement conditions. The position of the laser spot corresponds to the lower voltage levels in every reading cycle. In this example, the laser spot is found near the beginning of the array, and close to the narrow dip which marks the beginning of the reading cycle.*

To test the analog to digital conversion, one of the analog outputs of the array was internally connected to the embedded ADC, through the multiplexer. For every reading cycle (256 pixels), the converted digital data was transferred to the receptor computer via USB or RF transmission. Designed software running in the computer represents the results graphically in real time (figure 6.32).

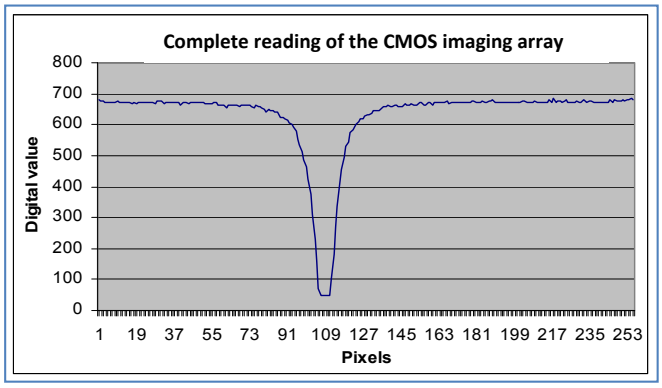

***Figure 6.32**: Complete reading of the CMOS imaging array including Analog to Digital conversion. Digital values of the analog voltage are represented in Y axis, while in X axis are represented the 256 pixels. The dip marks the position of the laser spot (around pixel 109).*

6.7.8 Response of CMOS imaging sensor to VCSEL light sources

To test the response of the image sensor to VCSEL light sources, the setup of figure 6.33 was arranged. With a die of 4 VCSELS from *EMCORE* bonded on a commercial open-window DIP package and a *Geltech Aspheric* lens of focal f=4.00mm and numerical aperture NA=0.62, positioned at a certain optical distance, we tried to focus the light beams on the CMOS imaging array. Images from the *Labview* software developed to process the data sent by the CMOS image sensor, in combination with electronics and communications module embedded in the PCB, demonstrate that the imaging array is able to sense this set of light beams.

Next step was to incorporate the CMOS image sensor into the experimental setup prepared for the optical detection of particles in microfluidic channels. The setup included the fabricated optoelectronic package (VCSELs and microlenses hybridly assembled in a silicon structure) presented in the previous chapters, which delivered four collimated light beams (figure 6.34). Graphical representations were obtained from the Labview software developed to process the digital information sent by the sensor device.

The performed measurements confirm that the CMOS double linear array of pixels is sensitive to the collimated light beams, which indeed is the aim of this researching work (figure 6.35). Thanks to the length of the CMOS double array and the optical collimation effect achieved by the optoelectronic device, several laser spots can be captured by the sensor once it is positioned in the image plane, as in figure 6.36 where four VCSELs were active.

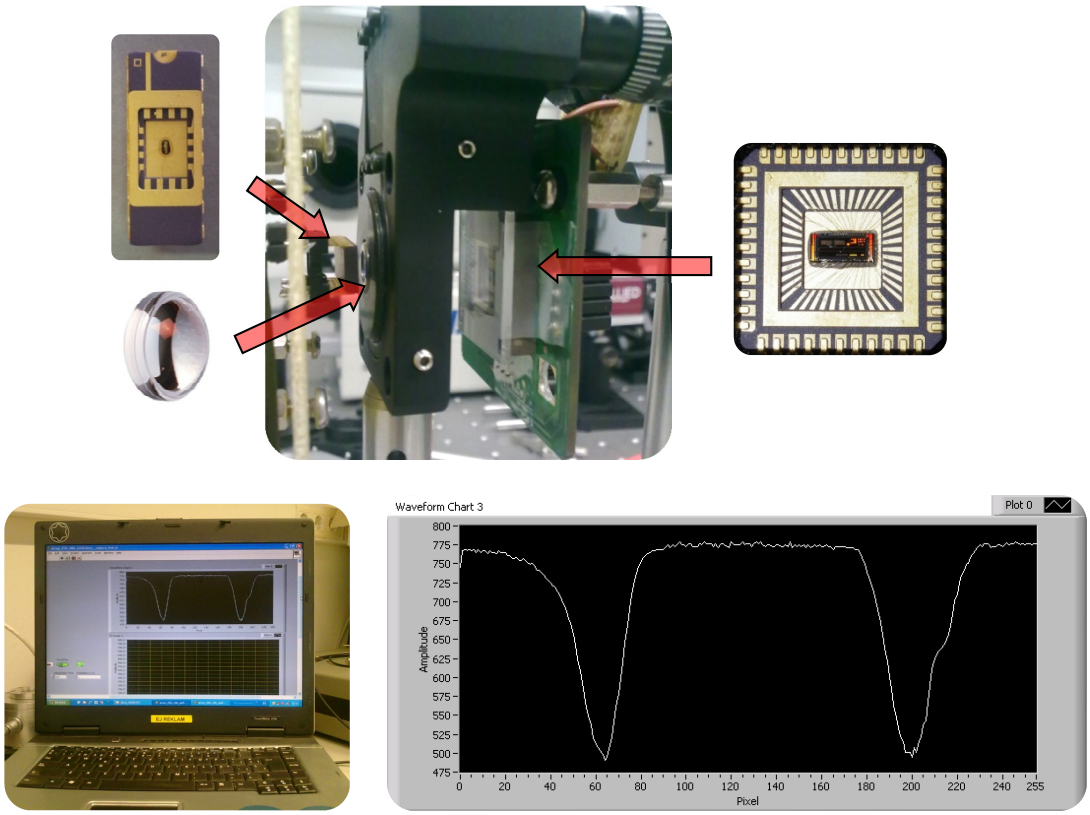

Figure 6.33: *Experimental measurement of the setup formed by a packaged die of 4 VCSELs, an aspheric lens with a focal of 4mm and the CMOS array image sensor. Only two VCSELs were active. Image corresponds to the direct reading of the digital values delivered by the imaging sensor, with an integration time of 400µs.*

Figure 6.34: *On the left side, setup of the system prepared for the optical detection application with the optoelectronic package, the microfluidic chip and the CMOS imaging sensor. Picture on the right side was captured by means of a commercial camera (ALLIED) thanks to a beam splitter placed over a glass substrate. On the right side, photograph of the fabricated CMOS image sensor with 3 active laser spots (red circle) emitted from the VCSELs integrated on the optoelectronic package reported in the previous chapters. These collimated spots are sensed by the image sensor, converted to digital values and processed.*

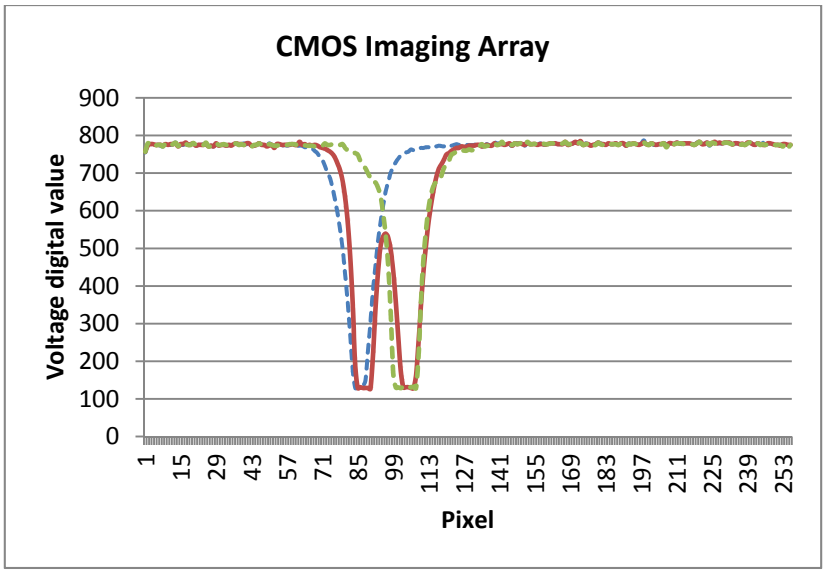

Figure 6.35: *Representation of the digital data read from the CMOS imaging array. In this case, 2 VCSELS were alternatively switched on (blue and green curves). The red curve corresponds to both VCSELs active. Integration time has been set to force the saturation of the pixels in order to have a better representation.*

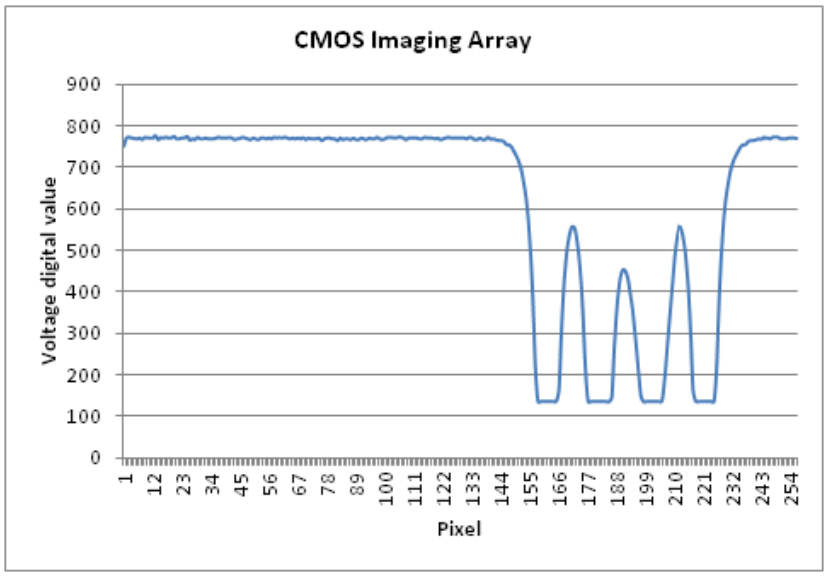

Figure 6.36: *Representation of the digital data read from the CMOS imaging array, for 4 VCSELs active. Thanks to the collimation effect produced by micro-optics, 4 spots are clearly distinguished. The length of the array would allow to sense up to 12 VCSEL spots.*

In figure 6.36, approximately 22 pixels separate the centers of each one of the spots. Considering that the pixels of the CMOS imaging array present a pitch of 10µm (11µm if the guard ring surrounding the pixels is included), that value corresponds to a distance of ≈ 220µm (242µm) which is almost equal to the defined pitch of the VCSEL light sources (250µm).

Measurements of the collimation effect for one of the VCSELs of the optoelectronic package were also carried out. Increasing the distance between the package and the CMOS sensor array a total of 1.5cm

with 1mm steps, the width of the beam keeps almost constant. Integration time was fixed at 100µs. The results of this case of study are presented in figure 6.37.

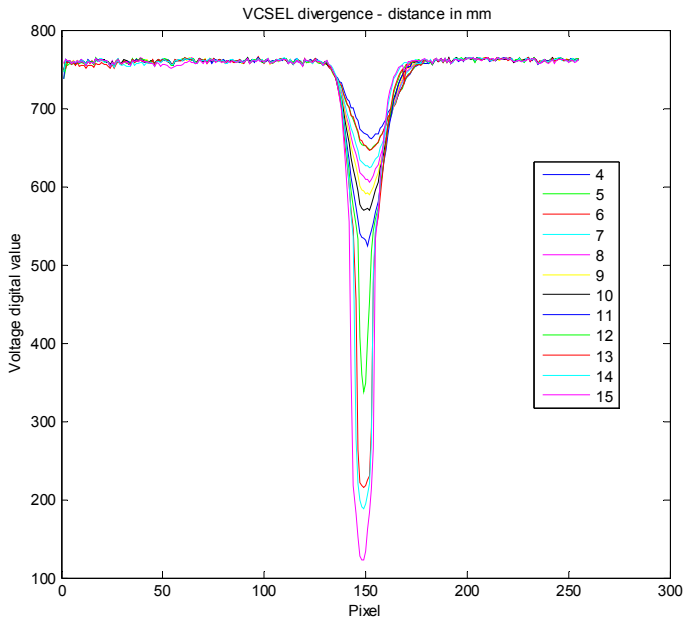

Figure 6.37: *CMOS image sensor measurement of the collimation effect achieved with the optoelectronic package, for a single VCSELs. Distance range between optoelectronic package and CMOS sensor form 4 to 15mm.*

When the optoelectronic package is positioned near the CMOS image sensor (below 1cm), the effect of optical replicas can be observed, as in simulations presented in chapter III. In the picture (figure 6.38), only one VCSEL is active and integration time has been set to 500µs (which can be considered a large value, not probable in normal scenarios) to make replicas more evident. Light sources possess a natural divergence which can be mathematically described as an emission cone with a certain solid angle. Though it is possible to correct this divergence effect with the use of microlenses, as it has been demonstrated in this work, when the image plane is proximate to the light source, surpassing the limit defined by the concrete optical system, replicas appear. Replicas are the result of part of the light rays from the emission cone of a particular light source, being collected by neighbouring lenses (off-axis).

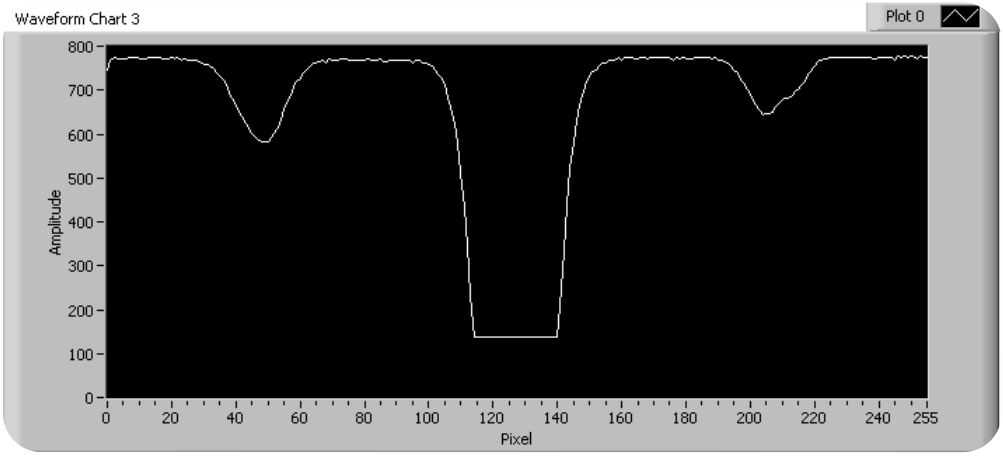

Figure 6.38: *CMOS image sensor measurement of the replicas effect produced by the optoelectronic package under conditions of excessive proximity with the optical sensor. For this case, CMOs sensor was nearly in contact with the optoelectronic package. Integration time was set to 500µs.*

6.8 Study of the differentiator

The study of the differentiator structure was accomplished by connecting one of the analog outputs of the array to the differentiator, using the multiplexer integrated in the chip. The spot of the laser diode was located in the center of the image sensor. With an oscilloscope, analog output of the differentiator was captured (figure 6.39, orange color). The obtained peaks correspond to the changes in voltage level from the analog output of the array (figure 6.39, blue color) due to the laser excitement, so the range of pixels of interest is delimited without having to read the 256 pixels of the array. Though the amplitude of the peaks for the experimental response of the differentiator is lower than expected, results can be considered acceptable to prove the global behavior of both blocks, the CMOS imaging array and the differentiator structure, working together. To improve the response, it is necessary to redesign the differentiator (resistors and capacities) attending the real rise and fall times for the analog output of the sensing array, or to add an electronic post processing stage to transform the peaks in standard digital pulses.

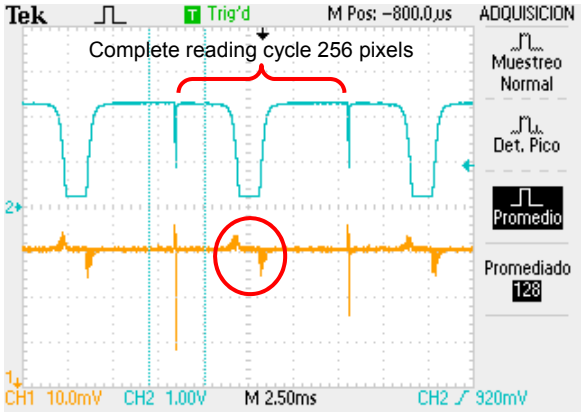

Figure 6.39: *Experimental results for the differentiator structure (orange colour). Red circle marks the peaks corresponding to the beginning and the end of the range of excited pixels in the array.*

6.9 Conclusions

The optical particle detection system presented in this thesis requires an optical sensing element able to detect and measure the changes in light intensity produced by the particles flowing through microfluidic channels. To achieve that goal, a full-custom CMOS imaging sensor has been designed and fabricated.

The CMOS imaging sensor contains a double linear array structure of a 256 pixels (512 pixels in total), designed in 0.35µm CMOS technology. Each active pixel integrates a 100µmX10µm area photodiode as basic sensing element, a capacitor acting as analog memory and several transistors. Total length of the arrays is ≈3mm. The double array architecture improves the detection process discarding false positive detected events.

Photodiode generates photocurrent proportional to the incident light exciting the pixel. Photocurrent discharges the initial voltage charge present at the capacitor according to the integration time parameter. The remaining voltage value is saved for reading in the readout phase.

The ASIC also includes 10 bits ADC, integrated logic control, a multiplexer and a differentiator block on the same chip. With the multiplexer, user can connect the outputs of the arrays to the AD Converter or to the differentiator block.

AD Converter delivers the digital signal corresponding to the reading of the 256 pixels of the array. Differentiator structure is designed to reduce the time devoted to locate the excited pixels.

The CMOS imaging sensor has been tested with red emitting laser diodes, as well as with a set of optically collimated NIR VCSEL light beams. The VCSELs, with a pitch of 250µm, were integrated in the optoelectronic package described in previous chapters. Each one of the spots was clearly detected. The length of the array would make possible in the future to detect simultaneously particles flowing through a total of 12 parallel microfluidic channels (some of them could work as reference channels) optically excited by means of an array of 12 VCSELs (pitch of 250µm).

The device has proven to be useful in biosensing applications such as the one described; i.e. optical detection of microparticles.

Values obtained during characterization of the pixels are in accordance with other developed CMOS image sensors. The experimental results obtained in the test phase presented good response, linearity (mean value of 6,09V/lux*s) and repetitivity.

References

[1] A.Mäkynen et al., «CMOS-compatible position-sensitive devices(PSDs) based on photodetector arrays» *Sensors and Actuators A,* Issue 105, pp. 261-270, 2003.

[2] R. Casanova, J. Lacort, A. Dieguez and A. Arbat, «A specific integrated controller for nanomicroscopy and cellular manipulation» *IEEE International Symposium on Circuits and Systems*, 2005.

[3] A. Arbat, A. Comerma, J. Trenado, D. Gascon, A. Vilà, L. Garrido and A. Dieguez, «High voltage vs. high integration: a comparison between CMOS technologies for SPAD cameras» *Detectors and Imaging Devices: Infrared, Focal Plane, Single Photon*, San Diego, California, 2010.

[4] A. Arbat, A. Comerma, J. Trenado, D. Gascon, A. Vilà, L. Garrido and A. Dièguez, «Comparison between technologies for APDs fabrication in particle detectors» *Procedia Engineering,* vol. 5, pp. 677–680, 2010.

[5] Zhu and Ozcan, «Wide-field fluorescent microscopy and fluorescent imaging flow cytometry on a cell-phone» *Journal of Visualized Experiments,* Issue 74, pp. 370-374, 2013.

[6] S. O'Driscoll, B. MacCraith and C. Burke, «A novel camera phone-based platform for quantitative fluorescence sensing» *Anal. Methods,* Issue 5, pp. 1904-1908, 2013.

[7] N.Darwish, "Numerical study of grating-waveguides for biosensing applications", *5ºconferencia de Dispositivos Electrónicos, CDE2005*, 2005.

[8] S. Kavadias, B. Dierickx, D. Scheffer, A. Alaerts, D. Uwaerts and J. Bogaerts, «A Logarithmic Response CMOS Image Sensor with On-Chip Calibration,» *IEEE JOURNAL OF SOLID-STATE CIRCUITS,,* vol. 35, Issue 8, 2000.

[9] Y. Oike, M. Ikeda and K. Asada, «High-sensitivity and wide-dynamic range range finder and its applications» *World Automation Congress*, 2002.

[10] N. Massari, L. Gonzo, M. Gottardi and A. Simoni, «A fast CMOS optical position sensor with high subpixel resolution» *IEEE Transactions on Instrumentation and Measurement,* 2004.

[11] F. De Nisi, F. Comper, L. Gonzo, M. Gottardi, D. Stoppa, A. Simoni and J. A. Beraldin, «A CMOS sensor optimized for laser spot-position detection» *Sensors Journal, IEEE,* 2005.

[12] H. Ji and P. A. Abshire, «A CMOS image sensor for low light applications», *ISCAS* , 2006.

[13] D. Stoppa, M. Vatteroni, D. Covi, A. Baschirotto, A. Sartori and A. Simoni, «A 120-dB Dynamic Range CMOS Image Sensor With Programmable Power Responsivity» *IEEE Journal of Solid-State Circuits,* 2007.

[14] M. Hadi. Izad and Karim. S. K. , «PIXEL ARCHITECTURES FOR DIGITAL X-RAY MAMMOGRAPHY IN MAMMOGRAPHY IN CRYSTALLINE SILICON TECHNOLOGY», *CCECE 2004- CCGEI 2004*, Niagara Falls, 2004.

[15] P. Lee, A. Simoni, A. Sartori and G. Torelli, «A photosensor array for spectrophotometry» *Sensors and Actuators A: Physical ,* vol. 47, Issue 1-3, pp. 449-452, 1995.

[16] G. Patounakis, K. L. Shepard and R. L. Levicky, «Active CMOS Array Sensor for Time-Resolved Fluorescence Detection», *IEEE Journal of Solid-State Circuits,* vol. 41, Issue 11, 2006.

[17] S. Li, S. Kleinfelder, L. Jin and N. H. Xuong, «A CMOS Sensor for Nano-Imaging», *IEEE,* 2006.

[18] C. Rao, X. Yuan, S. Zhang, L. Meng and C. Peng, «CMOS artificial subretinal chip for natural light illumination» *ELECTRONICS LETTERS 20th,* vol. 42, Isue 15, 2006.

[19] C. Niclass, A. Rochas, P.-A. Besse and E. Charbon, «Design and Characterization of a CMOS 3-D Image Sensor Based on Single Photon Avalanche Diodes» *IEEE JOURNAL OF SOLID-STATE CIRCUITS, ,* vol. 40, Issue 9, 2005.

[20] F. F. M. Tartagni, N. Manaresi, R. Canegalloy and R. Guerrieri, «A Comparative Analysis of Active and Passive Pixel CMOS Image Sensors», *ESSDERDC conference* , 2002.

[21] G. P. Weckler, «Operation of p-n Junction Photodetectors in a Photon Flux Integrating Mode», *Journal of Solid-State Circuits, IEEE ,* vol. 2, Issue 3, 1967.

[22] E. R. Fossum, «CMOS lmage Sensors: Electronic Camera on A Chip», *IEEE Trans. Electron Devices ,* vol. 44, 1997.

[23] G.Hornero, "Estudio y realización de arrays de fotodetectores CMOS aplicados a la medida de distancias", PhD dissertation, University of Barcelona, 2002.

[24] G. Hornero et al, «CMOS linear photosensor array for 3D reconstruction applications», *Optical Engineering,* vol. 43, Issue 10, pp. 2448-2453, 2004.

[25] G.Chapinal, «A 128x128 CMOS Image sensor whith analog memory for synchronous image capture», *IEEE sensors journal,* vol. 2, Issue 2, pp. 120-127, 2002.

[26] A. Arbat, A. Dieguez and J. Samitier, «A 1 to 8 bit resolution SAR-ADC in 0.12 m CMOS technology for low power micro-robotics applications», *Proceedings of the XX Conference on Design of Circuits and Integrated Systems (DCIS)*, Lisboa, 2005.

[27] R. Reshef, T. Leitner, S. Alfassi, E. Sarig, N. Golan and O. Berman, «Large-Format Medical X-Ray CMOS Image Sensor for High Resolution High Frame Rate Applications», *Proc. of 2009 International Image Sensor Workshop*, Bergen, NORWAY, 2009.

[33] A. Mäkynen, T. Rahkonen and J. Kostamovaara, «A binary photodetector array for position sensing», *Sensors and Actuators A.*

[34] N. Massari, M. Gottardi, L. Gonzo and A. Simoni, «High Speed Digital CMOS 2D Optical Position Sensitive Detector», *SSCIRC,* 2002.

[35] F. D. Nisi, F. Comper, L. Gonzo, M. Gottardi, D. Stoppa, A. Simoni and J.-A. Beraldin, «A Novel CMOS Sensor for Position Detection», *Proceedings of IEEE Sensors*, 2003.

[36] N. Viarani, M. Nicola, L. Gonzo, M. Gottardi, D. Stoppa and A. Simoni, «A fast and low power CMOS sensor for optical tracking», *Proceedings of the 2003 International Symposium on Circuits and Systems*, 2003.

[37] A. Mäkynen, T. Ruotsalainen, T. Rahkonen and J. Kostamovaara, «CMOS-compatible position-sensitive devices (PSDs) based on photodetector arrays», *Sensors and Actuators A: Physical.*

[38] R. D. Burns, J. Shah, C. Hong, S. Pepic, J. S. Lee, R. I. Hornsey and P. Thomas, «Object Location and Centroiding Techniques With CMOS Active Pixel Sensors», *IEEE TRANSACTIONS ON ELECTRON DEVICES,* vol. 50, Issue 12, 2003.

[39] C. Thomas, R. Homey, K. Yip, M. Mullins and P. J. Thomas, «CMOS Imager Design for Fast Centroid Readout», *CCECE 2004- CCGEI 2004*, Niagara Falls, 2004.

CHAPTER VII: OPTICAL PARTICLE DETECTION – EXPERIMENTAL RESULTS

7.1 Introduction

In this chapter, measurements performed with the aim of testing the capability of the designed system for optical detection of particles are presented. The measurement set-up, including the fabricated micro-optical package (Chapters III and IV), the microfluidic chips (Chapter V) and the CMOS sensor array (Chapter VI), as well as the followed procedures, are first described. Then, qualitative and quantitative results demonstrate that the integrated opto-electronic system achieves not only detection of particles flowing in liquid suspensions in the range from 10 to 90µm diameter, but also is able to distinguish particles of different diameters in a mixed solution. Benefits of CMOS double imaging array, such as improved Signal to Noise Ratio (SNR), are also discussed.

7.2 Measurement set-up

The setup for the experimental testing is presented in figure 7.1. Besides the micro-optical package, which delivers a set of collimated laser light beams, the designed CMOS imaging array and the microfluidic chip are also included, for in this step, they are essential to constitute the complete detection system.

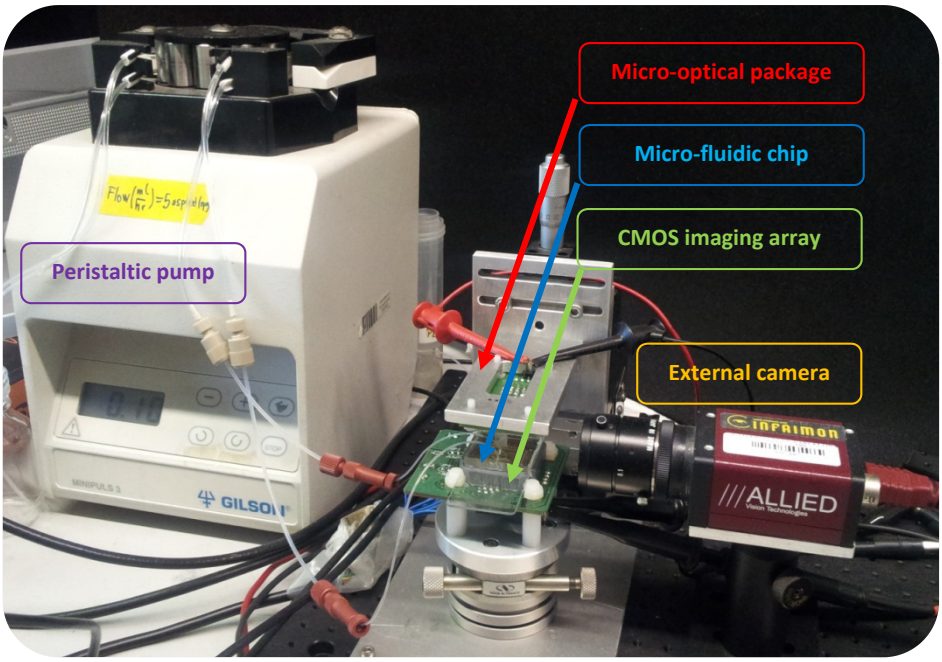

***Figure 7.1**: Measurement set-up overview. It includes: the micro-optical package, the designed CMOS imaging array and the microfluidic chip, as well as other external instrumentation and accessories necessary to perform the experiments (a peristaltic pump, flextubes and fittings for the microfluidic circuit, and an external camera). For detailed information about the different elements, refer to following sub-sections 7.2.1 and 7.2.2.*

Particles suspended in liquid flow through the microfluidic channels until they are confined into a detection window. Alignment of particles is achieved by active (i.e. 2D hydrodynamic focusing) or passive focusing (due to the geometry of the channels), depending on the microfluidic chip used for

the experiment. Each channel is centered in relation to one VCSEL, so they also share the same pitch distance of 250µm. Using a peristaltic pump (*Minipuls 3* from *GILSON*), motion of sample suspension with particles is achieved by pressure driven flow at a certain flow rate.

When the microbeads interfere with the light beams of the laser spots, the variation in the intensity of light is detected by the CMOS imaging sensor (i.e. the double linear array of photodetectors), placed just under the microfluidic chip. Parameters of the sensor (integration time, analog or digital reading operation mode and number of measurements) are adjusted according to the scenario. The signal is then readout, transferred to a computer and processed.

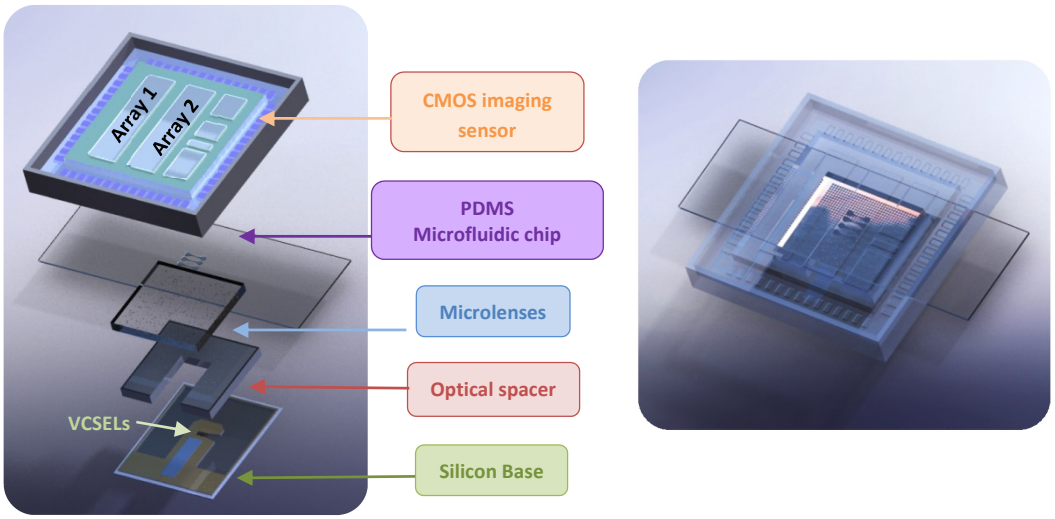

Figure 7.2: *Conceptual images for the components of the optical particle detection system. Silicon base, optical spacer, VCSELs and mcirolenses array compose the optoelectronic package. The microfluidic chip, fabricated in PDMS and glass, contains four parallel microchannels. The chip is placed between the optoelecotronic package and the CMOS image sensor.*

7.2.1 Optical detection system set-up

The micro-optical package is fixed into a solid aluminium structure attached to a 3-axis (XYZ) micro-positioner which allows a precise arrangement of the elements of the set-up (figure 7.3). With a goniometer is possible to accurately reorient the CMOS image sensor and improve the alignment of the light spots into the sensitive area of the arrays of photodetectors. For some of these measurements, where the aim is the detection of particles, the CMOS ASIC sensor takes advantage of the double array architecture to perform a simultaneous double measurement of the same sample.

This multiple interrogation procedure ("double checking") leads to an improvement of the Signal To Noise ratio, discarding false positives, and a reduction in the required analysis time. This, in addition to the possibility of measuring and analysing simultaneously several channels due to the length of the sensor and the multiple light sources, are some of the strong points of the system, along with others such as the embedded Analog to Digital Converter present in the ASIC. Bias voltages are in the range of 1.6-1.8V for the VCSELS in the micro-optical package, and 3.3V for the CMOS imaging sensor.

A special plastic piece was fabricated to place and support the microfluidic chips into the detection system, over the CMOS sensor (figure 7.3).

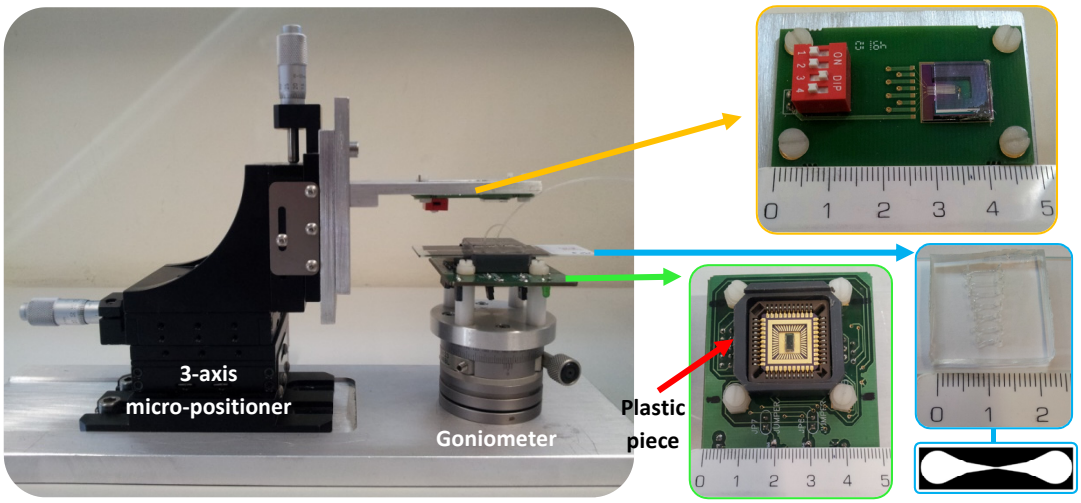

***Figure 7.3**: Detail of the measurement set-up. Micro-optical package (yellow) is placed into a solid aluminium structure attached to a 3-axis (XYZ) micro-positioner. Microfluidic chip (blue) and CMOS imaging sensor (green) are also included in the detection system. With the micro-positioner and the goniometer the elements can be accurately arranged. A special plastic piece (in grey colour, CMOS sensor picture) was designed to allow the placement of the microfluidic chips.*

A non-polarizing cube beam splitter from *Thorlabs* placed over the microfluidic chip allows to acquire black&white images simultaneously with an external camera (*AVT Marlin F-145B2*, equipped with a highly sensitive SONY 1/2" type progressive CCDarray, from *ALLIED*) while performing optical particle detection with the CMOS imaging sensor (figure 7.4).

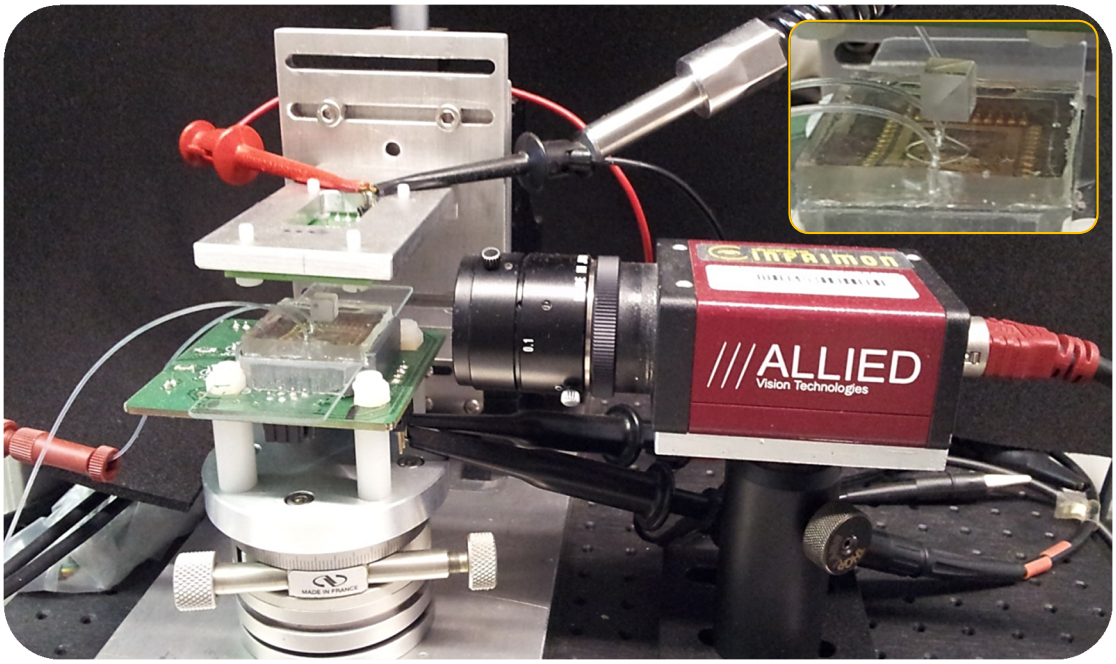

***Figure 7.4**: Detail of the measurement set-up. A beam splitter (zoom image at the upper right corner) placed over the microfluidic channel and a commercial camera are used as an external control system. Images from the camera will be compared with processed data from the CMOS imaging sensor.*

7.2.2 Procedure for the microfluidic chip

Different sets of experiments were planned in order to demonstrate not only the capability of the system for detecting microparticles, but also to evaluate its performance under different testing scenarios such as liquid suspensions with particles of different diameters, beads of different colours and materials, and also testing at different flow rates.

Previously to the experiments, microfluidic chips were thoroughly cleaned and conditioned for use following the next protocol: for each one of the channels, deionized (DI) water (*MiliQ* water from *Millipore®* with a measured conductivity of 2.1×10−4 S/m) was drawn through for 10 minutes. Then, the cleanse procedure was repeated drawing isopropanol (*Sigma-Aldrich*) for 5 minutes [1]. Finally, channels were rinsed with deionized water for another 5 minutes. At the end of each experiment, channels were cleansed with isopropanol circulating at high flow rate, and afterwards rinsed with DI water.

A similar protocol was applied to the flextubes and fittings used in the microfluidic circuit: *Upchurch Scientific® FEP* (fluorinated ethylene-propylene, a chemically inert material) tubings suitable for low pressure applications with 0.8mm/0.4mm output/inner diameters (OD/ID) for the inlets/outlets of the microchannels and 1.58mm/0.508mm OD/ID for the interconnections between the tubes of the peristaltic pump and the microchannels, as well as *Tygon® ST* and Silicone tubes with 1.02mm ID for the own circuitry of the pumps.

Cleaning solutions and samples in reservoirs were simply introduced into the inlets of the microfluidic channels and pumped through them to the outlets, by means of a peristaltic pump (*Minipuls 3* from *GILSON*). Anyway, some of the experiments were also performed with a pump (*P625/900.143* from *INSTECH*) of reduced dimensions (27 x 32 x 54 mm) able to provide flow rates in the range from 8 to 3300µl/min depending on the connected tube (e.g a 0.38mm ID tube deliver flow rates from 8 to 80ul/min). The utilization of this mini pump represents a reduction in the dimensions of the detection system, offering precise bi-directional speed control and power efficiency (i.e. typically drawing between 25-30 mA with a power supply of 8-12VDC) (figure 7.5).

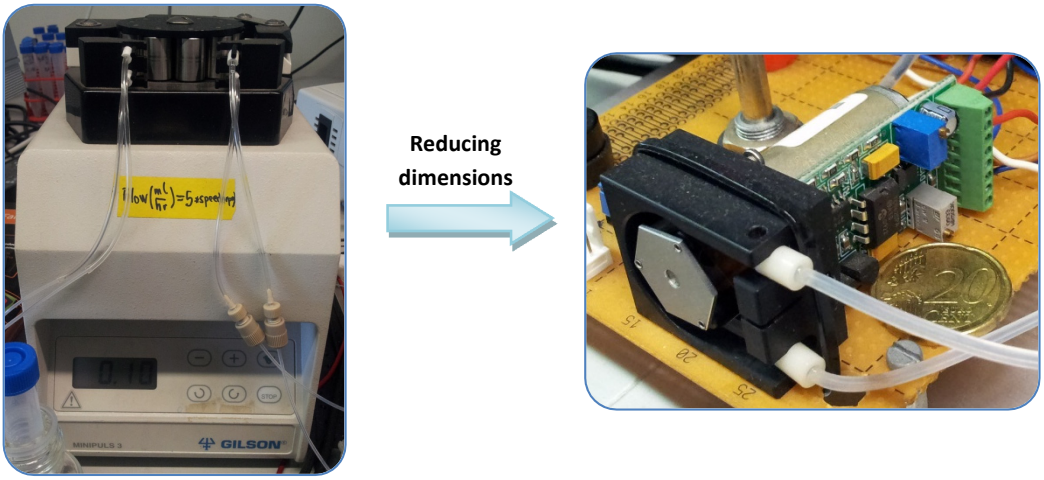

***Figure 7.5**: Peristaltic pumps used in the experimental setup to create flow motion into the microfluidic chips (pressure driven flow). On the left side, the standard peristaltic pump from GILSON. On the right side, a mini peristaltic pump from INSTECH, which allows reducing final dimensions of the detection system (printed with permission from the company).*

7.2.3 Tested particles

First, qualitative results will demonstrate that optical detection is feasible. Then, quantitative results along with real acquired images from the external camera will be introduced. Measurements are focused on a single microfluidic channel. Therefore, only one VCSEL is active.

Experiments were conducted with selected particles provided by "*Polysciences*" and "*Cospheric*" manufacturers. *Polybead ®* polystyrene microspheres from "*Polysciences, Inc.*" are available in sizes with nominal diameters from 50nm to 90µm, packaged in 2.5% solids (w/v) aqueous suspension. Samples were prepared with 10.00µm *Polybead®* Black Dyed Microspheres and 45.00µm *Polybead®* Microspheres suspended in deionized water and isopropanol solutions. Polyethylene microspheres from "*Cospheric*" are supplied in dry powder form. Due to the fact that these microspheres are hydrophobic, it is recommended to coat them with a non-ionic surfactant (i.e. detergent) prior to suspending in deionized water, such as *Tween 80* or *Triton X-100*. Black polyethylene (PE) microspheres of 53-63µm and 75-90µm diameter with a density (ρ) of 1.2g/cc were used. When dealing with these large size particles, concentration was finely adjusted to minimize particle sedimentation effects in the tubing and syringes.

Flow rate is related to the throughput of the system (though the critical constraints for this parameter are imposed by the response time of the imaging sensor and the electronics, since these times must ensure the detection of two consecutive microbeads) and also to the utility of the microfluidic channels in terms of useful life, i.e. the probability of avoiding clogging of the channels. Thus, selecting the proper flow rate is essential.

Adjusting the control parameters of the pumps, for the selected tubes (refer to section 7.2.2) the resulting flow rate is 10µl/min. This flow rate is applied in all the experiments. Otherwise, flow rate is indicated.

As results will demonstrate, the system is able not only to detect black-died and non-died particles of different diameters and materials, but it also distinguishes particles of different diameters and materials mixed in a liquid solution. In the quantitative results section, some of the included measurements were performed with the CMOS sensor operating in double array mode. Although finally the capabilities of this operation mode will not be fully exploited in this work, it is quite interesting to remark the benefits that may be achieved when using this configuration. Besides the ones previously commented in section 7.2.1, others could be found for example in applications for measuring the velocity of the particles flowing through the microfluidic channels.

Some of these ideas will be discussed in the conclusions and future work chapter.

7.3 Qualitative experimental results

This first section is devoted to present the set of experimental measurements performed with the aim for demonstrating the capabilities of the fabricated system in the field of particle optical detection. Microfluidic chips based on geometrical passive focusing of particles were used for these measurements (figure 7.6). Height of the channels was 100µm and the dimensions of the defined

detection window were 90µm for the width and 150µm for the length. Only a channel was filled with the sample solution, while the others remained empty.

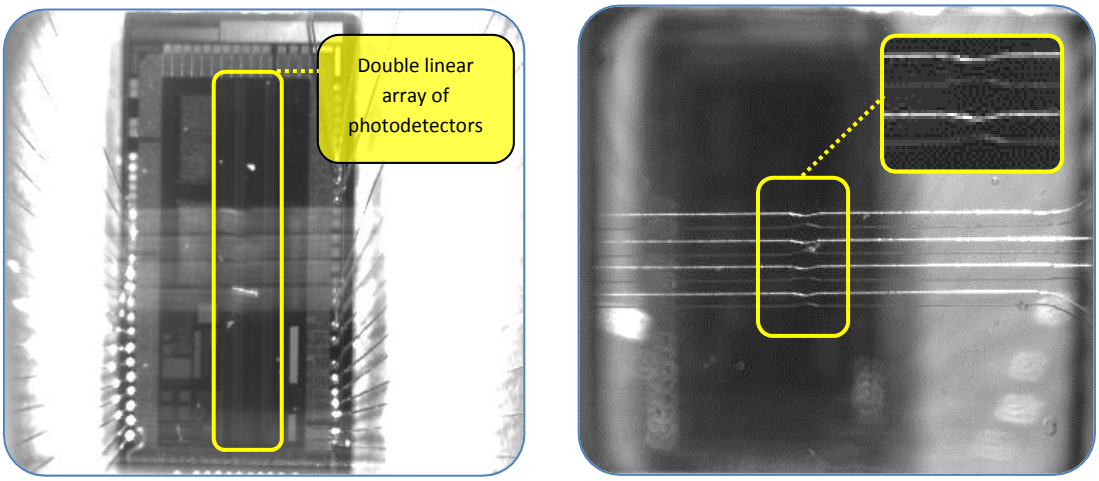

Figure 7.6: *Images captured with ALLIED external camera thanks to the beam splitter. On the left side, CMOS imaging sensor view through the microfluidic chip. The path of the four microfluidic channels can be also observed. On the right side, view of the microfluidic chip placed over the CMOS imaging sensor. Passive focusing of particles is achieved by geometrical confinement into a defined detection window, as can be appreciated in the central zone of the path of the channels.*

The following figures contain data from the results of different measurements, processed with *Matlab®* Software to create visual representations of the CMOS imaging sensor readout. Particular conditions for each experiment are described in the caption of the figure.

Figure 7.7 shows the graphical representation of the digital readout of the CMOS pixels array in an interval time of 132 seconds (800 measurements, Y-axis). The total readout (256 pixels) is zoomed in to represent only the pixels of interest (from pixel 50 to 150, X-axis), since only one VCSEL is active. The limits defined by the side walls (edges) of the channel can be observed stationary along time. The same effect could be appreciated in the simulations (refer to chapter III) due to the non-perfect orthogonal walls of the channels. The variations in the signal from low to high levels (white spikes), are caused by the beads (53-63µm diameter black polyethylene microspheres in isopropanol suspension) flowing through the channel. Some of the white spikes are not centered but displaced to the left or to the right of the detection window. This is due to the fact that passive alignment in microfluidics presents some limitations. In these cases, particles are flowing near the walls of the microfluidic channel.

In the left image of figure 7.8 the microfluidic channel is defined between pixels 25 and 35. Thus, the width of the channel is approximately 100µm (10 pixels*10µm/pixel), which corresponds to the theoretical width of the defined detection window (90µm). The 10 microns difference between both values is due to the fact that the microfluidic channel is projected over the CMOS sensor array (i.e. there is a certain air gap between the glass layer of the microfluidic chip and the sensitive area of the photodetectors). The white peaks denote the existence of a particle flowing through the detection window at the instant time of the measurement.

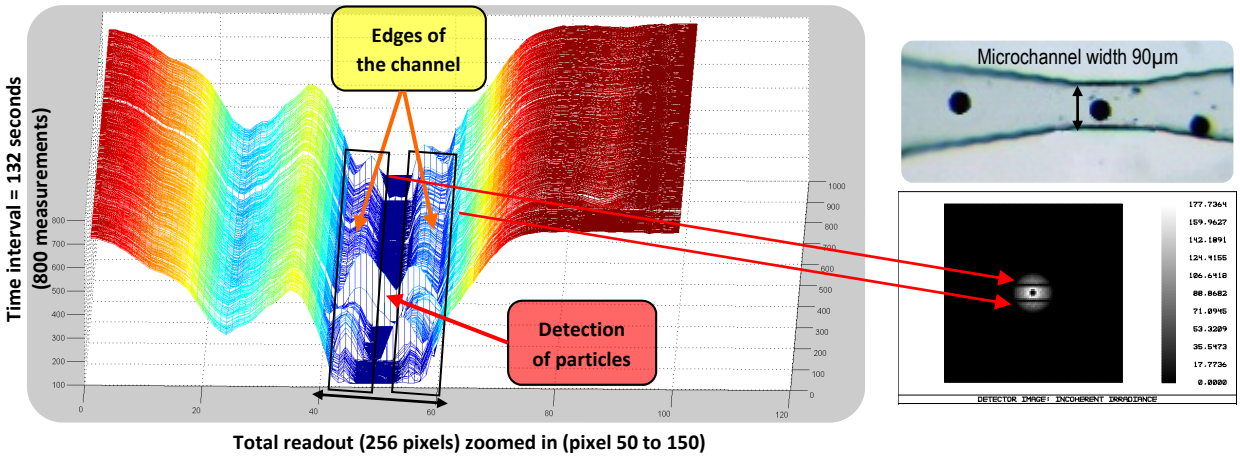

Figure 7.7: *3D graphical representation of the data from the CMOS sensor readout. Integration time set to 500µs. Sample solution with 53-63µm diameter black died polyethylene Cospheric particles. White spikes indicate the detection of particles. Right upper side: Photograph of micro beads flowing through the microfluidic channel used for the experiment. Right bottom side: ZEMAX simulation. The walls of the microfluidic channel are present in the image plane of the detector.*

The effect of stopping the flow of particles disconnecting the peristaltic pump can be observed in the image on the right side (figure 7.8). Detection of particles (white spikes) resumes when activating the pump. The relation between the spikes obtained in the processed image and the existence of flowing particles in the same time interval, confirms the capabilities of the system in the field of optical particle detection.

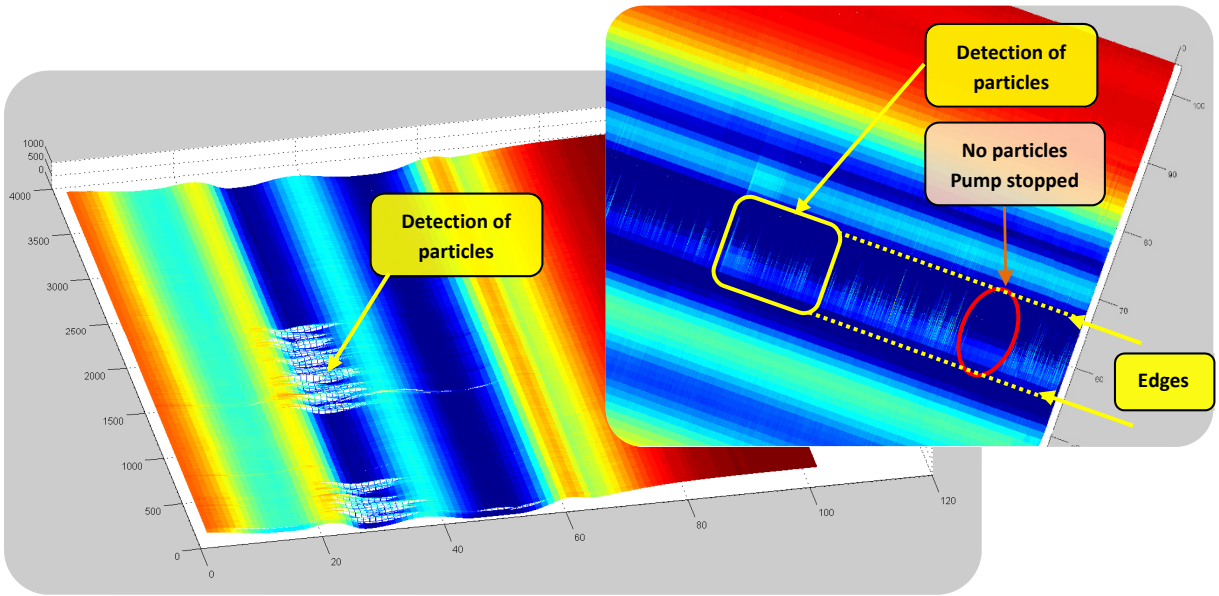

Figure 7.8: *Graphical representation of the data from the CMOS sensor readout. Pixel number is represented in X axis, while time interval - measurement number is presented in Y axis. Integration time set to 500µs. Sample solution with isopropanol and 53-63µm diameter black died polyethylene Cospheric particles. Left image: Data from 100 pixels is included. Microfluidic channel is defined between pixels 25 and 35. Right image: Effect produced by stopping the peristaltic pump, from time measurement 700 to 900 (zone indicated by the red circle). As there is no flow of particles, no detection occurs (no white spikes in the processed image). Microfluidic channel is defined between pixels 55 and 65.*

The changes in the fluids used as transport medium for particles produce a variation in the refractive index and thus, in the behaviour of light as the path followed by the light rays is modified. This effect is indeed detected by the system. As an example, in figure 7.9, CMOS image sensor collects the response of the system to three different fluids introduced in the microfluidic channel (air, water and isopropanol), until finally a solution with particles is injected. Air gaps in the microchannel are created on purpose between the changes in the liquid mediums. In this way, differences in the medium are pronounced and more evident.

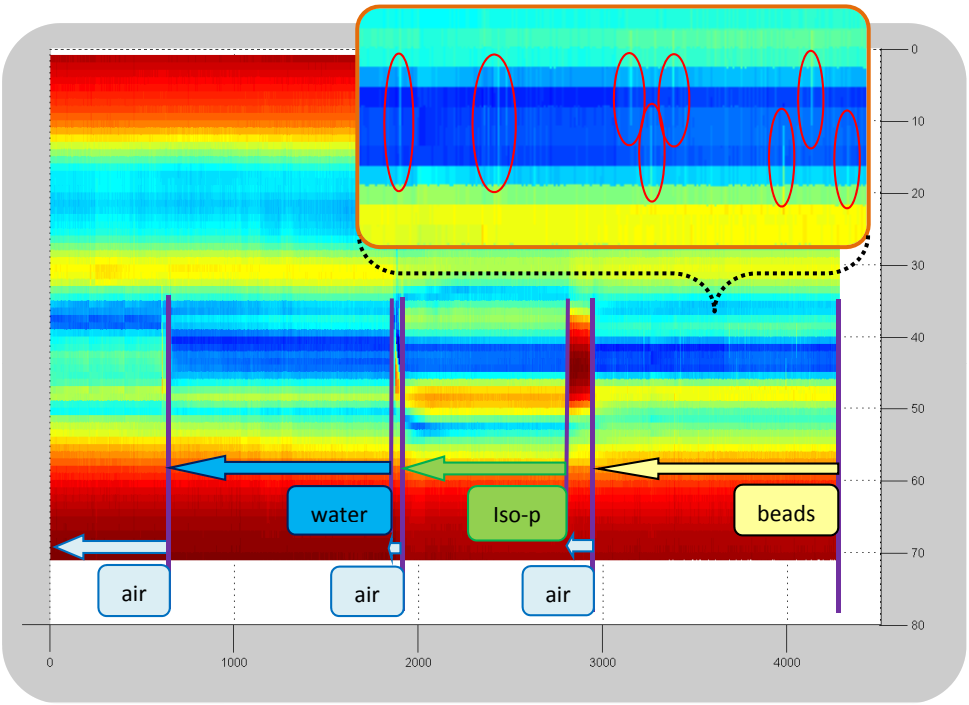

Figure 7.9: *Response of the detection system to different fluids (air, water and isopropanol) injected in the microfluidic channel. Changes in the refractive index of the medium are detected by the CMOS image sensor. A range of 70 pixels is represented (Y-axis). Finally isopropanol with microbeads of 45µm diameter were tested. Spikes corresponding to the detection of particles are marked in the upper box (zoom).*

Measurement data can be processed in order to remark the presence of peaks, removing additional information such as the referent to the side walls of the microfluidic channels (figure 7.10). Processing is as follows: data acquired when there is no particle flowing is taken as the reference measurement; this data contains information about the profile of the microfluidic channel, such as the sidewalls; this reference is subtracted from the rest of measurements, lowering the base line and remarking only the distinctive patterns. Results are shown for 45µm diameter translucent Polybead ® polystyrene microspheres (Polysciences, Inc.).

Finally, we introduce the results of applying different flow rates to a sample solution. In figure 7.11, measurements for four different flow rates (100µl/min, 50µl/min, 30µl/min and 15µl/min) are presented. In all cases, spikes indicate the detection of particles. Valid measurements begin after the detection of air bubbles, caused during the process of changing the liquid solution from simple DI water to the sample with particles. In figure 7.12, a detailed comparison between 10µl/min and 20µl/min flow rates can be observed. As expected, for a sample volume of a certain concentration, with a higher flow rate more particles are detected, since the probability of a particle flowing through the channel also increases. The detection limit is imposed by the frequency response of the electronics. Comparing

both figures, the number of detected events (white spikes in the zoomed section, marked with arrows) is larger[1] when flow rate is 20µl/min. Even when only higher white spikes in the 3D representation of the data are considered, for they correspond to particles flowing by the center of the channel.

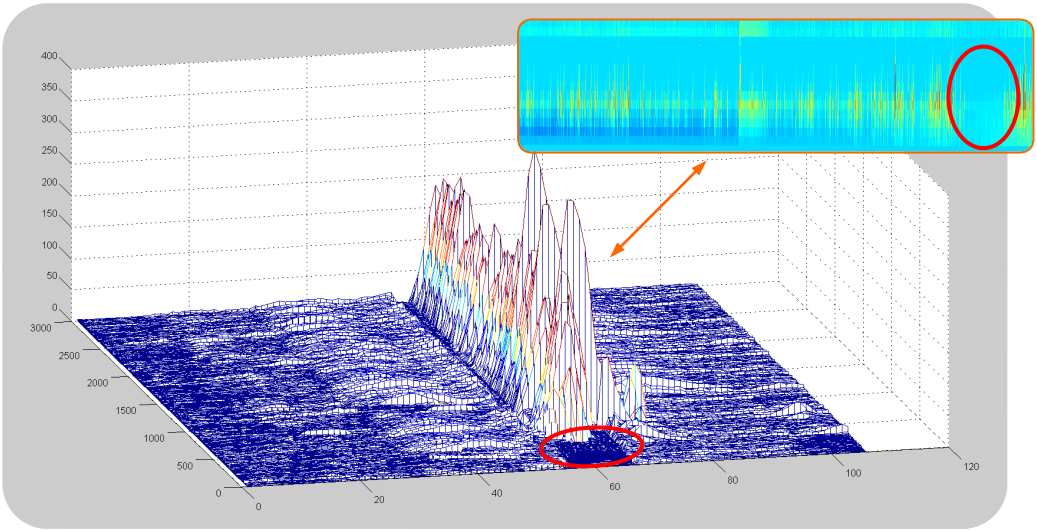

Figure 7.10: *Data can be processed to show only the presence/absence of peaks (digital value of amplitude in Z-axis). A range of 105 pixels is represented (X-axis). Time measurement in Y-axis. Microfluidic channel is defined between pixels 55 and 65. Integration time set to 500µs. At the top right corner of the image is included the linear representation of the complete sequence of measurements. In this processing, spikes corresponding to the detection of particles are presented in yellow-orange color. Red circles mark the zone with no flowing of particles.*

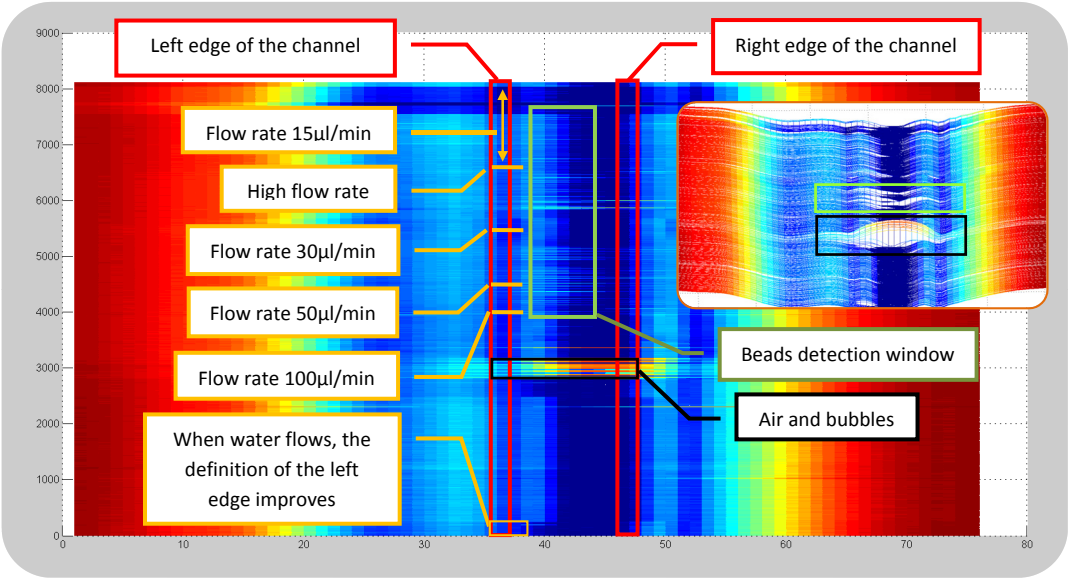

Figure 7.11: *Response of the detection system to different flow rates (100µl/min, 50µl/min,30µl/min and 15µl/min). In all cases, detection of particles is achieved (beads detection window). The bottom part of the image, on the left side, shows how after the injection of DI water into the microfluidic channel, the definition of the edges clearly improves (red rectangles). For this case, side walls correspond to pixels 37 and 47 (X-axis). Integration time was set to 300µs. On the right hand side, partial zoom with a 3D representation showing the effect of air bubbles (black square) and some spikes (green square) corresponding to the detection of particles.*

[1] Even when only higher white spikes in the 3D representation of the data are considered, for they correspond to particles flowing by the center of the channel.

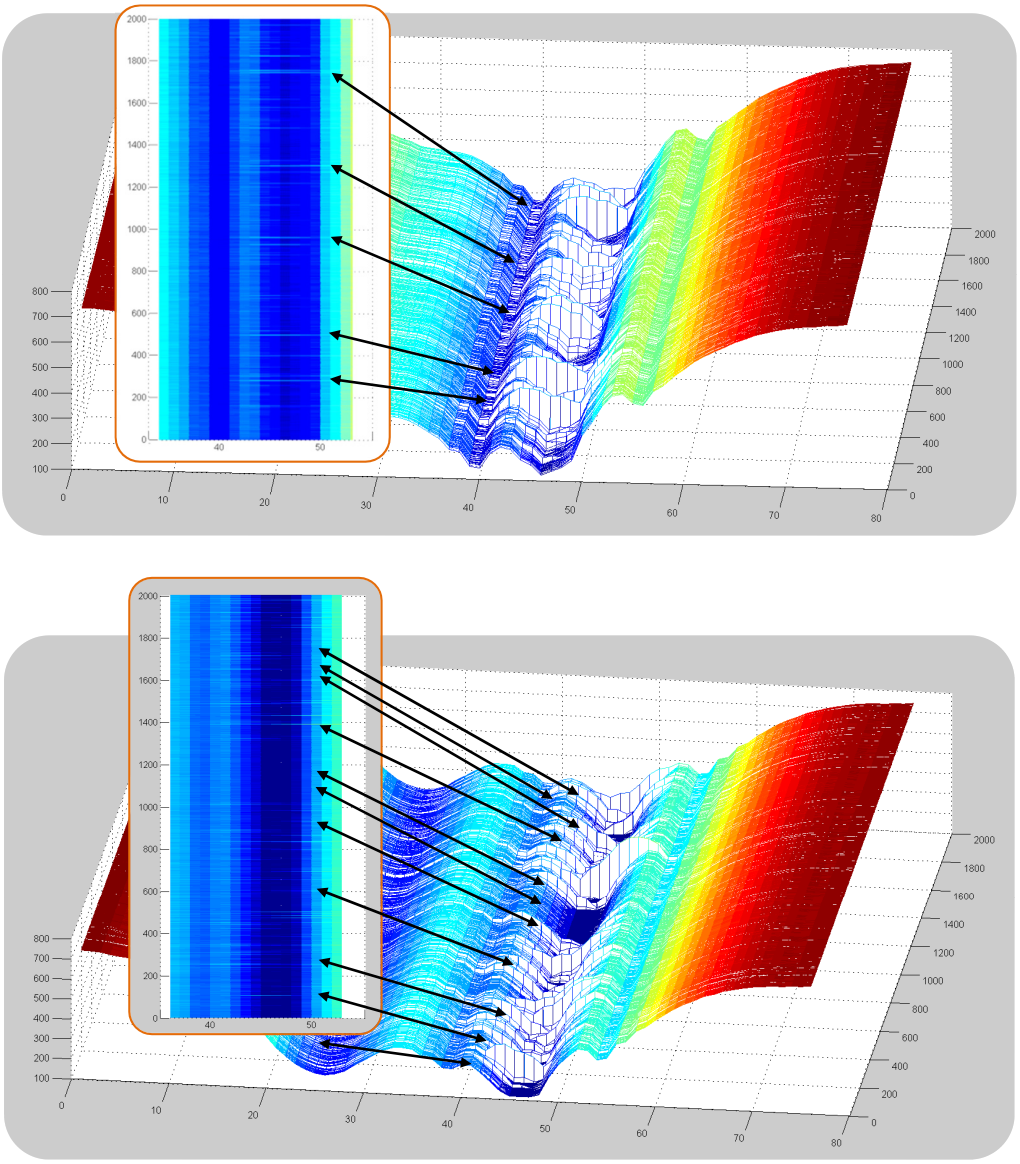

Figure 7.12: *Comparison of the responses for the detection system to 10µl/min (top) and 20µl/min (bottom) flow rates. For the 10µl/min scenario, integration time was set to 300µs. For the 20µl/min case, integration time was set to 200µs, reducing the processing time required by the electronics of the CMOS sensor, with the aim of delivering a faster response in accordance with the increase of the flow rate parameter. Therefore, amplitude of peaks is lower than in previous case. In the graph for this second case, it is possible to appreciate the existence of more detected events and even a time interval when the peristaltic pump was stopped.*

7.4 Quantitative experimental results

Once the capabilities of the system for optical particle detection have been demonstrated, this section offers a more accurate and detailed view of the results. In the figures here introduced, processed readout data from the CMOS image sensor is presented in a temporal line, as a sequential response where detected particles are represented as spikes of certain amplitude, measured in mV units. These amplitude values are directly related to the dimensions and characteristics of the particles, so it is possible to quantify the differences and identify the amount of particles of a certain group in a sample volume. Besides, some examples of measurements obtained with the double array architecture will

be presented, creating a space for comparing and discussing about the evident benefits offered by this operation mode.

For these testing, the measurement setup was completed with a commercial acquisition card from *National Instruments* (*NI USB-6251*), connected directly to the analog outputs of the CMOS sensor to perform analog to digital conversion of the signals, and managed by *NI LabVIEW SignalExpress* software. Otherwise, due to the limitations of the ADC hardware embedded in our ASIC CMOS sensor, it would not have been possible to perform the double readout and acquisition of both analog signals provided by the sensing photodetector arrays. Thanks to this acquisition data card, the limitation of a single conversion channel is surpassed, for it delivers up to 16 analog inputs of 16 bits, with a sample rate of 1.25 MS/s single-channel. This higher sample rate improves the signal processing.

Microfluidic chips with a single channel based on active alignment of particles by means of hydrodynamic focusing were chosen to work with (figure 7.13). Dimensions of the channel were 200µm width, 100µm height and 10mm length. The effective detection zone length is equivalent to the length of the photodetectors integrated in the CMOS imaging sensor (i.e. 100µm), and when working with the double array configuration, this length increases approximately up to 300µm (100µm for each photodetector plus 100µm of separation distance between the two sensing arrays). The shared focusing inlet of the microfluidic channel was filled with deionized water or isopropanol as sheath fluids, while the suspension with particles was pumped into the central sample inlet. As can be seen in the images of figure 7.13, particles travel centred along the channel.

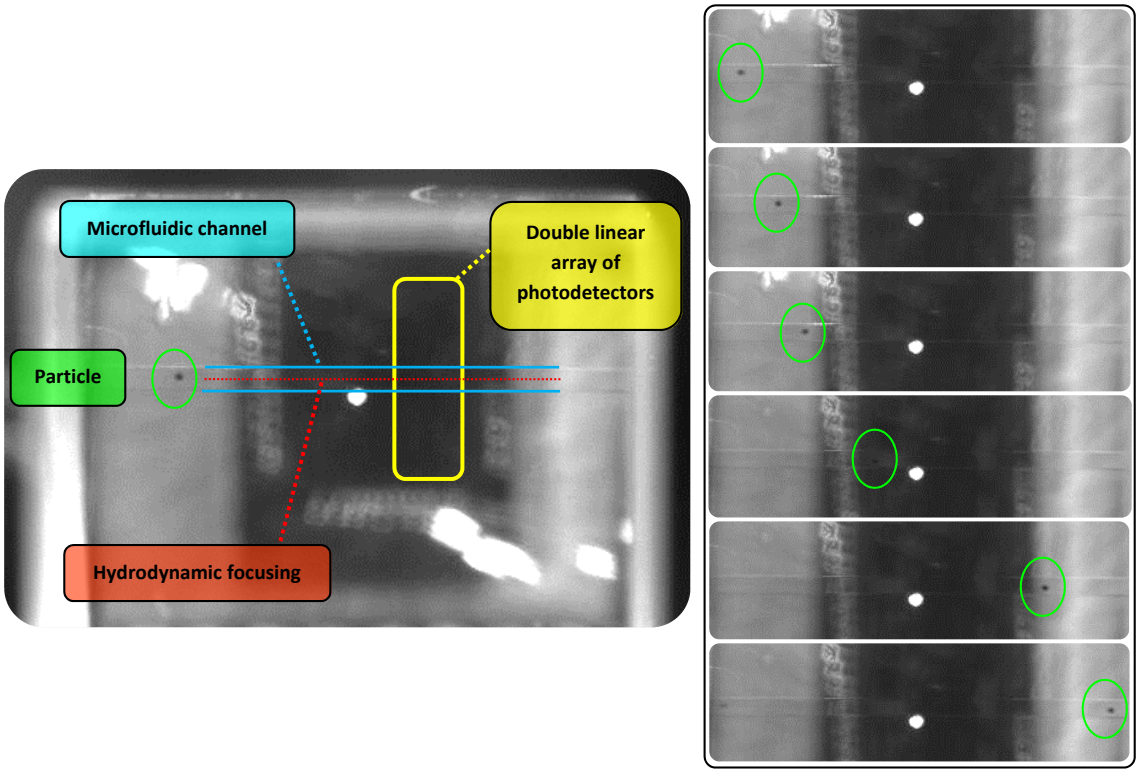

***Figure 7.13**. Images captured with the external ALLIED camera thanks to the beam splitter. Left: Real photograph of the microfluidic chip with a hydrodynamic focusing channel. Camera focal plane is on the channel. Right: Sequence of timeframe photographs showing the path travelled by a single focused particle along the channel.*

Graphs included in the following figures were obtained with Matlab ®software from the data provided by the CMOS imaging sensor.

7.4.1 Single array: temporal sequence

The effect produced by a flowing particle on the collimated light beam of a single spot, as sensed by the CMOS array, can be observed in the set of pictures gathered in figure 7.14. These images correspond to a sequence of successive reading cycles of the data delivered by the CMOS imaging array. Two dips, useful as reference for synchronising the signals in the processing phase, define the start and the end of the reading cycle (figure 7.14.a, right). In each one of the cycles, the 256 pixels are readout, and the spot of light exciting the sensor is transformed into a dip of a certain amplitude. For a concrete instant of time, the decrease in the amplitude of these dips is caused by particles.

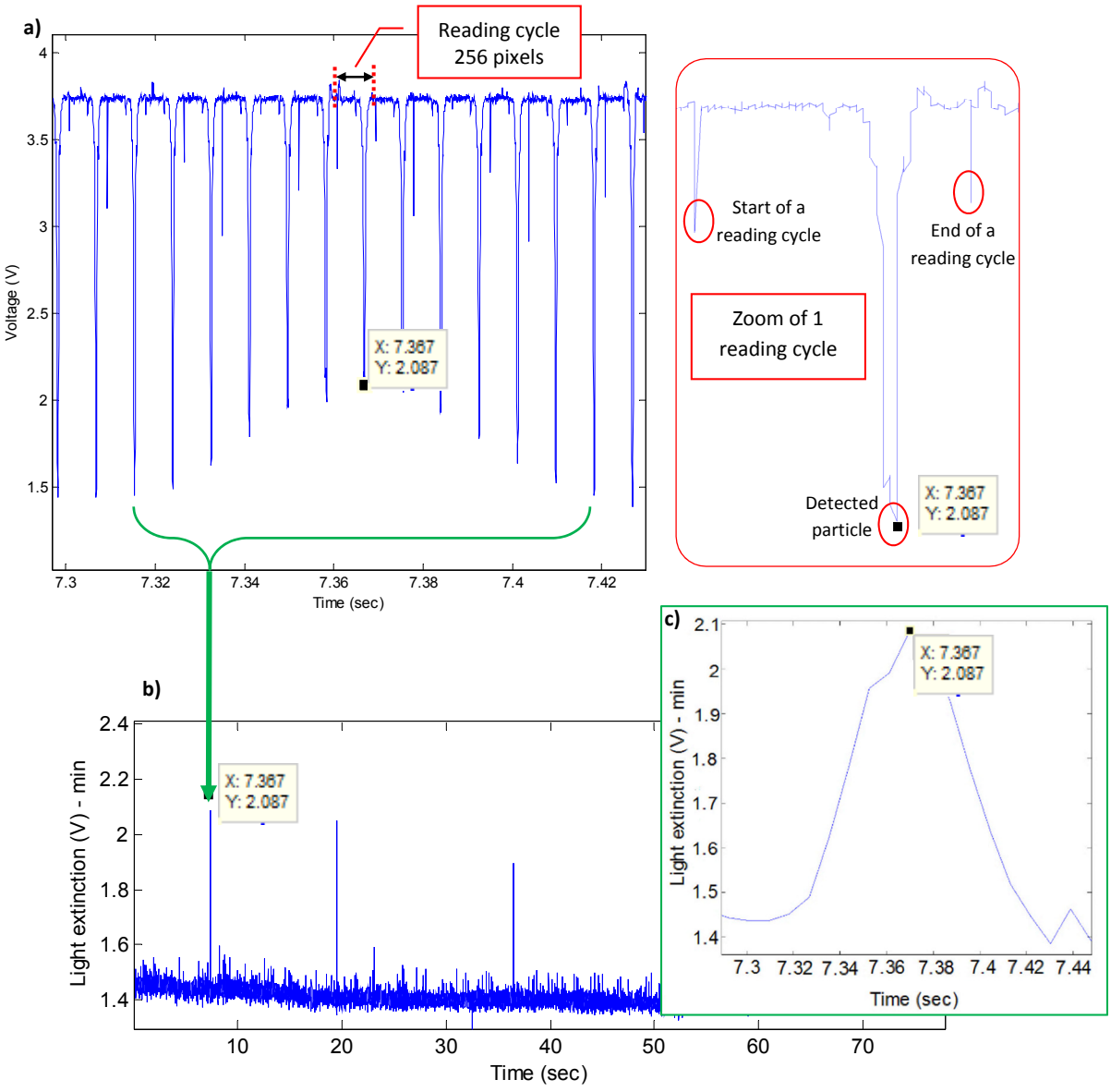

Figure 7.14: *(a) Left: Sequence of successive reading cycles of the data delivered by the CMOS imaging array. The decrease in the amplitude of these dips is caused by the particle flowing through the microfluidic channel and interfering with the collimated light beam. Sample with particles of 45µm diameter translucent Polybead ® polystyrene microspheres from "Polysciences, Inc.". Right: Zoom of one of the reading cycles of the CMOS image sensor (256 pixels). (b) Processed data. The spikes above the defined threshold correspond to the detection of a particle. (c) Zoom of one of the spikes of the processed data previous graph. The obtained peak presents a defined amplitude and width (temporal length).*

Due to high sample rate of the acquisition card, the effect of a single particle flowing through the detection window is detected multiple times (over sampling), from the initial moment in which the particle enters into the sensing zone, to the final moment in which it leaves, including the instant of time in which detection is at its maximum value (i.e. dip with the minimum amplitude).

Figure 7.14.b shows the result of processing this data, converting the sequential variations in the amplitude of the dips in a single peak of a defined amplitude and width (temporal length).

Results for a testing performed with 75-90µm diameter black died polyethylene *Cospheric* particles for 45 seconds, can be observed in figure 7.15 (next page). The sample solution was prepared to have a low concentration of particles. Thus, only four particles are detected during the testing time (four spikes can be clearly identified).

Differences in the amplitude of the spikes can be attributed to the range of diameters of the particles used for the preparation of the sample.

The two representations on the left side of the figure correspond to the same data but in the second one, a treatment based on a statistical reduction of the noise level was applied to remove this undesired effect, obtaining a clearer graph, where only the spikes are identified. In the mentioned processing, a threshold which sets the minimum amplitude value to consider a valid detection event (spike), is defined.

This threshold is statistically calculated from the results of each particular experiment and is equal to the mean of the measured values plus 3 or 4 times the standard deviation, depending on the case of study.

Images acquired with the external camera at certain instants of time (right side of the figure) prove the existing relation between the obtained spikes and the detected particles. In particular, the coloured circles distinguish two different particles and their respective spikes as detected by the CMOS double array sensor when passing through the detection window (sensitive area of the sensor).

7.4.2 Single array: several particle sizes

A number of measurements were performed with the aim of testing the detection of several samples, each one with particles of a particular dimension.

Figure 7.16 gathers information from some of these results. Microspheres *Polybead®* particles of 45µm diameter from *Polysciences* and black polyethylene (PE) microspheres of 53-63µm and 75-90µm diameter from *Cospheric* were used. CMOS imaging sensor worked in single array operation mode. In all cases, particles were successfully detected.

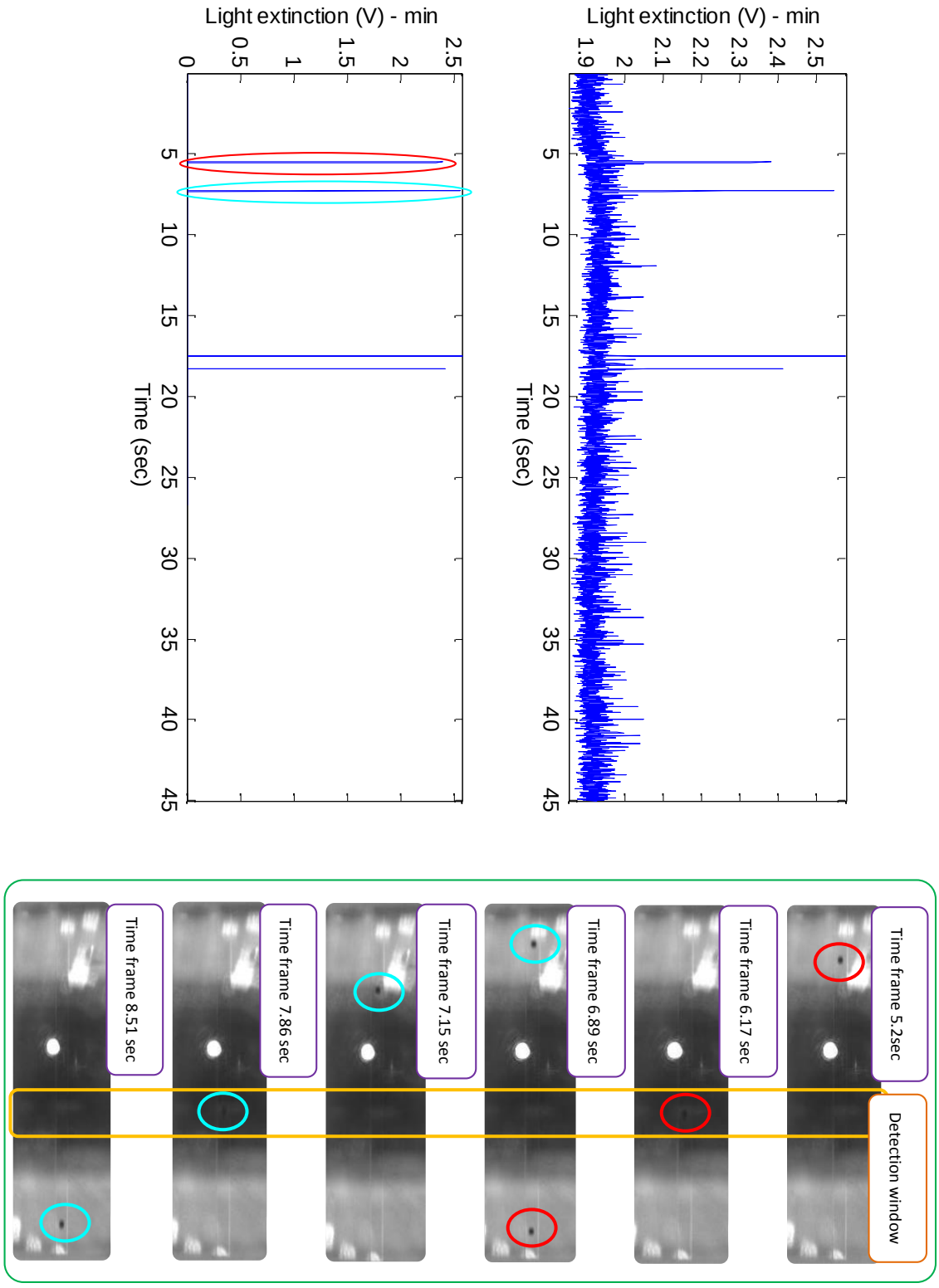

Figure 7.15. *Left: Temporal representation of the processed data corresponding to a test with a sample containing particles of 75-90µm diameter black died polyethylene Cospheric particles. Below, representation of the data after a treatment based on a statistical reduction of the noise level. Right: Images acquired with the external camera. Coloured circles mark the position of two particles at certain instants of time. Detection window of the CMOS sensor is defined by the orange rectangle.*

Regarding the variations in the amplitude of the base level signal (as can be seen in the first picture, where three “wide peaks” appear), the effect is caused by undesired movements of the flextubes in the microfluidic setup during the experiment.

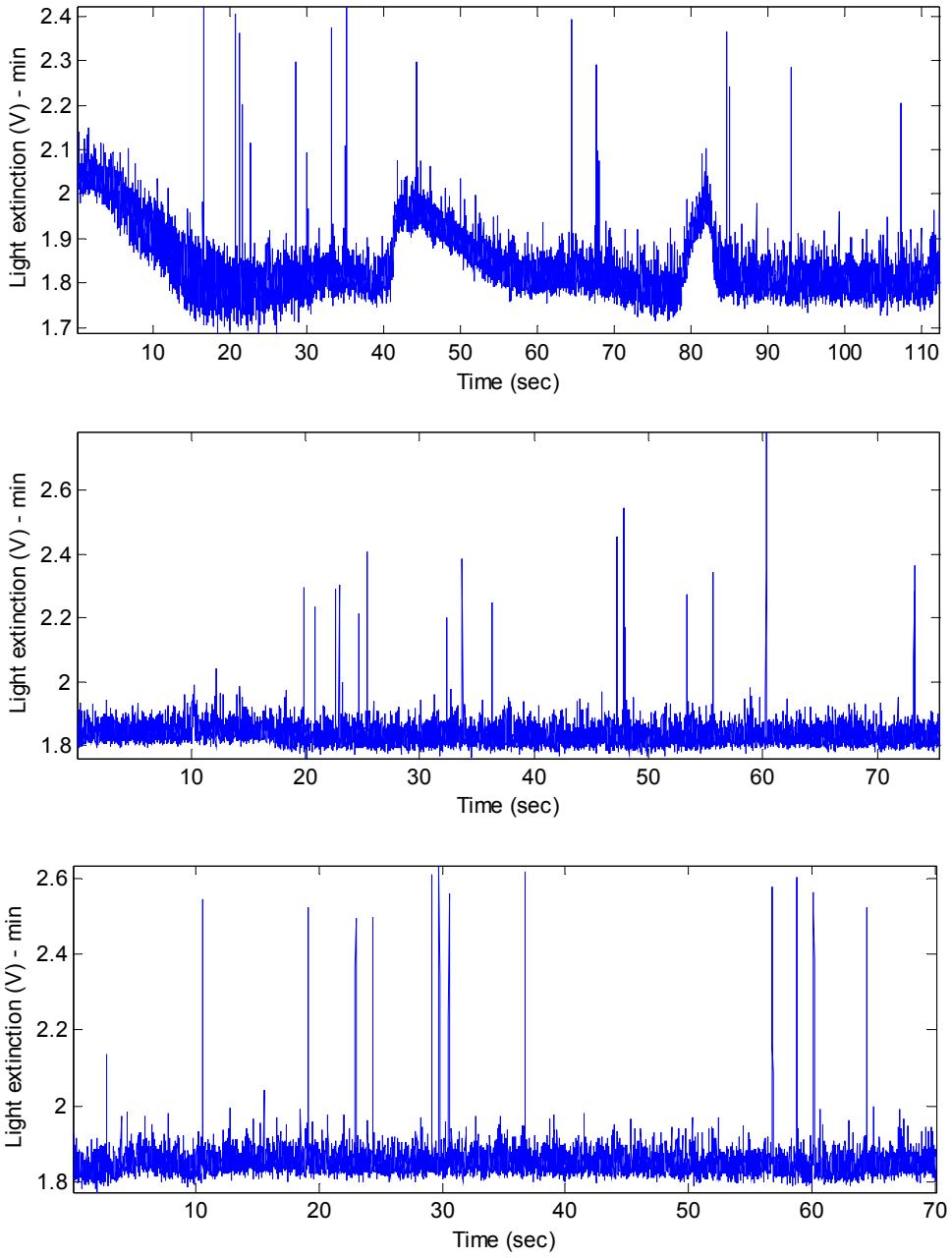

Figure 7.16: *Results of measurements with different samples. Top: sample with Polybead® particles of 45µm diameter. Middle: sample with black polyethylene particles of 53-63µm diameter. Bottom: sample with black polyethylene particles of 75-90µm diameter.*

Certainly, the amplitude values of the spikes for 75-90µm diameter particles are larger than the values for the other two studied cases. This fact, lead us to believe that the system is able to distinguish particles of several dimensions mixed in the same sample solution, as it will be demonstrated in the following subsections. The different amplitude values of the spikes within a measurement, as in the obtained results for the case with 53-63µm diameter particles, are due in part to the physical

limitations of hydrodynamic focusing (i.e. the defined central path can experiment variations caused by the peristaltic pump working cycles) and also to the presence of particles outside the expected dimension range (i.e. there is always a percentage of particles outside the standard mean values offered by manufacturer, defined by the Coefficient of variation).

Testing with black *Polybead®* microspheres particles of 10µm diameter were also performed with acceptable results (figure 7.17), though identification process is more difficult than in previous cases, for spikes present lower amplitudes. To improve signal to noise ratio of the measured signal, CMOS sensor should work in double array operation mode (as in section 7.4.4).

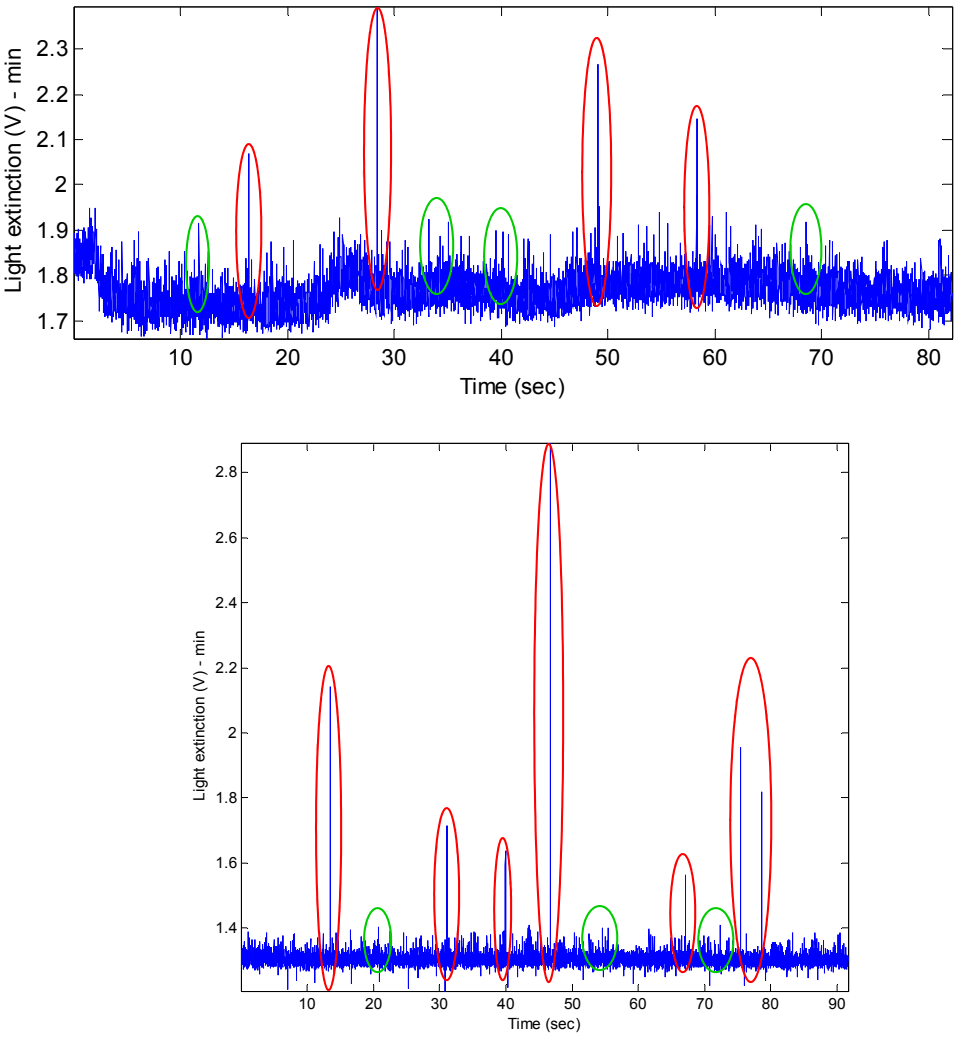

Figure 7.17: *Two examples of results with samples of black died Polybead® particles of 10µm diameter. Detected aggregates are marked with red circles, while some cases of particle detection are indicated in green colour.*

Anyway, hydrodynamic focusing of particles should be also corrected, readjusting the ratio of flow rates at the inputs of the inlets with the aim of obtaining a narrower central channel.

We also observed the apparition of large spikes in some of the experiments. Their existence is due to the formation of aggregates, i.e. groups of particles flowing together detected as a single particle of

larger dimensions. This undesired effect could be solved with a more accurate preparation of the sample solution, increasing the concentration of non-ionic surfactant component.

7.4.3 Single array: sample with mixture of particles

An interesting experiment with a sample containing a mixture of particles was carried out. The purpose of the test was to prove that the optical detection system is able to distinguish particles of different diameters mixed in a suspension.

The analysed sample included black polyethylene microspheres of 53-63µm and 75-90µm diameter. As expected and according to obtained results (figure 7.18), larger particles produce spikes of larger amplitude. These differences in the amplitude values are essential to discern and identify particles with different dimensions. Statistical information about this subject is found in section 7.4.5.

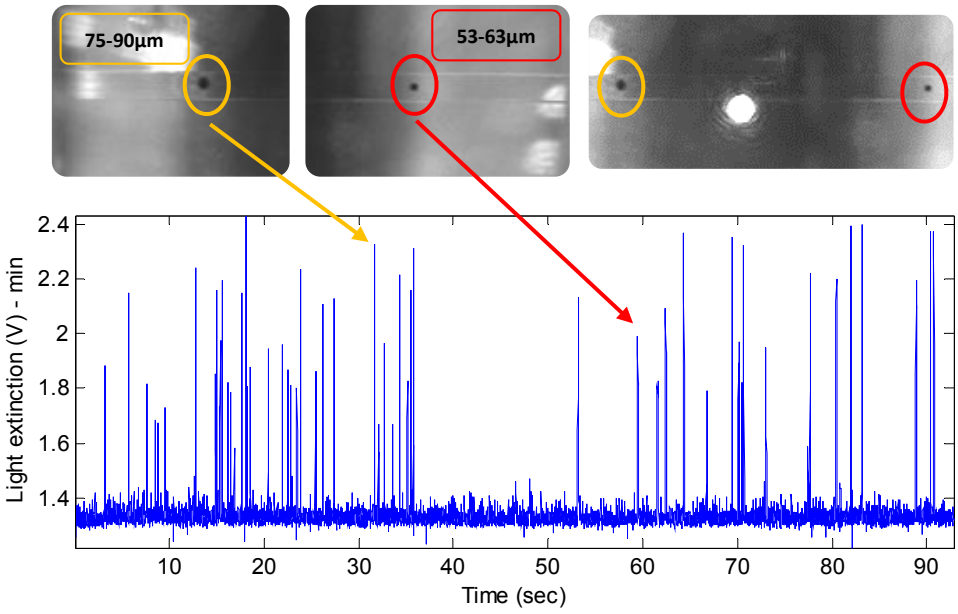

Figure 7.18: *Experimental results for a sample with a mixture of black polyethylene particles (53-63µm and 75-90µm diameters). Larger particles produce spikes of larger amplitude.*

A brief comment about the obtained results. As can be appreciated in figure 7.19, sometimes the amplitude measured for the spikes does not match the real diameter of the detected particle. In the example, a particle of 75-90µm diameter produces a spike of ≈ 500mV of amplitude, similar to the amplitude value for a 53-63µm diameter particle.

This deviation from the expected value is due to a poor hydrodynamic focusing effect[2]; i.e. particle flows outside the limits of the defined central path.

[2] Effectiveness of hydrodynamic focusing can be altered by undesired situations related with the microfluidic channel. For example, drops of pressure in one of the sheath inlets result in an unbalanced sheath fluid, which produces a deviation of particles from the central path.

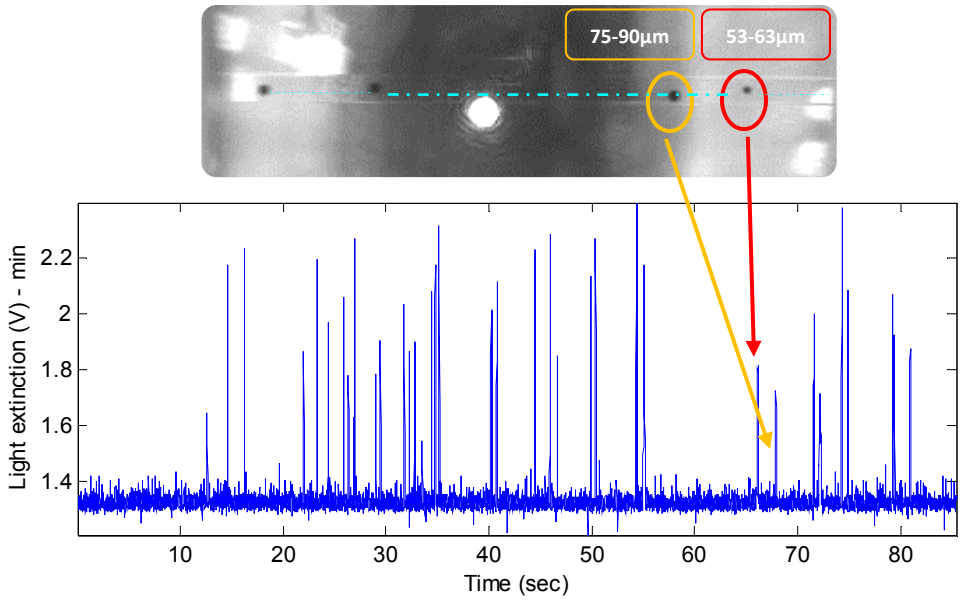

Figure 7.19: *When a particle deviates its path from the central channel defined by hydrodynamic focusing, the detected spike presents an amplitude value lower than expected. Direction of flow in upper image, from left to right.*

7.4.4 Double array sensor measurements

Two examples of CMOS image sensor working in double array operation mode are described in this subsection; the first one for a sample of 53-63µm diameter particles, and the second one for a sample with a mixture of 53-63µm (figure 7.20 top) and 75-90µm diameter particles (figure 7.20 bottom).

Particles flowing through the microfluidic chip are initially detected by the first array, and afterwards by the second. Therefore, there is a correspondence between the spikes in both arrays, which undoubtedly means that a particle was flowing at that instant of time. When this correspondence lacks, the detection of one of the arrays can be considered a false positive.

Of course, a temporal delay exists between spikes detected by each one of the arrays. It will depend on the velocity of the particles (fixed by the flow rate and the geometry of the microchannel), for the distance between sensitive arrays is constant and known (100µm).

This multiple interrogation technique (“double check”) presents advantages over a simple detection, such as the improvement of the measurements SNR, and opens a door to the possibility of exploring the determination of other interesting parameters, e.g. the velocity of the particles.

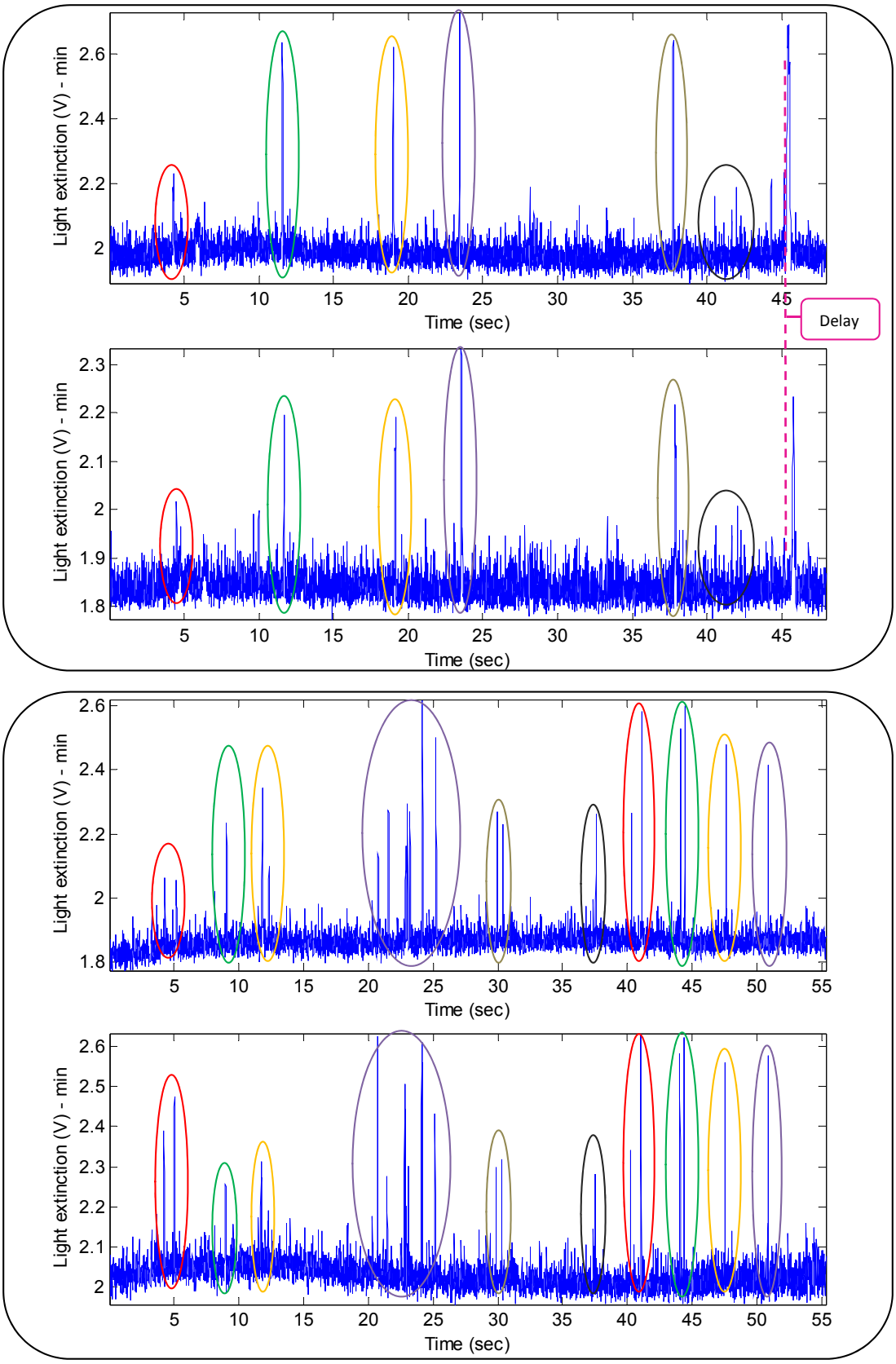

Figure 7.20: *Measurements performed with the CMOS sensor in double array operation mode for 53-63µm diameter particles (top) and a mixed sample with 53-63µm and 75-90µm (bottom) diameter particles. Correspondence of spikes in both arrays is marked with coloured circles. In top figure, dotted line indicates the delay effect between spikes.*

7.4.5 Histograms and statistical information from the results

To confirm the capability of the proposed device for discrimination of different sized particles, the results of several measurements are presented in the form of histogram analysis (figure 7.21), for particles of diameters 10µm, 45µm, 53-63µm and 75-90µm. Light extinction signal was measured individually for each group of particles in samples of low concentration. Histogram for a sample with a mixture of particles is also included (figure 7.22), to show that two different populations can be distinguished.

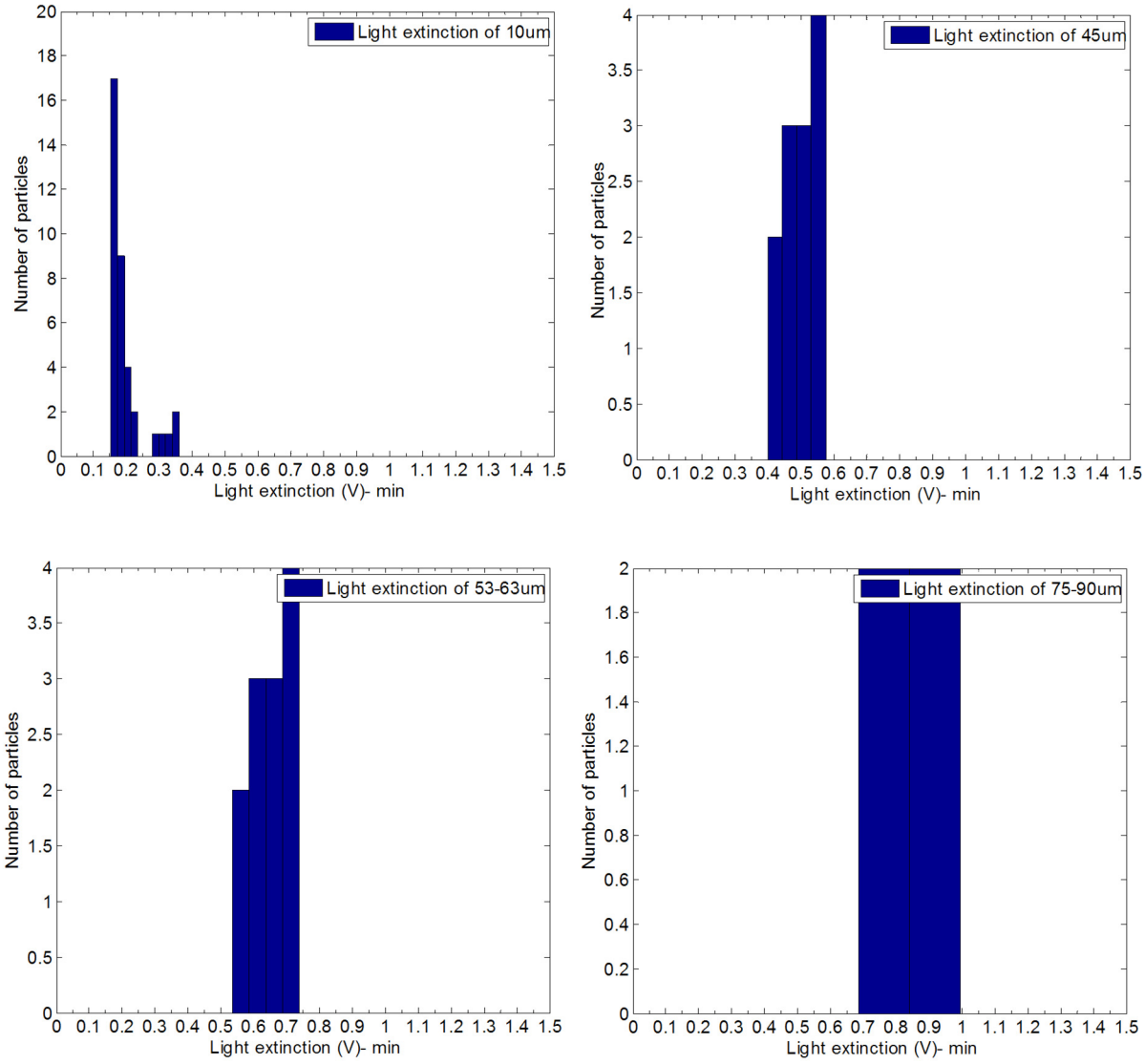

Figure 7.21: *Distributions of light extinction amplitude analysis for four different sizes of particles: 10µm (a), 45µm (b), 53-63µm (c) and 75-90µm (d) in the mean diameter. In the case of 10µm diameter particles, obtained values of amplitude above 250mV are the result of the formation of aggregates (i.e. groups of particles flowing together). To avoid the adhesion among these particles concentration of non-ionic surfactant in the solution should be readjusted.*

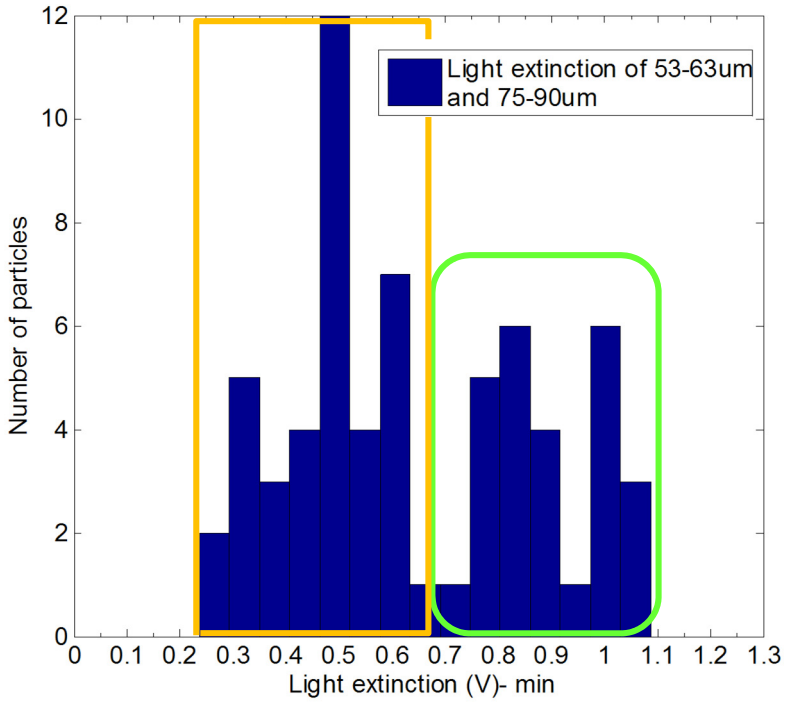

Figure 7.22: *Distribution of light extinction amplitude analysis for a sample with a mixture of particles: 53-63µm and 75-90µm in the mean diameter. Coloured boxes indicate the two different populations that can be observed (orange for 53-63µm and green for 75-90 µm).*

Histograms contain data of the number of events as a function of light extinction. The amplitude of the light intensity signal is influenced by the particle size. According to the data, statistical mean and standard deviation values are calculated for the groups of particles (table 7.1) as well as the coefficient of variation (CV), a normalized measure for the dispersion of the distribution.

Figure 7.23 presents the linear regression of light extinction mean values for the analysed particles. The graphical representation includes the minimum, maximum and mean amplitude values obtained for each group of particles. Results show that light extinction intensity is linearly proportional to particle size. In view of the results, discrimination of particles with different sizes is not only a possibility, but a reality. Mean values of light extinction signal amplitudes are well defined in differentiated ranges according to particle size, with low dispersion and excellent CV.

Table 7.1*. Statistical information from experimental distributions*

Particles diameter	Light extinction amplitude		
	Mean (mv)	Standard deviations (mV)	CV
10µm	170	0,049	0,029%
45µm	510	0,060	0,012%
53-63µm	655	0,056	0,009%
75-90µm	839	0,141	0,017%

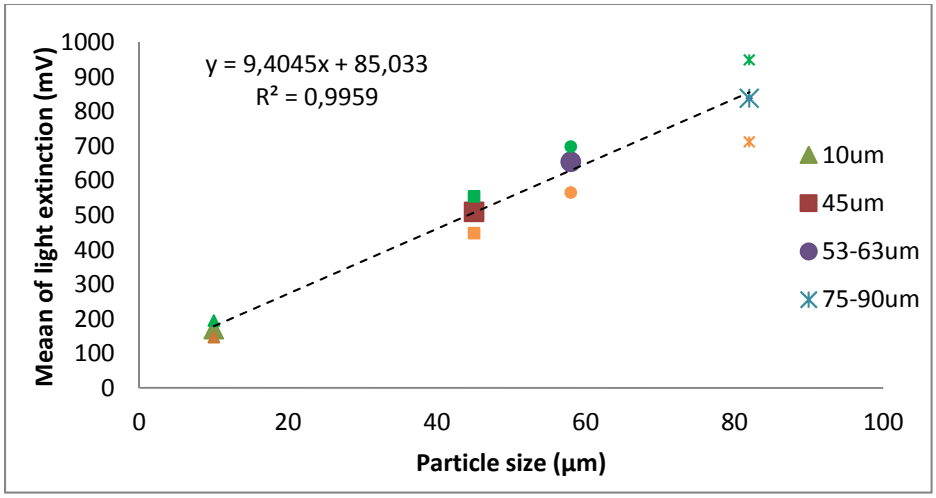

Figure 7.23: *Linear regression of the mean light extinction values for analyzed particles show the existence of a proportional relation between particle size and amplitude values. Minimum (orange) and maximum (green) values for each particle are also included.*

7.4.6 Throughput analysis

Throughput (counting rate) is an important performance index for a particle detection system, for it offers an idea of the number of cells/particles that can be analysed in a specific time period. The larger throughput value, the more particles can be analysed and the lower unit cost per test. In relation with throughput, flow rate is another factor which determines the performance of a particle detection system. With high flow rates, counting of events (detected particles) per second increases. However, special care with particle concentration in samples should be taken in order to avoid clogging of the channels.

To evaluate the efficiency of the proposed detection system, a set of experiments was developed at different flow rates: 15µl/min, 20µl/min and 30µl/min. Analysed samples contained a mixture of different size particles (53-63µm and 75-90µm diameter). Particle concentration was adjusted to avoid undesired effects. Figure 7.24 presents the results for these measurements.

With higher flow rates, an increase in the number of detected particles was observed. In the figure, 48, 65 and 88 particles were counted respectively for 15µl/min, 20µl/min and 30µl/min flow rates. Of course, concentration of particles in the prepared sample volume also influences the results, but we decided to preserve the functionality of the microfluidic chip instead of achieving the best possible counting rate causing clogging in the channels.

As shown in figure 7.25, a counting rate of 5-6 particles per second was accomplished; a value in accordance with values reported by other researchers [2].

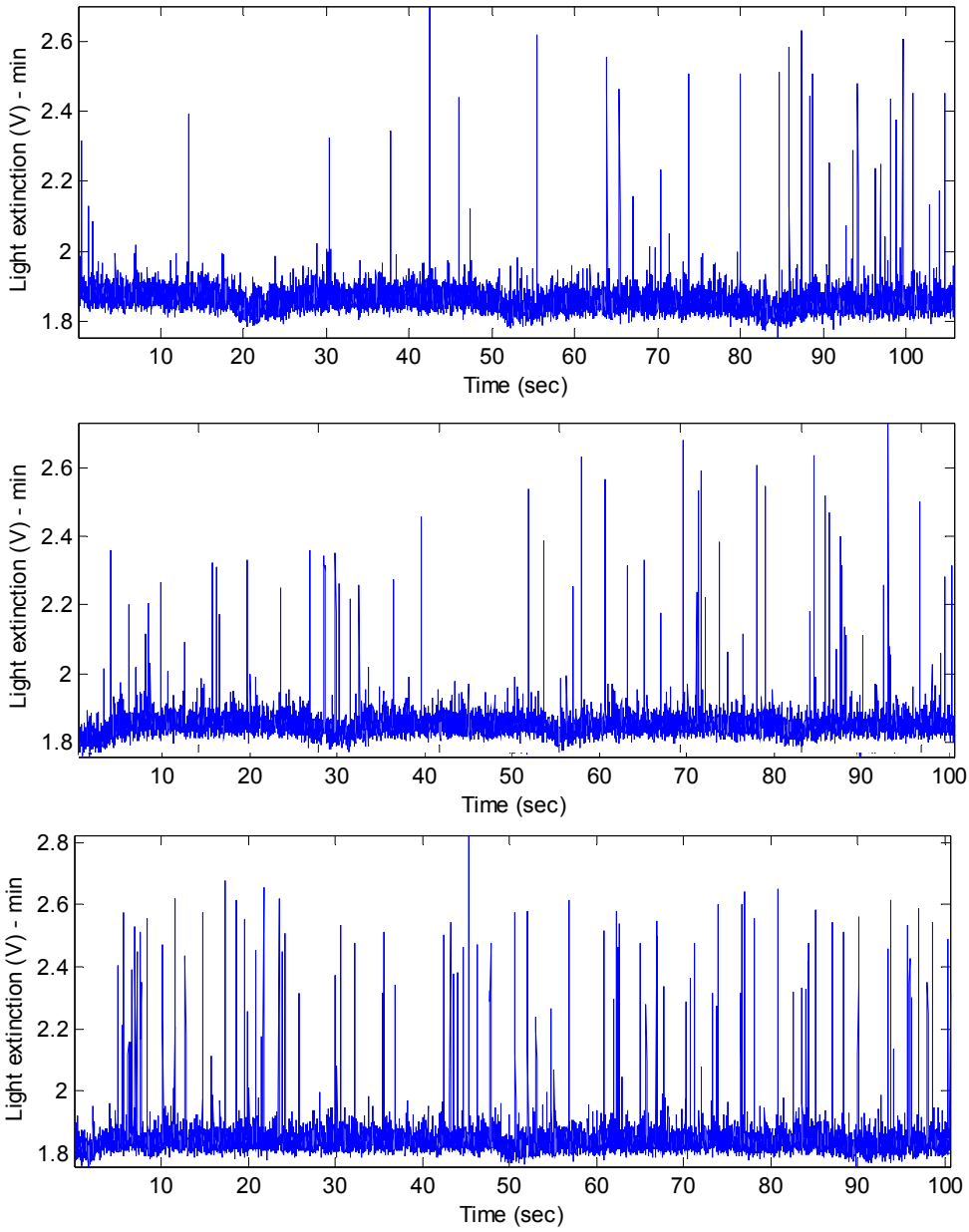

Figure 7.24: *Throughput analysis for different flow rates: 15µl/min (top), 20µl/min (middle) and 30µl/min (bottom). Analyzed samples contained a mixture of different size particles (53-63µm and 75-90µm diameter).*

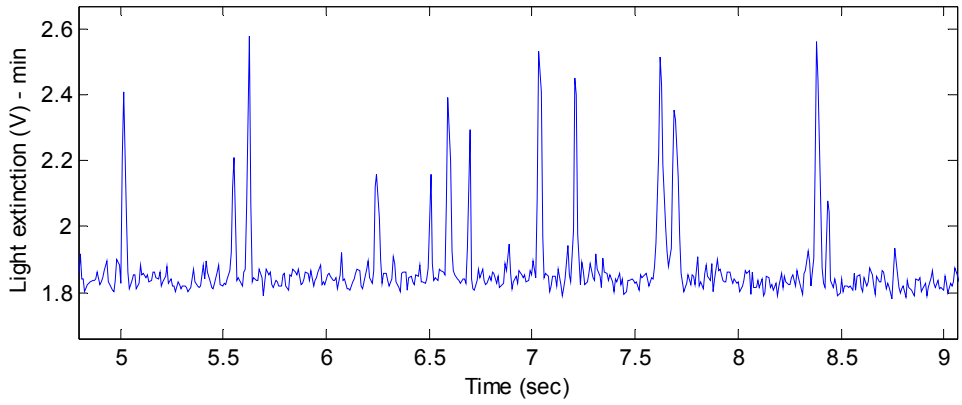

Figure 7.25: *Throughput analysis for a flow rate of 30µl/min. Zoom in the temporal line. In the example, from second 6 to second 7 a total of 5 particles are detected.*

Among the different factors that define and limit the throughput of the system, electronics of the CMOS image sensor should be also considered, as it plays an important role. A first bottle neck can be assumed by the Analog to Digital Converter (ADC) with a working frequency of 500 kHz, delivering a time of ≈5.6ms for a complete 256 pixels conversion; but the real problem is found in the times devoted to transfer the data stored in the microcontroller, which manages the sensor, to the computer, in part due to the communication protocol used (RS-232). As a result, an approximate time of 156ms is necessary to write the converted data of 256 pixels into a disk file, yielding in an effective particle detection frequency of ≈6Hz.

Besides an improvement in the performance of the external equipment (e.g. the computer), other possible solutions are to redesign the internal ADC of the sensor, improving its working frequency, or to use an enhanced external ADC connected directly to the analog outputs of the CMOS sensor; for example the one integrated in the microcontroller. However, this would not solve the question about excessive data transfer time, for the system would continue to use the same electronics in the acquisition and transfer processes. Better alternative is to take advantage of a commercial acquisition card, like the one we have used from National Instruments in the second block of our experiments. As it has been demonstrated, the powerful hardware included in these devices provide excellent results at high sampling frequencies, and the USB communication between them and hard disk drive units is more efficient than classical RS-232 protocol. We should reconsider new testing with higher concentration samples, to obtain a more reliable value of the throughput of the system, even at the risk of usability of the microfluidic chip.

In spite of all the questions here commented, it is interesting to note that the possibility of performing multiple parallel analysis could be considered as an improvement of the throughput parameter value, even when working with the electronics (the ADC embedded in the CMOS sensor) and the communication protocol (RS-232) designed for the system.

References

[1] M. Rosenauer and M. J. Vellekoop, «Characterization of a microflow cytometer with an integrated three-dimensional optofluidic lens system», *Biomicrofluidics,* nº 4, 2010.

[2] H.-T. Chen and Y.-N. Wang, «Optical microflow cytometer for particle counting, sizing and fluorescence detection», *Microfluidics and Nanofluidics,* vol. 6, Issue 4, pp. 529-537, 2009.

CHAPTER VIII: CONCLUSIONS AND FUTURE WORK

8.1 Conclusions

The present thesis is devoted to the design and fabrication of a complete optical microsystem for particle flow detection. For the conception of the proposed system, some target keys were defined: integration of the components for the final device should be optimized in order to deliver a miniaturized, portable and robust system, including on chip lenses and laser light sources, with acceptable performance values and suitable for point of care testing applications.

We have discussed about the present need for particle counters, describing the possible detection methods, their characteristics, advantages and drawbacks, to finally conclude that optical detection offers more benefits as being the approach commonly used in biological assays. Optical particle counters have been reviewed attending not only advances achieved in the fields of medicine and life sciences, but also from a practical point of view oriented to fabrication techniques.

The introduced system is based on hybrid integration of micro-optical commercial components and silicon micro-machined elements, creating an optoelectronic package, with the aim of performing optical particle detection of particles flowing through microfluidic channels.

In the **chapter of Optical Design**, two scenarios have been studied attending the restrictions imposed by selected commercial components (a linear array of four VCSELs from *ULM Photonics* in die format, and an array of fused silica microlenses from *SUSS Microoptics;* both sharing a pitch of 250 microns): collimated and focused light beams. The dimensions of the light spots obtained in the detection window (image plane of the fluidic channels) should allow detection of particles of different sizes in liquid suspensions.

With ZEMAX Radiance ® ray tracing software, simulations have been performed to analyse both cases, and results have demonstrated that, considering the physical limitations of a real implemented system, for the practical distances defined between the light sources and the detector, the collimated scenario is the best solution.

Some advanced alternatives have also been discussed with the aim of designing miniaturized and disposable chips combining self-designed microlenses and microfluidics, overcoming some of the spatial limitations of the current system. They have been defined as worthy future work lines.

In the **chapter of Hybrid Integration**, several fabrication alternatives have been discussed for the creation of a structure where commercial components can be placed, from the point of view of technologies and materials. Alignment between the microoptics and the light sources is considered a critical point.

According to the optical simulation results, two silicon pieces (base and optical spacer) have been fabricated with micromachining silicon processes at the Clean Room of the IBM-CNM-CSIC of Barcelona. Two different designs are proposed to accomplish with the optical requirement of

fe= 1.063mm (distance between the light sources and the array of microlenses). In the first, a 150µm depth single etching in the base piece for the placement of the VCSELs is combined with an optical spacer, fabricated in a non-standard wafer of 1230µm thickness. The second one, benefits from an optical spacer fabricated in a standard wafer of 1000µm thickness, with a 350µm depth double etching in the base piece. In both cases, standard wafers of 500µm thickness have been used for the base pieces.

The proposed solution benefits from passive alignment methodology: a pattern of pillars is designed on the top side of the optical spacer piece, according the geometrical properties of the commercial microlenses array. These pillars help to allocate and align the microlenses with the VCSEL light sources. Both alternative designs have been fabricated. Effects on the radius of the spots due to tolerances during fabrication have been discussed.

Assembly and packaging of the components has been accomplished. Optical testing have demonstrated the effectiveness of the collimated scenario with a minimum radius of 124µm in the range of 3 to 9mm (distance between VCSELs and rear detector), that increases up to 166µm at 2cm. From 1 to 3cm, divergence in the light beam increases only in 0.234°. Experimental results are in accordance with simulations.

The **chapter devoted to Microfluidics**, describes the fabrication process of the microfluidic chips where liquid suspensions with particles will be injected. In the final design, several parallel channels separated 250 microns are included in a single chip.

For their optical detection, particles need to be singly aligned when flowing through the defined detection windows. Several designs are presented to discuss about particle passive or active focusing mechanisms. A passive focusing design is presented based on a geometrical feature: a funnel. An active focusing design is also developed based on 2D hydrodynamic focusing. The relation of flow rates in the inlets (the sample and the sheath fluid inlets) define the width of the central path where the particles flow.

Microfluidic channels have been successfully fabricated with soft lithography and rapid prototyping techniques. SU-8 masters are replicated on PDMS. PDMS slabs are bonded to glass substrates by means of plasma cleaner. Experiments demonstrate the functionality of both designs in the focusing and alignment of particles.

In the **chapter for the CMOS photodetectors array,** the full-custom designed CMOS ASIC included in the detection system as the optical sensor, is introduced. The sensor contains not only a double linear array of 256 pixels but also other electronic circuitry such as control logic, 10 bits resolution ADC and a differentiator structure. Control logic runs the pixels readout process, sequentially selecting them and delivering their signal to the output of the array.

The architecture of each one of the pixels is based on a PN junction photodetector of dimensions 10x100 microns, and a set of transistors that control the phases of the detection process (Reset, Integration and Hold). The light sensed is converted into an electrical signal by means of discharging the reference voltage saved in a capacitor (“analog memory” effect). The discharge takes place during

the defined “integration time”. The area for the photodiodes is defined to offer good resolution (10 microns width) and good performance in terms of sensitivity to the variations of light intensity (100 microns length). The length of the sensor (= 3mm) is a plus for it allows multiple parallel detections. The IC has been fabricated in 0.35microns AMS opto technology.

Characterization of the pixels and the double linear array is performed, delivering acceptable results for sensitivity (6.09V/lux.s), spectral response, dark current (0.393fA/μm^2) and fixed pattern noise (74mV).

Finally, testing were carried out to study the response of the sensor to the VCSEL laser emitting sources of the fabricated optoelectronic package. Each one of the light sources delivers a single spot, identified by the sensor as a dip in the output signal. Integration time parameter improves the response in the case of low light levels.

Digital conversion and differentiator structure were also tested. The differentiator structure would represent an improvement in the execution time of each complete reading cycle of an array. It has been demonstrated that the structure delivers two peaks that indicate the extreme positions of the range of pixels excited by a laser source. However, the differentiator should be redesigned for a better response.

Finally, **the chapter about Experimental results** deals with the optical detection of particles. Thanks to the designed architecture, with more than one single VCSEL light source integrated into the optoelectronic package, multiple measurements can be performed simultaneously in parallel microfluidic channels. We have proven not only that the system provides four collimated light beams, but also that these light beams are detected by the CMOS image sensor. Experimental captures from the sensor demonstrate that the spots are respectful with the physical pitch of the VCSEL light sources (250µm). Unfortunately, no results about detection of particles can be presented in that sense, due to restrictions in the number of components for the microfluidic circuit.

Microfluidic chips based on passive alignment of particles are suitable for counting but these chips are not good enough to distinguish and identify particles with different diameters in a mixed sample solution. Maybe with a more accurate and complex processing of the data, this could be solved.

On the other hand, microfluidic chips based on active alignment hydrodynamic focusing are limited not only to count particles but also to determine their dimensions, thanks to the fact that particles flow through the detection window following a defined and restricted path, which means that exciting light conditions are constant for all the sample volume during the measuring process. Nevertheless, the number of inlets for channel increases, and managing the setup become more complex.

When hydrodynamic focusing does not ensure constant focusing (e.g. in particles of large size), some deviations can be observed in the results. Though particles are indeed detected, amplitude of spikes does not correspond to real dimensions.

The optical counter system is able to detect particles of different dimensions flowing through a microfluidic channel, and also to distinguish them when mixed in a sample solution. Results

demonstrate that detection and discrimination of particles is possible. Tests with 10µm, 45µm, 53-63µm and 75-90µm diameter particles confirm it. A linear relation between diameter of particles and voltage signal is established. However, measurements with 10µm diameter particles could be improved. Samples should be prepared adjusting the concentration of non-ionic surfactant component to avoid the formation of aggregates, and hydrodynamic focusing corrected.

The system also presents acceptable performance values when compared with other integrated devices in the academic field. Throughput of 5-6 particles per second is achieved though we believe the rate could be higher with some adjustments in the concentration of the samples.

Double array operation mode for the CMOS imaging sensor allows to improve the SNR of the system, as it performs a double check of the sample discarding false positives in the detection of particles. This operation mode is carried out without any special setup configuration.

To improve the detection sensitivity of the system, measurements should be performed in controlled environments with optimum working conditions, e.g. avoiding interferences of ambient light. Surely performance parameters would be better. Considering that the presented results were obtained in an open testing setup (ambient temperature and light conditions), the system proves to deliver satisfying results, which leads us to believe that it could be the first step in the way to create an alternative to present systems intended for point of care applications in environments with non-standard or controlled conditions.

Though in theory it is possible to perform fluorescent measurements with the system, still it has to be empirically proven. Hopefully, some results based on this future work line will demonstrate it.

8.2 Future Work

To continue with the work developed in this thesis, some future researching lines have been defined.

- **Multiple measurements:**

To demonstrate the ability of the presented system for the simultaneous detection of particles in parallel microfluidic channels, the external equipment of the microfluidics stage should be improved with an advanced peristaltic pump able to manage several channels.

- **Fluorescence measurements:**

Fluorescence measurements have been proposed in previous chapters as a feasible possibility, closer to reality when fabrication of VCSELs emitting at different wavelengths other than Near Infra-Red is emerging. Fluorescence measurements are also related to the choice of fluorochromes to functionalize the particles. Usually, fluorochromes in the market need to be excited with wavelengths in the visible spectrum range.

The presented optoelectronic package would serve to integrate this VCSELs with microoptics. Surely, the geometrical and optical parameters should be readjusted to work with the focused scenario.

As a proof of principle of the feasibility of the proposal, we have integrated a single VCSEL (from *Lasercomponents*) emitting at 670nm red visible wavelength in one of the fabricated silicon structures (figure 8.1).

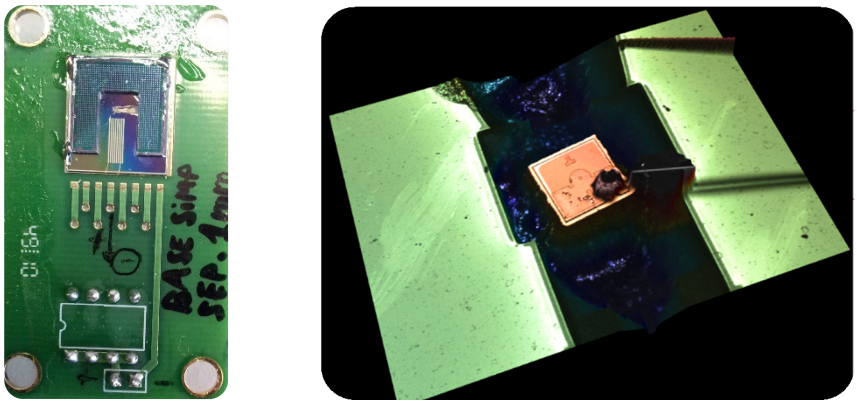

***Figure 8.1**. Left: Integration of a red emitting VCSEL in one of the silicon structures developed in this thesis. Right: Confocal photograph of the VCSEL bonded in the cavity defined in the base piece.*

In a further step, the combination of microfluidic chips with multiple parallel channels, with several VCSEL light sources emitting at different wavelengths, would allow to perform simultaneous measurements based for example on light obscuration and fluorescence, delivering a complete optical characterization system. This is undoubtedly the most ambitious proposal for future work.

- **Self-designed microlenses**

Sef-designed microlenses has been explored in the optical design chapter as a possible solution to achieve a more miniaturized system, even in combination with microfluidics. The aim in this research line would be the fabrication of disposable PDMS devices combining both elements.

In this line, we have started to replicate lenses on PDMS, and also to study the fabrication process of self-designed microlenses in polymers by means of thermal reflow (figure 8.2).

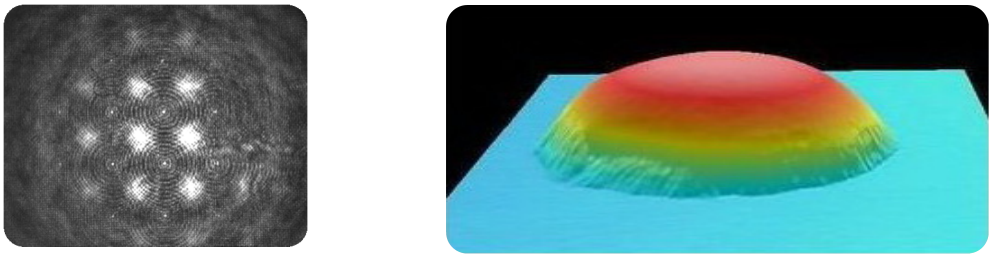

***Figure 8.2**. Left: PDMS replicated microlenses excited with VCSELs. Right: 3D image of a microlens fabricated in the clean room environment by means of thermal reflow. Diameter of 175µm. Images printed with permission of Farhan Badar (master thesis supervised by Dr. Moreno and I.Bernat).*

A more detailed study in the field of optics should be carried out. For example with ZEMAX Radiance ® simulator performing Montecarlo analysis for tolerances in the fabrication of microlenses.

- **Measurement of the velocity of particles**

As it has been reported, measurement of the velocity of particles is possible. Unlike in previous systems based on sensing the pass of particles through two lighted points, in our proposal we would take

advantage of the linear double array configuration. Knowing the distance between the two arrays of photodetectors (200µm), and the time elapsed between the two spikes produced by the same particle in each one of the arrays, velocity could be calculated.

- **Study of the possibility of scattering measurements**

In light scattering Optical Particle Counters, depending on the particle size range of interest, scattered light needs to be collected at large (from 15° and above for particles as small as 50nm) or small (from 4° to 15° for particles of 0.5-20µm) scattering angles, and thus, optics is often designed for one of these cases.

In the work developed for this thesis a question is raised about the possibility of the fabricated system to perform scattering light measurements. Taking profit of the total length of the optical detector (approximately 3mm length) and the defined pitch of the pixels (10microns), it would be possible in theory to perform scattering light measurements. A detailed study should be carried out in order to destine resources or to discard the measurement of forward scattered light (FSC) at narrow angles (e.g. 0.5° – 5°) or side scattered light (SSC) at wider angles (e.g. 20°- 25°).

- **Enhanced CMOS ASIC**

A redesign of the CMOS ASIC could also be developed in order to obtain an enhanced sensor with better performance values. This working line should include for example a faster Analog to Digital Converter.

RESUMEN EN CASTELLANO:

Desarrollo completo de un microsistema óptico para la detección de flujo de partículas

Introducción y objetivo de la tesis

Esta tesis doctoral resume el trabajo realizado en el Departamento de Electrónica de la Facultad de Física en la Universidad de Barcelona. El objetivo de la misma se centra en el diseño y fabricación de un microsistema óptico basado en la integración híbrida de componentes comerciales y piezas obtenidas mediante procesos de micromecanizado en silicio, destinado a la detección óptica de micropartículas en chips de microfluídica. Todo ello teniendo como principales metas la miniaturización y la integración de todos los componentes para obtener un sistema robusto, portátil y adecuado a las aplicaciones de tipo "*point of care*".

Actualmente existen varios métodos de detección y caracterización de partículas que utilizan diferentes mecanismos de sensado: desde los más clásicos (e.g. usando tamices o técnicas de sedimentación de partículas), hasta los más frecuentes, como los métodos de sensado eléctrico (e.g. los contadores *Coulter*) y sensado óptico (e.g. citometría óptica de flujo y los contadores ópticos de partículas), pasando por otros basados en técnicas cromatográficas o de análisis acústico. A modo de resumen acerca de los rangos de dimensiones de las partículas que pueden ser detectadas por de cada uno de ellos, puede consultarse la figura 1. En el mercado encontramos dispositivos destinados al ámbito industrial con funcionalidades adaptadas y desarrolladas específicamente de acuerdo a unas determinadas condiciones de trabajo. Aunque generalmente tales instrumentos son voluminosos, también es posible hallar dispositivos portátiles ("*handheld*") cuya utilidad se centra principalmente en la detección de partículas en aire. Recientemente, incluso algunos de estos dispositivos "de mano", como por ejemplo el "*Scepter*" de la empresa "*Millipore*", utilizan el principio *Coulter* de sensado eléctrico para la detección de partículas y células en suspensiones líquidas, midiendo los cambios que la circulación de partículas producen en el parámetro impedancia.

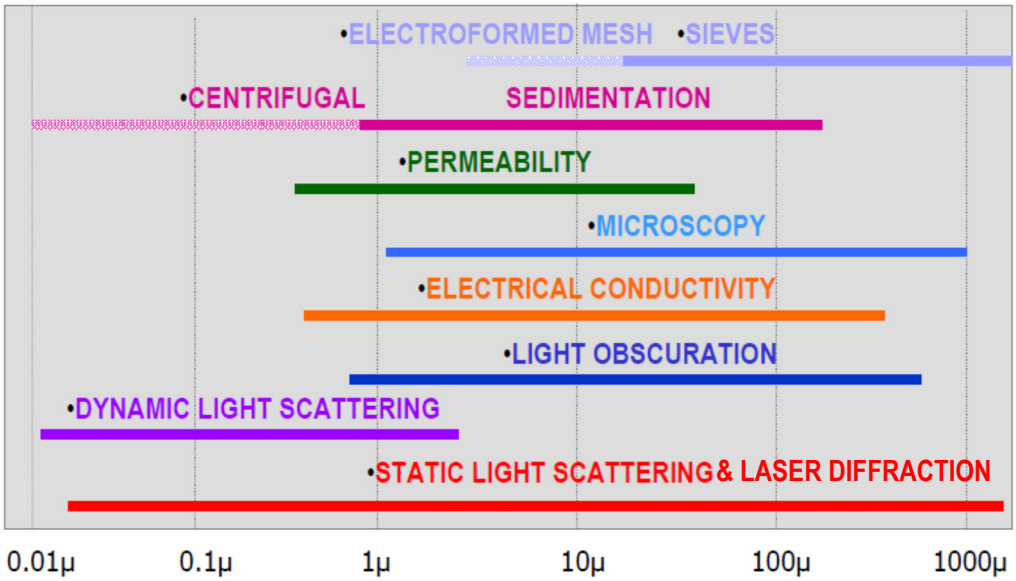

Figura 1. *Rangos de tamaño según la técnica usada. Reproducido con el permiso de "Horiba Company".*

En nuestro caso, decidimos centrarnos en los métodos de detección óptica de partículas, por ser los más afines a las medidas utilizadas en ensayos biológicos y cuyo ejemplo paradigmático es el citómetro de flujo. Las señales obtenidas como respuesta a la excitación luminosa de una partícula o célula (figura 2, izquierda) ofrecen información relativa no sólo a sus dimensiones (ausencia o extinción de luz), sino también a las características de su superficie y su granularidad (medidas de *scattering*) e incluso a la existencia de determinadas reacciones bioquímicas (medidas de fluorescencia). Actualmente existe un nicho en este campo, que está siendo explotado por numerosos grupos de trabajo con el objetivo de desarrollar sistemas ópticos de detección de partículas. Nuestro campo concreto serán los contadores ópticos de partículas basados en la detección de ausencia de luz (figura 2, derecha).

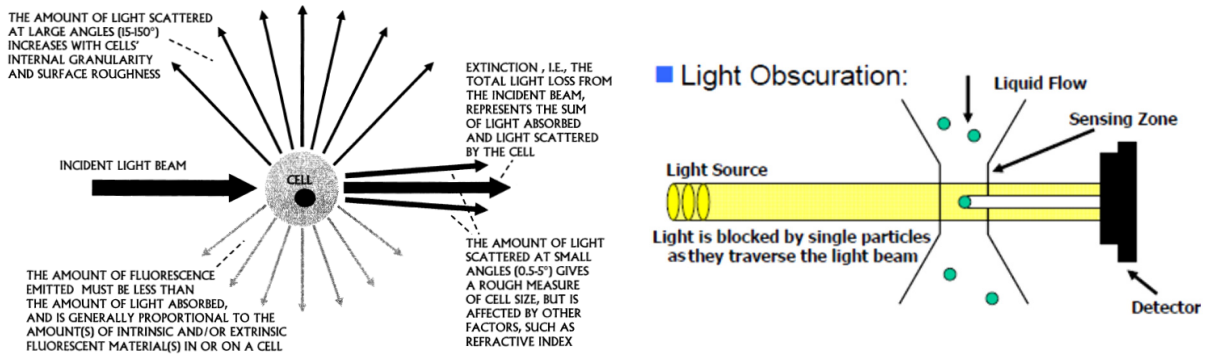

Figura 2. *Izquierda: Información que puede obtenerse acerca de una partícula o célula en respuesta a una excitación luminosa. Derecha: Esquema conceptual de un contador de partículas basado en la ausencia/extinción de luz.*

El sistema que presentamos parte de la existencia previa de varias patentes y artículos donde se abordan estos contadores desde la perspectiva de la integración y miniaturización de sus componentes, siguiendo los criterios que se aplican en los *Lab-on-a-chip* y los *Micro-total-analysis-systems*. El esquema general puede verse en la figura 3. Consta de un encapsulado optoelectrónico, un chip de microfluídica y un sensor óptico.

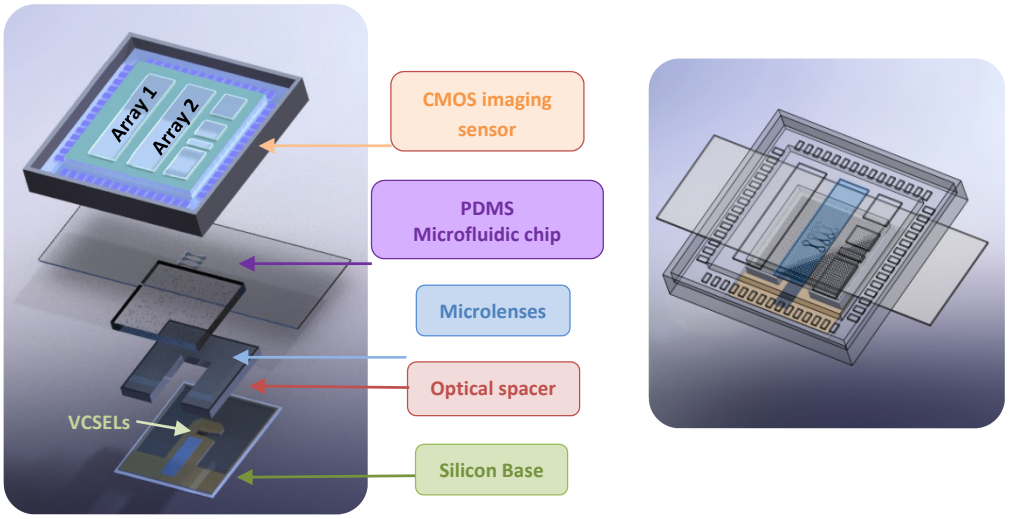

Figura 3: *Esquema general del Sistema de detección óptica de partículas. Las dos piezas fabricadas en silicio (base y separador óptico), los VCSELs y la matriz de microlentes componen el encapsulado optoelectrónico. El chip de microfluídica, fabricado en PDMS y vidrio, contiene 4 microcanales. Este chip se coloca entre el encapsulado y el sensor óptico CMOS.*

El detalle del encapsulado optoelectrónico se presenta en la figura 4. Dicho encapsulado contendrá un array de 4 VCSELs (láseres con emisión vertical) emitiendo en infrarrojo a 850nm, fabricado por *ULM Photonics*, y una matriz de microlentes de la empresa *SUSS MicroOptics* fabricada en *fused silica*.

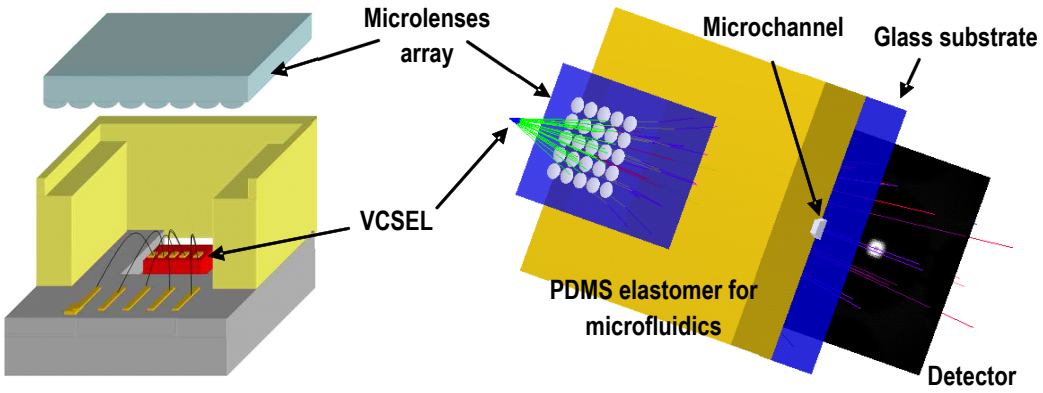

Figura 4. *Izquierda: Esquema del encapsulado optoelectrónico que incluye la base fabricada en silicio con los VCSELs integrados (color rojo) y los electrodos, la matriz de microlentes y el separador óptico en forma de "U" (color amarillo), fabricado también en silicio, que controla la distancia entre las microlentes y los VCSELs. Derecha: Diseño conceptual del sistema completo para la detección óptica de partículas, con el chip de microfluídica y el detector óptico.*

Ambos componentes comerciales se colocarán en la estructura formada por dos piezas fabricadas en silicio, llamadas base y separador óptico, en unas posiciones concretas determinadas mediante simulaciones ópticas. El objetivo es generar unos spots laser en zonas definidas de los canales de microfluídica (ventanas de detección), de forma que el proceso de detección pueda realizarse de forma simultánea en varios canales. Los escenarios ópticos previstos se analizarán en detalle (colimación o focalización) (figura 5).

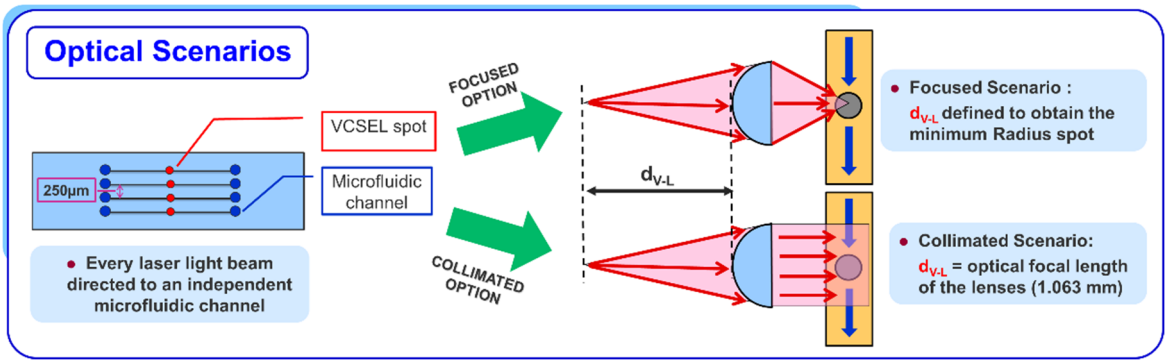

Figura 5: *Dos escenarios ópticos se estudiarán para obtener respectivamente haces de luz colimados o focalizados procedentes de las fuentes luminosas integradas (VCSELs). Cada uno de los spots obtenidos iluminará uno de os cuatro canales del chip de microfluídica. El efecto óptico deseado (colimación o focalización) puede controlarse mediante el ajuste de la distancia d_{V-L}; la distancia óptica entre las fuentes de luz y las microlentes.*

El sensor óptico, con un diseño *full-custom*, fabricado en tecnología CMOS será el responsable de detectar las partículas en base a las diferencias producidas en los niveles de intensidad luminosa (bloqueo de luz). El sensor presenta una arquitectura de doble array lineal de 256 píxels. Este diseño doble, permite mejorar el proceso de detección, ya que elimina falsos positivos: para que un evento se considere válido, debe detectarse por ambos arrays.

Diseño óptico

El sistema de detección óptica de partículas incluye dos componentes comerciales. Las características de los láseres VCSEL favorecen la integración y miniaturización del sistema global, produciendo haces de luz con unos parámetros favorables de acuerdo a las necesidades del sistema: divergencia reducida y elevada potencia óptica, además de su bajo consumo. La matriz de microlentes seleccionada se adapta al *pitch* que existe entre láseres (250 micras), cosa que la hace totalmente compatible en términos de alineación óptica. Ya que el sistema diseñado hace uso de componentes comerciales, éstos darán lugar a ciertas restricciones físicas en los parámetros de diseño.

Para determinar las posiciones óptimas de estos componentes, en términos ópticos, cumpliendo con la finalidad de la aplicación para la que se desarrolla el sistema, se plantea el uso de un simulador de trazado de rayos (*ZEMAX Radiance ®*) definiendo dos escenarios: el primero, basado en la obtención de haces de luz colimados; el segundo, basado en la obtención de haces de luz focalizados.

Mediante la definición de funciones de mérito, es posible calcular el valor *RMS* del radio del spot obtenido en un determinado plano imagen para unas condiciones particulares (i.e. $d_{V\text{-}L}$ la distancia óptica entre las fuentes de luz y las microlentes, y $d_{V\text{-}D}$ la distancia óptica entre las fuentes de luz y el plano imagen).

Las simulaciones ópticas se diseñan atendiendo a las restricciones físicas del sistema real: el espacio necesario entre el encapsulado optoelectrónico y el detector final, para poder manejar los chips de microfluídica ($d_{V\text{-}D} > 18$ mm).

El estudio de ambos escenarios concluye que es posible obtener spots de radios adecuados a las necesidades del sistema en torno a las 116 micras (escenario focalizado con $d_{V\text{-}L} \approx 1.118$ mm) y las 133 micras (escenario colimado con $d_{V\text{-}L} \approx 1.118$ mm), medidos en valores *RMS* para $d_{V\text{-}D} \approx 18$ mm en ambos casos (ver tabla 1).

Aun así, optamos por un diseño basado en la obtención de haces colimados (figura 6), ya que presenta mejores posibilidades técnicas al proporcionar también spots de 102 micras de RMS radio para $d_{V\text{-}D}$=13mm, cumpliendo con los requisitos establecidos en la teoría de la detección óptica de partículas (el spot debe cubrir el ancho total del canal de microfluídica, y como se verá más adelante la anchura mínima de los canales fabricados será de 100 micras, llegando incluso a las 200 micras en algunos casos) y haciendo posible una mayor miniaturización del sistema global, si las limitaciones prácticas del sistema lo permiten. Asimismo este diseño ofrece mayor versatilidad al poder reutilizar el encapsulado optoelectrónico en otro sistema que requiera el uso de haces de luz con divergencia reducida.

Tabla 1: *Resultados de las simulaciones para el sistema compuesto por el encapsulado optoelectrónico y el chip de microfluídica, analizando dos escenarios: colimado y focalizado.*

	Focused $I_{forward}$ = 8mA	Collimated $I_{forward}$ = 8mA		Focused $I_{forward}$ = 1mA	Collimated $I_{forward}$ = 1mA	
$d_{V\text{-}D}$ mm	RMS radius µm	RMS radius µm	Difference µm / %	RMS radius µm	RMS radius µm	Difference µm / %
9	38	86	48 / 126	38	80	42 / 111
10	48	89	41 / 85	48	83	35 / 73
11	55	92	37 / 67	55	87	32 / 58
12	64	97	33 / 52	65	92	27 / 42
13	73	102	29 / 40	73	98	25 / 34
18	116	133	17 / 15	116	130	14 / 12
23	165	169	4 / 2	159	167	8 / 5
28	201	207	6 / 3	202	207	5 / 2
33	243	247	4 / 2	243	247	4 / 2

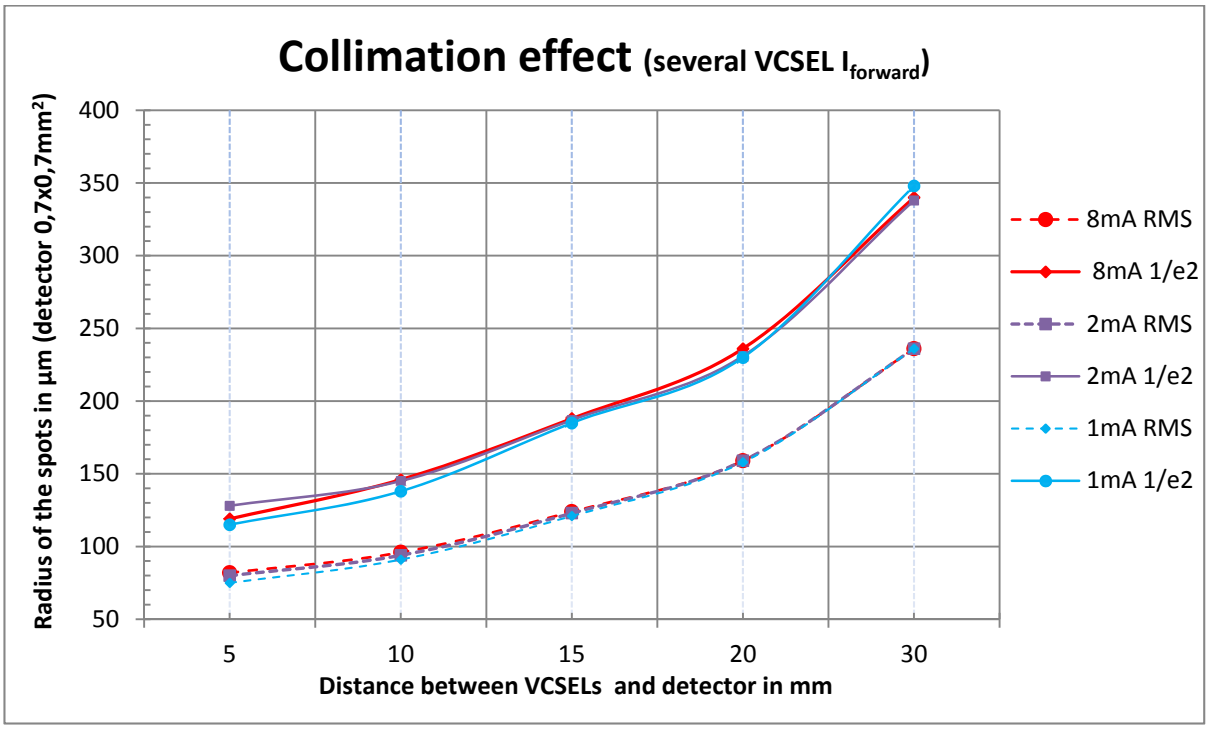

Figura 6: *Gráfica de los resultados de las simulaciones para el escenario colimado con los radios de los spots calculados según el valor RMS y el estándar 1/e² para varias corrientes $I_{forward}$ en los láseres VCSEL (8, 2 and 1mA). Las diferentes distribuciones angulares de los VCSELs según la $I_{forward}$ aplicada no tienen impacto alguno.*

Integración híbrida

Determinadas las posiciones de los componentes ópticos del sistema, es necesario fabricar una estructura robusta que permita alojarlos respetando los resultados de las simulaciones, creando así una especie de encapsulado optoelectrónico. Tras analizar otras tecnologías que podrían resultar útiles para la fabricación de dicha estructura (e.g. *Low temperature co-fired ceramics "LTCC"* y estereolitografía) se opta por el procesado en silicio, pues se trata de una tecnología conocida y que ofrece gran precisión. Así pues, el sistema propuesto se basará en la integración hibrida de los componentes comerciales en una estructura formada por dos piezas de silicio (base y separador óptico), y con alineación pasiva de las microlentes.

Se plantean dos alternativas para la fabricación de la estructura (figuras 7 y 8): un grabado simple en la base con una profundidad de 150 micras, suficiente para alojar el *die* de los VCSELs, o un grabado doble en la base, con una profundidad de 350 micras. La diferencia entre ambas propuestas se encuentra en la fabricación del separador óptico. Para el primer caso, se requiere una oblea no estándar de grosor 1230 micras, mientras que para el segundo, una oblea de 1000 micras de grosor es suficiente. En ambos casos, se conseguiría que la distancia focal efectiva entre los láseres y las lentes fuera del orden de 1.063 mm (la necesaria para el escenario de colimación), siendo más ajustada al valor deseado la obtenida con el grabado simple y el separador de 1230 micras de grosor (como desventaja, aparece el incremento de coste en la fabricación ex profeso de la oblea).

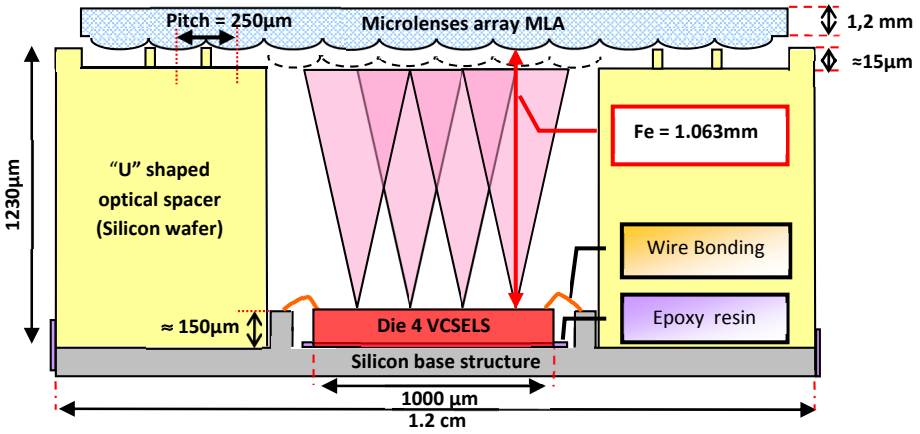

Figura 7: *Sección de la estructura propuesta para una base con grabado simple. El espaciador óptico se fabrica en una oblea de silicio de 1230 µm de grosor. La profundidad del grabado para la base es de 150 µm, creándose una cavidad con una altura igual a la del die de VCSELs, y un pozo en forma de "U" que permitirá el encaje del espaciador óptico.*

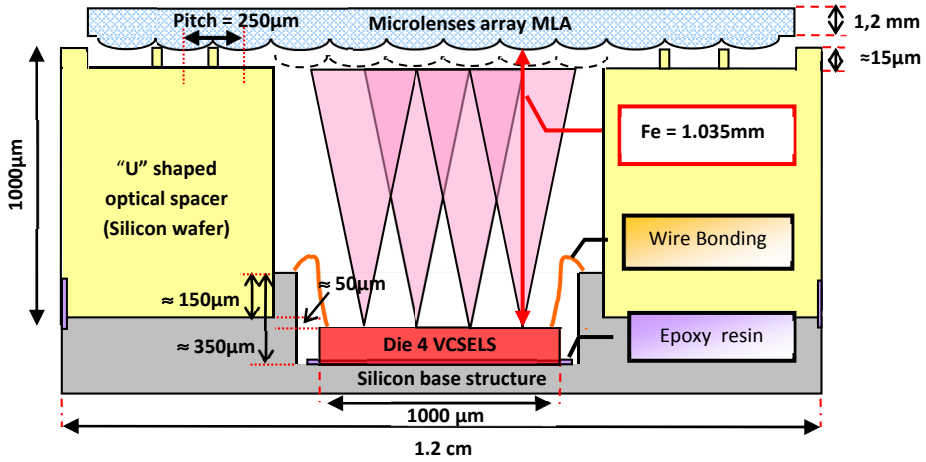

Figura 8*: Sección de la estructura propuesta para una base con doble grabado. El espaciador óptico se fabrica en una oblea de silicio de 1000 µm de grosor. En un primer paso, la base se graba 200 µm para crear la cavidad donde se alojarán los VCSELs. En un segundo paso, se incrementa la profundidad de grabado de esa cavidad hasta un total de 350 µm, y se crea el pozo en forma de "U" de 150 µm.*

Para asegurar la correcta alineación entre las lentes y los láseres, se fabrican en la cara top algunos de los espaciadores ópticos, unos pilares adaptados a las dimensiones de las microlentes, de forma que se puedan alinear pasivamente los componentes.

Tras definir las máscaras necesarias, se fabrican chips con ambas alternativas (figuras 9 y 10). Las piezas de silicio se procesan en obleas siguiendo los procesos de sala blanca indicados en los anexos correspondientes. En este punto debe agradecerse la colaboración del IBM-CNM de Barcelona. A pesar de las tolerancias existentes en los distintos pasos del procesado de las obleas de silicio, los resultados finales proporcionan distancias focales efectivas dentro del rango esperado

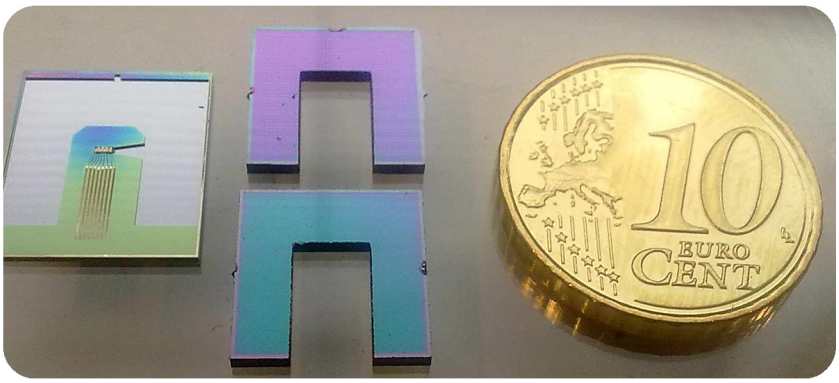

Figura 9: *Fotografías de las piezas fabricadas en silicio: una base con grabado simple y dos separadores ópticos con forma de "U", el superior con el patrón de pilares en la cara top, y el inferior sin dicho patrón. En la base se aprecia e pozo en forma de "U", las pistas metálicas para las conexiones eléctricas de los VCSELs en la zona central, y la cavidad con el die de VCSELs integrado.*

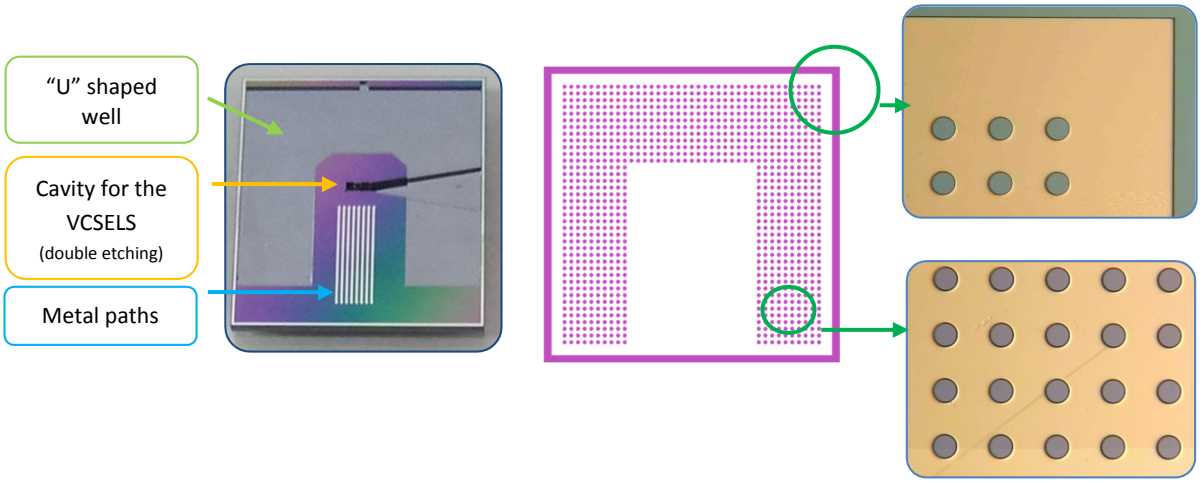

Figura 10: *Fotografía de una base con doble grabado. Detalle del patrón de pilares fabricados en la cara top de algunos espaciadores ópticos, para ayudar en el proceso de alineación óptica entre componentes.*

Con las piezas ensambladas y los componentes integrados, se procede a "empaquetar" la estructura en una PCB (*printed circuit board*) para poder manejarla con mayor facilidad y proveer las conexiones eléctricas necesarias (figura 11).

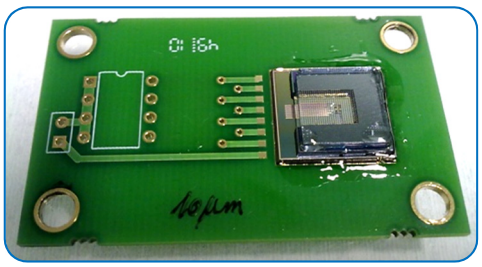

Figura 10: *Fotografía de la PCB donde se coloca el encapsulado optoelectrónico.*

Las medidas experimentales del efecto colimador obtenido se ajustan al rango de valores esperados tal y como se muestra en la figura 11.

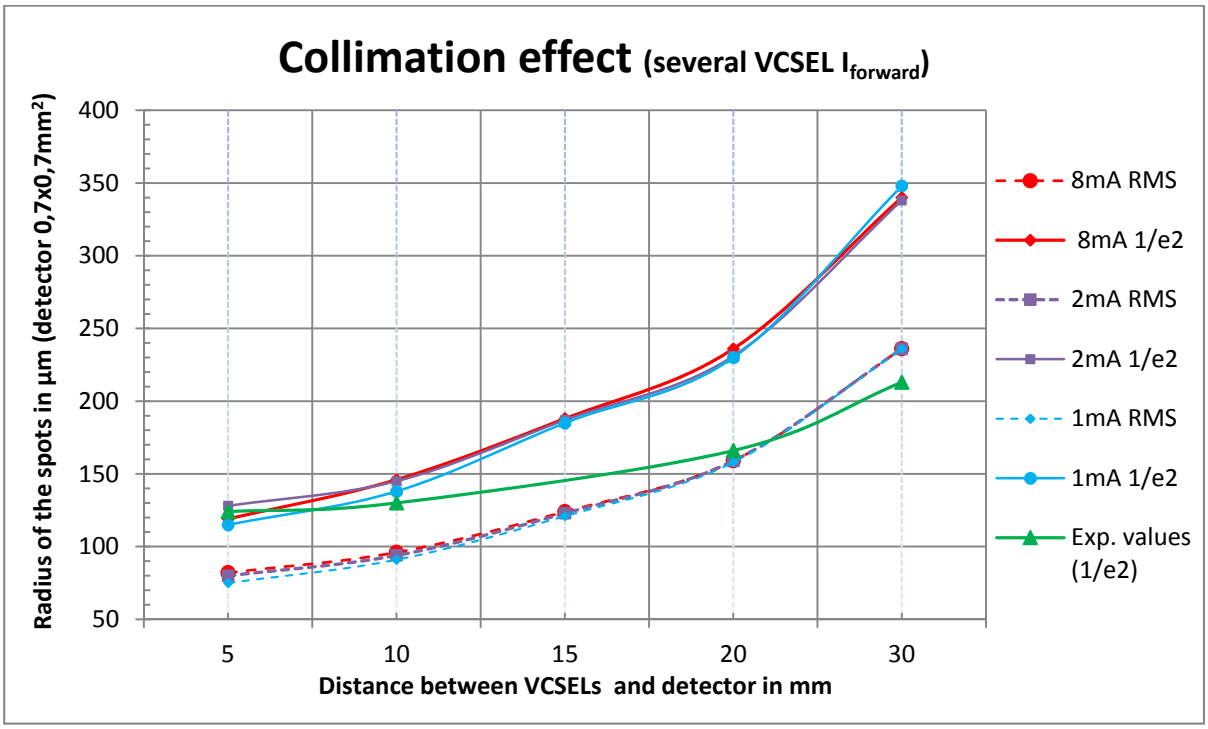

Figura 11: *Gráfica comparativa de los radios de los spots obtenidos para el escenario colimado según los resultados de las simulaciones (valor RMS ZEMAX y estándar 1/e²) y los resultados experimentales (estándar 1/e²).*

Microfluídica

Como pieza necesaria del sistema que aquí se presenta, se diseñaron y fabricaron diversos chips para el bloque de microfluídica. Dichos chips contienen los microcanales de fluídica por donde circularán las partículas que se pretende detectar, suspendidas en un medio líquido.

Los canales se fabrican siguiendo el protocolo establecido para técnicas de prototipado rápido, basadas en "*replica molding*"; concretamente en el subconjunto de técnicas englobadas bajo el concepto de "*soft lithography*" (llamadas así por ser técnicas de replicado en materiales como el PDMS). Los materiales escogidos en base a sus características (biocompatibilidad, precio, transparencia) son SU-8, para la fabricación de los masters, y PDMS (Polydimethylsiloxano) para la fabricación de los canales, siempre trabajando sobre sustratos de vidrio. Diseñados y fabricados los masters, el proceso continúa replicando los motivos en PDMS para finalmente completar la creación de los canales uniendo la lámina de PDMS a un sustrato de vidrio mediante una reacción con plasma de O_2.

Una de las características más llamativas del proceso de prototipado rápido es la rapidez con la que se pueden obtener dispositivos operativos (24/48horas), sin descartar el bajo coste del proceso (en la etapa de fotolitografía para la fabricación de los master, se trabaja con máscaras impresas en acetato, y no con máscaras estándar de vidrio-cromo). Esto evidentemente repercute en la resolución del nivel

de detalle que puede alcanzarse con estos procesos, pero a modo general, si se consigue una resolución apropiada en la etapa de impresión de la máscara (que dependerá básicamente de las características de la impresora), los resultados son más que aceptables. En nuestro caso trabajamos con la empresa *LEICROM* para realizar tales impresiones, ofreciendo una resolución de 10 micras a un precio razonable (impresión DIN-A4 a 35€).

Tras estudiar el efecto de "bloqueo" que aparece en canales con un diseño simplemente lineal, debido a la acumulación de partículas en ciertas zonas, se decide recurrir a un sistema capaz de focalizar, alinear y dirigir las partículas hacia la ventana de detección definida en los canales, donde tendrá lugar el proceso de detección óptica (al ser las zonas iluminadas por los spots procedentes de los láseres). Por ello, se estudian varias propuestas de diseño: canales con focalización pasiva del flujo y canales con sistemas de focalización activa (figura 12).

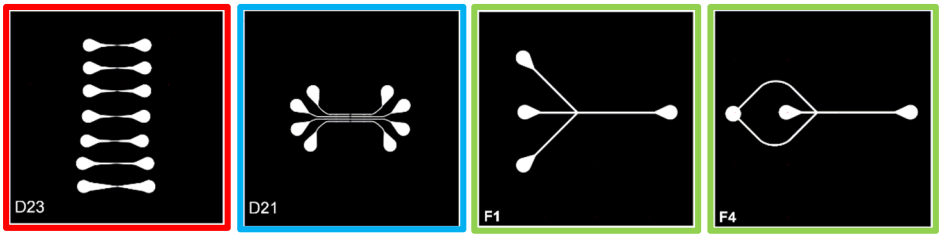

***Figura 12**: Mascaras de acetato con diseños que incluyen mecanismos de focalización pasiva (color rojo y azul) y focalización activa (color verde). El diseño final debe realizarse de acuerdo a los requisitos del sistema: 4 canales paralelos separados una distancia de 250 micras (color verde). Para la focalización pasiva, se definen unas ventanas de detección en forma de embudo. En el ejemplo (color verde) la anchura de los canales disminuye de las 100 a las 60 micras. En las máscaras para focalización activa, la anchura de los canales se fija en 200 micras. Se incluye una alternativa en la que se reduce el número de inlets necesarios (los inlets laterales unidos).*

En la primera de las técnicas de focalización (la focalización pasiva), la propia geometría del canal, con un embudo en la zona correspondiente a la ventana de detección, ejerce un efecto alineador. En cuanto a la focalización activa, los canales diseñados utilizan la técnica de focalización hidrodinámica 2D (figura 13). Esta técnica requiere un diseño en forma de tridente, de forma tal que la relación entre los *flow rates* de los *inlets* laterales (Q_f) y el *inlet* central (Q_s) define el ancho del camino central (w_s) por donde fluirán las partículas, de acuerdo con la ecuación 1.

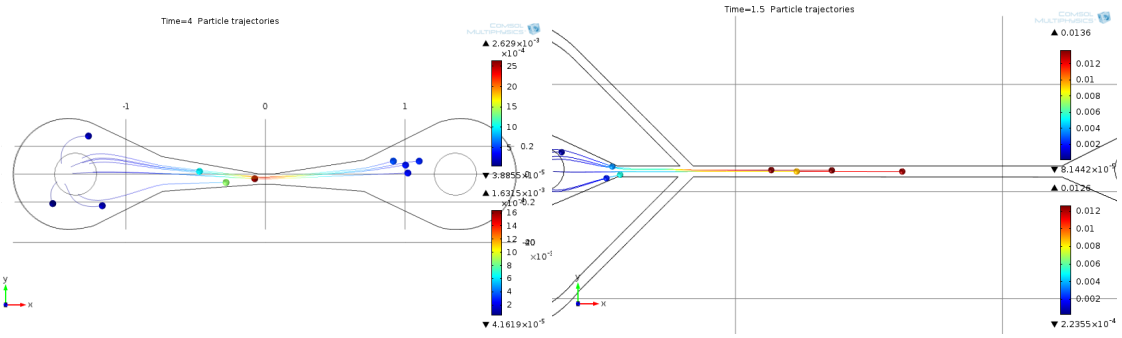

***Figura 13**: Simulaciones COMSOL para canales con focalización pasiva (izquierda) y activa (derecha). Los resultados demuestran que las partículas fluyen alineadas.*

$$\frac{w_s}{w} = \frac{1}{g(\lambda)} \cdot \frac{Q_s}{Q_s + Q_F} \quad (1)$$

$$with\ \lambda = {}^{height}/_{width}\ and$$

$$g(\lambda) = 1\ , when \lim_{\lambda \to 0} (h \ll w)\ or$$

$$g(\lambda) = (1+\lambda)^2(1 - 1.3553\lambda + 1.9467\lambda^2 - 1.7012\lambda^3 + 0.9564\lambda^4 - 0.2537\lambda^5)$$

Se fabrican diversos chips con canales de diferentes dimensiones: canales basados en focalización pasiva, con ventanas de detección en un rango de anchuras de 60 a 150 micras; canales basados en focalización activa con una anchura de 200 micras.

El desplazamiento del flujo se consigue mediante cambios de presión a la entrada de los canales, gracias a una bomba peristáltica conectada a los flextubes del circuito de microfluídica. Las pruebas experimentales con partículas de 45 a 90 micras de diámetro demuestran los efectos de focalización esperados (figura 14).

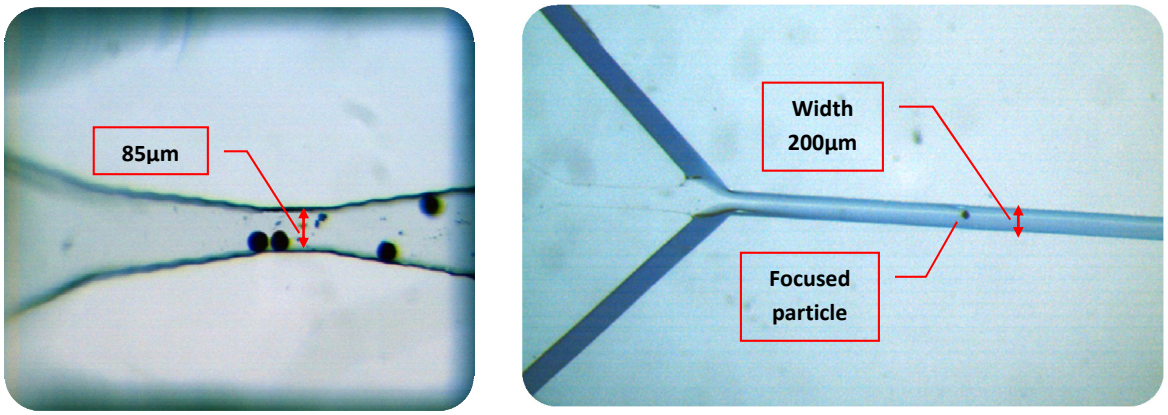

Figura 14. *Izquierda: Focalización pasiva basada en la geometría del canal. En la imagen, partículas de 45 micras de diámetro pasando por una ventana de detección de 85 micras de anchura. Derecha: Focalización hidrodinámica 2D. Canal de anchura 200 micras. La partícula de 45 micras de diámetro fluye alineada por el centro del canal definido mediante los líquidos laterales.*

Cámara CMOS – sensor óptico

El sistema de detección óptica de partículas requiere un sensor óptico encargado de detectar las variaciones en los niveles de intensidad luminosa causadas por la circulación de partículas. En esta tesis se plantea el diseño de un sensor de imagen basado en tecnología CMOS y con una arquitectura estructurada en un doble array lineal de 256 pixels. Estos pixels tienen como elementos sensores fotodiodos, que son capaces de generar señales eléctricas proporcionales a las señales luminosas que los excitan.

La estructura en doble array mejora el proceso de detección de partículas, al realizar un doble chequeo secuencial por cada uno de los eventos detectados que permite descartar falsos positivos, y repercute en una mejora del SNR, ya que las detecciones con una única medida que pudieran quedar enmascaradas por el nivel de ruido, tienen una alta probabilidad de aparecer en una segunda medida.

Esto resulta especialmente útil en el caso de detección de partículas de tamaño reducido (de 20 micras e inferiores), debido a que por volumen producen un efecto menor en el sensor.

El circuito diseñado *full-custom* contiene además otros componentes electrónicos, como por ejemplo un conversor analógico digital de 10 bits, la lógica de control de lectura de los pixels, y un derivador (que puede reducir el tiempo de procesado delimitando el rango de pixels excitado) (figura 15).

La arquitectura de cada uno de estos pixels se describe en la figura 16. El fotodiodo se simula como una fuente de intensidad dependiente del nivel de iluminación en paralelo con una capacidad de 1pF (correspondiente a la capacidad inherente a la unión PN), y similar a los valores resultantes una vez diseñado el layout. El rango de intensidades luminosas se fija entre 1 y 20nA. Dos transistores forman la puerta de paso que permite la descarga de la capacidad integrada en el pixel, con valor de 562fF. El buffer confiere el carácter de pixel activo a este diseño. A pesar de añadir una caída de aprox. 0.8V al valor almacenado en la capacidad, esta etapa evita que el proceso de lectura de los pixels afecte a los valores de carga de la memoria analógica (la capacidad de los pixels).

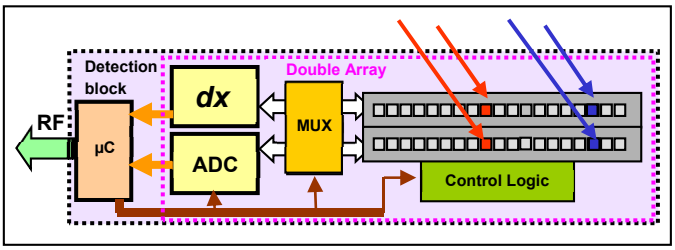

Figura 15: *Diagrama de bloques del sensor óptico diseñado en tecnología CMOS 0.35 micras. Se incluye un doble array lineal de 256 pixels, la lógica de control para la lectura de los pixels, el convertidor AD de 10 bits y un circuito derivador. El esquema también incluye componentes electrónicos off-chip: un microcontrolador y un puerto de comunicaciones.*

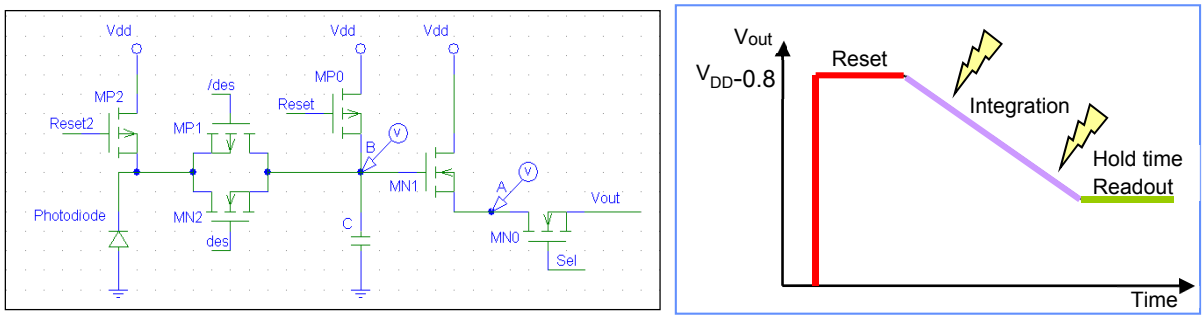

Figura 16*. Izquierda: Esquema gráfico de la estructura interna de un pixel activo. Derecha: Evolución temporal de la carga eléctrica en la memoria analógica del pixel (capacidad "C"). En la fase de Reset, la carga se fija a nivel alto. Durante la fase de Integración, esa carga disminuye según la fotocorriente generada. La carga restante se "guarda" hasta que el pixel es leído (fase de Lectura). A mayor tiempo de integración, mejor sensibilidad.*

El sensor óptico diseñado se fabrica en una *foundry* con tecnología CMOS 0.35 micras, por medio de la empresa *CMP*. La caracterización de los pixels (referirse a las figuras de la 6.23 a la 6.28 del documento principal para el análisis detallado) demuestra que estamos ante un sensor de valores acordes con otros sensores similares. Las prestaciones son suficientes para detectar los spots generados por el encapsulado optoelectrónico (figuras 17 y 18).

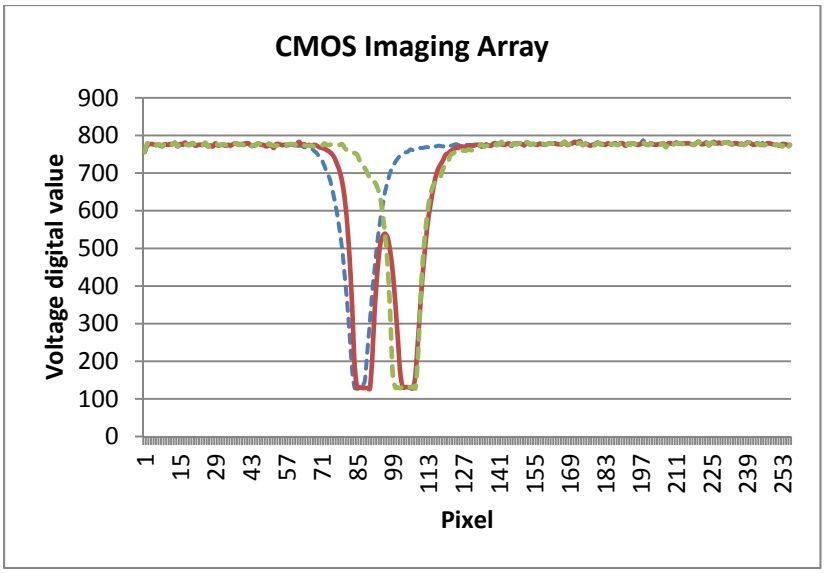

***Figura 17**: Representación de la lectura digital del sensor CMOS. En este caso, 2 VCSELs fueron alternativamente activados (curvas azul y verde). La curva en rojo corresponde a la situación en la que ambos VCSEL estaban activos simultáneamente. El tiempo de integración se fija para forzar la saturación de los pixels mejorando la representación.*

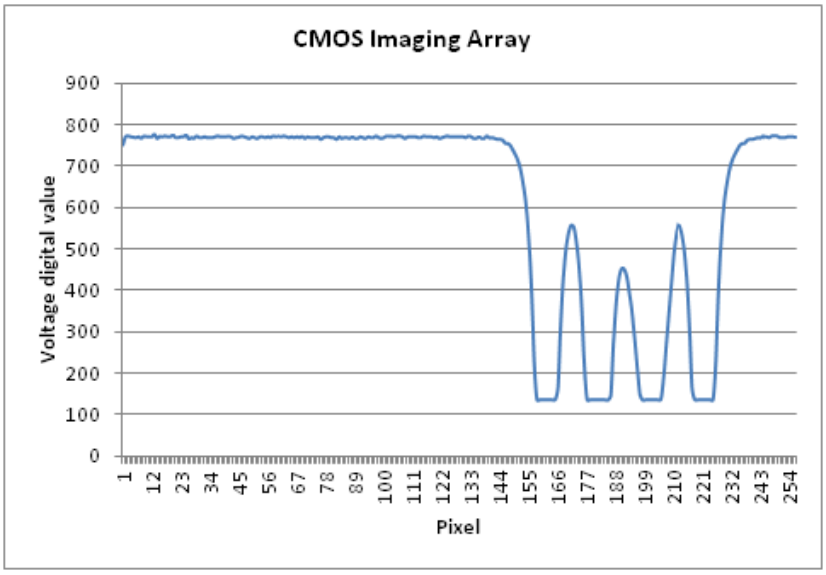

***Figura 18:** Representación de la lectura del sensor CMOS para 4 VCSELs activos. Gracias al efecto colimador del encapsulado optoelectrónico, se distinguen claramente los 4 spots separados unas 250 micras. La longitud del array permitiría trabajar con 12 spots VCSEL.*

Medidas experimentales

Para validar la funcionalidad del sistema fabricado, se realizó una batería de pruebas con el *setup* de la figura 19. Se prepararon diversas suspensiones líquidas en agua desionizada e isopropanol con partículas de diferentes dimensiones, materiales y fabricantes: *Coospheric* y *Polybead* en los rangos de 10 a 93 micras de diámetro. La concentración de las muestras se ajustó para evitar en lo posible el *clogging* de los canales. Mediante un *beam splitter* se pudieron tomar capturas con una cámara externa de forma simultánea al proceso de medida del sistema.

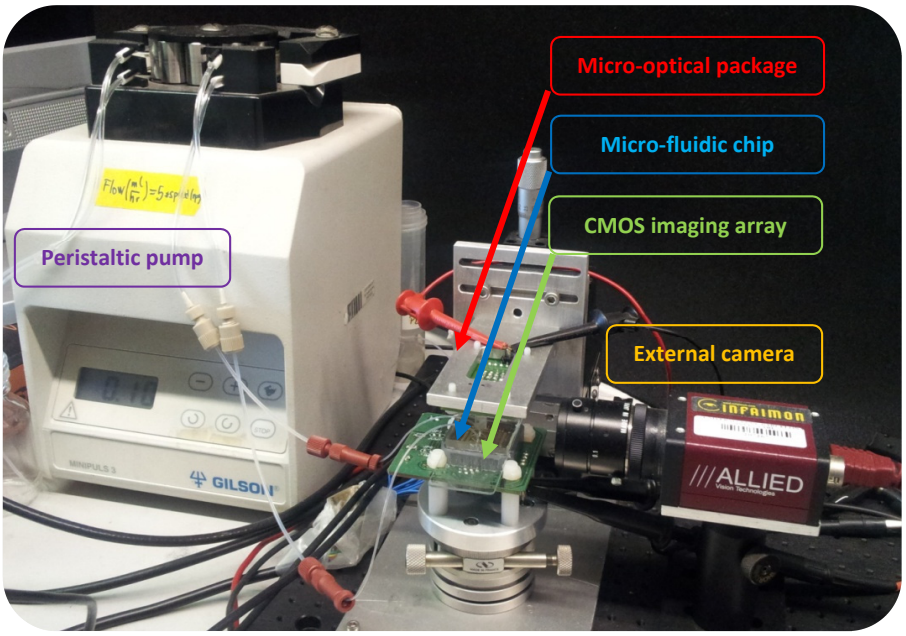

Figura 19: *Set-up para el sistema de medidas. Se incluyen: el encapsulado optoelectrónico, el sensor óptico diseñado y fabricado en tecnología CMOS y el chip de microfluídica, así como otros elementos externos (bomba peristáltica, flextubes y fittings, y una cámara comercial externa).*

Las primeras pruebas, realizadas con canales con focalización pasiva, fueron pruebas cualitativas que demostraron la capacidad del sistema para la detección de partículas. Es interesante remarcar como las paredes del canal aparecen definidas en todas las medidas (figura 20). Mediante un procesado de señal es posible quedarse únicamente con los picos de detección de las partículas. Varios líquidos se hicieron circular, detectándose cambios en los valores medidos por el sensor CMOS.

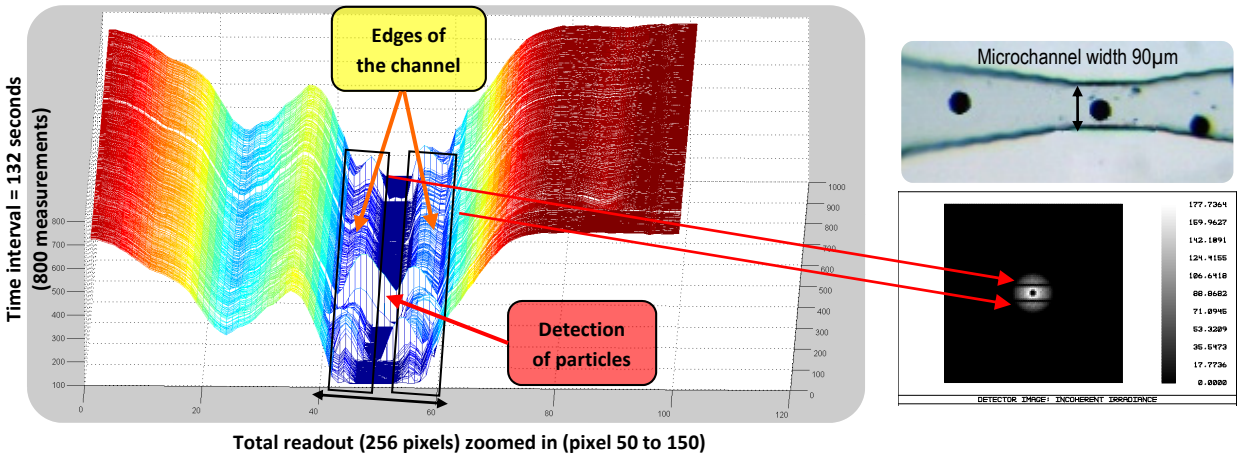

Figura 20: *Representación gráfica de los datos procedentes del sensor CMOS, correspondientes a una muestra de partículas negras de 53-63 micras de diámetro (Cospheric). Los picos blancos indican detección de partículas. El efecto de las paredes del canal, que ya aparecían en las simulaciones ZEMAX, está presentes en las medidas.*

Las medidas cuantitativas se realizaron con el sensor en modo array simple (figura 21) y array doble (figura 22), y para ambos casos se probaron suspensiones con partículas de un único tipo, y también mezclas (figura 23). El sistema fue capaz de identificar las partículas de diferentes tamaños, obteniéndose información en histogramas para cada uno de dichos tamaños.

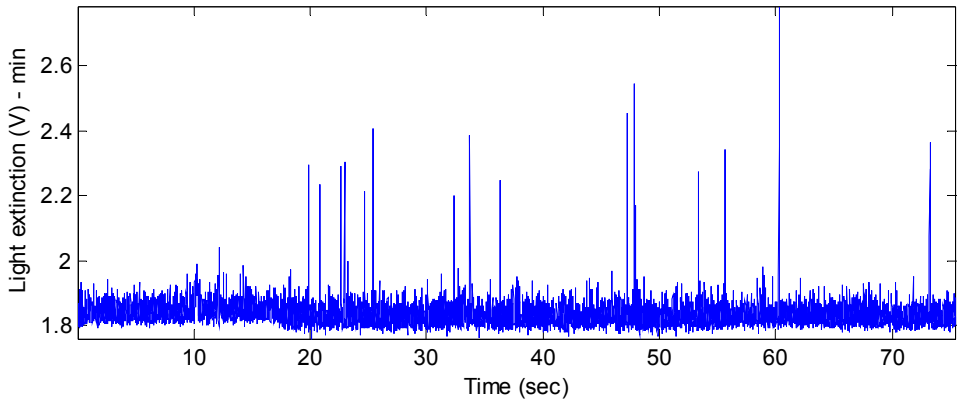

Figura 21: *Resultados de las medidas para una muestra de partículas negras de "polyethylene" de 53-63 micras de diámetro, con el sensor óptico CMOS trabajando en modo array simple.*

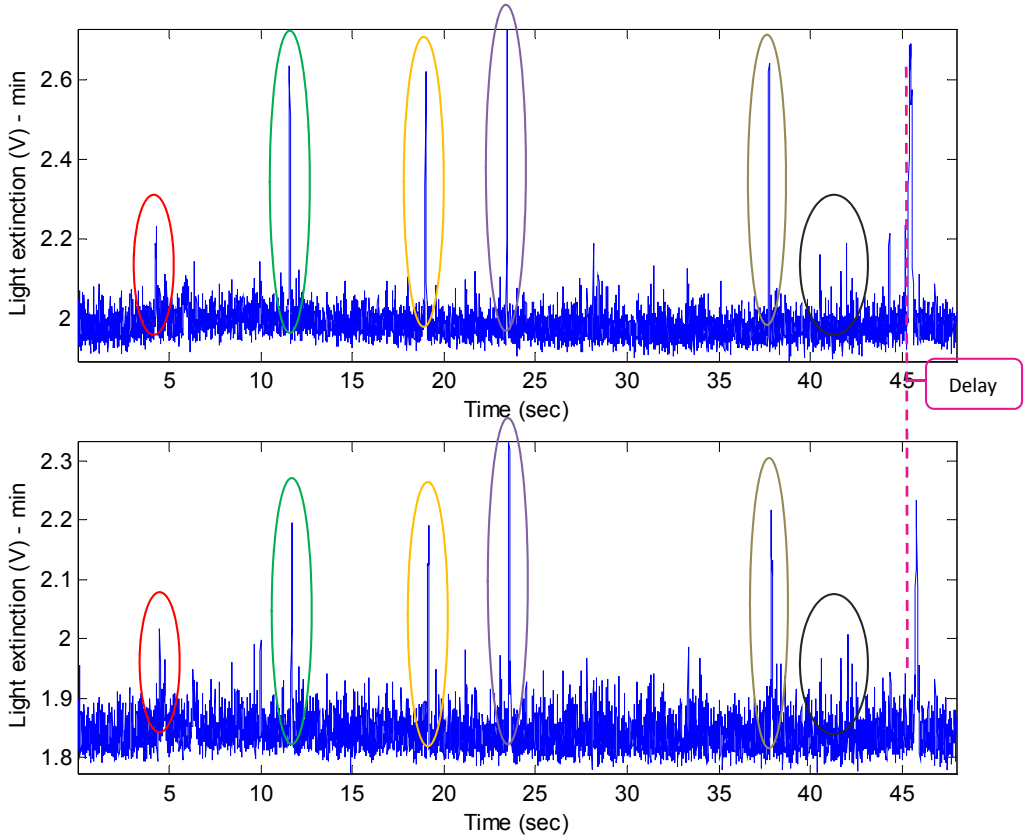

Figura 22: *Medidas realizadas con el sensor óptico CMOS en configuración doble array. Las muestras testeadas contienen partículas negras de "polyethylene" de 53-63 micras de diámetro. La correspondencia de picos en ambos arrays (algunos de los casos se indican marcados con círculos de color), indica detección "fiable" de partículas. La línea a puntos denota el "delay" temporal existente entre ambos arrays para una misma medida.*

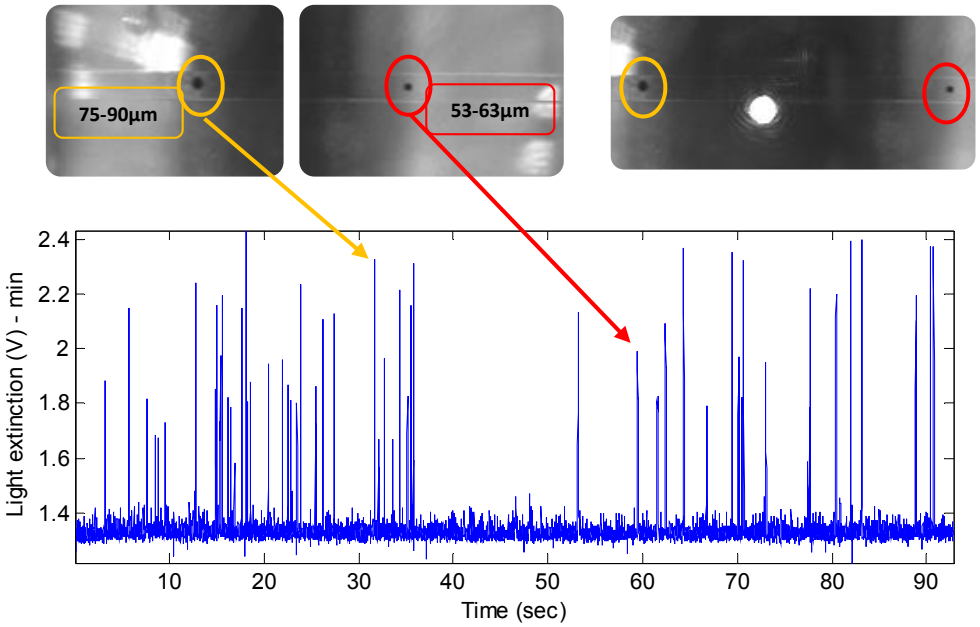

Figura 23: *Resultados experimentales para una muestra con una mezcla de partículas de diferentes tamaños (53-63 micras y 75-90 micras de diámetro) Los picos con mayor amplitud corresponden a las partículas de mayor diámetro. El sistema es capaz de diferenciar partículas de tamaños diversos.*

Los resultados fueron satisfactorios en todos los casos. El sensor CMOS diseñado, operando tanto en configuración simple como haciendo uso del doble array, proporciona resultados acordes con los valores en el ámbito académico. Es interesante remarcar las ventajas que aporta para la detección de partículas la configuración del sensor en modo doble array, mejorando el proceso al certificar doblemente que los eventos detectados no se corresponden con falsos positivos. El efecto indirecto es la mejora del SNR, sobretodo en los casos de muestras con partículas de pequeño tamaño (< 20 micras diámetro), ya que en estos casos, los eventos generados quedan enmascarados con la señal de base, lo que dificulta su detección.

De acuerdo con los resultados obtenidos es posible establecer una relación lineal entre el tamaño de las partículas y los valores de tensión facilitados por el sensor (tabla 2 y figura 24). Finalmente se estudió el *throughput* del sistema, fijado en un valor de 5-6 partículas por segundo.

Tabla 2: *Información estadística sobre las distribuciones obtenidas en las medidas experimentales.*

Particles diameter	Light extinction amplitude		
	Mean (mv)	Standard deviations (mV)	CV
10µm	170	0,049	0,029%
45µm	510	0,060	0,012%
53-63µm	655	0,056	0,009%
75-90µm	839	0,141	0,017%

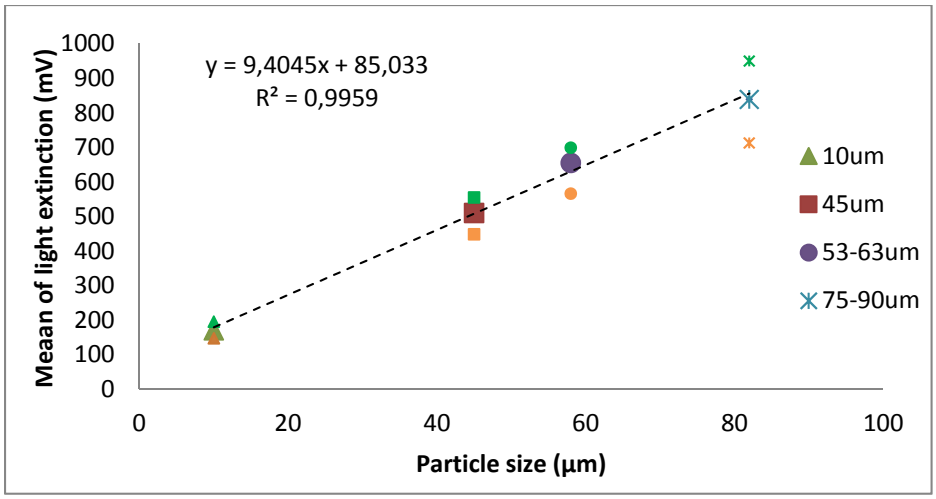

Figura 24: *Ajuste lineal de los valores medios de extinción luminosa obtenidos en las medidas experimentales realizadas. El ajuste confirma la existencia de una relación entre el tamaño de la partícula y la amplitud de la señal medida. Se incluyen también los valores de amplitud mínima (naranja) y máxima (verde) para cada rango de partículas.*

Conclusiones

Los resultados obtenidos son satisfactorios. El sistema presentado, de reducidas dimensiones, ha demostrado su capacidad en el ámbito de la detección y la caracterización de partículas de varios tamaños (rango de 10 a 90 micras). El diseño en doble array del sensor óptico CMOS mejora el proceso de detección. Aun así, se plantean varias líneas de trabajo futuro, que permitan explorar y potenciar la multifuncionalidad del sistema, permitiendo combinar por ejemplo, detección de partículas con medidas por fluorescencia en un mismo dispositivo. El diseño de nuestras propias lentes y su fabricación combinada junto a canales de microfluídica en materiales desechables de bajo coste permitiría aún más miniaturizar el sistema.